CRC Handbook of Atmospherics

Volume I

Editor

Hans Volland
University of Bonn
West Germany

CRC Press, Inc.
Boca Raton, Florida

Library of Congress Cataloging in Publication Data

Main entry under title

Handbook of atmospherics

Bibliography p
Includes index
1 Atmospheric electricity 1 Volland Hans
QC961 H33 551 5'6 81 674
ISBN 0-8493-3226-5 (v 1)
ISBN 0 8493-3227-3 (v 2)
AACR2

Direct all inquiries to CRC Press, Inc , 2000 N W 24th Street Boca Raton, Florida 33431

International Standard Book Number 0-8493 3226-5 (Volume I)
International Standard Book Number 0-8493-3227-3 (Volume II)

Library of Congress Card Number 81 674
Printed in the United States

PREFACE

Atmospherics, or sferics, which are the electromagnetic pulses radiated from lightning, have been intimately related with radio science since its beginnings. It was A.S. Popov, then in St. Petersburg, who in 1895 connected a wire to a detector and heard noise of an impulsive character. That was indeed the first observation of sferics in the audio frequency band.

"More generally, an atmospheric can also mean any incoming transient that stands out above the inevitable noise background in radio reception. The transient signal may originate naturally but not necessarily in lightning; blizzards, dust storms, and corona discharge are among the possible sources. The transients may also be due to man; signals are radiated, for example, by cars, by powerlines, and by electrical machinery. Indeed, the strongest atmospheric of all is man-made — the electromagnetic pulse created by a nuclear explosion.

When many transients arrive in rapid succession, with their effects often merging into each other, the resulting disturbance is usually termed "radio noise". Radio noise is distinguished according to its origin; thus we have atmospheric (dominantly due to lightning) noise, man-made noise and galactic (cosmic) noise".*

Radio noise of atmospheric and cosmic origin limits the system performance of radio transmission lines. Radio engineers have, therefore, extensively studied its variations with frequency, geographic location, time of day and season. Lightning currents are strong sources of very low frequency (VLF) and extremely low frequency (ELF) radio waves, which are very difficult to generate with commercial transmitters. These sferics are used by radio engineers as well as ionospheric physicits to study the characteristics of the wave guide between the Earth and lower ionosphere, in particular the behavior of the ionospheric D-layer. That wave guide behaves like a resonance cavity for waves near 7.5 Hz and its harmonics. Standing waves can be excited by lightning strokes (Schumann resonances). Electromagnetic pulses from lightning can also propagate along the geomagnetic lines of force into magnetospheric regions (whistler propagation) and allow indirect probing of the magnetosphere. The plasmaphere, a region of enhanced ion concentration in the near environment of the Earth at distances of a few Earth radii, was discovered from whistler measurements.

The wave forms of sferics from lightning depend on the electric charge stored within the lightning channel and also on channel characteristics such as channel length, diameter and orientation. An investigation of sferic wave forms thus affords insight into the physics of the various types of cloud-to-ground as well as intracloud strokes. Finally, lightning activity deduced from statistics of sferics is of interest to meteorologists, because a significant amount of latent heat within the troposphere is released in thunderclouds.

The participation of such diverse scientific and technical disciplines as meteorology, astronomy, atmospheric electricity, ionospheric and magnetospheric physics, electromagnetic wave propagation, and radio techniques in the research of atmospherics leads to the dilemma that the results published in scientific papers are widely spread in the literature. This Handbook is an attempt to collect the present knowledge on atmospherics in two volumes. Each chapter is written by an expert in his field. In order to be as complete as possible, some topics related to the study of atmospherics such as physics of thunderclouds, thunder, global atmospheric electric currents, biological aspects of sferics, and various space techniques for detecting lightning within our own atmosphere as well as in the atmospheres of planets, are included in the Handbook.

* Pierce, E. T., Atmospherics and radio noise, in *Lightning*,, Vol. 1, Golde, R. H., Ed., Academic Press, London, 1977, 351.

Sincere thanks are due to all contributors for their compliance with my suggestions and for their assistance in the preparation of this book. In particular, I am very much indebted to H. Dolezalek, without whose steady aid and helpful suggestions this book would probably not have been written.

Hans Volland

THE EDITOR

Hans Volland studied Geophysics and Meteorology at the Humboldt University in Berlin between 1948 and 1952. He worked as a scientist in the fields of geomagnetism and ionospheric physics at the German Academy of Sciences in East Berlin from 1952 until 1958. He completed his Doctor's thesis, entitled "On the Solar Eclipse Effect of the Geomagnetic Field" in 1956. In the years 1958 to 1964, he was a research associate at the Heinrich-Hertz-Institut in West Berlin where his main subject of research was VLF propagation and Atmospherics. He became a lecturer at the Technical University in West Berlin in 1963. In 1964 he became a lecturer at the Radio Astronomical Institute of the University of Bonn. He was named Professor there in 1967. His main interests cover physics of the atmosphere, magnetospheric physics, and solar radio astronomy. From 1967 to 1969 he was senior research associate of the U.S. National Academy of Sciences at the NASA Goddard Space Flight Center, Greenbelt, Maryland.

Dr. Volland is author of one book and more than 160 scientific papers. He is actively engaged in several international associations.

CONTRIBUTORS

Yam T. Chiu, Ph.D
Research Scientist
Space Science Laboratory
The Aerospace Corporation
El Segundo, California

Arthur A Few, Jr , Ph D
Associate Professor of Space Physics
and Environmental Science
Rice University
Houston, Texas

George H Hagn
Program Manager
Telecommunications Sciences Center
SRI International
Arlington, Virginia

Dr. Wolfgang Harth
Scientist
Max-Planck-Institut fur
Radioastronomie
Bonn
Federal Republic of Germany

Gunter Heydt
Associate Scientist
Heinrich-Hertz-Institute for
Communications Technology
Berlin
West Germany

Robert H Holzworth, Ph D.
Scientist
Space Sciences Laboratory
Aerospace Corporation
El Segundo, California

Edward A Lewis, Ph.D
Technical Consultant
Megapulse Inc
Bedford, Massachusetts

Toshio Ogawa, Ph.D
Associate Professor in Geophysics
Kyoto University
Japan

Richard E. Orville, Ph D.
Associate Professor of Atmospheric
Science
State University of New York at Albany
Albany, New York

Chung G Park, Ph D
Senior Research Associate
Radio Science Laboratory
Stanford University
Stanford, California

Charles Polk, Ph D
Professor of Electrical Engineering
University of Rhode Island
Kingston Rhode Island

Dr Reinhold Reiter
Director, Institute for Atmospheric and
Environmental Science
Garmisch-Partenkirchen
West Germany

Dr Klaus Rinnert
Scientist
Max-Planck-Institute for Aeronomy
Katlenburg-Lindau
West Germany

Arthur D Spaulding, Ph D
Mathematician, Senior Staff
Institute for Telecommunications
Sciences
National Telecommunications and
Information Administration
Boulder, Colorado

Dr. Hans Volland
Professor of Radioastronomy
University of Bonn
West Germany

Bernard Vonnegut, Ph.D
Professor of Atmospheric Science
Senior Research Scientist
Atmospheric Sciences Research Center
State University of New York at Albany
Albany, New York

TABLE OF CONTENTS

Volume I

Volume II

THE PHYSICS OF THUNDERCLOUDS

Bernard Vonnegut

TABLE OF CONTENTS

THUNDERCLOUDS

Many kinds of clouds are capable of generating the strong and extensive electric fields required to produce lightning These cloud types include volcanic clouds,[5] dust storms,[26] and snowstorms [41] Most of the lightning of the Earth is produced by strongly convective cumulus clouds, and preliminary observations indicate that convective clouds may also be important lightning producers in other planetary atmospheres as well [12 24] In our discussion of the physics of clouds we will confine our attention to the cumuliform clouds known as cumulonimbus clouds, thunderstorms, or thunderclouds

The common characteristic of thunderclouds is a vigorous system of updrafts and downdrafts Conditions producing such strong circulation occur when the atmosphere becomes unstable, and buoyant volumes of warm, moist air at lower levels rise in the presence of cooler, more dense air Because heating from the sun is the primary cause of the formation of temperature contrasts in the atmosphere, strong convective activity and thunderstorms are most common in the tropics, semitropics, and temperate zones They are rare, but not unknown, in the polar regions Thunderstorm activity is most intense and frequent during the spring and summer, but it can take place all times of the year It should be noted that under certain conditions, such as exist in the north Atlantic, the greatest convective instability occurs during the winter months when cold, polar air flows over the relatively warmer ocean waters Here thunderstorms are more frequent in winter than in the summer [43]

Satellite observations show that lightning discharges are far more common over land than they are over oceans [44] A possible explanation for this is that the temperature of the ocean surface rises much less under the influence of solar heating than the temperature of land masses under the influence of solar heating This is so because water has much greater heat capacity than land surfaces, the energy received from solar heating is dissipated to a considerable depth, and the temperature rise is reduced by evaporative cooling Because temperature contrasts are generally somewhat less over large bodies of water than over land, convective activity and thunderstorms are less common It is also conceivable that the lower incidence of electrical activity observed over the water may be related to differences between the electrical characteristics of land and water surfaces For example, much higher electric fields are required to produce point discharge over water surfaces than are required to produce point discharge from vegetation and other structures over land [45]

Thunderstorms occur both day and night, but the maximum storm and lightning activity usually occurs over land in midafternoon when solar heating and convection are at a maximum In some parts of the world, however, (for example, portions of the U S) the maximum frequency of thunderstorms and precipitation occurs late at night [79]

The electric currents flowing from thunderstorms to the Earth and to the upper atmosphere maintain the electrically conducting upper atmosphere at a positive potential of several hundred kilovolts with respect to the Earth [81] This movement of charge gives rise to a global fair weather electric field, which, at the surface of the Earth, is of the order of 100 V m^{-1} The period of greatest global thunderstorm activity occurs when the sun is shining on the land masses of the Earth, and the global fair weather electric field attains its maximum value during this time interval [8]

Meteorologists distinguish between two types of thunderstorms The first of these, the so-called "air mass" thunderstorm, is most common during the summertime It is produced by solar heating, which creates buoyant parcels of warm air near the surface that rise to form cumulus clouds, a few of which then develop to become isolated thunderstorms The second kind of thunderstorm, known as the "frontal" storm, is

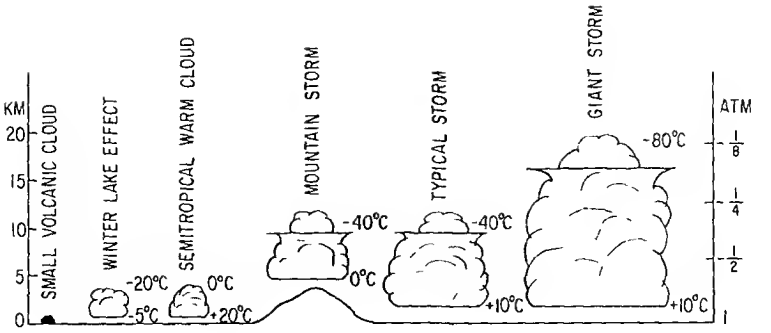

FIGURE 1 Approximate sizes of various lightning producing clouds.

produced at the interface between two contrasting regions of air, one warm and moist, and the other cool and dry. The frontal storms arise as a result of an overturning in which warm, moist air at the surface rises and is displaced by colder air. This process can produce long lines of large thunderstorm cells that have sometimes been observed to make horizontal lightning discharges 100 km long or more.[6,35,72] When the temperature contrast between air masses is very large, as is often the case in spring, the clouds have intense convective activity, rise to great heights, and produce unusually frequent and energetic lightning.[74]

Thunderstorms vary greatly in size. Except for volcanic clouds, which can produce lightning when they are only half a kilometer in height,[2] atmospheric clouds don't often produce lightning until they grow to a depth of at least 3 km. As is indicated in Figure 1, average thunderstorms are of the order of 10 km in altitude, while the rare, extraordinarily severe storms that sometimes produce tornadoes, have been measured at altitudes in excess of 20 km.[74]

The largest and probably the most active of all lightning generators are the enormous clouds produced by violent volcanic eruptions. These clouds penetrate far into the stratosphere, reaching altitudes in excess of 30 km.

Development of the Cloud

In the morning of a typical day when air mass thunderstorms will develop, the sky may be entirely free of clouds. As the sun rises and the morning progresses, heating of the ground under the influence of the sun warms the lower levels of the atmosphere, creating buoyant parcels of air. These accelerate and rise to some altitude, then lose their upward momentum and fall back. In its early stages, this process is invisible, but when parcels of the air, becoming more and more unstable, rise and cool slightly below the dew point temperature, a visible cloud begins to form. Small, spherical liquid water droplets of the order of tens of microns in diameter form by the condensation of water vapor on minute particles in the atmosphere known as condensation nuclei.[36] Typically the concentration of these droplets in the cloud is of the order of 10 to 100 per cubic centimeter. Because these droplets scatter sunlight, the updrafts become visible above the condensation level. Condensation occurs around only a few percent supersaturation, so the temperature of the cloud base is only very slightly below the dew point of the air mass from which the cloud is forming. The air mass is often quite homogeneous; therefore, the cloud base approximates a horizontal surface. Because the clear air under the cloud base cools at approximately 10°C for each kilometer it rises and because the vapor pressure of water decreases by a factor of 2 for each 10°C temperature drop, it is possible to estimate the height of the cloud base above the ground from measurement of the relative humidity on the ground beneath the cloud. For a relative

humidity of 50%, the height of the cloud base is approximately 1 km For a relative humidity of 25%, the cloud base is 2 km, etc Of course this rule applies only to cumulus clouds in a freely convective system

As the air rises above the cloud base, it continues to cool, and more moisture condenses to form cloud droplets Often this air may rise above its equilibrium level and then descend as a downdraft In this case, as the descending air is heated adiabatically, when it descends below the level of the cloud base, the condensed cloud particles will evaporate Flights with an airplane just below the base of a cumulus cloud show that although it appears to be flat and motionless like a ceiling, there are regions of strong updrafts and downdrafts This shows that the flat base is not a static interface between clear and cloudy air, but a level in a convective system where formation of cloud particles is occurring in updrafts or evaporation of cloud particles is occurring in downdrafts

The latent heat that is released when water condenses, approximately 600 cal/g, plays an important role in the dynamics of a cloud Because of the heat liberated by condensation, the moist air in a cloud cools much more slowly than dry air as it rises At a temperature of 20°C the so-called moist adiabatic lapse rate is about 6°C km^{-1} in contrast to the dry adiabatic lapse rate of about 10°C km^{-1} Due to heat released by droplet growth, rising clouds are often able to maintain their temperature above that of their environment The buoyancy of warmer air causes cloud parcels to experience upward accelerations over many kilometers of rise and to achieve high vertical velocities The cloud may be considered to be a giant heat engine putting air into motion from power that is derived from the heat released by the condensation of water

In severe storms, updrafts can reach vertical velocities in excess of 50 m sec^{-1} [59] Finally, because of its upward momentum, the once warm cloud air rises above the inversion at the tropopause into the stratosphere where it is colder than its environment It is now negatively buoyant, and its vertical velocity begins to decrease In the case of larger thunderstorms, the momentum of the rising air may be sufficient to carry it several kilometers into the stratosphere before it ceases to rise and then falls back [74] Such a penetrative cell is shown in Figure 2, a photograph of a thundercloud taken from a satellite By the time the rising air in the cloud has reached the altitude of the tropopause, its temperature will have dropped to approximately −50°C, and most of the moisture will have condensed out As a result, the rising air in the penetrative turrets of these clouds contains so little water that it cools at approximately the dry adiabatic rate of 10°C km^{-1} The temperatures in these very high clouds that have been observed to reach altitudes of more than 20 km can drop to as low as −80°C

When the rising currents of air in the thunderstorm reach their apogee, they fall back, achieving increasing downward velocity until they warm up through adiabatic compression to the point that their temperature is greater than that of their environment These downdrafts persist until finally they have descended to the point that their downward vertical momentum has been dissipated Observations of New Mexico thunderstorms show that the time of rise of the cumulus cloud top and the time of its descent are very nearly equal, being typically of the order of 6 or 8 min [64]

Vertical Extent

Because the height to which the cloud rises is a measure of the intensity of its updrafts, the cloud top temperature is a good indicator of the severity of the storm Satellite meteorologists now identify particularly severe storms by the unusually low temperatures of their cloud tops as determined by infrared techniques

Shackford's[55] (1958) observations (see Figure 3) have shown that in general, the higher the cloud top, the greater the frequency of lightning It appears probable on the basis of his findings that the colder the cloud top, the more frequent the occurrence

FIGURE 2. Thundercloud over Honduras viewed from Apollo 9 at an altitude of 190 km. The cell in the center of the cloud penetrating into the stratosphere casts a dark shadow. (From NASA, March 1979.)

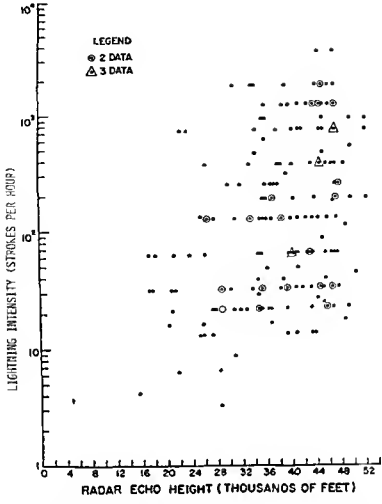

FIGURE 3 Lightning frequency as a function of cloud radar echo height.[4] (Permission to use this figure was granted by The American Meteorological Society, Boston, Mass.)

of the lightning discharges in the storm will be, although this has yet to be confirmed by direct measurements.

Formation of Precipitation

The vast majority of the clouds in the atmosphere form and dissipate without ever producing any precipitation. The cloud particles produced by condensation are so small that they fall extremely slowly, evaporate in the unsaturated air beneath the cloud base, and never reach the ground. In order to form precipitation, the moisture comprising the small droplets of the cloud must form much larger precipitation particles, millimeters in diameter, that have terminal velocities of many meters per second and that are capable of falling all the way to the Earth before they evaporate. Because the diameter of precipitation particles is approximately 100 times larger than that of the cloud particles, the formation of precipitation requires processes that will be capable of making a single large precipitation particle from about a million little cloud particles.

The formation of large particles in a cloud of small particles that leads to precipitation takes place by several mechanisms. Because of the Kelvin[27] effect, the smaller particles have a slightly higher vapor pressure than larger particles; therefore, the water evaporates from the smaller particles and condenses on the larger particles. If given

enough time, this process could result in the formation of precipitation; however, it takes place so slowly that it is usually not of importance. Two other much more effective mechanisms are recognized that are dominant in the formation of precipitation.

The first of these is the growth of large particles by coalescence. Collisions take place between the particles within the cloud as the result of Brownian movement of the smaller particles or as the result of larger, faster falling cloud particles overtaking smaller, slower falling cloud particles. When such collisions occur and the particles either coalesce or adhere to each other, it results in the formation of a larger particle. Because particles growing by this mechanism have an increasing rate of fall, their rate of collisions with smaller particles increases. In this way they grow into precipitation particles, such as rain, graupel, or hail, having terminal velocities of many meters per second. Growth of precipitation particles as the result of collisions is the primary process leading to the formation of rain in regions of the cloud warmer than 0°C. This process can also play a very important role in the formation of rain, graupel, and hail in portions of the cloud colder than 0°C where supercooled liquid water often is present.

A second mechanism, first recognized by Bergeron[3] and named in his honor, takes place in regions of clouds whose temperature is below 0°C. Even as low as −38°C,[52] far below the so-called freezing point of water, cloud droplets can exist as a liquid in what is known as the "supercooled" state. Such supercooled droplets are a common occurrence in clouds all over the world, not only in the winter, but also in the summer when even in the hottest weather the 0°C isotherm rarely extends more than 5 km above sea level. Because supercooled liquid water is a metastable phase, it has a significantly higher vapor pressure than ice at the same temperature. As a result, when ice crystals are present in a supercooled cloud as the result of formation on ice-forming nuclei or other processes, they rapidly grow at the expense of nearby supercooled water droplets until they become large enough to fall through the cloud as snow crystals or other types of ice precipitation. If such ice particles fall into air that is above 0°C for a sufficiently long distance, they will melt to form rain. Much of the rain falling upon the surface of the Earth originates within the cloud as ice particles produced by the Bergeron process. A supercooled cloud in which ice crystals or ice forming nuclei are absent can persist for long periods of time without forming precipitation. Under such conditions, the formation of snow or rain can be greatly accelerated by cloud seeding.[22] This technique catalyzes the formation of ice crystals by introducing into the cloud such agents as dry ice (solid carbon dioxide), which initiates ice crystal formation because of its low temperature, or by minute silver iodide particles, which serve as ice nucleation centers.

Although the formation of precipitation and the electrification of the cloud often take place at about the same time, the relationship between these two phenomena is quite variable. Clouds that are giving significant amounts of precipitation, either by coalescence or by the Bergeron process, sometimes produce strong electric fields and lightning, while in other instances such clouds produce extremely small electrical perturbations. Clouds giving little or no rain usually show very little electrical activity. In some instances, however, they may exhibit strong electrical perturbations before the presence of precipitation can be detected with radar.[76] In clouds where the electrification has developed sufficiently to cause lightning, precipitation is almost invariably present; however, on some occasions estimated rainfall rates can be as small as 1 mm hr^{-1} or less.[42] Observations of clouds suggest that in order for a cloud to develop into a lightning producing thunderstorm, appreciable vertical convective activity must also be present in addition to precipitation.[85]

CLOUD ELECTRIFICATION

Electric Fields

In the early fair weather cumulus stage of thunderstorm development, the electric field perturbations produced within and outside of the cloud are usually quite small and are often undetectable These perturbations arise from two causes Fast ions within the cloud rapidly become attached to cloud particles, so the cloud is a much poorer conductor of electricity than the surrounding clear air As a result, the presence of the cloud alters the fair weather conduction current and produces small perturbations of the electric field [8] Electrical perturbations are also produced when updrafts carry air into the cloud from below that has somewhat higher space charge density than the air surrounding the cloud Experiments have been carried out showing that electric field perturbations of the order of ± 100 V m^{-1} can be produced by artificially introducing space charge into the air rising from the ground up into the cloud [78]

The onset of thunderstorm electrification within the cloud is indicated when the fair weather electric field beneath the cloud and above the cloud changes from negative to positive, and begins to increase in the antifair weather sense This shows that the cloud has become approximately a vertical dipole, with positive charge in the upper and a negative charge in the lower part of the cloud As would be expected from the dipole distribution of charge, the antifair weather electric field intensity beneath the cloud decreases with distance, finally reversing and becoming intensified in the fair weather direction

The beginning of strong electrification is associated with a rapid vertical and horizontal development of the cloud Typically, the electric field grows exponentially with time, approximately doubling every few minutes Finally, when the electrical stresses within the cloud become sufficiently large, dielectric breakdown and lightning occur A history of a thunderstorm in New Mexico is shown in Figure 4 The sudden discontinuities appearing as vertical lines on the electric field record are produced by the rapid field changes caused by lightning flashes

The maximum intensity of the electric fields that can develop in a thunderstorm is limited by lightning and other dielectric breakdown processes Electric fields as high as 400 kV m^{-1} have been measured inside of the cloud,[82] and estimates of the maximum intensity are as high as 1000 kV m^{-1} [47]

Over land surfaces the intensity of the electric field at the surface beneath a thunderstorm is limited by a screening layer of space charge created by point discharge that occurs from vegetation and other structures [58] Usually the maximum electric field is only of the order of a few kilovolt m^{-1} On occasion, however, values somewhat in excess of 10 kV m^{-1} are observed Over the lakes and oceans, where much higher fields are required to produce point discharge, electric fields have been measured in excess of 100 kV m^{-1} [63] In the clear air a short distance above the top of a thunderstorm, electric fields reach values of the order of 40 kV m^{-1} [16]

How the electric field is affected by lightning discharges is strongly dependent on position with respect to the cloud Figure 5 shows that in the clear air above the top of the thunderstorm the electric field frequently is reversed or even intensified by the discharge [16] Inside of the cloud, as is shown in Figure 6,[93] the electric field is usually not reversed, but merely reduced in intensity On the ground beneath the cloud, the electric field is often reversed and intensified

The field reversal above the cloud is probably caused by a screening layer of space charge that is deposited on the cloud surface by the clear air conduction current flowing from the upper atmosphere [7] The field reversal beneath the cloud is probably caused by a region of space charge produced by point discharge from the surface of the Earth [58]

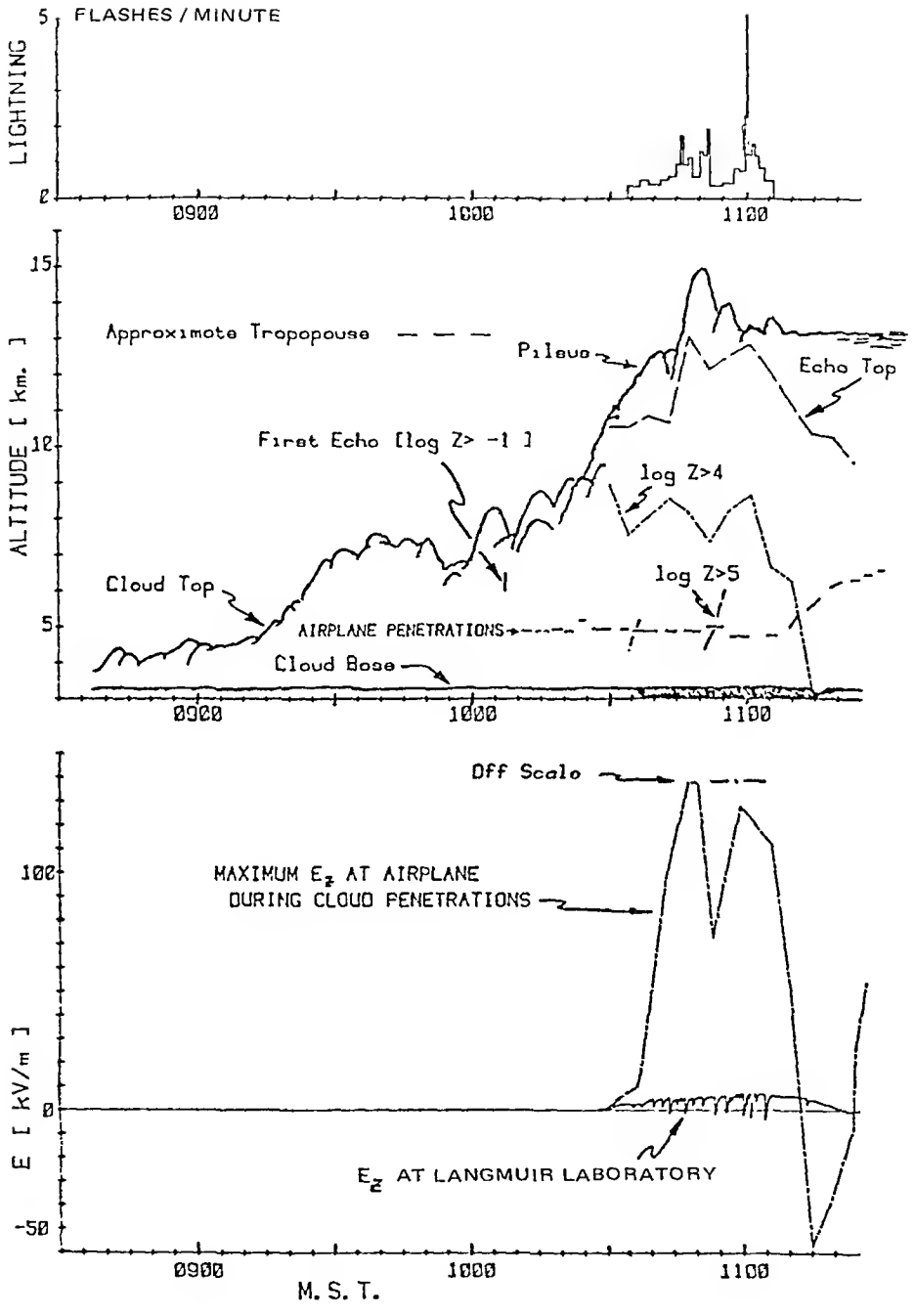

FIGURE 4. Time history of various features of a thundercloud formed over Langmuir Laboratory on August 17, 1977. (Courtesy Professor Charles B. Moore, New Mexico Institute of Mining and Technology.)

Most aerosol, cloud, and precipitation particles are electrically conducting, having electrical relaxation times of less than a second. As a result, the ambient electric field is intensified by charges induced on these particles. Spherical cloud droplets and raindrops cause a three-fold intensification, while ice particles and large raindrops distorted by aerodynamic and electrical forces may cause much greater intensification of the electric field. While the intensified fields caused by aerosol and cloud particles may reach values far in excess of 3000 kV m^{-1}, normally considered the dielectric strength

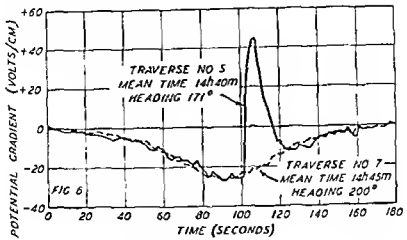

FIGURE 5 Field change produced by lightning recorded from aircraft flying in clear air above the top of a thunderhead [46]

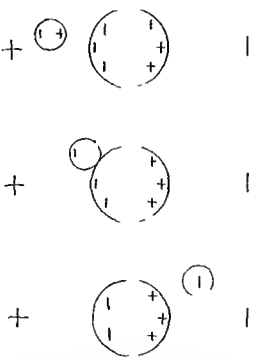

FIGURE 6 Schematic diagram showing how a collision between a big drop and a little drop in an electric field leads to a charge exchange that has the effect of increasing the electric field

of air, they do not initiate ionization because of their very small size. Larger particles, however, play a role in initiating various dielectric breakdown processes, particularly when they experience large distortions or collisions [49]. The even greater electrical perturbations[79] caused by aircraft and rockets undoubtedly can also trigger lightning.

The rapid electric field changes associated with lightning not only provide information on the details of the electrical discharge, but if measurements are made at several

locations under the cloud, such data can be used to calculate the magnitude and the location of the electrical charges deposited by the lightning flash and its individual strokes.[28]

Charged Particles

Charged particles are responsible for the electrical properties of the thunderstorm. The population of these particles and their distribution in space determine the strength and pattern of the electric field of the storm. Their movements under the influence of electrical, gravitational, and aerodynamic forces determine the development and dissipation of the electrical energy of the storm.

The experimental difficulties in obtaining reliable data in the storm concerning the distribution of electrical particles in space and time are so formidable that at present there is not enough information to characterize the electrical structure of the storm or the processes responsible for its development. It is possible, however, on the basis of present knowledge to indicate the various kinds of electrified particles that are undoubtedly present and the roles they may conceivably be playing.

In order of increasing size, the important charged particles involved in thunderstorm electrification are as follows: electrons, ionized atoms, molecules and molecular clusters (fast ions or small ions), charged aerosol particles (large ions), charged cloud ice particles, charged cloud droplets, charged snow crystals and snowflakes, charged raindrops, charged graupel particles, and charged hail. Although the movement of electrons is of dominant importance in the dielectric breakdown process and in the conduction of electric charge through plasmas,[11] free electrons have a very short lifetime and rapidly become attached to atoms and larger particles. They therefore are a negligible constituent of the accumulations of charged particles in the cloud responsible for thunderstorm electric fields.

Fast ions produced by cosmic rays play a dominant role in the electrical conduction processes in the clear air above and around the cloud.[25] Similarly, beneath the cloud, fast ions produced as the result of cosmic radiation, radioactive decay, and point discharge play an important role in conduction currents flowing as a result of the electric field of the storm and in the convection of charge by updrafts and downdrafts in the clear air beneath the thundercloud base. The space charge of fast ions above the cloud and beneath the cloud base probably plays an important role in determining the external electric fields of the cloud.

Fast ions are produced inside of the cloud by dielectric breakdown, cosmic rays, and radioactive disintegration. They are brought into the cloud from the clear air surrounding the cloud under the influence of electric fields and by advection resulting from the cloud circulation. Probably they play only a minor role in large-scale electrical conduction processes within the cloud, for they rapidly become attached to cloud particles through diffusion and through movement under the influence of the electric field. The steady-state concentration of fast ions in the cloud is so small that they probably are of minor importance as a constituent of the particles comprising the charged regions within the cloud.

Even the cleanest atmosphere always contains suspended particulate matter, either solid or liquid, that can serve as a carrier of electric charge.[36] These particles range in size from submicroscopic Aitken nuclei as small as 10^{-9}m up to large dust particles of 10^{-4}m in radius. These aerosols are produced by such natural sources as bursting bubbles from the ocean, volcanic eruptions, sand and dust storms, and the disintegration of meteors. In addition, biological activity generates spores and pollen as well as organic vapors that polymerize to form particles. In urban locations the population of aerosol particles is dominated by man-made particles arising from combustion processes, smelting, and manufacturing. Large quantities of aerosols become highly elec-

trified in volcanic eruptions and in sand or dust storms, and play a dominant role in the formation of lightning in these natural phenomena In the case of the ordinary thunderstorm, aerosols probably play a much less important role Beneath the thundercloud, ions of either sign released by point discharge will rapidly attach themselves to aerosol particles that may be present, thus causing these particles to become electrified with one sign or the other Because the mass and the aerodynamic drag of aerosol particles is vastly larger than that for small ions, electrified aerosol particles have mobilities several orders of magnitude lower than ions [8] Their motion under the influence of electric forces even in intense electric fields is small relative to the velocities of convective circulation in a storm [44] In the air beneath the cloud, these charged aerosols formed by attachment of ions caused by point discharge probably play an important role in determining the electric field on the ground surface under the storm When they are carried by the updrafts into the cloud, the electrified aerosol particles quickly lose their identity They collide with and become attached to small cloud particles or serve as nuclei for droplet formation Because of these processes, charges carried by the aerosol particles are rapidly transferred to cloud particles It is doubtful whether in the clouds of ordinary storms the charged aerosol particles are important either as charge carriers or as charged particles contributing significantly to the electrification of the cloud

Undoubtedly, small cloud particles, both ice crystals and water droplets, are a very important class of electrified particles within the thundercloud Not only is the mass of these particles far greater than the combined mass of all the other particulate matter in the storm, but in addition, because of their small size, these particles present by far the largest surface area available for carrying electric charge At the base of the cloud these particles can acquire charge by the attachment of fast ions carried up to the cloud under the influence of updrafts and electrical forces If they condense on or collide with aerosol particles carried up into the cloud, they will acquire whatever charge these may be carrying On the top of the storm, particles on the upper part of the cloud will become electrified by the attachment of ions attracted to the cloud under the influence of its electric field Within the cloud the small particles can become electrified by several processes When a cloud particle collides with and separates from another cloud or precipitation particle, a separation of charge generally takes place, either as the result of electrostatic induction in an electric field[36] or as a result of frictional or contact electrification [45] A consequence of these processes is that systematic electrification may occur, the cloud particles acquiring one sign of charge (usually positive), while the precipitation particles acquire the opposite charge (usually negative)

Other processes can also form electrified cloud particles, for example, the fragmentation of large precipitation particles when they break up by collision or by the action of aerodynamic forces When bubbles burst in melting ice particles or raindrops, the small droplets they eject can be highly charged The freezing of liquid drops often takes place with the formation of an outer sphere of ice and the consequent development of high internal pressures When the ice shell breaks, strongly electrified particles can be ejected The fracture of dendritic ice structures is also capable of producing small charged particles [37] Lightning or other varieties of dielectric breakdown processes occurring within a cloud result in the deposition of coulombs of positive or negative ions within the cloud While some of these ions may neutralize the charged cloud or precipitation particles that gave rise to the lightning discharge, others may cause the formation of other charged cloud particles by becoming attached to neutral or weakly charged droplets or ice particles.[45 73]

Laboratory experiments indicate that during the evaporation of electrified water drops, the electric charge remains on the drop surface so that the charge per unit area and electric field at the surface increase with time Finally, as the drop evaporates, the

Table 1
FALLING SPEEDS OF RAINDROPS AT 1 BAR ATMOSPHERIC PRESSURE

Drop diameter (cm)	m sec^{-1}
0.1	4.0
0.2	6.5
0.3	8.0
0.4	8.8
0.5	9.0
0.6	9.3

electrical stresses can become so large that either dielectric breakdown of the air occurs at the drop surface or the electric forces exceed those of surface tension and the droplet becomes unstable and breaks up.[14] In portions of the cloud where the relative humidity is less than saturation with respect to the charged water particle, evaporation may give rise to a class of very highly charged small water particles. Because of their extremely high charge-to-mass ratios, such water particles may have mobilities as high as several centimeters per second per volt per centimeter, comparable with that of small ions.

Electrified raindrops are another highly important carrier of charge within thunderstorms. Raindrops can become electrified by a variety of charging processes.[5] If a raindrop falling in a vertical electric field overtakes and collides with a smaller droplet, as is shown in Figure 6, an inductive charge transfer process can take place, in which the charge transfer process takes place in such a way that the falling raindrops augment the existing electric field. Drop electrification can also occur as the result of contact electrification when they collide and bounce off other water drops or ice particles. Raindrops may acquire a charge when they are formed as the result of the coalescence of charged cloud droplets or by the melting of electrified ice crystals. When bubbles within raindrops move to the drop surface and break, small highly electrified droplets may be ejected causing the raindrop to acquire the opposite charge.[15] When raindrops become large enough that they can be disrupted by aerodynamic forces or by electrical forces acting on the surface, the resulting drops formed by the breakup can become strongly electrified by induction or by charge separation processes taking place at the surface during its disruption.[56] Measurements show that raindrops reaching the ground often carry the same sign of charge that is being emitted by point discharge from nearby vegetation and other objects under the influence of the thunderstorm electric fields.[57] This situation, in which the rain carries the same sign of charge as the ions being released by point discharge, is sometimes called the "mirror image effect", for the record of the charge carried by rain mirrors the record of the electric field. It is undoubtedly the result of the attachment of upward moving point discharge ions to the falling raindrops. It is to be expected that when lightning events deposit charge in the form of fast ions near falling raindrops, some of the raindrops will become electrified by ion attachment. Gunn[21] has suggested that "hyper-electrification" will occur when ions moving toward the cloud under the influence of its electric field become attached to falling raindrops.

Because the force of gravity acting upon electrified raindrops can be large enough to carry charge in opposition to the electrical forces acting on the particle, falling rain may play an important role in generating the electric fields of thunderstorms. Table 1 shows the terminal velocities of various sizes of nonelectrified raindrops falling at 1 bar atmospheric pressure. Computer studies modeling the growth and electrification of water particles in a thundercloud[10] indicate that under the influence of electric

forces, charged drops in an average thunderstorm may experience a decrease in velocity of as much as several meters per second Some investigators have suggested that the electrical force acting upon highly charged raindrops in very strong electric fields may become large enough to levitate the charged raindrops or even cause them to move upwards [24] As yet there is no unequivocal experimental evidence of this phenomenon in thunderstorms

Frozen precipitation ranging from small graupel particles of the order of 1 mm in diameter up to hail, which has been observed in excess of 10 cm, is undoubtedly an important charge carrier in thunderclouds Because hail particles do not readily break up under the influence of aerodynamic forces and can reach sizes and masses far greater than the largest raindrop, they can reach higher terminal velocities than rain Hail particles 5 cm in diameter have a terminal velocity in excess of 30 m sec^{-1} [17] A hail particle has more surface area and falls at much higher speeds than a raindrop, thus it can transport charge at much higher rates Various investigators have, therefore, suggested that falling charged hail may be one of the primary contributors to the electrification of thunderclouds [47] It must be recognized, however, that although the falling hail can be an efficient transporter of electric charge, because of the relatively small number of hail particles available and their relatively limited total surface area, large hail probably is not an important charge carrier or component of charged regions in most thunderstorms

With the exception of the rather rare small thunderstorms in the tropics that do not extend above the freezing level,[41] most thunderstorms rise to levels where the temperature is far below freezing Frozen particles, particularly small hail and graupel, are commonly associated with electrification Estimates of the location of charged regions arrived at from calculations based on field changes associated with lightning show that the negatively electrified regions associated with cloud-to-ground strokes generally lie at altitudes where the temperature is 10 or 20°C below freezing [28]

Laboratory studies indicate that the ice phase can be important in electrification Experiments show that strong electrification occurs when freezing takes place in supercooled water[35a,b,5] and when collisions occur between ice crystals and other ice crystals or between ice crystals and liquid droplets

On the basis of these observations, many studies of thunderstorms have concluded that the ice phase or freezing processes are of dominant importance in the electrification of thunderstorms [37] Future investigations may well prove this to be true It must be recognized, however, that there are other electrification mechanisms capable of producing lightning such as those that are taking place in warm clouds,[41] volcanic eruptions,[2] and dust storms [26] It should also be noted that frequent energetic lightning has been noted in the atmospheres of Venus[62,29] and Jupiter[12] under conditions where it is unlikely that the ice phase could be playing a role

Electric Currents and Electrification Mechanisms

The motion in any direction of any of the charged particles described above under whatever influence constitutes an electric current To the extent that the motion has a component in the same direction as the electrical forces acting on the particle, the resultant current will dissipate the electrical energy of the storm To the extent that the motion occurs in a direction opposite to that of the electric field, it will contribute to the electrification in the storm by increasing its electrical energy The motions of all varieties of charged particles in various parts of the storm are capable of dissipating electrical energy Dramatic dissipative currents of the order of kiloamperes flow during the lightning flash through the movement of electrons in the plasma and, to a lesser extent, that of ions A similar flow of charge occurs within the cloud as the result of corona from solid[20] and liquid precipitation[49] particles and beneath the storm as the

result of corona from points on the surface of the Earth.[87] In the intense electric field in the clear air above the cloud, a current of small ions of the order of an ampere flows under the influence of the external electric field of the cloud.[16] The potential difference between the top of the cloud and the upper atmosphere is probably of the order of 10^8 V, so this current represents a power dissipation of the order of 10^5 kW. Beneath the cloud a similar dissipative current of comparable magnitude and power flows as the result of the movement of ions produced by point discharge from points on the surface of the Earth that move up toward the base of the cloud. If there is a high concentration of aerosol particles in the air beneath the cloud, these will become electrified as the result of ion attachment and may constitute a significant portion of the dissipative current if they are carried by updrafts to the cloud. Because of the low mobility of charged aerosol particles, small ice crystals, and cloud droplets, the motion of these particles under the influence of ambient electric fields inside and outside of the cloud does not contribute significantly to the dissipative currents that are flowing.[66a] On the other hand, if these small charged particles are carried by air motions so they move in the same direction as electric forces, they can cause a significant drain of electrical energy. Electrified precipitation particles have much higher mobilities and may constitute a significant dissipative current when they move under the influence of electric fields. If gravitational forces or winds carry them in the same direction as electric forces, their motion will also act to diminish the electrical energy of the storm.

In order for a cloud to develop electrification and lightning, it is necessary that there be electric currents in which charged particles moving in opposition to electrical forces develop electrical energy. The current must generate electrical energy at a sufficient rate that it exceeds the average rate at which the energy is being depleted by lightning and the other dissipative currents discussed above.

Because of the great difficulties in determining the charged particle population in various parts of the cloud as a function of time and how these particles move, we presently have only a poor understanding of the nature and magnitude of the currents responsible for cloud electrification. There are two possible mechanisms by which these currents might flow. In the first, electrical energy can be developed when electrified precipitation particles move downward under the influence of gravity in opposition to electrical forces.[8,36] In the second mechanism,[19,40] electrical energy can be developed when aerodynamic forces resulting from air motions within the cloud cause electrified cloud and precipitation particles to move in opposition to electrical forces. Doubtless both of these electrical energy generating processes are taking place in thunderstorms. Until better information is available concerning the distribution and motion of the charged particles within the storm, it will not be possible to evaluate the relative importance of the two mechanisms.

Charged Particle Accumulations

Through the action of gravitational and aerodynamic forces, water particles carrying one polarity of charge accumulate in some parts of the cloud while particles carrying the opposite polarity accumulate in other parts of the cloud. Ultimately, at some point, usually within the cloud, the electric field intensity becomes large enough to initiate ionization processes that develop into a lightning discharge.

There is general agreement among investigators that the cloud can be roughly approximated as a dipole with positively charged particles in the upper part of the cloud and negatively charged particles in the lower part of the cloud. There is evidence too that sometimes beneath the negative charge there is a smaller, lower positive charge.

Krehbiel et al.[28] have determined that cloud-to-ground flashes transfer of the order of 50 C of positive charge into the cloud. To the extent that it is possible to infer the

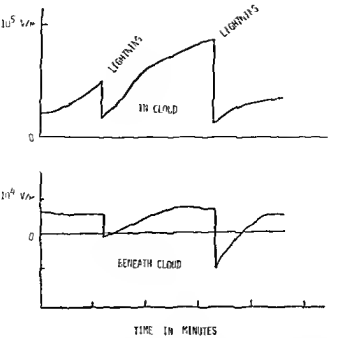

FIGURE 7 Field changes produced by lightning recorded from a balloon within the thunderstorm cloud and from a ground observation station beneath the cloud [83]

location of the charge accumulations responsible for lightning from the location of the charges deposited by lightning, the findings indicate that the *negatively charged* region is at a more or less constant elevation between −9 and −17°C extending over many kilometers Measurements made within the cloud[82] show that the lightning usually reduces the intensity of the electric field by about one-half (See Figure 7) This indicates that the negatively charged region is probably in excess of 100 C These findings are in accord with the *description*[85] that the negative accumulation in the cloud is fixed with respect to the *precipitation region*, and the positive accumulation is located upward and, in many cases, outward from the region as if it were blown there by air currents within the cloud

EFFECTS OF ELECTRIFICATION

Role of Electricity

Although much effort has been directed to studies designed to determine how cloud physical processes produce electrification, much less has been given to the effects that electrified particles, strong electric fields, and dielectric breakdown can have on the physical processes taking place in the thundercloud Scientists are agreed that fine weather electric fields of only hundreds of volts per meter and the small conduction current, 10^{-16} amp cm^{-2}, have little effect on cloud physical processes. There is a difference of opinion, however, on the role of thunderstorm electricity in the thundercloud While some scientists[36] have neglected the role of electrification in treatments of cloud physics, others believe that electrical effects may be of importance in physical processes taking place within the cloud.[33] In this section, some of the possible ways that thunderstorm electrification could be having an effect will be considered

Cloud Microphysics

It is well established by Wilson's[80] classic cloud chamber experiments that ions can

serve as centers for drop condensation. It has, therefore, been suggested from time to time that small ions produced by radioactive disintegrations, cosmic rays, brehmstrahlung, and dielectric breakdown could play an important role in the condensation of water vapor to form clouds (see, for example, Reference 64). Students of cloud physics, however, are generally agreed that this is unlikely, for the fourfold supersaturation of water vapor necessary to produce condensation on ions only very rarely exists in the free atmosphere of the Earth.[68]

It has been suggested that the acoustic wave produced by lightning near the channel where it is most intense may play a part in the formation of ice crystals. Laboratory experiments[66] show that the temperature lowering produced by the sudden adiabatic expansion of air is capable of producing very large numbers of minute ice crystals that are capable of seeding a cloud in a manner similar to that produced by dry ice. It is possible that cloud seeding effects resulting from lightning discharges in the colder portions of the cloud may play a significant role in cloud microphysical processes.[75]

In laboratory experiments with a supercooled cloud in a cold box,[53] it has been shown that small vegetable or animal fibers, such as lint or a spider web, raised to a potential of the order of a kilovolt can cause the production of enormous numbers of tiny ice crystals, again very similar to the seeding effects brought about by dry ice.[52] Extrapolating from such experiments to a thundercloud, it appears reasonable to suppose that such fibers will often be carried into thunderstorms on updrafts and that in the strong potential gradients of the cloud may give rise to the large-scale production of ice crystals that will accelerate the glaciation of the cloud.

Other experiments also carried out in the cold box have shown that the growth of ice crystals in a supercooled cloud is greatly accelerated in the presence of strong electric fields of the sort that exist in thunderclouds.[88] It would appear on the basis of these findings that the growth of ice crystals in supercooled regions of thunderstorms may be appreciably speeded up as the result of electrical effects. Work as yet unpublished[9] has shown that strong electric fields cause small ice crystals in a cloud to line up end to end and to form long slender ice fibers. Possibly these may play a role in the microphysics of the thundercloud.

Although the action of electrical forces in thunderstorm electrical fields produces only negligible distortion in the spherical shape of small cloud droplets, it causes appreciable distortion in the larger falling raindrops. As the electrical forces act on a drop in opposition to the forces of surface tension, strong electric fields have been shown to decrease the stability of falling randrops and to accelerate drop breakup.[38] Wind tunnel experiments show that strong electric fields are capable of deforming the falling raindrop into a teardrop shape and that under some conditions point discharge can occur from the pointed upper extremity.[49]

Experiments show that the optical properties of clouds composed of small ice crystals can be markedly affected by electric fields of thunderstorm intensity.[71] Normally small hexagonal ice platelets float in the air with their flat surface perpendicular to gravity. In strong electric fields, however, dipoles are induced that can align the ice crystals with their axes many degrees off the vertical direction. As a result, specular reflection of light from the ice crystals is strongly influenced by electric fields. Because the upper parts of most thunderstorm clouds are made of ice crystals, it is probable that they are influenced by the electric fields in the thunderstorm and the rapid changes in the intensity and direction of the electric field accompanying lightning discharges. Observations describing sudden changes in the cloud's appearance that are associated with lightning discharges may be explained by this phenomenon.[18]

Precipitation Formation

One of the possible conclusions that can be drawn from the close association be-

tween thunderstorm electricity and rain or other precipitation is that the falling precipitation is playing an important role in the electrification process Another conclusion is also conceivable, that the electrification process is playing a role in the formation of the precipitation One of the early suggestions that electricity may aid the formation of rain was offered by Lord Rayleigh [46] He showed that in a small vertical fountain water drops that bounce off each other in the absence of an electric field readily coalesce and form bigger droplets in the presence of an electric field, even as small as 1 kV m^{-1} He pointed out that because the behavior of a cloud was strongly dependent on the outcomes of encounters between water droplets, it is possible that through this mechanism electric fields may aid in the formation of rain

Electrical forces may be capable of accelerating the formation of rain and other precipitation not only by increasing the probability of coalescence, as suggested by Lord Rayleigh, but by the action of coulombic forces that cause particles to become attracted to each other and to experience collisions with each other that would not otherwise occur Laboratory experiments,[33] and theoretical calculations[51] show that significant increases in collision and coalescence can occur as the result of charges carried by cloud and precipitation particles or by charges induced on their surfaces as a result of ambient electric fields Field observations of precipitation from a thunderstorm in New Mexico indicate a possible enhancement of precipitation growth as the result of electric fields [39]

It is possible that the intense electrical effects within the thundercloud may have a significant effect on the chain reaction mechanism of rain formation proposed by Langmuir [50] According to this idea, falling raindrops growing by collision and coalescence with cloud droplets finally become so large that surface tension is no longer able to hold them together When they break up into two or more smaller raindrops, these in turn grow and subdivide, thus creating large numbers of raindrops by a chain reaction process If electric charges, induced or otherwise, are on the surface of the raindrop, they will oppose the forces of surface tension and thus reduce its stability under the action of aerodynamic forces As a result, it is to be expected that in a strongly electrified storm the time interval required for growth to break up size will be reduced with a consequent speeding up the chain-reaction drop multiplication process

It has long been observed that a nearby flash of lightning is often followed in a few minutes by a sudden, rather intense downpour Several mechanisms have been proposed to account for this so-called "rain gush" phenomenon One popular explanation is that as the intensity of the electric field within the cloud builds up, the electrical forces acting on charged raindrops become so great that they cease falling and are levitated [34] Then when the lightning occurs and the electric field is neutralized by the lightning, the rain is suddenly allowed to fall and arrives at the Earth as a burst of heavy precipitation Another possible explanation is that the intense acoustic wave of thunder produced by the lightning causes the cloud drops to collide and coalesce, leading to a sudden fall of rain [1] It has been suggested that the intense electric fields and the sudden deposition of charge by lightning greatly accelerate the coalescence process [42] Radar observations[60] show that there is often only very light precipitation present before the lightning discharge and that the development of the heavy rain occurs after the flash The fact that the intense radar echo from the precipitation forms many seconds after the lightning indicates that the phenomenon is probably caused by electrically accelerated particle growth rather than by acoustical forces or levitation

Cloud Dynamics

Although coulombic forces may play a significant role in the interaction of cloud and precipitation particles, it appears very doubtful that they are of importance in the large-scale motions of the cloud.[69] Estimates that the electrical component of energy

of the storm is small compared to its total energy[4] suggest that the electrical forces are probably of minor importance. The maximum intensity of large-scale electric fields within the cloud is limited by the dielectric breakdown strength of air to less than 3×10^3 kV m^{-1}. The maximum electrical force per unit area that can be exerted by this field corresponds to a pressure difference of only about 1 mb. Since this is small relative to the pressure differences to be found in the thunderstorm, it is unlikely that this is of importance.

While electrical energy probably plays a negligible part in the dynamics of the storm as a whole, it may be of importance in limited small regions. It has been suggested that the electrical heating resulting from repeated lightning discharges in the same path may produce localized regions of very hot air that could be significant in supplying energy to a tornado.[67]

Although electrical forces are probably of negligible importance in the dynamics of thunderstorms in the atmosphere of the Earth, it is conceivable that they may be far more important in the much denser atmospheres of other planets, such as Venus and Jupiter, where lightning has recently been observed.

The electric fields necessary to initiate dielectric breakdown vary directly with the atmospheric density. It is, therefore, possible that electric fields in these atmospheres may reach values orders of magnitude greater than on Earth. Because the electrical energy density and the intensity of electric forces varies as the square of the electric field, it is possible that the intensity of lightning discharges and the effect of electric forces may be far greater in these atmospheres than it is on Earth.

Oxides of Nitrogen Production

It has been recognized for over a century that lightning flashes contribute to the formation of nitrogen oxides in our atmosphere. Other processes as well are known to produce oxides of nitrogen. For example, they are also released from soils and generated as a result of the oxidation of ammonia in the atmosphere. In addition, large quantities of nitrogen oxides also originate from man's furnaces, internal combustion engines, and industrial processes.

Because of the uncertainties in making reliable measurements of these various sources, it has been difficult to determine the relative importance of lightning in the fixation of nitrogen. While some studies[65] conclude that lightning does not play a major role, others include estimates that its contribution may be as high as 50%. Theoretical studies[23] and consideration of various aspects of the problem[13] show that it will be necessary to learn much more about the physics of lightning and its global occurrence before it will be possible to assess accurately its importance as a source of nitrogen oxides.

REFERENCES

1. Agayan, L., Laboratory in the Caucasus mountains, *Prom. Ekon. Gaz.*, 4, March 1960.
2. Anderson, R., Bjornsson, S., Blanchard, D. C., Gathman, S., Hughes, J., Jonasson, S., Moore, C. B., Survilas, H. J., and Vonnegut, B., Electricity in volcanic clouds, *Science*, 148, 1179, 1965.
3. Bergeron, T., On the physics of cloud and precipitation, in *Proc. 5th Assembly UGGI*, Vol. 2, Union Geodesique Geophysique Internationale, Paris, 1935, 156
4. Braham, R. R., Jr., The water and energy budgets of the thunderstorm and their relation to thunderstorm development, *J. Meteorol.*, 9, 237, 1952.
5. Brook, M., Moore, C. B., and Sigurgeirsson, T., Lightning in volcanic clouds, *J. Geophys. Res.*, 79, 472, 1974.

6 Brook, M and Vonnegut, B , Visual confirmation of the junction process in lightning discharges, *J Geophys Res* , 65, 1320, 1960
7 Brown, K A , Krehbiel, P R , Moore, C B , and Sargent, G N , Electrical screening layers around charged clouds, *J Geophys Res* , 76 2825, 1971
8 Chalmers, J A , *Atmospheric Electricity*, 2nd ed , Pergamon Press New York, 1967
9 Cheng, Roger, personal communication, 1980
10 Chiu, C-S, Numerical study of cloud electrification in an axisymmetric, time-dependent cloud model, *J Geophys Res* 83, 5025 1978
11 Cobine, J D , *Gaseous Conductors* Dover, New York, 1958
12 Cook, A F , II, Dusbury, T C , and Hunt, G E , First results on Jovian lightning, *Nature (London)*, 280, 794 1979
13 Dawson, G A , Nitrogen fixation by lightning *J Atmos Sci* 37 174, 1980
14 Doyle, A , Moffett, D R , and Vonnegut, B , Behavior of evaporating electrically charged droplets, *J Colloid Sci* 19 136, 1964
15 Drake, J C , Electrification accompanying the melting of ice particles *Q J R Meteorol Soc* , 94, 176 1968
16 Gish, O H and Wait, G R , Thunderstorms and the earth's general electrification, *J Geophys Res* , 55, 473 1950
17 Gokhale, N R , *Hailstorms and Hailstone Growth*, State University of New York Press, Albany, 1975
18 Graves, M E , Gall, J C , Jr and Vonnegut, B , Meteorological phenomenon called crown flash, *Nature (London)*, 231, 258 1971
19 Grenet, G , Essai d'explication de la charge electrique des nuages d'orages *Ann de Geophys* , 3, 306, 1947
20 Griffiths, R F and Latham, J , Electrical corona from ice hydrometeors, *Q J R Meteorol Soc* 100, 163, 1974
21 Gunn, R , The hyperelectrification of raindrops by atmospheric electric fields, *J Meteorol* , 13, 283, 1956
22 Havens, B S , Jiusto, J E , and Vonnegut, B , *Early History of Cloud Seeding*, New Mexico Tech Press, Socorro, 1978
23 Hill, R D , Rinker, R G , and Wilson, H D , Atmospheric nitrogen fixation by lightning, *J Atmos Sci* , 37 179 1980
24 Hunten, D M , View of Venus from Moscow, *Nature (London)*, 280, 794, 1980
25 Israel, H , *Atmospheric Electricity* Vol II, Israel Program for Scientific Translations, Jerusalem, 1973
26 Kamra, A K , Measurements of the electrical properties of dust storms, *J Geophys Res* , 77 5856, 1972
27 Kelvin, Lord, On the equilibrium of vapour at a curved surface of a liquid *Proc R Soc Edin* , 7, 1870
28 Krehbiel, P , Brook, M , *and McCrory, R , An analysis of the charge structure of lightning discharges* to ground, *J Geophys Res* 84, 2432, 1979
29 Ksanfomaliti, L I , Discovery of frequent lightning discharges in clouds on Venus, *Nature (London)*, 284, 244, 1980
30 Langmuir, I , Production of rain by a chain reaction in cumulus clouds at temperatures above freezing *J Meteorol* , 5 175 1948
31 Latham, J , The electrification of frost deposits, *Q J R Meteorol Soc* , 89, 540, 1963
32 Latham, J , Influence of electrical forces on cloud physical development, *Planetary Electrodynamics*, Vol 1, Gordon and Breach, New York, 1969, 359
33 Latham, J , Experimental studies of the effect of electric fields on the growth of cloud particles, *Q J R Meteorol Soc* 95, 349, 1969
34 Levin, A , and A Ziv, The electrification of thunderclouds and the rain gush *J Geophys Res* , 79, 2699, 1974
35 Ligda, M G H , The radar observation of lightning, *J Atmos Terr Phys* , 9, 329, 1956
35a Magono, C , *Thunderstorms*, Elsevier, Amsterdam, 96 1980
36 Mason, B J , *The Physics of Clouds*, 2nd ed Clarendon, Oxford, 1971
37 Mason, B J , The physics of the thunderstorm, *Proc R Soc London Ser A*, 327, 433, 1972
38 Matthews, J B , Mass loss and distortion of freely falling water drops in an electric field, *J Geophys Res* , 72, 3007, 1967
39 Moore, C B , and Vonnegut, B , Estimates of raindrop collection efficiencies in electrified clouds, in *Physics of Precipitation*, Monogr 5, American Geophysical Union, Washington, D C , 1960, 291
40 Moore, C. B and Vonnegut, B , *Lightning*, Vol 1, Golde, R H , Ed , Academic Press New York, 1977, chap 3

41. Moore, C. B., Vonnegut, B., Stein, B. A., and Survilas, J. H., Observations of electrification and lightning in warm clouds, *J. Geophys. Res.*, 65, 1907, 1960.
42. Moore, C. B., Vonnegut, B., Vrablik, E. A., and McCaig, D. A., Gushes of rain and hail after lightning, *J. Atmos. Sci.*, 21, 646, 1964.
43. Neville, M., Report E. L. 1489, Royal Aircraft Establishment, Farnborough, England, 1958.
44. Orville, R. E. and Spencer, D. W., Global lightning flash frequency, *Mon. Weather Rev.*, 107, 934, 1979.
45. Phelps, C. T. and Vonnegut, B., Charging of droplets by impulse corona, *J. Geophys. Res.*, 75, 4483, 1970.
46. Rayleigh, Lord, The influence of electricity on colliding water droplets, *Proc. R. Soc.*, 28, 406, 1879.
47. Reynolds, S. E., Compendium of Thunderstorm Electricity, New Mexico Inst. Mining and Tech., Socorro, N.M., 1954.
48. Reynolds, S. E., Brook, M., and Gourley, M. R., Thunderstorm charge separation, *J. Meteorol.*, 14, 426, 1957.
49. Richards, C. N., and Dawson, G. A., The hydrodynamic instability of water drops falling at terminal velocity in vertical electric fields, *J. Geophys. Res.*, 76, 3445, 1971.
50. Sartor, J. D., The role of particle interactions in the distribution of electricity in thunderstorms, *J. Atmos. Sci.*, 24, 601, 1967.
51. Sartor, J. D., Accretion rates of cloud drops, raindrops, and small hail in mature thunderstorms, *J. Geophys. Res.*, 75, 7547, 1970.
52. Schaefer, V. J., The production of clouds containing supercooled water droplets or ice crystals under laboratory conditions, *Bull. Am. Meteorol. Soc.*, 29, 175, 1948
53. Schaefer, V. J., The generation of large numbers of ice crystals in an electric field, *J. Appl. Meteorol.*, 7, 452, 1968.
54. Schonland, B. F. J., *The Flight of Thunderbolts*, 2nd ed., Clarendon, Oxford, 1964.
55. Schackford, C. R., Radar indications of a precipitation-lightning relationship in New England thunderstorms, *J. Meteorol.*, 17, 15, 1960.
56. Simpson, G. C., On the electricity of rain and its origin in thunderstorms, *Philos. Trans. R. Soc. (London), Ser.* A, 209, 379, 1909.
57. Simpson, G. C., Atmospheric electricity during disturbed weather, *Geophys. Mem. London*, 84, 1, 1949.
58. Standler, R. B. and Winn, W. P., Effects of coronae on electric fields beneath thunderstorms, *Q. J. R. Meteorol. Soc.*, 105, 285, 1979.
59. Steiner, R. and Rhyne, R. H., Some Measured Characteristics of Severe Storm Turbulence, U.S. Weather Bureau, National Severe Storms Project Report 10, Washington, D.C., July 1962.
60. Szymanski, E. W., Szymanski, S. J., Holmes, C. R., and Moore, C. B., An observation of a precipitation echo intensification associated with lightning, *J. Geophys. Res.*, 85, 1951, 1980.
61. Takeuti, T., Nakano, M., Brook, M., Raymond, D. J., and Krehbiel, P., The anomalous winter thunderstorms of the Hokuriku coast, *J. Geophys. Res.*, 83, 2385, 1978.
62. Taylor, W. W. L., Scarf, F. L., Russell, C. T., and Brace, L. H., Evidence for lightning on Venus, *Nature (London)*, 279, 614, 1979.
63. Toland, R. B. and Vonnegut, B., Measurement of maximum electric field intensities over water during thunderstorms, *J. Geophys. Res.*, 82, 438, 1977.
64. Vampola, A. L., VLF transmission induced slot electron precipitation, *Geophys. Res. Letters*, 4, 569, 1977.
65. Viemeister, P. E., Lightning and the origin of nitrates found in precipitation, *J. Meteorol.*, 17, 681, 1960.
66. Vonnegut, B., Production of ice crystals by the adiabatic expansion of gas, *J. Appl. Phys.*, 19, 959, 1948.
66a. Vonnegut, B., Possible mechanism for the formation of thunderstorm electricity, Proc. Conf. Atmos. Elec., AFCRL Geophys. Res. Paper 4Z, Air Force Cambridge Research Laboratory, Bedford, Mass., 169, 1955.
67. Vonnegut, B., Electrical theory of tornadoes, *J. Geophys. Res.*, 65, 203, 1960.
68. Vonnegut, B., Wilson cloud chamber effect under natural conditions, *J. Atmos. Sci.*, 19, 194, 1962.
69. Vonnegut, B., Some facts and speculations concerning the origin and role of thunderstorm electricity, *Meteorol. Monogr.*, 5, 224, 1963.
70. Vonnegut, B., Electrical Behavior of an Airplane in a Thunderstorm, Report FAA-ADS-26, Arthur D. Little, Inc., Cambridge, Mass., 1965.
71. Vonnegut, B., Orientation of ice crystals in the electric field of a thunderstorm, *Weather*, 20, 310, 1965.
72. Vonnegut, B., Lightning observation from space, *Weather*, 34, 291, 1979.
73. Vonnegut, B., Production of charged cloud particles by lightning, *Trans. Am. Geophys. Union (EOS)*, 60, 834, 1979.

74 Vonnegut, B and Moore, C B , Giant electrical storms, in *Recent Advances in Atmospheric Electricity*, Pergamon Press New York 1959, 399
75 Vonnegut, B and Moore, C B , Nucleation of ice formation in supercooled clouds as the result of lightning *J Appl Meteorol* 4 640, 1965
76 Vonnegut, B , Moore, C B , and Botka, A T , Preliminary results of an experiment to determine initial precedence of organized electrification and precipitation in thunderstorms, *J Geophys Res* , 64 347, 1959
77 Vonnegut, B , Moore, C B Espanola, R P , and Blau, H H , Jr , Electric potential gradients above thunderstorms, *J Atmos Sci* , 23, 764, 1966
78 Vonnegut, B , Moore, C B , Semonin, R G , Bullock, J W , Staggs, D W , and Bradley, W E , Effect of atmospheric pace charge on initial electrification of cumulus clouds *J Geophys Res* 67, 3909, 1962
79 Wallace, J M , Diurnal variations in precipitation and thunderstorm frequency over the conterminous United States, *Mon Weather Rev* , 103 406 1975
80 Wilson, C T R , Condensation of water vapour in the presence of dust free air and other gases, *Philos Trans R Soc (London) Ser A*, 189, 265, 1897
81 Wilson, C T R , Investigations on lightning discharges and on the electric field of thunderstorms, *Philos Trans R Soc (London), Ser A* 221, 73 1920
82 Winn, W P , Measurements of electric fields in thunderclouds, *J Geophys Res* 79 1761, 1974
83 Winn, W P and Byerley, L G , III, Electric field growth in thunderclouds, *Q J R Meteorol Soc* , 101, 979, 1975
84 Workman, E J and Reynolds, S E , Time of rise and fall of cumulus cloud tops, *Bull Am Meteorol Soc* , 30, 359, 1949
85 Workman, E J and Reynolds, S E , Electrical activity as related to thunderstorm cell growth, *Bull Am Meteorol Soc* 30, 142 1949
86 Workman, E J and Reynolds, S E , Electrical phenomena occurring during the freezing of dilute aqueous solutions and their possible relationship to thunderstorm electricity *Phys Rev* , 78, 254 1950
87 Wormell, T W , Vertical electric currents below thunderstorms and showers *Proc R Soc (London) Ser A*, 127, 567, 1930
88 Zawidzki, T W and Papée, H M , Pseudo-whiskers of ice grown from clouds of supercooled water in an electric field, *Nature (London)* 196, 568 1962

THE LIGHTNING CURRENT

Toshio Ogawa

TABLE OF CONTENTS

INTRODUCTION

Atmospherics are generated from various electric discharges There are many kinds of discharge processes of either natural or artificial origin The familiar discharge phenomena of natural origin are lightning from thunderstorms, dust storms, volcanic eruptions, tornadoes and so on Of artificial origin are nuclear detonation and other small scale man-made machinery such as cars, power lines, etc The most significant among these is lightning from thunderstorms

The history of lightning research is very old and numerous papers on lightning have been published Lightning has been investigated from both the physical and the electrical-engineering points of view Physicists have been interested mainly in the discharge mechanism of lightning, the spatial and temporal scales of which are extremely large compared with artificial laboratory discharges Engineers have been interested primarily in the protection methods from lightning hazard (regardless of the lightning discharge mechanism), while physicists have done more or less nothing with lightning protection

For these reasons physicists and engineers have taken different approaches to lightning research Physicists have made research of lightning with regard to thunderstorm-electricity generation mechanism, while engineers have paid little attention to thunderstorm clouds Physicists have made measurements of electric and magnetic fields, of optical, photographic and acoustic features of lightning discharges to determine the position and magnitude of charges associated with lightning of both cloud-to-ground and intracloud discharges, and physical properties such as temperature and electron density of lightning channel Engineers, on the other hand, have worked to determine magnitude of lightning currents and their wave-shapes necessary to design lightning warning devices such as the lightning counter Physicists tend to be interested in natural lightning, lightning which strikes open ground, while engineers tend to be concerned with rather special lightning, lightning which strikes artificial structures, such tall buildings as the Empire State Building and tall towers of transmission lines More and more importance is recognized for such lightning in today's society From the point of view of atmospherics, however, such lightning is extraordinary We are, therefore, mostly concerned with natural lightning, lightning which strikes open ground

Two books on lightning have been published The title of both books is the same, *Lightning* One is written by Martin A Uman[75] and the other is edited by R H Golde [14] The former is based on the physical analysis of lightning, while the latter is based on both the physical and the engineering approaches As both books are carefully written and edited and cover most of important features of lightning, there seems to be very little to add to these comprehensive books of lightning We will therefore, in this chapter summarize the recent results of lightning research published mostly in 1970s and present a general picture of lightning without neglecting the essential mechanism and features of lightning

CHARGE STRUCTURE OF THUNDERSTORM AND LIGHTNING

Charge Structure

The thunderstorm electricity consists of two main positive and negative charges with a small positive charge The upper portion of a thunderstorm cloud is filled with the main positive charge and the lower portion with the main negative charge The small positive charge is surrounded by the negative main charge near the cloud base We often call this small positive charge the positive pocket charge (see Figure 1)

Suppose a sign of charge distributes in a spherical fashion The spherical distribution of charge gives the same electric field in space as does a point charge The thunder-

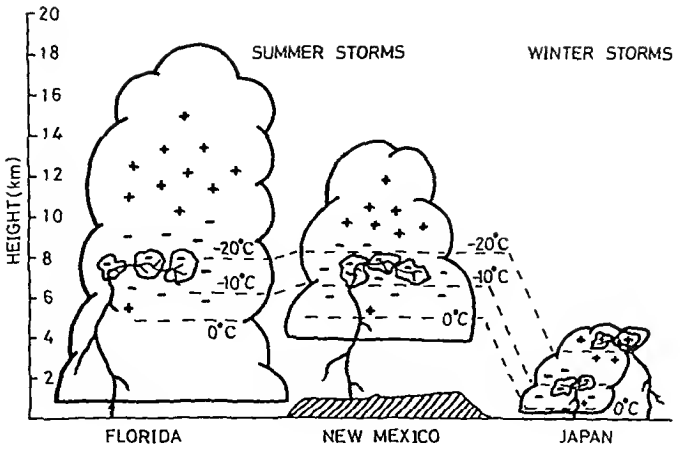

FIGURE 1. Model charge structure of lightning and thunderstorm clouds in three different locations. (From Krehbiel, P. R., Brook, M., Lhermitte, R. L., and Lennon, C. L., paper presented at the 6th International Conference on Atmospheric Electricity, Manchester, July 28 to August 1, 1980. Copyright owned by New Mexico Tech. With permission.)

storm and lightning charges are often assumed as point charges mainly because of simplicity. This assumption has been proved adequate to be representative of cloud charges which are lowered by lightning strokes to ground.[23]

Neglecting the small positive pocket charge, the two positive and negative point charges give the superposed effect of electric fields in space. The measurement is made usually on the ground surface and we will further add the effects of image charges under the ground surface to match the boundary condition assuming the ground to be a perfect conductor. Then we have the familiar expression of electric field, E_z, on the ground surface due to the thundercloud charges:

$$E_z = \frac{1}{4\pi\epsilon_0} \sum_{i=1}^{2} \frac{2Q_i Z_i}{[(x_i - x_0)^2 + (y_i - y_0)^2 + z_i^2]^{3/2}} \qquad (1)$$

where ϵ_0 is the permittivity of free space, Q_i is the amount of positive or negative charge, x_i, y_i and z_i are the position coordinates in space of the positive and negative charges, and x_0, y_0 and z_0 are the coordinates of the observing station. The electric field on the ground has only the vertical component and is usually defined downward as positive. It is easily understood that the right hand side of Equation 1 has eight unknown variables. This means that if we have eight simultaneous electric fields observed at eight different stations distributed near the position of the charges we can solve the simultaneous eight equations and estimate the charge amounts and their positions in the space. If both magnitudes of positive and negative charges are identical, then we only need seven-station electric-field measurements. This may apply to the study of cloud-discharge charge structure. In the case of the ground discharges the only one sign of charge in the cloud is effectively associated. So we principally need only four station electric fields to get complete information of ground-discharge charge structure.

Applications of this method have been made at different places on the globe. The most famous measurements were made in New Mexico,[55,96] in Florida,[20] and in Japan.[16,72] Very recently Krehbiel et al.[23] made a very accurate estimation of ground-discharge associated charge-structure in New Mexico using the least squares fitting

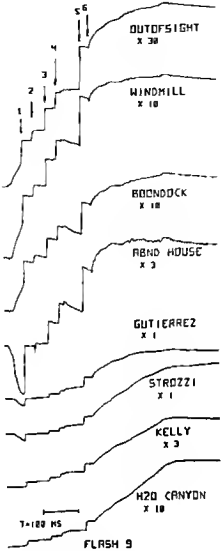

FIGURE 2 Electric field changes of ground discharge observed at eight stations simultaneously Total field change values range from 19 1 kV/m at the Strozzi station to 2 28 kV/m at the Outofsight station in New Mexico (From Krehbiel P R, Brook, M, and McCrory, R A, *J Geophys Res*, 84, 2432, 1979 With permission)

method which was originally introduced by Jacobson and Krider [20] An example of the simultaneous electric field records from eight stations is shown in Figure 2 This flash produced six major strokes (numbered in the Figure) to ground, the last of which initiated a long continuing current of 220-msec duration The analyzed results from four such flashes are shown in Figure 3 This figure shows sources of charge for the individual strokes of multiple-stroke flashes to ground The centers of charge for successive strokes of each flash developed over large horizontal distances within the cloud, up to 8 km, at more or less constant elevation between the − 9 and − 17°C environmental (clear air) temperature levels

Jacobson and Krider[20] compared the lightning charges, altitudes, corresponding air temperatures, and electric-moment changes in various geographical locations The

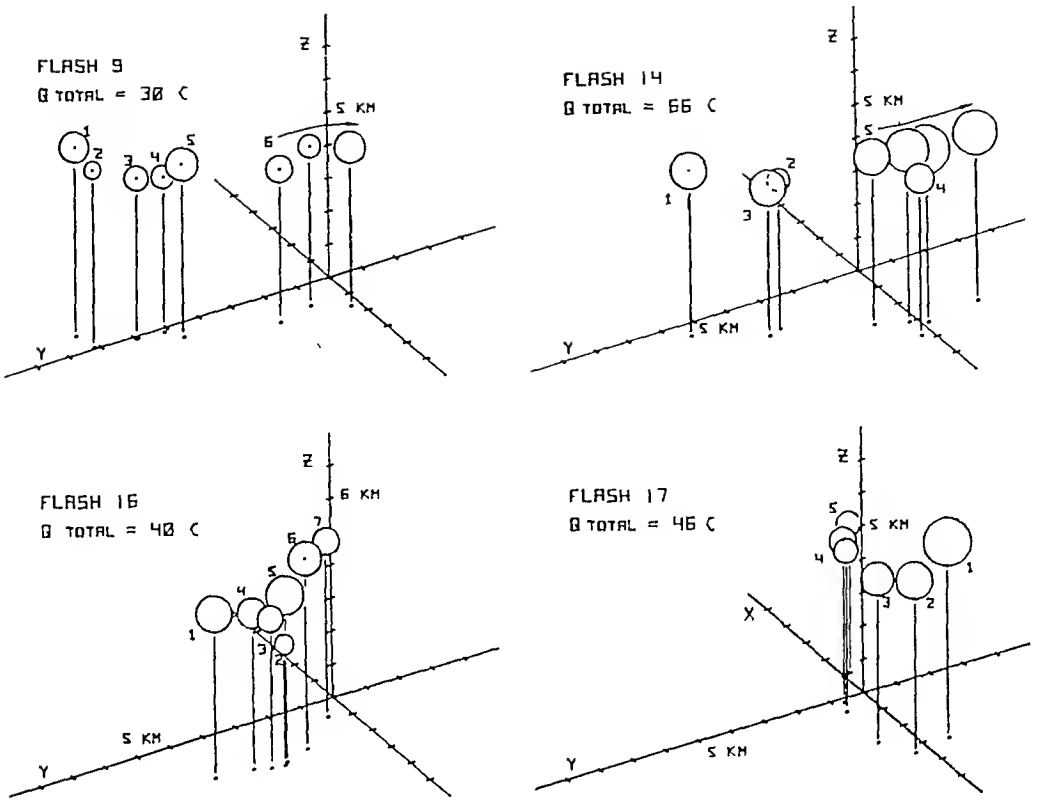

FIGURE 3. Ground stroke charge structure for four flashes to ground. The circles denote the size of spherical volumes which would have contained the individual stroke charges at a uniform density of 20 C/km³. Arrows indicate charge volumes for the continuing current. (From Krehbiel, P. R., Brook, M., and McCrory, R. A., *J. Geophys. Res.*, 84, 2432, 1979. With permission.)

summaries of this comparison are given in Table 1, which indicates that the ground discharge neutralizes cloud charges of −10 to −40°C in the air temperature range from −5 to −30° C. Model charge distributions in thunderstorm clouds are given in Figure 1, which was originally sketched by Krehbiel et al.[102] and is modified here. The charge structure depends primarily on the air temperature.

Lightning Channel Orientation

The orientation of the lowest part of the lightning channel to Earth can be studied by photography. The visual portion looks more or less vertical with some sideward branches. The visible channel is, however, not the entire lightning channel. The channel inside the cloud cannot be seen. The lightning channel hidden within cloud was only studied by the electrical method. Such study was made early by Malan and Schonland.[31,32] They found that the negative charge lowered to Earth in a flash-to-ground is distributed in a vertical column extending up to 6 km in length. Hacking[15] supported this result for South African storms as well. Pierce,[44] using the J-change-slope analysis (see the discussion on multiple strokes in the section entitled "Lightning Discharge Mechanism") given by Malan and Sohenland,[32] concluded that most return strokes originated at roughly the same height, i.e., the intervening streamers between successive return strokes travelled horizontally, suggesting a horizontal distribution of negative charge.

Using a network of eight field-change recordings simultaneously, Workman et al.[96] concluded that horizontal separation of intracloud discharges was on the average more

Table 1
LIGHTNING CHARGES, ALTITUDES, AND MOMENT CHANGES IN VARIOUS GEOGRAPHICAL LOCATIONS

Geographical location	Charge (C)	Local terrain height above sea level (km)	Altitudes above local terrain (km)	Range of air temperatures (°C)	Moment changes (C km)	Ref
England	-11 5—-46	0 1	7	-34	33—430	93
England	20	0 1	2	-0 5	100 (av)	94
England	-10—-40	0 1	4 5—5	-16—-19	220 (av)	97
England	—	—	—	—	150 (av)	44
South Africa	15	1 8	3	13	93 (av)	59
South Africa	4— 40	1 8	2 5—8 7	-10—-48	41—495	2
South Africa	—	1 8	4—8 5	-7—-38	—	32
New Mexico	-24 (av)	1 6	4—7	5— 25	—	96
New Mexico	-5— 20	2 1	4 3—7 2	-7— 33	—	55
New Mexico	-5— 60	1 8	3—8	-3— 36	249 (av)	7
New Mexico	-30— 66	1 8	4 5—6	-9— 17	—	23
Florida	-10— 40	0	6—9 5	-10— 34	100—600 400 (av)	20
Japan	50— 150	0 1	4—8	4— 25	—	16
Japan	-6—-55	0 1	6—8	-11— 24	—	71
Japan	-20 (av)	0 1	3 5—5 5	3— 8	—	67
Hong Kong	-25 (av)	0 1	4	-1	210 (av)	91
Australia	-17 (median)	0 1	3 (median)	5	150 (av)	30

than three times greater than the vertical separation Reynolds and Neill,[55] in a study similar to the Workman et al [96] study, also found that the negative charges brought to the Earth in successive strokes were displaced horizontally

Ogawa and Brook,[40] based on a study of electric field changes measured at two stations, concluded that the horizontal component of the in-cloud channel of the ground discharges on the average exceeds the vertical component The negative charge involved in lightning flashes to ground is distributed in a manner strongly dependent upon the direction of movement of the storm

A nonelectrical method to determine the lightning channel orientation was reported by Teer and Few[75] with an analysis of thunder recorded by an array of microphones Lightning channel reconstructions derived by them indicated that the horizontal lightning structures are persistent and much extended A typical ratio was 3 2 1 of long horizontal axis to short horizontal axis to vertical axis in their ellipsoid model of intracloud lightning and the intracloud portions of ground lightning All channels analyzed by them aligned along the same direction and perpendicular to the direction of storm motion This observation does not agree with Ogawa and Brook[40] who reported that the intracloud channel aligned with the direction of storm motion Nakano[37] with the thunder technique, discussed the relationship between the channel direction and the storm characteristics and showed that the ground discharge channel inside the cloud tilted to downstream of upper atmospheric wind

Additional observations of the horizontal nature of lightning discharges were made by using the polarization of the electromagnetic radiation from lightning These results also indicated horizontal EM field amplitudes several times larger than the vertical [18 65] Proctor[50] made space-time mapping of lightning discharge processes by using VHF technique in South Africa, and reported that the flash pervaded a volume $3 \times 4 \times 6$ km^3. Taylor,[74] using a similar technique in Florida showed that most lightning activity occurred about 5 to 6 km high, near the −10°C temperature level, and considerable movement of discharge centers occurred as the lightning-processes permeated the thunderstorm volume at progression speed of about 50 to 150 km/sec

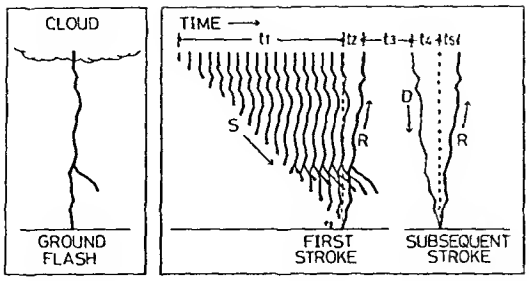

FIGURE 4. Schematic presentation of still and time-resolved lightning discharge to ground. $t_1 = 20$ msec, $t_2 = 70$ μsec, $t_3 = 50$ msec, $t_4 = 1.5$ msec and $t_5 = 60$ μsec. S: Stepped-leader; R: Return stroke; D: Dart Leader.

The charge structures of lightning are modeled in Figure 1. As described above, intracloud lightning discharge channel and the portion within the cloud of lightning channel to ground are considerably inclined: the horizontal extent of the channel is sometimes more than the vertical extent. Furthermore, the in-cloud part of the ground discharge may be composed of more than one channel. Such nature of lightning channel orientation makes modeling of the lightning current and the radiated electric and magnetic fields complex. No theory may be applicable to the actual lightning current if such nature is taken into account.

LIGHTNING DISCHARGE MECHANISM

Ground Discharge

Lightning is a transient, high-current electrical discharge, having a path length of several kilometers. Lightning occurs between a cloud and the ground. This type of discharge is called cloud-to-ground discharge, or simply ground discharge. Lightning also occurs between clouds, between a cloud and air, and within clouds. These are essentially of the same mechanism, so we do not differentiate them in this chapter. We call them intracloud discharge, or simply cloud discharge. In this subsection we are concerned only with ground discharge.

Each ground discharge is made up of one or more intermittent partial discharges. A total lightning discharge whose time duration is about 1/3 sec is called a flash, and each component discharge whose luminous time duration is measured in tenths of milliseconds is called a stroke. There are usually three or four strokes per flash, the successive strokes typically being separated by about 50 msec. Each lightning stroke is preceded by a barely luminous predischarge, the so-called leader process, which produces a negatively charged and ionized path between cloud and ground for the return stroke to follow (see Figure 4).

The leader discharge which precedes the first return stroke is called a stepped-leader because it moves downward stepwise every about 50 m. There are pauses of about 50 μsec between the steps. Typical average velocity of the stepped-leader is 1.5×10^5 m/sec. It takes about 20 msec to reach the ground from the cloud base of about 3 km height. During the process about 5 C of negative charge is distributed along the leader channel and the average current of the order of 100 A flows. The diameter of the stepped leader channel photographed seems to be 1 m or more but the current flows in a small conducting arc channel whose diameter is the order of 1 cm. The portion that looked luminous in the photograph is considered as the corona sheath which envelopes the high conducting channel.

The stepped-leader brings down toward the ground high negative potential from the

cloud the stepped-leader arc channel is a good conductor and is a high negative potential column When the stepped-leader is within a distance of about a few tens of meters from the ground surface, a very strong electric field is produced between the leader tip and the ground Then an electrical breakdown occurs between the leader tip and the ground A positive streamer propagates up toward the leader tip from a raised point on the ground surface When the streamer touches the downward coming stepped-leader tip, the potential of the bottom of the leader channel is raised to that of the Earth, rest of the leader channel remaining at the high negative potential There the first return stroke begins The wavefront of ionizing potential waves drived by the strong electric field carries the potential of the Earth along the channel already made by the preceding stepped-leader This wavefront propagates at a velocity of ⅓ to 1/10 the speed of light The velocity decreases every time the wavefront traverses the channel branches It attains the cloud base in about 70 μsec The return stroke discharges to the ground the negative charge which is distributed in the stepped-leader channel A large amount of current flows between the front and the ground and it reaches typically 20 kA within a few microseconds, then decreases to half the peak value within 40 to 50 μsec Then the current of the order of a few hundred amperes flows continuously for several milliseconds

The initial gas density in the return stroke channel is the same as the gas density of the leader channel, while the temperature is raised very high due to the high energy carried by the return stroke current, and it becomes much higher than that in the leader channel Then gas pressure of the stroke channel exceeds the pressure of surrounding air, and as a result the channel will expand This expansion is made at supersonic velocity and generates the cylindrical shock-wave making thunder This phase lasts about 5 to 10 μsec The gas density of the current channel decreases as the shock wave propagates outward the channel In the later phase of the shock wave the channel temperature observed from the optical spectrum is near 30,000 K After completion of the shock-wave phase due to the channel expansion, the high-temperature low-density channel approaches, in microseconds or a few tens of microseconds, a state of approximate pressure equilibrium with the surrounding air, and the current density in the channel stabilizes at about 1 kA/cm^2 At this time the diameter of the channel will be approximately a few centimeters

After the current stopped, if there are still negative charges in the cloud region near the old channel top, the next stroke may occur Such type of lightning discharge is called multiple-stroke flash If a new charge is transferred from the negative charge region to the previous return-stroke channel, within about 100 msec by the small discharge (called K streamer), then the next high speed leader (called dart leader) runs down The dart leader recreates ionization of the channel and draws the cloud potential toward the ground again Thus, a second or later return stroke occurs In the dart leader a luminous portion of about 50 m in length runs toward the ground surface at the speed of about 2×10^6 m/sec The dart leader that precedes subsequent strokes carries less charges than the stepped leader The dart leader current is of the order of 1 kA The subsequent return stroke velocity is relatively constant with height

There are other types of discharges which occur in less common circumstances Those are

1 Positive downward leader followed by the negative upward return strokes — this type of discharge often happens in the winter thunderstorm in which the cloud charge distribution is largely shifted from the vertical
2 Positive upward leader from the tall structure followed by the negative downward return stroke — as the height of structure increases the proportion of producing upward discharge increases, having more probability with the height of 100 m

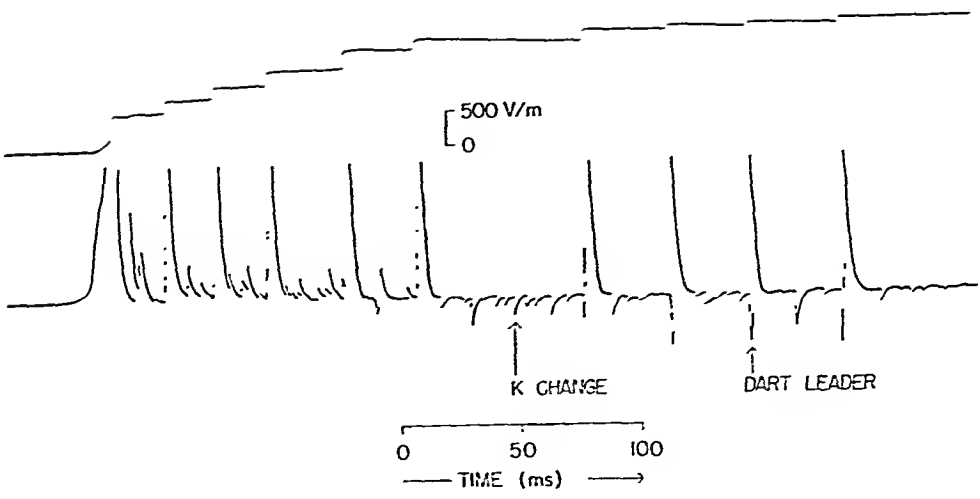

FIGURE 5. Electric field changes observed with fast antenna (upper portion) and slow antenna (lower portion) at an intermediate distance approximately 8 km from the lightning discharge to ground.

or more;[13] the leader which is initiated from towers is not necessarily followed by the return stroke while the subsequent downward leaders are followed by the subsequent return strokes.

3. Negative upward leader followed by the downward positive return stroke — this type of discharge is initiated from an object on Earth under a cloud portion of positive charges.

Discussion on Multiple Strokes

Lightning discharge processes have been studied by electric field measurements in which both the slow and fast antennas have been used to be very useful in providing the microscopic view of discharges.[22]

In Figure 5 are shown the electric field changes simultaneously measured with the slow antenna (upper portion) and the fast antenna (lower portion) for a ground discharge which occurred at the intermediate distance, approximately 8 km from the lightning discharge. Small impulsive discharges which occur in the return stroke intervals are called K change. The K change and the dart leader show positive field change in the first half period of whole discharge duration and then change sign from positive to negative almost simultaneously. It is suggested from this example that the K change and the dart leader are initiated at the same height suggesting that the K change and the dart leader are of similar character.

The discharge process between successive return strokes is called the Junction process or simply the J process. The slope of the electric field during the period of this process is negative for near storms and positive or zero for distant storms. When the storm is in the intermediate distance (6 to 10 km from the observing station), the electric field changes its slope from positive to negative as the order of strokes increases. The discharge channel length apparently increases upward with the stroke order. Based on these observational facts, Malan and Schonland[31,32] concluded that the positive streamer proceeds upward during the return stroke intervals from the cloud base toward the top of the negatively charged column in the cloud. The stroke multiplicity of the ground discharge was thus interpreted by this positive junction streamer theory.

Kitagawa and Brook[22] found that the later half portion of the cloud discharge is the same as the J process in the ground discharge and is essentially the integrated effect

of K field changes Ogawa and Brook[39] investigated the cloud discharge mechanism and concluded that the K change in the cloud discharge is due to the upward negative recoil current to the trunk channel from the tip of the initial downward positive streamer channel

Suppose a negative electric dipole moment, $-M$, at the position in the cloud where K change occurs in the ground discharge The electric field change at the ground surface, ΔE, produced by a disappearance of this dipole moment is given by

$$\Delta E = M(1 - 3\sin^2\theta)/2\pi\epsilon_0 L^3$$

or

$$\Delta E = M(1 - 3\sin^2\theta)\cos^3\theta/2\pi\epsilon_0 D^3 \qquad (2)$$

where L is the distance of the dipole to the observation point and $\cos\theta = D/L$, D is the horizontal distance It is clear from Equation 2 that ΔE changes its sign at $\theta = \sin^{-1}(1/3)^{1/2} = 35°\ 16'$ from positive to negative as θ increases at a fixed horizontal distance Consequently the effective electric field in the J period changes its slope from positive to negative This feature is just identical with the expected from the positive J-streamer theory by Malan and Schonland,[21,22] but the physical meaning is different It will be suggested from the above discussion that the J process between strokes is no more the process of junction streamer which proceeds upward because production of the K change in the J period requires a discharge channel already made Toward the end the positive upward streamer in the return stroke is to make a new channel in the negative fresh charge region in the cloud Sometimes this positive upward streamer appears as a continuing current

The continuing current was investigated in detail by Brook et al [7] They discussed the luminous portion which lasts more than 40 msec after the return stroke, and attributed it to the continuing current flowing from the ground to the cloud portion of concentrated negative charges It is however tentative that the lowest limit of the duration of the continuing current was defined as 40 msec There are continuing luminosities of the duration shorter than 40 msec The same amount of current of the order of 100 A flows during the periods as well In the ground discharge without continuing current the positive streamers progress into the new negative charge region within a few milliseconds and the channels thus made are readily followed by the K changes from the tip of the channel A large K change appears as the next dart leader

In the above subsections we have briefly discussed the discharge processes in the ground discharge but details are still not very well understood The numerical data on ground discharge parameters are listed in Table 2, which was originally compiled by Uman[28] and is modified with the data by Cianos and Pierce[9] and the Japanese data collected by Ikeda and Sumi [10]

Cloud Discharge

It is difficult to describe a common knowledge of cloud discharge, because the study of the cloud discharge has been much behind compared with that of the ground discharge Although more than half of all lightning flashes occur within clouds, the cloud discharges have been almost an ignored subject in the long history of lightning research, and therefore, there are very few data accumulated on the cloud discharge to date It is, however, important from the point of view of atmospherics because the cloud discharge produces atmospherics as well as the ground discharge

The cloud discharge occurs within clouds, illuminating the whole clouds Duration of the cloud flash is about the same as the ground discharge, about half a second The

Table 2
NUMERICAL DATA FOR GROUND DISCHARGE

Parameter	Minimum	Typical	Maximum
Stepped leader			
Length of step, m	3	50	200
Time interval between steps, μsec	30	50	125
Average velocity of propagation of stepped leader, m/sec	1.0×10^5	1.5×10^5	2.6×10^5
Charge deposited on stepped-leader channel, C	3	5	20
Dart leader			
Velocity of propagation, m/sec	1.0×10^6	2.0×10^7	2.1×10^7
Charge deposited on dart-leader channel, C	0.2	1	6
Return stroke			
Velocity of propagation, m/sec	2.0×10^7	5.0×10^7	2.0×10^8
Current rate of increase, kA/μsec	1	10	210
Time to peak current, μsec	0.5	2	30
Peak current, kA	1	20	250
Time to half of peak current, μsec	10	40	250
Charge transferred excluding continuing current, C	0.2	2.5	20
Temperature, K	0.8×10^4	2×10^4	3.6×10^4
Electron density, m^{-3}	1×10^{23}	3×10^{23}	3×10^{24}
Channel length, km	2	5	14
Continuing current			
Duration of continuing current, msec	50	150	500
Peak continuing current, A	30	150	1600
Charge in continuing current, C	3	25	330
Lightning flash			
Number of strokes per flash	1	3	26
Time interval between strokes in absence of continuing current, msec	3	50	380
Time duration of flash, sec	0.01	0.3	2
Charge transferred including continuing current, C	1	20	400

discharge path is not usually seen but sometimes comes out between portions of clouds. This type of discharge is called the intercloud or cloud-to-cloud discharge. The discharge path sometimes comes outside the cloud, probably toward the transparent space-charge accumulated region around the cloud. This type of discharge is called the air discharge. These two types of discharges present chances to see details of cloud discharge channels. As these two kinds of discharges may be produced by the same mechanism as the cloud discharge, we can investigate the discharge mechanism of cloud discharge using the photographs and simultaneous measurements of electric fields on the ground surface. This was done by Ogawa and Brook,[39] and the mechanism of the cloud discharge was barely unveiled.

The cloud discharge initiates with the slow positive streamer from the upper portion of the boundary region between positive and negative charges in the cloud. This initial streamer extends downward as well as horizontally. The streamer has the velocity of the order of 10^4 m/sec, and continues for about half the total duration; about 250 msec. The current of the streamer is of the order of 100 A. The streamer distributes positive charges along the path. When the streamer reaches the space-charge concentrated region of opposite sign, the recoil streamer runs back along the already made channel by the previous positive streamer and neutralizes the distributed positive charges. The electric field produced by this recoil streamer is called K change. The K change has the speed of the order of 10^6 m/sec and neutralizes the charge of about 1 C. As the duration of the K change is about 1 msec, the corresponding current is the order of 1 kA. Recognizable K changes in the electric field record repeat the order of

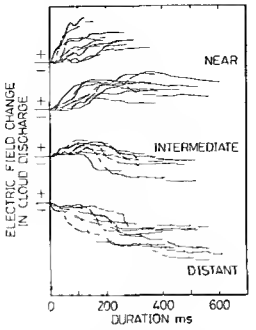

FIGURE 6 Types of electric field changes in cloud discharges observed near (approximately 4 to 7 km), intermediate (6 to 9 km) and distant (≥~10 km) from the cloud discharges The maximum field change amplitude is about 700 v/m for near discharges and 200 v/m for distant discharges

ten times during the latter half of the total duration A time series of cloud discharge field change data from an isolated thunderstorm is shown in Figure 6 where the field changes are classified into three groups for near, intermediate, and distant flashes The field changes show different curves from each other group From an analysis of these field-change data Ogawa and Brook[39] concluded that the cloud discharge is the combination of the initial positive streamer process and the series of recoil-current K-change process Detailed examination of the time-resolved photograph of the cloud-to-air discharge channel shows that each branched channel has few streaks parallel to the channel The relative brightness of the streaks offered an evidence that the K streamer starts the end point of the branched streamer and recoils back toward the main trunk of the initial streamer This process repeats few times from each branch tips The speed of the K streamer is the same as that of the dart leader in the ground discharge

The initial streamer goes sometimes upward from the lower negative-charge cloud portion toward the upper positive charge This was reported by Smith[64] with two-station electric-field measurements Takagi's[66] statistical result agrees with Ogawa and Brook's[39] result These contradictory results and still not-clear mechanism of K change initiation offer a future interesting field of investigation. The numerical data collected by Brook and Ogawa[6] are listed in Table 3 with references

EXPERIMENTAL MODEL OF LIGHTNING PARAMETERS

Cumulative Frequency Distribution

There are many lightning parameters which characterize the properties of lightning discharges to the ground The parameters often referred to are number of return

Table 3
NUMERICAL DATA FOR CLOUD DISCHARGE

	Total discharge	Initial streamer	*K* change		Ref.
Charge (C)	32				95
	21				55
	90				16
	32		0 47		19
	15				92
	10				51
	30		1·4		39
	33 ± 27			Average value	
Moment (C km)	70				95
	21				55
	81				44
	20				72
	200				92
	100				30
	120		3 6		39
	87 ± 62			Average value	
Height (km)	5 8—4 7				95
	5·8—5·2				96
	5·5—5·1				55
	10—6				16
	6				72
	(7—11)—(3—6)				66
	8·2—4 8				92
	5				75
	6·0—4 0		5 3—4 0		39
Duration			<1		22
(msec)	500	250			39
Speed		5×10^4	$(3—4) \times 10^6$		19
(m/sec)		10^4	10^6		66
		8×10^3	$1 \cdot 3 \times 10^6$		39
Current		100(max)			30
(A)		120	1,400		39

strokes per flash (N), duration of flash (Tg), return stroke intervals (Ts), return stroke peak current (Ip), charge quantity per flash (Cg), charge quantity per stroke (Cs), time to peak current (Tp), rate of current rise (It), time to current half-value (Th), duration of continuing current (Tc), continuing current (Ic), charge in continuing current (Cc), etc. Such lightning discharge parameters vary over a wide range like most of other geophysical parameters.

Most of the instruments which enable us to collect such data have been designed so as to measure an average or a moderate picture of lightning quantity. As a result, the extreme values in both larger and smaller regions have often been cut out from the data obtained. Giant lightning was often over-scaled in the data and minor lightning was usually neglected in analysis. It is necessary to remember, therefore, that the lightning picture available in the literature is representative usually of moderate lightning characteristics and not necessarily of all lightning.

The probability of occurrence of these parameters is often statistically given by the log-normal form. The log-normal distribution is a normal distribution in which the variables are given by logarithm, and probability density function P(log χ) is given by

$$P(\log x) = \frac{1}{\sigma\sqrt{2\pi}} \exp\left[-\frac{(\log x - \log m)^2}{2\sigma^2}\right] \qquad (3)$$

Table 4
STATISTICAL DISTRIBUTIONS FOR LIGHTNING PARAMETERS

Parameter	Occurrence %				
	2	10	50	90	98
Duration of flash(Tg) msec	850	480	180	68	36
Return stroke interval(Ts) msec	320	170	60	20	11
Return stroke peak current(Ip) kA	140	65	20	6 2	3 1
Charge quantity per flash(Cg) C	200	75	15	2 7	1
Time to peak current(Tp), μsec	12	5 8	1 8	0 66	0 25
Rates of current rise(It) kA/μsec	100	58	22	9 5	5 5
Time to current half value(Th), μsec	170	100	45	17	10 5
Duration of continuing current(Tc) msec	400	260	160	84	58
Continuing current(Ic) A	520	310	140	60	33
Charge in continuing current(C c), C	110	64	26	12	7

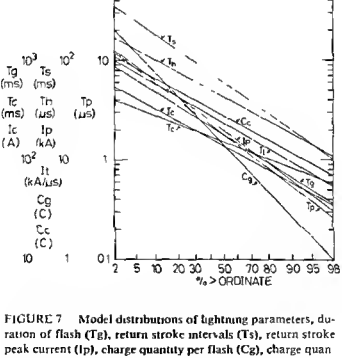

FIGURE 7 Model distributions of lightning parameters, duration of flash (Tg), return stroke intervals (Ts), return stroke peak current (Ip), charge quantity per flash (Cg), charge quantity per stroke (Cs), time to peak current (Tp), rate of current rise (It), time to current half-value (Th), duration of continuing current (Tc), continuing current (Ic) and charge in continuing current (Cc)

where σ is the log of the standard deviation relative to the median value m The log-normal distribution is to be expected for any process that consists of a number of independent contributing factors

Cianos and Pierce[9] have collected data for lightning parameters and made statistical model distributions of these parameters The model values are tabulated in Table 4 where the values of the parameters for cumulative frequencies at 2%, 10%, 50%, 90%, and 98% are given These values are shown in Figure 7 where cumulative frequency distributions of all parameters are plotted together.

Table 5
LIGHTNING RETURN STROKE VELOCITY

Number of strokes	Mean velocity $\times 10^5$ m/sec	Velocity range $\times 10^5$ m/sec	Ref.
27	0.47	0.20—1.1	62
			63
20	0.62	0.30—0.85	34
—	1.0	—	53
18	—	0.5—2.0	56
8	0.81	0.58—1.2	4
4	1.3	1.2—1.4	99

The parameter with the largest range of distribution is the charge quantity per flash (Cg) and the parameter with the smallest range of distribution is the duration of the continuing current (Tc). The rest of parameters are divided into two groups. The return stroke peak current (Ip), the time to peak current (Tp), the return stroke intervals (Ts), and the flash duration (Tg) are of a group of larger range of distribution, while the rate of current rise (It), the time to current half-value (Th), the charge in continuing current (Cc) and the peak continuing current (Ic) are of another group of smaller range of distribution.

The lightning return stroke velocity is another important parameter for modeling of lightning current. Boyle and Orville[4] measured two-dimensional return stroke velocities within 1 km from the ground using a multislit channel isolator with narrow vertical and wide horizontal fields of view on a high-speed streaking camera. Measurements of 12 strokes in three multistroke flashes yielded return stroke velocities which range from 2.0×10^7 to 1.2×10^8 m/sec with an estimated systematic error of 30 to 60%. Velocities in one multistroke flash vary by a factor of 4 between the lowest and highest values. Radda and Krider's[53] results, on the other hand, indicate the narrow range of return stroke velocities, the mean vertical speed near the ground level being 10^5 m/sec for all strokes estimated.

Subsequent return stroke velocities are collected from the literature by Lin et al.[27] They are listed in Table 5, in which the values range from 2.0×10^7 to 2.0×10^8 m/sec, an order of magnitude variation.

Latitude Dependence

Thunderstorms are produced frequently in tropical latitudes but produced also in temperate and higher latitudes. Thunderstorms are not only produced frequently over mountainous lands but are also produced over the ocean. Thunderstorms are produced most frequently in summer, but are also produced in spring and autumn as well as in winter. All these thunderstorms have their own characteristics depending on such various geographical locations and meteorological and seasonal circumstances.

The characteristics of lightning which is produced in the thunderstorms, therefore, are reasonable to be dependent on many of such spatial and temporal factors. It is necessary to take these factors into account in modeling of lightning but no precise data are collected yet. Among these factors some discussions have been made on latitude dependence for some parameters.

Prentice and Mackerras[48] collected the observations of the ratio of cloud lightning flashes to ground flashes and obtained an empirical relationship between this ratio (z) and latitude (λ). The 29 observations, covering a latitude range 69°N to 37°S, gave a mean value of z of 3.35. The empirical relationship proposed between z and λ is

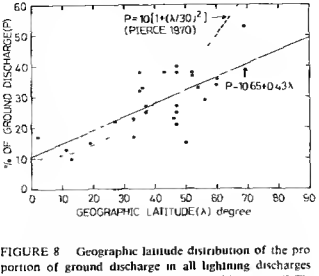

FIGURE 8 Geographic latitude distribution of the proportion of ground discharge in all lightning discharges. Data are from Table 1 in Prentice and Mackerras.[44] The solid line is the regression line to fit the data. The curve fitted to the different set of data by Pierce[45] is shown by dashed curve for comparison.

$$z(\lambda) = 4.16 + 2.16 \cos 3\lambda \quad 0 \leq \lambda \leq 60^{\circ} \tag{4}$$

The relationship between z and λ was interpreted by probable dependence on the variation of freezing level height with latitude, the lower the freezing level in the higher latitudes, the larger the probability of occurrence of discharges to ground.

Percentage of occurrence of ground discharge of all lightning flashes (P) can be calculated from the values of ratio z, and the result is given in Figure 8 where the regression line is given by

$$P = 10.65 + 0.43\lambda \tag{5}$$

Pierce[45] obtained the different form of relation from a different set of data which he had collected

$$P = 10\left[1 + \left(\frac{\lambda}{30}\right)^2\right] \tag{6}$$

Equation 6 is also plotted in Figure 8 for comparison with Equation 5.

Thomson[76] examined the latitude dependence of the number of strokes per lightning flash to ground by statistical analysis from data published so far. Thomson[76] concluded that the distribution of the parameter is more sensitive to local influences, including measurement and sampling techniques, than it is to latitude effect. This suggests that the lightning characteristics depend on many elements and it is difficult to detect the dependency on any one of these elements. Nevertheless the data collected by Thomson[76] are very informative and we plotted the mean number of strokes per flash (N) with latitude in Figure 9. If we neglect a point at λ = 34° in Figure 9 there seems to be a clear dependence. The regression line relating N to λ is

$$N = 3.64 - 0.01\lambda \tag{7}$$

Temperature and Electron Density

Determination of temperature and electron density of the lightning channel is im-

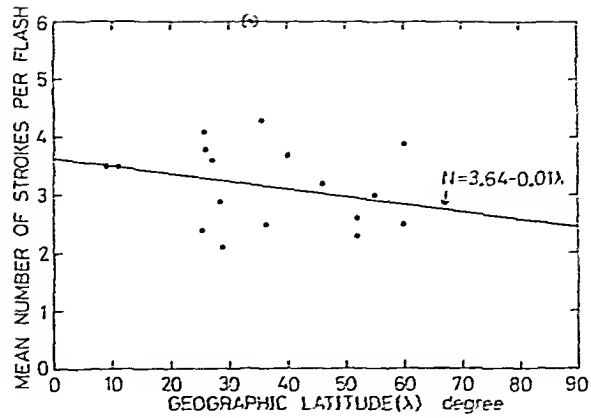

FIGURE 9. Mean number of strokes per flash, N, plotted as a function of geographic latitude, λ. Data are from Table 1 in Thomson.[74]

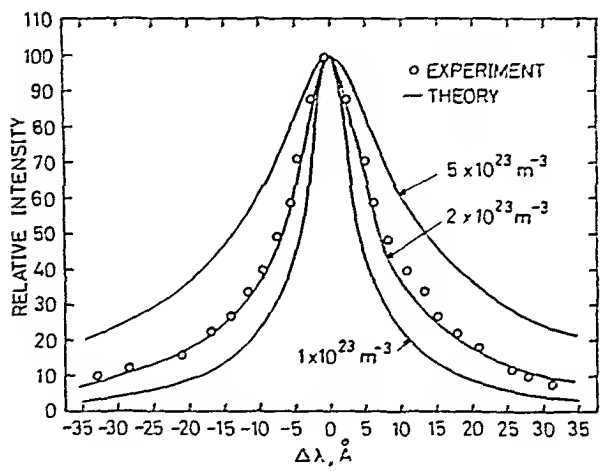

FIGURE 10. Comparison of the measured and calculated line profiles for Hα in lightning stroke. Theoretical profiles are given for three electron densities at 2×10^4 K (From Uman, M. A. and Orville, R. E., *J. Geophys. Res.*, 69, 5151, 1964. With permission.)

portant for discussing the discharge mechanism. They can be determined by the optical spectrum analysis The spectroscopic study of lightning has been done since more than a century ago but the lightning spectra obtained before 1960 gave only the time integrated effect of whole lightning. Since Salanave[57] succeeded in having separate spectra for each stroke, Salanave et al.,[58] Krider,[24] Orville,[41] etc., developed their own spectrometers and obtained much data of lightning channels. These data have enabled us to study physical properties of the lightning channel.

Before using this technique the opacity and the LTE (local thermodynamic equilibrium) of the channel should be examined. Uman and Orville[83] proved by examining the strength ratio of multiple spectral lines of singly ionized nitrogen (NII) that the lightning channel is optically thin, and that the channel is not in the perfect LTE but the temperature which would be obtained by this technique will represent approximately the actual temperature. If the temperature is known, the electron density of the channel will be determined by using the Saha equation. If the temperature and the electron density are known, the electrical conductivity of the channel can be calculated.

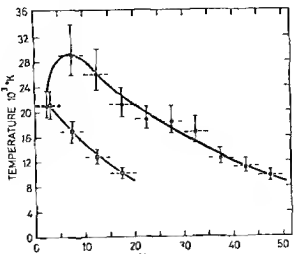

FIGURE 11 Return stroke temperature as a function of time for two strokes Horizontal dashed lines indicate the time resolution vertical bars the error limits (From Orville, R E *J Atmos Sci*, 25, 852, 1968 With permission)

Using these techniques Prueitt[53] obtained the channel average temperature of 24,000 to 28,000 K Uman et al [66 67] obtained the channel electron density of $3 \times 10^{24}/m^3$ The electrical conductivity of the channel calculated by Uman[77] was $1.8 \times 10^4/\Omega/m$

Uman and Orville[82] determined the electron density by using Stark broadening of spectral line of H_α in Balmar series The result is shown in Figure 10 where the experimental result agrees very well with the theoretical result From these results obtained for three return strokes the electron density was determined to be 1×10^{23}–$5 \times 10^{23}/m^3$ These values are more reliable than the value obtained by using the Saha equation

Orville[42] obtained the time variation of temperature for the return stroke with the time-resolved spectrum In Figure 11 are shown the results of average temperature for 5 μsec in which the exposure was made Typical maximum temperature is about 30,000 K The temperature reaches maximum within initial 10 μsec and decreases steadily thereafter

Orville[42] also estimated the channel electron density as a function of time calculated from the measured half width of H_α line The result is shown in Figure 12 The electron density was of the order of $10^{24}/m^3$ in the initial 5 μsec of the return stroke and decreased to $1 \times 10^{23}/m^3$ during the next 25 μsec, then it stayed at rather constant value during next 50 μsec after which the temperature decreased

If the channel temperature and the electron density are known as functions of time as in above, then pressure and other properties of the channel can be calculated Orville[42] showed that the channel pressure will be of the order of 10 at at the temperature of 30,000 K and the electron density of $10^{24}/m^3$ As the channel pressure exceeds that of the surrounding air, the channel expands until the pressure equilibrium will attain It will be suggested in Figure 12 that the channel pressure approaches to the atmospheric pressure in about 20 μsec

As described above most lightning flashes consist of more than one stroke In order for the second and later discharges to progress along the same channel as the first stroke channel, it needs to keep the preceding channel in a state of relatively high ionization during several tens of milliseconds before the next dart leader starts Brook et al [7] discussed a possibility of the order of 10A of the current flowing during that period keeping the channel conductive. McCann,[33] on the other hand, reported that

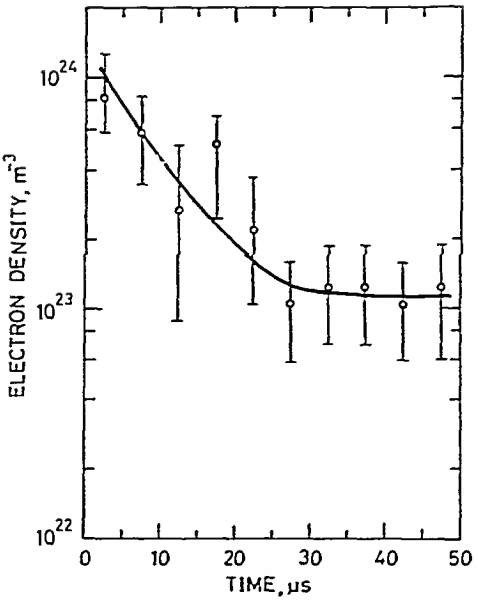

FIGURE 12. Return stroke electron density as a function of time calculated from the measured half width of Hα line (From Orville, R. E., *J. Atmos. Sci.*, 25, 852, 1968. With permission.)

the amount of current during the period between strokes is less than 0.1 A. Loeb[29] suggested the ionization wave due to K change which cannot be seen in the photograph.

Apart from these estimations Uman and Voshall[84] calculated the cooling rate of the channel in the case without energy input; they calculated temperature decay as a heat transfer problem. They solved the following four equations simultaneously: (1) the energy balance equation, (2) the momentum transfer equation, (3) the mass conservation equation, and (4) the equation of state. They assumed that these four equations hold in the discharge channel as well as in the surrounding air.

An example of the calculated results is shown in Figure 13. Assuming the initial temperature of 8000 K at the moment when the return stroke current stopped, the temperature at the center of the channel is shown taking the channel radius as a parameter. The calculated temperature does not decrease so much during the average duration of about 40 msec between successive strokes. At 4000 K the electron density and the conductivity of dry air are $10^{19}/m^3$ and about $1/\Omega/m$, respectively, then the air will be conductive.

At 2000 K the electron density is $10^{13}/m^3$ and the conductivity is $10^{-6}/\Omega/m$, then the air will be nonconductive.[98] The channel at the temperature between 2000 K and 4000 K as shown in Figure 13, therefore, is in a state between good conductor and insulator, but will be conductive enough to draw the next dart leader.

Diameter of Lightning Channel

Measurements of the lightning return-stroke channel diameter have been made in basically two ways, (1) from measurements of channel images in photographs and (2) from measurements of the size of the region of interaction of lightning and material objects. Besides these, theoretical calculations of the return stroke parameters lead to estimates of the current-carrying core of the channel.

Estimated results were summarized by Orville *et al.*[43] and listed in Table 6, which shows that the luminous diameter of the channel is the order of 10 cm while the current flowing diameter is the order of 1 cm.

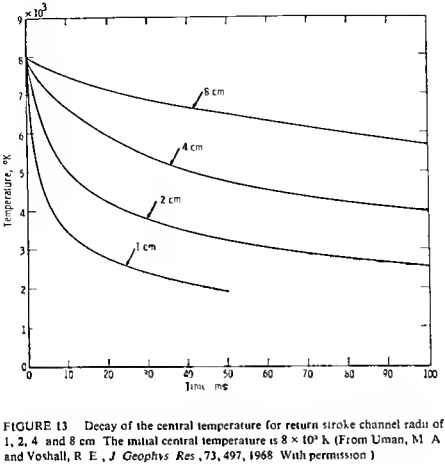

FIGURE 13 Decay of the central temperature for return stroke channel radii of 1, 2, 4 and 8 cm The initial central temperature is 8×10^3 K (From Uman, M A and Voshall, R E , *J Geophys Res* , 73, 497, 1968 With permission)

Table 6
DIAMETER OF THE LIGHTNING RETURN STROKE CHANNEL

Method of determination	Diameter (cm)	Ref
Photographic	15—23	60
Photographic	3—12	12
Photographic	6—7	43
Fulgurites in sand	≤5	61
Fulgamites	0 03—0 52	17
Holes in fiberglass bonnets	0 2—0 5, 2—3 5	77
Tree trunk damage	0 05—0 3, 1—8	73
Discharge craters in aluminum	0 1—0 3	21
Spark discharge model	0 3—2	5
Electrical circuit models	0 1—8	38
Temperature decaying model	0 5—2 5	84
Spark discharge model	0 33—1 76	47

MODELING OF LIGHTNING RETURN STROKE

Bruce-Golde and Transmission Line Models

If the spatial distributions and temporal variations of the currents energizing the lightning channel were known, then the electric and magnetic fields radiated from the channel can be calculated as a function of time Then the temporal variations of fields can be transformed into amplitude and phase spectra by Fourier transform An example of observed time profiles of lightning return-stroke currents for three strokes

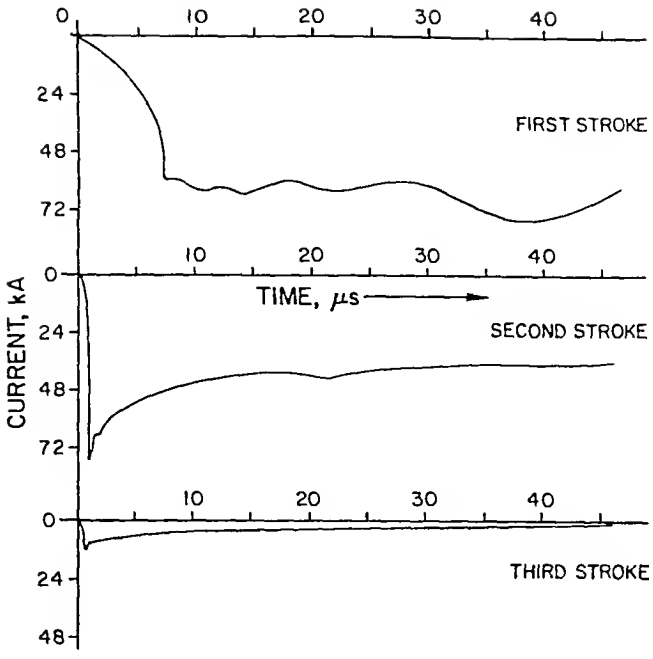

FIGURE 14. Lightning return stroke currents for three strokes observed in South Africa (From Lin, Y. T., Uman, M. A., and Standler, R. B., *J. Geophys. Res.*, 85, 1571, 1981 With permission.)

obtained in South Africa[11] is shown in Figure 14.[27] The first and second stroke magnitudes are unusually large, but the wave shapes of all three strokes are typical. The spatial distribution of the current along the channel, however, is not yet precisely known.

The first successful lightning return-stroke model was given by Bruce and Golde[8] who suggested a double exponential expression of the form:

$$I_t = I_0 (e^{-\alpha t} - e^{-\beta t}) \tag{8}$$

The current is instantaneously uniform from ground to the return stroke tip. This tip ascends at the velocity of v. Then the current moment at a time t is given considering the image current by $2I_t \int_0^t v dt$, from which the radiated fields can be calculated. Bruce and Golde,[8] based on the direct experimental measurements at the ground end of the channel, found the average values of I_0, α and β to be about 30 kA, 4.4×10^4 s^{-1} and $4.6 \times 10^5 s^{-1}$, respectively. The first return stroke velocity was represented from the photographic data by

$$v_t = v_0 e^{-\eta t} \tag{9}$$

where v_0 is 8×10^7 m/sec and η is $3 \times 10^4 s^{-1}$. The velocity for subsequent strokes in a multiple flash is relatively constant. As the peak current for the subsequent strokes is about half that of the first return stroke, thus an average current model for the subsequent strokes is given by

$$I_t = \frac{I_0}{2} (e^{-\alpha t} - e^{-\beta t}) \tag{10}$$

Pierce[46] gave the model values of these parameters as $\alpha = 2 \times 10^4 s^{-1}$, $\beta = 2 \times 10^6 s^{-1}$, $I_0 = 20kA$, $v_r = 10^8$ m/s, and $\eta = 3 \times 10^4 s^{-1}$

The double exponential expression of the lightning current given by Equation 8 can be interpreted as follows [54] Suppose the stepped leader channel is charged with an amount of charge Q A fraction of α of this charge is removed at the return stroke tip in unit time

$$dQ = -\alpha Q\, dt \tag{11}$$

where α depends on the charge density and the channel dimension The solution to Equation 11 is

$$Q_t = Q_0\, e^{-\alpha t} \tag{12}$$

where Q_0 is the total charge deposited in the stepped-leader channel at $t = 0$ The charge flowing down from the cloud would not stop after the initiation of return stroke This charge also contributes to the lightning current at the return stroke tip The decay of this charge is

$$Q_t' = Q_0'\, e^{-\beta t} \tag{13}$$

The total change rate of charge at the tip of the return stroke channel is given by

$$I_1 = \frac{d}{dt}\left(-Q_t + Q_t'\right) = Q_0 \alpha\, e^{-\alpha t} - Q_0' \beta e^{-\beta t} \tag{14}$$

$I_1 = 0$ at $t = 0$, then

$$I_t = I_0 \left(e^{-\alpha t} - e^{-\beta t}\right) \tag{15}$$

where $I_0 = Q_0 \alpha = Q_0 \beta$

Calculating the lightning currents using Equations 8 and 10 they become small for times larger than a few hundred microseconds, that is, the currents are much less than 1 kA In practice, a current of the order of 1 kA or so usually flows for a few milliseconds Cianos and Pierce[9] suggested the intermediate current of another double exponential form

$$I_{t1} = I_{01}\left(e^{-\gamma t} - e^{-\delta t}\right) \tag{16}$$

where $I_{01} = 2$ kA, $\gamma = 10^5 s^{-1}$ and $\delta = 10^6 s^{-1}$ The resultant current models for the first and subsequent return strokes are then, respectively,

$$I_0\left(e^{-\alpha t} - e^{-\beta t}\right) + I_{01}\left(e^{-\gamma t} - e^{-\delta t}\right) \tag{17}$$

and

$$\frac{I_0}{2}\left(e^{-\alpha t} - e^{-\beta t}\right) + I_{01}\left(e^{-\gamma t} - e^{-\delta t}\right) \tag{18}$$

Equations 17 and 18 are calculated for $I_0 = 20$ kA and $I_{01} = 2$ kA and the results are shown in Figure 15

The magnitude of the continuing current, I_c, is nearly constant, flowing for a duration, T_c I_c is generally about 150 A, and T_c is about 150 msec When a continuing current phase follows a return stroke, the total current model will be given by adding I_c to either Equation 17 or 18

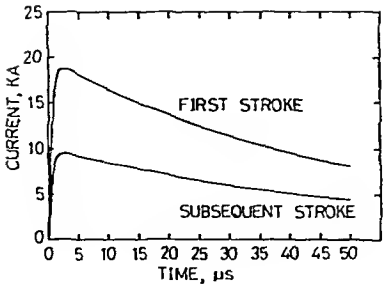

FIGURE 15. First and subsequent return stroke currents with time calculated by adding the intermediate current from Equations 17 and 18.

The charge transfer can easily be obtained by integrating the equations for each of the currents above, and are given as follows: For the first return stroke

$$Q_R = I_o \left(\frac{\beta - \alpha}{\alpha\beta}\right) \tag{19}$$

For the subsequent return strokes

$$Q_{SR} = \frac{I_o}{2}\left(\frac{\beta - \alpha}{\alpha\beta}\right) \tag{20}$$

For the intermediate current

$$Q_I = I_{oi}\left(\frac{\delta - \gamma}{\gamma\delta}\right) \tag{21}$$

For the continuing current

$$Q_C = I_c T_c \tag{22}$$

For the numerical values of the constants given by Cianos and Pierce[9] the respective transferred charges are $Q_R = 1.0$ C, $Q_{SR} = 0.5$ C, $Q_I = 1.8$ C and $Q_c = 22.5$ C. The charge transfer by the complete first and subsequent return strokes without continuing current are thus 2.8 C and 2.3 C. When the return strokes are followed by the continuing current, the complete charges transferred by the first and subsequent return strokes are 23.5 C and 23 C, respectively. These values are in good agreement with experimental values.

In the Bruce-Golde model, the return stroke current at any given time is assumed to be uniform with height below the return stroke wavefront and zero above. The current in the channel below the wavefront is identical to the current at ground level:

$$\begin{aligned} I(z,t) &= I(0,t) \qquad z \leq \ell \\ I(z,t) &= 0 \qquad\quad z > \ell \end{aligned} \tag{23}$$

As the return stroke propagates upward for times after the current peak is reached, the current in the channel decreases. As a result, the Bruce-Golde type return stroke

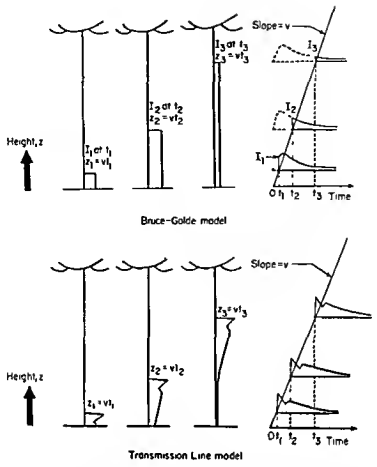

FIGURE 16 Return stroke current distributions for the Bruce Golde and transmission line models (From Lin, Y T Uman, M A, and Standler R B J Geophys Res 85 1571 1980 With permission)

lowers charge from the channel to ground, charge originally stored in the corona envelope of the leader The current that characterizes the Bruce-Golde model is schematically shown in Figure 16 [37]

The Bruce-Golde model has been much used for analytical computations However, it is not physically reasonable for the return stroke current to be uniform instantaneously with altitude Dennis and Pierce[10] modified the Bruce-Golde model to correct this deficiency They suggested that the current wave travels up the channel with a velocity which is not larger than the velocity of the Bruce-Golde model This concept of a traveling wave of current regards the channel as a quasi-transmission line which is charged by the preceding leader process and then discharged by the return stroke.

In this transmission line model the current waveform at ground level is assumed to propagate up the channel as it would propagate along an ideal transmission line

$$\begin{aligned} I(z,t) &= I(t - z/v) \qquad z \leq \ell \\ I(z,t) &= 0 \qquad\qquad\quad z > \ell \end{aligned} \tag{24}$$

where the return stroke velocity v is assumed constant Because the transmission line model requires the same current to propagate across any height of the channel, as schematically shown in Figure 16, no leader corona charge can be removed from the return stroke channel during the return-stroke propagation time, charge being only

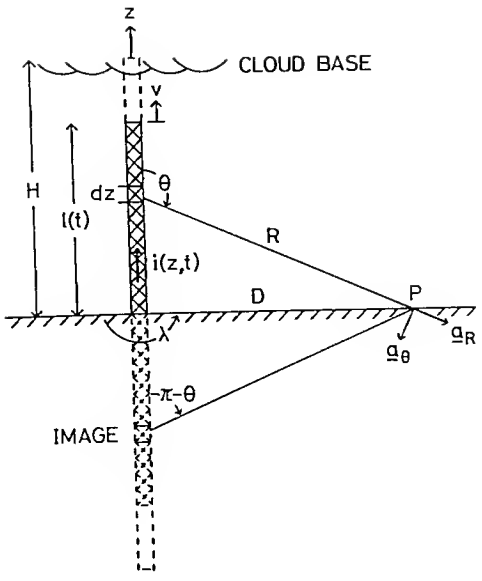

FIGURE 17. Geometry of an idealized lightning return stroke channel.

transferred from the top to the bottom of the channel. This transmission-line return-stroke model has been widely used by Uman and co-workers,[26 81 89 90] Leise and Taylor,[25] and Price and Pierce[49] to find a typical current wave shape and return stroke velocity from the measured electric and magnetic fields produced by lightning within about 200 km. If this approach proves to be valuable, it will enable us to study the characteristics of "normal" lightning in different geographical locations and under a variety of meteorological conditions. Here the "normal" lightning does not necessarily discharge to the special instrumented tower but discharge to any natural land.

Electromagnetic Radiation

Uman and co-workers[27 28 35 79-81 85 88] have developed a general theory of the electromagnetic radiation from a finite-length antenna which is regarded as an assumed lightning channel, and applied it to a large amount of experimental data. It is very instructive to follow closely with their theory.[85]

Consider a straight vertical antenna of height H above a perfectly conducting ground plane as an idealized lightning channel. Geometry of the antenna with self-explanatary notations is shown in Figure 17. Boundary conditions at the plane are satisfied by adding the image antenna shown dashed in Figure 17. The radius of the antenna cross-section is assumed to be very small compared with the wavelength of any radiation under consideration. The current at any height is assumed to be some arbitrary continuous function, i(z,t), which is zero everywhere at $t = 0$.

Consider an infinitesimal vertical current dipole of length dz having a current i(z,t) on the antenna as shown in Figure 17. The electric and magnetic fields at an observation point on the plane a horizontal distance D from the antenna base are the sum of the fields from the real and image dipoles.

The differential magnetic flux density $d\underline{B}$ of the dipole can be determined from the differential retarded vector potential $d\underline{A}$, i.e.

$$d\underline{B} = \nabla \times d\underline{A} \tag{25}$$

As the assumed current has only vertical component, the differential vector potential in Equation 25 has only a z-component, which is given by

$$dA_z = \frac{\mu_0}{4\pi} \frac{i(z,t - R/c)}{R} dz \tag{26}$$

where μ_0 is permeability of space and c is the velocity of light If we use a spherical coordinate system with an origin at the dipole, then

$$d\underline{A} = \frac{\mu_0}{4\pi} \left[i(z,t - R/c) \frac{\cos\theta}{R} \underline{a}_R - i(z,t - R/c) \frac{\sin\theta}{R} \underline{a}_\theta \right] dz \tag{27}$$

where a_R, a_θ and a_λ (in Equation 28) are the unit vectors sketched in Figure 17 Evaluating the curl gives

$$\nabla \times d\underline{A} = \frac{\mu_0 dz}{4\pi} \left[-\frac{\sin\theta}{R} \frac{\partial i(z,t - R/c)}{\partial R} + \frac{\sin\theta}{R^2} i(z,t - R/c) \right] \underline{a}_\lambda \tag{28}$$

Converting the space derivatives to time derivatives

$$\frac{\partial i(z,t - R/c)}{\partial R} = -\frac{1}{c} \frac{\partial i(z\ t - R/c)}{\partial t} \tag{29}$$

we have

$$d\underline{B} = \frac{\mu_0 dz}{4\pi} \sin\theta \left[\frac{i(z,t - R/c)}{R^2} + \frac{1}{cR} \frac{\partial i(z\ t - R/c)}{\partial t} \right] \underline{a}_\lambda \tag{30}$$

The differential magnetic induction from the image dipole can be calculated in the same way with replacing θ by $\pi - \theta$ Then total magnetic induction at the observation point can be calculated by adding the both effects from the actual and image dipoles The resultant magnetic induction is in the λ direction,

$$dB_\lambda(R,\theta,t) = \frac{\mu_0 dz}{2\pi} \sin\theta \left[\frac{i(z,t - R/c)}{R^2} + \frac{1}{cR} \frac{\partial i(z,t - R/c)}{\partial t} \right] \tag{31}$$

The electric field is given in terms of retarded scalar and vector potentials as

$$\underline{\Gamma} = -\nabla\phi - \frac{\partial \underline{A}}{\partial t} \tag{32}$$

where the scalar potential is given by

$$\phi(\underline{R},t) = -c^2 \int_0^t \nabla \cdot \underline{A}\, d\tau \tag{33}$$

Evaluating the divergence of the differential vector potential gives

$$\nabla \cdot d\underline{A} = \frac{dz\mu_0 \cos\theta}{4\pi} \left[-\frac{1}{R^2} i(z,t - R/c) + \frac{1}{R} \frac{\partial i(z,t - R/c)}{\partial R} \right] \tag{34}$$

The differential scalar potential $d\phi$ is

$$d\phi(R,\theta,t) = \frac{dz \cos\theta}{4\pi\epsilon_0} \left[\frac{1}{R^2} \int_0^t i(z,\tau - R/c)\, d\tau + \frac{i(z,t - R/c)}{cR} \right] \tag{35}$$

From Equations 27, 32, and 35 we obtain the following expression for the differential electric field due to the infinitesimal source dipole:

$$\begin{aligned} d\underline{E}(R,\theta,t) = \frac{dz}{4\pi\epsilon_0} \Bigg\{ & \cos\theta \left[\frac{2}{R^3} \int_0^t i(z,\tau - R/c)\, d\tau \right. \\ & \left. + \frac{2}{cR^2} i(z,t - R/c) \right] \underline{a}_R \\ & + \sin\theta \left[\frac{1}{R^3} \int_0^t i(z,\tau - R/c) d\tau \right. \\ & + \frac{1}{cR^2} i(z,t - R/c) \\ & \left. + \frac{1}{c^2 R} \frac{\partial i(z,t - R/c)}{\partial t} \right] \underline{a}_\theta \Bigg\} \end{aligned} \tag{36}$$

The total electric field is the vector sum of the fields from the real and image dipoles and is in the vertical direction:

$$\begin{aligned} dE_z(R,\theta,t) = \frac{dz}{2\pi\epsilon_0} \Bigg[& \frac{(2 - 3\sin^2\theta)}{R^3} \int_0^t i(z,\tau - R/c)\, d\tau \\ & + \frac{(2 - 3\sin^2\theta)}{CR^2} i(z,t - R/c) \\ & - \frac{\sin^2\theta}{c^2 R} \frac{\partial i(z,t - R/c)}{\partial t} \Bigg] \end{aligned} \tag{37}$$

The total electric and magnetic fields from the complete vertical antenna of height H are obtained by integrating the infinitesimal dipole solutions 31 and 37 over the antenna.

$$B_\lambda(D\,t) = \int_0^H dB_\lambda(R,\theta,t)$$

$$= \frac{\mu_o}{2\pi}\int_0^H \frac{\sin\theta}{R^2}\,i(z,t-R/c)\,dz \qquad (38)$$

$$+ \frac{\mu_o}{2\pi}\int_0^H \frac{\sin\theta}{cR}\,\frac{\partial i(z\,t-R/c)}{\partial t}\,dz$$

The first term on the right of Equation 38 is the induction magnetic field and the second term the radiation magnetic field

And

$$E_z(D\,t) = \int_0^H dE_z(R\,\theta\,t)$$

$$- \frac{1}{2\pi\epsilon_o}\int_0^H \frac{(2-3\sin^2\theta)}{R^3}\int_0^t i(z\,\tau - R/c)\,d\tau dz$$

$$+ \frac{1}{2\pi\epsilon_o}\int_0^H \frac{(2-3\sin^2\theta)}{cR^2}\,i(z,t-R/c)\,dz \qquad (39)$$

$$- \frac{1}{2\pi\epsilon_o}\int_0^H \frac{\sin^2\theta}{c^2R}\,\frac{\partial i(z,t-R/c)}{\partial t}\,dz$$

The first term on the right of Equation 39 is the electrostatic field, the second term the induction electric field and the third term the radiation electric field

Uman et al [45] demonstrated solutions to Equations 38 and 39 for the transmission line model The results of computer calculations are shown in Figure 18 In these calculations they assumed that the current terminates at H in Figure 17 and that no current reflected downward from the top of the antenna The height, H = 4 8 km, and the speed of propagation, v = 8 × 10⁷ m/sec, were assumed The input current waveform (a) in Figure 18 was chosen to resemble a return stroke in a lightning discharge to ground

In Figure 18, the radiation field terms dominate the E and B waveforms at the initial time for all distances because the initial time derivative of the current is large At 1 km, the near field terms produce a large hump in E_z, which represents the integrals of the current being modulated by the geometrical factors as the current propagates upward The magnetic field at 1 km is dominated by the induction field term The final value of the magnetic field is zero at all distances because the final current and time-rate-of-change of current were chosen to be zero The electric field, on the other hand, has a finite final value because the current waveform results in the effective transfer of a charge

$$Q = \int_0^\infty i\,dt \qquad (40)$$

from ground to the top of the antenna which creates a dipole field given by the well-known relation

$$E_z(D=\infty) = -\frac{1}{2\pi\epsilon_o}\,\frac{QH}{(H^2+D^2)^{3/2}} \qquad (41)$$

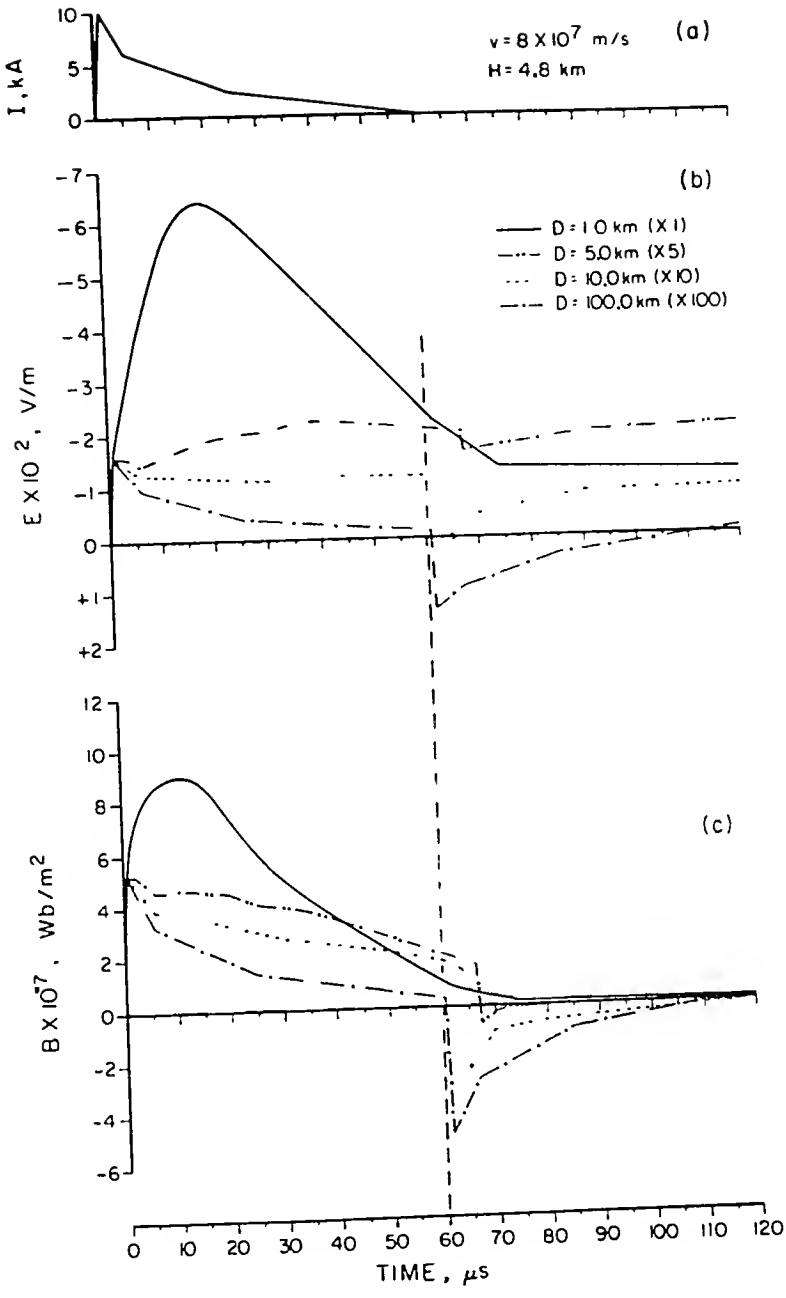

FIGURE 18. Return stroke electric (middle) and magnetic (bottom) fields as a function of distance for the current shown in the top panel and the return stroke velocity $v = 8 \times 10^7$ m/sec calculated by the transmission line model (From Uman, M. A., Brantley, R. D., Lin, Y. T., Tiller, J A., Krider, E. P., and McLain, D. K., *J. Geophys. Res.*, 80, 373, 1975. With permission.)

There are seen the "mirror images" of the initial field peak at large distances in Figure 18 for times after the current pulse reaches the top of the antenna. The initial radiation field peak arises because a propagating current wave was turned on at the bottom of the antenna, and the mirror image field peak arises because the same current has been turned off at the top. Field behavior that could be interpreted as indicating these features has been only occasionally observed and only for first return strokes.[28]

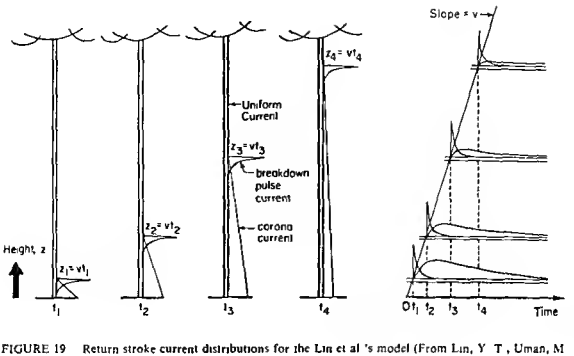

FIGURE 19 Return stroke current distributions for the Lin et al 's model (From Lin, Y T, Uman, M A and Standler R B, *J Geophys Res* 85, 1571 1980 With permission)

The Model of Lin et al

The Bruce-Golde model and the transmission line model represent two extreme cases of what might be expected to occur in the return stroke channel

Lin et al [27] tested these two most commonly used lightning return stroke models, Bruce-Golde and transmission line models, against subsequent-stroke electric- and magnetic-field waveforms measured simultaneously at near and distant stations and showed that these models do not fit very well to the experimental data Lin et al [27] then proposed a new return stroke model which is schematically shown in Figure 19 The new model is composed of three separate current components (1) A short-duration upward propagating pulse of current associated with the upward-propagating electrical breakdown at the return-stroke wavefront It will traverse the channel with the return-stroke wavefront velocity and is treated by the transmission line model The velocity cannot be determined by the new model and is assumed to be 10^8 m/sec The current pulse is assumed to be responsible for the initial peak of the electric and magnetic radiation fields (2) A uniform current that may already be flowing (leader current) or may start to flow soon after the return stroke begins In order to determine the uniform current, I_u, is measured the slope, dE/dt, of the electric field near the lightning in the linear ramp region when the field is primarily electrostatic, and I_u is computed from the time rate of change of the relation between a point or spherical charge located at the top of the channel and the resultant electrostatic field

$$I_\mu = -\frac{2\pi\epsilon_0 (H^2 + D^2)^{3/2}}{H} \frac{dE(D,t)}{dt} \tag{42}$$

Lin et al [27] assumed that H for subsequent strokes in Florida is 7 5 km [20] (3) "Corona current" which is caused by the radially inward and then downward movement of the charge initially stored in the corona sheath around the leader channel The corona current is idealized as a number of current sources distributed along the channel Each source is turned on when the peak of the return stroke breakdown-pulse current reaches the altitude of the source At each height the corona-current wave shape injected into the channel is assumed to be identical, but its magnitude decreases exponen-

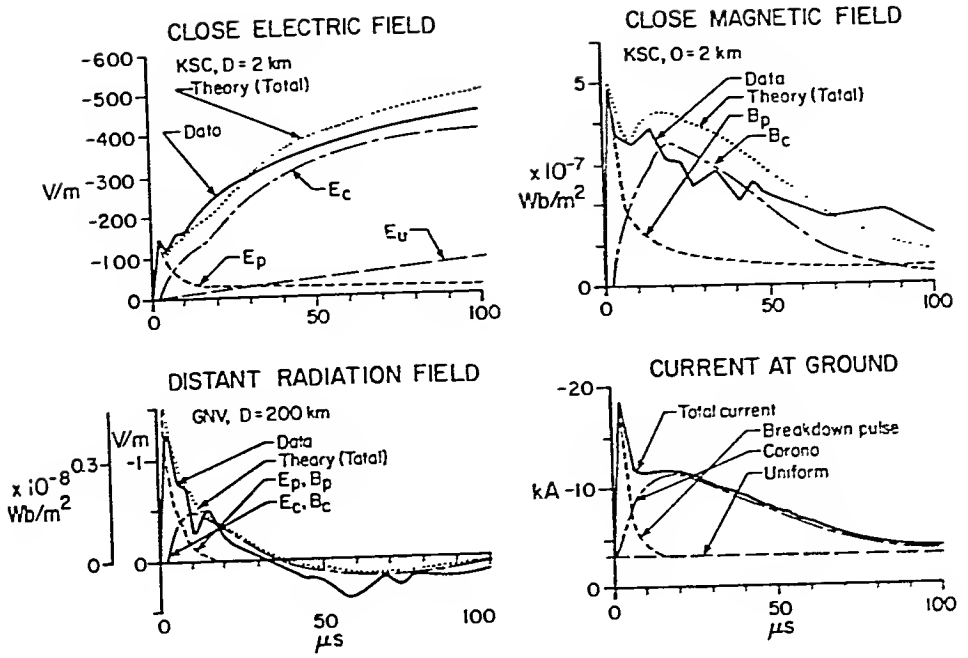

FIGURE 20. An example of Lin et al.'s model fit to two-station electric and magnetic field measurements. KSC is Kennedy Space Center and GNV is Gainesville, Fla. (From Lin, Y. T., Uman, M. A., and Standler, R. B., *J. Geophys. Res.*, 85, 1571, 1980. With permission.)

tially with height. The corona current is assumed to flow into the channel and to ground with the speed of light.

An example of two-station data analyzed by Lin et al.[27] using the new model is shown in Figure 20. The matching of the model fields to the data is considered adequate. The subsequent stroke current waveforms shown in Figure 20 agree reasonably well with the subsequent return-stroke current waveform obtained by direct measurement as illustrated in Figure 14.

The properties of the current for subsequent return strokes derived from the new model were presented as histograms of the peak current, the uniform current, the charge transfer by breakdown pulse current, the charge transfer by corona current, and the total charge transfer in Figures 21, 22, 23, 24, and 25, respectively. The mean value of the subsequent return stroke peak current in Fig. 21 is 23 kA and the median value is 20 kA. The latter value is a factor of 2 higher than the 12-kA median of Berger et al.[3] The mean of uniform current amplitude for subsequent return strokes in Figure 22 is 3.2 kA and the median is 2.3 kA. The origin of the uniform current can be considered to be the continuation of dart leader current. As the dart leader lasts about 1 msec, the median charge transfer is about 2.3 C. This value agrees well with the estimate given by Uman[78] from data of Brook et al.[7] The mean of charge transfer by the breakdown pulse current for subsequent return strokes in Figure 23 is 0.093 C. The majority of breakdown pulse current contain charge of less than 0.1 C. The mean of corona current charge in Figure 24 is 0.56 C and the median is 0.45 C.

The total charge transferred by the return stroke in the first 100 μsec is the time integral of the sum of the breakdown pulse current, the corona current and the uniform current. The mean of total charge transfer in Figure 25 is 0.95 C and the median is 0.85 C. These values agree well with the measurements made by Brook et al.[7] for subsequent return strokes without continuing current following the strokes.

As described above the new model of lightning return-stroke current presented by

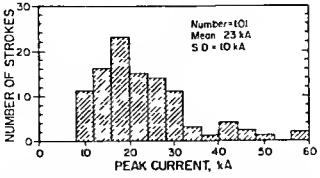

FIGURE 21 Histogram of subsequent return stroke peak current derived from 101 electric field data observed simultaneously at two stations within about 200 km distances (From Lin Y T Uman M A and Standler R B *J Geophys Res* 85, 1571, 1980 With permission)

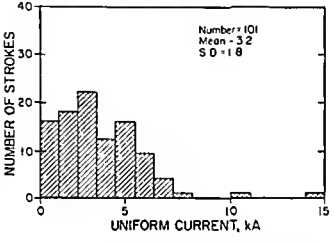

FIGURE 22 Histogram of subsequent return stroke uniform current derived from 101 electric field data observed simultaneously at two stations within about 200 km distances (From Lin Y T, Uman M A and Standler R B *J Geophys Res* 85 1571 1980 *With permission*)

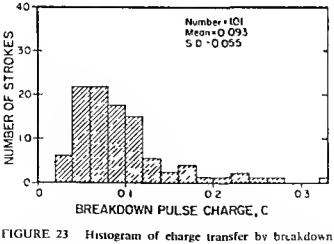

FIGURE 23 Histogram of charge transfer by breakdown pulse current for subsequent return strokes derived from 101 electric field data observed simultaneously at two stations within about 200 km distances (From Lin, Y T, Uman, M A, and Standler, R B, *J Geophys Res*, 85, 1571, 1980 With permission)

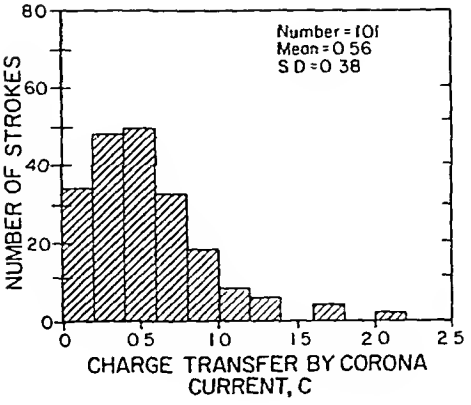

FIGURE 24. Histogram of charge transfer by corona current for subsequent return strokes derived from 101 electric field data observed simultaneously at two stations within about 200 km distances (From Lin, Y. T., Uman, M. A., and Standler, R. B., *J. Geophys. Res.*, 85, 1571, 1980. With permission.)

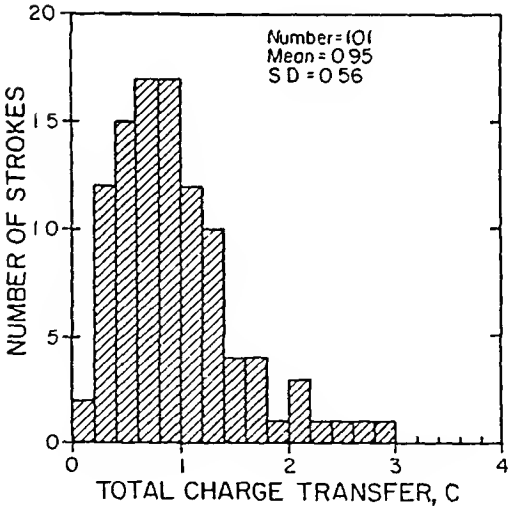

FIGURE 25. Histogram of subsequent return stroke total charge transfer derived from 101 electric field data observed simultaneously at two stations within about 200 km distances (From Lin, Y. T., Uman, M. A., Standler, R. B., *J. Geophys. Res.*, 85, 1571, 1980. With permission.)

Lin et al.[27] is physically plausible and has reproduced reasonably acceptable lightning characteristics. The major disadvantage of the new model is, however, the need to choose arbitrarily the value for return stroke velocity.

Discussion on Space Dependent Nature

Time and space dependent nature of lightning return stroke was discussed by Rai[54] who applied the theory of ionizing potential waves. Albright and Tidman[1] derived the relation between the velocity v and the electric field E at the wavefront of the ionizing potential waves

$$v = \frac{e(1 + T_e/V_i)}{m\nu}\Gamma \tag{43}$$

where m and e are electron mass and charge respectively, ν is elastic scattering frequency of electrons, T_e is the electron temperature of the return stroke channel ($\simeq 3 \times 10^4$K), V, is the ionization potential of constituent gases, and $(T_e/V_i)^2 \ll 1$ was assumed The conductivity of the stepped-leader channel in the immediate neighborhood of the return stroke tip during the return stroke ascent is assumed at time t^{3a}

$$\sigma_t = \sigma_0 e^{-\rho t} \tag{44}$$

where σ_0 and ρ are the constants If the return stroke current can be assumed as $I = \sigma_t E_t$ then Equation 43 is transformed to

$$v_t = \frac{e(1 + T_e/V_i)}{m\nu}\frac{J_t}{\sigma_t} \tag{45}$$

where $J_t = I_t/A$, A being the area of cross-section of the channel which is assumed to be constant with time at all points along the channel The time dependent return stroke velocity can be obtained by combining Equations 8, 44 and 45

$$v_t = v_0 (e^{-at} - e^{-bt}) \tag{46}$$

where

$$v_0 = \frac{e(1 + T_e/V_i)I_0}{m\nu A\sigma_0}, \quad a = \alpha - \rho \quad \text{and} \quad b = \beta - \rho$$

The distanee travelled by the tip of the return stroke can be found from Equation 46

$$\begin{aligned} z &= \int_0^t v_t dt \\ &= v_0 \left(-\frac{e^{-at}}{a} + \frac{e^{-bt}}{b} + \frac{1}{a} - \frac{1}{b}\right) \end{aligned} \tag{47}$$

The second term on the right of Equation 47 can be ignored because it is much smaller than other terms when t is large enough Then Equation 47 is solved for the time t,

$$t = -\frac{1}{a} \ln \frac{aH}{v_0}\left(1 - \frac{z}{H}\right) \tag{48}$$

where $H = v_0(1/a - 1/b)$ is the total length of the return stroke channel Elimination of t from Equations 44 and 48 yields the spatial variation of conductivity of the stepped-leader channel in the immediate neighborhood of the return stroke tip, i e ,

$$\sigma_z = \sigma_0 \left(1 - \frac{a}{b}\right)^{\rho/a} \left(1 - \frac{z}{H}\right)^{\rho/a} \tag{49}$$

Eliminating t from Equations 46 and 48 yields the spatial velocity variation of the tip of the return stroke:

$$v_z = v_0 \left(1 - \frac{a}{b}\right)\left[\left(1 - \frac{z}{H}\right) - \left(1 - \frac{a}{b}\right)^{b/a-1}\left(1 - \frac{z}{H}\right)^{b/a}\right] \tag{50}$$

The spatial variation of the return stroke current at the tip, Iz, is found from Equations 45, 49, and 50:

$$I_z = I_{0,0}\left[\left(1 - \frac{z}{H}\right)^{\rho/a+1} - \left(1 - \frac{a}{b}\right)^{b/a-1}\left(1 - \frac{z}{H}\right)^{(b+\rho)/a}\right] \tag{51}$$

where

$$\begin{aligned} I_{0,0} &= \frac{Am\nu}{e(1 + T_0/V_i)}\sigma_0 v_0 \left(1 - \frac{a}{b}\right)^{\rho/a+1} \\ &= I_0\left(1 - \frac{a}{b}\right)^{\rho/a+1} \end{aligned} \tag{52}$$

Equation 51 gives the current at the moment when the tip of the return stroke arrives at a height z. As the tip moves up to distances larger than z, the constituted current arrives at that point until the channel extends into the cloud. Thus at a given point there is also a time variation of the current. From a point above z the current waveform comes to z at a time z/v later. For a time less than z/v, the current is zero. Hence both the spatial and temporal variation of current may be combined together,

$$I_{z,t} = I_{z,0}\left[e^{-\alpha(t - z/v)} - e^{-\beta(t - z/v)}\right] \tag{53}$$

where

$$\begin{aligned} I_{z,0} &= I_{0,0}\left[\left(1 - \frac{z}{H}\right)^{\rho/a+1} - \left(1 - \frac{a}{b}\right)^{b/a-1}\left(1 - \frac{z}{H}\right)^{(b+\rho)/a}\right] \\ &= I_0\left(1 - \frac{a}{b}\right)^{\rho/a+1}\left[\left(1 - \frac{z}{H}\right)^{\rho/a+1} - \left(1 - \frac{a}{b}\right)^{b/a-1}\left(1 - \frac{z}{H}\right)^{(b+\rho)/a}\right] \end{aligned} \tag{54}$$

To see the spatial variation of the return stroke current and velocity, $I_{z,0}$ in Equation 54 and v_z in Equation 50 were calculated as a function of z/H, where I_0 = 22 kA, v_0 = 9×10^7 m/sec, a = 6×10^4 s^{-1}, b = 7×10^5 s^{-1} and ϱ = a were assumed. The results are shown in Figure 26. The value of $I_{z,0}$ becomes maximum at a height of z/H≃0.08. This is a little larger than the height where the breakdown streamer from the ground meets the downward propagating stepped-leader tip. Because of the maximum ionization near the tip of the stepped-leader, the current attains a maximum at this height. The calculated return stroke velocity increases initially, attains a maximum around z/H≃0.13 and then decreases steadily.

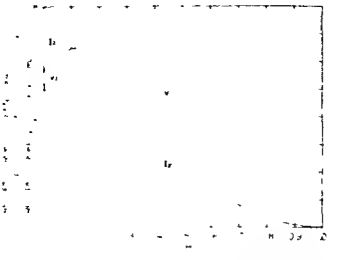

FIGURE 26 Variations of return stroke current and velocity with increasing length of channel calculated from Equations 50 and 54. H is the total stroke channel length

CONCLUDING REMARKS

The 6th International Conference on Atmospheric Electricity held at the University of Manchester during July 28 to August 1, 1980 revealed that much development of lightning-current related research has been made during the past few years. There are some topics presented at the Conference.

Some attention has been drawn to winter lightning since Takeuti et al.[65] reported "abnormal" features of winter lightning observed at the Japan sea coast. Later New Mexico's group had much interest in such thunderstorms in this wet and cold area which is opposite to the dry and hot New Mexico. Then they made joint measurements for winter thunderstorms at Hokuriku coast in Japan.

Takeuti et al.[65,66] reported that in Hokuriku area positive lightning often occurs as does usual negative lightning. They first suspected that the charge distribution in clouds and then the charge generation mechanism in winter thunderstorms are different from those of summer thunderstorms. As a result of more measurements for later years they concluded that the charge distribution in the winter thunderstorm is fundamentally the same as that in the summer thunderstorm, but strong wind shear in the upper atmosphere makes the upper positive charge shift downwindward. Moreover the cloud height is so low that lightning is sometimes produced from the upper shifted-portion of the cloud where the positive charge exists (see Figure 1). The laboratory experiment has shown that the positive breakdown occurs more easily than does the negative breakdown if the other conditions are the same. This applies to the case of the winter thunderstorm.

Takeuti et al.[106] also found that electric field oscillations are often associated with positive ground discharges observed in the winter storms in Japan and in summer storms in Sweden. The oscillations last for 40 to 150 μsec and contain frequencies 16 to 67 kHz. This is interpreted as follows: the electric conductivity of the lightning channel in the positive ground discharge is high enough to produce lightning current oscillations because of the shorter channel length of winter and high latitude lightning.

Easier artificial triggering of winter lightning than summer lightning also drew attention. Although the frequency of occurrence of winter lightning is very small compared with summer lightning, transmission line damages due to winter lightning have often been reported, and it is worthwhile investigating more detailed mechanism of winter lightning.

Lightning channel locations have been further developed by Hayenga and Warwick[101] in addition to the works by Proctor[50] and Taylor[74] outlined in the section, "Charge Structure." They used two antennas interferometer 8.7 m spacing each other. Measurements of the lightning source can be made every 2.5 μsec (400,000/sec) using 34.3 MHz pulses with 3.4 MHz bandwidth.

Proctor,[105] Taylor,[107] and Hayenga and Warwick[101] made a comparative exhibition of space-time mapping of VHF lightning source positions which jumped around in clouds. Such a dynamic nature of lightning will make modeling of the lightning current complex.

LeVine and Meneghini[104] discussed on effects of lightning channel tortuousity on the electric fields radiated from return strokes. Computer simulations using two paired exponentials of the Bruce-Golde type lightning current waveform and a piecewise linear traveling wave (i.e., transmission line) model showed that the simulated return stroke electric field could well reproduce the measured radiation field. An important consequence of tortuousity is to increase the high frequency energy in the radiated signal. A calculated radiation spectrum was in good agreement with observed data when tortuousity was taken into account.

Correlated measurements of lightning radiation fields and whistlers were made by Weidman et al.[109] The whistler measurements were made at Roberval in Canada and at Siple in Antarctica. The lightning field measurements were made at Roberval and Gainesville, Fla. It was found from these measurements that 80% of lightning which produces whistlers were ground discharges, and 10% were intracloud discharges; multiple return strokes occupied 66% of whistler-producing lightning and single return strokes did 34%. The mean peak field amplitude was 0.22±0.10 V/m for whistler producing lightning and 0.13±0.05 V/m for nonwhistler producing lightning. The maximum excitation range of these whistlers was greater than 2,200 km.

Turman[108] detected by the Vela satellite very powerful lightning flashes, the superbolts, the optical power of which ranged $10^{11}\sim10^{13}$ watts. The DMSP satellite lightning sensor has also been sampling the superbolts.[100] The average duration of the superbolts was about 1 msec. Most of them occurred in the northern hemisphere between 30° and 40° N. A significant number occurred in the northwest Pacific Ocean and the Sea of Japan.

Planetary lightning and radio emission measurements are also planned[103] for the Jupiter thunderstorms. Such satellite borne lightning observations will provide an interesting field of lightning investigation in the future.

REFERENCES

1. Albright, N. W. and Tidman, D. A., Ionizing potential waves and high-voltage breakdown streamers, *Phys. Fluids*, 15, 86, 1972.
2. Barnard, V., The approximate mean height of the thundercloud charges taking part in a flash to ground, *J. Geophys. Res.*, 56, 33, 1951.
3. Berger, K., Anderson, R. B., and Kroninger, H., Parameters of lightning flashes, *Electra*, 41, 23, 1975.
4. Boyle, J. S. and Orville, R. E., Return stroke velocity measurements in multistroke lightning flashes, *J. Geophys. Res*, 81, 4461, 1976.
5. Braginskii, S. I., Theory of the development of a spark channel, *Sov. Phys. JETP*, (Engl. transl.), 34, 1068, 1958.
6. Brook, M. and Ogawa, T., The cloud discharge, in *Lightning*, Vol. 1, Golde, R. H., Ed., Academic Press, London, 1977, chap. 6.

7 Brook, M , Kitagawa, N , and Workman, E J , Quantitative study of strokes and continuing currents in lightning discharges to ground, *J Geophys Res* , 67, 649, 1962

8 Bruce, C E R and Golde, R H , The lightning discharge *J Inst Electr Eng Part 2*, 88, 487, 1941

9 Cianos, N and Pierce, E T , A Ground-Lightning Environment for Engineering Usage, Tech rep 1, Stanford Research Institute, Menlo Park, Calif , 1972

10 Dennis, A S and Pierce, E T , The return stroke of the lightning flash to earth as a source of VLF atmospherics, *Radio Sci* 68D, 777 1964

11 Eriksson, A J , A Discussion on Lightning and Tall Structures, Special Rep ELEK 152, Council for Scientific and Industrial Research Pretoria, S Africa, July 1978

12 Evans, W H and Walker, R L , High-speed photographs of lightning at close range, *J Geophys Res* 68, 4455, 1963

13 Golde, R H , *Lightning Protection* Edward Arnold, London, 1973

14 Golde, R H , *Lightning* Vol 1 and 2 Academic Press, London, 1977

15 Hacking, C A , Observations on the negatively charged column in thunderclouds, *J Geophys Res* , 59 449, 1954

16 Hatakeyama, H , The distribution of the sudden change of electric field on the earth's surface due to lightning discharge, in *Recent Advances in Atmospheric Electricity*, Smith, L G , Ed , Pergamon Press London, 1958, 289

17 Hill, R D , Determination of charges conducted in lightning strokes *J Geophys Res* , 68, 1365, 1963

18 Hughes, H G , Differences between pulse trains of ELF atmospherics at widely separated locations, *J Geophys Res* , 76, 2116, 1971

19 Ishikawa, H , Nature of lightning discharge as origins of atmospherics *Proc Res Inst Atmospherics Nagoya Univ* 8A, 1, 1961

20 Jacobson, E A and Krider, E P , Electrostatic field changes produced by Florida lightning, *J Atmos Sci* , 33, 103 1976

21 Jones, R C , Return stroke core diameter, *J Geophys Res* 73, 809, 1968

22 Kitagawa, N and Brook, M , A comparison of intracfoud and cloud to ground lightning discharges, *J Geophys Res* , 65, 1189, 1960

23 Krehbiel, P R , Brook, M , and McCrory, R A , An analysis of the charge structure of lightning discharges to ground, *J Geophys Res* , 84, 2432, 1979

24 Krider, E P , Time resolved spectral emissions from individual return strokes in lightning discharges, *J Geophys Res* 70 2459 1965

25 Leise, J A and Taylor, W L , A transmission line model with general velocities for lightning, *J Geophys Res* , 82, 391 1977

26 Lin, Y T and Uman, M A , Electric radiation fields of lightning return strokes in three isolated Florida thunderstorms *J Geophys Res* 78, 7911 1973

27 Lin, Y T , Uman, M A , and Standler, R B , Lightning return stroke models, *J Geophys Res* , 85, 1571, 1980

28 Lin, Y T , Uman, M A , Tiller, J A , Brantley, R D , and Beasley, W H , Characterization of lightning return stroke electric and magnetic fields from simultaneous two station measurements, *J Geophys Res* , 84, 6307 1979

29 Loeb, L B , The mechanism of stepped and dart leaders in cloud-to ground lightning strokes, *J Geophys Res* 71, 4711 1966

30 Mackerras, D , A comparison of discharge processes in cloud and ground lightning flashes, *J Geophys Res* 73, 1175 1968

31 Malan, D J and Schonland, B F J , The electrical processes in the intervals between the strokes of a lightning discharge *Proc R Soc London Ser A*, 206, 145, 1951

32 Malan, D J and Schonland, B F J , The distribution of electricity in thunderclouds, *Proc R Soc London, Ser A*, 209, 158 1951

33 McCann, G D , The measurement of lightning currents in direct strokes, *Trans Am Inst Electr Eng* , 63, 1157, 1944

34 McEachron, K B , Photographic study of lightning, *Trans Am Inst Electr Eng* , 66 577, 1947

35 McLain, D K and Uman, M A , Exact expression and moment approximation for the electric field intensity of the lightning return stroke, *J Geophys Res* 76, 2101, 1971

36 Misra, R P and Rai, J , Radius of the lightning return stroke, *Inst J Electron* , 43, 369, 1977

37 Nakano, M , Characteristics of lightning channel in thunderclouds determined by thunder, *J Meteorol Soc Jpn* , 54 441, 1976

38 Oetzel, G N , Computation of the diameter of a lightning return stroke, *J Geophys Res* , 73, 1889, 1968

39 Ogawa, T and Brook, M , The mechanism of the intracloud lightning discharge, *J Geophys Res* , 69, 5141, 1964

40. Ogawa, T. and Brook, M., Charge distribution in thunderstorm clouds, *Q. J. R. Meteorol. Soc*, 95, 513, 1969.
41. Orville, R. E., High-speed, time-resolved spectrum of a lightning stroke, *Science*, 151, 451, 1966.
42. Orville, R. E., A high-speed time-resolved spectroscopic study of the lightning return stroke. III. A time-dependent model, *J. Atmos Sci.*, 25, 852, 1968
43. Orville, R. E., Helsdon, J. H., Jr., and Evans, W. H., Quantitative analysis of a lightning return stroke for diameter and luminosity changes as a function of space and time, *J. Geophys. Res.*, 79, 4059, 1974.
44. Pierce, E. T., Electrostatic field-changes due to lightning discharges, *Q. J. R. Meteorol. Soc.*, 81, 211, 1955.
45 Pierce, E. T., Latitudinal variation of lightning parameters, *J. Appl. Meteorol.*, 9, 194, 1970.
46. Pierce, E. T., Atmospherics and radio noise, in *Lightning*, Vol. I, Golde, R. H., Ed., Academic Press, London, 1977, chap. 10.
47. Plooster, M. N., Numerical model of the return stroke of the lighting discharge, *Phys. Fluids*, 14, 2124, 1971.
48. Prentice, S. A. and Mackerras, D., The ratio of cloud to cloud-ground lightning flashes in thunderstorms, *J. Appl. Meteorol.*, 16, 545, 1977.
49. Price, G. H. and Pierce, E. T., The modeling of channel current in the lightning return stroke, *Radio Sci.*, 12, 381, 1977.
50. Proctor, D. E., A hyperbolic system for obtaining VHF radio pictures of lightning, *J. Geophys. Res.*, 76, 1478, 1971.
51. Proctor, D. E., VHF Radio Pictures of Lightning, Special Rep. TEL 120, Council for Scientific and Industrial Research, Johannesburg, S Africa, 1974.
52 Prueitt, M. L., The excitation temperature of lightning, *J. Geophys. Res.*, 68, 803, 1963.
53. Radda, G. J. and Krider, E. P., Photoelectric measurements of lightning return stroke propagation speed (abstract), *Eos Trans. AGU*, 55, 1131, 1974
54. Rai, J., Current and velocity of the return stroke lightning, *J. Atmos. Terr. Phys.*, 40, 1275, 1978.
55. Reynolds, S. E. and Neill, H. W., The distribution and discharge of thunderstorm charge-centers, *J. Meteorol.*, 12, 1, 1955
56. Saint-Privat-D'Allier Research Group, Research in artificially triggered lightning in France, in *Proceedings of the Third Symposium on Electromagnetic Compatibility*, Dvorak, T., Ed., Zentrum, E. T. H., Zurich, 1979.
57 Salanave, L. E., The optical spectrum of lightning, *Science*, 134, 1395, 1961.
58. Salanave, L. E., Orville, R. E., and Richards, C. N., Slitless spectra of lightning in the region from 3850 to 6900 Angstroms, *J. Geophys. Res.*, 67, 1877, 1962
59. Schonland, B. F. J., The interchange of electricity between thunderclouds and the Earth, *Proc. R. Soc. London, Ser. A*, 118, 252, 1928.
60. Schonland, B. F. J., The diameter of the lightning channel, *Philos. Mag.*, 37, 503, 1937.
61. Schonland, B. F. J., *The Flight of Thunderbolts*, Oxford University Press, London, 1950, 63.
62. Schonland, B. F. J. and Collens, H., Progressive lightning, *Proc. R. Soc. London, Ser. A*, 143, 654, 1934.
63. Schonland, B. F. J., Malan, D. J., and Collens, H., Progressive lightning. II., *Proc. R. Soc. London, Ser. A*, 152, 595, 1935.
64. Smith, L. G., Intracloud lightning discharges, *Q. J. R. Met. Soc.*, 83, 103, 1957.
65. Stanford, J. L., Polarization of 500 kHz electromagnetic noise from thunderstorms: A new interpretation of existing data, *J. Atmos. Sci.*, 28, 116, 1971.
66. Takagi, M., The mechanism of discharges in a thundercloud, *Proc Res. Inst. Atmospherics, Nagoya Univ.*, 8B, 1, 1961.
67. Takeuti, T., Studies on thunderstorm electricity. II. Ground discharge, *J. Geomagn. Geoelectr.*, 18, 13, 1966.
68. Takeuti, T., Nakano, M., and Yamamoto, Y., Remarkable characteristics of cloud-to-ground discharges observed in winter thunderstorms in Hokuriku area, Japan, *J. Meteorol. Soc. Jpn.*, 54, 436, 1976.
69. Takeuti, T., Nakano, M., Nagatani, M., and Nakada, H., On lightning discharges in winter thunderstorms, *J. Meteorol. Soc. Jpn.*, 51, 494, 1973.
70. Takeuti, T., Nakano, M., Brook, M., Raymond, D. J., and Krehbiel, P., The anomalous winter thunderstorms of the Hokuriku coast, *J. Geophys. Res.*, 83, 2385, 1978.
71. Tamura, Y., An analysis of electric field after lightning discharges, *J. Geomagn. Geoelectr.*, 6, 34, 1954.
72. Tamura, Y., Ogawa, T., and Okawati, A., The electrical structure of thunderstorm, *J. Geomagn. Geoelectr.*, 10, 20, 1958.
73. Taylor, A. R., Diameter of lightning as indicated by tree scars, *J. Geophys. Res.*, 70, 5693, 1965.
74. Taylor, W. L., A VHF technique for space-time mapping of lightning discharge processes, *J. Geophys. Res.*, 83, 3575, 1978.

75 Teer, T L and Few, A A , Horizontal lightning *J Geophys Res* 79, 3436, 1974
76 Thomson, E M , The dependence of lightning return stroke characteristics on latitude, *J Geophys Res* 85 1050 1980
77 Uman, M A , The conductivity of lightning *J Atmos Terr Phys* , 26, 1215 1964
78 Uman, M A , *Lightning* McGraw Hill, New York, 1969
79 Uman, M A and McLain, D K , Magnetic field of lightning return stroke *J Geophys Res* , 74, 6899 1969
80 Uman, M A and McLain, D K , Radiation field and current of the lightning stepped leader, *J Geophys Res* 75, 1058, 1970
81 Uman, M A and McLain, D K , Lightning return stroke current from magnetic and radiation field measurements *J Geophys Res* 75 5143, 1970
82 Uman, M A and Orville, R E , Electron density measurement in lightning from Stark-broadening of Hα *J Geophys Res* 69 5151 1964
83 Uman, M A and Orville, R E , The opacity of lightning, *J Geophys Res* , 70, 5491, 1965
84 Uman, M A and Voshall, R E , Time interval between lightning strokes and the initiation of dart leaders *J Geophys Res* 73 497 1968
85 Uman, M A , McLain, D K , and Krider, E P , The electromagnetic radiation from a finite antenna *Am J Phys* 43 33, 1975
86 Uman, M A , Orville, R E , and Salanave, L E , The density, pressure, and particle distribution in a lightning stroke near peak temperature, *J Atmos Sci* 21 306, 1964
87 Uman, M A , Orville, R E , and Salanave, L E , The mass density, pressure, and electron density in three lightning strokes near peak temperature *J Geophys Res* 69 5423, 1964
88 Uman, M A , Brantley, R D , Lin, Y T , and Tiller, J A , Correlated electric and magnetic fields from lightning return strokes *J Geophys Res* 80 373 1975
89 Uman, M A , McLain, D K , Fisher, R J , and Krider, E P , Electric field intensity of the lightning return stroke *J Geophys Res* 78 3523, 1973
90 Uman, M A , McLain, D K , Fisher, R J , and Krider, E P , Currents in Florida lightning return strokes, *J Geophys Res* 78 3530 1973
91 Wang, C P , Lightning discharges in the tropics I Whole discharges, *J Geophys Res* , 68, 1943, 1963
92 Wang, C P , Lightning discharges in the tropics II Component ground strokes and cloud dart streamer discharge, *J Geophys Res* 68 1951, 1963
93 Wilson, C T R , On some determination of the sign and magnitude of electric discharges in lightning flashes, *Proc R Soc London, Ser A* 92 555 1916
94 Wilson, C T R , Investigations on lightning discharges and on the electric field of thunderstorms *Philos Trans R Soc London, Ser A* 221, 73 1920
95 Workman, E J and Holzer, R E , A Preliminary Investigations of the Electrical Structure of Thunderstorms Tech Notes Nat Advis Comm Aeronaut No 85 1942
96 *Workman, E J , Holzer, R E , and Pelsor, G T , The Electrical Structure of Thunderstorms,* Tech Notes Nat Advis Comm Aeronaut , No 864, 1942
97 Wormell, T W , The effects of thunderstorms and lightning discharges on the earth's electric field *Philos Trans R Soc London A* 238 249, 1939
98 Yos, J M , Transport Properties of Nitrogen, Hydrogen Oxygen and Air to 30,000°k, Tech Mem RAD TM 63 7 Avco Corporation Wilmington Mass , 1963
99 Orville, R E , Lala, G G , and Idone, V P , Daylight time resolved photographs of lightning, *Science* 201, 59 1978
100 Edgar, B C , The Distribution of Lightning Superbolts, paper presented at the 6th International Conference on Atmospheric Electricity, Manchester, July 28 to August 1, 1980
101 Hayenga, C O and Warwick, J W , Interferometric Determination of VHF Lightning Source Positions and Movement, paper presented at the 6th International Conference on Atmospheric Electricity Manchester, July 28 to August 1, 1980
102 Krehbiel, P R , Brook, M , Thermitte, R L , and Lennon, C L , Lightning Charge Structure in Thunderstorms, paper presented at the 6th International Conference on Atmospheric Electricity Manchester, July 28 to August 1, 1980
103 Lanzerotti, L J , Rinnert, K , Krider, E P , Uman, M A , Dehmel, G , Ghem, F O , and Axford, W I , Planetary Lightning and Lightning Measurements on the Galileo Probe to Jupiter's Atmosphere, paper presented at the 6th International Conference on Atmospheric Electricity, Manchester, July 28 to August 1, 1980
104 LeVine, D M and Meneghini, R , Effects of Channel Tortuousity on the Electric Fields Radiated from Return Strokes, paper presented at the 6th International Conference on Atmospheric Electricity, Manchester, July 28 to August 1, 1980

105. Proctor, D. E., Radio Pictures of Consecutive Lightning Flashes, paper presented at the 6th International Conference on Atmospheric Electricity, Manchester, July 28 to August 1, 1980.
106. Takeuti, T., Israelson, S., Lundquist, S., Aström, E., and Nakano, M., Fine Structures of Field Changes Due to Positive Ground Flashes, paper presented at the 6th International Conference on Atmospheric Electricity, Manchester, July 28 to August 1, 1980.
107. Taylor, W. L., Lightning Location and Progression Using VHF Space-time Mapping Technique, paper presented at the 6th International Conference on Atmospheric Electricity, Manchester, July 28 to August 1, 1980.
108. Turman, B. N., Detection of lightning superbolts, *J. Geophys. Res.*, 82, 2566, 1977.
109. Weidman, C. D., Krider, E. P., Park, C. G., and Blockley, B., Correlated Measurements of Lightning Radiation Fields and Whistlers, paper presented at the 6th International Conference on Atmospheric Electricity, Manchester, July 28 to August 1, 1980.
110. Ikeda, G. and Sumi, S., Lightning parameter in Japan, private communication, 1980.

QUASI-ELECTROSTATIC FIELDS WITHIN THE ATMOSPHERE

Hans Volland

TABLE OF CONTENTS

INTRODUCTION

This chapter deals with natural electromagnetic fields within the atmosphere which have periods of the order of hours or longer Three sources of such fields are known

1 Thunderstorm electricity and related phenomena
2 Interaction between tidal winds and the ionospheric plasma
3 Interaction between the solar wind and the magnetosphere

It has been known since the middle of the 18th century that the terrestrial atmosphere is always and everywhere in an electrified state Lord Kelvin called this condition the atmospheric electric field It is also known as the atmospheric potential gradient During the last 2 decades of the 19th century, it was discovered that the atmosphere has a small but measurable electric conductivity In the presence of an electric field, therefore, there must be incessant currents These currents decay within a characteristic time of

$$\tau \simeq \epsilon_0/\sigma \gtrsim 7 \text{ min} \qquad (1)$$

($\epsilon_0 = 8.85 \times 10^{-12}$ F/m, $\sigma \gtrsim 2 \times 10^{-14}$ S/m) if they are not continuously maintained by external nonelectric forces Since atmospheric electricity does not disappear, the "Fundamental Problem of Atmospheric Electricity" was evident there must be some replenishing mechanism

It was discovered from balloon measurements during the early years of this century that the electric conductivity is caused mainly by cosmic rays and that its magnitude increases nearly exponentially with altitude Wilson[115] developed the hypothesis that the earth surface and an equipotential layer at some height ($\gtrsim 40$ km) must behave like a huge capacitor The thunderstorms in which electric charge is separated act like current generators which maintain the potential gradient on a global base Observations of the electric field at oceanic stations showed that this field undergoes variations which are simultaneous over the globe To date this is the strongest argument in favor of the validity of Wilson's hypothesis For more details about the history of atmospheric electricity, see Israel [48]

The dynamo theory of the geomagnetic Sq variations presumes a horizontally extended electric polarization field at ionospheric E layer heights, e g , Chapman and Bartels [11] Only recently has that field configuration been deduced from backscatter measurements [90] A magnetospheric electric field which could be related to global plasma convection was theoretically predicted by Axford and Hines[6] and was first measured *in situ* at ionospheric heights by Heppner[49] and Frank and Gurnett [24] The problem of downward mapping of these fields into the middle and lower atmosphere was first considered by Mozer and Serlin [72]

In this chapter the main emphasis will be the electrostatic component of these fields as observed within the lower and middle atmosphere We shall only briefly mention field and current configurations within the ionospheric dynamo region or the magnetosphere Likewise, we shall not discuss electromagnetic induction effects within the Earth interior and the magnetosphere Since the conductivity plays a crucial role for electric fields and currents, a brief summary about its origin and properties will be given in the next section, followed by an outline of basic features of the three sources of atmospheric electric fields In the third section, we discuss observations made at ground based stations, at balloon altitudes, and at ionospheric heights In the last section we review theoretical approaches for describing global electric fields and currents

Methods of measurements will not reviewed. For more details the reader is referred to Chalmers,[10] Israël,[48-49] and Fahleson.[19]

BACKGROUND INFORMATION

Electric Conductivity

Lower and Middle Atmosphere

The electric conductivity depends on the existence of positive and negative ions and on their mobility. Ions and electrons are produced by cosmic rays within the lower and middle atmosphere and by radioactivity from the ground over the continents within the first 100 m. Electrons attached to molecules as well as positive ions, form molecular clusters via a hydration process within a fraction of a second. These clusters, called small ions, are among others $H^+ \cdot (H_2O)_n$ (positive ions) and $O_2^- \cdot (H_2O)_n$ and $CO_4^- \cdot (H_2O)_n$. (negative ions). The number of attached water molecules, n, depends on the water vapor content of the air and is of the order of 4 to 8.[68] Additional ions form above 15-km altitude. The ion chemistry of the atmosphere is extremely complicated and far from being completely understood. For more details see, e.g., Israel,[48] Ferguson,[20] and Arnold.[4]

Small ions disappear either by recombination with each other or by attachment to large ions or to aerosol particles. In the steady state the number of small ions can be derived from an equation of recombination.[48]

$$\frac{dn_\pm}{dt} = 0 = q - \alpha n_+ n_- - \beta n_\pm Z = q - \alpha n^2 - \beta n Z \qquad (2)$$

as

$$n = \frac{-\beta Z + \sqrt{\beta^2 Z^2 + 4\alpha q}}{2\alpha} \qquad (3)$$

where $n_+ = n_- = n$ = concentration of positive and negative small ions, q = production rate of ions, α = recombination coefficient, β = effective attachment coefficient, and Z = aerosol concentration. Equation 3 is simplified because β depends on the aerosol spectrum. Furthermore, the electric charge of the aerosol particles has to be taken into account. Production and annihilation of small ions is schematically shown in Figure 1. Only the mobile (or fast) small ions are of significance for the electric conductivity:

$$\sigma = e(n_+ k_+ + n_- k_-) \qquad (4)$$

with $k\pm$ = mobility of the ions and e = electric elementary charge.
The mobility of small ions is inversely proportional to the air density:

$$k_\pm(z) = k_{o\pm} \frac{p_o T(z)}{p(z) T_o} \qquad (5)$$

where p_o and T_o are STP pressure and temperature, and p and T are pressure and temperature at height z. Under STP conditions, $k_{o\pm}$ is a reduced mobility. Table 1 gives values of k, α, and β for different heights.

Figure 2 shows measured altitude profiles of the positive polar electric conductivity $\sigma_+ = en_+k_+$ for three stations in 30°N, 48°N, and 68°N latitude. The increase of σ_+

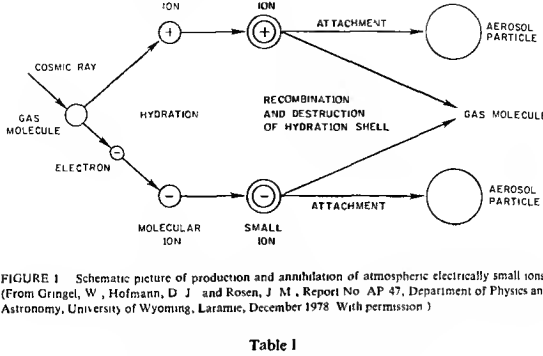

FIGURE 1 Schematic picture of production and annihilation of atmospheric electrically small ions (From Gringel, W , Hofmann, D J and Rosen, J M , Report No AP 47, Department of Physics and Astronomy, University of Wyoming, Laramie, December 1978 With permission)

Table 1
AVERAGE MOBILITY OF SMALL IONS (k), RECOMBINATION COEFFICIENT (α), AND ATTACHMENT COEFFICIENT (β) IN VARIOUS HEIGHTS (z)[30]

z (km)	k (cm/s per V/cm)	α (10^{-6} cm³/s)	β (10^{-6} cm³/s)
4	2	1 6	7
8	3	1 8	10
12	5	1 6	12
16	10	0 95	13
20	18	0 6	13
24	35	0 45	13
28	70	0 35	13

with latitude reflects the latitudinal dependence of cosmic ray intensity at the surface of the Earth [23]

From Equation 3 it follows that an increase of the aerosol concentration decreases the number of small ions The aerosol concentration over the continents depends on meteorological conditions, time of day, season, and also on man-made factors The conductivity thus varies significantly with time and space over the continents, in particular within the atmospheric exchange layer in the first 1000 m above the ground Although ion production rate over the continents is five times larger than over the oceans due to radioactivity, the loss rate due to attachment to aerosol is five times larger over the continents Therefore, the number density of fast ions is about 10^9 m^{-3} over the continents and over the oceans

The mean conductivity profile can be analytically described by the formula,[26]

$$\frac{1}{\sigma} = (2\,94\,e^{-4\,527z} + 1\,39\,e^{-0\,375z} + 0\,369\,e^{-0\,121z})10^{13}\ \Omega\ \text{m} \qquad (6)$$

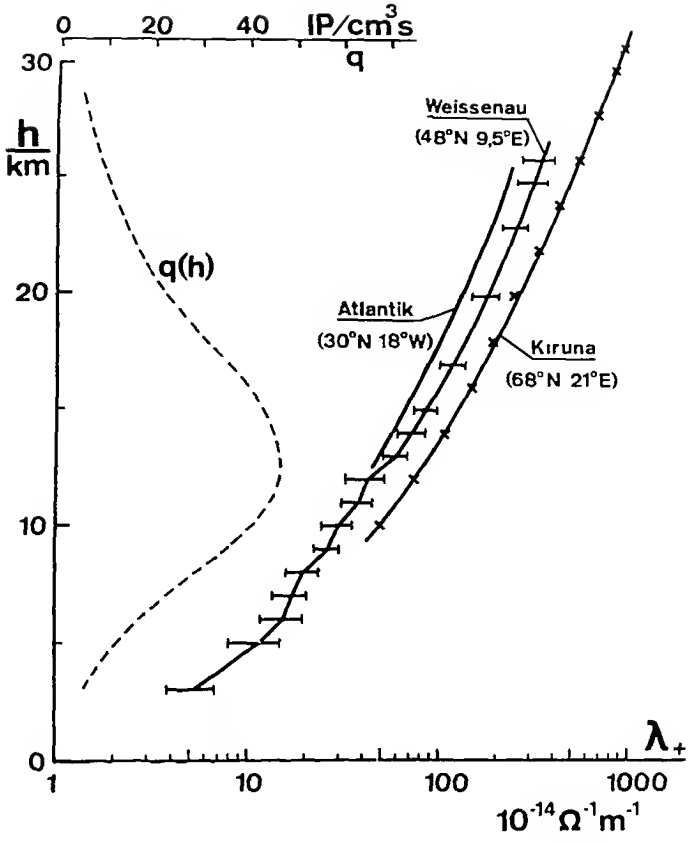

FIGURE 2. Observed electric conductivity at three different latitudes based on balloon measurements and mean ion production rate q versus height. (From Gringel, W., *Prometheus*, 7, 13, 1977 With permission)

valid at mid latitudes (z in km; σ in S/m). Figure 3 shows a mean height profile of the conductivity. Due to meteorological and other factors, deviations from that average up to several hundred percent can occur within the exchange layer. Layers of increased aerosol can significantly reduce the conductivity within the atmosphere. Gringel and Mühleisen[34] found a reduction of σ between 2- and 4-km altitude over the North Atlantic west of Africa, which they attribute to a dust layer of sand from the Sahara. The Junge layer, a region of enhanced aerosol concentration between about 17- and 25-km altitude, can act in the same manner to reduce σ in an irregular way, (e.g., Rosen and Hofmann[95]). Cipriano et al.[13] claim that σ attains a relative maximum near 40-km altitude. There is a steeper exponential increase of σ above 60 km. According to Cole and Pierce,[15] electrons become significant in that height region (see also Pierce[85]). Cosmic ray events, including cosmic rays of solar origin, can significantly influence σ due to the change in ion production.[31 87] The solar wind tends to exclude cosmic ray particles from the Earth, thus explaining why the cosmic ray flux, and therefore the ion production rate, is lower on the average during solar maximum and more intense during solar minimum.[74] A change in conductivity may not necessarily reflect a change in ionization levels, but rather a change in mobility. Significant structure has been seen in the vertical profile of mobility at mesospheric altitudes.[114]

The columnar resistance between ground and ionosphere is of the order

$$\bar{\Lambda} = \int_0^\infty \frac{dz}{\sigma} \simeq 1.3 \times 10^{17}\ \Omega\ m^2 \qquad (7)$$

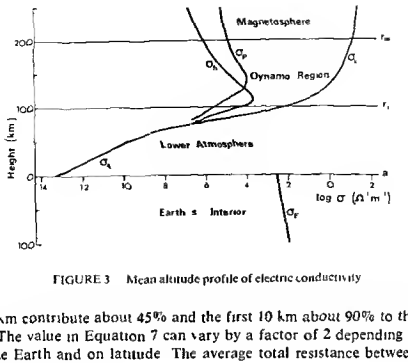

FIGURE 3 Mean altitude profile of electric conductivity

The first 2 km contribute about 45% and the first 10 km about 90% to that columnar resistance The value in Equation 7 can vary by a factor of 2 depending on the orography of the Earth and on latitude The average total resistance between Earth and ionosphere amounts to about

$$\bar{\lambda}/A \simeq 250\,\Omega \tag{8}$$

with $A = 5.1 \times 10^{14}\,m^2$ being the surface area of the Earth That value may vary with solar activity

Ionosphere

The extreme UV and soft X-radiation from the sun that produce the ionospheric layers are almost entirely absorbed above the mesopause near 85-km altitude There is a small contribution from harder X-rays, particularly during solar flares when the flux of hard X-radiation can increase by two or three orders of magnitude over its normal value within the ionospheric D layer between about 60- and 90-km altitude O_2^+ and NO^+ are the major positive ions which are produced in that region [88] N_2^+ and O^+ become increasingly important above about 100-km altitude, e g , Whitten and Poppoff [113]

The electric conductivity in these regions is governed by collisions between neutrals and ions and electrons and by the influence of the geomagnetic field on the mobility of the plasma components The mobility of the electrons is restricted by the geomagnetic field at levels above 80 km, while the ions are bound to the geomagnetic lines of force above about 140 km The differential motion of the ions and the electrons in the dynamo region between about 80- and 200-km altitude gives rise to an anisotropic behavior of the conductivity The conductivity parallel to the geomagnetic lines of force B_o, symbolized by $\sigma_\parallel$, is not affected by B_o It therefore increases strongly with height (see Figure 3) The conductivity parallel to an electric field E, however orthogonal to B_o, is called the Pedersen conductivity σ_p That conductivity is reduced with respect to $\sigma_\parallel$ and has a maximum where the ion-neutral collision rate equals the gyrofrequency of the ions That occurs near 140 km at mid latitudes The conductivity orthogonal to both E and B_o is called the Hall conductivity, σ_h Its maximum occurs near 110-km altitude and decreases with height more rapidly than σ_p (Figure 3) The effective conductivity for horizontal currents within the dynamo region is the Cowling conductivity $\sigma_c = \sigma_p + \sigma_h^2/\sigma_p$ It may reach values as large as five times the Pedersen conductivity near the geomagnetic equator

The Pedersen conductivity is carried by electrons below about 105 km and by ions above that height. The Hall conductivity is mainly due to electrons. Both conductivities depend on time of day, season, and latitude in a complicated manner. For more details see Whitten and Poppoff[113], Rishbeth and Garriott[93], or Maeda and Matsumoto.[61]

Space Charges

The surplus of one kind of charged particles within a certain volume is called space charge. Its SI unit is C/m^3. According to Poisson's law, the space charge q is related to an electric field E:

$$\nabla \cdot E = q/\epsilon \qquad (9)$$

with $\varepsilon \simeq \varepsilon_o$ the dielectric constant of the air. The global electric field decreases nearly exponentially with altitude. A space charge is therefore always present within the lower and middle atmosphere. It decreases from a few pC/m^3 at the ground to about 0.01 pC/m^3 at 10-km altitude in fair-weather areas.

An electrically inactive cloud contains positive space charge in its upper part and negative charge in its lower part, with values of the order of 1 pC/m^3. The electric conductivity is reduced in local dust and fog, so that enhanced layers of space charge with strong horizontal gradients may form.[16] In thunderclouds space charges can reach values up to tens of nC/m^3.

One source of space charge near the ground is the electrode effect, e.g., Anderson.[3] The positive and negative small ions drift in opposite directions under the influence of the vertical electric field. Since they are formed only within the air, a depletion of negative ions occurs near the ground, giving rise to positive space charges of the order of 0.1 nC/m^3 within the first 10 m above ground. This effect is most pronounced above areas covered with water, ice, or snow. Above solid soil the effect is normally absent because of the strong vertical turbulent mass exchange there. Negative ions emanating from a waterfall, positive ions created by breaking surf in a salty ocean, or fire, air, pollution, etc. are other sources of space charges.[49]

Recent electric field measurements by sounding rockets seem to indicate that space charge layers of unknown origin may be present within the middle atmosphere near 50- to 70-km altitude.[37 104] However, these measurements are still controversial.[7]

Horizontal gradients of space charge at ionospheric heights are built up by the different motion of ions and electrons driven by the tidal wind. They will be discussed in the section on "Ionospheric Dynamo Field," page 73.

Equivalent Electric Circuits

Thunderstorm Field

Figure 4 shows a schematic electric circuit simulating atmospheric electric fields and currents and their sources. Electric charge separation within thunderstorms with positive charge stored in the upper part and negative charge stored within the lower part of the cloud and convection currents maintaining that charge separation constitute an electric current source with about 1 A strength per cloud area and voltage differences between cloud top and the Earth's surface U_T of about 10 to 100 MV. The Earth and the atmosphere above about 10 km are good conductors. They behave like a spherical condensor with capacitance

$$C_A = \frac{\epsilon_o A}{d} \simeq 2\ F \qquad (10)$$

where $d \simeq 2.5$ km is the virtual distance of the plates, and A is the surface area of the Earth.

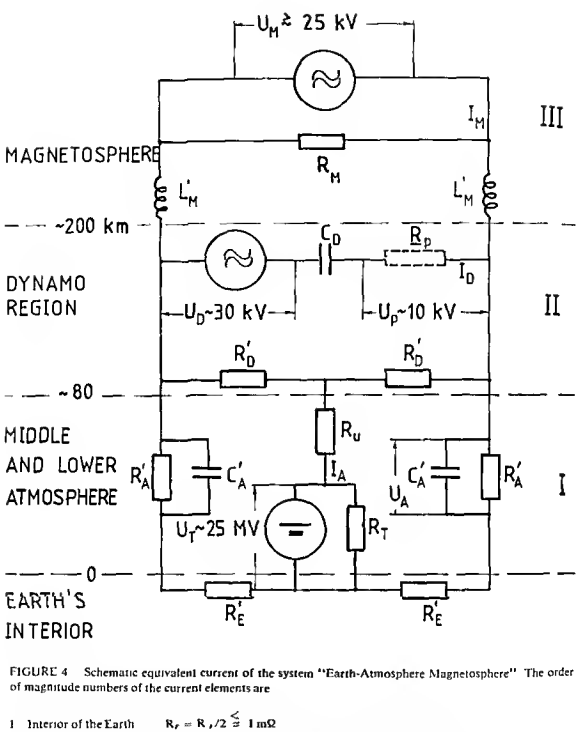

FIGURE 4 Schematic equivalent current of the system "Earth-Atmosphere Magnetosphere" The order of magnitude numbers of the current elements are

1	Interior of the Earth	$R_T = R_{T/2} \lesssim 1$ mΩ			
2	Lower and middle Atmosphere (region I)	$R_A = R_{A/2} \simeq 250\ \Omega$	$R_A \simeq 25$ kΩ	$R_T \simeq 100$ kΩ	
		$C_A = 2\,C_{A'} \simeq 2$ F	$I_A \simeq 1$ kA	$U_A \simeq 250$ kV	$\overline{U}_T \simeq 25$ MV
3	Dynamo region (Region II)	$R_D \simeq 2\,R_{D'} \simeq 20$ mΩ	$\lvert R_A \rvert \simeq 0.1\ \Omega$ (complex impedance)		
		$C_D \simeq 200$ kF	$I_D \simeq 100$ kA	$\overline{U}_D \simeq 30$ kV	
4	Magnetosphere (Region III)	$R_M \simeq 0.2\ \Omega$	$L_M \simeq 2L_{M'} \simeq 30$ H ?		
		$I_M \lesssim 1$ MA	$\overline{U}_M \lesssim 25$ kV		

Since the resistance R_M between top of the thundercloud and ionosphere is smaller than R_T between top and ground, most of the current flows from the top into the ionosphere. Because of the large height-integrated Cowling conductivity within the dynamo region ($R_D \simeq 20$ mΩ), no significant horizontal potential gradient can be maintained by this DC current there, and the electric charge will distribute nearly equally over all the dynamo region, from which it flows downward to the Earth within the

fair-weather areas. The average resistance of the fair weather area has been estimated to $R_A \simeq 250\ \Omega$ (see Equation 8). The interior of the Earth is a good conductor, with overall resistance of not more than $R_E < 1\ m\Omega$.

The interior of the Earth, like the ionosphere, can thus be considered in a first order approximation as an equipotential layer for DC currents. The return currents from the ground to the clouds are carried mainly by lightning flashes. Each thunderstorm area covering a number of active clouds transports about 0.5 to 1 A into the ionosphere.[28] With 1000 to 2000 thunderstorms at any time all over the globe, one arrives at a total current of $I_A \simeq 1$ kA and a potential difference between ground and ionosphere of about $U_A \simeq 250$ kV. The observations scatter between 180 and 400 kV.[73]

The internal resistance of the sum of all thunderstorm generators is symbolized by R_T. That resistance is of the order

$$R_T \simeq \frac{\Lambda_o}{F} \simeq 100\ k\Omega \tag{11}$$

with

$$\Lambda_o = \int_0^{z_o} \frac{dz}{\sigma} \simeq 0.8\ \bar{\Lambda}$$

the columnar resistance between ground and cloud top at z_o, and $F \simeq 10^{12} m^2$ the total area covered by thunderstorms.[52]

A smaller part of the current ($\simeq 20\%$) flows within that resistance down to the Earth in the environment of the clouds. Another small part may flow along the geomagnetic lines of force from one hemisphere into the other (simulated in Figure 4 by the resistance R_M of the magnetosphere). That resistance acts like a shunt of the dynamo resistance R_D.

The electric charge stored on one plate of the condensor can be estimated to

$$Q_A = C_A U_A \simeq 500\ kC$$

The voltage U_A would then decrease to 1/e after a delay time of

$$\tau_A = R_A C_A \simeq 500\ sec \tag{12}$$

if the thunderstorm activity should suddenly cease. In order to maintain the potential difference U_A, thunderstorm activity must be present at all times.

From the foregoing discussion, it is evident that the DC currents and voltages measured at the ground or within the lower atmosphere are rather noisy. The sources themselves (the thunderstorm voltage U_T) change with time and location, influencing U_A and I_A with characteristic times as small as several minutes. Changes in R_u, R_T, or R_A may also give rise to variations of U_A and I_A. In particular, a varying column resistance (Equation 7) modulates the local electric field and current density. The fair weather fields and currents are modified significantly near thunderstorms. In addition, precipitation, blowing snow and dust, and rising or descending space charge layers all behave like local generators of electric current systems.

Ionospheric Dynamo Field

Tidal wind systems generated within the entire atmosphere by differential heating of the sun interact with the ionospheric plasma above about 80-km altitude. Collisions

between neutrals and electrons become of minor importance above 80 km, and the electrons start to gyrate along the geomagnetic lines of force This happens above about 140-km altitude for ions, so that they essentially move with the neutral wind below that height It is this differential motion of electrons and ions in the height region between 80 and 200 km that is responsible for an essentially horizontal electric current

Charge separation between electrons and ions generates a secondary electric polarization field E_p The configuration of that field is such that its contribution to the electric current together with the current driven by the Lorentz field $V \times B_o$ leads to a source-free electric current density j

$$\operatorname{div} j = \operatorname{div} [\bar{\sigma} (E_p + V \times B_o)] = 0 \qquad (13)$$

with V the horizontal tidal wind and σ the horizontal conductivity tensor, e g , Chapman and Bartels [1] It is that horizontally directed polarization field E_p which can be measured by an observer moving with the Earth

Only those tidal winds can generate observable dynamo currents which have vertical wavelengths comparable to or larger than the thickness of the dynamo layer The most important wind systems belong to the diurnal (1,−2) tidal wave which is evanescent below 100-km altitude,[53 100 103] and to the semidiurnal (2,2) and (2,4) tidal waves [91]

Feedback between tidal wind and plasma can be simulated by the equivalent current II in Figure 4 [107] The AC voltage source U_o with period τ/m (τ = 24 hr, m = 1, 2,) is the solar differential heating The capacitance C_D acts like an internal resistance of the source depending only on nonplasma parameters

$$C_D = \frac{\bar{\rho}_o \, \Delta z}{4 B_o^2} \qquad (14)$$

($\bar{\rho}_o$ = mean density of the air at the center of the dynamo region, Δz = effective thickness of the dynamo region, and B_o = geomagnetic field) The voltage U_p is the meridionally averaged zonal potential difference of the electric polarization field during one half-period A voltage of 10 kV in Figure 4 corresponds to the diurnal tide, thus yielding a half-period of 12 hr This voltage U_p is proportional to the current I_A, the proportional factor being a complex impedance R_p

The total dynamo current I_D within one hemisphere is of the order of 100 kA The load resistance R_D is the global mean height-integrated reciprocal Cowling conductivity within the dynamo region

$$R_D = 2R'_D \simeq \frac{1}{\int_{z_1}^{z_2} \sigma_c \, dz} \simeq \frac{1}{\sigma_c \, \Delta z} \simeq 20 \text{ m}\Omega \qquad (15)$$

Note that all values in Figure 4 are only order-of-magnitude numbers The actual numbers may vary by at least a factor of 2

The movement of an electrically conducting medium (the ionospheric plasma), driven mechanically by the neutral wind against an external magnetic field (the geomagnetic field), and the induction of electric voltages and currents in that system (the polarization field and the Sq current) correspond to a technical dynamo The load resistance of the technical dynamo where energy is dissipated corresponds to R_p in Figure 4, while the self-inductance of the coil corresponds to R_p in Figure 4 Even if

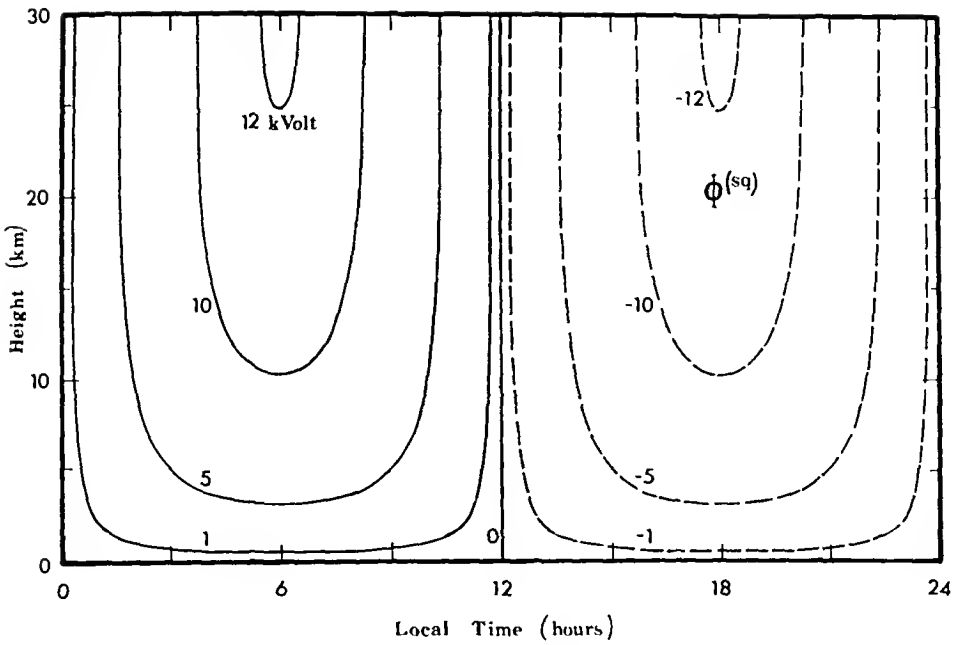

FIGURE 5. Equipotential lines of the electric polarization field of the Sq current versus local time and height within lower and middle atmosphere. Equatorial cross section (From Volland, H., *J. Geophys. Res.*, 77, 1961, 1972. With permission.)

the load resistance is zero (short circuit), the self-inductance (charge separation) prevents the current from becoming infinitely large.

The magnetospheric resistance R_M and the atmospheric resistance R_A act like shunts within current system II in Figure 4. Currents through the magnetosphere along geomagnetic field lines can only flow if a significant voltage difference exists between the two conjugate footpoints of a given line. That may be the case during solstice conditions. Maeda and Murata[62] estimated that not more than 10% of the dynamo currents flow along geomagnetic field lines during solstice.

The currents flowing within the lower atmosphere and the ground are of the order of

$$I \simeq \frac{R_D}{R_A} I_D \simeq 10^{-4} I_D \simeq 10\,A \qquad (16)$$

which is only about 1% of the thunderstorm current I_A.

Note that this current is an AC current varying with local time and latitude.

Mapping the horizontal electric polarization field E_p down to the lower atmosphere leads to equipotential lines as shown in Figure 5. These equipotential lines, which are nearly vertical down to about 20-km altitude, progress into a horizontal direction near the well-conducting Earth. The vertical field strength at the ground is of the order of 1 V/m, which is smaller by a factor of about 100 as compared with the thunderstorm field at the ground. Therefore, it appears to be rather difficult to filter that small signal out of the noisy thunderstorm field.

The AC dynamo current behaves like a huge antenna system from which electromagnetic waves are emitted. The system "dynamo region-earth interior" can be considered as a transformer with the dynamo region as the primary winding, and the interior of the Earth as the secondary winding of a coil. The induced electromagnetic

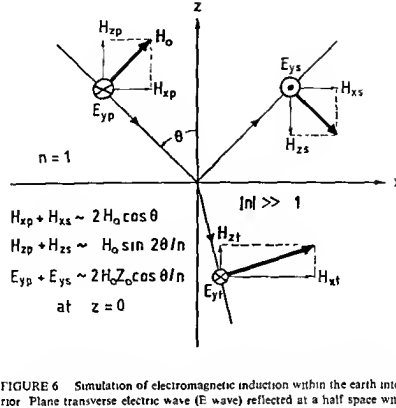

FIGURE 6 Simulation of electromagnetic induction within the earth interior Plane transverse electric wave (E wave) reflected at a half space with large refractive index n (|n|>>1) ("p" = primary wave, "s" = reflected wave, "t" = transmitted wave)

waves within the secondary winding are superimposed onto the primary waves The simplest way to describe that induction effect is to consider the reflection of plane transverse electric waves on a well-conducting half space as indicated in Figure 6 While the horizontal electric fields cancel nearly to zero just outside the half space, the magnetic fields add, thus leading to an enhancement of the horizontal field and to a reduction of its vertical component near the ground

These magnetic fields can be observed at the ground as the geomagnetic Sq variations The primary field is proportional to the dynamo current, and the secondary field is proportional to the induced current within the Earth The strength and phase of the induced currents depend on the period of the primary wave and on the configuration of the electric conductivity within the Earth Longer periods penetrate deeper into the Earth than shorter periods (skin effect) For more details see Price[88] and Rikitake [92]

Magnetospheric Convection Field

The solar wind, a plasma flow from the sun of high electric conductivity, cannot directly penetrate the geomagnetic field, but leaves a cavity, the magnetosphere, in the wider environment of the Earth The boundary of the magnetosphere, the magnetopause, is located where the kinetic energy of the solar wind matches the magnetic energy of the geomagnetic field The mean distance of the magnetopause from the Earth is about 10 Earth radii at the subsolar point The magnetosphere stretches several hundred Earth radii into space on the night side (see Figure 7)

In the polar cap regions of the magnetosphere, the solar wind plasma blows across geomagnetic field lines which merge with the interplanetary magnetic field These regions therefore behave like a hydromagnetic generator in which the kinetic energy of the solar wind is converted into electric energy In plasma physics the effect is known as channel flow or Hartmann flow [99] In order to allow the solar wind plasma to pene-

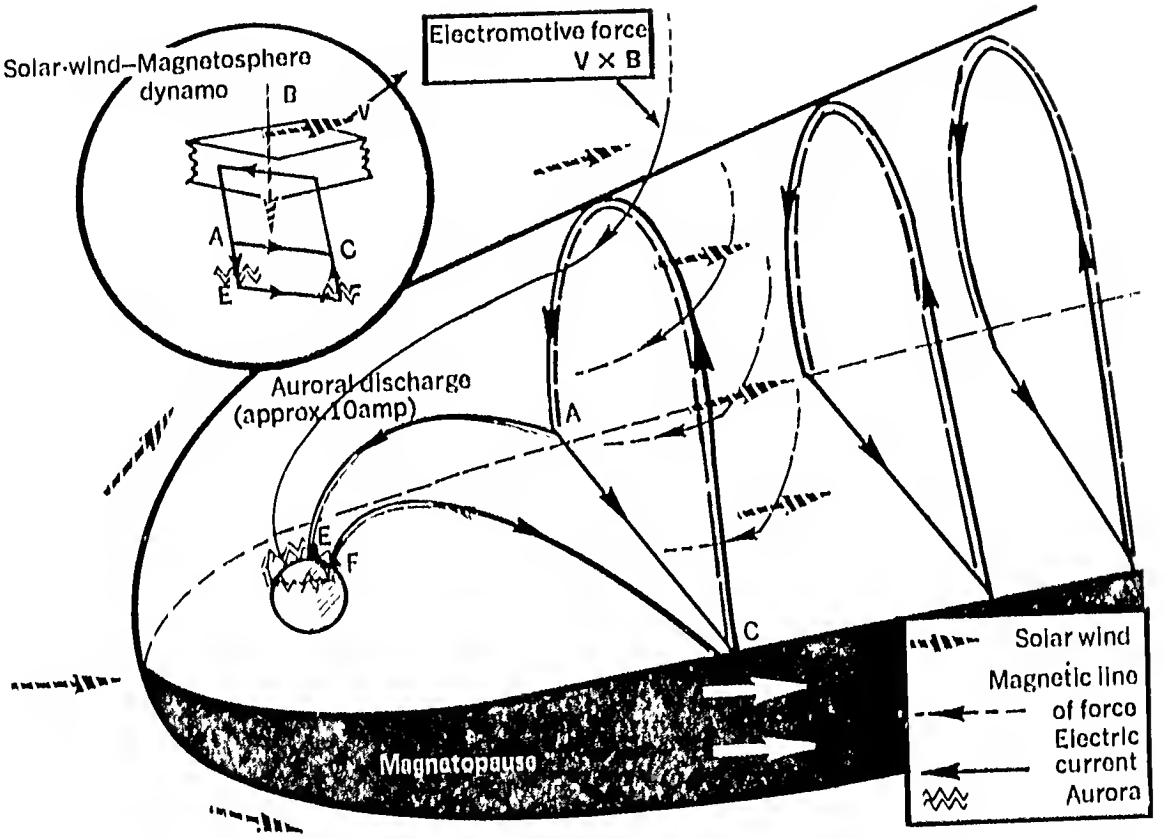

FIGURE 7. Dynamo from interaction of solar wind and magnetosphere. The solar wind plasma blows across the geomagnetic field lines that originate in the polar-cap region and merge with the interplanetary magnetic field lines. The resulting voltage, current, and power are of the order of 50 kV, 2×10^7 A and 10^{12} W. Much of the current is discharged directly across the magnetosphere (AC), but about 10^6 A is discharged through the polar upper atmosphere and the ionosphere along the geomagnetic lines shown in the diagram (AEFC). (From Akasofu, S.-I. and Lanzerotti, L. J., *Phys. Today*, 28, 28, 1975. With permission.)

trate into that region, an electric polarization field directed from dawn to dusk must be built up which compensates the Lorentz field $\mathbf{v} \times \mathbf{B}_z$, where $\mathbf{v}$ is the solar wind velocity directed from noon to midnight and $\mathbf{B}_z$ is the polar cap geomagnetic field directed to the south

Discharging electric currents can flow along the magnetopause, along the magnetospheric tail (AC in Figure 7), and along the geomagnetic field lines which are interconnected via the dynamo region of the ionosphere (AEFC in Figure 7) The resulting voltage, current, and power are of the order of 50 kV, 20 MA, and 1 TW About 1 MA flows along the line from A via E on the morning side into the ionosphere to F on the evening side, and from F to C into the magnetosphere These field-aligned currents have been observed [47] The electric polarization field which drives those currents is accompanied by large-scale plasma convection within the nighttime magnetosphere and is therefore called the convection field [5]

Since the geomagnetic lines of force are well conducting, they are practically electric equipotential lines and the electric field vector must be orthogonal to these lines The electric field can thus map downward into ionospheric heights where it drives electric Pedersen and Hall currents The convection field has been measured *in situ* by satellites [24 40] For an observer at ionospheric heights who rotates with the Earth, this field is an AC field with a basic period of 1 solar day Its dawn to dusk potential difference is about $\bar{U}_M = 25$ kV during very quiet conditions It can increase up to 100 kV and more during disturbed conditions [41] Maximum field strengths are observed near the low latitude borders of the auroral zones, from which the field decays rapidly toward the lower latitudes For a review, see Stern [101]

Voltage sources and currents of magnetospheric origin are very crudely simulated by the current system III in Figure 4 Again, part of that current can flow through the lower atmosphere Here one expects effects on the ground which in the auroral zones may locally be of the same order of magnitude as the thunderstorm field effects The locally and temporally varying ionospheric currents of magnetospheric origin which are associated with magnetospheric substorms' can induce a whole spectrum of secondary electric currents within the Earth [29 92] Secondary induced electric fields within the magnetosphere due to fluctuating primary fields are discussed by Kim et al [58] The time constant of magnetospheric currents is of the order of $L_M/R_D \simeq 25$ min

OBSERVATIONS

Ground-Based Measurements

Globally Representative Stations for the Thunderstorm Field

The atmospheric electric field measured at the ground is orthogonal to the surface of the Earth because the Earth behaves like an equipotential layer In the fair weather regions far away from thunderstorm areas, the field of thunderstorm origin is directed downward In the literature of atmospheric electricity, that direction is defined as positive [10] In this book, however, we apply a coordinate system with the z-axis positive upward, so that the fair weather field is negative according to our definition To avoid confusion, we shall explicitly mention any deviation from our definition if it occurs in the following text

Fair weather in the atmospheric electric sense is during a time in which the action of local generators remains unimportant Local generators are those generators which do not contribute significantly to the global electric current and influence only their immediate environment Convection currents (precipitation), corona discharges, and blowing snow or dust belong to local generators A thunderstorm is also a local generator in its immediate vicinity

A globally representative station for the thunderstorm field is a station where, for

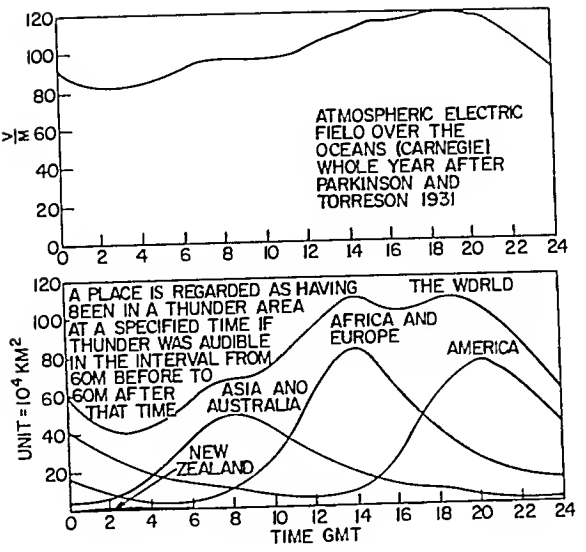

FIGURE 8. Annual mean of field strength at the ground versus universal time (in GMT) measured at oceanic stations (upper Figure; field strength is positive downward), and thunderstorm activity versus GMT in the four main centers of the world (lower Figure). (From Israël, H., *Atmospheric Electricity*, Vol. II, National Science Foundation, Washington, D.C., 1973. With permission.)

all fair weather conditions, the vertical columnar resistance $\bar{\Lambda}$ (see Equation 7) remains nearly constant,[17] so that the measured electric current density j_A reflects only the variation of the potential difference U_A:

$$U_A = -\bar{\Lambda} j_A \tag{17}$$

This condition is approximately true for ocean and for polar stations. Figure 8 shows the results of field strength measurements on board the research ship *Carnegie*. The upper part of Figure 8 gives annual averages of hourly means of E_z (positive downward) plotted vs. universal time (GMT). The striking feature is a dependence on universal time with maximum near 19.00 GMT at locations of different longitude. The lower part of Figure 8 gives the areas of thunderstorm activity on the different continents. Although the thunderstorm activity depends on local time maximizing during early afternoon, the sum of all active areas on the Earth closely follows the field strength curve.

Presently, this correlation is the most convincing argument in favor of Wilson's theory that the thunderstorms are the generators of the global electric field. However, there remain some discrepancies. The electric field in Figure 8 varies by only 40%, while the thunderstorm areas vary by about 100%. Moreover, Krumm,[59] preparing seasonal curves of thunderstorm activity, found a less convincing correlation between the seasonal parameters. Ogawa et al.[77] split the thunderstorm data into monthly curves and showed that electric field and thunderstorm activity do not follow the same hourly trend for individual months. Since the time constant of the atmosphere is of the order of 500 sec (see Equation 12), the global electric potential should adjust to changes in the global generator strength within the same time, and one would expect a rather strong correlation between electric field and thunderstorm activity, at least for time scales of 1 hr. Recent simultaneous measurements of the current density in

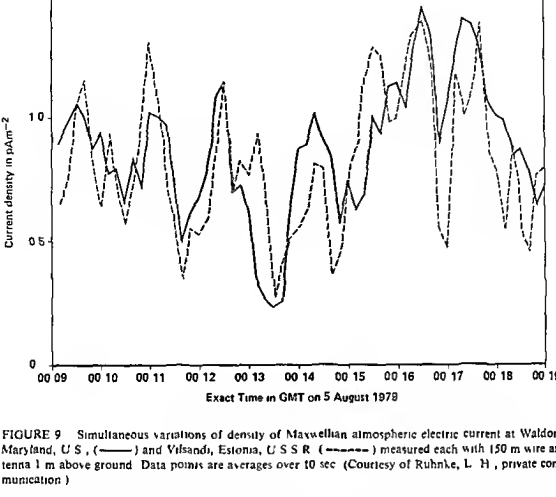

FIGURE 9 Simultaneous variations of density of Maxwellian atmospheric electric current at Waldorf, Maryland, U S , (——) and Vilsandi, Estonia, U S S R (– – – –) measured each with 150 m wire antenna 1 m above ground Data points are averages over 10 sec (Courtesy of Ruhnke, L H , private communication)

Maryland, U S and in Estonia, U S S R show similar synchronous world-wide fluctuations with time constants even smaller than 1 min, (Figure 9) [97]

Another argument against the Wilson hypothesis is that the annual variation of the daily mean of the oceanic field and the corresponding annual variation of the thunderstorm activity are anticorrelated The electric field shows a minimum during north summer, while thunderstorm activity has a maximum there [105]

One way out of the discrepancy may be that measurements of thunderstorm activity are still based on the World Meteorological Organization (WMO) tables which give numbers of the "day with thunder heard" This is certainly not a representative measure of thunderstorm activity, particularly in regions of sparse meteorological stations It should be mentioned, however, that observations of the energy of Schumann resonances show a similar large amplitude variation, to the total thunderstorm activity in the lower part of Figure 8 [14] Schumann resonances are considered to represent the lightning activity of the major storm centers (see the chapter, "Schumann Resonances") Thus, the question remains unsolved whether additional sources have to be considered to generate the global electric circuit, e g , a convective generator,[117] or an Austausch generator,[53] or whether our assumption about a linear relationship between lightning activity and the generator strength of thunderclouds must be modified

Typical values of E_z at ocean stations near the equator are 120 V/m The electric current density measured at ocean stations closely follows the electric field with typical values of 2 to 3 pA/m^2, e g , Gringel et al [33] Regional effects of the global field are discussed by Takagi [102]

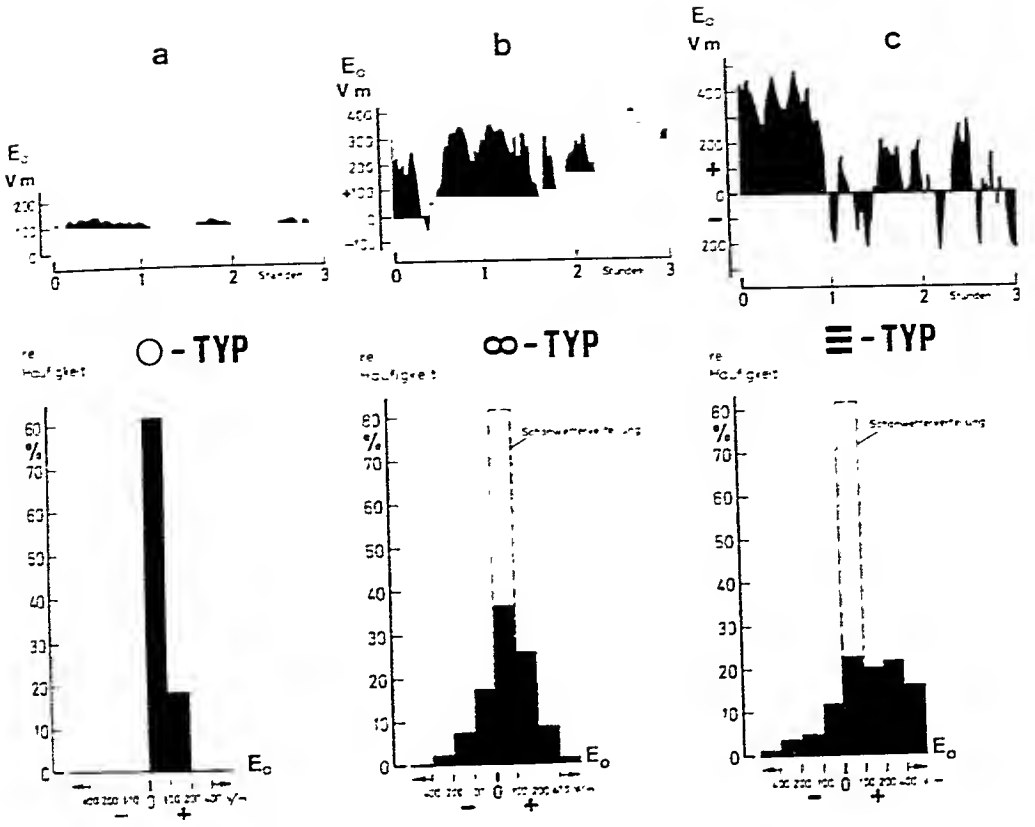

FIGURE 10. Typical variations of electric field on the ground and relative amplitude distribution during fair weather (0), haze (∞), and fog (≡). (+ means field strengths positive downward) (From Fischer, H. J., *Prometheus*, 7, 4, 1977. With permission.)

Continental Stations

Meteorological and anthropogenic influences on electric conductivity are stronger over the solid Earth than over the ocean, in particular within the atmospheric exchange layer in the first few km above ground. The electric field observed on the ground can vary considerably. Figure 10 shows typical variations of E_z at a continental mid latitude station during fair weather, haze, and fog (the plus sign in Figure 10 means fields positive downward). Also shown in Figure 10 is the relative occurrence of the field amplitudes. During fair weather the variation is small and the mean value of E_z is about 120 V/m. No negative fields (field directions positive upward) are observed. During haze and fog the variation can become quite substantial, with occasional negative values of E_z. The amplitude distribution flattens reaching large magnitudes.

The mean field strength is still positive. The large positive amplitudes are the result of a local decrease in the electric conductivity due to the attachment of small ions to haze and fog droplets. The negative fields are probably caused by space charges.

Anthropogenic influences on the field on the ground are shown in Figure 11. The station east of a big city (Stuttgart, Germany) exhibits the character of the fair weather field because the wind from the north does not transport man-made pollution into that area. However, pollution from industrial areas in the north of the city reaches the western station, resulting in strong variations of the field, including negative values.

Figure 12 shows field variations and amplitude spectra during rain of various strength. The negative fields now become a substantial part of the picture with maximum values of more than 400 V/m increasingly dominating with increasing strength

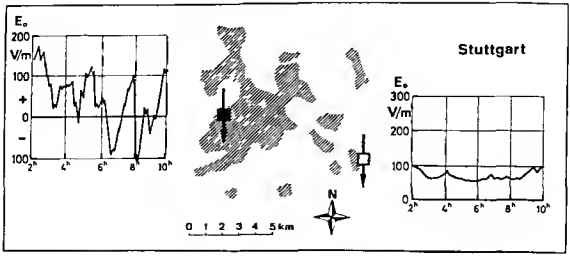

FIGURE 11 Anthropogenic influences on the electric field on the ground Simultaneous measurements at two stations east and west of Stuttgart Germany (+ means field strengths positive downward) (From Fischer H J *Prometheus* 7, 4 1977 With permission)

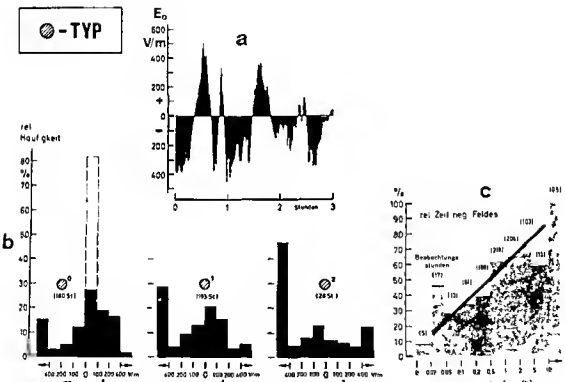

FIGURE 12 Typical variations of electric field on the ground during rain (a), relative amplitude distribution for various rain intensities (b), and time of negative fields (in percentage) vs intensity of the rain (c) (+ means field strengths positive downward) (From Fischer, H J *Prometheus*, 7, 4, 1977 With permission)

of the rain fall The situation becomes more complex during snow The U form of the amplitude distributions in Figure 12 becomes even more pronounced during thunderstorms, and the maximum amplitudes can be as high as 1000 V/m

Seasonal means of the diurnal variation of E_z show two distinct types (Figure 13), both depending on local time Whereas a single oscillation type (Figure 13a) is predom-

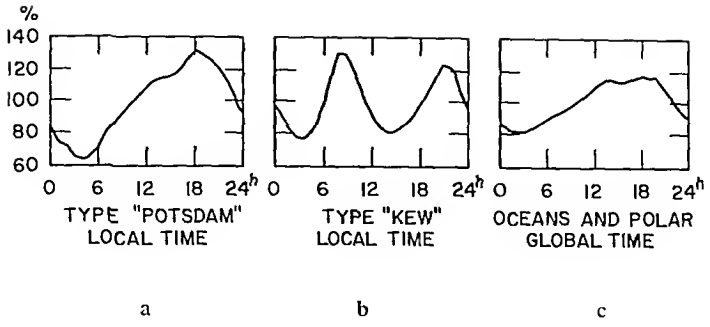

FIGURE 13. The three main types of diurnal variation of the electric field on the ground. Types 1 and 2 (left and middle Figures) are continental types depending on local time. Type 3 (right Figure) is an oceanic type depending on universal time (see also Figure 8). (From Israel, H., *Atmospheric Electricity*, Vol. II, National Science Foundation, Washington, D.C., 1973. With permission.)

inant during winter in many stations, the double oscillation type generally dominates during summer. However, some stations have double oscillations throughout the year, and others have only single oscillations diurnally. The first occurs more often in cities, the second predominates in rural areas.[49]

For comparison, Figure 13c shows the behavior of a typical oceanic station which depends on universal time as discussed in the foregoing section. Figure 13 gives the impression that the diurnal variation is generally made up of two components, a 24-hr component and a secondary overlapping fluctuation of shorter period which gradually becomes more significant from winter to summer. That local time fluctuation apparently masks the superimposed universal time fluctuation which is seen at ocean stations.

The double-oscillation type is limited to plains and disappears above several tens of meters above ground, where a clearly marked change toward the single-oscillation type is observed.

The local time-dependence of E_z at continental stations is remarkably similar to the variation of water vapor pressure (Figure 14). The single-oscillation type of vapor pressure is called the maritime diurnal variation. It occurs when the ground at the observation point ensures a continuous and adequate supply of water vapor by evaporation. The vapor pressure will then approximately follow the diurnal temperature curve and thus influences the columnar resistance within the atmospheric exchange layer; this explains the corresponding behavior of E_z.

The double-oscillation type of the diurnal variation of vapor pressure stems from the single diurnal variation with the added effect of convection. Convection, with its maximum effect at noon, can reduce water vapor content near the ground during summer, thus overcompensating for the evaporation effect during day time.

In contrast to the electric field variations, not much characteristic diurnal fundamental behavior can be recognized for the electric current density at continental stations. Similarly, an arrangement according to universal time does not indicate a strong common behavior. The reason for this follows.[49]

The electric field E_z, the thunderstorm potential U_A, the electric current density j_A, the columnar resistance $\bar{\lambda}$ (see Equation 7), and the local conductivity on the ground σ are interconnected as

$$E_z = \frac{j_A}{\sigma} = -\frac{U_A}{\sigma \bar{\lambda}} \tag{18}$$

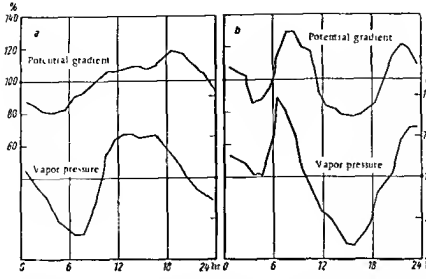

FIGURE 14 The two continental types of electric field on the ground versus local time as compared with the diurnally varying vapor pressure in percentage as recorded in Potsdam 1934 to 1937 (From Israel, H., *Atmospheric Electricity*, Vol I, National Science Foundation, Washington, D C., 1973 With permission.)

and

$$J_A = -U_A/\bar{\lambda} \qquad (19)$$

Therefore, E_z depends on three parameters, while J_A depends on only two Now, the local conductivity σ shows diurnal variations and can dominate the behavior of E_z For J_A, it depends on whether the global influences U_A or the local influences $\bar{\lambda}$ are stronger

The total mean of J_A on flat ground is about 2pA/m², which is probably somewhat smaller than the corresponding value at ocean stations In mountain areas, J_A is larger

If the local variations are removed by appropriate averaging processes, both electric field and current density on the ground indeed show the universal time dependence exhibited by the ocean stations [80]

Effects of Solar Activity

The electric fields and currents discussed in the two previous sections are caused by the thunderstorm generator It is still doubtful whether electric fields of ionospheric or magnetospheric origin have been observed on the ground[78] although claims in that direction have been made [49,79]

An influence of solar activity on the thunderstorm field may occur either via a variation of the electric conductivity or via a modulation of the thunderstorm activity in a yet unknown manner [44] Claims about a solar activity modulation of the thunderstorm field are still controversial (e g , Israel,[49] Herman and Goldberg[42]) For example, Reiter[89] reported an increase of the vertical electric field and current at a mid latitude station a few days after sector boundary crossings of the interplanetary magnetic field, whereas Park[81] found a decrease of E_z during the same events at an Antarctic station Markson and Muir[45] observed an anticorrelation between the thunderstorm voltage and the solar wind velocity

Observations at Balloon Altitudes

Vertical Electric Fields

Figure 15, shows the decrease of the vertical electric field with altitude during fair

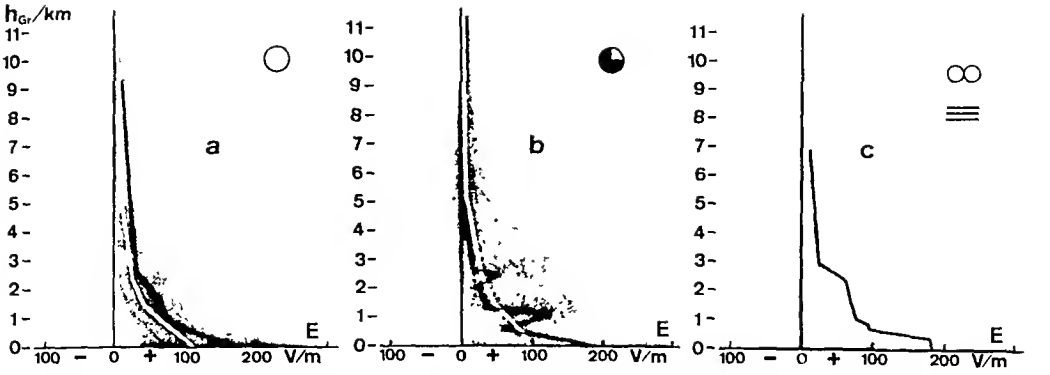

FIGURE 15. Electric field versus altitude during fair weather (○), cloudiness (◔), and fog (≡). Black curves show typical measurements; white curves are mean values; hatched regions indicate the scattering of the data (+ means field strengths positive downward). (From Fischer, H J., *Prometheus*, 7, 4, 1977. With *permission.*)

weather, during cloudiness without rain, and during haze and fog. The positive sign in Figure 15 means positive downward. The black lines show typical individual altitude profiles, the shaded regions indicate the range of scattering, and the white curves gives averages. An analytical formula of Gish[27]

$$E_z = -[81.8 \exp(-4.527\, z) + 38.6 \exp(-0.375\, z) + 10.27 \exp(-0.121\, z)] \quad (20)$$

(E_z in V/m; z in km) approximates rather well the mean profile of E_z. According to Equation 20, the field at 10-km altitude decreases to about 2% of its value on the ground.

The scattering in Figure 15 is mainly due to the variation of the local electric conductivity rather than to a change in the thunderstorm voltage U_A. This scattering can increase substantially during cloudiness and during fog. The black saw-toothed curve in Figure 15b during cloudiness characterizes the attachment of the small ions to water droplets within the cloud, thus giving rise to a reduction of the conductivity there.

During rain or snow, and particularly in thunderclouds, the electric field profiles show much larger scattering, including even regions of negative fields (negative in the sense that the direction is positive upward). The temporal variations are fast, and the horizontal field components can become of the same order of magnitude as the vertical field components.

The electric current density, which is the product of the exponentially decreasing electric field and the exponentially increasing conductivity, remains nearly constant with height. As an example, Figure 16 shows a vertical profile of the polar vertical electric current density over the North Atlantic together with the electric field and the electric conductivities. This is true over the continents as well.[33]

Vertical electric field measurements by rocket-borne instruments have been made by Tyutin[104] and by Hale and Croskey[37] up to heights of 70 km. They claim that they observe large vertical electric fields with a total potential of 100 kV near 50- to 60-km altitude in the auroral zones during quiet conditions, which then vanish during disturbed conditions. However, Bering et al.[7] criticized these results on the basis that the payloads were traveling at or above Mach one speed. Holzworth and Mozer[44] measured the vertical electric field at 30-km altitude during the August 1972 magnetic storm event and found an anticorrelation of the electric field with the intensity of the solar proton flux.

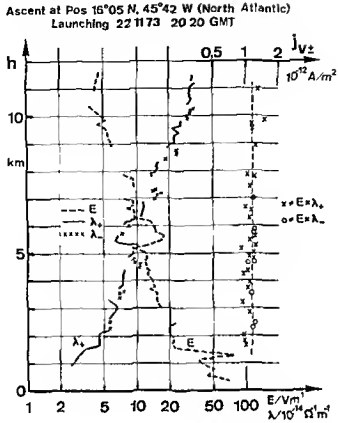

FIGURE 16 Balloon borne measurements of the polar conductivities λ_+ (= σ+) and λ_- (= σ−) and of the electric current density (From Gringel, W Leidel J , and Muhleisen R , Meteor Forschungsberichte Reihe B Nr 13 41 1978 With permission)

Muhleisen[73] observed differences in the ionospheric potential up to 60 kV over a horizontal distance of 6600 km The effect of the orography is to reduce the columnar resistance over mountain areas, which thereby increases the local electric current density (see Equation 19 and also Hoppel,[45] and Ogawa et al [70]) The thunderstorm potential has the same diurnal UT dependence as the electric field over the ocean [49] For recent measurements, see Markson[63] and Muhleisen [73]

Many observations exist within and above thunderclouds Gish and Wait's[28] airplane measurements of the electric conductivity and the electric field confirmed Wilson's[115] prediction that the currents over thunderclouds were of the order of 1 A and were conveying positive charge to the upper atmosphere Observations above thunderclouds from a U2 airplane reported by Vonnegut et al [102] revealed that the strong electric fields and currents were confined to the convection cells rising above the top of the clouds (see Moore and Vonnegut[67] for a review)

Horizontal Electric Fields

In the proximity of thunderclouds, or local generators, the electric field differs substantially from a homogeneous vertical field These inhomogeneous components decay rapidly away from the source (see section on the Thunderstorm as a Local Generator, page 96) Electric fields of ionospheric and magnetospheric origin have horizontal components of planetary scale These fields decay downward (see Figure 5) However, their magnitudes are comparable to the vertical thunderstorm field at stratospheric heights A measured horizontal field of magnetospheric origin is shown in Figure 17

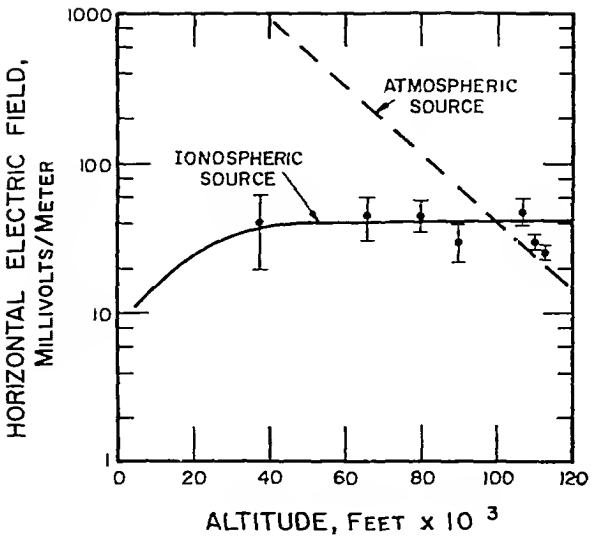

FIGURE 17. Balloon borne measurements of horizontal electric fields (solid lines) and vertical electric fields (dashed lines) versus altitude (1 km = 3281 ft). (From Mozer, F. S and Serlin, R., *J. Geophys. Res.*, 74, 4739, 1969. With permission.)

as a function of altitude. It remains nearly constant down to 15-km altitude and its magnitude exceeds that of the thunderstorm field above approximately 35 km.

Mozer and collaborators[71] have made extensive balloon-borne measurements of horizontal electric fields of magnetospheric origin at high latitudes. Their result will be discussed in the next section in connection with *in situ* observations of electric fields at ionospheric heights.

Observations at Ionospheric Heights

Electric Field of Sq Current

The evaluation of electric field measurements made *in situ* within the ionospheric dynamo layer is difficult because satellites cannot orbit freely below 150-km altitude. Rocket-borne observations yield only a localized snapshot of a global field configuration. Barium cloud releases, allow in addition only twilight measurements.[36]

So far, the most reliable quasi-continuous measurements on a global base of the electric polarization field of the Sq current at low and middle latitudes are due to ground-based backscatter observations.[18] Figure 18 shows an empirical model of the ionospheric dynamo field, based on drift data at F layer heights from five low and mid-latitude stations.[90] The values are valid between 0 and 60° latitude. Electric fields due to the magnetospheric generator must be considered at higher latitudes. During geomagnetic storms, the dynamo field may be enhanced somewhat. Although the data in Figure 18 are F-layer data, they are believed to reflect the dynamo field which maps into the F layer. The potential in Figure 18 peaks at 0700 hr LT (maximum) and at 2000 hr LT (minimum) at the equator. A second maximum at 40° latitude is at 0300 hr LT. The maximum potential difference between morning and evening is 7 kV. Figure 18 is valid during equinox conditions. One would expect an additional antisymmetric component during solstices.

Electric Convection Field

The electric convection field is generated within the magnetosphere and maps down into the ionosphere. OGO 6 *in situ* measurements, revealed a typical field configura-

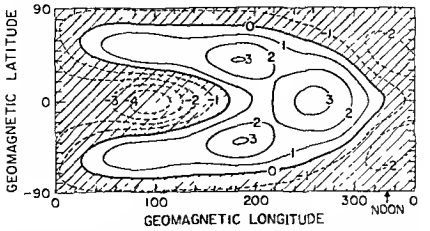

FIGURE 18 Equipotential lines of the electric potential of the dynamo field during quiet conditions as derived from backscatter measurements (numbers in kV) (From Richmond A D , *J Geophys Res* 81, 1447, 1976 With permission)

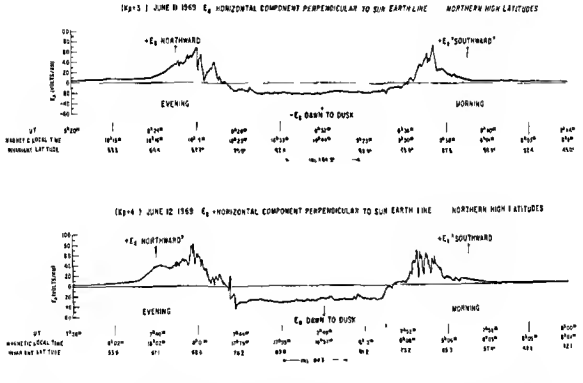

FIGURE 19 The horizontal component of the electric field perpendicular to the sun-earth line along two polar traverses of OGO-6 across the north magnetic pole (From Heppner, J P , in *Magnetospheric Physics*, Dyer, E R , Ed , National Academy Sciences, Washington, D C , 1972, 107 With permission)

tion at ionospheric heights above the F layer maximum as shown in Figure 19 [40] The satellite crosses the northern pole along the dawn-dusk meridian One notices a transition from southward-directed fields over the polar cap to northward-directed fields beyond about 75° magnetic latitude The field decays rapidly towards lower latitudes

Figure 19 shows observations during moderately disturbed conditions, but the configuration remains essentially the same during quiet conditions The main differences are that the maximum amplitude decreases to about 20 mV/m, and the transition range shifts to higher latitudes and shrinks

Observations of this type, together with balloon results,[71] incoherent scatter data,

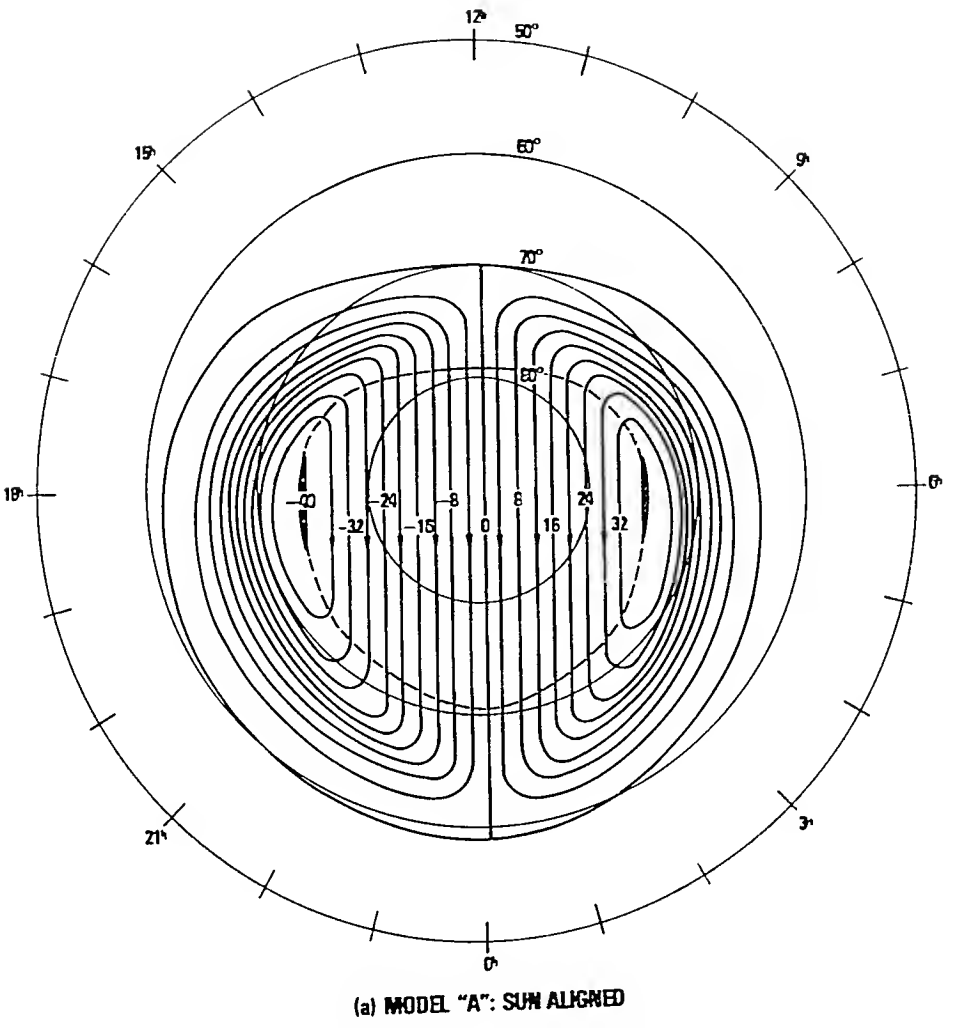

FIGURE 20. Semiempirical model of the electric convection field at ionospheric heights. Equipotential lines (in kV) of the ionospheric electric potential on the northern hemisphere during moderately disturbed conditions. (From Heppner, J. P., *J. Geophys. Res.*, 82, 1115, 1977. With permission.)

and barium cloud observations (for a review see Rostoker[96]), yield an empirically derived electric potential configuration at ionospheric altitudes as shown in Figure 20 during moderately disturbed conditions with a potential difference between dawn and dusk of about 75 kV. During quiet conditions that potential difference is reduced to about 25 kV. That pattern depends on local time for an observer on the Earth. For an observer within a fixed magnetospheric frame of reference, it is necessary to add a corotation field which is due to unipolar induction within the corotating magnetospheric plasma in the presence of the geomagnetic field.[101]

Polar Cap Field

Heppner[40] detected a relationship between the polarity of the interplanetary magnetic field (IMF) and an antisymmetric configuration of the electric convection field. This is schematically shown in Figure 21. During away polarity of the IMF (upper figures), the maximum amplitudes are on the morning side on the northern hemisphere and on the evening side on the southern hemisphere. During toward polarity of the IMF (lower figures), the situation is reversed.

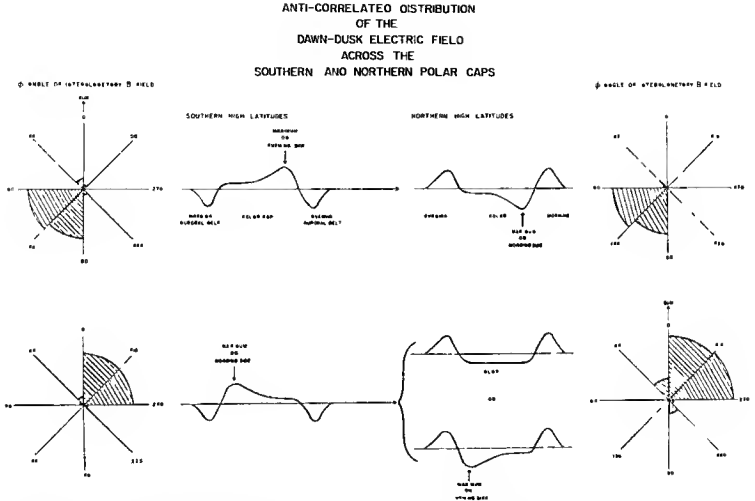

FIGURE 21 Superposition of convection field and polar cap field (schematic) depending on the interplanetary magnetic field direction (angle ϕ) Upper figure away polarity of the interplanetary magnetic field Lower figure toward polarity (From Heppner, J P , *J Geophys Res* , 82, 1115, 1977 With permission)

According to Friis-Christensen et al.[25], it is the azimuthal component of the IMF which is responsible for that effect. The electric potential of that polar cap field which is superimposed onto the convection field in Figure 21 is nearly independent of local time and is limited to the polar caps. Its maximum value is about 3 to 4 kV at the poles, decaying to zero at about ± 75° magnetic latitude. It is antisymmetric with respect to the equator and changes direction with changing polarity of the IMF, the time delay being of the order of 20 min.[57]

THEORY

Basic Equations

Electromagnetic Equations

The basic equations are the two Maxwell equations,

$$\nabla \times \mathbf{B} = \epsilon\mu \frac{\partial \mathbf{E}}{\partial t} + \mu \mathbf{j} \tag{21}$$

$$\nabla \times \mathbf{B} = -\frac{\partial \mathbf{B}}{\partial t} \tag{22}$$

Ohm's law in the general form

$$\mathbf{j} = \bar{\sigma} \cdot (\mathbf{E} + \mathbf{v} \times \mathbf{B}_0) \tag{23}$$

together with

$$\nabla \cdot (\epsilon \mathbf{E}) = q \tag{24}$$

and

$$\nabla \cdot \mathbf{B} = 0 \tag{25}$$

with **E** the electric field (in V/m), **B** the magnetic induction (in T), **j** the electric current density (in A/m^2), q the electric charge density (in C/m^3), $\epsilon \simeq \epsilon_0 = 8.854 \times 10^{-12}$ F/m the dielectric constant, $\mu \simeq \mu_0 = 1.256 \times 10^{-6}$ H/m the permeability, σ the electric conductivity tensor (in S/m), $\mathbf{B}_0$ an external magnetic field (in general, the magnetic field of the Earth), and **v** the (nonrelativistic) velocity of the gas, including its plasma component (in m/sec).

The Lorentz field $\mathbf{v} \times \mathbf{B}_0$ in Equation 23 accounts for the transformation of the electric field from the frame of reference of the moving gas into the frame of reference of the observer.

Hydrodynamic Equations

In order to solve Equations 21 to 25 consistently, one must also consider the hydrodynamic and thermodynamic equations of the plasma. For large-scale tidal and planetary motions within the thermosphere, it is possible to separate the horizontal wave structure from the vertical wave structure to a first order approximation, so that only the horizontal momentum equations are directly coupled with the electromagnetic forces, e.g., Volland and Mayr:[111]

$$\frac{\partial V}{\partial t} + 2\Omega\hat{r} \times V\cos\theta + \frac{1}{\rho_o}(\nabla p)_{hor} = \frac{j \times B_o}{\rho_o}$$

$$\frac{\partial p}{\partial t} + g\rho_o h\,\nabla\cdot V = 0 \qquad (26)$$

with V the horizontal wind of the system "neutral gas-plasma", $\Omega = 7.29 \times 10^{-5} s^{-1}$ the angular frequency of the rotation of the Earth, $\hat{r}$ the unit vector in the radial direction, θ the polar distance, ρ_o the mean density, p the pressure amplitude, $g = 9.81$ msec^{-2} the gravitational acceleration, and h a separation constant (in m) known as the equivalent depth

The term $j \times B_o$ in Equation 26 is a mechanical force (ampere force) That term, together with the Lorentz field in Equation 23, is responsible for a feedback between neutral gas and plasma

Quasi-Electrostatic Approach

If one wants to consider only the electrostatic field, ignoring induction effects, one assumes that $\partial B/\partial t = 0$ in Equation 22, from which follows a scalar potential Φ for the electric field

$$\underline{E} = -\nabla\Phi \qquad (27)$$

This greatly simplifies the treatment of Maxwell's equations, because the feedback from the magnetic field to the electric field is ignored, and the number of possible electric field configurations is reduced Moreover, electric fields of different origin can be combined by simply adding their potentials

In order to estimate the range of validity of Equation 27, Equations 21 to 23 are combined as follows (with σ = constant and scalar, $v = 0$)

$$\frac{\epsilon}{\sigma}\frac{\partial^2 B}{\partial t^2} + \frac{\partial B}{\partial t} + \frac{1}{\sigma\mu}\nabla \times (\nabla \times B) = 0 \qquad (28)$$

If τ is a characteristic time and $L \lesssim a$ (a = radius of the Earth) is a characteristic length, one arrives from a comparison between the second and third terms of Equation 28 at

$$\tau >> \sigma\mu L^2 \qquad (29)$$

as the range of periods where Equation 27 is valid

In the lower and middle atmosphere, one finds $\sigma \lesssim 10^{-6}$ S/m (see Figure 3), and Equation 29 thus requires $\tau >> 40$ sec Within the dynamo layer, one has $\sigma \simeq 10^{-4}$ S/m, so that $\tau >> 1$ hr It follows that in the whole atmosphere, with the possible exception of the maximum of the dynamo layer,[110] the quasi-static approximation is a reasonable approach for periods larger than 1 hr

Comparing the first and second terms in Equation 28 yields

$$\tau >> \frac{\epsilon}{\sigma} \lesssim 7 \text{ mm} \qquad (30)$$

indicating the range of periods where the displacement current in Equation 21 can be neglected as compared with the conduction current

Current measurements on the ground have to take into account the displacement

current at periods smaller than about 10 min. Kasemir[51] describes a method to eliminate the displacement current from the observations.

Mapping of Electric Fields

Lower and Middle Atmosphere

Outside of thunderstorm areas or other local generators, the electric current is source free. Potential fields can map up and down within the lower and middle atmosphere where the scalar conductivity increases nearly exponentially with altitude:

$$\sigma = \bar{\sigma}\, e^{z/H} \tag{31}$$

From Equations 23, 27, and 31 one derives the differential equation

$$\nabla\cdot(\sigma\nabla\Phi) = 0 \tag{32}$$

With the potential difference between earth and ionosphere developed into a series of spherical functions P_{nm}:

$$\Phi = \sum_{n,m} \bar{\Phi}_{nm} h_{nm}(r) \quad P_{nm}(\theta) e^{im\lambda} \tag{33}$$

one obtains from Equation 32 an equation for the height structure functions $h_{nm}(r)$:

$$\frac{1}{r^2}\frac{\partial}{\partial r}\left(r^2 \frac{\partial h_{nm}}{\partial r}\right) - \frac{n(n+1)}{r^2} h_{nm} + \frac{1}{H}\frac{\partial h_{nm}}{\partial r} = 0 \tag{34}$$

which has the solution

$$h_{nm} \simeq (e^{\alpha_1 z} - e^{-\alpha_2 z}) \quad ; \quad (z = r - a;\ 0 \leqq z \leqq z_i) \tag{35}$$

and

$$\left.\begin{matrix}\alpha_1 \\ \alpha_2\end{matrix}\right\} = \mp\left(\frac{1}{a} + \frac{1}{2H}\right) + \sqrt{\left(\frac{1}{a} + \frac{1}{2H}\right)^2 + \frac{n(n+1)}{a^2}} \simeq \left\{\begin{matrix}\beta_n/H \\ 1/H\end{matrix}\right. \tag{36}$$

The last approximation is valid for large and mesoscale structures

$$\beta_n = H^2 n(n+1)/a^2 << 1/4 \tag{36a}$$

for $n \lesssim 100$.

The lower boundary condition, $\Phi = 0$ at $z = 0$, has been adopted in Equation 35. The upper boundary condition is the potential at ionospheric heights at z, which is

$$\Phi_i \simeq \sum_{n,m} \bar{\Phi}_{nm} P_{nm}(\theta)\, e^{im\lambda} \qquad \text{for } n \lesssim 100 \tag{37}$$

because

$$h_{nm} \simeq h = 1 - e^{-z/H} \qquad (n \lesssim 100) \tag{38}$$

and $h(z_i) \simeq 1$ for $z_i \gtrsim 100$ km.

The vertical electric current density is

$$J_z = -\sigma \frac{\partial \Phi}{\partial r} \simeq -\frac{\bar{\sigma}}{H} \Phi_1 \qquad (39)$$

and the electric field components become

$$E_\theta \simeq -\frac{h(z)}{a} \sum_{n,m} \bar{\Phi}_{nm} \frac{dP_{nm}}{d\theta} e^{im\lambda}$$

$$E_\lambda \simeq -\frac{ih(z)}{a} \sum_{n,m} m \bar{\Phi}_{nm} \frac{P_{nm}}{\sin\theta} e^{im\lambda} \qquad (n \leqq 100) \qquad (40)$$

$$E_z = \frac{e^{-z/H}}{H} \sum_{n,m} \bar{\Phi}_{nm} P_{nm} e^{im\lambda}$$

The zeroth order mode ($n = 0$) is the globally averaged potential of thunderstorm origin $U_A = \Phi_{00} \simeq 250$ kV (see Figure 4). Potential, electric current, and field of the zeroth mode vary with height according to

$$\Phi_{00}(z) = U_A h(z)$$

$$J_A = -\frac{\bar{\sigma}}{H} U_A = \text{constant} \qquad (41)$$

$$E_A = -\frac{e^{-z/H}}{H} U_A$$

The essential features of this component are the exponential decrease of the vertical electric field and the constant vertical electric current density. With the numbers $H \simeq 6$ km, and $\sigma \simeq 5 \times 10^{-14}$ S/m, one arrives at the ground level ($z = 0$) values of $|J_A| \simeq 2$ pA/m², $|E_A| \simeq 40$ V/m which are the right orders of magnitude for average currents, fields, and conductivity unmodified by turbulence within the exchange layer.

At the height

$$z \simeq H \ln \frac{a}{H} \simeq 40 \text{ km} \qquad (42)$$

the vertical and the horizontal components of the large-scale fields in Equation 40 have the same orders of magnitude, and the vertical component has been reduced to about 0.1% of its value at the ground.

The horizontal components in Equation 40 decrease downward. The large-scale fields still possess 90% of their ionospheric amplitudes at 14-km altitude. This is reduced further to 50% at 4 km, and at the ground the horizontal components disappear. Figure 5 shows the equipotential lines of a field of zonal wave number, $m = 1$, which depends on local time.

For small-scale fields with a horizontal extent $\lambda \leqq 500$ km, the height structure functions h_{nm} in Equation 35 deviate significantly from their large-scale form (Equation 38). The result is a stronger attenuation of the horizontal field downward as indicated in Figure 22.* Here, $h(\lambda,z)$ (applying plane model calculations) is plotted vs altitude z for various values of λ. The curve with $\lambda = \infty$ corresponds to h in Equation 38. Figure 22 also takes into account the effect of the displacement current in Equation 21. The damping effect increases with increasing frequency. The upward or downward

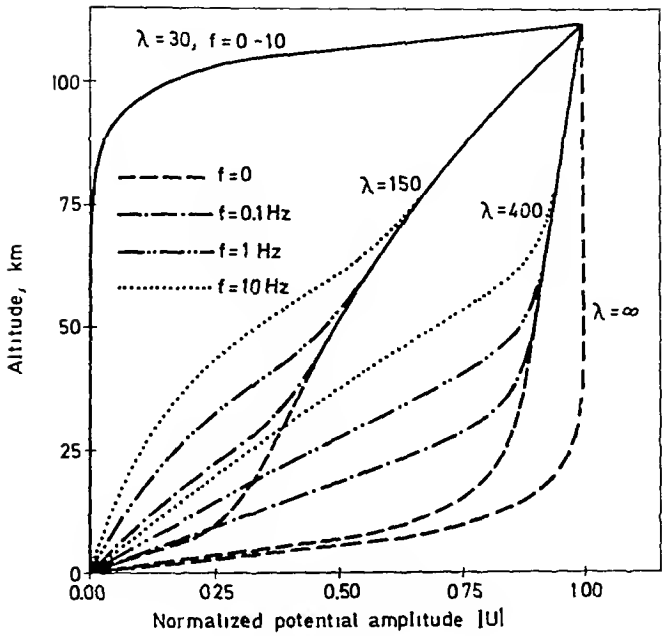

FIGURE 22 Height structure function h (λ,z) versus altitude for various horizontal scales λ and frequency scales f. (From Boström, R. and Fahleson, U., in *Electrical Processes in Atmospheres*, Dolezalek, H. and Reiter, R., Eds., Steinkopf, Darmstadt, 1977, 529. With permission.)

mapping of small-scale structures ($\lambda \lesssim 100$ km) with small periods ($\tau \lesssim 10$ sec) is rather ineffective. The mapping of small-scale structures becomes more complex if the conductivity tensor in Equation 23 at ionospheric heights is taken into account.[9,12,82,83]

To date, the most sophisticated calculation of downward mapping of Sq fields (from Figure 18) and convection fields (such as in Figure 20) is due to Roble and Hays.[94] These authors considered in their model the latitude dependence of the conductivity and also the orography of the surface of the Earth. Since those fields are large-scale fields, their downward mapping is rather efficient, and perturbations of ± 20% in the vertical electric field on the ground at high latitudes are expected to be superimposed on the thunderstorm field even during quiet conditions. The perturbations become larger during disturbed conditions, but are generally highly variable.

Upward mapping of fair weather fields in a two layer model (exchange layer and above), taking into account the day-night pattern and the influence of mountain areas, was calculated by Kasemir.[53]

Magnetosphere

The very large parallel conductivity at ionospheric and magnetospheric heights above about 100 km generally prevents electric fields parallel to the geomagnetic field lines. The possibility of parallel electric fields is discussed by Stern.[101] For most practical purposes, however, the geomagnetic field lines are equipotential lines of the electric field, and the electric fields must be orthogonal to the magnetic field lines:

$$E \cdot B_o = 0 \qquad (43)$$

For quasi-static electric fields, this implies that the electric potential is parallel to the magnetic field lines, and Φ can be any function of L:

$$\Phi = f(L) \tag{44}$$

where L is the equation of the geomagnetic field lines. In the case of a coaxial geomagnetic dipole, one has

$$L = \frac{r}{\sin^2\theta} = r_b \tag{45}$$

with (r,θ) spherical coordinates, and r_b the equatorial distance of the line.

For instance, a potential at ionospheric heights at latitude θ, which depends on $\sin^{-r}\theta_c e^{im\lambda}$ | remains constant along the L shell and maps like

$$\Phi = A\, L^{p/2}\, e^{im\lambda} \tag{46}$$

Its electric field components are

$$E_r = -\frac{p}{2r}\Phi \tag{47}$$

$$E_\theta = \frac{p}{r}\cot\theta\,\Phi \tag{48}$$

$$E_\lambda = -\frac{im}{r\sin\theta}\Phi \tag{49}$$

In the equatorial plane of the magnetosphere, the θ-component disappears, and the r-component diminishes to the fraction

$$E_r(r_b)/E_r(r_i) = r_i/r_b \tag{50}$$

of its ionospheric value $E_r(r_i)$.

Mapping along the real non-dipole and non-coaxial geomagnetic field is somewhat more complicated and needs numerical treatment [66-70].

Generators of Electric Fields and Currents

The Thunderstorm as a Global Generator

Thunderstorms are considered as generators of electric currents which drive the global electric current system [66]. One thunderstorm area is believed to contribute about 0.5 to 1 A on the average to the global electric current. With 1000 to 2000 thunderstorms acting simultaneously on the Earth, one arrives at the measured total fair weather current of about 1 kA.

A thunderstorm area can be simulated by a point source of strength $\bar{I} \simeq 1$ A located at height $z_o = r_o - a$ km above the surface of the Earth on the axis of a spherical coordinate system at $\theta = 0°$ [19]

$$J_s = \frac{\bar{I}\,\delta(r - r_o)\,\delta(x - 1)}{\pi r_o^2} \tag{51}$$

with δ Delta functions, $x = \cos\theta$, $r_o \simeq a$ the radial distance of the point source from the center of the Earth, $\sigma_o = \sigma(r_o)$. Furthermore

$$\delta(x - 1) = \sum_n \frac{(2n+1)}{4} P_n(x) \tag{52}$$

with $P_n(x)$ the zonal spherical functions. Again assuming electric potential fields, one need only replace Equation 32 by

$$\nabla\cdot(\sigma\nabla\Phi) = J_s \tag{53}$$

We assume the same height dependence of the conductivity as in Equation 31 up to the center of the dynamo layer at height z_i, from where it drops exponentially to zero:

$$\sigma = \begin{cases} \bar{\sigma} e^{z/H} & \text{for } 0 \leqq z \leqq z_i \\ \bar{\sigma} e^{(2z_i - z)/H} & \text{for } z \geqq z_i \end{cases} \tag{54}$$

We then develop the potential into a series of spherical functions as in Equation 33. Because of the location of the point source, only zonal spherical harmonics remain ($m = 0$). Region I ($0 \geqq z \geqq z_o$) from the Earth to the source is source free, and Equation 35 is valid:

$$\Phi_I = \sum_n \bar{\Phi}_n^{(1)} \left(e^{\beta_n z/H} - e^{-z/H} \right) P_n(x) + 0(\beta_n) \tag{55}$$

In region II ($z_o \leqq z \leqq z_i$), we write

$$\Phi_{II} = \sum_n \bar{\Phi}_n^{(2)} \left\{ e^{\beta_n z/H} + 2\beta_n e^{(z_i - z)/H} \right\} P_n(x) + 0(\beta_n) \tag{56}$$

and in region III ($z_i \leqq z$), the solution is

$$\Phi_{III} = \sum_n \bar{\Phi}_n^{(2)} e^{\beta_n (2z_i - z)/H} P_n(x) + 0(\beta_n) \tag{57}$$

with $O(\beta_n)$ small terms of the order β_n ($\beta_n z_i/H << 1$ for $n \lesssim 100$). The terms in the Φ are selected in such a way that the boundary conditions at z_i of continuous Φ and $\partial\Phi/\partial z$ are fulfilled. In region III, it is $j_z \to 0$ for $z \to \infty$. There remain the boundary conditions at z_o, which are continuity of Φ, and

$$\left\{ \left.\frac{\partial \Phi_I}{\partial z}\right|_{z_o - 0} - \left.\frac{\partial \Phi_{II}}{\partial z}\right|_{z_o + 0} \right\} = \int J_s \, dz = \frac{\bar{I}}{\sigma_o A} \sum_n (2n+1) P_n(x) \tag{58}$$

where A is the surface area of the Earth. This yields (apart from terms of the order $O[\beta_n]$)

$$\bar{\Phi}_n^{(1)} = \frac{(2n+1) H \bar{I} \left(1 + 2\beta_n e^{(z_i - z_o)/H} \right)}{\bar{\sigma} A \left(1 + 2\beta_n e^{z_i/H} \right)} \tag{59}$$

and

$$\bar{\Phi}_n^{(2)} = \frac{(2n+1) H \bar{I} \left(1 - e^{-z_o/H} \right)}{\bar{\sigma} A \left(1 + 2\beta_n e^{z_i/H} \right)} \tag{60}$$

If the upper boundary at z_i is an electric wall ($j_z = 0$ at z_i), the expression, Equation 55, remains the same, and one has only to replace $2\beta_n$ by β_n in Equations 56, 59, and 60

The quantity

$$\bar{\Phi}_o^{(s)} = \frac{H\bar{I}}{\bar{\sigma}A}\left(1 - e^{-z_o/H}\right) \simeq 200\ V \qquad (61)$$

is the globally averaged potential at ionospheric heights generated by one thunderstorm (with $\bar{I} = 1$ A, $z_o = 10$ km, and the numbers from Equation 41) N thunderstorms are then responsible for a total global potential of

$$U_A = N\Phi_o^{(s)} = \frac{N A_o \bar{I}}{\bar{A}} = 250\ kV \qquad (62)$$

with

$$A_o = \bar{A}\left(1 - \frac{\bar{\sigma}}{\sigma_o}\right)$$

the columnar resistance between Earth and cloud top at z_o (see Equation 11) Comparison with Equation 41 and Equation 8 yields

$$|A|_A| = |I_A| = \frac{A_o}{\bar{A}} N\bar{I} \qquad (63)$$

indicating an efficiency of the thunderstorms of about 80% ($N \simeq 1250$) to drive the global current I_A Twenty percent of the thunderstorm current flows directly downward to the Earth via the resistance R_T in Figure 4

According to Equation 63, the efficiency depends on the ratio of the columnar resistance from the Earth to the cloud top A_o to the total columnar resistance $\bar{A}$ That efficiency increases if the height of the cloud tops increases Tropical thunderstorms *thus appear to be more efficient than thunderstorms at higher latitudes The efficiency* would drop to zero in an atmosphere with constant conductivity ($H \to \infty$). Since U_A does not depend on the upper boundary conditions, it would remain the same if σ should increase indefinitely with altitude

The higher order terms of Equations 55 and 56 are also nearly independent of the upper boundary within the lower and middle atmosphere

Since $\beta_n \exp(z_i/H) \ll 1$ ($n \leqq 1$) for reasonable z_i ($z_i \geqq 100$ km), these terms may be approximated by

$$\Phi_n \simeq \begin{cases} (2n+1)\dfrac{\bar{A}\,\bar{I}}{A} e^{-z_o/H}\left(1 - e^{-z/H}\right) P_n(x) & z \leqq z_o \\ (2n+1)\dfrac{\bar{A}\,\bar{I}}{A}\left(1 - e^{-z_o/H}\right) e^{-z/H} P_n(x) & z_o \leqq z < z_i \end{cases} \quad \text{for} \quad (n \leqq 1 \lesssim 100) \qquad (64)$$

indicating in region I the same height dependence as in Equation 38, and an exponential decrease of Φ_n in region II corresponding to a current which is positive upward Comparison with Equation 52 suggests that the thunderstorm field is limited to the immediate environment of a narrow, vertical cylindrical column above and below the cloud. Evidently, the bulk of the current which flows upward from the top of a thundercloud reaches the region of maximum conductivity before it spreads horizontally

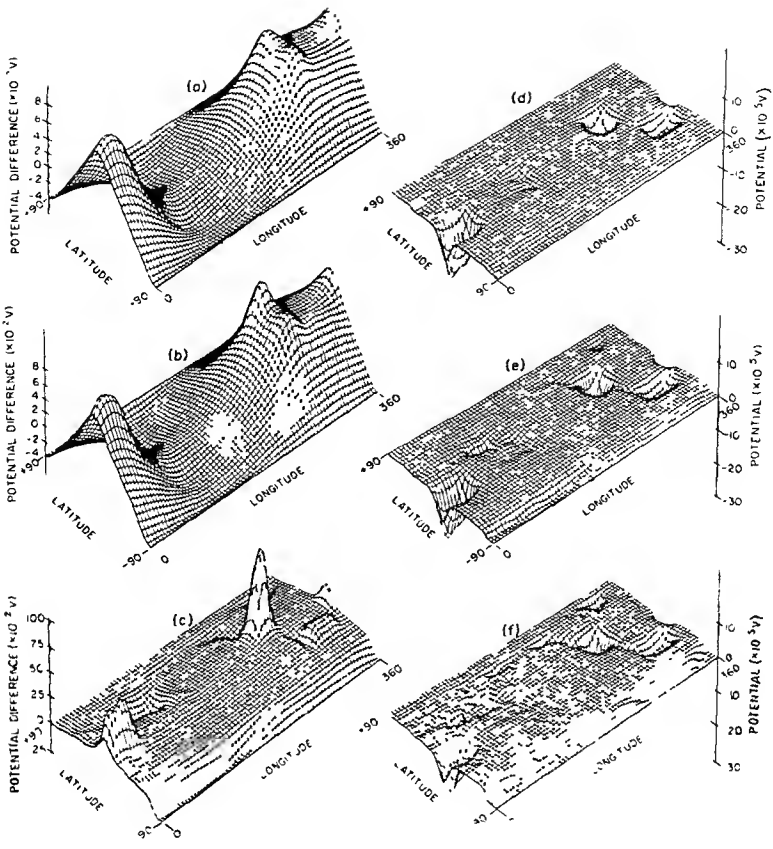

FIGURE 23. Perspective illustrations of the calculated potential of the fair weather field along various constant conductivity surfaces (a), (b), and (c) illustrate the calculated potential difference $(\phi - \phi_\infty)$ volts along, respectively, $\sigma = 4.54 \times 10^{-6}$ S/m (approximately 105 km at the equator), $\sigma = 4.74 \times 10^{-10}$ S/m (approximately 50 km at the equator), and $\sigma = 7.3 \times 10^{-12}$ S/m (approximately 25 km at the equator); $\phi_\infty = U_A$ is the ionospheric potential. (d) is the potential $\phi(\sigma_i)$ along $\sigma_i = 4.3 \times 10^{-13}$ S/m (approximately 8 km at the equator). (e) is the potential ϕ(4 km) at a constant 4-km height, and (f) is the potential ϕ(2 km) at a constant height of 2 km. (From Hays, P. B. and Roble, R. G., *J. Geophys. Res.*, 84, 3291, 1979. With permission.)

over the globe.[52] The currents use the way of least resistance. The "exchange layer" is therefore the dynamo region rather than some arbitrarily selected height within the middle atmosphere.

These estimates are verified by more sophisticated calculations. Hays and Roble[39] determined global and mesoscale structures of the thunderstorm field, taking into account the orographic features of the Earth as well as a realistic distribution of thunderstorms. They chose an electric wall as upper boundary at $z_t = 105$ km, and they considered the geomagnetic field lines to be electric equipotential lines. Figure 23 taken from Hays and Roble, shows contours of the calculated potential difference $\Phi - \overline{\Phi}_{oo}$ at various constant surfaces of the conductivity (σ = const.) corresponding to altitudes of 2, 4, 8, 25, 50, and 105 km, respectively. The thunderstorm regions are considered to be located between 8- and 15-km altitude. The potential differences above the three main thunderstorm areas in Africa and Central and South America are positive above 15-km altitude, indicating positive currents upward into the ionosphere. The potential differences are negative within the thunderstorm areas below 8 km, corresponding to

downward currents The deviation is negative in fair-weather regions where the return currents flow to the Earth Orographic features become important below 8 km The regions of deviation from the average potential, which are limited to the thunderstorm areas at lower altitudes, broaden with increasing height Horizontal differences of even 1 kV are maintained at 105-km altitude The total averaged potential U_A is 291 kV in Hays and Roble's calculations [39]

It is clear that the fine structure of the field in the immediate environment of a thunderstorm cannot be adequately modeled To discriminate horizontal structures of the order of 1 km, one would need about 40,000 terms in the series of spherical functions in Equations 55 and 56, a task clearly beyond any reasonable possibility Local structures of a thunderstorm field will be discussed in the next section

The Thunderstorm as a Local Generator

A current point source of strength $\bar{I}$, located at height z_o within an infinitely extended atmosphere with exponentially increasing conductivity, has the electric potential in a cylindrical coordinate system (ϱ,z)[52] of

$$\Phi_c = \frac{\bar{I}}{4\pi\sigma_0} \frac{\exp\left\{-\left(\sqrt{\rho^2+(z-z_0)^2}+z-z_0\right)/(2H)\right\}}{\sqrt{\rho^2+(z-z_0)^2}} \qquad (65)$$

The streamlines of the currents of such a point source, which are radial away from the source near the origin, bend to the vertical upward under the influence of the exponentially increasing conductivity

The effect of the well-conducting Earth can be taken into account by an image point source of strength $-\bar{I}$ located at height $-z_o$ However, only the part

$$-\bar{I}_v = -\frac{\bar{\sigma}}{\sigma_0}\bar{I} \qquad (66)$$

is necessary to compensate the downward flowing current from the primary source at the ground so that the total potential becomes

$$\Phi = \frac{\bar{I}}{4\pi\bar{\sigma}}\left[\frac{\exp\left\{-\frac{(R_1+z-z_0)}{2H}\right\}}{R_1} - \frac{\exp\left\{-\frac{(R_2+z+z_0)}{2H}\right\}}{R_2}\right] \qquad (67)$$

with

$$\left.\begin{matrix}R_1\\R_2\end{matrix}\right\} = \sqrt{\rho^2+(z\mp z_0)^2}$$

Note that $\Phi = 0$ for $z = 0$ is assumed

The charge of the rest of the image source fills the plane $z = 0$ homogeneously and is responsible for a negative vertical homogeneous current in region $z > 0$ of strength

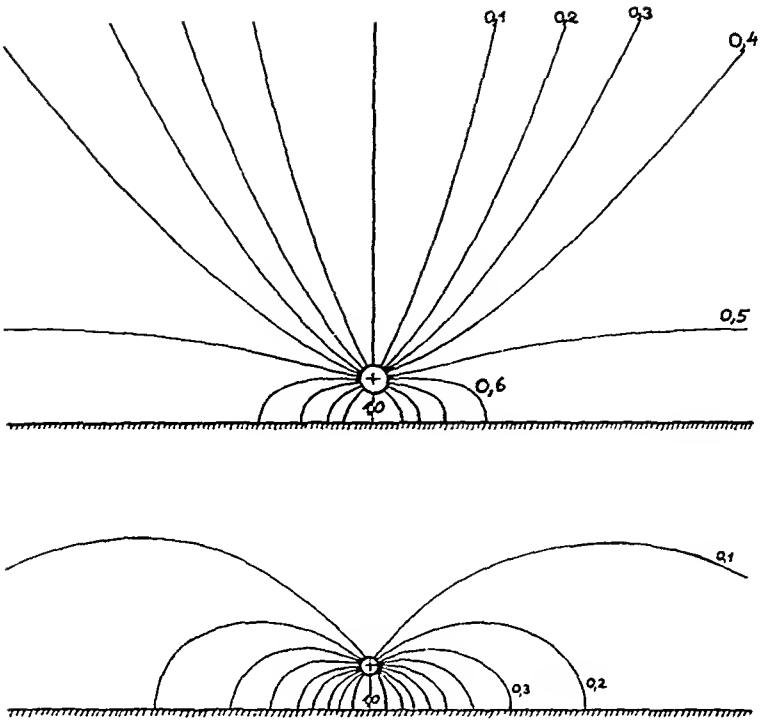

FIGURE 24. Current streamlines of a current point source embedded within an atmosphere with exponentially increasing conductivity over a perfectly conducting earth (upper Figure), and the same point source embedded within an atmosphere of constant conductivity (lower Figure). (From Kasemir, H. W., *Z. Geophys.*, 25, 33, 1959. With permission.)

$$-I_r = -\bar{I}\left(1 - \frac{\bar{\sigma}}{\sigma_o}\right) \tag{68}$$

That current is the fair-weather current compensating the current of the primary source, which flows upward above the source, bending downward at infinitely great heights (or within the ionosphere) away from the source. In this model with infinitely extended horizontal scales, the fair-weather current diminishes to zero. The effective strength of the primary source to produce the fair-weather current, which is $+I_r$, corresponds exactly to the number $\Lambda_o\bar{I}/\bar{\Lambda}$ in Equation 63.

Figure 24a taken from Kasemir[52] shows the current streamlines of the point source, Equation 67, with an efficiency of $I_r/\bar{I} = 1/2$. The equivalent electric current system is drawn in Figure 4. The resistance R_T is the internal resistance of the source, where the part I_r of the current flows from the source directly to the Earth (lines 0.5 to 1 in Figure 24a). The remaining current I_r flows upward into the ionosphere and returns to the Earth within the fair-weather areas (indicated by R_A in Figure 4). This latter part of the current system is not modeled by Equation 67.

Figure 24b gives the current streamlines of the point source within an atmosphere with constant conductivity. The efficiency is zero in this case, and the current of the primary source flows directly to the image source so that no fair-weather current exists.

The electric charge of the point source is related to its strength, according to Kasemir,[52]

$$\bar{Q} = \frac{\epsilon_o}{\sigma_o}\bar{I} \tag{69}$$

where $\varepsilon_o/\sigma_o = \tau_o$ is a time constant (see Equation 1) With $\sigma_s \simeq 5\sigma_o$, $\tau_o \simeq 33$ sec, and $\bar{I} \simeq 1$ A, one obtains $Q \simeq 33$ C, which is a reasonable estimate of the positive charge accumulation in thunderclouds (see that chapter)

A more realistic model has to account for the negative electric charge distribution near the bottom of a thundercloud Such a model can be very simply constructed by the superposition of a positive and a negative source with the strength of the negative source

$$\tilde{I} = -\bar{t}\left(1 - \frac{\bar{\sigma}}{\tilde{\sigma}_o}\right) \tag{70}$$

at a height $\bar{z}_o < z_s$ below the positive source, and $\tilde{\sigma}_o = \tilde{\sigma}(z_s)$ Now, the efficiency of this dipole source becomes

$$I_s/\bar{I} = \left(\frac{\bar{\sigma}}{\tilde{\sigma}_o} - \frac{\tilde{\sigma}}{\sigma_o}\right)$$

which is smaller than the strength of the monopole However, as Kasemir[42] showed, the reduced electric conductivity within the cloud compensates for that decrease to a certain extent Any other more complicated source configuration can be constructed by combining a number of point sources

Holzer and Saxon,[43] who also simulated the ionosphere by an electric wall, considered the potential of a dipole source in a similar manner Park and Dejnakarintra[44] calculated the electric field above monopoles and dipoles and considered the anisotropic conductivity of the ionosphere and magnetosphere Figure 25 shows the horizontal electric field E_ρ vs horizontal distance ϱ of a monopole located at 15-km height for different heights The field first rises to a maximum and then falls off exponentially at distances greater than about 50 km As z increases, the E_ρ curve becomes broader, and the peak moves outward until it reaches about 40 km at z = 100-km altitude E_ρ decreases rapidly with height at first, but levels off near 90 km The narrow range of disturbance which a thunderstorm produces within the lower and middle atmosphere is apparent in Figure 25

At ionospheric altitudes, the electric field depends sensitively on the electric conductivity model and on the thunderstorm model, thus suggesting that giant thunderstorms may be an important source of localized fields that can form field-aligned density irregularities in the ionosphere and magnetosphere [44]

Tidal Winds

The system of coupled electrodynamic and hydrodynamic equations in Equations 21 to 26 can be solved analytically only if severe model restrictions are made For example, if one assumes a conductivity tensor with constant height-integrated elements

$$\underline{\Sigma} = \int \underline{\sigma}\, dz = \begin{pmatrix} \Sigma_p & \Sigma_h \\ -\Sigma_h & \Sigma_p \end{pmatrix} \tag{71}$$

with Σ_p a Perdersen conductivity and Σ_h a Hall conductivity, and if one considers a thin spherical layer of thickness Δz in which the current flows, as well as a coaxial geomagnetic dipole field, one can approximate the diurnal symmetric (1,−2) tidal wave by analytical functions [105] The electric potential of that wave becomes

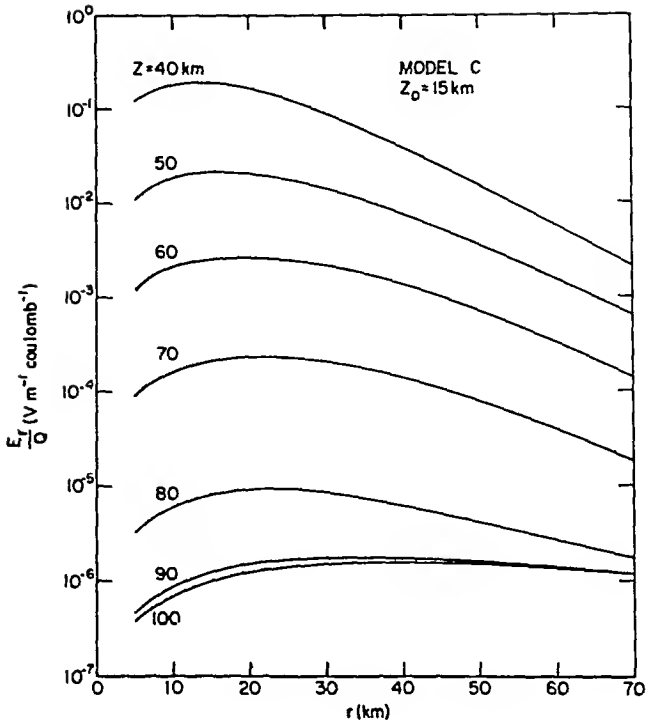

FIGURE 25. Normalized horizontal electric field of current point source at 15 km altitude versus horizontal distance r ($\simeq \varrho$) at different heights. (From Park, C. G. and Dejnakarintra, M., *J. Geophys. Res.*, 78, 6623, 1973. With permission.)

$$\Phi = -V - \frac{\Sigma_h}{\Sigma_p} W \tag{72}$$

with

$$\left.\begin{aligned} V &= i(4c - 1 + 4c\cos^2\theta)\sin\theta \\ W &= -(4c - 1)\sin\theta\cos\theta \end{aligned}\right\} \frac{U_o B_o r_i}{5} e^{i(\Omega t + \lambda)} \tag{73}$$

where

$$c = \frac{1 + i\delta/3}{1 + 4i\delta/c} \qquad \delta = \frac{\Sigma_c B_o^2}{\Delta z \Omega \bar{\rho}_o}$$

$\Sigma_c = \Sigma_p + \Sigma^2_h/\Sigma_p$ is the Cowling conductivity, $B_o = 3 \times 10^{-5}$ T is the geomagnetic field at the equator, $U_o \simeq 40$ m/sec is the wind amplitude at the poles, $\Omega = 7.29 \times 10^{-5}$ sec^{-1} is the angular frequency of the rotation of the Earth, r_i is the radial distance of the dynamo layer, and $\bar{\varrho}_o$ is the mean density in the center of the layer.

The electric current system can be found from a stream function $\Sigma_c W$ as

$$j = \Sigma_c \nabla \times W \hat{r} \tag{74}$$

That current system is mainly responsible for the geomagnetic Sq current.[55] With the

numbers $\Sigma_h/\Sigma_p \simeq 2$ and $\delta \simeq 1$, the potential pattern of Equation 72 is similar to that of Figure 18 [108] Corresponding formulas exist for the wind and the pressure field of the (1,−2) tidal wave They approximate reasonably well the exact solutions.

After integrating Equations 23 and 26 over a meridional circle, the meridional components disappear, and the zonal components can be written as

$$\begin{aligned} U &= \bar{U}_D - R_t I_D \\ R_D I_D &= U_p + U \\ U_p &= R_p I_D \end{aligned} \tag{75}$$

where U_p corresponds to the driving force (the solar radiation) and is an external or source voltage, U corresponds to the Lorentz field $V \times B_z$, I_D to the height-integrated electric current, U_p to the polarization field, and finally

$$R_D = \frac{l}{\Sigma_t} \qquad R_t = \frac{l}{\pi C_D} \qquad C_D = \frac{\bar{R}_0 \Delta z}{4 B_0^2}$$

$$R_p = -\frac{13}{3} R_D + \frac{R_t}{9} \qquad \delta = \frac{1}{4\pi C_D R_D}$$

where R_p is a load resistance, R_t an internal resistance, and R_t a complex resistance related to the polarization field The equivalent current system of Equation 75 is shown in Figure 4 [107]

A dynamo in which feedback between plasma and neutral gas is taken into account is called a hydromagnetic dynamo If that feedback is neglected, and if the wind is considered as an external driving force for the current, one speaks about a kinematic dynamo The term δ determines the feedback If $\delta = 0$, feedback is neglected, and

$$R_t = 0 \quad \text{and} \quad R_p = -\frac{13}{3} R_D$$

The consequences of neglecting the feedback can be seen immediately in Figure 4 Now, the source voltage is the wind, $\bar{U}_p = U$, and I_D increases with decreasing load resistance In the case of a short circuit, $R_p = 0$, current becomes infinite On the other hand, with feedback, $\delta \neq 0$, I_D and U reach asymptotic, but finite, short circuit values if $R_p \to 0$ This is analogous to a technical dynamo where the current remains finite in case of a short circuit because of the self-inductance of the coil, which is space charge in the atmospheric dynamo

Numerical calculations of kinematic dynamos based on the generation and propagation of several tidal driving wind systems are due to Richmond et al ,[91] Möhlmann,[67] and Forbes and Lindzen,[22] The reciprocal approach, i e , a determination of winds and electric fields from the currents which are derived from geomagnetic Sq variations, was applied by Kato [54] Winds and electric fields based on that method are now published regularly by the Data Analysis Center for Geomagnetism and Spacemagnetism of Kyoto University, Japan

Solar Wind Interaction with the Magnetosphere

There does not as yet exist a self-consistent model of solar wind interaction with the magnetospheric plasma Therefore, in order to describe the magnetospheric electric

field generated by that interaction, it is often convenient to omit any detailed consideration of magnetospheric plasma convection, and to start with electric field or current configurations based on observations. This is possible for stationary large-scale fields with periods longer than several hours.

Electric potential fields have been developed by McIlwain[60] from observed particle fluxes at synchronous orbits during and after substorms, and by Heppner[41] from *in situ* electric field measurements on the satellite OGO-6. Numerical stationary models often follow one of three basic cause-and-event approaches

$$\begin{aligned} j_{\parallel} &\rightarrow E, I \rightarrow B \\ E &\rightarrow I, j_{\parallel} \rightarrow B \\ B &\rightarrow I \rightarrow E, j_{\parallel} \end{aligned} \tag{76}$$

where $j_{\parallel}$ is the field-aligned electric current density (corresponding to I_M in Figure 4) which is related to the ionospheric current at dynamo layer heights I via the condition that the total current must be source free:

$$j_{\parallel}\Big|_{r=r_i} = -\nabla \cdot \underline{I} / \sin \chi \tag{77}$$

r_i is the height of the dynamo layer, χ is the angle of inclination of the geomagnetic field, and B is the geomagnetic variation on the ground caused by the ionospheric and magnetospheric currents.

Models based on the first approach are those of Yasuhara and Akasofu,[116] Nisbet et al.,[75] Nopper and Carovillano,[76] and Kamide and Matsushita.[50] The second approach was followed by Kawasaki and Fukushima,[56] Stern,[101] Gurevich et al.,[35] and by Volland.[109] The third approach is due to Hughes et al.[46]

Following the second approach, one can construct electric potentials for the convection field of the form (Equation 46) in several regions of the magnetosphere, which are symmetric about the equator and which depend on local time τ:

$$\Phi = A L^{p/2} \sin(\tau - \tau_m) \tag{78}$$

Since the potential and the ionospheric current must be continuous at the boundaries of those regions, the field-aligned current follows uniquely if the conductivity tensor of the dynamo layer is given. A reasonable approximation of the convection field at lower latitudes is $p = 4$ in Equation 78. It simulates sufficiently well the observed electric fields at ionospheric heights (such as in Figure 19) and also the configuration of the plasmapause within the equatorial plane of the magnetosphere. The parameter $p = -1$ in Equation 78 is valid at polar latitudes, thus yielding a nearly constant electric field over the polar cap ($\theta \lesssim 15°$) at ionospheric heights, as seen in Figure 19. In the auroral zone ($15° \lesssim \theta \lesssim 20°$), more complicated analytical functions must be applied in order to simulate the transition region.[109]

The polar cap field, which is antisymmetric about the equator and does not depend on local time, can be simulated in a similar way. The reader is referred to Harel et al.[38] for time-dependent solutions treating substorm conditions.

The electric fields and currents cause Joule heating at thermospheric heights. That Joule heating is responsible for the generation of neutral winds, which in turn can cause secondary electric fields and currents via dynamo action. Blanc and Richmond[8] calculated these winds and their associated electric fields and currents and showed that they may have an appreciable influence at lower and middle latitudes.

ACKNOWLEDGMENT

I am very much indebted to H Dolezalek and H Kasemir for their helpful advice and stimulating discussions

REFERENCES

1 Akasofu, S -I , *Physics of Magnetospheric Substorms*, Reidel, Dordrecht Holland, 1977
2 Akasofu, S -I and Lanzerotti, L J , The earth's magnetosphere, *Phys Today* 28, 28, 1975
3 Anderson, R V , Atmospheric electricity in the real world, in *Electrical Processes in Atmospheres*, Dolezalek, H and Reiter, R , Eds , Steinkopf, Darmstadt 1977, 87
4 Arnold, F , The middle atmosphere ionized component, *Proc ESA Symposium on Rocket-and Balloon Programmes*, Bournemouth April 1980, in press
5 Axford, W I , Magnetospheric convection, *Rev Geophys Space Phys* , 7, 421, 1969
6 Axford, W I and Hines, C O , A unifying theory of high latitude geophysical phenomena and geomagnetic storms, *Can J Phys* 39 1433, 1961
7 Bering, E A , Benbrook, J R , and Sheldon, W R , Problems with mesospheric electric field measurements *Nature (London)* 283 695, 1980
8 Blanc, M and Richmond, A D , The ionospheric disturbed dynamo, *J Geophys Res* , 85, 1669, 1980
9 Bostrom, R and Fahleson, U , Vertical propagation of time-dependent electric fields in the atmosphere and ionosphere, in *Electrical Processes in Atmospheres*, Dolezalek, H and Reiter, R , Eds , Steinkopf, Darmstadt 1977, 529
10 Chalmers, J A , *Atmospheric Electricity* Pergamon, London, 1967
11 Chapman, S and Bartels, J , *Geomagnetism* Clarendon, Oxford, 1951
12 Chiu, Y T , Self consistent electrostatic mapping in the high-latitude ionosphere, *J Geophys Res* , 79 2790, 1971
13 Cipriano, J P , Hale, L C , and Mitchell, J D , Relations among low ionospheric parameters and A3 radio wave absorption, *J Geophys Res* 79 2260, 1974
14 Clayton, M and Polk, C , Diurnal variation and absolute intensity of world wide lightning activity, September 1970 to May 1971 in *Electrical Processes in Atmospheres*, Dolezalek, H and Reiter, R , Eds , Steinkopf, Darmstadt 1977, 440
15 Cole, R K and Pierce, E T , Electrification in the earth's atmosphere for altitudes between 0 and 100 km *J Geophys Res* 70 2735 1965
16 Dolezalek, H , The atmospheric electric fog effect, *Rev Geophys* , 1, 231, 1963
17 Dolezalek, H , Discussion of the fundamental problem of atmospheric electricity, *Pure Appl Geophys* , 100, 8, 1972
18 Evans, J V , Measurements of horizontal drifts in the E and F region at Millstone Hill, *J Geophys Res* , 77, 2341, 1972
19 Fahleson, U V , Theory of electric field measurements conducted in the magnetosphere with electric probes, *Space Sci Rev* , 7, 238, 1967
20 Ferguson, E E , Ion chemistry of the middle atmosphere, in *Middle Atmosphere Electrodynamics*, Mavnard, N C Ed , NASA Report CP-2090, Washington, D C , 1979, 1
21 Fischer, H J , The atmospheric electric field and its dependence on weather and pollution (in German) *Prometheus*, 7, 4, 1977
22 Forbes, J M and Lindzen, R S , Atmospheric solar tides and their electrodynamic effects I The global Sq current system *J Atmos Terr Phys* 38, 897 1976
23 Forbush, S E , Time variations of cosmic rays, in *Handbuch der Physik, Geophysik III*, Bartels J , Ed , Springer, New York, 1966
24 Frank, L A and Gurnett, D A , Distribution of plasmas and electric fields over the auroral zones and polar caps, *J Geophys Res* 76, 6829, 1971
25 Friis-Christensen, E , Lassen, K , Wilhelm, J , Wilcox, J M , Gonzales, W , and Colburn, D S , Critical component of the interplanetary magnetic field responsible for large geomagnetic effects in the polar cap, *J Geophys Res* 77, 3371, 1972
26 Gish, O H , Evaluation and interpretation of the columnar resistance of the atmosphere, *Terr Magn Atmos Electr* , 49, 159, 1944

27. Gish, O. H., Atmospheric electricity, in *Physics of the Earth*, Fleming, J A., Ed., New York, 1949, 149.
28. Gish, O. H. and Wait, G. R., Thunderstorms and the earth's general electrification, *J. Geophys. Res.*, 55, 473, 1950.
29. Gregori, G. P. and Lanzerotti, L. J., Geomagnetic depth sounding by induction arrow representation, *Rev. Geophys. Space Phys.*, 18, 203, 1980
30. Gringel, W., Air ions, electric conductivity, and their dependence on aerosol (in German), *Promethcus*, 7, 13, 1977.
31. Gringel, W., The Effect of Solar Activity on Atmospheric Electrical Conductivity, *6th Int. Conf. Atmospheric Electricity*, Manchester, July 1980, in press
32. Gringel, W., Hofmann, D. J., and Rosen, J. M., Results of Balloon Borne Atmospheric Electrical Measurements to 33 km, Part 1, *Report No AP-47*, Department of Physics and Astronomy, University of Wyoming, Laramic, Wyo., December 1978.
33. Gringel, W., Leidel, J., and Mühleisen, R., The air-earth current density at the water surface and in the free atmosphere above the ocean, *Meteor Forschungsergeb.*, Reihe B, 13, 41, 1978.
34. Gringel, W. and Muhleisen, R., Sahara dust concentration in the troposphere over the North Atlantic derived from measurements of the air conductivity, *Beitr. Phys Atmos*, 51, 121, 1978
35. Gurevich, A. V., Krylov, A. L., and Tsedilina, E. E., Electric fields in the earth's magnetosphere and ionosphere, *Space Sci Rev.*, 19, 56, 1976
36. Haerendel, G. and Lüst, R., Electric fields in the ionosphere and magnetosphere, in *Particles and Fields in the Magnetospherc*, McCormac, B M., Ed., Reidel, Dordrecht, 1970, 213
37. Hale, L. C. and Croskey, C. L., An auroral effect on the fair weather electric field, *Nature (London)*, 278, 239, 1979.
38. Harel, M., Wolf, R. A., and Reiff, P. H., Computer modeling of events in the inner magnetosphere, in *Quantitative Modeling of Magnetospheric Processes*, Olson, W. P., Ed , Geophysical Monograph 21, American Geophysical Union, Washington, D C., 1979, 499.
39. Hays, P. B. and Roble, R. G., A quasi-static model of global atmospheric electricity 1. The lower atmosphere, *J. Geophys. Res* , 84, 3291, 1979
40. Heppner, J. P., Electric fields in the magnetosphere, in *Critical Problems of Magnetospheric Physics*, Dyer, E. R., Ed., National Academy of Sciences, Washington, D.C., 1972, 107.
41 Heppner, J. P., Empirical models of high latitude electric fields, *J. Geophys. Res* , 82, 1115, 1977.
42. Herman, J. R. and Goldberg, R. A., Sun, Weather, and Climate, Scientific and Technical Information Branch, National Aeronautics and Space Administration, Washington, D C., 1978.
43. Holzer, R. E. and Saxon, D. S., Distribution of electric conduction currents in the vicinity of thunderstorms, *J. Geophys. Res* , 57, 207, 1952
44. Holzworth, R. H. and Mozer, F. S., Direct evidence of solar flare modification of stratospheric electric fields, *J. Geophys. Res.*, 84, 363, 1979.
45. Hoppel, W. A., Altitude variations in the electric potential resulting from orographic features, *Pure Appl. Geophys.*, 84, 57, 1971.
46. Hughes, T. J., Oldenburg, D. W., and Rostoker, G., Interpretation of auroral oval equivalent current flow near dusk using inversion techniques, *J. Geophys. Res* , 84, 450, 1979.
47. Iijima, T. and Potemra, T. A., The amplitude distribution of field-aligned currents at northern high latitudes observed by Triad, *J. Geophys. Res.*, 81, 2165, 1976.
48. Israël, H., *Atmospheric Electricity*, Vol. I, National Science Foundation, Washington, D.C., 1971.
49. Israël, H., *Atmospheric Electricity*, Vol. II, National Science Foundation, Washington, D.C., 1973.
50. Kamide, Y. and Matsushita, S., Simulation studies of ionospheric electric fields and currents in relation to field-aligned currents, *J. Geophys. Res.*, 84, 4083, 1979.
51. Kasemir, H. W., Measurement of the air-earth current density, *Geophys. Res. Pap.*, 42, 91, 1955.
52. Kasemir, H. W., The thunderstorm as a generator in the global electric circuit (in German), *Z. Geophys.*, 25, 33, 1959.
53. Kasemir, H. W., Theoretical problems of the global atmospheric electric circuit, in *Electrical Processes in Atmospheres*, Dolezalek, H. and Reiter, R., Eds., Steinkopf, Darmstadt, 1977, 423.
54. Kato, S., Horizontal wind systems in the ionospheric E region deduced from the dynamo theory of the geomagnetic Sq variations, *J. Geomagn. Geoelectr.*, 8, 24, 1956.
55. Kato, S., Diurnal atmospheric oscillations, *J. Geophys. Res.*, 71, 3201, 1966.
56. Kawasaki, K. and Fukushima, N., Equivalent current pattern of ionospheric and field-aligned currents generated by geomagnetic S_q' fields with closed equatorward auroral boundary, *Rep. Ionos. Space Res., Jpn.*, 28, 187, 1974.
57. Kawasaki, K., Yasuhara, F., and Akasofu, S.-I., Short period interplanetary and polar magnetic field variations, *Planet. Space Sci.*, 21, 1743, 1973.
58. Kim, J. S., Graham, D. A., and Wang, C. S., Inductive electric fields in the ionosphere-magnetosphere system, *Rev. Geophys. Space Phys.*, 8, 2049, 1979.

59 Krumm, H , The universal time dependence of thunderstorm occurrence (in German), *Z Geophys* 28 85 1962

60 Mcllwain, C E , Substorm injection boundaries, in *Magnetospheric Physics* McCormac, B M , Ed Reidel Dordrecht Holland 1974, 143

61 Maeda, K and Matsumoto, H , Conductivity of the ionosphere and current system, *Rep Ionos Space Res Jpn* 16, 1 1962

62 Maeda, K and Murata, H , Ionospheric dynamo theory with consideration for magnetospheric current along the geomagnetic lines of force *Rep Ionos Space Res , Jpn* 19, 272, 1965

63 Markson, R , Ionospheric potential variations obtained from aircraft measurements of potential gradient *J Geophys Res* ,81 1980, 1976

64 Markson, R , Solar modulation of atmospheric electrification and possible implications for the sun-weather relationship, *Nature (London)* 273 103 1978

65 Markson, R and Muir, M , Solar wind control of the earth's electric field, *Science*, 208, 979, 1980

66 Matsushita, S , Interactions between the ionosphere and the magnetosphere for Sq and L variations, *Radio Sci* , 6, 279 1971

67 Mohlmann, D , Ionospheric electrostatic fields, *J Atmos Terr Phys* 39, 1325, 1977

68 Mohnen, V A , Formation nature and mobility of ions of atmospheric importance, in *Electrical Processes in Atmospheres* Dolezalek, H and Reiter, R , Eds , Steinkopf, Darmstadt, 1977, 1

69 Moore, C B and Vonnegut, B , The thundercloud, in *Lightning Vol 1*, Golde, R H , Ed , Academic Press, New York, 1977, 51

70 Mozer, F S , Electric field mapping in the ionosphere at the equatorial plane *Planet Space Sci* , 18, 259, 1970

71 Mozer, F S and Lucht, P , The average auroral zone electric fields *J Geophys Res* , 79, 1001, 1974

72 Mozer, F S and Serlin, R , Magnetospheric electric field measurements with balloons *J Geophys Res* ,74 4739, 1969

73 Muhleisen, R , The global circuit and its parameters, in *Electrical Processes in Atmospheres*, Dolezalek H and Reiter, R Eds Steinkopf Darmstadt, 1977, 467

74 Neher, H V , Cosmic ray particles that changed from 1954 to 1958 to 1965, *J Geophys Res* , 72, 1527 1967

75 Nisbet, J S , Miller, N J , and Carpenter, L A , Currents and electric fields in the ionosphere due to field aligned auroral currents, *J Geophys Res* 83, 2647, 1978

76 Nopper, R W and Carovillano, R L , Polar-equatorial coupling during magnetically active periods, *Geophys Res Lett* 5, 699, 1978

77 Ogawa, T , Tanaka, Y , and Yasuhara, N , Schumann resonances and world wide thunderstorm activity, *J Geomagn Geoelectr* ,21 447 1969

78 Ogawa, T , Tanaka, Y , Huzita, A , and Yasuhara, M , Three-dimensional electric fields and currents in the stratosphere, in *Electrical Processes in Atmospheres*, Dolezalek, H and Reiter R , Eds , Steinkopf Darmstadt 1977, 552

79 Olson, D E , Evidence for auroral effects on atmospheric electricity, *Pure Appl Geophys* 84, 118, 1971

80 Paramonov, N A , Determination of the global diurnal variation of the potential gradient of the electric field in the atmosphere and the vertical conduction current (in Russian), *Meteorol Gidrol* , 12, 89, 1971

81 Park, C G , Solar magnetic sector effects on the vertical electric field at Vostok, Antarctica, *Geophys Res Lett* , 3, 475, 1976

82 Park, C G , Downward mapping of high latitude electric fields to the ground, *J Geophys Res* , 81, 168, 1976

83 Park, C G , Comparison of two and three-dimensional mapping of ionospheric electric fields, *J Geophys Res* ,84 960, 1979

84 Park, C G and Deynakaruntra, M , Penetration of thunderstorm electric fields into the ionosphere and magnetosphere I Middle and subauroral latitudes, *J Geophys Res* , 78, 6623, 1973

85 Pierce, E T , Stratospheric electricity and the global circuit, in *Electrical Processes in Atmospheres*, Dolezalek, H and Reiter R , Eds Steinkopf, Darmstadt, 1977, 582

86 Price, A. T , Electromagnetic induction within the earth, in *Physics of Geomagnetic Phenomena*, Matsushita, S and Campbell, W H , Eds , Academic Press, New York, 1967

87 Reagan, J B , Meyerott, R E , Evans, J E , and Imhof, W L , The Effects of Energetic Particle Precipitation on Global Atmospheric Electric Circuit, 6th Int Conf Atmospheric Electricity, Manchester, July 1980, in press

88 Reid, G C , The middle atmosphere, in Middle Atmosphere Electrodynamics, Maynard, N C Ed , *NASA Report CP 2090* 1979, 27

89. Reiter, R., Influences of solar activity on the electric potential between the ionosphere and the earth, in *Solar-Terrestrial Influences on Weather and Climate*, McCormac, B. M. and Seliga, T. A., Eds., Reidel, Dordrecht, Holland, 1979, 243.
90. Richmond, A. D., Electric fields in the ionosphere and plasmasphere on quiet days, *J. Geophys. Res.*, 81, 1447, 1976.
91. Richmond, A. D., Matsushita, S., and Tarpley, J. D., On the production mechanism of electric currents and fields in the ionosphere, *J. Geophys. Res.*, 81, 547, 1976
92. Rikitake, T., Electromagnetism and the earth's interior, *Dev Solid Earth Geophys.*, 2, 1, 1976.
93. Rishbeth, H. and Garriott, O. K., *Introduction to Ionospheric Physics*, Academic Press, New York, 1969.
94. Roble, R. G. and Hays, P. B., A quasi-static model of global atmospheric electricity II. Electrical coupling between the upper and lower atmosphere, *J. Geophys. Res.*, 84, 7247, 1979.
95. Rosen, J. M. and Hofmann, D. J., Balloon borne measurements of condensation nuclei, *J. Appl. Meteorol.*, 16, 56, 1977.
96. Rostoker, G., Electric and magnetic fields in the ionosphere and magnetosphere, *J. Geomagn. Geoelectr.*, 30, 67, 1978.
97. Ruhnke, L. H. and Tammet, H. F., Atmospheric Electric Currents at Widely Spaced Stations, 6th Int. Conf. Atmospheric Electricity, Manchester, July 1980, in press
98. Shaw, G. E. and Hunsucker, R. D., A study of possible correlation between the fair-weather electric field and auroral activity, in *Electrical Processes in Atmospheres*, Dolezalek, H and Reiter, R., Eds., Steinkopf, Darmstadt, 1977, 576.
99. Seshadri, S. R., *Fundamentals of Plasma Physics*, Elsevier, New York, 1973.
100. Stening, R. J., An assessment of the contributions of various winds to the Sq current system, *Planet. Space Sci.*, 17, 889, 1969.
101. Stern, D. P., Large-scale electric fields in the earth's magnetosphere, *Rev. Geophys Space Phys.*, 15, 156, 1977.
102. Takagi, M., On the regional effect in the global atmospheric electric field, in *Electrical Processes in Atmospheres*, Dolezalek, H. and Reiter, R., Eds , Steinkopf, Darmstadt, 1977, 477.
103. Tarpley, J. D., The ionospheric wind dynamo. 2 Solar tides, *Planet. Space Sci.*, 18, 1091, 1970.
104. Tyutin, A. A., Mesospheric maximum of the electric field strength, *Cosmic Res.*, 14, 132, 1976.
105. Uchikawa, K., Annual variations of the ionospheric potential, the air-earth current density and the columnar resistance measured by radiosondes, in *Electrical Processes in Atmospheres*, Dolezalek, H. and Reiter, R., Eds., Steinkopf, Darmstadt, 1977, 460.
106. Volland, H., Mapping of the electric field of the Sq current into the lower atmosphere, *J. Geophys. Res.*, 77, 1961, 1972.
107. Volland, H., The atmospheric dynamo, *J. Atmos. Terr. Phys.*, 38, 869, 1976.
108. Volland, H., Coupling between the neutral wind and the ionospheric dynamo current, *J. Geophys. Res.*, 81, 1621, 1976.
109. Volland, H., Semiempirical models of magnetospheric electric fields, in *Quantitative Modeling of Magnetospheric Processes*, Olson, W. P., Ed., Geophysical Monograph 21, American Geophysical Union, Washington, D.C., 1979, 261.
110. Volland, H. and Grellmann, L., A hydromagnetic dynamo of the atmosphere, *J. Geophys. Res.*, 83, 3699, 1978.
111. Volland, H. and Mayr, H. G., Theoretical aspects of tidal and planetary wave propagation at thermospheric heights, *Rev. Geophys. Space Phys.*, 15, 203, 1977.
112. Vonnegut, B., Moore, C. B., Espinola, R. P., and Blau, H. H., Electric potential gradients above thunderstorms, *J. Atmos. Sci.*, 23, 764, 1966.
113. Whitten, R. C. and Poppoff, I. G., *Fundamentals of Aeronomy*, John Wiley & Sons, New York, 1971.
114. Widdel, H. U., Rose, G., and Borchers, R., Experimental results on the variation of electric conductivity and ion mobility in the mesophere, *J. Geophys. Res.*, 81, 6217, 1976.
115. Wilson, C. T. R., Investigations on lightning discharges and on the electric field of thunderstorms, *Philos. Trans R. Soc. London*, A221, 73, 1920.
116. Yasuhara, F. and Akasofu, S.-I., Field-aligned and ionospheric electric fields, *J. Geophys. Res.*, 82, 1279, 1977.
117. Markson, R., Airborne atmospheric electrical measurements of the variation of ionospheric potential and electrical structure in the exchange layer over the ocean, in *Electrical Processes in Atmospheres*, Dolezalek, H. and Reiter, R., Eds., Steinkopf-Verlag, Darmstadt, West Germany, 1977, 450.

SCHUMANN RESONANCES

Charles Polk

TABLE OF CONTENTS

INTRODUCTION

In 1952 Schumann suggested in a series of papers[1-3] that the surface of the Earth and the lower edge of the ionosphere form the boundaries of a cavity resonator He calculated resonant frequencies[4] and attenuation factors[2] predicting a lowest resonance of the order of 10 Hz and a cavity Q of about 12 Between 1954 and 1959 Schumann[4-6] further amplified his theoretical work and he and his student, Konig,[5-7] published the first experimental data showing that such resonances can actually be observed In 1960 Balser and Wagner[8-9] obtained spectra based on more elaborate processing of 5 to 35 Hz natural electric field noise and gave values for the first five resonant frequencies of 8, 14 1, 20 3, 26 4, and 32 5 Hz Their data, obtained on June 27 and 28, 1960, gave a cavity Q of about 4 at the lowest resonant frequency

Since then considerable theoretical work[10-37] on Earth-ionosphere cavity resonances has been published Summaries of the theory are contained in books by Watt[13] and Galejs [16] The most recent developments are due to Bliokh,[30] Greifinger,[31] Tran,[33-35] Booker,[36] and Behroozi [37] In addition experimental observations of both electric and magnetic noise fields at several locations[38-51] have led to data on diurnal variation of noise amplitude and spectral content [38-43-48-50-51] Such data have also been used to obtain information about the distribution and intensity[45-50-52] of the lightning activity which is responsible for the excitation of the cavity and for extracting some information on the variation of electrical conductivity with altitude [24-54-55]

In the following sections theory, experimental techniques and experimental results will be reviewed

THEORY OF THE CONCENTRIC SPHERE RESONATOR

Resonances in a Cavity with Sharp, Homogeneous, Isotropic Boundaries

Referring to the coordinate system of Figure 1 and using the nomenclature generally employed for electromagnetic systems with spherical symmetry, we call those modes which have no radial component of the magnetic field "transverse magnetic" (TM) and those for which $E_r = 0$ "transverse electric" (TE) When the free space wavelength λ is large compared with the distance (h) between two concentric spherical shells, only the lowest order TM mode can propagate [12] This is clearly the case at ELF (λ = 30,000 km at 10 Hz) in the Earth-ionosphere cavity (h $\sim$ 100 km) Calculating the cut-off frequency of modes with zero electric field in the vertical direction, within a parallel-plane waveguide of height h, shows that TE modes are not significant in the Earth-ionosphere cavity at ELF (except in the immediate vicinity of a radiating source) That cut-off frequency[56] is

$$f_c = \frac{c}{2h} \qquad (1)$$

where $c = (1/\sqrt{\mu\varepsilon})$ = velocity of light in vacuum This gives $f_c \approx 1500$ Hz when h $\sim$ 100 km Since the attenuation in a waveguide well below cut-off[56] is approximately equal to 2π/cut-off wavelength, the attenuation for TE waves in the Earth-ionosphere cavity well below 1500 Hz is of the order of 200 to 300 dB/1000 km This is to be compared with a calculated and measured attenuation of the order of 0 5 dB/1000 km for the lowest order TM mode at 8 Hz

It follows from Maxwell's equations[57] that the TM fields can be expressed in terms of a scalar function ψ which satisfies the scalar Helmholtz equation

$$(\nabla^2 + k^2)\psi = 0 \qquad (2)$$

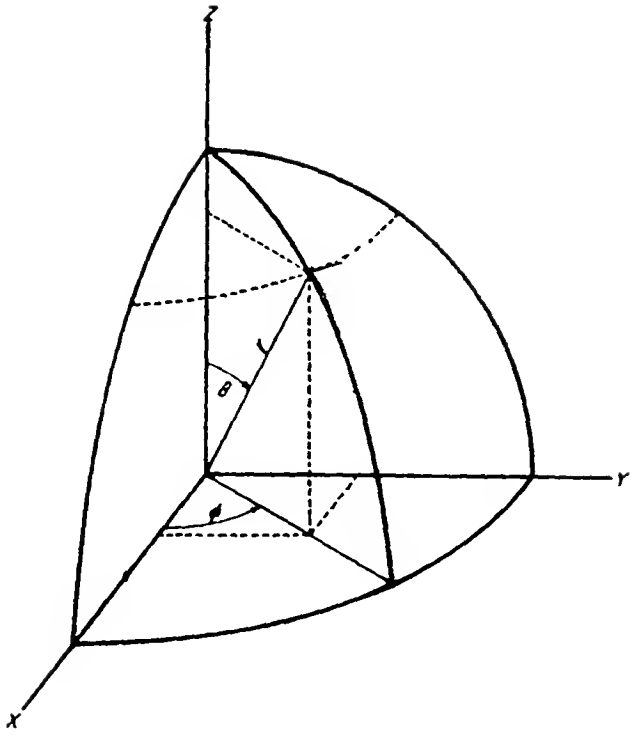

FIGURE 1. Spherical coordinates r, θ, ϕ.

where $k = \omega(\mu\varepsilon)^{-1/2}$ is the complex wave number of the medium in which wave propagation takes place. The fields are given by

$$E_r = \frac{k}{j\omega\epsilon}\left(\frac{\partial^2}{\partial r^2} + k^2\right)(r\psi) \tag{3}$$

$$E_\theta = \frac{k}{j\omega\epsilon r}\frac{\partial^2}{\partial r\partial\theta}(r\psi) \tag{4}$$

$$E_\phi = \frac{k}{j\omega\epsilon r\sin\theta}\frac{\partial^2}{\partial r\partial\phi}(r\psi) \tag{5}$$

$$H_\theta = \frac{k}{\sin\theta}\frac{\partial\psi}{\partial\phi} \tag{6}$$

$$H_\phi = -k\frac{\partial\psi}{\partial\theta} \tag{7}$$

$$H_r = 0 \tag{8}$$

For the cavity with azimuthal symmetry $\partial/\partial\phi\,(\ ) = 0$ and $E_\phi = H_\theta = H_r = 0$. Furthermore in this case the last term in the expression for $\nabla^2\psi$ below vanishes

$$\nabla^2\psi = \frac{1}{r^2}\frac{\partial}{\partial r}\left(r^2\frac{\partial\psi}{\partial r}\right) + \frac{1}{r^2\sin\theta}\frac{\partial}{\partial\theta}\left(\sin\theta\frac{\partial\psi}{\partial\theta}\right) + \frac{1}{r^2\sin\phi}\frac{\partial^2\psi}{\partial\phi^2} \tag{9}$$

such that E_r from Equation 3 can also be written, using Equation 2 and Equation 9

$$E_r = \frac{jk}{r\omega\epsilon \sin\theta} \frac{\partial}{\partial\theta}\left(\sin\theta \frac{\partial\psi}{\partial\theta}\right) \tag{10}$$

Solutions of Equation 2 can be expressed as sums of products involving spherical Bessel or Hankel functions,[58] Associated Legendre Polynomials P^m_n (cos θ) and trigonometric functions

$$\psi = \sum_{m=0}^{N} \sum_{n=0}^{\infty} D_{n,m} z_n(kr) P_n^m(\cos\theta) \begin{cases} \cos m\phi \\ \sin m\phi \end{cases} \tag{11}$$

or for the cavity with azimuthal symmetry as

$$\psi = \sum_{n=0}^{\infty} D_n z_n(kr) P_n(\cos\theta) \tag{12}$$

where

$$z_n(kr) = j_n(kr) + b_n n_n(kr) \tag{13}$$

and the constants D_n and b_n must be found from the appropriate boundary conditions For the cavity with perfectly conducting walls neither the origin ($r = 0$) nor $r = \infty$ are included in the region where the field is evaluated and therefore the radial function can take the form of Equation 13 with b_n and D_n real numbers In the more general case, involving a finitely conducting ground and a realistic model for the ionosphere, $z_n(kr)$ becomes a combination of Hankel functions

$$z_n(kr) = \begin{cases} a_n h_n^{(1)}(k_g r) & 0 \le r \le a \\ h_n^{(1)}(kr) + b_n h_n^{(2)}(kr) & a \le r \le (a+h) \\ c_n h^{(2)}(k_i r) & r \ge (a+h) \end{cases} \tag{14}$$

where $h_n^{(1)}$ (kr) and $h_n^{(2)}$ (kr) represent, respectively, incoming and outgoing waves and k_g, k, and k_i are the wave numbers for the ground, air, and the ionosphere

The series of zonal harmonics Equation 12 converges very slowly, although it can be used at ELF to obtain useful field expressions[18 20] employing 2 ka to 10 ka terms [15] Another approach, which is particularly useful if calculations are to be extended to higher frequencies, involves the Watson transformation as described by Wait[13] (p 110) where the summation of Equation 12 is replaced by a contour integral The residues of that integral are evaluated at the poles of the integrand ν. The result[13] (p 157) is

$$\psi(r,\theta) = \sum_{\nu} D_\nu z_\nu(kr) P_\nu(-\cos\theta) \tag{15}$$

where the argument $-\cos\theta$ rather than $+\cos\theta$ has been chosen to assure that P_ν has singularities at the source ($\theta = 0$) and not at the antipode ($\theta = \pi$) [59 60] The radial functions $z_\nu(kr)$ are given by Equation 14 with u replacing n

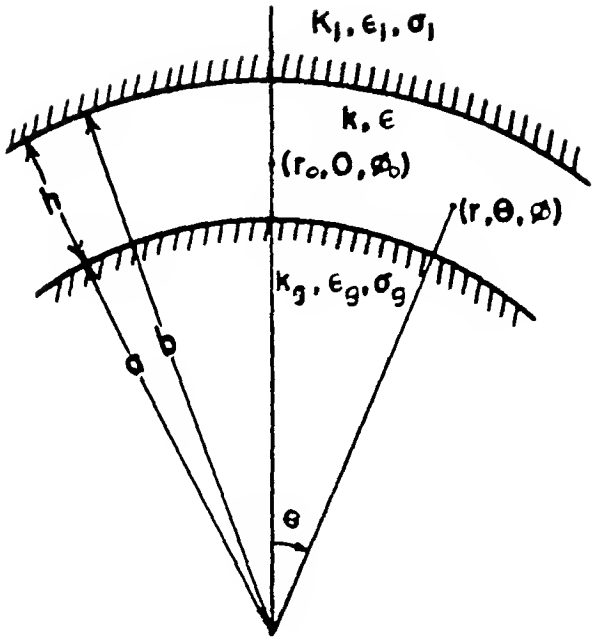

FIGURE 2. Geometry of Earth-ionosphere cavity.

The factor D_ν is obtained by requiring that ψ reduces to the proper form at the source at $r = r_o$ (Figure 2).

$$\psi_o(r, \theta) = \frac{Ids}{4\pi r_o k} \frac{e^{-ikr}}{R} \tag{16}$$

where Ids is the current moment of the source and R the distance from the source

$$R = (r_o^2 + r^2 - 2rr_o \cos \theta)^{1/2} \tag{17}$$

Employing over the neighborhood of the source the approximations $z_\nu(kr) \approx z_\nu(kr_o)e^{-ikR} \approx 1$ and $(1/R) \approx r_o^{-1}(\eta^2 + \theta^2)^{-1/2}$, where $-\varepsilon < \eta < +\varepsilon$, $\varepsilon \ll 1$, the result[13] (p. 160) is

$$\psi(r, \theta) \approx \frac{jIds}{2khr_o} \sum_{n=0,1,2}^{\infty} \frac{z_\nu(kr_o) z_\nu(kr) P_\nu(-\cos \theta)}{z_\nu(ka) z_\nu(ka) \sin \nu\pi} \delta_n \tag{18}$$

where the z_ν ( ) are functions of n[13] (p. 158) and

$$\delta_n = \frac{1}{1 + \dfrac{\sin 2khC_n}{2khC_n}} \tag{19}$$

and C_n is the cosine of the angle of incidence for the nth mode. Also $\delta_o \approx \frac{1}{2}$ and $\delta_n = 1 (n \neq 0)$.

It has been pointed out[13,15] that at ELF when $h \ll \lambda$ only the $n = 0$ mode in Equation 18 is significant. Thus

$$\psi(r, \theta) \approx \frac{jIds}{4khr_o} \frac{z_\nu(kr_o) z_\nu(kr)}{z_\nu(ka) z_\nu(ka)} \frac{P_\nu(-\cos \theta)}{\sin \nu\pi} \tag{20}$$

We now make the approximation $r \simeq r_e \simeq a$ and note[13 59] that

$$\frac{1}{\sin\theta}\frac{\partial}{\partial\theta}\left(\sin\theta\,\frac{\partial P_\nu(-\cos\theta)}{\partial\theta}\right) + \nu(\nu+1)P_\nu(-\cos\theta) = 0 \qquad (21)$$

Combination of Equations 10, 21, and 18 then gives

$$E_r = \frac{k}{r\omega\epsilon}\,\frac{Ids}{4\pi ka}\,\nu(\nu+1)\,\frac{P_\nu(-\cos\theta)}{\sin\nu\pi} \qquad (22)$$

Using the expansion formula[13] (p 164)

$$\frac{P_\nu(-x)}{\sin\nu\pi} = -\frac{1}{\pi}\sum_{n=0}^{\infty}\frac{2n+1}{n(n+1)-\nu(\nu+1)}P_n(x) \qquad (23)$$

we obtain

$$\Gamma_r = \frac{Ids}{4\pi a^2\epsilon\omega h}\,\nu(\nu+1)\sum_{n=0}^{\infty}\frac{2n+1}{n(n+1)-\nu(\nu+1)}P_n(\cos\theta) \qquad (24)$$

Referring to Equations 4 and 20 and considering first a cavity with perfectly conducting walls, it is clear that $E_\theta = 0$ at the boundaries requires

$$\frac{\partial^2}{\partial r\,\partial\theta}\left[z_\nu(kr)\,\frac{P_\nu(-\cos\theta)}{\sin\nu\pi}\right] = 0 \qquad \text{at } r = a,\ r = a+h \qquad (25)$$

At ELF the radial functions may be approximated either by exponentials[16] or by a Taylor series expansion[16 33] Employing the Taylor series expansion one obtains[33] for perfectly conducting boundaries at $r = a$, $(a+h)$ the following relation for the eigenvalues ν of this problem

$$\nu(\nu+1) = (ka)^2 \qquad (26)$$

The Schumann resonances are then those frequencies for which the denominator in Equation 24 becomes zero

$$\omega_{n\infty} = \frac{c}{a}\sqrt{n(n+1)} \qquad (27)$$

The subscript ∞ is used to indicate that this result is applicable only to an Earth and ionosphere with infinite conductivity The first four frequencies are

$$f_{n\infty} = 7.5\sqrt{n(n+1)} = 10.6,\ 18.36,\ 25.6,\ 33.54\ \text{Hz}$$

If the boundaries of the cavity are not perfectly conducting, the condition of Equation 25 is replaced by the requirement for continuity of E_θ and H_ϕ at $r = a$ and $r = a+h$ If only the ground ($r = a$) remains perfectly conducting — a reasonable approximation at ELF where, for example, the ratio of conduction current to displacement current $(\sigma/\omega\epsilon) \simeq 10^5$ at 14 Hz even over dry land ($\sigma \simeq 10^{-3}$ S/m) — Equation 25 still applies at $r = a$ or, equivalently, the surface impedance of the ground $Z_s = 0$ How-

ever at r = a + h, the surface impedance $Z_i = (E_\theta/H_\phi)$ at the lower boundary of the ionosphere is in general a frequency dependent complex number determined by the properties of the ionosphere. In this case[33] Equation 26 must be replaced by

$$\nu(\nu+1) = (ka)^2\,[1 - jZ_i/(\eta kh)] \tag{28}$$

where $\eta = (\mu_o/\varepsilon_o)^{1/2}$ and $k = \omega\,(\mu_o\varepsilon_o)^{1/2}$.

Since the values of ν given by Equation 28 are now complex, $|E_r|$ given by Equation 24 now remains finite at the "resonances" which are defined as the maxima of $|E_r|$. Several of the pertinent papers[24] and books[13,16] also employ a complex propagation constant defined by

$$jkS_\nu = \alpha + j\beta \tag{29}$$

$$\nu(\nu+1) = (kaS_\nu)^2 \tag{30}$$

where $S_\nu = \sin\gamma_\nu$ and γ_ν is the "virtual complex angle of incidence"[33] at the lower boundary of the ionosphere (γ_ν would be the actual complex angle of incidence only in a parallel plane guide without curvature[33]). With this definition

$$\text{Re } S_\nu = \frac{\beta}{k} = \frac{c}{v} = \frac{\text{free space velocity}}{\text{phase velocity in guide}} \tag{31}$$

$$\text{Im } S_\nu = \frac{\alpha}{k} = \alpha\frac{c}{\omega} \tag{32}$$

$$\alpha \approx 1.36\,\text{Im}\nu \quad \text{dB/Mm} \tag{33}$$

Since typical values[33] of ν for a realistic ionosphere are usually such that Re $S_\nu \gg$ Im S_ν (for example $\nu \approx 1 - j0.2$ and ka $S_\nu \approx 2 - j0.3$ near 10 Hz), the "resonant frequencies" or maxima of Equation 24 are given by

$$\omega_n \approx \frac{\omega_{n\infty}}{\text{Re}S_\nu} = 2\pi\,\frac{7.5\,[n(n+1)]^{1/2}}{\text{Re}S_\nu} \tag{34}$$

and typical observed values of the lowest resonant frequencies[8,55] are approximately 8, 10, and 14 Hz. The spectra take the general appearance illustrated by Figure 3 and the cavity Q, which is inversely proportional to attenuation, may be related to the widths of the resonance peaks.

Q is defined as the ratio of the product of ω and energy stored per cycle to the average power dissipated with steady sinusoidal excitation. When the numerical value of Q is high ($\geqslant$10) this analytical definition is equivalent to the experimentally useful definition of Q = (resonance frequency)/(bandwidth between half power points). Based on the analytical definition, Galejs[16,63] derived the following expressions applicable to the Earth-ionosphere cavity

$$Q = \frac{(\text{Re}S)^2 + 1}{4(\text{Re}S)(\text{Im}S)} \tag{35}$$

$$Q = \frac{1}{2(\text{Re}S)(\text{Im}S)} \tag{36}$$

$$Q = \frac{\text{Re } S}{2(\text{Im } S)} \tag{37}$$

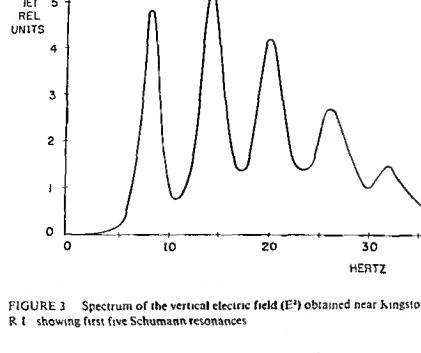

FIGURE 3 Spectrum of the vertical electric field (E^2) obtained near Kingston, R I showing first five Schumann resonances

In Equation 35, both the electric and magnetic stored energies are considered, in Equation 36 only the stored magnetic energy, and in Equation 37 only the stored electric energy Equations 35 to 37 were derived by considering only the leading terms (i e , resonance terms) in Equation 24 But since Q is below 10 for the Schumann resonances, the terms in the series expansion just above and below the nth resonance term significantly affect the actual power spectra and expressions in Equations 35 to 37 give different values from the "operational" 3 dB-point definition of Q which was applied by Jones[22-24] to the frequency-dependent part of Equation 24 All of these definitions are mutually consistent only if Q is high, in that case Re S ≈ 1 and Equations 35, 36, and 37 are obviously identical For the Schumann resonances, when Q is usually well below 10, the 3 dB definition gives, however, a value which is less than any of the other definitions [25]

When the object of an investigation is to relate experimental power spectra to atmospheric parameters it is probably best not to employ any of the above definitions Instead it can be shown by numerical experiments[55] that Imv is simply related to the width of the experimental data at the 90% level (i e , at $|E(\omega)|^2 = 0.90\,|E(\omega_n)|^2$)

Resonances in a Cavity Bounded by a Radially Inhomogeneous but Isotropic "Ionosphere" Extending to Ground Level

Layered ionosphere profiles[22-24] and profiles in which the electrical conductivity varies exponentially with height[14] have been used by various authors to obtain analytical models which give resonance spectra similar to those observed experimentally Following the theoretical development of Wait[12 13] it has been shown by Tran and Polk[53 54] that the approximation of planar stratification is adequate for the computation of the lowest three ELF resonance frequencies to within 0 1 Hz However, planar stratification will lead to errors in cavity Q or wave attenuation with increasing frequency (1 5% at 10 Hz, 23% at 45 Hz) Finally, computation of resonance frequencies to within 0 1 Hz requires the extension of the lower boundary of the "ionosphere" to a height where the ratio of conduction current to displacement current is less than 0 3, this means that the height of the lowest layer in the stratification illustrated by Figure 4 becomes about 30 km at 7 5 Hz Computation of wave attenuation and Q also requires that the nonzero conductivity even of that lowest layer,[35] $\sigma_e \sim 3\ 3\ [10^{-1}]$S/m, be taken into account.

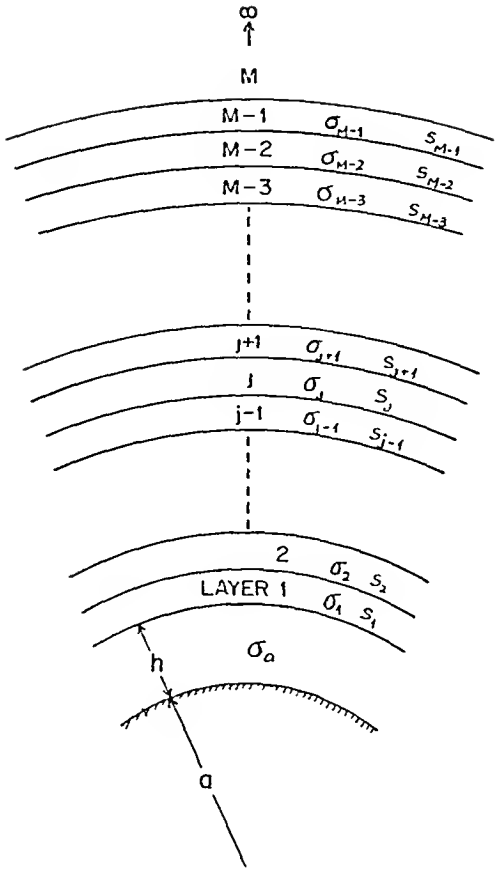

FIGURE 4. Geometry of stratified ionosphere.

The computation of the eigenvalues ν still involves Equation 28, but the surface impedance Z_1 at the top of the lowest layer in Figure 4 is modified to take into account the effect of all the higher layers. Each of the M layers is made so thin that it can be considered homogeneous — that is its thickness is made much smaller than the local wavelengths. The uppermost layer is chosen at an altitude where the change of conductivity has no calculable effect on the waves in the cavity and therefore any inhomogeneity beyond this layer is disregarded. Thus the M'th layer is assumed to extend to infinity with constant conductivity, therefore no downcoming (reflected) wave needs to be considered in this layer. For each of the other layers the solution of Equation 2 takes the form of Equation 15 with a single value of ν; thus for the jth layer

$$\psi_j = a_j h_\nu^{(1)}(k_j r) - b_j h_\nu^{(2)}(k_j r)\, P_\nu(-\cos\theta) \tag{38}$$

The tangential electric and magnetic fields E_θ and $H_\bullet$ must be continuous across all boundaries. This is equivalent to the continuity of the surface impedances

$$Z_j = \left.\frac{E_{\theta,j+1}}{H_{\phi,j+1}}\right|_{r=r_j} = \left.\frac{E_{\theta,j}}{H_{\phi,j}}\right|_{r=r_j} \tag{39}$$

which leads to a very complicated expression[33] for Z_j containing Z_{j+1}, $\eta_{j+1} = \sqrt{\mu_{j+1}/\epsilon_{j+1}}$

and the spherical Hankel functions $h_\nu^{(1)}$ $h_\nu^{(2)}$ with arguments $(k_{\rho+1}\, r_j)$ and $(k_{\rho+1} r_{\rho+1})$ as well as their logarithmic derivatives $\ln' [k_{\rho+1} r_j h_\nu^{(1)(2)}(k_{\rho+1} r_j)]$ The latter are given by

$$\ln' \left[z\, h_\nu^{(1)}(z) \right] = \frac{(\nu+1)}{z} - \frac{H_{\nu+3/2}^{(1)}(z)}{H_{\nu+1/2}^{(1)}(z)} \tag{40}$$

Details of the precautions which must be taken in evaluating these functions numerically have been discussed by Tran [33]

As pointed out above, spherical stratification is only needed for the evaluation of cavity Q or attenuation, or if the resonance frequencies must be evaluated with an error of less than 0 1 Hz Differences obtained[32] when comparing Re ν evaluated by the much simpler planar stratification[32 33] with the results of spherical stratification were less than 0 5% below 30 Hz

Wait[33] (p 321) using the second order or Debye approximation for the spherical Hankel functions showed that the surface impedance Z, at the lower boundary of the ionosphere can be evaluated by modeling the ionosphere as a plane stratified medium However that approximation requires

$$\left| \frac{\nu + \frac{1}{2}}{kr} \right| << 1 \tag{41}$$

$$\left| \nu + \tfrac{1}{2} \right| >> 1 \tag{42}$$

$$\left| kr \right| >> 1 \tag{43}$$

and for frequencies below 50 Hz neither Equation 42 nor $|ka| \gg 1$ are satisfied, nevertheless results obtained by planar stratification[33] do not deviate greatly from those obtained by the more appropriate spherical stratification

Another approach[31] to calculating the eigenvalue which gives phase velocity (and resonance frequency) as well as attenuation within the cavity consists of an approximation which assumes that details of the conductivity profile are important only in two limited altitude ranges the lower where conduction current and displacement current are equal ($\sigma = \omega\varepsilon_o$) and the upper where the character of the propagation process changes from wave-like to diffusion-like That latter height, h_i, is shown to be given by $4\,\mu_o\omega\sigma_i\xi_i^2 = 1$, ξ_i being the conductivity scale height (i e , the distance over which σ changes by a factor e^{-1}) at h_i Calculations using this approach have been published[31] only for frequencies of 50 Hz and 100 Hz — above the Schumann resonances — but should also give useful approximate results at lower frequencies At 50 Hz and 100 Hz the results for phase velocity and attenuation agree very well with those obtained by more standard full-wave calculations

Realistic conductivity profiles are needed with all of these methods for the evaluation of the eigenvalues ν (or S = kr ν) Here one notes that over the entire Schumann resonance frequency range the wave frequency is always far smaller than the collision frequency in the lower ionosphere The effective electrical conductivity of the ionosphere plasma can then be obtained[44] from

$$\sigma_j = \sum_k \frac{N_k e^2}{m_k u_k} \tag{44}$$

where N_k, m_k, u_k are the number density, mass, and collision frequency of the kth ion

species, and e is the electronic charge (all particles are assumed to be singly charged). Collision frequencies can be calculated from the following equations[65 66]

$$u_e = u_{en} + u_{ei} \tag{45}$$

$$u_i = u_{in} + u_{ie} \approx u_{in} \tag{46}$$

where the subscripts e, i, and n refer to electrons, ions, and neutral particles.

$$u_{en} = (5.4)\ 10^{-16}\ N_n T^{1/2}$$

$$u_{in} = (2.6)\ 10^{-15}\ N_n M_i^{-1/2} \tag{47}$$

$$u_{ei} = (10^{-6})(59.0 + 4.18 \log_{10} T^3/N_e) N_e T^{-3/2}$$

T is the temperature in degrees K, $N_{e,n}$ the number density per m^3, and M_i is the ionic molecular weight, which is chosen to be 29 for all illustrations used in this chapter. Values of N_n and T are tabulated in the U.S. Standard Atmosphere[67] and the ionosphere is assumed to be neutral ($N_+ = N_- + N_e$); some typical values are also given in Table 1. Below 60 km ionic conductivity becomes significant[24 54] and ions rather than electrons are primarily responsible for the conductivity below 50 km. Galactic cosmic rays are probably the most important source of ionization at these elevations[68] and available ion density data have been obtained by measurements from rockets,[69,70] balloons,[71,72] and rocket launched parachutes.[73] Data on electron and ion densities, temperature, and collision frequencies are also given in Whitten and Poppoff[76] and Banks and Kockarts.[77]

An analytic approximation to the electron density profile of the D-, E-, F-1, and F-2 layer has been derived by Booker.[74] His purpose was to obtain a profile without discontinuities of slope which cause difficulties in evaluating exact solutions for propagation of waves through the ionosphere. Booker's published analytic profile[74] for the day ionosphere starts at 55 km and that for the night ionosphere at 80 km; however, the method can be applied to fit a variety of experimental data. No attempt was made to evaluate positive or negative ion densities at lower elevations in this profile, but Pappert and Moler[75] in a related paper concerned with ELF propagation at 75 Hz summarize results of ion and electron density data down to ground level.

Effects of the Earth's Magnetic Field

In an ionized medium which is subjected to a steady magnetic flux density $\bar{B}_o$, charged particles acquire velocities perpendicular to the applied fields and as a consequence the complex dielectric permittivity ε or the complex conductivity σ assume tensor form.[64,70] If we use rectangular coordinates with the z-axis along $\bar{B}_o$, the components of σ are given by

$$<\sigma> = <\sigma_i> + <\sigma_e> = \omega_{p,i}^2 [\ ] + \omega_{p,e}^2 [\ ] \tag{48}$$

where the squares of the ion and electron plasma frequencies ω_{p_i} and ω_{p_e} are

$$\omega_{pi}^2 = \frac{Z_i^2 |e|^2 N_i}{m_i \epsilon_o} \qquad \omega_{pe}^2 = \frac{|e|^2 N}{m \epsilon_o} \tag{49}$$

and Z_i = number of electronic charges per ion; e = charge of electron; N_i, N number

of ions and electrons per m^3, m_e, m ion and electron mass, ε_o = dielectric permittivity of free space and

$$\langle \sigma_e \rangle = \omega_{pe}^2 \varepsilon_o \begin{vmatrix} \frac{u + j\omega}{(u + j\omega)^2 + \Omega^2} & \frac{-\Omega}{(u + j\omega)^2 + \Omega^2} & 0 \\ \frac{\Omega}{(u + j\omega)^2 + \Omega^2} & \frac{u + j\omega}{(u + j\omega)^2 + \Omega^2} & 0 \\ 0 & 0 & \frac{1}{u + j\omega} \end{vmatrix} \tag{50}$$

u = electron collision frequency u_i as defined by Equation 45, and Ω = electron gyro frequency = $B_o e/m$ The form of $\langle \sigma_e \rangle$ is identical to that of $\langle \sigma_e \rangle$ with u_i replacing u and Ω_i = $(BZ_i e)/m$, replacing Ω It is obvious that for $u \gg \omega$ and $\Omega = 0$ the off-diagonal terms in Equation 50 vanish and $\langle \sigma \rangle$ reduces to the scalar value given by Equation 44 so that current density and electric field are related by $\bar{J} = \sigma \bar{E} = (\sigma_1 + j\omega\varepsilon_1)\bar{E}$ where σ_1 and $\varepsilon_1 = \varepsilon_o$ are the real parts of the complex conductivity σ and complex dielectric permittivity ε As illustrated in Table 1 $u \gg \omega$ and $u_i \gg \omega$ are satisfied at all elevations which are of interest at ELF below 50 Hz Also at very low elevations ($h < 50$ km) $u \gg \Omega$ and $u_i \gg \Omega_i$ are satisfied However, it is clear from Table 1 that for higher elevations, for example at 75 km, $u \sim \Omega$ such that the components of $\bar{J}$ transverse to $\bar{B}_o$ are modified Examination of Equation 50 indicates that the diagonal terms σ_{11} and σ_{22} with and without B_o field (without B_o $\sigma_{11} = \sigma_{22} = \sigma_{33}$) are related by

$$\frac{\sigma_{11}}{\sigma_{33}} \approx \left[1 + \frac{\Omega^2}{u^2}\right]^{-1} \qquad u >> \omega \tag{51}$$

and that the off-diagonal terms, the "Hall" conductivities, are related to the isotropic medium conductivity σ_{33} by

$$\frac{|\sigma_{12}|}{\sigma_{33}} \approx \frac{\left(\frac{\Omega}{u}\right)}{1 + \left(\frac{\Omega}{u}\right)^2} \qquad u >> \omega \tag{52}$$

Thus one would expect that at elevations where Ω/u becomes significant, the presence of the magnetic field might affect propagation However, propagation inside the cavity, that is propagation at very low elevation, is only affected by reflection of waves from the upper boundary One must therefore look primarily for effects of B_o upon the reflection coefficient For TEM waves in isotropic media the reflection coefficient $R = (Z - \eta_o)/(Z + \eta_o)$ is given, when the medium with impedance Z is a very good conductor,[57] by

$$R \approx 1 - 2\sqrt{j\frac{\omega\varepsilon_o}{\sigma}} \tag{53}$$

Consequently for slight deviations from the isotropic case, one would expect differences in R due to changes in conductivity to be roughly proportional to the square root of the quantity

$$\frac{\omega\varepsilon_o}{\sigma_{33}} \approx \frac{\omega\varepsilon_o u}{\omega_p^2 \varepsilon_o} = \frac{\omega}{\omega_t} \tag{54}$$

Table 1
TYPICAL LOWER IONOSPHERE PARAMETERS

	Quiet ionosphere				Disturbed ionosphere				
	Day (noon)		Night		Day (noon)		Night		
	45 km	75 km	45 km	75 km	45 km	75 km	45 km	75 km	Ref.
N_e m^{-3}	$8(10^{4})$	$5(10^{8})$	0	$1(10^{6})$	$1(10^{8})$	$2(10^{11})$	0	$1(10^{8})$	76 (p. 128, 146) 65 (p 83)
N_i m^{-3}	$1(10^{9})$	$8(10^{7})$	$1(10^{9})$	$2(10^{8})$	$1(10^{11})$	$7(10^{10})$	$1(10^{11})$	$2(10^{11})$	55 37
N_n m^{-3}	$5(10^{22})$	$9(10^{20})$	$5(10^{22})$	$9(10^{20})$	$5(10^{22})$	$9(10^{20})$	$5(10^{22})$	$9(10^{20})$	67
T K	265	200	265	200	265	200	265	200	67
u_{en} s^{-1}	$5(10^{8})$	$3(10^{6})$	$5(10^{8})$	$3(10^{6})$	$5(10^{8})$	$3(10^{6})$	$5(10^{8})$	$3(10^{6})$	76 (p. 169) Eq. 47
u_{in} s^{-1}	$2.4(10^{7})$	$4.3(10^{4})$	$2.4(10^{7})$	$4\ 3(10^{5})$	$2.4(10^{7})$	$4.3(10^{5})$	$2.4(10^{7})$	$4.3(10^{5})$	Eq. 47
ω_p^2s^{-2}	$2.53(10^{8})$	$1.59(10^{12})$	—	$3.17(10^{9})$	$3.17(10^{11})$	$6.34(10^{14})$	—	$3.17(10^{11})$	Eq. 49
σ_{1e} S/m	$4.5(10^{-12})$	$4.7(10^{-6})$	—	$9.3(10^{-9})$	$5\ 6(10^{-9})$	$1\ 9(10^{-3})$	—	$9\ 3(10^{-7})$	Eq. 44
σ_{1i} S/m	$2.3(10^{-11})$	$1(10^{-10})$	$2.3(10^{-11})$	$2.5(10^{-10})$	$2\ 3(10^{-9})$	$8.8(10^{-8})$	$2.3(10^{-9})$	$2\ 5(10^{-7})$	
$\sigma_{12e}/\sigma_{13e}$	10^{-2}	0.43	10^{-2}	0.43	10^{-2}	0.43	10^{-2}	0.43	Eq. 50 Eq.52
$\sigma_{12i}/\sigma_{33i}$	$4.2(10^{-6})$	$2.4(10^{-4})$	$4.2(10^{-6})$	$2.4(10^{-4})$	$4.2(10^{-6})$	$2\ 4(10^{-4})$	$4.2(10^{-6})$	$2.4(10^{-4})$	B_o = 0.3 G
ω_e s^{-1}	0.5	$5.3(10^{5})$	—	10^{3}	634	$2.1(10^{8})$	—	10^{5}	Eq. 55
Ω_e/u_{en}, B = 0.3 G	10^{-2}	1.75	10^{-2}	1 75	10^{-2}	1 75	10^{-2}	1 75	Eq 50
$\frac{\sigma_{1e}+\sigma_{1i}}{\omega\varepsilon_0;\omega = 50}$	0.052	10^{4}	0.052	21.0	5.2	$4.3(10^{6})$	5.2	2100	Cond. curr. / Displ curr

where

$$\omega_r = \frac{\omega_p^2}{\upsilon} \tag{55}$$

Propagation in the cavity, where the B_o field is parallel to the E field or transverse to the direction of propagation (in the Earth-ionosphere cavity at high latitudes), should therefore depend upon both parameters, ω, and Ω_T/υ where

$$\Omega_T = \Omega \sin \alpha \tag{56}$$

α = angle between direction of propagation and $\overline{B}_o$.

Before proceeding to a discussion of quantitative results obtained by computations which are directly applicable to Schumann resonances in the Earth-ionosphere cavity in the presence of $\overline{B}_o$, we note also from Equation 50 and Ampere's law, $\nabla \times \overline{H} = j\omega\langle\varepsilon\rangle\overline{E} = \langle\sigma\rangle\overline{E}$ (where ε_{jk} and σ_{jk} are complex), that changes in the diagonal components of $\langle\sigma\rangle$ affect only the field components in one type of propagation mode. Thus, for example, for propagation of a TE mode ($E_z = 0$) in the x-direction (transverse to B_o) indicated by $\exp j(\omega t - k_1 x)$ and a time varying H in the z direction

$$-\frac{\partial H_z}{\partial x} = jk_1 H_z = \sigma_{22} E_y \quad \text{when } \sigma_{21} = 0 \tag{57}$$

On the other hand the off-diagonal terms in $\langle\sigma\rangle$ produce mode coupling. Thus starting with the same TE mode ($E_z = 0$), we find that H_z propagating in the x-direction is related to E_y and to an E_z of a TM mode when $\sigma_{21} \neq 0$

$$-\frac{\partial H_z}{\partial x} = jk_1 H_z = \sigma_{21} E_x + \sigma_{22} E_y \tag{58}$$

In general, an electromagnetic wave entering the ionosphere is traveling at some arbitrary angle to the magnetic field of the Earth. The index of refraction

$$\mu = \frac{\text{velocity of wave in vacuum}}{\text{phase velocity}} \tag{59}$$

is then given by the Appleton-Hartree formula[13 15 65 78 80]

$$\mu^2 = 1 - \frac{X}{1 - jZ - \dfrac{\frac{1}{2}Y_T^2}{1 - X - jZ} \pm \left\{ \dfrac{\frac{1}{4}Y_T^4}{(1 - X - jZ)^2} + Y_L^2 \right\}^{1/2}} \tag{60}$$

where

$$X = \frac{\omega_{pe}^2}{\omega^2} \quad Z = \frac{\upsilon}{\omega} \quad Y = \frac{\Omega}{\omega} \quad Y_L = Y\cos\alpha \quad Y_T = Y\sin\alpha$$

At ELF only the case $Y > 1$ is of interest. When propagation is perpendicular to the magnetic field $Y_L = 0$, Equation 60 gives two values

$$\mu_o^2 = 1 - \frac{X}{1 - jZ} \tag{61}$$

and

$$\mu_x^2 = 1 - \frac{X}{1 - jZ - \dfrac{Y^2}{1 - X - jZ}} \tag{62}$$

The value of μ_o given by Equation 61 determines the behavior of the "ordinary" wave in which electron motion is not affected by the magnetic field of the Earth, μ_o being independent of Y. The value of μ_x determines the behavior of the "extraordinary wave".

When propagation is parallel to the magnetic field of the Earth ("longitudinal") $Y_T = 0$ and Equation 60 reduces to

$$\mu^2 = 1 - \frac{X}{1 - jZ \pm Y} \tag{63}$$

The minus sign in the denominator in this case implies a real value of μ for all $Y > 1$ when $Z \approx 0$ which is the Whistler mode.[80-82] It can also be shown[13] that the longitudinal mode is circularly polarized and that the indices of refraction for the two waves of opposite circular polarization are given by the two values corresponding to $\pm Y$ in Equation 63.

A very detailed discussion of Equation 60 with consideration of many possible special cases has been given by Budden.[80] The application of magneto-ionic theory to reflection from stratified media with particular application to VLF and ELF has been carried out in considerable detail by Galejs[16] and Wait.[13] We use here Wait's quantitative results for the evaluation of the reflection coefficient in a stratified magnetoplasma as applied to the Earth-ionosphere waveguide or cavity.

Using Booker's "quasi-longitudinal" approximation[83] for the case when the magnetic field of the Earth is steeply dipping (applicable at medium and high latitudes) Wait shows that at ELF

$$A_1 = \frac{\text{Attenuation with magnetic field}}{\text{Attenuation without magnetic field}} \simeq \frac{\cos\left(\dfrac{\tau}{2}\right)}{(\cos\tau)^{1/2}} \tag{64}$$

where

$$\tan\tau = \frac{\Omega\cos\alpha}{u} \tag{65}$$

We note then from Table 1 that $\tan\tau$ will always be below 1 at an altitude of 45 km and reach 3 only at very high altitudes. The values of A_1 corresponding to $\tan\tau = 1$, 2 and 3 are 1.10, 1.27, 1.44. Since Equation 64 with $\tan\tau > 1$ should apply only to a small part of the reflecting surface which is effective at ELF, the effect upon attenuation or cavity Q averaged over the entire cavity should be less than that indicated by these numbers.

Equation 64 is only valid when

$$\frac{\Omega_T^4}{4\omega^2\Omega_L^2} << \left|\left(1 - \frac{\omega_p^2}{\omega^2} - j\frac{u}{\omega}\right)^2\right| \tag{66}$$

where $\Omega_L = \Omega \cos \alpha$ When Ω_T is large, for example for propagation along the magnetic equator, Wait[13] shows that the reflection coefficient from the plane boundary of a magneto-ionic plasma is

$$R = \frac{C - \Delta}{C + \Delta} \tag{67}$$

where C = cosine of complex angle of incidence, and

$$\Delta = \left[\frac{j\omega}{\omega_r}\right]^{1/2} X_1 \tag{68}$$

with ω_r as given by Equation 55 and

$$X_1 = \frac{\left(1 + \frac{j\omega}{\omega_r}\right)^{1/2}\left(1 + \frac{j\omega}{\omega_r} + j\frac{\Omega_T^2\omega}{u^2\omega_r}\right)^{1/2} - \frac{\Omega_T}{u}\left(j\frac{\omega}{\omega_r}\right)}{\left(1 + j\frac{\omega}{\omega_r}\right)^2 - \frac{\Omega_T^2\omega^2}{u^2\omega_r^2}} \tag{69}$$

The value of S, corresponding to S_r of Equation 29, which gives attenuation and phase velocity is

$$S = \left[1 - j\frac{\Delta}{kh}\right]^{1/2} \tag{70}$$

Substituting values of $(\Omega_T/u) \leqslant 2$ and $\omega_r \simeq 5(10^5)$ for 75 km, as indicated by Table 1, and $\omega \leqslant 63$ (frequencies $\leqslant$ 10 Hz), shows that phase velocity (or resonance frequency) and attenuation (cavity Q) are affected only by a few percent, but that the effect is greater at 20 Hz than at 10 Hz

In a series of papers Large and Wait[64-67] extended the theory outlined above and applied it directly to the problem of ELF resonances in the Earth-ionosphere cavity The theoretical work which probably comes closest to achieving a realistic representation of the physical situation[67] treats a ring magnetic source which includes excitation by a vertical electric dipole as a special case All ionization below 50 km was disregarded to avoid excessive difficulties in the numerical evaluation Conclusions of this paper are

1 In agreement with what was derived from Equations 67 to 70 magnetic field effects become larger as the frequency increases
2 The geomagnetic field has more influence on the cavity resonances over the night than over the day hemisphere
3 Coupling between TM and TE modes due to the geomagnetic field produces no calculable effect when a typical day-time ionosphere conductivity profile is used For a night-time ionosphere profile, mode coupling lowers resonance frequencies by about 5% and cavity Q by about 10% (The Q for a night-time ionosphere extended over the entire Earth is considerably lower, even without the effect of $\overline{B}_o$, than the Q for a day-time ionosphere)

In a recent paper, Booker and Lefeuvre[68] used an approximate approach which neglects the curvature of the Earth and involves the phase-integral method[69] above a critical reflection level to calculate ELF phase velocities and attenuation rates Propa-

gation of ordinary and extraordinary waves is considered, but coupling between these waves is disregarded. Collisional absorption below the reflection level is also taken into account. Although the paper is concerned primarily with propagation at higher ELF frequencies (above 45 Hz), Schumann resonances are considered as a limiting case. Higher than experimentally observed attenuation at 7.5 Hz is predicted "not because of undue leakage of energy through the E-region in association with the low night-time ionization density . . . but because electronic and ionic collisions caused too much absorption of energy below the reflection level." Booker and Lefeuvre state that, "to avoid this, it is necessary to give the E-region a sharp bottom at night" (at about 90 km) "similar to that existing during the daytime at 80 km."

Greifinger and Greifinger[31] have extended their approximate method for the evaluation of ELF propagation parameters which was discussed in "Resonances in a Cavity Bounded by a Radially Inhomogeneous, but Isotopic Ionosphere Extending to Ground Level" above to include the effects of a steeply dipping magnetic field.[89] As before they derive two critical heights: h_o is the altitude at which the conduction current parallel to the magnetic field is equal to the displacement current; h_1, defined in the section just mentioned, is the altitude where the absolute value of the local reciprocal wave number becomes equal to the local scale height of the refractive index. Concerning Schumann resonances they conclude that "although all of the heating dissipation takes place in a narrow altitude region around h_o, the local attenuation rate (i.e., the ratio of the local heating rate to the horizontal flow rate at the same level) is an increasing function of altitude. Thus an unweighted average of the local attenuation rate will exceed the actual horizontal attenuation rate. For a given profile, the difference between the two values increases with decreasing frequency duc to the lowering of the altitude h_o. This perhaps accounts for the difficulty experienced by Booker and Lefeuvre[88] in reconciling the observability of the nighttime Schumann resonance with generally accepted nighttime profiles."

Bezrodny et al.[28] in their analysis of the Schumann resonances in a cavity with anisotropic boundaries predict resonance line splitting of the first resonance into three lines at 7.6, 8.05, and 8.5 Hz when the ratio of gyrofrequency to electron-neutral collision frequency is 0.5. However this result is obtained by assuming a radial magnetic field of constant amplitude over each hemisphere which abruptly changes sign over the equator — an assumption which probably greatly exaggerates any real effect. Furthermore Bezrodny et al.[28] point out that despite the predicted "line splitting" the actual observable resonance spectra, such as Figure 3, should be "smooth", i.e., have single resonance peaks, because the low Q implies that the separation of the split maxima is smaller than the individual line width.

In view of the many approximations which must be made in evaluating the effects of the magnetic field of the Earth upon the Schumann resonances — for example, planar stratification of the ionosphere, neglect of ionization below 50 km and specification of $\bar{B}_o$ with constant magnitude and dip over the entire cavity — and the very small changes in resonance frequencies and Q predicted by these anisotropic ionosphere models, it appears that analysis employing an isotropic ionosphere is useful for comparison of theory with experimental results in this frequency range. However, in view of the prediction that the effect of the magnetic field of the Earth upon the Schumann resonances should become larger as the frequency increases, it is desirable to employ only the lower part of the spectrum (below 20 Hz and preferably below 15 Hz) when the isotropic theory is used to deduce from experimental data information about upper atmosphere or ionosphere conductivity, or about the location of excitation sources as discussed in "Interpretation and Use of Data", page 155.

Effects of Lateral Inhomogeneities

The real ionosphere varies not only with height, but also in the "horizontal" direc-

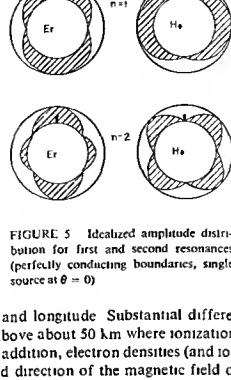

FIGURE 5 Idealized amplitude distribution for first and second resonances (perfectly conducting boundaries, single source at $\theta = 0$)

tion, i e , with latitude and longitude Substantial differences exist between the day and night hemispheres above about 50 km where ionization is due to solar rather than cosmic ray radiation In addition, electron densities (and ion densities at low altitudes), as well as magnitude and direction of the magnetic field of the Earth, vary with latitude During solar disturbances which give rise to "PCA" (Polar Cap Absorption) events, the ionosphere down to latitudes of approximately 60° can be profoundly modified

Effects of various lateral inhomogeneities upon the Schumann resonances have been analyzed in considerable detail by Madden and Thompson[25] and by Large and Wait [27]

Madden and Thompson proposed a two-dimensional network in which the constants of individual sections of the Earth-ionosphere TM, transmission line are represented by lumped parameters They outlined methods for numerical evaluation and analyzed errors resulting, for example, from using a 10° by 20° grid They also predicted changes in the lowest (8 Hz) resonance frequency due to a typical SID event (perturbation over one third of the surface of the Earth on the daylight hemisphere) of 0 1 Hz to 0 6 Hz depending upon the observation point Similarly predicted changes due to the July 2, 1962 "Starfish" high-altitude nuclear explosion (perturbation over one third of the surface of the Earth on the night hemisphere) were also 0 1 Hz to 0 6 Hz, while a typical PCA event (more intense perturbation restricted to the auroral zones) gave shifts of 0 1 Hz to 0 2 Hz in the lowest resonance frequency

Frequency shifts due to ionosphere perturbations are not uniform over the entire Earth, because the observable "resonance frequency" itself, as defined below Equation 26 and by Equation 34, is not constant over the entire Earth The $P_n(\cos\theta)$ terms multiplying each term in the summation of Equation 24 are obviously functions of the angular separation θ between source and receiver, therefore the resultant sum, which contains terms of significant magnitude corresponding to values of n above and below the n of Equation 34, peaks at slightly different frequencies depending upon the relative position of source and receiver This effect is illustrated by Figure 5 and discussed in more detail below in "Location of Major Thunderstorm Regions "

Madden and Thompson[25] also discussed the "mode splitting" which is predicted by Equation 11 for a cavity which is nonuniform in the azimuthal (ϕ) direction Depending upon the type of nonuniformity each single term multiplying $P_n(\cos\theta)$ is replaced by several terms, each containing $(\sin m\,\phi)\,P_n^m(\cos\phi)$ or $(\cos m\,\phi)\,P_n^m(\cos\phi)$ Madden and Thompson conclude that the line-splitting, though present, will be masked in view of the low Q values which are characteristic of the Schumann resonances

Large and Wait[87] analyzed several models: (1) constant surface impedance over each global hemisphere with the "day-night" boundary at $\theta = \pi/2$; (2) surface impedance varying continuously with θ corresponding to the variation with θ of a dipolar magnetic field with "day-night" boundary at $\theta = \pi/2$; (3) surface impedance depending upon θ and ϕ (day-night boundary at an arbitrary position with respect to source). Numerical results were given for (1) and (2). One particularly interesting result obtained from (1) was that the field strength in the cavity is lower whenever the source is located in the night hemisphere. The discontinuities of (1), (2), and (3) produce cross-coupling between several TM modes as well as between TM and TE modes, but the numerical results show that the effect of such coupling upon the resonance frequencies is negligible (below 5%). A more important effect is a lowering of the quality factor, for example, from 4.6, obtained by averaging day and night results (i.e., results obtained by using in succession a day and a night ionosphere over the entire globe), to 3.0 obtained by a more rigorous day-night model. However these results are probably "slightly exaggerated by the assumption of an abrupt transition between night and day" and the authors suggest that a smooth day-night transition would reduce mode coupling and the resulting effects upon Q. They conclude that the "regular diurnal changes in the peak frequencies and quality factors of the Schumann modes are primarily due to interference, or overlapping of the cavity modes" which will be discussed in "Location of Major Thunderstorm Regions."

Paul[91] performed several numerical experiments to see whether either the assumption of a constant magnetic field or various lateral inhomogeneities — simulating the day/night discontinuity and PCA events — can produce resonance line splitting. The frequency resolution was 0.1 Hz. Realistic ionosphere profiles and many different source/receiver/discontinuity geometries were employed. Line splitting (i.e., a double resonance peak or a peak separation less than approximately 5 Hz between successive resonances) was not obtained in any case.

ELF MEASUREMENT TECHNIQUES

General Considerations and Horizontal Electric Fields

To a first approximation the Earth-ionosphere cavity with dipole excitation has azimuthal symmetry and in this case the only field components are E_r, E_θ, and H_ϕ as indicated below Equation 8. The vertical electric field is E_r and the horizontal fields are E_θ and H_ϕ.

For plane wave propagation in unbounded space, one would expect that the orthogonal field components would be related by the wave impedance of free space $\eta = 377$. In the cavity this is not true at ELF where cavity dimensions and wavelength are of comparable magnitude. However, when the excitation source is on the surface of the Earth ($r = r_o = a$), it follows from Equations 7, 20, and 22 that

$$\left| \frac{E_r}{H_\phi} \right| = \frac{\nu(\nu+1)}{a\,\omega\,\epsilon} \frac{P_\nu(-\cos\theta)}{\frac{\partial}{\partial\theta} P_\nu(-\cos\theta)} \qquad (71)$$

Thus this ratio is a function of both frequency and the angular separation θ between source and receiver. In the cavity with perfectly conducting boundaries Equation 26 gives $\nu(\nu+1) = (ka)^2$ and in the cavity bounded by the real ionosphere $\nu(\nu+1)$ is given by Equation 28. Substituting into Equation 71 we obtain, exactly with Equation 26 and approximately with Equation 28 —

$$\left|\frac{E_r}{H_\phi}\right| \approx \eta(ka)\frac{P_\nu(-\cos\theta)}{\frac{\partial}{\partial\theta}P_\nu(-\cos\theta)} \qquad (72)$$

At the first resonance $ka = \sqrt{2}$ by Equation 27 and $|E_r/H_\phi| = \eta = 377\ \Omega$ occurs at[52] $\theta \approx 55°$. At 8 Hz measured values[50] of E_r are in the vicinity of 10^{-4} Vm^{-1} $Hz^{-1/2}$ and measured values[52] of H_ϕ in the vicinity of $5(10^{-7})$ Am^{-1} $Hz^{-1/2}$, corresponding to $B_\phi \approx$ 0.6 milligamma = $6(10^{-13})$ Tesla. Thus measurements give $(E_r/H_\phi) \approx 200$ which can be expected from Equation 72.

At ground level the tangential field components must be related by the surface impedance of the ground

$$\frac{E_\theta}{H_\phi} = Z_g \qquad (73)$$

which is for a good conductor given by[56 57 92]

$$Z_g = \sqrt{\frac{j\omega\mu}{\sigma}} \qquad (74)$$

From Equations 72 and 73 the order of magnitude of the ratio of the horizontal to the vertical electric field is

$$\left|\frac{E_\theta}{E_r}\right| \approx \frac{Z_g}{377} \qquad (75)$$

Thus for dry land,[92] when $\sigma \approx 2(10^{-3})$ S/m,

$$\left|\frac{E_\theta}{E_r}\right| \sim 5(10^{-4}) \quad \text{at 8 Hz} \qquad (76)$$

Very few measurements of the horizontal ELF field at ground level are available. The reason is that an electrically very short (length $\ll \lambda$) horizontal wire antenna near ground[41] essentially responds to the vertical electric field (E_r) which exists across the capacitor formed by the horizontal antenna and the ground, but is not nearly as efficient a receiver for that field component as a vertical antenna of the same length.[13] The horizontal wire also exhibits directional properties.[13 95] The true horizontal electric field at ELF is probably best obtained from measurements of the potential difference between electrodes inserted into the ground. Such measurements are difficult, require extreme precautions in the design of electrodes, and are usually employed only for the measurement of lower, "micropulsation" frequencies where the field strength is higher than at ELF.[93] Word, Smith, and Bostick[94] did extend such measurements to 10 Hz although their principal interest was lower frequencies and the determination of the electrical properties of the ground. They employed electrodes separated horizontally about 200 m and reported $|E_{rms}|^2$ values at 8 Hz between 10^{-5} and 10^{-3} $(mV/km)^2/Hz$. This corresponds to E_r between 10^{-7} and $3(10^{-9})$ $Vm^{-1}Hz^{-1/2}$ and is 2 to 0.06 times what one obtains from Equation 76 and the value of E_r quoted above, $E_r \approx 5(10^{-4})$ $(10^{-4}) = 0.5(10^{-7})$ Vm^{-1} $Hz^{-1/2}$. However, in view of the local (θ) dependence of the fields indicated by Equation 72 and the dependence upon the exact value of ground conductivity σ implied by Equation 74 the value is not unreasonable.

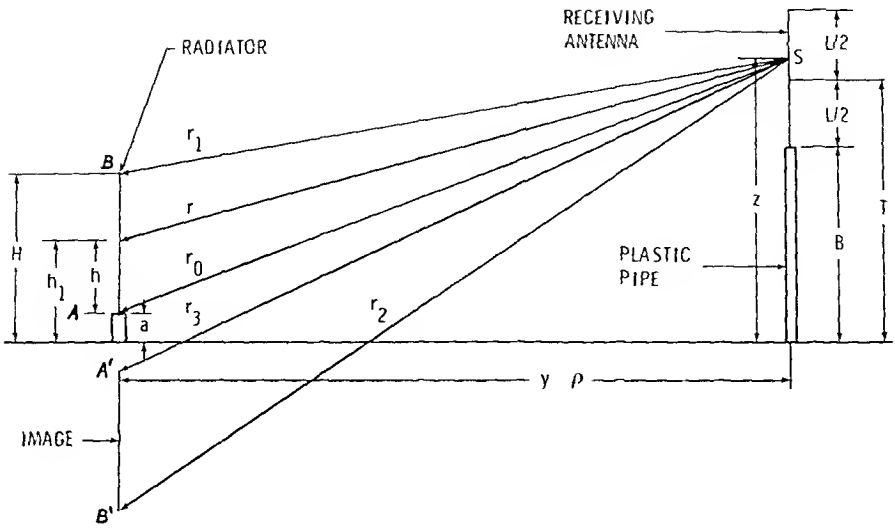

FIGURE 6. Radiator and receiver geometry for calibration of electric field sensor.

The measurement of horizontal electric fields is also important at ELF when one is interested in field strength in the ocean. There measurement of the potential difference between floating electrodes is relatively convenient and such measurements were reported by Soderberg.[95] He obtained the potential difference between carbon electrodes at a horizontal separation of 5 m at depths below the ocean surface between 30 and 300 m several miles from the coast of Baja California. He gives values for 8 Hz, at a depth of 60 m, between −161 dB below 1 V/m and − 165 dB below 1 V/m per 1.25 Hz frequency interval, corresponding to E_θ values of $5(10^{-9})$ to $8(10^{-9})$ Vm^{-1} $Hz^{-1/2}$. Since for sea water with $\sigma \approx 4$ Sm^{-1} Equation 74 gives, at 8 Hz, $Z_\epsilon \approx 4(10^{-3})$ Ω, we obtain from Equation 75 $E_\theta \approx 10^{-5}$ E_r. Thus for $E_r \approx 10^{-4}$ Vm^{-1} $Hz^{-1/2}$, one would expect at the sea surface a horizontal field strength $E_\theta \approx 10^{-9}$ V/m. Although the electric field in sea water at 8 Hz would decrease by a factor of 0.5 over a depth of 60 m, the measured value is again not unreasonable in view of the expected variability of E_r.

In view of the greater ease of measurement and calibration most of the field intensity values quoted in the literature involve vertical electric fields[5 8 42 46 48 50] and horizontal magnetic fields.[39,44,47 48] Methods for such measurements are now summarized.

Vertical Electric Fields

Vertical electric ELF fields can be measured most conveniently with a vertical "whip" antenna or with some metallic element, usually a plate, cylinder or sphere, which is mounted several meters above the conducting ground and electrically insulated from it.[46] The principal difficulty with this measurement is not insufficient field strength since the vertical electric field component of the Schumann resonances is generally well above most other electric field noise in this frequency range as discussed in "Field Intensity Levels — Spatial, Diurnal, and Seasonal Variations." The main difficulty is rather determination of the absolute level of the received ELF field. This requires calculation or measurement of the true effective antenna height or of antenna capacitance, which can be significantly affected by details of mounting arrangements. Furthermore pick-up by antenna to preamplifier cables (including cable shields) must either be eliminated or considered in the calibration.

Clayton et al.[50] have shown that for an electrically short linear receiving antenna, as well as for a spherical antenna, the open circuit terminal voltage V is equal to the average of the undisturbed potential to ground V_o (i.e., the potential which would exist

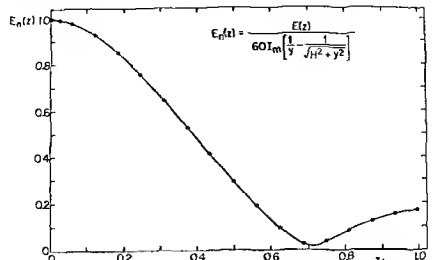

FIGURE 7 Relative magnitude of $E(z)$ near an electrically very short antenna at ground level ($a = 0$)

with the antenna removed) at the location of the antenna. Thus for a linear antenna of length L mounted on an insulating base of height B, as illustrated by Figure 6,

$$V = \frac{1}{L}\int_{B}^{B+L} V_o(z)\,dz \tag{77}$$

For an incident uniform electric field $V_o(z) = E_o z$ and

$$V = F_o\left[B + \frac{L}{2}\right] \tag{78}$$

which is also equal to

$$V = \int_{0}^{B+\frac{L}{2}} E(z)\,dz \tag{79}$$

For a spherical antenna with its center at height T above ground

$$V = \int_{0}^{T} E(z)\,dz = \Gamma_o(T) \tag{80}$$

provided the capacitance C of the sphere of radius R at the height T above the conducting plane does not differ appreciably from the capacitance $C_o = 4\pi\epsilon_o R$ of the sphere in free space. This condition is satisfied when the ratio of mounting height to radius is sufficiently large since $(C/C_o) \leq 1.02$ when $(T/R) > 2.5$.

Equations 77 to 79 give only the open circuit terminal voltage. Since the antenna capacitance is of the order of 20 pF, the input impedance at 8 Hz will be a capacitive reactance of about $10^9\Omega$! The input stage of the preamplifier must therefore be designed appropriately and the capacitance of any connecting cables must be considered.

In view of the uncertainties involved in relating the voltage actually measured at the output of an impedance transformer and through cables, or a preamplifier, to the true

open circuit voltage, it is essential that the system be calibrated with a field of known magnitude. This can be done by using the arrangement illustrated by Figure 6 in which a linear radiator is supplied with a known input current. When the calibrating antenna length H, the distance y between that antenna and the receiving antenna base, and the height T, and length L of the receiving antenna are all very much smaller than the free space wavelength, the field due to the calibrating antenna is given[50] by

$$E(z) = 30\, I_m \left\{ -\frac{1}{r_1} - \frac{1}{r_2} + \frac{1}{r_3} + \frac{1}{r_o} - \frac{(z+a)(H-a)}{r_o^3} + \frac{(z-a)(H-a)}{r_o^3} \right\} \tag{81}$$

and I_m is related to the antenna base current I_b by

$$I_m = \frac{I_b}{k(H-a)} \qquad k = (2\pi/\lambda) \tag{82}$$

The behavior of $|E(z)|$ as a function of z/y for a calibrating antenna at ground level ($a = 0$) is shown on Figure 7.

Determination of the base current I_b in Equation 82 requires measurement of a conveniently large voltage at the input of the calibrating antenna. One should note that with an input impedance of the order of $10^9\ \Omega$ the base current $I_b \approx 1\ \mu A$ even if the voltage applied between feedpoint and ground is 1 kV! If that voltage is known, however, I_b in Equation 82 can be determined by measuring the input capacitance of the calibrating antenna. A typical value of this capacitance (for a 1.8-m antenna at ground level) is 19.0 pF. A possible circuit for measuring it is described by Clayton et al.[50] and empirical formulas for its calculation have been given by Watt[97] and Küpfmuller:[98]

$$C = \frac{24.16(L)}{\log_{10}(2L/d) - k'}\ \text{pF} \tag{83}$$

where L is the antenna length, d the antenna diameter and k′ is a function of a/L with a being the mounting height of the antenna base above ground (k′ = 0.42 for a/L = 0.01 and k′ = 0.144 for a/L = 10).

Calibration by a known ELF field is, of course, applicable to receiving antennas of any shape. A particularly useful antenna for ELF is the spherical antenna, mentioned above, in which, as suggested by Ogawa,[46] the preamplifier is mounted inside the antenna to avoid the need for transmitting low level signals through cables (whose capacitance is also larger than that of the antenna). A practical arrangement of such an antenna[50] is illustrated on Figures 8 and 9. The antenna height T was 9.87 m and the radius of the sphere R was 15 cm.

Several additional precautions must be observed in measurements of the vertical electric field. (1) The mounting of the receiving antenna must be sufficiently rigid to avoid motion due to wind which would modulate the antenna to ground capacitance and thereby the amplitude of the received field. (2) Large moving objects must be kept out of the vicinity of the antenna for the same reason. (3) Generally, data must be discarded during heavy local precipitation, although during light rain a dielectric "radome", such as the plexiglass sphere shown on Figures 8 and 9, minimizes precipitation noise. (4) Data must also be discarded when the Schumann resonance spectrum is contaminated by "local" thunderstorms, that is by lightning which is so close that TE modes and higher order TM modes are not sufficiently attenuated; generally this will

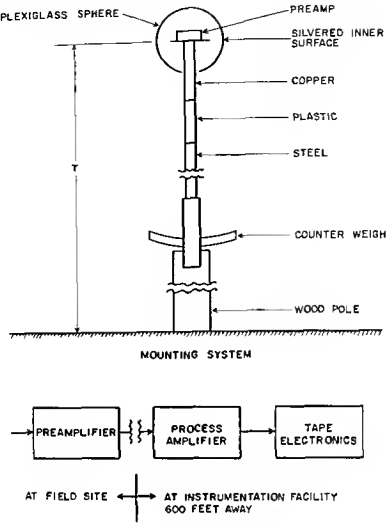

FIGURE 8 Spherical antenna system

be the case if lightning occurs within about 100 km of the station which can be checked by independent recording of HF noise (5) Semiconductor devices in the impedance transformer, the high sensitivity first amplifier stage, and succeeding stages, will generally have to be protected against burnout due to very large impulses (of the order of kilovolts) which are picked up by the antenna and cables during lightning activity in the immediate vicinity (within 2 or 3 km) of the antenna At the Kingston, R I field site[99] RCA type 8393 "NuVistor" vacuum tubes rather than I C s were used in the preamplifier, because they were found to withstand surge voltages better than transistors or I C s In addition zener (break-down) diodes were used at several locations between the "hot" side of the low voltage DC power supplies and ground [99] (6) Filters must usually be used to eliminate high level natural noise[93] below about 3 Hz and man-made noise from power lines and other sources, as discussed in the following section on field intensity levels (7) As discussed in more detail by Ogawa et al [46] and by Clayton et al ,[50] the receiving antenna must extend to sufficient height above the ground to minimize the effect of random field fluctuations which occur within the first meter above ground and are possibly due to motion of ions produced by radon gas emanating from the soil [100]

Magnetic Fields

Schumann resonance magnetic flux densities are reported[44 47 52 99] to lie between 0 47

FIGURE 9. Spherical antenna used near Kingston, R.I. (schematic on Figure 8).

milligamma $Hz^{-1/2}$ = 4.7(10^{-13}) Tesla $Hz^{-1/2}$ and 11.7(10^{-13}) T $Hz^{-1/2}$. Compared with other naturally occurring magnetic fields in neighboring frequency bands, such as mi-

cropulsations,[93] and man-made interference, these are extremely low level fields Therefore detectors must be placed in locations which are far from sources of man-made interference such as power lines, electric railroads, telephone lines, ignition noise, or radio transmitters with ELF modulation As will be discussed below, detectors must also be isolated from ground transmitted and airborne acoustic vibrations

In the past either induction coils with ferromagnetic cores[39 40 44 101 102] or air-core loops[99 102 105] have been used, although there are some indications that it may be more convenient in the future to use Josephson-junction "SQUID" (super conducting quantum interference devices)[105 107] Dinger et al [106] have reported on a three-axis "SQUID" ELF detector with a sensitivity of 10^{-14} T $Hz^{-1/2}$ The response of the SQUID device is, in principle, independent of frequency, while the response of induction coils, which depends upon the time rate of change of the magnetic flux Φ linking the N-turn coil, increases linearly with frequency $V = (d\Phi/dt) = \omega N\Phi$

Both ferromagnetic and air-core coils must be electrostatically shielded to prevent response to slowly varying electric fields The self-inductance and sensitivity of coils with high permeability cores depend less upon the exact value of the core permeability than upon the length to diameter ratio of the core as a result of the demagnetizing factor of long slender rods [101] Eddy current losses in the core can be minimized by using insulated laminations, but the resistance at ELF (reported for 8 8 Hz)[101] can be substantially above the DC resistance as a result of residual eddy current losses and hysteresis The principal danger of using ferromagnetic cores for low level measurements is the presence of Barkhausen noise[102] and possible variation of the response characteristics due to the nonlinear variation of permeability in the presence of a relatively large, slowly time-varying field (the magnetic field of the Earth during magnetic storms) and more rapidly varying interference fields (micropulsations and power line fields) Generation of spurious signals at the sum and difference frequencies of unwanted interference as a result of core nonlinearity is also a possibility Nevertheless, iron or ferrite core induction coils are useful when small distortions of the received signal can be tolerated and when only relative signal amplitude is of interest, but they are of questionable value for very precise measurements of wave shape, phase, and absolute field amplitude They are light and portable compared with air core loops which become very bulky and large when they are designed for adequate sensitivity to detect Schumann resonances

Air core induction loops can be optimized[99 104] for the best signal-to-noise (S/N) ratio It can be shown that S/N is independent of the wire size[99] but is proportional to the square root of the "window area" (Figure 10)

$$\frac{S}{N} = Kr^{3/2}\sqrt{\alpha\sigma A_w} \qquad (84)$$

where $K = (\omega\pi B)/(8\pi kT\Delta f)^{1/2}$, B is the incident flux density, k Boltzmann's constant, T the absolute temperature in degree K, Δf the filter bandwidth, α the fill factor (i e , the fraction of the window area actually filled by wire, typically $\alpha \simeq 0\,6$), and σ the conductivity of wire in Sm^{-1} The magnitude of the induced open-circuit voltage V_{OC}, however, does depend on wire size

$$V_{OC} = \omega NAB = \omega AB\frac{\alpha A_w}{s} \qquad (85)$$

where N is the number of turns, A is the cross-section area of the loop $\simeq \pi r^2$, and s is the cross-section area of the wire

From Equation 84 it follows that for a fixed winding radius r, the S/N ratio is proportional to the square root of the weight of wire used

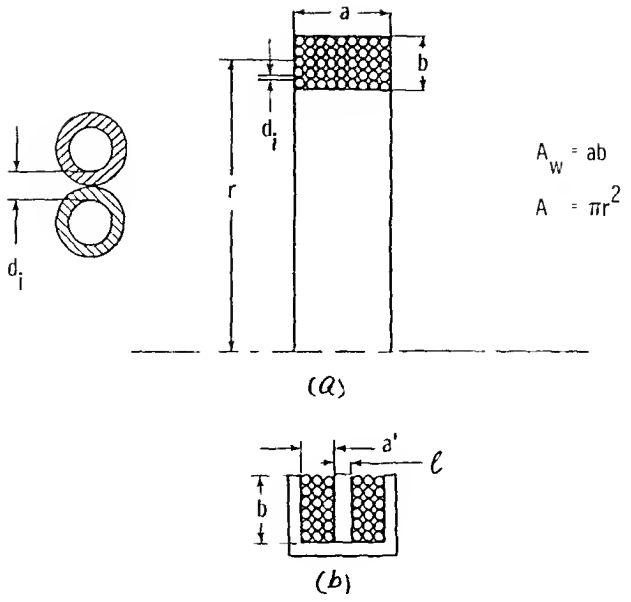

FIGURE 10. Air core induction loop. (a) Cross-section through one half of coil showing "window" with windings. (b) Window sectionalized to reduce distributed capacitance.

$$\frac{S}{N} = \frac{Kr}{\sqrt{2\pi}} \sqrt{W \frac{\sigma}{\theta}} \tag{86}$$

where W is the weight of the wire and θ is the density of the wire material (kg^{-3}).

Another important consideration in coil design is the value of the distributed capacitance C_d. If the coil response is to be kept linear with frequency, C_d must be sufficiently small to keep the self-resonant frequency of the coil well above the desired maximum operating frequency.[99] (Self-resonance may, of course, be used to enhance the response of the receiving system over a narrow frequency band.) C_d is affected by window shape (see Figure 10) and the number of coil layers: it can be reduced by making b > a for fixed values of A, A_w, N, and d, (copper to copper distance between layers); this can be done by dividing the coil into sections of width a', insulated from each other as shown in Figure 10. To reduce intersection capacitance, the separation distance ℓ should be as large as possible, which reduces the open-circuit voltage given by Equation 85, and S/N given by Equation 86, since the effective window area becomes smaller. The complete coil design clearly requires compromises between such conflicting requirements, and one possible design procedure is given by Keefe et al.[99]

For large coils other considerations are also important, such as ruggedness, waterproofing (particularly if the coil is to be mounted below ground level), and mounting to reduce vibration. For a large-diameter high-sensitivity coil, minute coil motion in the magnetic field of the Earth can produce signals which are much larger than the temporal variations which are to be measured. For example, distant city traffic,[108] microseisms,[109] and a helicopter flying above the magnetic field test site[110] have been recorded by induction loop magnetic field sensors. To remove this source of error an accelerometer can be mounted on or near the magnetic field sensor and its output recorded simultaneously with $\overline{dB}/dt$ on a multitrack tape system.[99]

Very high sensitivities and good S/N ratios can be obtained with large air core coils even at the lowest end of the ELF band. For example, the flux density detected with S/N = 1 by an electrostatically shielded 2-m-diameter 4-section 44,000-turn coil of

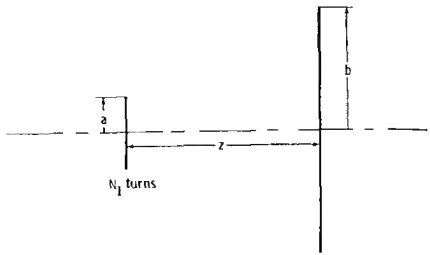

FIGURE 11 Setup for calibration of large induction loop (radius b) by field from smaller loop (radius a)

No 30 copper wire[99] in the frequency band 3 Hz to 30 Hz was 3 $2(10^{-14})$ T $Hz^{-1/2}$, this coil had a self-resonant frequency of 80 Hz A circular 2-m-diameter coil with 16,000 turns of 0 127-mm-diameter wire[111] had a natural frequency of 144 Hz and gave 0 3 μV for a 10^{-12} T signal at 1 Hz Using elaborate signal processing, White and Willim[102] detected 45-Hz and 75-Hz narrow-band signals at the 10^{-14} T level using an antenna with a turns-area product of 909 2 m^2

Magnetic field sensors can be calibrated[111] rather conveniently even outside the laboratory [99] For a very large diameter coil (e g , 1 m or 2 m) a calibration field can be set up by locating a smaller diameter loop (e g , with 100 turns) coaxial with the large loop at a relatively short distance (e g , 5 m) In this instance the calibration field is not uniform over the area of the receiving antenna, and computation of the induced signal $(d/dt) \int \vec{B} \cdot d\vec{s}$ requires integration of the calibration field over the receiving area The field on the axis of the calibration antenna (see Figure 11) is

$$B = \mu_0 \frac{N_1 I_1}{2} \frac{a^2}{(a^2 + z^2)^{3/2}} \tag{87}$$

The error introduced by using a uniform B, given by Equation 87 over the entire area of the receiving loop, to calculate the induced voltage is[99]

$$\frac{V}{V_0} = \frac{z^3}{[z^2 + (a+b)^2]^{3/2}} \tag{88}$$

where V_0 is the voltage calculated by using Equation 87 for $\Phi_2 = B \pi b^2$ and $V_0 = \omega N_2 \Phi_2$, and V is the correct voltage obtained by integrating the off-axis B using approximations of elliptic integrals suitable for dimensions of the order of $z \approx 10a$, $b \approx 2a$

EXPERIMENTAL DATA AND DATA ANALYSIS

Methods of Spectral Analysis and Effects of Data Treatment on Resulting Spectra

The Earth-ionosphere cavity is usually excited simultaneously by many different thunderstorms [113] Although one or a few large source regions may provide the major excitation at any particular time, each of these sources consists of a large number of

lightning "flashes" (each of which may consist of three to four "strokes"),[114] which are distributed randomly in time and space. Although it is occasionally possible to measure an individual impulse response of the cavity,[49] one is usually forced to extract information from a mass of uncorrelated, individual signals which are randomly distributed, but partially overlapping in time. No phase information is available, the measured amplitude fluctuates rapidly and the signal as a function of time has the general appearance of random noise. The power spectrum of such a signal can be obtained and is determined by the excitation functions[15] and by the propagation, or cavity transfer function which are defined below.

Since the expression for the vertical electric field in Equation 24 represents only the response of the cavity to a single impulse of current moment Ids located at r = a and $\theta = 0$, the actually measurable $|E_r|^2$ due to many lightning flashes confined to an area limited by $-\Delta_\phi \leqslant \phi \leqslant \Delta_\phi$ and $-\Delta \leqslant \theta \leqslant \Delta$ (using the coordinates of Figure 1) will be

$$|E_r(\omega)|^2 = \int_{-\Delta_\phi}^{\Delta_\phi} \int_{-\Delta}^{\Delta} Mg(\omega)\,|F_e(\theta,\omega)|^2\, a^2 \sin\theta \, d\theta \, d\phi \qquad (89)$$

where $F_e = E_r/(Ids)$, n = number of lightning flashes per unit area, M = magnitude squared of n vertical lightning current moments per unit area, $= n^2$ (average lightning current)^2 (average lightning path length)^2, $= (Am)^2/m^2$, $g(\omega)$ = power spectrum of average lightning flash (discussed in "Monitoring of Worldwide Thunderstorm Intensity"). When $\Delta_\phi \ll \theta$ and $\Delta \ll \theta$ Equation 89 reduces to

$$|E_r(\omega)|^2 \approx G(\omega)\,|F_e(\theta,\omega)|^2 = S_e(f) \qquad (90a)$$

where

$$G(\omega) = \int_{-\Delta_\phi}^{\Delta_\phi} \int_{-\Delta}^{\Delta} Mg(\omega) a^2 \sin\theta \, d\theta \, d\phi \qquad (91)$$

is the excitation function and $|F_e(\theta,\omega)|^2$ the square of the absolute value of the transfer function or frequency response function. Similarly, for the magnetic field

$$|H_\phi(\omega)|^2 = G(\omega)\,|F_m(\theta,\omega)|^2 = S_H(f) \qquad (90b)$$

where $F_m = H_\phi/(Ids)$ is given by Equations 7 and 20 or by Equations 24 and 71.

$S_e(f)$ and $S_H(f)$ are the power spectral density functions[115] which can be determined from the measured electric and magnetic fields considered as random signals x(t) varying with time t. These power spectral density functions give the frequency composition of the received fields in terms of the spectral density of their mean square values.

The mean square value ψ^2_x of a random signal x(t) is[115]

$$\psi_x^2 = \lim_{T\to\infty} \frac{1}{T} \int_{-\frac{T}{2}}^{\frac{T}{2}} x^2(t)dt = \lim_{T\to\infty} \frac{1}{T} \int_0^T x^2(t)dt \qquad (92)$$

If the signal is passed through a group of parallel connected narrow band filters (each of width Δf), the mean square response of the nth filter centered at frequency f is

$$\psi_{xn}^2(f) = \lim_{T\to\infty} \frac{1}{T} \int_{-\frac{T}{2}}^{\frac{T}{2}} x_n^2(t,f,\Delta f)\,dt \tag{93}$$

In terms of $\psi_{xn}^2(f)$ the power spectral density function S(f) is then

$$S(f) = \lim_{\Delta f\to 0} \frac{\psi_{xn}^2}{\Delta f} = \lim_{\Delta f\to 0} \lim_{T\to\infty} \frac{1}{\Delta f} \frac{1}{T} \int_{-\frac{T}{2}}^{\frac{T}{2}} x_n^2(t,f,\Delta f)\,dt$$

$$\text{If } x_T(t) = x(t) \quad \text{for } |t| < \frac{T}{2} \tag{94}$$

$$= 0 \qquad |t| > \frac{T}{2}$$

and if $\underline{X}_T(\omega)$ is the Fourier transform of x(t)

$$\underline{X}_T(f) = \int_{-\infty}^{\infty} x_T(t) e^{-j\omega t}\,dt \qquad \omega = 2\pi f \tag{95}$$

it follows from Equation 92, and Parseval's theorem

$$\int_{-\infty}^{\infty} x_T^2\,dt = \int_{-\infty}^{\infty} |\underline{X}_T(f)|^2\,df$$

that

$$\psi_x^2 = \int_{-\infty}^{\infty} \lim_{T\to\infty} \frac{|\underline{X}_T(f)|^2}{T}\,df = 2 \lim_{T\to\infty} \int_0^{\infty} \frac{|\underline{X}_T(f)|^2}{T}\,df \tag{96}$$

If the power spectral density function S(f) is defined, in agreement with Equation 94, by

$$\psi_x^2 = \int_0^{\infty} S(f)\,df \tag{97}$$

it follows from Equations 94, 95, and 97 and Parseval's theorem that an estimate of S(f) with the narrowest possible resolution $f = (1/T)$ is given[117] by

$$S_o(f) = \lim_{T\to\infty} \frac{2}{T} \left| \int_0^T x(t) e^{-j\omega t}\,dt \right|^2$$

$$= \lim_{T\to\infty} \frac{1}{T} \left| \int_{-\frac{T}{2}}^{\frac{T}{2}} x(t) e^{-j\omega t}\,dt \right|^2 \tag{98}$$

where $x_T(t) = x(t)$. However it is not necessarily true that $S_o(f) = S(f)$ as discussed in Davenport and Root [117]

Also useful for the evaluation of S(f) is the Wiener-Khinchin relation valid for a random process which is at least "wide sense" or "weakly stationary" (i.e., a process for which expected values equal average values and the autocorrelation function is only a function of the delay τ and not of time)

$$S(f) = \int_{-\infty}^{\infty} R(\tau) e^{-j\omega\tau}\, d\tau \tag{99}$$

where $R(\tau)$ is the autocorrelation function

$$R(\tau) = \lim_{T\to\infty} \frac{1}{T} \int_{0}^{T} x(t)x(t+\tau)\, dt \tag{100}$$

From Equations 100 and 92 it also follows that the mean square value ψ_x^2 of x(t) is the autocorrelation function with zero delay

$$R(0) = \psi_x^2 \tag{101}$$

The power spectrum can be evaluated from the experimental data either digitally or by use of an analog or hybrid analog-digital analyzer. Implementation of Equation 94 involves the following operations:

1. The instantaneous, received signal x(t) is passed through n band-pass filters of width Δf, centered at f_k. This is done either by parallel analog filters or by a Fast Fourier Transform (FFT) algorithm.
2. The output of these filters is squared.
3. The squared narrow-band signal is averaged over the sampling time T.
4. The mean square output is divided by the filter bandwidth Δf.

As the center frequency f of the filters is moved (or as the output of parallel filters of width f centered at frequencies f_k is recorded in succession), a plot of the power spectral density function — the power spectrum — is obtained.

If either method is used, FFT or an analog or analog-hybrid scheme, the resulting power spectrum can be only an estimate of the actual power spectrum of the received signal, because the integration time T can, of course, not be infinite.

The integration time T must be limited, not only because data must be taken over some limited time interval, but, more importantly, because the process involved, the excitation of the Earth-ionosphere cavity by lightning sources, is really not "stationary": the "transfer functions" $F_e(\theta,\omega)$ and $F_m(\theta,\omega)$ are varying continuously with time. The source to receiver separation θ is varying continuously and therefore P_n (cos θ) in Equation 24 is varying continuously; the day-night boundary moves continuously and therefore the position of source and receiver relative to the day and night ionosphere is shifting; the level of cosmic ray as well as solar activity is changing continuously, affecting local and world averaged ionosphere properties which determine ω in Equation 24. Thus the stationarity implied by the use of power spectral analysis is only an approximation. While one wants to make T as long as possible to improve the estimate of S(f), and thereby the estimates of cavity properties and excitation function, T can not be longer than the time period over which neither the source to receiver spacing, nor the cavity properties, change appreciably. Since we do not really know what that period is, the selection of the interval T is somewhat arbitrary, but periods between 2.33 min[119] and 34 min[55] have been used. In the absence of solar disturbances

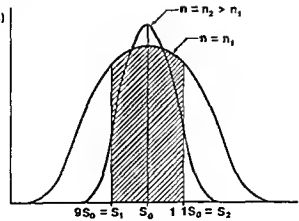

FIGURE 12 Normal probability density distribution for different size samples

(PCA events, SID's, major X-ray bursts, etc), when world average properties of the ionosphere do not change rapidly, the longer integration periods are likely to give more reliable results, particularly since the position of major thunderstorm regions, which excite the cavity, remains constant within ±5° of latitude and longitude over periods of several hours [120]

In band limited white noise data samples separated by the "Nyquist interval" $T = 1/(2\,\Delta f)$ are uncorrelated, or

$$n = 2(\Delta f)T \tag{102}$$

samples taken during this interval are statistically independent (For a discussion of these considerations see, for example, Bendat and Piersol [115 117]) Although the statistical independence is not strictly satisfied for noise such as that considered here, it is nevertheless useful to employ Equation 102 as the definition of the number of "degrees of freedom", i e , the number of independent random variables whose squares are summed in evaluating S(f) as given by Equation 94 Infinite sampling time would give $n = \infty$ and the true value of S(f)

It can be shown[115 116] that the probability density function describing the estimate of S (obtained with $n \leqslant \infty$) about the true power density S_0 (corresponding to $n = \infty$) within the band Δf is the chi-square distribution However, when n is large ($n > 30$) this distribution approaches the normal distribution shown on Figure 12 which illustrates the improvement in the estimate of S as n is increased The shaded area represents the "confidence" one has that the estimate will be within ±10% of the mean value S_0 This area, the integral of the probability density function p(S), will give the probability P that S will be within a given range about S_0,

$$P\left\{S_1 < S < S_2\right\} = 1 - \alpha = \int_{S_1}^{S_2} p(S)dS \tag{103}$$

$100\,\alpha$ is the "significance" level

It is also useful and customary to calculate the normalized standard error ε Its square, the normalized mean square error ε^2 is defined by

$$\varepsilon^2 = \frac{E\left\{|\bar{S}(f) - S(f)|^2\right\}}{S^2(f)} \tag{104}$$

where E = expected value and $\tilde{S}(f)$ = estimated value of S(f). As illustrated by Figure 12, ϵ should be inversely related to the number of degrees of freedom and it can be shown[115-117] that it is given by

$$\epsilon^2 = \frac{2}{n} = \frac{1}{(\Delta f)T} \tag{105}$$

For the normal distribution, the probability is 68.3% that S will fall within

$$\pm \frac{|\tilde{S} - S|}{S} = \epsilon$$

or 95.4% that it will fall between

$$\pm \frac{|\tilde{S} - S|}{S} = 2\epsilon$$

Thus the true power density S will fall within ±10% of S with a confidence of 95.4% of $\epsilon = 0.05$ or if $(\Delta f)T = 1/[25(10^{-4})] = 400$. For this level of confidence, namely, the probability of 95.4% that the calculated power spectral density will fall within ±10% of S, and a frequency resolution $\Delta f = 0.1$ Hz, a sampling or integration time of 4000 sec or 66.6 min would be required. For most of the data described in succeeding sections of this review, f = 0.125 Hz and either T = 1024 sec = 17.067 min or T = 2056 sec = 34.267 min were employed.

The use of FFT algorithms for evaluating power spectra estimates by the "direct Fourier transform" or "Cooley-Tukey" method has been discussed by Bendat and Piersol[117] and Oppenheim and Schafer[118] (p. 555). The starting point for this procedure is Equation 98. An older, computationally less efficient method is based on Equations 99 and 100.

In applying Equation 98 the record length must again be finite. For the FFT analysis we will call the length of the initially analyzed record section T_1, since it will be shown that $T_1 \neq T$, where T is the length of the entire record available for analysis. If a "boxcar function", Figure 13, is used to limit the record length, the following operation is substituted for Equation 98:

$$S(f) \approx \frac{1}{T_1}\left[\int_{-\infty}^{\infty} x(t)u(t)e^{-j\omega t}\,dt\right]^2$$

$$\text{where} \quad u(t) = 1 \qquad -\frac{T_1}{2} \leq t \leq \frac{T_1}{2} \tag{106}$$

$$u(t) = 0 \qquad |t| > \left|\frac{T_1}{2}\right|$$

However the Fourier transform

$$F[x(t)u(t)] = \bar{X}(\omega)^* U(\omega) = \int_{\infty}^{\infty} \bar{X}(y)U(\omega - y)\,dy \quad \text{and}$$

$$U(\omega - y) = T_1 \sin\frac{(\omega - y)T_1}{2} \Big/ \frac{(\omega - y)T_1}{2}$$

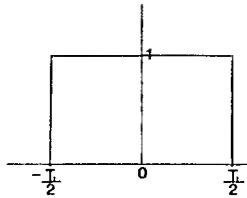

FIGURE 13 "Box-car" time function

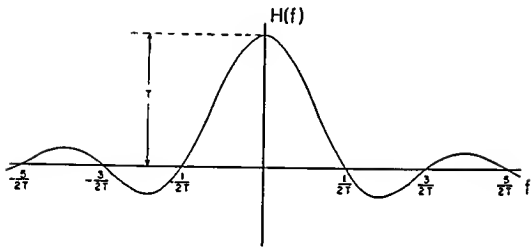

FIGURE 14 Fourier transform of "box car" window

Thus the "boxcar" time window will give in place of the desired F[x(t)] its convolution with the $(\sin \alpha/\alpha)$ function. This causes "leakage", i.e., the main lobe of the true power density function is distorted and an infinite number of side lobes is added as illustrated in Figure 14. It turns out that this leakage can be reduced by using a smooth filter shape with a "taper" (for example, a cosine function) at each end. This can substantially reduce sidelobes, but introduces a scale factor which must be applied as a correction to the final estimate of S(f) as explained by Bendat and Piersol[117] (p. 327).

The finiteness of the sampling time T, also introduces another difficulty. If x(t) is sampled at N equally spaced points which are $\Delta t = h$ apart, the total record length T is Nh. The time interval h cannot be smaller than allowed by the cut-off frequency (Nyquist frequency or folding frequency).

$$f_c = \frac{1}{2h} \tag{107}$$

if aliasing is to be avoided. (It is assumed that x[t] has been prefiltered so that it does not contain any frequency components above f_c.) The Fourier transform is evaluated at frequencies

$$f_k = \frac{k}{Nh} \qquad k = 0, 1, 2, \ldots, N-1 \tag{108}$$

which requires N^2 multiply-add operations. FFT procedures are based on decomposing N^2 into composite factors and carrying out Fourier transforms over smaller numbers of terms in each of the composite factors, but even if the procedure is carried out over the entire record length $T_1 = Nh$, that length is much too short to give any reasonable confidence limits or a sufficiently small standard error ε defined by Equation 105. For example if the cut-off frequency for the record is 25 Hz, $h = 0.02$ sec by Equation 107. If the desired frequency resolution $f = 0.1$ Hz, then Equation 108 gives $T_1 = (1/Nh) = 10$ sec, since the increments Δf of f_k are $(1/Nh)$. Consequently Equation 102 gives $n = 2(0.1)10 = 2$ as the number of degrees of freedom. The chi-square distribution is then the appropriate probability density function and the resulting mean square error, ε^2, is 2 or the normalized standard error is $100\sqrt{2} = 141\%$! Clearly further averaging or smoothing is necessary. This is achieved by evaluating the spectrum for r successive periods of length T_1 until the total length $T = rT_1$ is sufficient to give the desired standard error as determined by Equation 105. The spectrum obtained for each of the successive sampling periods T_1 is stored and the average is obtained by integration.

Digital processing of data, either to obtain the power spectrum by an FFT algorithm, or over the entire recording and analysis process when digital recording is employed, introduces also other errors than those discussed thus far. They are (1) errors due to quantization of the input into discrete levels; (2) inaccuracies produced by representation of filter coefficients by finite length numbers (i.e., B bits per coefficient), for example if a digital filter is used for the initial limitation of the received signal or for suppression of power line interference; and (3) roundoff errors which can arise whenever numbers are multiplied since data registers can only accommodate a finite number of bits (multiplication of words of length B' and B'' produces a new word of length $B' + B''$). In the use of FFT algorithms an additional error, closely related to roundoff errors occurs, particularly when fixed point arithmetic is used: it can be shown[121] that the numbers necessary to describe a record of fixed duration at discrete frequencies in the frequency domain is larger than those which describe the signal in the time domain; consequently scaling may be necessary at each iteration of the FFT.

A discussion of these errors can be found in books by Oppenheim and Schafer[118] and Peled and Liu.[121] Among the various errors, roundoff error is likely to be the most important.

Resonance Line Splitting

Resonance line splitting in observations of the Schumann resonances, as illustrated by Figure 15, has been reported by Gendrin and Stefant[44] (only in the second and higher resonances), by Hughes,[119] Jones,[49] Ogawa et al.[51] and Paul.[91] In view of the limitations of power spectral analysis discussed in the preceding section, the question arises whether such line splitting represents a real physical phenomenon or is an artifact resulting from the data analysis. Since this question can only be answered if complete details of the analysis procedure are known, the following discussion will be restricted to data obtained in the author's laboratory.

Electric as well as magnetic field data obtained over a period of several years,[91] show that resonance line splitting is a relatively common phenomenon. However there seemed to be some indication that it occurred more frequently during geomagnetic disturbances and this hypothesis was therefore tested by Paul[91] for several periods of 3- to 12-days duration between March 1970 and August 1972. Included were several geomagnetically quiet periods as well as disturbed periods with minor and major PCA events and two periods (March 5 to 10, 1970 and August 2 to 14, 1972) when major solar proton events occurred. A summary of the resulting statistical evaluation is reproduced on Table 2 for those 21 days during which power spectra over the complete 24-hr period were available.

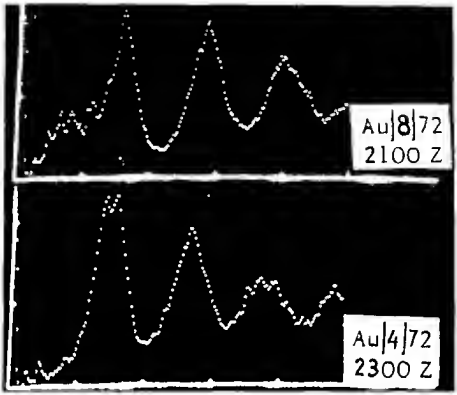

FIGURE 15 Electric field power spectra showing resonance line splitting (Blips' at the bottom of graph are 5 Hz markers indicating 5 Hz to 25 Hz, frequency resolution 0 125 Hz, averaging time T = 17 min)

Detailed examination of all available data showed that correlation between line splitting and solar or geomagnetic activity indices was much stronger during a major solar event than during minor events or during quiet periods "Splits" were more often observed in the third than in the second resonance and only very rarely — only during a period of unusually high solar proton flux — in the first resonance

Since higher order resonances in our data, and in most other data available in the literature, are "split" more often than the first (8 Hz) resonances, this relation was further examined It was noticed that the "Q" values of the first few resonances are almost the same and that as a consequence the resonance bandwidths are larger for the higher order resonances An examination of the relation between "split" occurrence and resonance bandwidth or cavity Q seemed therefore indicated However cavity Q is not uniquely defined for the Schumann resonances, as explained in "Resonances in a Cavity with Sharp, Homogeneous Isotropic Boundaries" (Equations 35 to 37), and is not equal to the resonance frequency divided by the half power beam width On the other hand it is apparent from the discussion in the section just mentioned that Imν and Im S, are related to the width of the cavity response in the immediate vicinity of the resonance peak, also noise is less likely to contaminate the power spectra at the higher levels near the resonance peaks The 80% level bandwidth was therefore chosen for the comparison with the occurrence frequency of split peaks

Since experimentally obtained power spectra, such as that shown on Figure 15, are often quite irregular and nonsymmetric about the resonance peaks, it was necessary for quantitative, statistical analysis to differentiate between "split" peaks and "broken" peaks for a power spectrum with frequency resolution Δf and minimum amplitude resolution δ a split peak in a section of power spectrum $\pm 8\,\Delta f$ about a resonance peak was defined by.

Table 2
CORRELATION BETWEEN OCCURRENCE OF RESONANCE LINE SPLITTING DURING 24 HR PERIODS AND SOME GEOPHYSICAL INDICES

ELF Data	Geophysical parameter	R Correlation coefficient	P Level of significance
Magnetic field H_{EW} First resonance	Riometer absorption 30 MHz Thule	0.287	<0.005
Magnetic field H_{EW} Second resonance	Riometer absorption 30 MHz Thule	0.492	<0.001
Magnetic field H_{EW} Third resonance	Riometer absorption 30 MHz Thule	0.533	<0.001
Electric field First resonance	Riometer absorption 30 MHz Thule	0.424	<0.001
Electric field Second resonance	Riometer absorption 30 MHz Thule	0.252	<0.02*
Electric field Third resonance	Riometer absorption 30 MHz Thule	0.390	<0.001
Electric field First resonance	Solar proton flux $E_p \geq 60$ MeV Explorer 41	0.225	<0.05*
Electric field Third resonance	Solar proton flux $E_p \geq 60$ MeV Explorer 41	0.347	<0.001
Magnetic field H_{EW} Second resonance	Solar proton flux $E_p \geq 60$ MeV Explorer 41	0.275	<0.01
Magnetic field H_{EW} Third resonance	Solar proton flux $E_p \geq 60$ MeV Explorer 41	0.215	<0.05*
Electric field First resonance	Solar proton flux E_p: 5-20 MeV ATS-1	0.302	<0.02*
Electric field Third resonance	Solar proton flux E_p: 5-20 MeV ATS-1	0.247	<0.05*
Magnetic field H_{EW} Second resonance	Solar proton flux E_p: 5-20 MeV ATS-1	0.358	<0.005

Note: The indices considered were Magnetic A-Index (Fredericksburg), 24 hr average of X-ray flux (Explorer 37), Solar proton flux (ATS-1 and Explorer 41) and 30 MHz Thule riometer absorption. The A-index is a daily weighted mean of the 3-hr K values. The level of significance P was determined by reference to tables of the student-t probability with N-2 degrees of freedom: N = number of observations, r = correlation coefficients, P = probability that a value of r equal to or greater than that computed would be obtained from a pair of purely independent (uncorrelated) variables. The correlation has been considered significant when $P < 0.01$. Probabilities $0.01 < P < 0.05$ are listed with asterisks indicating a doubtful case. For $P > 0.05$ the correlation is not considered significant.

1. A drop of at least δ takes place over each of two consecutive data points and a drop of 2δ occurs in at least one of them.
2. These two data points must be followed by a third data point at least δ above the preceding point.
3. A gap of $b \geq 3\,\Delta f$ must exist between the two successive subpeaks which form a "split" peak. (For some parts of the analysis $b = 3\,\Delta f$ was used.)

Thus for a "split" peak to occur, a set of at least four consecutive points (i, i + 1, i + 2, i + 3) must exist such that their amplitudes x(i), x(i + 1), x(i + 2), x(i + 3) satisfy

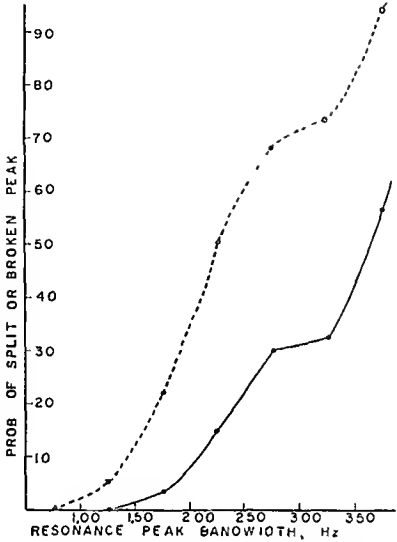

FIGURE 16 Probability of "split" and "irregular" peaks vs resonance peak bandwidth Magnetic field (522 samples, each with T = 17 min) "Broken peak" ———, "Split" peak —

$$\left.\begin{aligned} x(i+1) &< x(i) - \delta \\ x(i+2) &< x(i+1) - \delta \\ x(i+3) &> x(i) \end{aligned}\right\} \qquad (109)$$

A broken peak was defined by substituting Δf or $2\,\Delta f$ as the distance between subpeaks in listing 3

As expected the probability of finding a "split" or "broken" peak in the experimental power spectra increased with increasing resonance peak bandwidth as illustrated by Figures 16 and 17 Similar curves were obtained for other integration times (= T = sample length in Equation 105). The probability of "split" or "broken" peaks decreased, in general, with integration time as illustrated by Figure 18, which shows the observed frequency of occurrence of split peaks versus integration time for various ranges of 80% resonance line widths

To obtain a limiting value for the relation between record length (or integration time) T in Equation 105 and the degree of irregularity of the power spectrum (i e , the

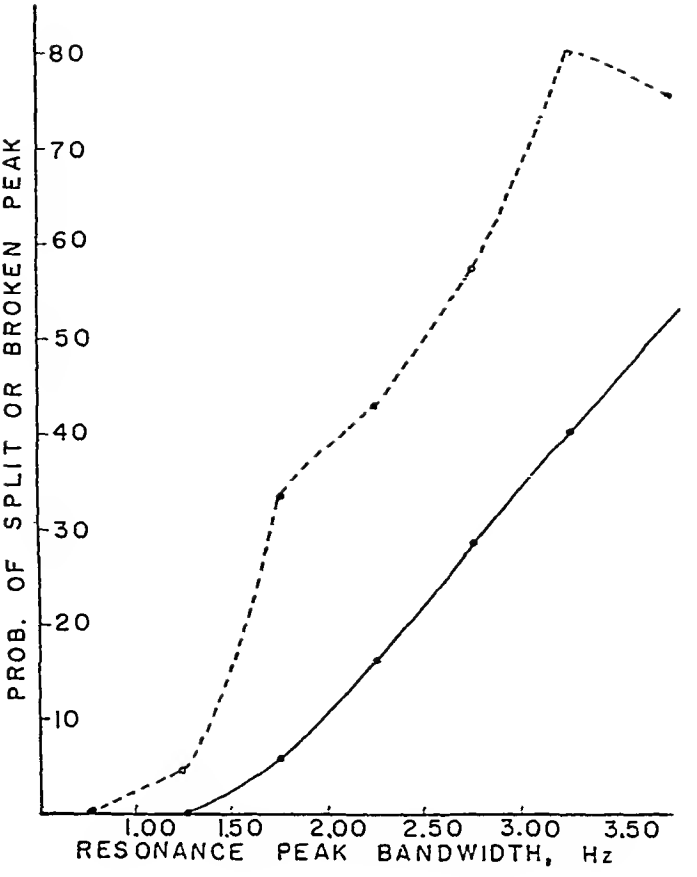

FIGURE 17. Probability of "split" and "irregular" peaks vs. resonance peak bandwidth. Electric field (548 samples, each with T = 17 min) "Broken" peak ———, "Split" peak —.

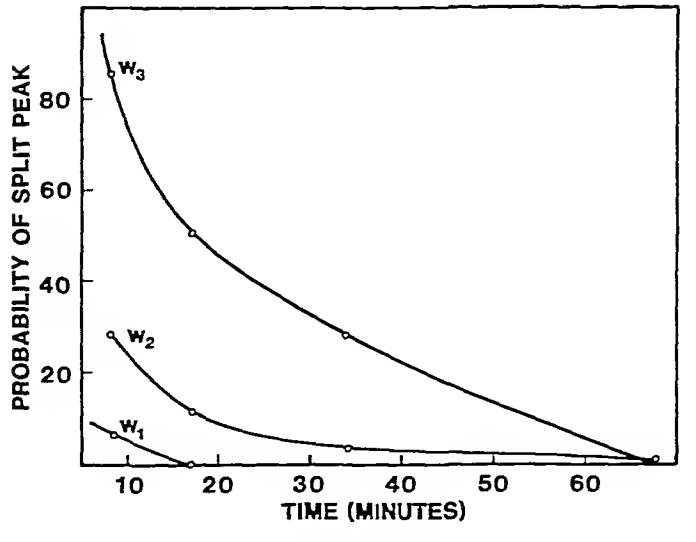

FIGURE 18. Experimental probability of split peak vs. sampling time T for electric field records.(Parameter: 80% width of resonance peak $0.5 \leqslant w_1 \leqslant 1.0$ Hz, $1.5 \leqslant w_2 \leqslant 2.0$ Hz, $2.5 \leqslant w_3 \leqslant 3.0$ Hz).

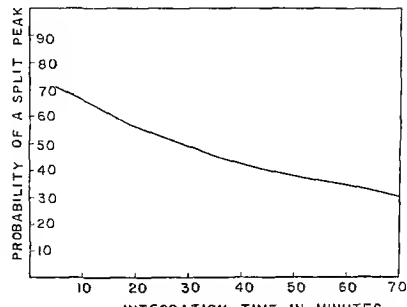

FIGURE 19 Probability of split peak, defined by Equation 109, vs integration time for white noise

probability of "split" or "broken" peaks), the white noise spectrum, $f(\omega)$ = constant, was examined Based a rather lengthy derivation given by Paul,[9] the predicted probability of a double or multiple peak defined by Equation 109 with $b = 3\,\Delta f$ was calculated for such a spectrum The results are shown on Figure 19 Finally an attempt was made to predict the probability of obtaining a double peak in a resonance type spectrum The assumed form of that spectrum was

$$G(f) = \frac{1}{1 + \left(\frac{f - f_0}{2}\right)^2} \qquad (110)$$

where B is the 80% band-width of the peak The calculation is very lengthy and it was feasible only to calculate the probability $P(B_i)$ of obtaining a split peak at one particular point on the resonance curve $P(B_i)$ varies in a rather complex manner with the distance $(f_i - f_o) = n_i(\Delta f)$ and Figure 20 shows the probability of obtaining a split peak starting at the point $B_i \approx f_o - 2\Delta f$ A split peak in the sense of Equation 109 could, of course, also start at $B_i = f_o - 5\Delta f$ or at $B_i = f_o + \Delta f$, etc The total probability P(B) of finding a split peak in a complete resonance curve is given by

$$P(B) = \sum_{i=-8}^{i=8} P(B_i)$$

$$(f_o - 8\Delta f) \leq B_i \leq (f_o + 8\Delta f) \qquad (111)$$

Although Figure 20 is applicable to only one point on the resonance curve, two comparisons with experimental data are possible (1) The predicted probability of obtaining a split peak for white noise, from Figure 19, can be compared with the experimental data for the largest 80% bandwidth w, 3 5 to 4 0 Hz, which according to Figure 20, should approach the probability of obtaining a split peak in a white noise spectrum

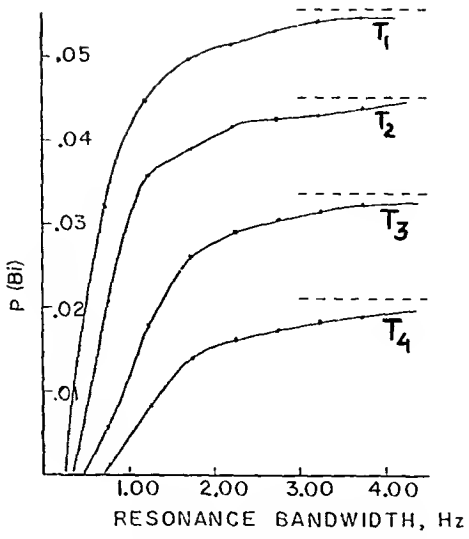

FIGURE 20. Probability of split peak, defined by Equation 109 with $b = 3\,\Delta f$, starting at $f = f_o - 2\,\Delta f$, against resonance line 80% bandwidth. (Parameter: integration time $T_1 = 8.53$ min, $T_2 = 17.07$ min, $T_3 = 34.13$ min, $T_4 = 68.26$ min, ——— white noise).

For an integration time of T = 17 min the number of experimental samples was large enough (522 magnetic field spectra, Figure 16) to obtain a meaningful comparison. For this integration time the measured probability of obtaining a split peak was 56.2% (Figure 16) as compared with a predicted probability (T = 17 min, $w \to \infty$) of 58.4% from Figure 19. (2) Although Figures 19 and 20 cannot be used to predict the exact value of the probability P(B) of finding a split peak in a resonance curve of 80% width $w < \infty$, they can be used with one supplementary calculation to establish lower and upper bounds on P(B).

Even for white noise P(B) cannot be obtained by just multiplying the value of $P(B_i)\big|_{w\to\infty}$ from Figure 20 by the number of discrete frequency points (equal to 17) in the range $(f_o - 8\,\Delta f) \leqslant f \leqslant (f_o + 8\,\Delta f)$. For example for

$$T = 1024 \text{ sec} = 17 \text{ min}$$

$$P(B_1)\Big|_{w\to\infty} = 0.045 \qquad \text{(from Figure 20)}$$

$$P(B)\Big|_{w\to\infty} = 0.584 \qquad \text{(from Figure 19)}$$

$$\frac{P(B)}{P(B_1)}\Big|_{w\to\infty} = 12.978 \qquad f_i = f_0 - 2\Delta f$$

It can be shown[91] that $P(B_i)$ is higher for points $f < f_o$ than for points $f > f_o$ and that it decreases monotonically with f. For a given finite resonance bandwidth, for example w = 2.75 Hz, we may therefore calculate the values of $P(B_i)$ corresponding to $f_i = f_o - 8\Delta f$ and $f_i = f_o + 8\Delta f$ and then approximate the ratios $[P(B)/P(B_i)]_{w=2.75}$ and $[P(B)/P(B_i)]_{w=2.75}$ by the ratio $[P(B)/P(B_i)]_{w\to\infty}$ at the intermediate value of $f_i = f_o - 2\Delta f$. This will then give an estimate of upper and lower bounds for $P(B)_{w=2.75}$. Doing this we obtain

$T = 17$ min $\quad w = 2.75$ Hz

$P(B_i) = 0.0462$ for $f_i = f_o - 8\Delta f$ giving $P(B)_{max} = 0.0462(12.978)$

$P(B_j) = 0.0283$ for $f_j = f_o + 8\Delta f$ giving $P(B)_{min} = 0.0283(12.978)$

Thus we obtain for $T = 17$ min and $w = 2.75$ Hz

$$0.367 \leqslant P(B) \leqslant 0.600$$

This can be compared with experimental values of 28.6% for the electric field spectra and 29.7% for the magnetic field spectra as shown on Figures 16 and 17.

In the analytical predictions of P(B) only $b = 3\Delta f$ was used in Equation 109. This is not very realistic since many subpeaks were observed to be at least $4(\Delta f)$ and $5(\Delta f)$ apart. Introducing more points in the definition of the "split" would have made the already lengthy calculation even more cumbersome. However in view of this $b = 3\Delta f$ assumption it is not surprising that the calculated P(B) is higher than the experimentally obtained P(B) for a "split" peak. The calculated probability is however lower than the experimentally observed probability for obtaining a "broken" peak (defined by $b = \Delta f$ or $b = 2\Delta f$) which was 57.2% for the electric field (Figure 17), and 68% for the magnetic field (Figure 16).

This entire examination shows that while the frequency of resonance line splitting increases during some types of ionospheric disturbances, it is also correlated with resonance line width (i.e., with inverse Q) and inversely with the length of the data sample. Thus while some major ionospheric disturbances are responsible for lower cavity Q, as discussed again in "Determination of the Electrical Conductivity of the Lower Ionosphere and 'Non-conducting' Atmosphere Below 40 km," it is not possible on the basis of the available experimental data to state that such disturbances cause resonance line splitting. Double and triple resonance peaks may be a characteristic of the cavity, but they may also be a consequence of unavoidable statistical error produced by the use of a data sample of finite length.

Field Intensity Levels — Spatial, Diurnal, and Seasonal Variations

Some representative magnetic flux density levels and electric field intensity levels measured in the Schumann resonance range, principally between 3 Hz and 30 Hz, are given in Table 3.

The values in Table 3 should only be considered approximate. For conversion to a per $Hz^{1/2}$ basis some calculations had to be based on frequency response curves which could be read only to very limited accuracy in the published literature. In any case, values of the electric and magnetic field vary widely with location, time of day, season, and frequency. As illustrated by Figures 3 or 15 the amplitude of different resonance peaks is not the same and the amplitude ratio between peaks and valleys of the power spectrum ($|E|$ rather than $|E|^2$ as shown on the figures) can vary roughly between 1.3 and 2.5.

Although it is sometimes possible to obtain Schumann-type spectra, such as Figure 3, without interruption over several days for contiguous sampling periods, there are other times when either all, or all but one or two of the resonance peaks disappear. This can be due to man-made interference as discussed below in "Sources of Man-Made and Natural Interference," to "local" thunderstorm activity within about a 500-km radius, to isolated, extremely intense lightning activity, or due to large ionospheric disturbances. Sudden enhancements of atmospherics ("SEA" phenomena) have been discussed by Sao et al.[125] and Ogawa et al.[126] Jones and Kemp[49] analyzed discrete light-

Table 3
REPRESENTATIVE FLUX DENSITY AND ELECTRIC FIELD VALUES IN THE SCHUMANN RESONANCE BAND (LOWEST THREE RESONANCES 8 Hz TO 21 Hz)

Magnetic field H or flux density B = μ_oH		Electric field[b]	
In units reported	B[a] in [Tesla/Hz]$^{-1/2}$	(mV/m)Hz$^{-1/2}$	Ref.
3.5 (10^{-10}) Watt/m^2/Hz	12.1	—	44
—	—	vert. 0 06—0 20	42
—	—	vert. 0.34	43
−1.5—−6.5 dB below 1(milligamma)^2/Hz	4.7—8 4	—	47
4(10^{-7})—2.9(10^{-6}) (A/m)Hz$^{-1/2}$	5.0—36.0	vert. 0.06—0.24	122
—	—	vert. 0.1—0.30	46
2.6—5.2 (milligama) ^{2}/Hz	16.0—23.0	—	124
−122—−134 dB/A/m/Hz$^{1/2}$	2.50—9.98	—	123
—	—	hor. over water σ = 4 S/m 1.1(10^{-5})—1 7(10^{-5})	95
—	—	hor over land σ = 10^{-3} S/m 3(10^{-6})—10^{-4}	94

[a] 0.1 milligamma = 10^{13}T
[b] Electric field: vert. = vertical; hor. = horizontal.

ning events which are substantially larger than those producing the normal Schumann "background".

In the Schumann spectra not only the amplitude, but also the Q values of the various resonance peaks and the resonance frequencies themselves vary with time. Some resonance frequency shifts were directly attributable to known world-wide ionospheric disturbances,[127] while other diurnal variations in frequency and amplitude can be attributed to changes in location and level of worldwide thunderstorm activity.[38 108] An example showing the variation of the first resonance frequency with time of day for three different days, approximately 1 month apart, is shown on Figure 21. Variation of the relative amplitude of successive resonance peaks is illustrated by Figure 22.

In "Effects of Lateral Inhomogeneities," this shift of resonance frequencies and relative amplitudes of resonance peaks was already discussed referring to Equation 24 and Figure 5. In "Location of Major Thunderstorm Regions," the use of experimentally established changes in frequency and relative amplitude for locating the position of major thunderstorm regions will be explored, and in "Monitoring of Worldwide Thunderstorm Intensity," the variations of resonance frequencies, relative spectral amplitudes and absolute field levels will be related to changes in total, world-wide thunderstorm activity.

Sources of Natural and Man-Made Interference

Approximate amplitude levels of "micropulsation" natural magnetic field noise, based on Campbell's work,[128] are shown on Figure 23. Below 3 Hz the natural ambient noise increases as $\sim 1/f^n$ ($1.5 < n < 2.5$) and generally it is already much larger than the Schumann level at about 2 Hz. Therefore a high pass filter with relatively sharp cut-off at the low end of the Schumann band is necessary to avoid overloading of receiving equipment for the detection of the magnetic field component of the cavity resonances.

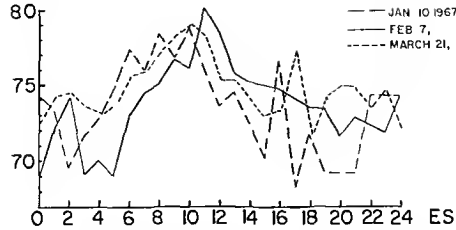

FIGURE 21 Diurnal variation of frequency of first resonance peaks

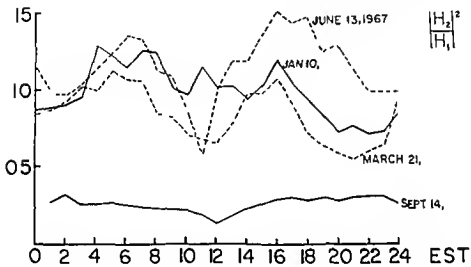

FIGURE 22 Diurnal variation $|H_2/H_1|^2$, ratio of magnetic field power densities at first and second resonance peaks

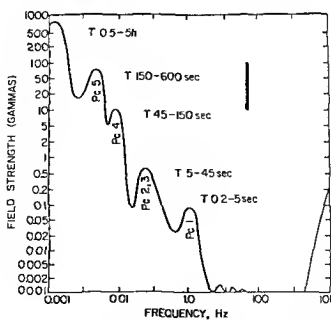

FIGURE 23 Field strength vs frequency of micropulsations

Similarly noise below about 4 Hz is picked up by electric field sensors, but its level decreases, as was pointed out in "Vertical Electric Fields" and by Ogawa et al.,[46] when the height of the sensor above ground is increased. This noise, probably due to ion motion near the ground, can also become very bothersome if a horizontal wire at close proximity to the ground is used as a receiving antenna.

In "Magnetic Field," it was already pointed out that motion of a high sensitivity induction coil in the steady magnetic field of the Earth can produce an e.m.f. of a few Hertz of much larger amplitude than the noise, of the order of 10^{-13} T $Hz^{-1/2}$, from distant thunderstorms. Magnetic field sensors for Schumann resonance frequencies must therefore be located far from road traffic or other man-made vibrations.[108 110] However, natural ground vibrations,[109] for example, due to surf at a shore line at a few miles from the receiving site, can also become a source of interference. If a large coil is mounted so as to isolate it from ground vibrations, it becomes of course essential that the mechanical natural resonance frequency of the coil and mount system be well below the passband of the electrical receiving system. In this context, it is worth noting that many available rubber or rubber-like materials become stiffer with age when they are subjected to continuous compression. Since the mechanical resonance frequency $\omega_o/2\pi$ of a vibrating system is given by

$$\omega_o^2 = \frac{k}{m} \tag{112}$$

where k = stiffness coefficient of the "spring" material, a system originally designed for a mechanical resonance frequency of 2 Hz may vibrate at an unacceptable 4 Hz after a few months of operation.

In considering pick-up of undesired natural as well as man-made signals one has to differentiate between pick-up by the principal sensor and pick-up, after preamplification, on long transmission lines between the sensor-preamplifier and a building where timing and recording equipment may be housed. If it is not possible to avoid such lines (by using subminiaturized receiving and telemetering equipment at the antenna), they must be extremely well shielded and appropriately grounded to avoid pick-up on ground loops.[129]

Unless a location far from sources of man-made noise can be found, such noise is almost always orders of magnitude larger than the Schumann oscillations. This is particularly true for magnetic fields. The primary noise source is, of course, power lines (60 Hz in the U.S., 50 Hz in most other countries); however power lines from low frequency railway systems, such as the 16.67 Hz German net,[7] can be particularly bothersome. If there are nonlinearities in the receiving system sum and difference frequencies of the interference, such as 50 − 16.67 = 33.33 Hz, may also appear. In the U.S. most telephone ringing systems employ frequencies in the vicinity of 20 Hz and ELF fields measured near telephone lines may be dominated by this source.

Modulation of higher frequency communication carriers (particularly VLF carriers, 10 kHz to 100 kHz) may also be detected by nonlinearities in ELF-measurement systems when the carrier level is large enough to overload high sensitivity input circuitry. Thus König et al.[130] measured a strong 30 Hz signal whenever ship-borne ELF detecting equipment was brought to within perhaps 100 km of a "Loran" navigation transmitter. The reasons for this are illustrated by Figure 24, which depicts the modulation of a Loran signal.

INTERPRETATION AND USE OF DATA

Location of Major Thunderstorm Regions

The electric field due to a single vertical current source in the Earth-ionosphere cav-

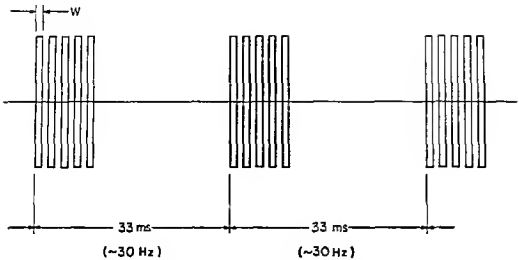

FIGURE 24 "Loran" (navigational) signal causing 30 Hz interference

ity is given by Equation 24 In "General Considerations and Horizontal Electric Fields," the ratio and E_r/H_ϕ can be obtained From Equations 71 and 24 it then follows that the horizontal magnetic field is

$$H_\phi = -\frac{Ids}{4\pi ah}\sum_{n=0}^{\infty}\frac{2n+1}{n(n+1)-\nu(\nu+1)}\frac{d}{d\theta}P_n(\cos\theta) \qquad (113)$$

As was pointed out in deriving Equation 72, the ratio $|E_r/H_\phi|$ near the resonance frequencies is approximately

$$\frac{E_r}{H_\phi} \approx \omega\mu a\frac{\sum_{n=0}^{\infty}\frac{2n+1}{n(n+1)-\nu(\nu+1)}P_n(\cos\theta)}{\sum_{n=0}^{\infty}\frac{2n+1}{n(n+1)-\nu(\nu+1)}\frac{d}{d\theta}P_n(\cos\theta)} \qquad (114)$$

and neglecting all but the "resonance" term in the summation, i e , the term corresponding to the frequency when $|n(n+1)-\nu(\nu+1)| = \min$,

$$\frac{E_r}{H_\phi} \approx \omega_r\mu a\frac{P_n(\cos\theta)}{\frac{d}{d\theta}P_n(\cos\theta)} \qquad (115)$$

As a consequence the ratio of the electric to the magnetic field amplitudes near the resonance frequencies is not very sensitive to the details of the model assumed for the ionosphere The ratio is not completely independent of the ionosphere parameters since Equation 71 contains $\nu(\nu+1)$ and since terms other than the resonance term are significant in the summations of Equation 114 Nevertheless Equation 115 suggests that near the resonance frequencies the ratio $|E_r/H_\phi|$ is strongly affected by the source receiver separation θ and only secondarily by the ionosphere parameters which determine ν Referring to Figure 5 it is apparent then that, for example, at the first resonance frequency and $\theta = (\pi/2)$ $(E_r/H_\phi) \to 0$ The ratio $|E_r/H_\phi|$ at the resonance frequencies can then be used as a sensitive indicator of the source-receiver separation Application

of Equations 71 or 24 and 113 to realistic cavity models[55,131] shows that this is a useful procedure. Similarly the dependence on ν, that is the dependence on the ionosphere parameters, becomes relatively weak when the ratio of the amplitudes of the electric or magnetic field at two successive resonance peaks is evaluated. For example from Equation 113 for the H field first and second resonance peaks

$$\left|\frac{H_{\phi 2}}{H_{\phi 1}}\right| \approx \left|\frac{S}{6-\nu_2(\nu_2+1)}\,\frac{2-\nu_1(\nu_1+1)}{3}\right|\left|\frac{\frac{d}{d\theta}P_2(\cos\theta)}{\frac{d}{d}P_1(\cos\theta)}\right| \tag{116}$$

The dependence on υ is not strong because at the resonance peaks

$$\begin{aligned} &n(n+1)-\nu(\nu+1) = \text{MIN} \\ &\nu \approx n - j\epsilon \qquad \text{where } \epsilon << 1 \end{aligned} \tag{117}$$

therefore Equation 116 becomes

$$\left|\frac{H_{\phi 2}}{H_{\phi 1}}\right| \approx \frac{5}{3}\,\frac{3\epsilon_1}{8\epsilon_2}\,\frac{\frac{d}{d\theta}P_2(\cos\theta)}{\frac{d}{d\theta}P_1(\cos\theta)} \tag{118}$$

Typical values of ε showing that $\varepsilon_1/\varepsilon_2$ depends only weakly on the characteristics of the ionosphere model are given by Tran and Polk.[54]

These considerations[52] have led then to the idea of using ratios such as Equations 114 and 116, obtained from experimental data, to locate sources of cavity excitation. Since many lightning flashes excite the cavity simultaneously, power spectral amplitudes must be used, as discussed in the section on methods of spectral analysis. Also the size of the excitation area r = a, $(\theta-\Delta) \leqslant \theta \leqslant (\theta+\Delta)$, $(\phi-\Delta_\phi) \leqslant \phi \leqslant (\phi+\Delta_\phi)$ must be considered as indicated by Equations 89 to 91.

Using Equations 89 to 91 for a source centered at (θ,π) which has an angular spread $\pm\Delta$ in the θ-direction and $\pm\Delta_\phi$ in the ϕ-direction, and assuming that Mg(ω), the current moment and power spectrum of the average lightning flash, is independent of θ and ϕ, the desired ratios are[131]

$$\left|\frac{E_{n+1}}{E_n}\right|^2 = \frac{\int_{\theta-\Delta}^{\theta+\Delta} G_{E_{n+1}}(\theta',\phi')\sin\theta'\,d\theta}{\int_{\theta-\Delta}^{\theta+\Delta} G_{E_n}(\theta',\phi')\sin\theta'\,d\theta'} \qquad n = 1,2,\ldots, \tag{119}$$

$$\left|\frac{H_{n+1}}{H_n}\right|^2 = \frac{\int_{\theta-\Delta}^{\theta+\Delta} G_{H_{n+1}}(\theta',\phi')\sin\theta'\,d\theta'}{\int_{\theta-\Delta}^{\theta+\Delta} G_{H_n}(\theta',\phi')\sin\theta'\,d\theta'} \qquad n = 1,2,\ldots, \tag{120}$$

$$\left|\frac{E_n}{H_n}\right|^2 = \frac{2\Delta_\phi \int_{\theta-\Delta}^{\theta+\Delta} G_{E_n}(\theta',\phi') \sin\theta' \, d\theta'}{[\Delta_\phi - \tfrac{1}{2}\sin 2\Delta_\phi \cos 2(\phi-\alpha)] \int_{\theta-\Delta}^{\theta+\Delta} G_{H_n}(\theta',\phi') \sin\theta' \, d\theta'} \qquad n = 1,2, \quad , \qquad (121)$$

where

$$G_{E_n}(\theta',\phi') = M a^3 g(\omega_n) \left| \frac{\nu(\nu+1)}{4\pi a^2 \omega_n \epsilon_0 h} \sum_{n=0}^{\infty} \frac{2n+1}{n(n+1) - \nu(\nu+1)} P_n(\cos\theta) \right|^2 \qquad (122)$$

$$G_{H_n}(\theta',\phi') = M a^3 g(\omega_n) \left| \frac{1}{4\pi a r} \sum_{n=0}^{\infty} \frac{2n+1}{n(n+1) - \nu(\nu+1)} \frac{d}{d\theta} P_n(\cos\theta) \right|^2 \qquad (123)$$

and α in Equation 121 is the angle of the receiving coil axis with the ϕ reference line which, for example, could be the east-west direction The subscript n denotes the order of the resonance

Amplitude ratios r, are obtained from spectra of experimental data and ratios $f_i(\theta,\Delta)$ are calculated from Equations 119 to 121 Different sets of (θ,Δ) are tried in the following expression

$$q = \sum_{i=1}^{N} \left[\frac{r_i - f_i(\theta,\Delta)}{r_i} \right]^2 \qquad (124)$$

where N is the number of ratios used The set (θ,Δ) which gives a minimum q defines the source

Sometimes more than a single major thunderstorm region excites the cavity at one time It is generally believed that the three major thunderstorm regions are tropical America, Africa, and Asia The occurrence of thunderstorms depends on local time with most activity taking place in the local late afternoons Most of the time not more than two major thunderstorm regions are active simultaneously [132] To extend the method to locate two such simultaneously active regions it is assumed that they are centered at θ_A and θ_B and have equal spread in the θ-direction $\Delta_A = \Delta_B = \Delta$ The ratio of azimuthal spread of the two sources is $\delta = (\Delta_{\phi A}/\Delta_{\phi B})$

For two sources the ratios of resonant peak amplitudes are

$$\left|\frac{E_{n+1}}{E_n}\right|^2 = \frac{\mathcal{E}_{n+1}^A + \delta \mathcal{E}_{n+1}^B}{\mathcal{E}_n^A + \delta \mathcal{E}_n^B} \qquad n = 1,2,3 \qquad (125)$$

$$\left|\frac{H_{n+1}}{H_n}\right|^2 = \frac{\mathcal{H}_{n+1}^A + \delta \mathcal{H}_{n+1}^B}{\mathcal{H}_n^A + \delta \mathcal{H}_n^B} \qquad n = 1,2,3 \qquad (126)$$

$$\left|\frac{E_n}{H_n}\right|^2 = \frac{\mathcal{E}_n^A + \delta \mathcal{E}_n^B}{\mathcal{H}_n^A + \delta \mathcal{H}_n^B} \qquad n = 1,2,3 \qquad (127)$$

where the superscripts denote source A or B, and

$$\mathcal{E}_n(\theta,\Delta) = \int_{\theta-\Delta}^{\theta+\Delta} G_{E_n}(\theta')\, z^2 \sin\theta'\, d\theta' \tag{128}$$

$$\mathcal{H}_n(\theta,\Delta) = \int_{\theta-\Delta}^{\theta+\Delta} G_{H_n}(\theta')\, z^2 \sin\theta'\, d\theta' \tag{129}$$

Equations 125 to 127 can be rewritten in the following general form.

$$f_i(\delta) = \frac{A_i + \delta B_i}{C_i + \delta D_i} \tag{130}$$

For a specified θ_A and θ_B, δ may be obtained for given experimental values r_i by minimizing the following quantity:

$$q = \sum_{i=1}^{N} \left[r_i - \frac{A_i + \delta B_i}{C_i + \delta D_i} \right]^2 \tag{131}$$

To avoid the need for solving a higher order polynomial in δ which is obtained by minimizing q, an alternative approach is introduced. Rewriting Equation 130 as

$$f_i(C_i + \delta S_i) = (A_i + \delta B_i) \tag{132}$$

one obtains

$$q = \sum_{i=1}^{N} \left[r_i(C_i + \delta D_i) - (A_i + \delta B_i) \right]^2 \tag{133}$$

Minimizing Equation 133 gives

$$\delta = \frac{\sum_{i=1}^{N} (A_i - C_i r_i)(D_i r_i - B_i)}{\sum_{i=1}^{N} (D_i r_i - B_i)^2} \tag{134}$$

since

$$\frac{\partial^2 q}{\partial \delta^2} = \sum_{i=1}^{N} (D_i r_i - B_i)^2 \geq 0 \tag{135}$$

For a specified θ_A, θ_B, there will always be a minimum q with δ given by Equation 134. Therefore, different combinations of (θ_A,θ_B) can be tried and the location of the two thunderstorm regions is determined by the set (θ_A,θ_B) which gives minimum q.

Since the resonance frequencies for different values of θ are not identical, the determination of A_i, B_i, C_i, and D_i in Equations 130 to 135 requires the following iterative procedure.

1 Amplitude ratios at the experimental resonance frequencies are used to obtain the initial values of θ_A, θ_B, and δ
2 Resonance frequencies are calculated for this combination of θ_A, θ_B, and δ
3 These resonance frequencies are compared with the experimentally determined resonance frequencies (or with the resonance frequencies obtained in the previous iteration as explained below)
4 If the calculated resonance frequencies are not identical with the experimentally determined values, Step 1 is repeated with the resonance frequencies calculated in Step 2 replacing the experimental values (thus A_1, B_1, C_1, and D_1 in Equation 133 are now based on the calculated resonance frequencies) This will give a different set of θ_A, θ_B, and δ

The iteration indicated by Steps 1 to 4 is continued until two successive sets of resonance frequencies (in Step 2) are identical It can be shown[131] that the ratios of resonance amplitudes display only a second order variation with Δ (compared with the dependence on θ), provided Δ is in the range $0° \leq \Delta \leq 10°$ which probably includes most realistic thunderstorm regions A value of $\Delta = 5°$ was therefore used for the experiments described below The average source spectrum was represented by a relation due to Galejs,[133] based on earlier work by Williams[134] and Raemer [17]

$$g(\omega) = K \exp[-9.1(10^{-3})\omega] \qquad Hz^{-1} \qquad (136)$$

In several numerical experiments other forms of $g(\omega)$ were tried, but Equation 136 gave the best fit to Schumann resonance data The constant K is arbitrary, but in "Monitoring of Worldwide Thunderstorm Intensity," $K = 0.0447$ will be used to obtain $\int_{\omega_1}^{\omega_2} g(\omega)\,d\omega = 1$ over the frequency range $12\ Hz < f < 21\ Hz$

Although two simultaneously active major thunderstorm regions can be located from ELF spectra obtained at a single observation site, the information is ambiguous in that four possible azimuth locations are given for each of the two values of the angular source-receiver separation θ Frequently several of these sources can be eliminated from such considerations as the unlikeliness of a major thunderstorm occurring over the North Atlantic in winter, but for unambiguous location of major thunderstorm centers on the surface of the Earth two widely separated ELF receiving sites would be required Figure 25 indicates how locations from two such stations, one in the Northeastern U S and one in Honshu, Japan, would give intersecting loci for given values of θ (60 J = locus of all points at $\theta = 60°$ from the Japanese station, etc) Unfortunately long term and detailed spectral data were available to the author only for the one receiving station near Kingston, R I at 71°43'53"W, 47°37'18"N Results of source locations using these data were compared with results obtained by the VLF system of Heydt and Volland[135-137] and, in one case, with satellite cloud photographs [138]

Details of the comparison of the ELF with VLF data were reported by Polk and Clayton [139] Among 31 useful data samples one or more of the four θ values determined by ELF location coincided with a source located by VLF in 22 cases Among these, 12 were based on ELF data taken exactly at the same time as the VLF data, while 10 were taken 1 hr before or after the VLF reception Among the nine angles θ which did not locate sources confirmed by VLF, six or 66 7% of the data, were taken 1 hr before or after the VLF recordings The comparison with satellite data (and surface observations) reported by Tran and Polk[55] involved the location of a major thunderstorm system over Utah and Colorado in the U S during the period June 6 to 12, 1967 Five power spectra covering the period 00 00 to 02 00 UT on June 7, 1967, each with an integration time of 17 min, located the source at $24° < \theta < 26°$ while radar precipitation

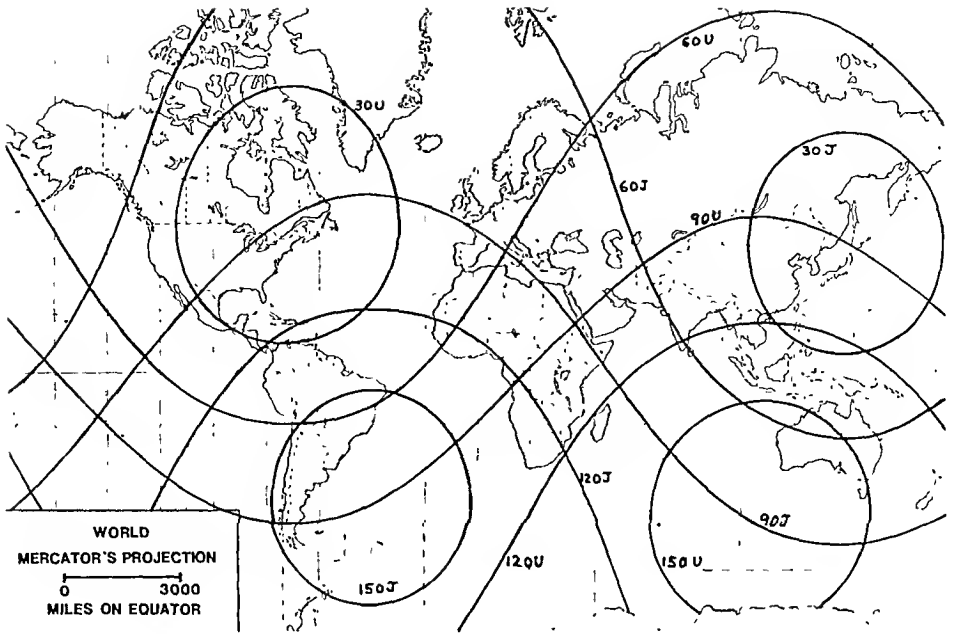

FIGURE 25. Loci of constant angular separation from observation sites in New England (U) and Kakioka, Japan (J).

data located the center of activity near Salt Lake City, Utah at $\theta = 29°$ and indicated an extent of the system of about $0.81(10^6)$ km[L] corresponding roughly to $\Delta = 5°$ and $\Delta_\phi = 3.5°$.

Toomey[131] also investigated the effect of "background noise", consisting of relatively light thunderstorm activity uniformly distributed over an equatorial belt, upon the location of the major thunderstorm regions. The Schumann resonance method clearly assumes that the one or two large regions of intense activity have a much greater effect upon the resonance spectrum than simultaneous low density lightning activity which is more or less uniformly distributed over the rest of the world. As a test of how well this assumption is satisfied it was specified that 100 flashes per second occur[132] worldwide and that they are distributed between a region of major activity, having area $A_M = 10^6$ km^2 with flash density ϱ_M, and a larger region, of area A_B, with smaller flash density ϱ_B. Thus

$$N = 100 = N_M + N_B = \rho_M A_M + \rho_B A_B \qquad (137)$$

Using a realistic ionosphere conductivity profile[131] and $g(\omega)$ given by Equation 136 for both regions — but with different constant K determined by Equation 137 — the source location procedure was implemented for northern winter (A_B over the equatorial belt 10°N to 40°S), spring-fall (A_B 30°S to 30°N) and northern summer (A_B 10°S to 60°N). The spring-fall results shown on Figure 26 display the deviation of the estimated location from the true location as uniform background activity increases. The value of the deviation is very sensitive to the area A_M of the major thunderstorm region; for example, if the assumed size of a major thunderstorm region is increased to $5(10^6)$ km^2 the signal to noise ratio is greatly improved. It is also apparent from Figure 26 that the extent to which it becomes possible to confirm ELF location results by direct surface or satellite observations, also provides information about the relative magnitude of "major" and "background" lightning activity. For example, if it should turn out

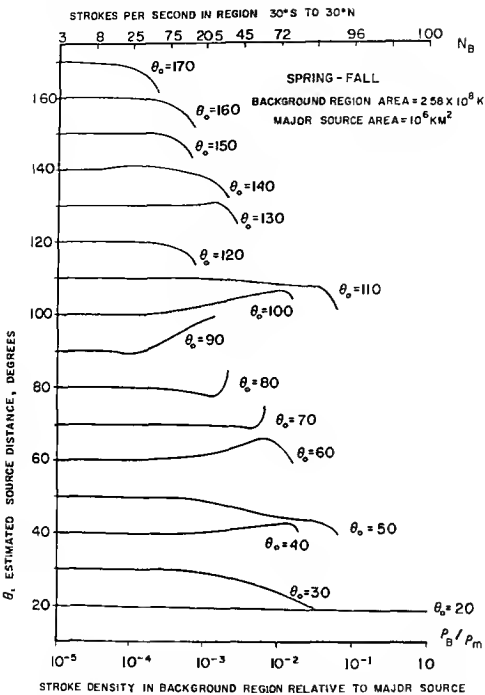

FIGURE 26 Effect of widely distributed thunderstorm activity upon location estimates

that the ELF resonance location method gives consistently correct thunderstorm positions during certain periods, but not during others, it would be possible to draw conclusions concerning the distribution in time of the "background" activity

Toomey[131] also investigated the effect of extra terrestrial low frequency $1/f^{\alpha}$ noise, which is particularly likely to contaminate the magnetic field data as was discussed in "Sources of Man-Made and Natural Interference" If the power spectrum resulting from thunderstorm activity is designated by T(f) and the noise spectrum $Af^{-\alpha}$ by N(f), then the total received spectrum is

$$S(f) = N(f) + T(f) \tag{138}$$

provided N and T are power spectra of uncorrelated random processes Assuming a

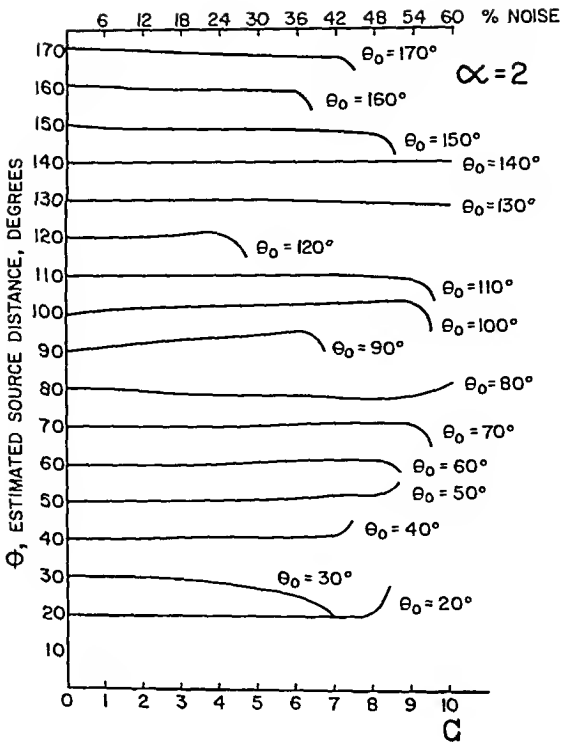

FIGURE 27. Estimated erroneous source location θ for given true location θ_0 as a function of A $f^{-\alpha}$ noise.

source location and strength, one can evaluate S(f) for different values of A and α and use these "noisy" spectra in the source location procedure. Figure 27 illustrates the results of such a numerical experiment; θ_0 is the true location of the thunderstorm source and the abscissa is the ratio of spectral power at 2 Hz to the spectral power at the first resonance, i.e.,

$$C = \frac{S(2)}{S(f_1)} \tag{139}$$

Since thunderstorm-produced power at 2 Hz is usually negligible compared to the noise power at 2 Hz

$$C = \frac{N(2)}{N(f_1) + T(f_1)} \tag{140}$$

C was chosen in this form. The abscissa in Figure 27 can also be roughly interpreted as the percent noise power at the apparent first resonance

$$P_n(f_1) = 100 \frac{N(f_1)}{N(f_1) + T(f_1)} = 100C \frac{N(f_1)}{N(2)} \tag{141}$$

since f_1 is approximately constant (f_1 depends on A, α, and the source location and strength, but varies at most ± 1 Hz) and $N(f_1) + T(f_1) = N(2)/C$ from Equation 140. Varying P_n corresponds to varying A in $N(f) = Af^{-\alpha}$. It is apparent from Figure 27

that the source location procedure is fairly insensitive to this type of noise In part this is due to the fact that the procedure uses the received power spectrum at or near the resonance peaks where the effect of contamination by background noise is less than at the valleys of the resonance curve (Figure 3)

Monitoring of Worldwide Thunderstorm Intensity

If the Schumann resonances are excited exclusively, or almost exclusively, by lightning-generated radiation, they should provide information not only about relative diurnal and seasonal variation of global lightning activity,[15 38 63 108] but also about its absolute value Attempts to do this were made by Clayton and Polk[53] using records of the period September 1970 to May 1971

The calculation of absolute levels clearly requires accurate determination of the absolute values of the received electric and magnetic fields as discussed in "Experimental Data and Data Analysis " Furthermore, the diurnal and seasonal variations of amplitudes and peak frequencies at any particular receiving site must also be corrected for source-receiver spacing since Equations 24 and 113 indicate a dependence on θ A source location method such as that discussed in "Location of Major Thunderstorm Regions" is therefore a prerequisite for the deduction of absolute levels of world lightning activity from Schumann resonance records

Determination of absolute levels of lightning activity amounts to finding the product of lightning activity area and the factor M in Equation 89 M is the magnitude squared of the total vertical lightning current moment per unit area No information about individual lightning flashes is obtained and the world-integrated effect of all flashes can be translated into a number of flashes per second only if something is known about the current moment Ids of the "average" flash Also since the propagating TM, mode is only very inefficiently excited by horizontal electric currents, the estimate obtained from Schumann resonance data will contain only a small contribution due to horizontal cloud to cloud flashes On the other hand, estimates obtained from Schumann resonances are likely to be influenced by slowly varying components of the lightning flash which have much less effect at higher frequencies, for example contributions of the "corona current" may be significant as pointed out in Chapter 3 of Galejs' book [16]

To obtain M and the required area some asumption has to be made about the power spectrum $g(\omega)$ of the average flash, particularly if data from more than one frequency are used Clayton and Polk[53] used the form given by Equation 136 which is due to Raemer[17] and has also been discussed by Galejs [16] It assumes that the interstroke interval is distributed about a median value of 33 msec with a standard deviation of 7 msec and that the probabilities of n return strokes in each flash vary between 0 23 (for n = 3) and 0 01 (for n = 10), the median value of n is 2 5

Since the θ dependence of the spectrum given by Equation 24 is different at different resonant peaks as illustrated by Figure 5, use of spectrum which includes at least two such peaks tends to reduce dependence of the final result for total lightning activity T upon an exact knowledge of θ Data integrated over the frequency band 12 Hz to 21 Hz were therefore used by Clayton and Polk[108] as shown below Data at individual resonances were only used to find θ as outlined in "Location of Major Thunderstorm Regions " The lower cut-off frequency (f_c = 12 Hz) of the band was taken above the first resonance ($f \approx 8$ Hz), because the Schumann spectrum is sometimes contaminated below 10 Hz by noise which is presumably due to extraterrestrial sources either in the ionosphere or the magnetosphere as discussed in "Sources of Man-Made and Natural Interference " (See also Abbas.[44])

To calculate both θ and T, it was necessary to assume an average electrical conductivity profile extending from ground level to about 80 km altitude In the section on determining electrical conductivity, it is shown that the need for changes in conductiv-

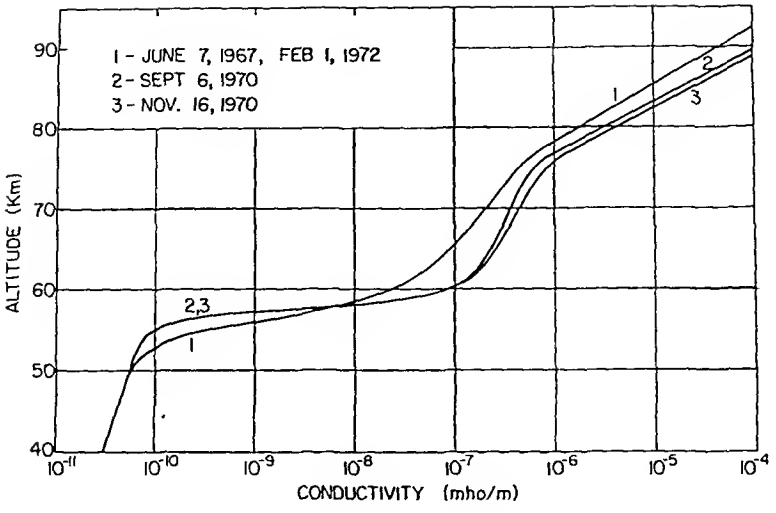

FIGURE 28. Electrical conductivity profiles used for source strength computations (from Clayton and Polk[140]).

ity profiles appropriate for Schumann resonance calculations is indicated very well by changes in 10.7 cm solar radio flux in the absence of "solar proton" or "PCA" events. One of the conductivity profiles shown on Figure 28 was therefore used depending upon the 10.7 cm flux reported for the particular day.

The starting point of the calculation of the total lightning activity T $(Am)^2$ = T $(Cm)^2/s^2$ are Equations 90 and 91. If electric field data are used, the power spectrum is

$$|E_r(\omega)|^2 = G(f)\,|F_e(\theta,f)|^2 \qquad (\text{Volt m}^{-1})^2/\text{Hz} \qquad (90)$$

and the source location procedure of "Location of Major Thunderstorm Regions" gives two values of θ as well as the ratio of source strengths D. Knowing θ_A and θ_B and given appropriate ionosphere parameters as well as $g(\omega)$ given by Equation 136, one can evaluate $|E_r(f)|_A^2$ and $|E_r(f)|_B^2$ from Equations 24 and 89 except for as yet unknown amplitude factors $T_{A,B}$ = M × Area. It is also useful to evaluate an average of the measured power spectral densitites over the selected frequency range

$$|E|^2 = \frac{1}{(f_2 - f_1)} \int_{f_1}^{f_2} |E_r(f)|^2\, df \quad (\text{Vm}^{-1})^2/\text{Hz} \qquad (142)$$

as well as spectral averages of the calculated values $E_r(\omega)_A$ and $E_r(\omega)_B$:

$$\frac{\text{Average power spectral density}}{\text{Unknown amplitude factor}} = F_{A,B} = \frac{1}{T_{A,B}\,(f_2 - f_1)} \int_{f_1}^{f_2} |E_r(f)|_A^2\, df \qquad \frac{(\text{Volt m}^{-1})^2}{(\text{Am})^2\,\text{Hz}} \qquad (143)$$

Since the experimental data provide values of $|E|^2$ and $D = (T_B/T_A)$, one can write

$$|E|^2 = T_A(F_A + DF_B)$$

and find (144)

$$T = T_A + T_B = \frac{|E|^2}{F_A + DF_B}(1 + D) \qquad (\text{Am})^2$$

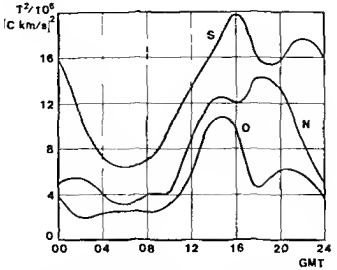

FIGURE 29 Diurnal variation of lightning activity from Schumann resonance data September, October, and November 1970 (6 days each month)

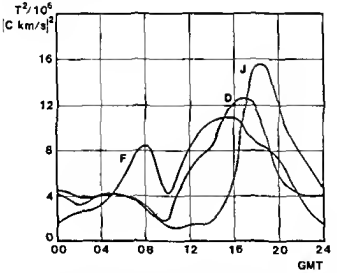

FIGURE 30 Diurnal variation of lightning activity from Schumann resonance data December 1970, January and February 1971 (6 days each month)

T may also be expressed in (coulomb meters per second)^2 which is probably more useful since total charge transfer for the average lightning flash is better established than total current flow Hence the results of the ELF calculations can therefore be more easily compared with other data

Results of these calculations of world lightning activity are given on Figures 29 to 31. (Similar curves in the paper by Clayton and Polk[140] give an incorrect scale in terms of C^{2}m^2/sec rather than C^{2}m^2/sec^2 which must be corrected by a factor of 9 proportional to the frequency bandwidth which was used) The values of T vary from 1170 C km/sec at 1000 GMT in January 1971 to 4450 C km/sec at 1600 GMT in September 1970 If one assumes, based on data given by Uman,[114] a transfer of 20 C, over a 3 km path for the average lightning flash, this corresponds to minimum of 19 5 and a maximum of 74 flashes per second

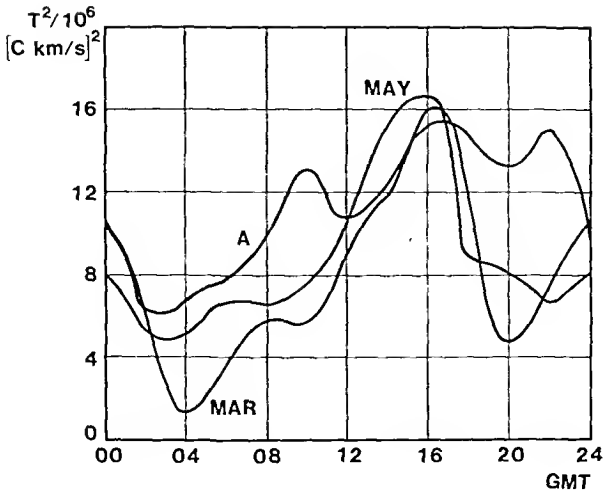

FIGURE 31. Diurnal variation of lightning activity from Schumann resonance data: March, April, and May 1971 (6 days each month).

Determination of the Electrical Conductivity of the Lower Ionosphere and "Nonconducting" Atmosphere below 40 km

While the ratios of the field amplitudes at successive resonance peaks depend only weakly on the characteristics of the ionosphere, the precise values of the resonance frequencies and the widths of the resonance peaks are a sensitive indicator of upper atmosphere and ionosphere properties. These values also depend upon source-receiver separation as illustrated by Figure 32. Ogawa and Murakami[143] have used the dependence on the vertical conductivity profile to test various atmosphere and ionosphere models. To correct for source-receiver separation they used annual averages for the diurnal variation of global lightning distribution published by Israël[144] and came to the conclusion that "either diurnal variation of local lightning activity is more drastic (than the annual averages), or that the diurnal variation of peak frequencies is caused by some reasons other than the variation of worldwide lightning activity." The first conclusion, that actual diurnal variation of lightning activity during a particular period deviates considerably from annual averages, is confirmed by the results summarized on Figures 29 to 31. It is therefore desirable to use information on actual source locations during the periods for which ELF data are available, when resonance frequencies and Q-values are employed to test various ionosphere models.

The other difficulty with using ELF data to deduce ionosphere profiles is the computational complexity of taking into account either the magnetic field effects discussed in "Effects of the Earth's Magnetic Field," or the lateral ionosphere variations discussed in "Effects of Lateral Inhomogeneities." Recent advances in digital computer power may make it possible to combine the techniques outlined by Madden and Thompson[25] for handling lateral inhomogeneities with Tran's[33 35] refinements for calculating the effects of a multilayer ionosphere to greater accuracy (avoiding planar approximations, considering the diffusivity of the lower boundary), or with Booker's[36] and Behroozi-Toosi-Booker's[37] techniques for evaluating the effect of the magnetic field of the Earth. Nevertheless this has not been done thus far and the discussion which follows will be limited to calculations of world-averaged ionosphere profiles to match experimental ELF power spectra when the location of the exciting regions is known.

Tran and Polk[55] used the source location method outlined in "Location of Major

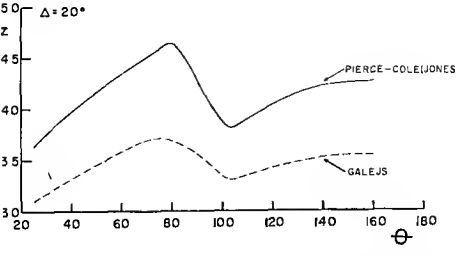

FIGURE 32 Dependence of resonance frequency upon source-receiver separation (θ) and ionosphere profile for source size $\Delta = \theta_1 - \theta_2 = 20°$ (Profiles used by Toomey[131] based on Jones,[34] electrons and ions, and Galejs,[44] electrons only Profiles differ particularly between 0 and 45 km altitude)

Thunderstorm Regions" and essentially Wait's[13] method for handling a stratified isotropic ionosphere (described in the section on resonances bounded by an ionosphere) to obtain a world average ionosphere profile This was done iteratively starting with an assumed ionosphere profile to obtain a first guess of the source locations (θ) Resonance frequencies were then used to obtain a conductivity profile in the 40- to 100-km altitude range, which was then used to obtain a better source location which, in turn, was used in a second calculation of an ionosphere profile The 90% width (related to cavity Q) was then used to obtain an average value, σ_a, of the conductivity for the lowest, 0- to 40-km altitude range, as well as corrections to the ionosphere profile from 60 to 75 km The 60- to 75-km profile was necessary because the 90% width depends upon that part of the profile as well as σ_a

The results of these calculations are shown on Figures 28, 33, and 34 for four different observation days (1) On June 6 through 12, 1976, a major thunderstorm system was located by satellite and surface observations as well as by ELF techniques over Utah and Colorado For this period the correction needed for source-receiver separation (θ), which can be made from the ELF data alone, was therefore verified by independent (surface and satellite) observations Solar activity as indicated by the relative sunspot number R, (Table 4) was low Since Lyman-α is the dominant ionizing agent in the 60- to 85-km region during low solar activity, the relatively low value of 10 7 cm flux (Table 4), which is indicative of XUV radiation, suggests lower ionization in the upper D-region during this period (and on February 1, 1972) than on September 6 and November 16, 1970 (Five power spectra, each with 17 min of integration time, were used.) (2) September 6, 1970 was selected because it was characterized by relatively high solar activity as indicated by R. The average solar 10 7 cm flux on this day indicated intermediate level XUV radiation (compared with June 7 or November 16) (Three electric and magnetic field spectra with 34-min, integration time) (3) R, on November 16, 1970 was only slightly lower than on September 6, 1970, but 10.7 cm flux was unusually high (Three electric and magnetic field spectra with 34-min integration time.) (4) On February 1, 1972, sunspot number and XUV radiation were about the same as during the June 6 through 12, 1967 period (Three electric and magnetic field spectra with 34-min integration time)

Galactic cosmic ray activity — which is inversely related to solar activity — is the

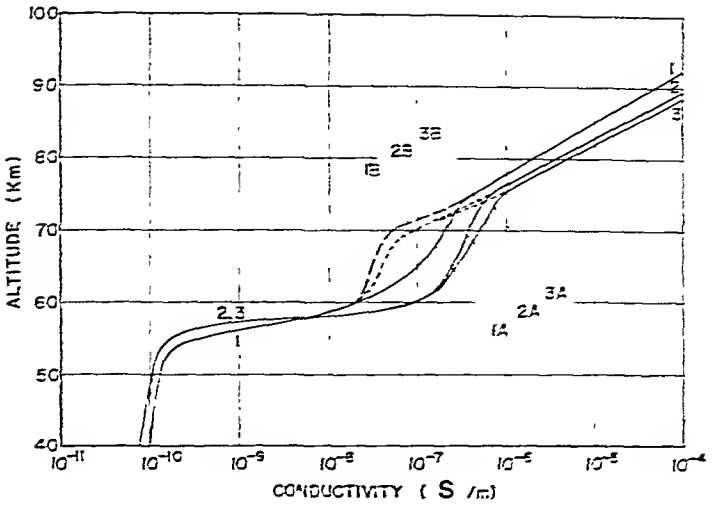

FIGURE 33. Conductivity profiles evaluated from Schumann resonance data. $\sigma_s = 3.5\ (10^{-11})$ S/m for 1A, 2A, 3A; $\sigma_s = 3.35\ (10^{-11})$ S/m for 1B, 2B, 3B.

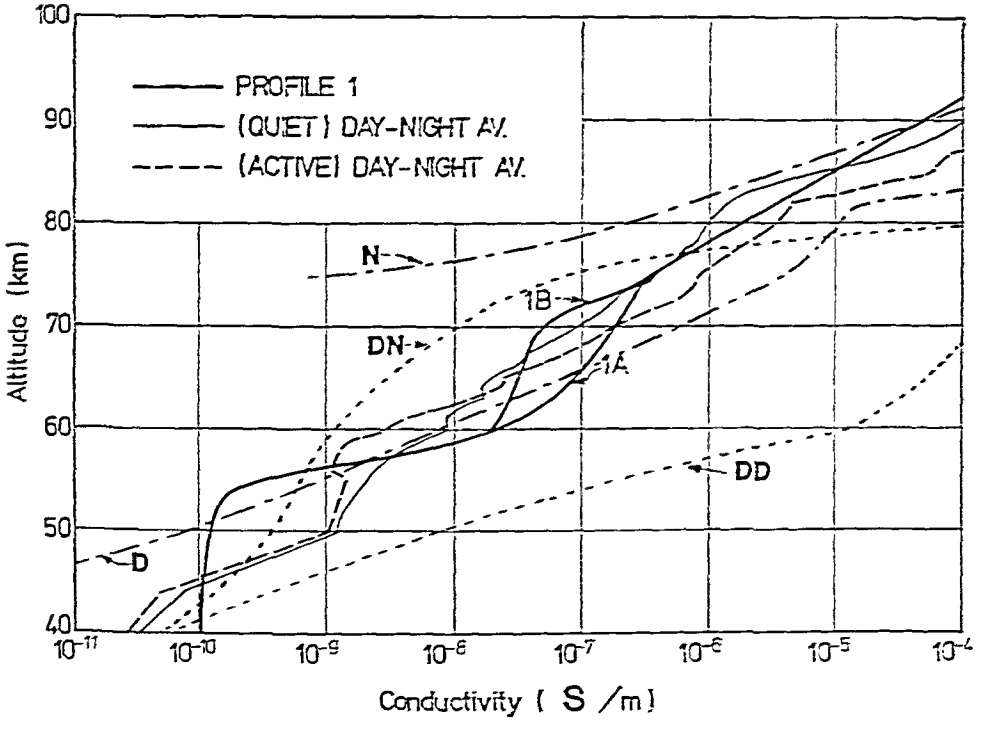

FIGURE 34. Comparison of world-average conductivity profile evaluated from Schumann resonance data during low solar activity ($R_z = 53$) with other profiles.

major ionizing agent in the lower D- or C-region. Therefore higher conductivity below the 55- to 60-km level can be expected during the two periods of low solar activity (1) and (4), as shown on Figure 34, than on the selected 1970 days. (2) and (3), above. In all cases the frequency resolution of the experimental power spectra[55] was 0.125 Hz. It was found that Profile 1 on Figure 33 gave the best match (resonance frequencies to within 0.09 Hz, 90% peak widths to within 0.1 Hz), to the data for periods (1) and

Table 4
10.7 CM SOLAR FLUX AND RELATIVE SUNSPOT NUMBER R, ON JUNE 7, 1967, SEPTEMBER 6, 1970, NOVEMBER 16, 1970 AND FEBRUARY 1, 1972

Date	Observed flux (10^{-22} W m^{-2} Hz) Ottawa 2800 MHz (10 7 cm)	Relative sunspot number R,
6/7/76	115 6	53
9/6/70	159 0	133
11/16/70	193 5	126
2/1/72	106 7	53

(4) of low solar activity, while Profile 2 provided the best match for the periods (2) and (3) with high solar activity The profiles of Figure 33 with $\sigma_s > 0$ provided a better match with resonance bandwidth data than the profiles of Figure 28 ($\sigma_s = 0$)

Profile 1 from Figure 33 is compared on Figure 34 with two day-night average profiles based on ion density data due to Widdel et al [69] below 60 km and electron distributions due to Mechtly et al [145] (Details are given in Reference 55) Night-time electronic conductivity was disregarded at all heights below 90 km, because it is usually an order of magnitude smaller than day-time conductivity

The average conductivities for the region below 40 km, $\sigma_a = 3\ 5\ (10^{-12})$ S/m or 3 35 (10^{-12}) S/m, are not unreasonable if one considers other available data on atmospheric conductivity If the average conductivity of the lowest 40 km is

$$\sigma_a = \frac{1}{40}\left\{10(10^{-13}) + \int_{10}^{40} \sigma_1 e^{\frac{h-10}{b}} dh\right\} \qquad (145)$$

implying an average conductivity of 10^{-13} S/m for the first 10 km (based on Israel[144] or Ishikawa et al [72]), and if $\sigma_1 = 1\ 7\ (10^{-12})$ with a scale height b = 5 95 km for the 10 to 40 km range, which matches rather well the data of Ishikawa[72] [$\sigma = 3(10^{-12})$ S/m at 15 km], Paltridge[71] [$\sigma = 2(10^{-12})$ S/m at 24 km], and Maeda et al [146] [$\sigma = 3\ 6(10^{-12})$ S/m at 28 km], Equation 145 gives an average conductivity $\sigma_a = 3\ 875\ (10^{-12})$ S/m for the 0- to 40-km atmosphere A change of scale height to b = 6 11 km, giving $\sigma = 3\ 24(10^{-12})$ at 28 km, would lead to $\sigma_a = 3\ 50(10^{-12})$ S/m Leaving the scale height b at 5 95 km and changing the value of conductivity σ_1 at 10 km to 1 47(10^{-13}) S/m [giving $\sigma = 3\ 02\ (10^{-12})$ S/m at 28 km] leads to $\sigma_a = 3\ 35\ (10^{-12})$ S/m Since the measurement of atmospheric conductivity by balloon or rocket-borne instrumentation is difficult[148] and since relatively little data are available, there is no basis at the present time to indicate which of the two values of σ_a represents a better characterization of the lower atmosphere The value of σ_a given by Equation 145 depends, of course, mostly on conditions above 20 km

The profiles for the higher elevations, 40 km to 90 km, are world averages and neglect differences between the day and night hemispheres They have validity only to the extent that the Schumann resonances, particularly at 8 Hz and 14 Hz, depend to a large extent on the conductivity profile below 60 km which is due to galactic cosmic rays and probably has little day-night dependence (Near the ground conductivity is higher at night than during the day, see page 98 in Israel [144])

Table 5
VALUES OF ν FOR CONDUCTIVITY PROFILES OBTAINED FROM ELF DATA

Frequency Hz	Profile 1A Re ν	1A -Im ν	1B -Im ν	Profile 2A Re ν	2A -Im ν	2B -Im ν	Profile 3A Re ν	3A -Im ν	3B -Im ν
5.0	0.531	0.104	0.103	0.510	0.0945	0.0932	0.507	0.0924	0.0911
7.5	0.925	0.129	0.128	0.894	0.116	0.115	0.889	0.114	0.113
10.0	1.333	0.150	0.149	1.293	0.133	0.133	1.287	0.131	0.131
12.5	1.746	0.170	0.170	1.699	0.150	0.150	1.691	0.148	0.148
15.0	2.162	0.189	0.190	2.107	0.165	0.166	2.097	0.164	0.164
17.5	2.580	0.208	0.210	2.517	0.181	0.183	2.505	0.179	0.181
20.0	2.997	0.227	0.230	2.927	0.196	0.200	2.914	0.195	0.198
22.5	3.413	0.247	0.251	3.337	0.212	0.217	3.322	0.211	0.215
25.0	3.829	0.267	0.272	3.747	0.228	0.234	3.730	0.227	0.232
27.5	4.245	0.287	0.294	4.157	0.244	0.252	4.138	0.243	0.250
30.0	4.660	0.307	0.316	4.566	0.260	0.271	4.546	0.260	0.267

From Tran, A. and Polk, C., *J. Atmos. Terr. Phys.*, 41, 1249, 1979. With permission.

One interesting way to obtain visualization of this dependence on the region below 60 km is to apply the method of Greifinger and Greifinger[31,89] for the isotropic ionosphere (neglecting magnetic field effects) to the ELF data which led to the profiles of Figures 33 and 34. The eigenvalues ν for Profile 1B as a function of frequency are reproduced on Table 5.

As discussed earlier under "Theory of the Concentric Sphere Resonator", Greifinger and Greifinger[31] have shown that peaks in the rate of energy dissipation occur at ELF at two altitudes. The lower of these, h_o, is given by $\sigma = \omega\epsilon_o$. The upper level, h_1, where the energy dissipation rate seems to be somewhat lower than near h_o, occurs where the absolute value of the local wave number k_1 is equal to the local scale height of the index of refraction. For a good conductor

$$k = \sqrt{j\omega\mu\sigma} \tag{146}$$

$$\text{complex } n = \sqrt{\sigma'/\omega\epsilon_0} \tag{147}$$

σ' = complex conductivity. If the real conductivity varies as

$$\sigma = \sigma_1 \exp\left[(z - h_1)/\xi_1\right] \tag{148}$$

and if $\sigma' = \sigma$

$$n = \sqrt{\sigma_1/\omega\epsilon_0} \exp\left[(z - h_1)/2\,\xi_1\right] \tag{149}$$

Thus $|k_1| = 1/(2\xi_1)$ gives the condition

$$4\,\omega\,\mu_0\sigma\,\xi_1^2 = 1 \tag{150}$$

Greifinger and Greifinger also show, using a planar stratified ionosphere, cylindrical geometry, and an exponential representation of the conductivity profile, that an approximation of the eigenvalue S (virtual complex angle of incidence) defined by Equations 29 and 30 is given by

Table 6
ν AND S FOR 7.5, 10 0, AND 15.0 Hz FOR DATA OF TABLE 5

f Hz	Re ν	Im ν	Re S	Im S	h_1/h_o	$\xi_1/h_o + \xi_1/h_1$
7 5	0 925	O 128	1 2678	0 12987	1 6074	0 13042
10	1 333	0 149	1 3156	0 11549	1 7308	0 11177
15	2 162	0 190	2 3008	0 09620	1 6921	0 09416

Table 7
CONDUCTIVITIES, HEIGHTS, AND SCALE HEIGHTS FOR 7.5, 10.0, AND 15.0 Hz

		from 3-(151)				
Frequency of exper data Hz	σ_o S/m	h_o km	ξ_o km	h_1 km	ξ_1 km	σ_1 S/m
7 5	4 166(10 $^{-16}$)	47 0	2	75 55	6 64	9 57(10 $^{-4}$)
10 0	5 555(10 $^{-16}$)	47 575	2	80 51	5 61	1 01(10^{-4})
15 0	8 332(10 $^{-16}$)	48 386	2	81 87	4 32	1 13(10^{-4})

$$S_o = \left(\frac{h_1}{h_o}\right)^{3/2}\left[1 + j\frac{\pi}{a}\left(\frac{\xi_o}{h_o} + \frac{\xi_1}{h_1}\right)\right] \qquad (151)$$

where ξ_o is the conductivity scale height in the vicinity of h_o. As discussed in the section on "Theory of the Concentric Sphere Resonator", the real part of S_o is equal to c/v as given by Equation 31 and the imaginary part of S_o is proportional to the wave attenuation in the guide or cavity as given by Equation 32 $\text{Im}S = (\alpha/k)$

Table 6 lists the values of ReS and ImS obtained by converting the ν values for 7.5 Hz, 10 Hz, and 15 Hz on Table 5 by Equation 30 Also listed are the resulting values of (h_1/h_o) and $(\xi_o/h_o + \xi_1/h_1)$ in Equation 151

A conductivity of 4 166 (10^{-16}) S/m results from requiring $(\sigma/\omega\varepsilon_o) = 1$ at 7.5 Hz This corresponds to a level of h_o = 47 km if those conductivity curves on Figure 34 are used which are based on rocket measurements The h_o level of conductivity is directly proportional to frequency and this now permits calculation of the h_o levels for 10 Hz and 15 Hz using a scale height ξ_o = 2 km which seems appropriate in view of Figure 34 The data on Table 6 and Equation 151 then give the results shown on Table 7.

Since most experimental Schumann resonance data[24,32,55] exhibit very small variations in the phase velocity, or ReS, while Q values, or ImS (or Imν) can vary substantially as indicated by Table 5, calculations based on Equation 151, such as those leading to Table 7, suggest that the ratio (h_1/h_o) varies very little, while the rates of variation of conductivity with height — indicated by ξ_o and ξ_1 — can exhibit large diurnal and seasonal changes If the conductivity at the lower level, at about 45 km — or at least its rate of change — is relatively constant (as was assumed in obtaining Table 7 by setting ξ_o = 2), the slope of the conductivity profile at about 75 km to 85 km must vary considerably

However, while an interpretation of world average data using an electrically isotropic and laterally homogeneous atmosphere is not unreasonable for elevations below 60 km, day-night effects, and probably also magnetic field effects should be considered

Table 8
COMPARISON OF 7.5 Hz PHASE VELOCITY AND ATTENUATION VALUES

	Quiet ionosphere, propagation along magnetic equator		Enhanced ionization/ magnetic latitude 75°		Quiet ionosphere 1B, Fig. 34
	Noon equinox	Night 0° latitude	Day	Night	Day-night average
c/v	1.30 (1.30)	1.18 (1.16)	1.36 (1.31)	1.34 (1.35)	1.27
α dB/Mm	0.074 (0.071 WE 0.075 EW)	0.16 (0.14)	0.24 (0.23)	0.18 (0.17)	0.17

Note: Numbers in parentheses are results of the Pappert-Moler computations; EW indicates East to West propagation and WE indicates West to East propagation.

for higher elevations. It is desirable therefore to compare the data discussed here with the analytical predictions of Behroozi-Toosi-Booker[37] and full-wave calculations by Pappert and Moler[75] quoted in their paper. These calculations are for various mathematically continuous ionosphere profiles, and take into account magnetic field effects.

The Behroozi-Toosi-Booker[37] electron distributions for a quiet ionosphere (their Figures 2 and 3 for sunspot number = 10) are shown on Figure 34 as D (day, 0° zenith angle) and N (night, 0° latitude) translated into conductivity by Equation 44 and an expression for the electron-neutral collision frequency

$$\log_{10} u_{en} = 5.4 - 0.077\,(z - 90) \qquad (152)$$

given by Behroozi-Toosi-Booker,[37] where the altitude z is in km. The ion density and electron density distributions (their profiles "2") used in their computations for a highly disturbed ionosphere at a magnetic latitude of 75°, are shown as DD (disturbed day) and DN (disturbed night). Their expression

$$\log_{10} u_{in} = 4.6 - 0.077\,(z - 90) \qquad (153)$$

was used to compute the ion neutral collision frequency in Equation 44 for the ionic conductivity which is significant at 40 and 45 km in the day profile and below 75 km in the night profile. Results given for 7.5 Hz in the Behroozi-Toosi-Booker[37] paper are compared in Table 8 with the Tran-Polk data shown in Tables 5 to 7. Im ν or ImS was converted to dB/Mm. The ratios c/v obtained from the Behroozi-Toosi-Booker profiles[37] are generally higher (1.30 to 1.36) than those based on the Schumann resonance data and obtained from Profile 1B (1.27), except for the quiet night ionosphere profile (N) which does not seem to take into account conductivity at the 40 km to 50 km level. The Tran-Polk[55] attenuation value of 0.17 dB/Mm is the same as the Pappert-Moler value for the enhanced ionization night profile, which is similar to Profile 1A between 50 and 75 km and gives lower conductivity than used by Tran-Polk below 50 km. Although it is impossible to draw conclusions on agreement between experimental results and various ionosphere models using only single frequency data, this comparison suggests again that the conductivity profile below 60 km plays a major role in the determination of cavity Q, at least at the low frequency end of the Schumann resonance band. If the ionosphere parameters at higher elevations could be well established from other measurements, Schumann resonance data would be very useful for obtaining global information about the electrical properties of the atmosphere below 60 km.

REFERENCES

1 Schumann, W O , Uber die strahlungslosen Eigenschwingungen einer leitenden Kugel, die von einer Luftschicht und einer Ionospharenhulle umgeben ist, *Z Naturforsch* , 7a, 149, 1952
2 Schumann, W O , Uber die Dämpfung der elektromagnetischen Eigenschwingungen des Systems Erde Luft Ionosphare, *Z Naturforsch* , 7a, 250, 1952
3 Schumann, W O , Uber die Ausbreitung sehr langer elektrischer Wellen und der Blitzentladung um die Erde, *Z fur Angew Physik*, 1V(12), 474, 1952
4 Schumann, W O , Uber die Oberfelder bei der Ausbreitung langer, elektrischer Wellen im System Erde-Luft Ionosphare und 2 Anwendungen (horizontaler und senkrechter Dipol), *Z fur Angew Physik* V1(1) 35 1954
5 Schumann, W O and Konig, H , Uber die Beobachtung von Atmospherics bei geringsten Frequenzen, *Naturwissenschaften*, 41, 183 1954
6 Schumann, W O , Uber elektrische Eigenschingungen des Hohlraumes Erde-Luft-Ionosphare erregt durch Blitzentladungen, *Z fur Angew Physik*, IX(8), 373, 1957
7 Konig, H , Atmospherics geringster Frequenzen, *Z fur Angew Physik*, X1(7), 264, 1959
8 Balser, M and Wagner, C A , Observation of earth ionosphere cavity resonances, *Nature (London)*, 188, 638 1960
9 Balser, M and Wagner, C A , Measurements of radio noise from 50 to 100 cycles per second *J Res Nat Bur Stand Sect D* 64(4), 415, 1960
10 Watt, J R , Terrestrial propagation of very low frequency radio waves, *J Res Nat Bur Stand , D* Radio Propagation, 64, 153, 1960
11 Watt, J R , Mode theory and propagation of ELF radio waves *J Res Nat Bur Stand , D* Radio Propagation 64, 387 1960
12 Watt, J R , On the propagation of ELF radio waves and the influence of a non homogeneous ionosphere, *J Geophys Res* 65, 597, 1960
13 Watt, J R , *Electromagnetic Waves in Stratified Media*, Pergamon Press, New York, 1970, chap 10
14 Galejs, J , ELF waves in presence of exponential ionospheric conductivity profiles, *I R E Trans Antennas Propagation* AP-9 554, 1961
15 Galejs, J , Terrestrial extremely-low-frequency propagation in *Natural Electromagnetic Phenomena Below 30 KC/S*, Bleil, D F , Ed , Plenum Press, New York 1964, 205
16 Galejs, J , *Terrestrial Propagation of Long Electromagnetic Waves*, Pergamon Press, New York, 1972
17 Raemer, H R , On the extremely low frequency spectrum of earth-ionosphere cavity response to electrical storms, *J Geophys Res* ,66(5) 1580, 1961
18 Row, R V , On the electromagnetic resonant frequencies of the earth-ionosphere cavity, *I R E Trans Antennas Propagation* AP-10 766, 1962
19 Johler, J R and Berry, L A , Propagation of terrestrial radio waves of long wavelength — theory of zonal harmonics with improved summation techniques, *J Res Nat Bur Stand , D Radio Propagation*, 66, 737, 1962
20 Johler, J R and Lewis, R L , Extra low frequency radio-wave field calculations with the zonal harmonic series, *J Geophys Res* ,74(10), 2459, 1969
21 Harris, F B and Tanner, R L , A method for the determination of lower ionosphere properties by means of field measurement of sferics, *J Res Nat Bur Stand , D Radio Propagation*, 66, 463, 1962
22 Jones, D L , The calculation of the Q factor and frequencies of earth-ionosphere cavity resonances for a two-layer ionosphere model, *J Geophys Res* , 69(19) 4037, 1964
23 Jones, D L , Numerical computations of terrestrial ELF electromagnetic wave fields in the frequency domain, *Radio Sci* , 5(5), 803, 1970
24 Jones, D L , Schumann resonances and e l f propagation for inhomogeneous, isotropic ionosphere profiles, *J Atmos Terr Physics*, 29, 1037, 1967
25 Madden, T and Thompson, W., Low-frequency oscillations of the earth-ionosphere cavity, *Rev Geophys* , 3(2), 211, 1965
26 Nickolaenko, A P and Rabinowicz, L M , Speeding up the convergence of the zonal harmonic series representations in the Schumann resonance problem, *J Atmos Terr Physics*, 36, 979, 1974
27 Nickolaenko, A P , On the features of ELF noise spectra of the earth-ionosphere resonator excited by cosmic radiation, (in Russian), *Geomagn Aeron* , X11(3), 462, 1972
28 Bezrodny, V G , Nickolaenko, A P , and Sinitsin, V G , Radio propagation in natural waveguides, *J Atmos Terr Physics*, 39, 662, 1977

29. Murakami, Y., The waveguide mode theory of propagation of ELF electromagnetic waves over the spherical surface of the earth, *J. Atmos. Terr. Phys.*, 38, 371, 1976.
30. Bliokh, P. V., Nickoalenko, A. P., and Filippov, Y., *Global Resonances in the Earth-Ionosphere Cavity*, (in Russian), Naukova Dumka, Kiev, 1977.
31. Greifinger, C. and Griefinger, P., Approximate method for determining ELF eigenvalues in the earth-ionosphere waveguide, *Radio Sci.*, 13, 831, 1978.
32. Bannister, P. R., Some notes on ELF earth-ionosphere waveguide daytime propagation parameters, *IEEE Trans. Antennas Propag.*, AP-27, 696, 1979.
33. Tran, A. and Polk, C., The earth-ionosphere cavity, *Radio Sci* , 11, 803, 1976.
34. Tran, A., Generalization of ELF mode theory to include unequal surface impedance at the lower ionosphere boundary, *Radio Sci.*, 13(1), 139, 1978.
35. Tran, A., ELF fields for an inhomogeneous ionosphere with diffusive lower boundary, *J. Atmos. Terr. Phys.*, 42, 1980.
36. Booker, H. G., A simplified theory of ELF propagation in the earth-ionosphere transmission line, *J. Atmos. Terr. Phys.*, 43, 1981.
37. Behroozi-Toosi, A. B. and Booker, H. G., Application of a simplified theory of ELF propagation to a simplified worldwide model of the ionosphere, *J. Atmos. Terr. Phys.*, 43, 1981.
38. Balser, M. and Wagner, C. A., Diurnal power variations in the earth-ionosphere cavity modes and their relationship to worldwide thunderstorm activity, *J Geophys. Res* , 67(2), 619, 1962.
39. Polk, C. and Fitchen, F., Schumann resonances of the earth-ionosphere cavity — ELF reception in Kingston, R.I., *J. Res. Nat. Bur. Stand* , Sect. D, 66(3), 313, 1962
40. Sao, K., Jindo, H., and Yamashita, M., Preliminary observations of ELF atmospheric waveforms, *J. Geomag. Geoelectr.*, 15, 43, 1963
41. Rycroft, M. J. and Wormell, T. W., The natural ELF electromagnetic noise in the band 2-40 c/s; apparatus and some preliminary results, in *Propagation of Radio Waves at Frequencies Below 300 Kc/s*, Blackband, W. T., Ed., Pergamon Press, New York, 1964, 421
42. Jones, D. L. and Chapman, F. W., Earth-ionosphere cavity resonances and effective ionospheric parameters, in *Propagation of Radio Waves at Frequencies Below 300 Kc/s*, Blackband, W. T., Ed., Pergamon Press, New York, 1964, 413.
43. Rycroft, M. J., Resonances of the earth-ionosphere cavity observed at Cambridge, England, *Radio Sci.*, 1071, 1965.
44. Gendrin, R. and Stefant, R., Magnetic records between 0 2 — 30 c/s, in *Propagation of Radio Waves at Frequencies Below 300 Kc/s*, Blackband, W. T., Ed., Pergamon Press, New York, 1964, 371.
45. Nelson, P. H., Ionospheric Perturbations and Schumann Resonance Data, Ph.D thesis, MIT, Project NR-371-401, Geophysics Lab., MIT, Cambridge, Mass., 1967
46. Ogawa, T., Tanaka, Y., Miura, T., and Yasuhara, M., Observations of natural ELF and VLF electromagnetic noises by using ball antennas, *J Geomag. Geoelectr.*, 18(4), 443, 1966.
47. Shand, J. A., Some quantitative characteristics of Schumann-ELF natural electromagnetic background, *Can. J. Phys.*, 44, 449, 1966.
48. Sao, K., Propagation of atmospherics and ELF radio noise, in *Proc. Res. Inst. Atmospherics, Nagoya Univ.*, 14, 61, 1967.
49. Jones, D. L. and Kemp, D. T., Experimental and theoretical observations on the transient excitation of Schumann resonances, *J. Atmos. Terr. Phys.*, 32, 1095, 1970.
50. Clayton, M. D., Polk, C., Etzold, H., and Cooper, W. W., Absolute calibration of antennas at extremely low frequencies, *IEEE Trans. Antennas Propag.*, AP-21(4), 514, 1973.
51. Ogawa, T., Kozai, K., and Kawamoto, M., Schumann resonances observed with a balloon in the stratosphere, *J. Atmos. Terr. Phys.*, 41, 135, 1979.
52. Polk, C., Relation of ELF noise and Schumann resonances to thunderstorm activity, in *Planetary Electrodynamics*, Vol. 2, Coroniti, S. C. and Hughes, J., Eds., Gordon and Breach, New York, 1969, 55.
53. Clayton, M. and Polk, C., Diurnal variation and absolute intensity of worldwide lightning activity, September 1970 to May 1971, in *Electrical Processes in Atmospheres*, Dolezalek, H. and Reiter, R., Eds., Verlag, Darmstadt, West Germany, 1977, 440.
54. Tran, A. and Polk, C., Schumann resonances and electrical conductivity of the atmosphere and lower ionosphere. I. Effects of conductivity at various altitudes on resonance frequencies and attenuation, *J. Atmos. Terr. Phys.*, 41, 1241, 1979.
55. Tran, A. and Polk, C., Schumann resonances and electrical conductivity of the atmosphere and lower ionosphere. II. Evaluation of conductivity profiles from experimental Schumann resonance data, *J. Atmos. Terr. Phys.*, 41, 1249, 1979.
56. Ramo, S., Whinnery, J. R., and Van Duzer, T., *Fields and Waves in Communication Electronics*, John Wiley & Sons, New York, 1965.

57 Harrington, R F, *Time-Harmonic Electromagnetic Fields*, McGraw Hill New York, 1961, chap 6
58 Morse, P M and Feshbach, H, *Methods of Theoretical Physics* McGraw Hill, New York, 1953
59 Bateman, H, *Higher Transcendental Functions* Vol I McGraw-Hill, New York, 1953, 164
60 Sommerfeld, A, *Partial Differential Equations in Physics* Academic Press, New York, 1949, 156
61 Wait, J R, On the theory of Schumann resonances in the earth-ionosphere cavity, *Can J Phys* 12(4) 575 1964
62 Al'pert, Ya L and Fligel, D S, *Propagation of ELF and Waves near the Earth*, Consultants Bureau New York 1970
63 Galejs J, Schumann resonances, *Radio Sci* 69D(8) 1043 1965
64 Holt, E H and Haskell, R E, *Foundations of Plasma Dynamics* Macmillan, New York, 1965
65 Rishbeth, H and Garriott, O K, *Introduction to Ionospheric Physics*, Academic Press, New York, 1969 130
66 Cole, R K and Pierce, E T, Electrification in the earth's atmosphere at altitudes between 0 and 100 kilometers, *J Geophys Res* 70(12) 2735 1965
67 U S Standard Atmosphere, U S Government Printing Office, Washington, D C, 1962
68 Ratnasiri, P A J, D region processes at equatorial latitudes, *J Atmos Terr Phys*, 39, 999, 1977
69 Widdel, H U, Rose, G, and Borchers, R, Experimental results on the variation of electrical conductivity and ion mobility in the mesosphere, *J Geophys Res*, 81 6217, 1976
70 Maeda, K, Study of electron density profile in the lower ionosphere *J Geomag Geoelectr Jpn* 23, 133 1971
71 Paltridge, G W, Experimental measurements of the small-ion density and electrical conductivity of the stratosphere, *J Geophys Res* 70 2751 1965
72 Ishikawa, H, Morita, Y, and Takagi, M, Balloon observation of atmospheric electrical conductivity up to 24 km in altitude in *Planetary Electrodynamics* Vol 2, Coroniti, S C and Hughes, J, Eds, Gordon and Breach, New York, 1969
73 Cipriano, J P, Hale, L C, and Mitchell, J D, Relations among low ionosphere parameters and A3 radio wave absorption, *J Geophys Res* 79(15), 2260, 1974
74 Booker, H G, Fitting of multi-region ionospheric profiles of electron density by a single analytic function of height, *J Atmos Terr Phys* 39, 619, 1977
75 Pappert, R A and Moler, W F, A theoretical study of ELF normal mode reflection and absorption produced by night time ionospheres, *J Atmos Terr Phys*, 40, 1031 1978
76 Whitten, R C and Poppoff, I G, *Physics of the Lower Ionosphere*, Prentice Hall, New York, 1965
77 Banks, P M and Kockarts, G, *Aeronomy*, Academic Press, New York, 1973
78 Ratcliffe, J A, *Physics of the Upper Atmosphere* Academic Press, New York, 1960
79 Uman, M A, *Introduction to Plasma Physics*, McGraw Hill, New York, 1964
80 Budden, K G, *Radio Waves in the Ionosphere* Cambridge University Press, Cambridge, 1961
81 Helliwell, R A, *Whistlers and Related Ionospheric Phenomena* Stanford University Press, 1965
82 Helliwell, R A, Whistlers and VLF emissions, in *Physics of the Magnetosphere*, Carovillano et al, Eds, D Reidel Publishing, Dordrecht Holland 1968
83 Ratcliffe, J A, *The Magneto-Ionic Theory and its Applications to the Ionosphere*, Cambridge University Press Cambridge, 1959
84 Large, D B and Wait, J R, Resonances of the thin-shell model of the earth ionosphere cavity with a dipolar magnetic field *Radio Sci*, 2 (7), 695, 1967
85 Wait, J R and Large, D B, Electromagnetic fields in a spherical cavity with a concentric anisotropic shell system, *Can J Phys*, 46 1505, 1968
86 Large, D B and Wait, J R, Influence of a radial magnetic field on the resonances of a spherical plasma cavity, *Radio Sci*, 3(6), 633 1968
87 Large, D B and Wait, J R, Theory of electromagnetic coupling phenomena in the earth ionosphere cavity, *J Geophys Res*, 73(13), 4335, 1968
88 Booker, H G and Lefeuvre, F, The relation between ionospheric profiles and ELF propagation in the earth ionosphere transmission line *J Atmos Terr Phys* 39, 1277, 1977
89 Greifinger, C. and Greifinger, P, On the ionospheric parameters which govern high latitude ELF propagation in the earth ionosphere waveguide, *Radio Sci*, 14(5), 889, 1979
90 Reid, G C, Solar cosmic rays and the ionosphere, in *Physics of the Earth's Upper Atmosphere*, Hines, C O, et al, Eds, Prentice Hall Englewood Cliffs, N J, 1965, chap 11
91 Paul, A M, Study of Resonance Line Splitting at Extremely Low Frequency (ELF) in the Earth Ionosphere Cavity, Ph D dissertation, University of Rhode Island, Kingston, R I, 1975
92 Jordan, E C, *Electromagnetic Waves and Radiating Systems*, Prentice Hall, New York, 1950

93. Polk, C., Sources, propagation, amplitude and temporal variation of extremely low frequency (0 - 100 Hz) electromagnetic fields, in *Biological and Clinical Effects of Low Frequency Magnetic and Electric Fields*, Llaurado et al., Eds., Charles C Thomas, Springfield, Ill., 1974.
94. Word, D. R., Smith, H. W., and Bostick, F. X. Jr., An Investigation of the Magnetotelluric Tensor Method, Technical Report 82, Electronics Research Center, University of Texas, Austin, Tex., March 15, 1970.
95. Soderberg, E. F., ELF noise in the sea, *J. Geophys. Res.*, 74, 2376, 1969.
96. Bannister, P. R., Summary of image theory expressions for the quasistatic fields of antennas at or above the earth's surface, *Proc. IEEE*, 67(7), 1001, 1979.
97. Watt, A. D., *VLF Radio Engineering*, Pergamon Press, New York, 1967, 41.
98. Küpfmüller, K., *Einführung in die Theoretische Elektrotechnik*, Springer Verlag, Berlin, 1965, 82.
99. Keefe, T. J., Etzold, H., and Polk, C., Detection and Processing of ELF (3 - 30 Hz) Natural Electromagnetic Noise, Air Force Cambridge Research Laboratory Report AFCRL-TR-0077 (Contract F 19628-70-C-0090) January 1973.
100. Huzita, A., Effect of radioactive fallout upon the electrical conductivity of the lower atmosphere, in *Planetary Electrodynamics*, Coroniti, S. C. and Hughes, J., Eds., Gordon and Breach, New York, 1969, Chap. 1 to 5.
101. Hill, L. K. and Bostick, F. Y., Micropulsation Sensors with Laminated Mumetal Cores, Report 126, Electrical Engineering Research Lab., University of Texas, Austin, 1962.
102. Lokken, J. E., Instrumentation for receiving electromagnetic noise below 3000 C.P.S., in *Natural Electromagnetic Phenomena Below 30 KC/S*, Bleil, D. F , Ed., Plenum Press, New York, 1964.
103. White, D. P. and Willim, D. K., Propagation measurements in the extremely low frequency (ELF) band, *IEEE Trans. Commun.*, COM-22 (4), 457, 1974.
104. Campbell, W. H., Induction Loop Antennas for Geomagnetic Field Variation Measurements, ESSA, Res. Lab. (U.S. Dept. of Commerce), Report ERL-ESL6, Boulder, Colo., 1969.
105. Polk, C., Measurements of ELF field strength, *IEEE Trans. Antennas Propag.*, AP-28 (1), 140, 1980.
106. Dinger, R. J., Davis, J. R., Goldstein, J. A., Meyers, W. D., Nisenoff, M., Wolf, S. A., and Kennedy, J. J., SQUID ELF Receiving Antenna for Submarine Applications, Final Report, U.S Office of Naval Research, NRL 8118, Washington, D.C., 1977.
107. Zimmerman, J. E. and Campbell, W. H., Test of cryogenic squid for geomagnetic field measurements, *Geophysics*, 40(2), 269, 1975.
108. Fraser, B. J. and Ellyett, C. D., Man made magnetic micropulsations, *J. Geophys. Res.*, 69(17), 3603, 1964.
109. Frantti, G. E., The nature of high-frequency earth noise spectra, *Geophysics*, 28(4), 547, 1963.
110. Setian, L., Investigation of Extremely Low Frequency Noise from Helicopters, M.S. thesis, University of Rhode Island, Kingston, R.I., 1966.
111. Campbell, W. H., An Introduction to Geomagnetic Instruments and Observing, U.S. Dept. of Commerce, Boulder, Colo., ESSA Tech. Report ERL 183-ESL, 1970.
112. Greene, F. M., NBS field strength standards and measurements (30 Hz — 1000 MHz), *Proc. IEEE*, 55, 970, 1967.
113. Crichlow, W. Q., Davis, R. C., Disney, R. T., and Clark, M. W., Hourly Probability of Worldwide Thunderstorm Occurrence, Telecommunications Research Report OT/ITS RR 12, U.S. Department of Commerce, Boulder, Colo., April 1971.
114. Uman, M. A., *Lightning*, McGraw-Hill, New York, 1969.
115. Bendat, J. S. and Piersol, A. G., *Measurement and Analysis of Random Data*, John Wiley & Sons, New York, 1966.
116. Blackman, R. B. and Tukey, J. W., *The Measurement of Power Spectra*, Dover Publications, New York, 1958.
117. Bendat, J. S. and Piersol, A. G., *Random Data: Analysis and Measurement Procedures*, Interscience, New York, 1971.
118. Oppenheim, A. V. and Schafer, R. W., *Digital Signal Processing*, Prentice-Hall, Englewood Cliffs, N.J., 1975.
119. Hughes, H. G., Power spectral analysis of modulated earth-ionosphere cavity resonances, *J. Geophys. Res.*, 69(21), 4709, 1964.
120. Jarvis, E. C., The Identification and Movement of Meso-Scale Thunderstorm Systems, CIR-4346, TEC-591, Department of Transportation, Meteorological Branch, Toronto, Canada, December 14, 1965.
121. Peled, A. and Liu, B., *Digital Signal Processing*, John Wiley & Sons, New York, 1976.
122. Polk, C., Extremely low frequency noise, Section 3, in *Geophysics and Space Data Bulletin*, Carrigan, A. L. and Oliver, N. J., Eds., Space Physics Laboratory, Air Force Cambridge Research Laboratories, Bedford, Mass., vols. 4 to 10, 1967 to 1973.

123 Ginsberg, L H , Extremely low frequency H F I atmospheric noise level statistics for project Sanguine, *IEEE Trans Commun* 22(4) 555, 1974
124 Yanagihara, K , Extremely low frequency (magnetic field records and spectra), Kakioka Magnetic *Observatory*, Japan private communication, 1968
125 Sao, K , Yamashita, M , and Jindoh, H , SI A phenomena on e l f atmospherics, *J Atmos Terr Phys* , 28 97 1966
126 Ogawa, T , Tanaka, Y , Miura, T , and Owaki, M , f l f noise bursts and enhanced oscillations associated with the solar flare of July 7 1966 *Ionosphere Space Res Jpn* , 20(4) 528, 1966
127 Gendrin, R and Stefani, R , Effects of the very high altitude nuclear explosion of July 9, 1962 on the earth to ionosphere cavity resonances experimental results and interpretation, *C R Acad Sci* , 255, 2273 1962
128 Campbell, W H , Geomagnetic pulsations in *Physics of Geomagnetic Phenomena* Matsushita S and Campbell, W H Eds Academic Press New York 1967
129 Morrison, R , *Grounding and Shielding Techniques in Instrumentation* John Wiley & Sons, New York, 1967
130 Konig, H L , Finkle, H , and Polk, C , Measurement of Electric Fields Between 3 cps and 10,000 cps With a Vertical Antenna Over the Atlantic Ocean Near the East Coast of Florida, University of Rhode Island Department of Electrical Engineering Report 396(10)-1 1969
131 Toomey, J and Polk, C , Location of Sources of E L F Noise in the Earth Ionosphere Cavity by Analysis of Schumann Spectra Report AFCRI 70 0226 Part II Air Force Cambridge Research Laboratories, Bedford Mass 1970
132 Smith, L G , Atmospheric electricity in *Handbook of Geophysics* (revised edition), Macmillan, New York 1961
133 Galejs, J , Terrestrial extremely low frequency noise spectrum in the presence of exponential ionospheric conductivity profiles *J Geophys Res* 66(9) 2787 1961
134 Williams, J C , Thunderstorms and Very Low Frequency Noise Ph D thesis Harvard University, Cambridge Mass 1959
135 Heydt, G and Volland, H , Eine Anlage zur statistischen Untersuchung von Atmospherics im Längswellengebiet *Zeitschr fur Angew Physik* 16(1) 40 1963
136 Heydt, G , Experiments for the Intercontinental Location of Sources of Atmospherics through the Determination of Direction of Arrival and Group Delay Differences Technical Report 136 Henrich Hertz Institut fur Schwingungsforschung Berlin Charlottenburg 1971
137 Heydt, G , V l f — Atmospherics — Analyzer Network — Data Derived from Photographic Records Taken in Berlin Waidmannslust December 1 1970 to December 31, 1971 Henrich Hertz Institut fur Schwingungsforschung Berlin Charlottenburg, 1972
138 Kealoha, J H S , Setebteny, S M , and Smith, M I , Final Report on Stanford Research Project 6806, Stanford Research Institute Menlo Park, Calif 1968
139 Polk, C and Clayton, M , Location of many thunderstorm regions employing ELF noise, Proc , Waldorf Conf on Long Range Geographic Estimation of Lightning Sources, NRL Report 7763, U S Naval Research Laboratory Washington, D C , 1974 242
140 Clayton, M , Estimation of Worldwide Thunderstorm Activity from Schumann Resonance Data, Ph D thesis, University of Rhode Island Kingston, R I 1974
141 Clayton, M , and Polk, C , Diurnal variation and absolute intensity of world wide lightning activity September 1970 to May 1971 in *Electrical Processes in Atmospheres* Dolezalek, H and Reiter, R , Eds , Dietrich Steinkopff Verlag Darmstadt, 1977
142 Rao, M , Note on the corona currents in a lightning discharge and the emission of ELF waves *Radio Sci* ,2 (new series) 11 1394 1967
143 Ogawa, T and Murakami, T , Schumann resonance frequencies and the conductivity profiles in the atmosphere, *Contributions, Geophysical Institute Kyoto University* 13 13 1973
144 Israel, H , (in cooperation with Dolezalek, H ,) Atmospheric Electricity Vols I and 2, Israel Program for Scientific Translations, U S Department of Commerce Boulder Colo , 1973
145 Meehtly, E. A , Bowhill, S A , and Smith, L G , Changes of lower ionosphere electron concentrations with solar activity, *J Atmos Terr Phys* , 34, 1899, 1972
146 Maeda, S , Handa, S , Ogawa, T , Kawahira, K , and Miura, T , Short period variations of atmospheric temperature and electrical conductivity in the stratosphere, *Contributions Geophysical Institute, Kyoto University*, 13, 21, 1973
147 Davenport, W B and Root, W L , *An Introduction to the Theory of Random Signals and Noise*, McGraw-Hill, New York, 1958, 107
148 Ogawa, T , Analyses of measurement techniques of electric fields and currents in the atmosphere, *Contributions, Geophysical Institute, Kyoto University*, 13, 117, 1973
149 Abbas, M , Hydromagnetic wave propagation and excitation of Schumann resonances, *Planet Space Sci* , 16, 831, 1968

LOW FREQUENCY RADIO NOISE

Hans Volland

TABLE OF CONTENTS

INTRODUCTION

Organization of the Chapter

The electric currents flowing within a lightning channel during return strokes (R strokes), leader strokes (L strokes), and intracloud strokes (K strokes) are the main sources for the generation of pulse-type electromagnetic radiation known as atmospherics or sferics While this radiation dominates at frequencies less than about 100 kHz, a continuous noise component becomes increasingly important at higher frequencies (Figure 1)

This paper deals with the generation and the radiation properties of such electromagnetic impulses from an observational as well as from a theoretical point of view Some basic definitions concerning dipole radiation are provided early in this chapter In the second section, observations of electromagnetic wave forms from cloud-to-ground strokes (mainly R strokes) and from intracloud strokes (mainly K strokes) both near and far from the source are reviewed Theoretical considerations concerning the electric currents within lightning channels are presented in the third section The fourth section deals with the electromagnetic radiation from lightning channels and with dispersion effects within the atmospheric wave guide In the last section, methods of deriving source and wave guide properties from the observations of sferics are described

The international system of units is used throughout this chapter. Also used is a coordinate system with the z-axis positive upward, contrary to the general usage in the literature of atmospheric electricity where the electric field is taken positive "in the sense of lowering negative charge to the ground "[113]

Radiation from Dipoles

Electrostatic Component

The simplest model of a typical R stroke is a negative charge $\bar{Q} = -|\bar{Q}|$ stored at time $t < 0$ at a height $\bar{l}$ above the surface of the Earth (Figure 2a) At time $t \geq 0$ that charge is lowered to the ground in an impulsive way with a time dependence F (t)

$$Q = -\bar{Q}\,\Gamma(t) \tag{1}$$

where

$$\Gamma(t) = \begin{cases} -1 & t = 0 \\ > -1 \quad \text{for} & t > 0 \\ 0 & t \to \infty \end{cases} \tag{2}$$

The electrostatic field at a distance R between charge and a receiver on the ground is directed toward the charge and has the value

$$E_R = -\frac{\bar{Q}\,\Gamma(t)}{4\pi\,\epsilon_0 R^2} \tag{3}$$

Since the surface of the Earth can be considered to be a perfectly well-conducting medium as a first approximation, the horizontal component of the electric field must disappear at the ground The usual way to describe the electric field in this case is to put a virtual positive charge at the image distance $-\bar{l}$ under the surface of the Earth

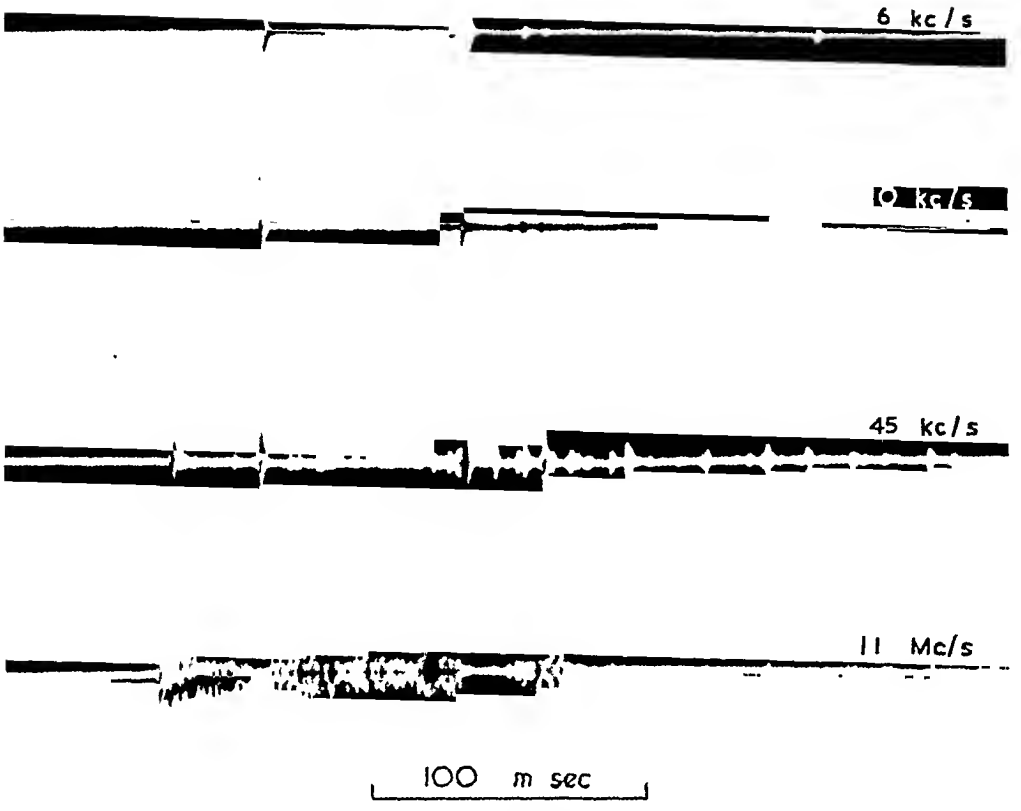

FIGURE 1 Atmospherics from a near discharge observed at four different frequencies (From Horner, F. and Bradley, P. A., *J. Atmos. Terr Phys* , 26, 1155, 1964 With permission.)

as shown in Figure 2a. The new charge configuration is an electric dipole with its axis positive downward having the dipole moment of

$$\bar{M} = 2\bar{\ell}\,\bar{Q} < 0 \tag{4}$$

The electrostatic field at the ground has now only a vertical component given by

$$E_z = \frac{\bar{Q}\,F(t)\sin\xi}{2\pi\epsilon_0 R^2} = \frac{\bar{M}\,F(t)}{4\pi\epsilon_0 R^3} \tag{5}$$

This electric field has its maximum at time $t = 0$. Negative charge is lowered during the stroke process, or, according to Figure 2a, the negative charge is compensated to zero by the ascending positive image charge. The electric field due to that charge decreases to zero as $t \to \infty$. This electrostatic field is often described differently in the literature. The electrostatic potential at time $t = 0$ is defined as zero, and the electric field is considered as increasing to an asymptotic positive value as negative charge is lowered to the ground. According to the definition used in this chapter, this corresponds to a field in the form

$$\Delta E_z(t) = E_z(0) - E_z(t) \qquad \text{for} \qquad t \geqq 0 \tag{6}$$

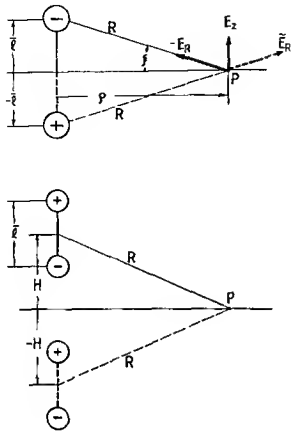

FIGURE 2 Point charge configuration simulating (a) a return stroke and (b) an intracloud stroke

Induction Component

The electric current flowing in the channel is the time derivative of Q

$$I = \frac{dQ}{dt} = -\bar{Q}\frac{d\tilde{r}}{dt} = -\frac{\bar{M}}{2\bar{\ell}}\frac{d\tilde{r}}{dt} \tag{7}$$

Since the electric current must be upward directed in order to discharge a negative charge, and since $\bar{M} < 0$, it follows from Equation 7 that $d\tilde{r}/dt > 0$ for $t > 0$. According to the Biot-Savart law, this current element generates a positive azimuthal magnetic field of strength

$$B_\phi = \mu_0 \frac{2\bar{\ell}I}{4\pi R^2} \simeq -\frac{\bar{M}}{4\pi c^2 \epsilon_0 R^2}\frac{d\tilde{r}}{dt} \tag{8}$$

where $c = 1/\sqrt{\epsilon_0\mu_0}$ is the velocity of light,

$$\mu_0 = 4\pi \times 10^{-7} = 1.2566 \times 10^{-6}\ \mathrm{Hm^{-1}}$$

is the permeability of free space, and

$$\epsilon_0 = \frac{1}{c^2\mu_0} = 8.8542 \times 10^{-12}\ \mathrm{Fm^{-1}}$$

is the dielectric constant of free space. The field (Equation 8) that falls off as R^{-2} is called the induction component or the intermediate component. The electric field contains also a component of that form which can be derived from first principles.[11]

Radiation Component

As is well known from electromagnetic theory (see the section on "Electromagnetic Radiation from Lightning Channels"), a radiation component of the electric field is generated in addition to the electrostatic and induction components. This is given by

$$E_z = -cB_\phi = \frac{\bar{M}}{4\pi\epsilon_0 c^2 R}\frac{d^2F}{dt^2} \tag{9}$$

so that the total field of a vertical electric dipole located on the ground for a receiver also on the ground becomes (see chapter on Theory of Low Frequency Wave Propagation by Harth, Volume II)

$$\begin{aligned} E_z &= \frac{\bar{M}}{4\pi\epsilon_0}\left\{\frac{F}{R^3} + \frac{1}{c}\frac{dF/dt}{R^2} + \frac{1}{c^2}\frac{d^2F/dt^2}{R}\right\} \\ cB_\phi &= -\frac{\bar{M}}{4\pi\epsilon_0}\left\{\frac{1}{c}\frac{dF/dt}{R^2} + \frac{1}{c^2}\frac{d^2F/dt^2}{R}\right\} \end{aligned} \tag{10}$$

where now in Equation 10, the expressions must be evaluated at the retarded time t_r given by

$$t_r = t - R/c \tag{11}$$

The electric field E_z and the magnetic field cB_ϕ in Equation 10 have the same unit (Vm^{-1}) and have the same induction and radiation components. In typical K strokes, for which positive charge is lowered within a channel at height H without connection to the Earth (Figure 2b), $\bar{M} = 2\bar{l}\bar{Q} > 0$ and Equation 10 is still approximately valid provided $R \gg H$.

Impulse Forms of Lightning Currents

Type 1 Current

Typical temporal variations of observed channel currents of R strokes have the following aperiodic wave form:[7]

$$I = \bar{I}(e^{-\alpha t} - e^{-\beta t}) \quad ; \quad (0 < \alpha < \beta, \text{ real} \quad ; \quad t \geq 0) \tag{12}$$

According to Equation 7, one may thus derive

$$F(t) = -\frac{\beta e^{-\alpha t} - \alpha e^{-\beta t}}{\beta - \alpha} \tag{13}$$

and

$$\bar{Q} = -\frac{\bar{I}(\beta - \alpha)}{\alpha\beta} \tag{14}$$

This wave form is referred to as a type 1 wave The parameters $\bar{I}$, α, and β can be derived from the observations and allow an estimate of the sign and magnitude of the charge stored at time $t = 0$ within the channel

Type 2 Current

Observations of sferics from R strokes as well as from K strokes suggest another form of F(t), which is of the type of damped oscillations

$$I = 2\bar{I} \sin \delta t \, e^{-\gamma t} \quad , \quad (\gamma, \delta > 0, \text{ real} \quad , \quad t \geq 0) \tag{15}$$

Hence,

$$F(t) = -\left(\cos \delta t + \frac{\gamma}{\delta} \sin \delta t\right) e^{-\gamma t} \tag{16}$$

and

$$\bar{Q} = -\frac{2\delta \bar{I}}{\gamma^2 + \delta^2} \tag{17}$$

This wave is called type 2 wave The time dependences F(t) given by Equations 13 and 16 are identical for

$$\left.\begin{matrix} \alpha \\ \beta \end{matrix}\right\} = \gamma \mp i\delta \tag{18}$$

Whereas Equation 16 is valid for real δ, Equation 13 is valid for imaginary δ If $\delta = 0$, Equations 13 and 16 degenerate to

$$F(t) = -(1 + \gamma t) e^{-\gamma t} \quad , \quad (\gamma > 0, \text{ real} \quad , \quad t \geq 0) \tag{19}$$

and the current becomes

$$I = -\bar{Q} \gamma^2 t e^{-\gamma t} \tag{20}$$

Evidently, $\bar{I}$ is not defined in this case

Electromagnetic Field of a Vertical Electric Dipole

The electromagnetic field (in Vm^{-1}) of a vertical electric dipole situated above a perfectly electrically conducting plane at height H for an observer on the ground is[104]

$$\begin{aligned} E_z &= 9\bar{M} \left\{ \frac{G_1}{D} \sin^2\theta + \left(\frac{G_2}{D^2} + \frac{G_3}{D^3}\right) (1 - 3\cos^2\theta) \right\} \\ cB_\phi &= -9\bar{M} \left(\frac{G_1}{D} + \frac{G_2}{D^2}\right) \sin\theta \end{aligned} \tag{21}$$

Table 1
WAVE FORMS

m		Aperiodic wave (Type 1)	Damped oscillation (Type 2)	$\delta = 0$ (Type 3)
1	G_1	$\frac{\alpha\beta\bar{R}^2}{(\beta-\alpha)c^2}\{\beta e^{-\beta t} - \alpha e^{-\alpha t}\}$	$(\gamma^2+\delta^2)\frac{\bar{R}^2}{c^2}\{\cos\delta t - \frac{\gamma}{\delta}\sin\delta t\}e^{-\gamma t}$	$\frac{\gamma^2\bar{R}^2}{c^2}(1-\gamma t)e^{-\gamma t}$
2	G_2	$\frac{\alpha\beta\bar{R}}{(\beta-\alpha)c}\{e^{-\alpha t} - e^{-\beta t}\}$	$\frac{(\gamma^2+\delta^2)\bar{R}}{\delta\ c}\sin\delta t\, e^{-\gamma t}$	$\frac{\gamma^2\bar{R}t}{c}e^{-\gamma t}$
3	G_3	$\frac{1}{(\beta-\alpha)}\{\alpha e^{-\beta t} - \beta e^{-\alpha t}\}$	$-\{\cos\delta t + \frac{\gamma}{\delta}\sin\delta t\}e^{-\gamma t}$	$-(1+\gamma t)e^{-\gamma t}$
1	t_1	$\frac{2}{(\beta-\alpha)}\ln\left(\frac{\beta}{\alpha}\right)$	$\frac{2}{\delta}\arctan\left(\frac{\delta}{\gamma}\right)$	$\frac{2}{\gamma}$
1	R_1	$\frac{\alpha}{\beta}e^{\beta t_1}$	$e^{\gamma t_1}$	e^2
2	t_2	$t_1/2$	$t_1/2$	$t_1/2$
2	$\bar{G}_2$	$\frac{\beta\bar{R}}{c}e^{-\beta t_2}$	$\frac{(\gamma^2+\delta^2)\bar{R}}{\gamma\ c}\cos\delta t_2\, e^{-\gamma t_2}$	$\frac{\gamma\bar{R}}{ec}$
	$\bar{I}/\bar{Q}$	$-\frac{\alpha\beta}{(\beta-\alpha)}$	$-\frac{(\gamma^2+\delta^2)}{2\delta}$	∞

Note: Wave forms of radiation component (G_1), of induction component (G_2), and of electrostatic component (G_3) to be included in (21) and (66). Note that the time t must be replaced in (21) by the retarded time t_r. t_1 is the time of the first minimum of G_1, $R_1 = |G_1(0)/G_1(t_1)|$ is the ratio between first maximum and first minimum, t_2 is the time of the first maximum of G_2 and $\bar{G}_2 = G_2(t_2)$ is its maximum amplitude. $t_2 = t_1/2$ is also the cross-over time of G_1 from positive to negative values. $\bar{I}/\bar{Q}$ is the ratio between current amplitude and electric charge (see Eqs. 14 and 17). The function G_2 is proportional to the channel current (see Eqs. 12, 15 and 20).

with $\bar{M} = 2\bar{Q}\bar{\ell}$ the electric dipole moment $\bar{Q}$ in C, $\bar{\ell}$ in m, $\sin\theta = \varrho/R$, $\cos\theta = -H/R$, $D = R/\bar{R}$ and $\bar{R} = 1$ km. The functions

$$G_m = \left(\frac{\bar{R}}{c}\right)^{3-m}\frac{d^{3-m}F}{dt^{3-m}} \qquad (22)$$

are given in Table 1 for the three cases considered: aperiodic type 1 waves (Equation 13), type 2 damped oscillations (Equation 16), and the intermediate case (Equation 19). The three components symbolized by the subscript "m" are, respectively, the radiation component (m = 1), the induction component (m = 2) and the electrostatic component (m = 3). Table 1 also contains the maximum amplitude $G_2 = G_2(t_2)$ of the induction component, the time of maximum t_2 which is also the crossover time of the radiation component, the time t_1 of the first minimum of the radiation component, and the ratio R_1 between maximum at time t = 0 and first minimum at time t_1 of the radiation component: $R_1 = |G_1(t_1)/G_1(0)|$. Note that $t_1 = 2t_2$. The last row of Table 1 gives the ratio of the current amplitude to the electric charge $\bar{I}/\bar{Q}$.

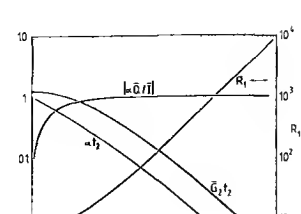

FIGURE 3 Type 1 strokes Functions αt_2, $\overline{G}_2 t_2$, and $|\alpha\overline{Q}/\overline{I}|$ (left ordinate) and R_1 (right ordinate) from Table I vs β/α

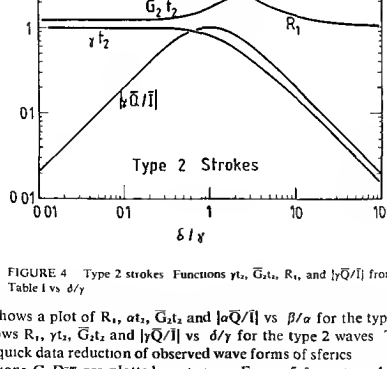

FIGURE 4 Type 2 strokes Functions γt_2, $\overline{G}_2 t_2$, R_1, and $|\gamma\overline{Q}/\overline{I}|$ from Table I vs δ/γ

Figure 3 shows a plot of R_1, αt_2, $\overline{G}_2 t_2$ and $|\alpha\overline{Q}/\overline{I}|$ vs β/α for the type 1 waves, and Figure 4 shows R_1, γt_2, $\overline{G}_2 t_2$ and $|\gamma\overline{Q}/\overline{I}|$ vs δ/γ for the type 2 waves These plots are useful for a quick data reduction of observed wave forms of sferics

The functions $G_m D^{-m}$ are plotted vs time in Figure 5 for a type 1 wave with the parameters from Table 2 These represent the electromagnetic field contributions of a typical first return stroke of type 1 In order to make the magnitudes of the G_m comparable, the value D = 10 (or a distance of 10 km) has been chosen One notices a large peak in the radiation component (m = 1) at t = 0 in Figure 5, a fast decrease to a crossover point at t_2 = 13 μsec, a minimum at time t_1 = 26 μsec, and a slow rise to

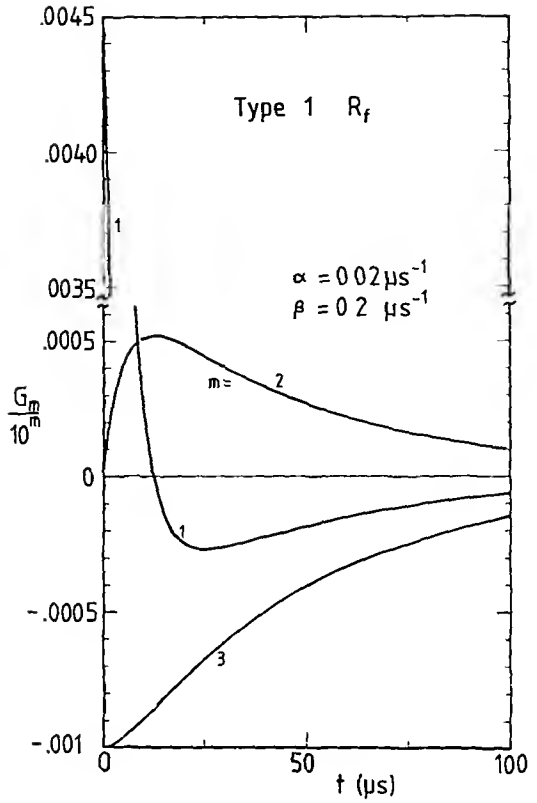

FIGURE 5. Type 1 first return stroke. Functions G_m from Table 1 with the parameters of R_f from Table 2 at 10 km distance (D = 10). It is m = 1: radiation component; m = 2: induction component; m = 3: electrostatic component.

zero. The ratio between maximum and minimum of the radiation component is R_1 = 17. The induction component (m = 2) peaks at t_2 with a maximum amplitude of $\bar{G}_2$ = 0.0516, while the electrostatic component (m = 3) rises slowly from −1 at t = 0 to zero within the first several 100 μsec.

Figure 6 shows the functions $G_m D^{-m}$ of a type 2 wave (D = 10 again) with the parameters from Table 3. This wave represents a typical wave form of sferics from R strokes. In this case, the crossover time of the radiation component is t_2 = 48 μsec, and the ratio between maximum and minimum is R_1 = 3. Both the induction and electrostatic components are of the oscillatory form with first crossover points near 135 and 80 μsec, respectively.

Figure 7 gives the functions G_m of a type 2 wave with the parameters from Table 3 which represent intracloud K strokes. All three components here have the same order of magnitude at a distance of 1 km (D = 1). The crossover point of the radiation component is now at t_2 = 5.5 μsec, and the ratio between maximum and minimum is again $R_1 \approx 3$.

Spectral Functions

Since Maxwell's equations are linear, a temporal variation of the electromagnetic field can be decomposed into its spectral components via a Fourier integral transformation. A component of the electric field which is zero at times t < 0, for example, may be written

Table 2
TYPE I RETURN STROKES

Stroke	n	α_n μs^{-1}	β_n μs^{-1}	$\bar{I}_n$ kA	$\bar{Q}_n$ C	ℓ km	$\bar{\ell}$ km	$\bar{M}_n$ C km	$\sqrt{\alpha\delta}/\sqrt{S\pi}$	R kΩ	P_{∞} MJ	P_{rad} kJ	P_{rad}/P_{∞} %
R_f	1	0 02	0 2	30	−1 35	7 9	5 0	−13 6	1 55	4 2	35	740	2 1
R_s	1	0 00086	6 0	2 50	−2 9	7 9	5 0	−29	0 32	99	180	210	0 12
	2	0 0072	6 0	4 84	−0 67	—	—	2 2	—	—	80	82	0 11
	3	0 019	6 0	4 74	−0 25	—	—	−0 51	—	—	29	31	0 10

Note The parameters (α β) of the wave form of the first return stroke (R_f) are taken from Dennis and Pierce [4] the parameters (α_n, β_n) of the subsequent return stroke (R) are derived in "Type 2 Subsequent Return Stroke " $\bar{I}_n$ is the current amplitude $\bar{Q}$ the total electric charge, ℓ the channel length $\bar{\ell}$ the effective antenna length (Equation 44) $\bar{M}_n$ the electric dipole moment (Equation 43), σ the electric conductivity of the channel d its diameter R the total resistance of the channel P_{∞} the total electromagnetic energy radiated from the channel (Equation 48) and P_{rad} its radiation component at large distances (Equation 70)

Table 3
TYPE 2 STROKES

Stroke	n	γ_n μs^{-1}	d_n μs^{-1}	$\bar{I}_n$ kA	$\bar{Q}_n$ C	ℓ km	$\bar{\ell}$ km	$\bar{M}_n$ C km	$\sqrt{\alpha\delta}/\sqrt{S\pi}$	R kΩ	P_{∞} MJ	P_{rad} kJ	P_{rad}/P_{∞} %
R_f	1	0 0115	0 023	7 0	−0 49	18 7	11 9	−11 9	4 56	1 15	1 96	143	7 3
R_s	1	0 026	0 026	9 0	−0 35	13 2	8 4	−5 8	3 05	1 81	1 41	133	4 7
k	1	0 1	0 2	−1 2	0 01	2 2	2 8	0 053	1 61	2 1	0 012	1 9	16 0

Note The parameters (γ,d) of the first return stroke R_f, the subsequent return stroke R and the k stroke were determined from Figures 12 and 19 The meaning of the other parameters is the same as in Table 2 Note that the effective antenna length $\bar{\ell}$ of the K stroke is determined from Equation 52

Table 4
FOURIER TRANSFORMS OF WAVE FORMS

	Type 1		Type 2	
m	$\lvert \hat{G}_m \rvert$	$\tan \Phi_m$	$\lvert \hat{G}_m \rvert$	$\tan \Phi_m$
1	$\dfrac{\bar{R}^2\,\omega\,\bar{\omega}^2}{c^3\,I}$	$\dfrac{\omega^2-\bar{\omega}^2}{\omega(\alpha+\beta)}$	$\dfrac{\bar{R}^2\,\omega\,\bar{\omega}^2}{c^3\,F}$	$\dfrac{\omega^2-\bar{\omega}^2}{2\gamma\omega}$
2	$\dfrac{\bar{R}\,\bar{\omega}^2}{c\,E}$	$\dfrac{\omega(\alpha+\beta)}{\bar{\omega}^2-\omega^2}$	$\dfrac{\bar{R}\,\bar{\omega}^2}{c\,L}$	$\dfrac{2\gamma\omega}{\bar{\omega}^2-\omega^2}$
3	$\dfrac{\sqrt{\omega^2+(\alpha+\beta)^2}}{L}$	$\dfrac{\omega(\alpha^2+\beta^2+\bar{\omega}^2+\omega^2)}{(\alpha+\beta)\,\bar{\omega}^2}$	$\dfrac{\sqrt{\omega^2+4\gamma^2}}{F}$	$\dfrac{\omega(2\gamma^2+2\delta^2+\bar{\omega}^2+\omega^2)}{2\gamma\bar{\omega}^2}$
$\bar{\omega}$	$\sqrt{\alpha\beta}$		$\sqrt{\gamma^2+\delta^2}$	
E	$\sqrt{(\alpha^2+\omega^2)(\beta^2+\omega^2)}$		$\sqrt{[\gamma^2+(\omega-\delta)^2][\gamma^2+(\omega+\delta)^2]}$	
$\lvert \hat{G}_1(\bar{\omega}) \rvert$	$\dfrac{\bar{R}^2\,\alpha\beta}{c^2(\alpha+\beta)}$		$\dfrac{\bar{R}^2(\gamma^2+\delta^2)}{c^2\,2\gamma}$	
$\dfrac{\partial^2\Phi_1}{\partial\omega}$	$\dfrac{2\gamma(\omega^2+\bar{\omega}^2)}{4\gamma^2\omega^2+(\omega^2-\bar{\omega}^2)^2}$		$(2\gamma = \alpha+\beta)$	
$\dfrac{\partial^2\Phi_1}{\partial\omega^2}$	$\dfrac{4\gamma\omega(3\bar{\omega}^4-\omega^4-2\omega^2\bar{\omega}^2-4\gamma^2\bar{\omega}^2)}{(4\gamma^2\omega^2+(\omega^2-\bar{\omega}^2)^2\}^2}$			

Note Fourier transforms of the functions G_m in Table 1 (amplitude $\lvert \hat{G}_m \rvert$ and phase Φ_m) $\hat{G}_1(\bar{\omega})$ is the maximum amplitude of $\lvert \hat{G}_1 \rvert$ at frequency $\bar{\omega}$. Also given are the first and second derivative of the phase Φ_1 with respect to frequency.

from Table 3. These functions asymptotically approach constant values for $f = 0$ and fall off as f^{-1} and f^{-3}, respectively, for $\omega \gg \bar{\omega}$. Their phases change from −180° to 0° and from 0° to 90°, respectively, with increasing frequency. This is the general behavior of these two components.

OBSERVED WAVE FORMS OF SFERICS

Wave forms of sferics observed at some distance from the origin depend on the antenna characteristics of the lightning channel (electric current distribution, channel configuration, and orientation), on the dispersion characteristics of the propagation medium between surface of the Earth and ionosphere (electric conductivity of Earth and ionosphere varying with location, time of day, and season), and on the transmission function of the receiver (bandwidth, amplification factor, and time delay depending on frequency). Since about 100 strokes per second are generated all over the globe, interference between the electromagnetic fields of two or more strokes excited at nearly the same time may furthermore complicate the interpretation of the data. A certain

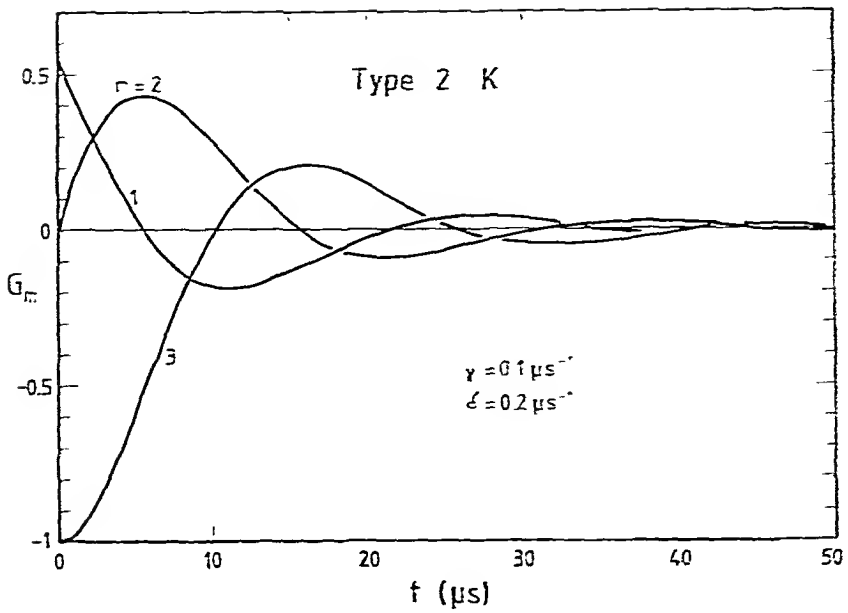

FIGURE 7. Type 2 intracloud stroke. Functions G_m from Table I with the parameters of K from Table 3 at 1 km distance (D = 1). It is m = 1: radiation component, m = 2: induction component; m = 3: electrostatic component.

bias toward the stronger strokes is thus unavoidable in general if wave forms of individual strokes are recorded. However, these stronger strokes need not reflect the typical behavior of an average stroke.

Because of these complications, it is impossible to present in this review a complete selection of observed wave forms of sferics. Kimpara[55] and Wang[124] have presented examples of a wide variety of wave forms observed both during the day and at night. In the following, the discussion is restricted primarily to recent observations of wave forms of intracloud and R strokes at near and at far distances from the source.

Return Strokes

Near Field Wave Forms

Since each receiver has a finite bandwidth and a finite time constant, it is impossible to measure with a single instrument the exact electromagnetic field which exists at the location of the receiving antenna. An instrument with a large time constant (e.g., a field mill) will measure mainly the total field changes due to the electrostatic component while the transient changes due to the induction and the radiation component are suppressed. On the other hand, receivers with short time constants measure the temporal variation of single strokes more or less accurately. Figure 10 shows electric field changes following three giant R strokes which were recorded at three different distances (2, 11, and 19 km) from the lightning flash.[117] These fields are the electrostatic components. The vertical electric field in this figure is presented as positive downward according to the definition used in this chapter (see Equation 6). Figure 11, taken from the same paper, shows the corresponding short-time variations of the electric and the magnetic field of the same three R strokes at an 11-km distance.

According to Figure 6, the stroke R1 apparently belongs to the damped oscillation type 2 with a fast decaying electrostatic component on which the two other components are superimposed during the first 40 μsec. The maximum of the magnetic field results from the superposition of the induction and the radiation components.

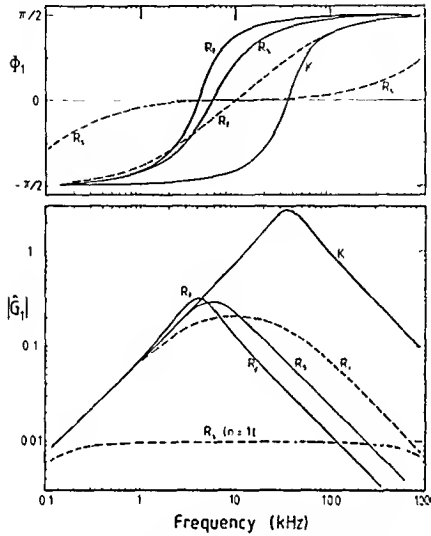

FIGURE 8 Spectral amplitudes $|\hat{G}_1|$ and phases Φ_1 of the Fourier transform of G_1 (Table 4) vs. frequency for type 1 currents (dashed lines) with the parameters from Table 2 and for type 2 currents (solid lines) with the parameters from Table 3

Comparison between the wave forms of strokes R2 and R3 with Figure 5 suggests that these strokes belong to the aperiodic waves of type 1 with a slower decay of the electrostatic component, and with a radiation component which possesses a short high initial peak.

Figure 12 shows typical electric and magnetic field strengths vs. time of sferics observed at various distances from the source between 1 and 200 km [72]. The solid lines represent first return strokes, and the dashed lines represent subsequent R strokes. These wave forms are again of the type 2 as immediately apparent from a comparison with Figure 6. In particular, the radiation component at a 200-km distance has a cross-over time of about $t_2 = 50$ μsec and its ratio R_1 is of the order 2 to 3. The parameters (γ,δ) in Figure 6 and Table 3 have been derived from the wave forms of the first R stroke in Figure 12 (see the section on "Antenna Characteristics of Lightning Currents").

Figure 13 shows further examples of sferics wave forms observed at distances less than 500 km [107]. According to Taylor,[107] 80% of all measured sferics belong to his groups 1+ and 2+. Evidently, his groups 1+ and 2+ have the same characteristics of their wave forms as in Figure 12, namely a ratio between initial peak and first

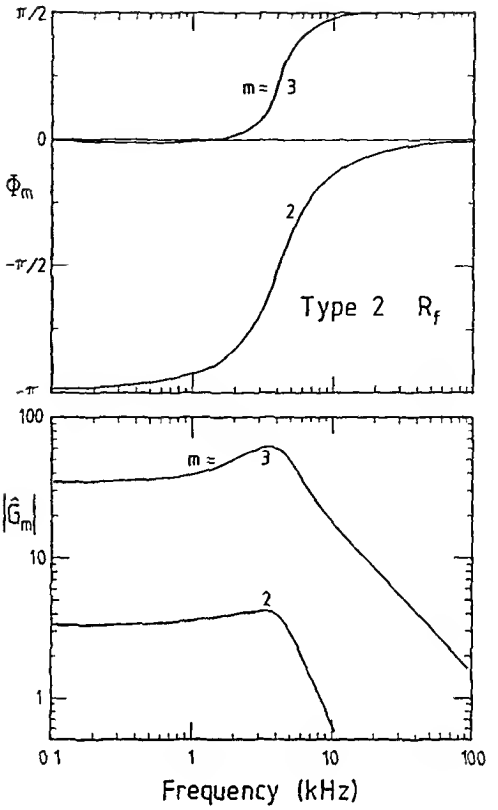

FIGURE 9. Spectral amplitudes $|\hat{G}_m|$ and phases Φ_m of the Fourier transforms of G_2 and G_3 from Table 4 vs. frequency for a type 2 first return stroke with the parameters of R_f from Table 3.

minimum of about $R_t = 1$ to 3, a crossover point at typically 50 μsec, and an initial positive polarity; i.e., $\Delta E_z > 0$ in Equation 6 in a sense of lowering negative charge. These wave forms can be attributed to R strokes and are of type 2 according to my definition. Groups 4 and 5 in Figure 13 are also of type 2 with shorter crossover times of typically 25 μsec. However, their initial peaks are predominantly negative (in 78 out of 89 cases), which indicates lowering of positive charge either from cloud-to-ground or within the cloud. The only type 1 wave form in Figure 13 appears to be group 3 with a large value of R_t. Note that the limiting ratio for type 1 waves is $R_t = 7.4$ (see Table 1 or Figure 4).

The rise time to the initial peak of the electric field depends on the distance. For shorter distances they are between 1 and 5 μsec with smaller values for the subsequent return strokes (Figure 14A). Figure 14B presents the amplitudes of the initial peaks vs. distance. Figure 15 shows the ramp starting time (see Figure 12) as a function of distance, which varies between about 10 and 60 μsec over the range 1 to 10 km.[111] Typical rise times are 3 μsec for first return strokes, and 2.5 μsec for subsequent return strokes at distances greater than 100 km.[71] The rise times can decrease to the submicrosecond range if the propagation path is over seawater (Figure 16). The small impulses preceding the R strokes in Figure 16, labeled "L", are due to stepped leaders. The large subsidiary peaks following the initial peak of the R strokes in Figure 16 seem to be limited to a maritime environment.[127] Typical nighttime sferics wave forms contain trains of pulses which may result from the generally better propagation conditions during night.[124]

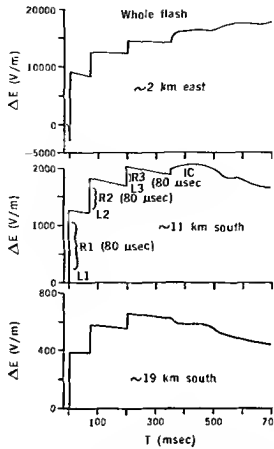

FIGURE 10 Electric field changes at 2, 11, and 19 km from a flash On the 11 km field, the leader portions of the field changes are labeled L1, L2, and L3, and extended from the bottom of the R bracket downward to the field break, the return strokes are bracketed and labeled R1, R2, and R3, the intracloud discharge beginning around 360 msec is labeled IC The orientation of the electric field is according to Equation 6 (positive downward) (From Uman, M A , et al , *Science*, 201, 9, 1978 With permission)

Far Field Wave Forms

At distances beyond 1000 km, the wave guide characteristics between Earth and ionospheric D layer substantially modify the sferics wave forms Figure 17 shows representative wave forms for east-to-west propagation at distances between 1250 and 4480 km [106] The essential feature of these wave forms is the bandpass filtering effect of the wave guide Only the VLF waves survive The damped oscillations in Figure 17 suggest that they are excited by type 2 lightning currents

Some lightning currents, probably mainly subsequent R strokes, contain a long "continuous" component, corresponding to relatively large spectral amplitudes in the ELF range (f < 3 kHz) (see Figure 8) The terrestrial wave guide has a pronounced attenuation maximum around 1 to 3 kHz (see the section on "Electromagnetic Radiation from Lightning Channels") so that the spectral components within this range are severely suppressed Furthermore, the group velocity is smaller at lower frequencies so that the dispersive terrestrial wave guide separates the lower ELF waves near 100 Hz from the VLF waves near 5 kHz This "slow tail" wave form in distant sferics may be seen in Figure 18, which is taken from Taylor and Sao [109]

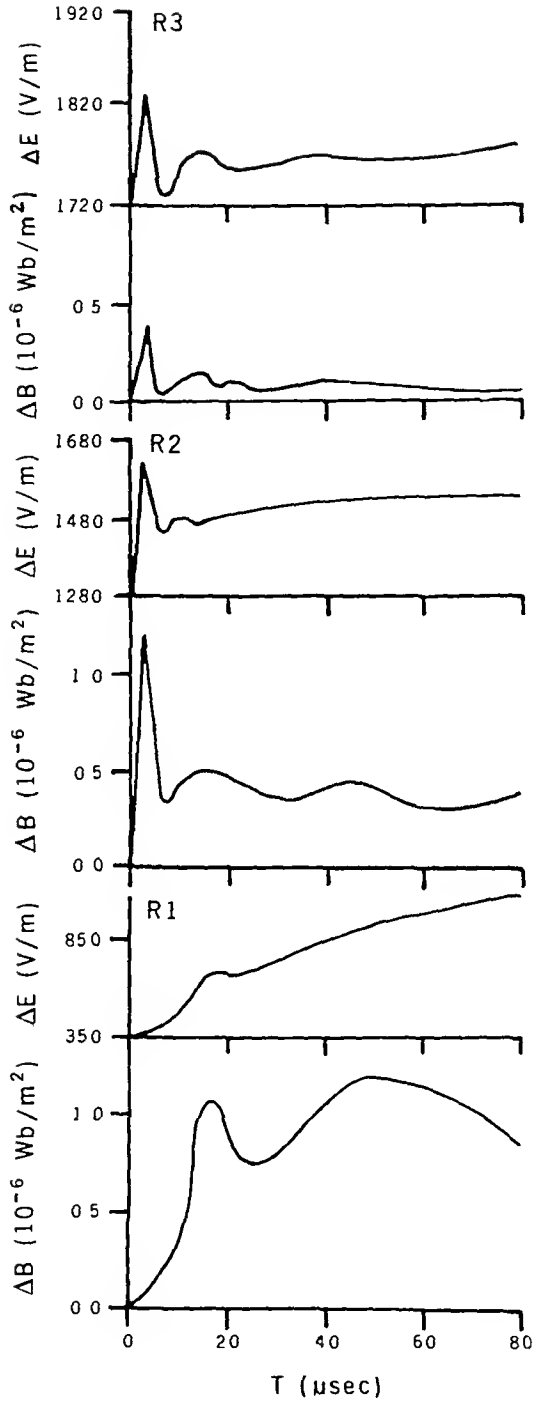

FIGURE 11. Details of the three return stroke electric field changes in Figure 10 with the corresponding magnetic field changes, as observed 11 km from the flash. The return strokes are labeled R1, R2, and R3 as in Figure 10. The orientation of the electric field is according to Equation 6 (positive downward). (From Uman, M. A. et al., *Science*, 201, 9, 1978. With permission.)

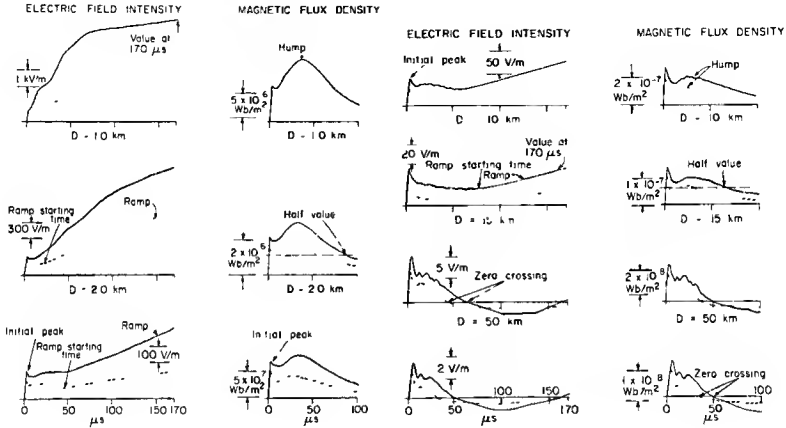

FIGURE 12 (A) Typical electric field intensity (left column) and magnetic flux density (right column) for first (solid lines) and subsequent (dotted lines) return strokes at distances 1, 2, and 5 km. The following characteristic features of the wave forms are identified: for electric field, initial peak, ramp-starting time, ramp, and 170 μsec value, for magnetic field, initial peak, hump, and half-value. (B) Typical fields as described in Figure 12A for distances of 10, 15, 50, and 200 km. Characteristic wave force features identified in addition to those in Figure 12A are electric and magnetic field zero crossings. Electric field orientation is according to Equation 6 (positive downward). (From Lin Y. T. et al., *J. Geophys. Res.* 84, 6307, 1979. With permission. Copyrighted by American Geophysical Union.)

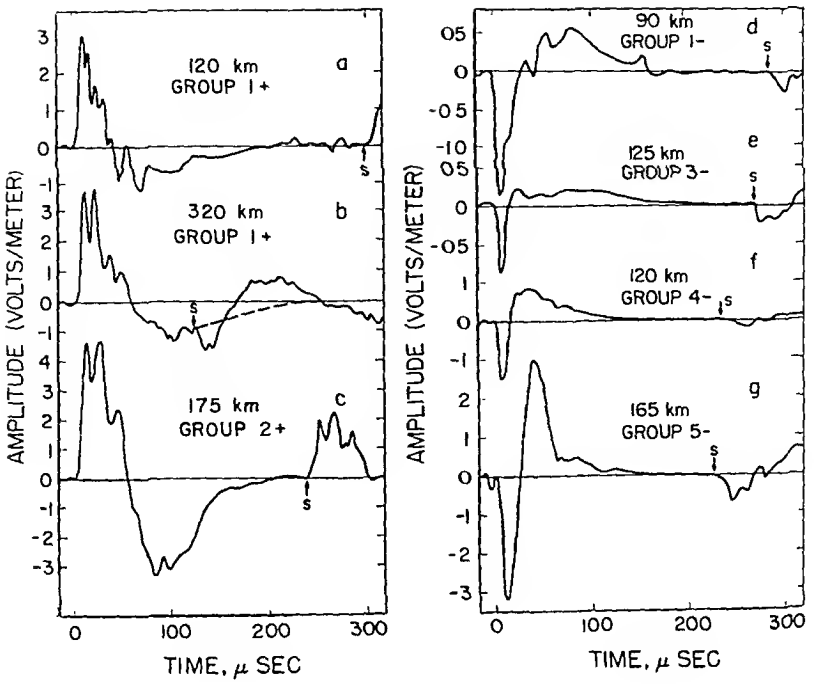

FIGURE 13 Examples of atmospheric wave forms. Electric field orientation is according to Equation 6 (positive downward). (From Taylor, W L., *J. Res. Nat. Bur. Stand*., 67D, 539, 1963 With permission. Copyrighted by American Geophysical Union.)

Intracloud Discharges

K strokes are intracloud discharges in channels without contact with the Earth. An internal discharging process occurs where, in general, positive charge stored in the upper half of the channel neutralizes the negative charge stored in the lower half.[6] Lowering positive charge corresponds to an initial "negative" polarity $\Delta E_z < 0$ in the sense of Equation 6.

Figure 19, taken from Weidman and Krider,[128] shows examples of the radiation field of K strokes observed at distance between 15 and 30 km from the source. One notices large pulses of bipolar wave form belonging to type 2 according to the nomenclature in this chapter. Fast smaller pulses of unipolar (type 1) form precede the larger pulses. The parameters (γ,δ) used in Figure 7 have been chosen to simulate the K stroke in Figure 19b. Typical ratios between maximum and minimum of the larger pulses are $R_1 = 2$ to 3. The crossover times are of the order $t_2 = 5$ to 10 μsec. The rise times to the initial peak are within the submicrosecond range, and the total pulse width is of the order of 40 to 50 μsec. Most of these strokes occur in isolation, i.e., they are not followed by R strokes.

On the other hand, sequences of pulses of type 2 with "positive" polarity ($\Delta E_z > 0$) are usually produced in the several tens of milliseconds prior to the first R stroke (Figure 20 taken from Weidman and Krider[128]). The time interval between the pulses is between about 50 and 200 μsec, which are typically followed 50 msec later by the associated R stroke. The amplitudes of the pulses are comparable with those of the R strokes. These pulse sequences are probably related to in-cloud leader processes.

Figure 21, taken from Krider et al.,[64] shows a high resolution record of pulses produced by stepped leaders immediately preceding R strokes. They apparently belong to type 1 and have a total pulse width of only a few microseconds. Sequences of that kind of pulses with time intervals between pulses of typically 5 μsec have been recorded

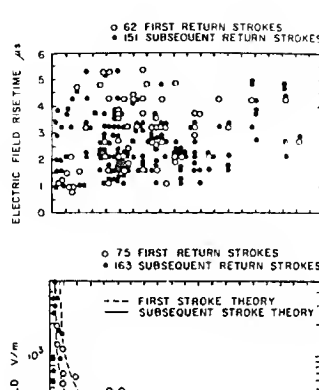

FIGURE 14 (A) Electric field rise time vs distance (B) Initial peak magnitude vs distance The theoretical curves of part (B) were calculated by using an inverse distance relationship and the normalized initial peak field means for first and subsequent strokes (From Tiller, J A , et al , *J Geophys Res* , 81, 4430, 1976 With permission Copyrighted by American Geophysical Union)

during a large fraction of intercloud discharges [63] Measurements of sferics from intracloud strokes in correlation with the associated radio frequency radiation have been made by Krider et al [65]

Spectral Amplitudes and Phases

Spectral amplitudes and phases can be derived from individual wave forms of sferics via a Fourier transformation (see Equation 24), or they can be measured directly with narrow band receivers (see the section on "Source and Wave Guide Properties Derived from Sferics") Evidently, the second method is a statistical approach where all kinds of wave forms (R, K, and L, type 1 and 2) contribute to the amplitude spectrum Therefore, results of those measurements cannot be directly compared with spectra of individual wave forms However, such comparison does give some indication of the relative contributions of the various types of waves to the total spectrum

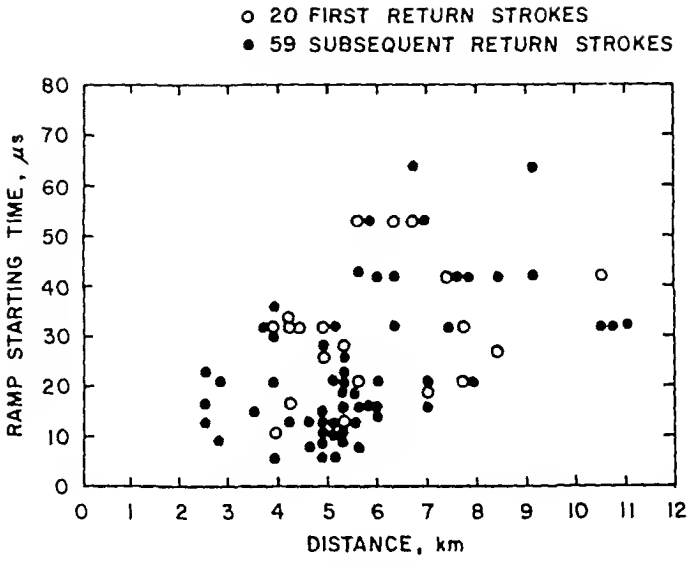

FIGURE 15. Ramp starting time vs. distance (from Tiller, J. A., et al, *J. Geophys. Res*, 81, 4430, 1976. With permission. Copyrighted by American Geophysical Union.)

The spectra of individual pulses depend on the distance. Figure 22 gives the spectral amplitudes of the wave forms of the first return stroke in Figure 12 at various distances.[103] The amplitude at large distances (curves A and B), where only the radiation component is significant, peaks near 4 kHz. The spectrum falls off as f^{-1} for $f < 100$ kHz and even faster for higher frequencies. This is due to the influence of the finite electric conductivity of the Earth (see the section on "Electromagnetic Radiation from Lightning Channels"). At distances less than 10 km (Curves C to H in Figure 22) the spectrum shows a steady increase with decreasing frequency down to 1 kHz. This is a result of the increasing dominance of the induction and the electrostatic components at these distances (Figure 9A).

The subsequent strokes contain a larger amount of high frequencies than the first return strokes.[103] The results of Figure 22 are consistent with Taylor's[107] spectral analysis of his group 1 and 2 wave forms in Figure 13. The spectral functions of the far field wave forms in Figure 17 peak between 7 and 10 kHz, increasing with distance. Spectral peaks of R strokes between 4 and 10 kHz have been reported in the literature (e.g., Horner and Bradley,[39] Dennis and Pierce,[16] and Croom[15]).

The ELF spectrum of the slow tail wave form of Figure 18 is shown in Figure 23.[98,109] The peak is attained near 70 Hz (Figure 23A), and the phase increases by several cycles between 10 and 400 Hz. The spectral peak broadens and shifts to higher frequencies with decreasing distance from the source.[54]

The spectrum of intracloud strokes contains a larger amount of high frequencies, which is evident from the much shorter total pulse width. Peak amplitudes between 20 and 70 kHz have been reported.[2,24] The spectral function $\hat{G}_1$ of the K stroke in Figure 8, which simulates the observations of Weidman and Krider[128] shown in Figure 19, represents that kind of spectrum. The spectra of stepped leaders such as those in Figure 21 peak even as high as $f = 200$ kHz.[63]

Overview

The electric current configuration within a lightning channel as well as the geometry of the channel determine the antenna characteristics for the radiation of electromagnetic energy Measurements of channel lengths and electric currents within strokes are discussed in the chapter, "The Lightning Current" The average vertical extensions of R stroke channels are reported to be of the order of 5 km,[5 113] while those of K strokes are about 2 km long [6] The channels are in general obliquely orientated Their horizontal components may be as large as 10 km [110]

Channel diameters are typically a few centimeters in thickness The Bruce-Golde formula (Equation 12) is a good description of the average wave form of observed electric currents at the foot point of the channel on the ground The electric conductivity within the channel is about 10^4 S/m Optical observations seem to indicate an upward traveling ionized wave front, moving along the channel with velocities of between 0 1 and 0 3 c [5 113] Bruce and Golde[7] assumed that the R stroke expands upward at a rate

$$v_t = v_0 e^{-\gamma t} \tag{26}$$

with $v_o = 8 \times 10^7$ m/sec, $\gamma = 3 \times 10^4$ sec^{-1} for the first R stroke, and $\gamma = 0$ for the subsequent R strokes The electric current remains uniform in the channel up to its tip, located at the height

$$\ell_t = \int_0^t v_t \, dt \tag{27}$$

and zero above Charge is therefore transferred instantaneously from the base to the wave front of the R stroke Hill[34] derived another velocity from the condition that the total charge below the pulse front is equal to the initial charge less that amount which has flown to the Earth Rai[9] developed a model for the velocity which has a double exponential expression Dennis and Pierce[16] modified the Bruce-Golde model, introducing a finite velocity for the charge transfer to the tip of the channel

Finite charge transfer also occurs in the so-called transmission line model of Uman and McLain [114] Here, the current has the time and height dependence

$$i = i(t - z/u)$$

where I (t) is the current at the base of the channel and of the form (Equation 12) The height in the channel is $z \leq \ell_t$, and the current wave front propagates with constant velocity u upward Above ℓ_t the current is again zero A transmission line model with variable velocity u has been developed by Leise and Taylor [68] An even more refined transmission line model is due to Price and Pierce [90]

For times immediately after the return stroke has reached the top of the channel, the transmission line models predict an exact replica of the initial field peak but with opposite polarity[115 116] while the Bruce-Golde model yields a field discontinuity Both effects are rarely observed

In order to overcome these deficiencies, Lin et al [73] have proposed a new model which is composed of three separate current components· (1) a short-duration upward-

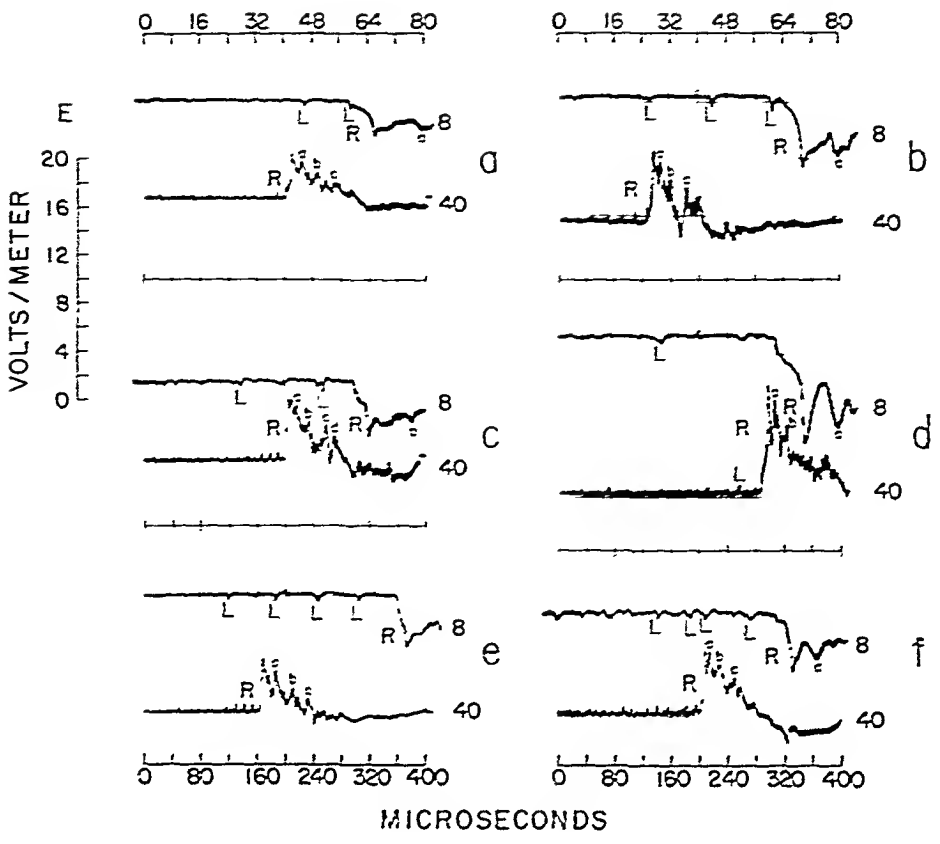

FIGURE 16. Electric field wave forms produced by first return strokes in Florida at distance 100 to 200 km over seawater. Each wave form is both shown on a fast (8 μsec/div) and inverted on a slow (40 μsec/div) time scale. The origins of the time scales have been chosen to be at the left edge of each trace. The large return stroke fields R are preceded by stepped leader pulses L and are followed by large subsidiary peaks a, b, c etc. (From Weidman, C. D. and Krider, E. P., *J. Geophys. Res.*, 83, 6239, 1978. With permission. Copyrighted by American Geophysical Union.)

propagating pulse of current associated with the upward-propagating electrical breakdown at the return-stroke wavefront, (2) a uniform current which may already be flowing (leader current) or may start to flow soon after the return stroke begins, and (3) a "coronal current" caused by the radially inward and downward movement of the charge initially stored in the corona sheath around the leader channel. They then determined the various free parameters involved by trial and error in order to reproduce observed sferics wave forms (e.g., such as those in Figure 12).

The major disadvantage of all these models is that they are based more on phenomenological aspects than on physical arguments of first principles and that they are not able to simulate in a consistent manner both types of electric currents which are suggested from the observations.

In the following part of this section, a wave guide model is outlined; this model is directly associated with the channel parameters length l and diameter d and will turn out to be surprisingly simple.

Lumped Circuit Model

The evaluation of sferics wave forms in the section, "Observed Wave Forms of

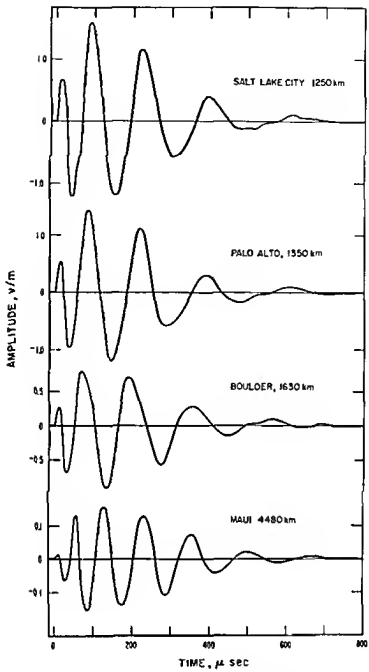

FIGURE 17 Representative atmospheric wave forms, east to west at great distances Electric field orientation is according to Equation 6 (positive downward) (From Taylor, W L, *J Res Nat Bur Stand*, 64D, 349, 1960 With permission Copyrighted by American Geophysical Union)

Sferics" already suggested that the type 1 wave (Equation 12) of Bruce and Golde[7] *cannot be the only type, but rather type 2 currents of the form of Equation 15 predominate* in many cases A lumped circuit model proposed by Oetzel[44] can simulate both types of currents in an R stroke

In this model (see Figure 24) negative charge $Q = -|Q|$ is stored on the upper plate of a condenser C at time $t < 0$ This corresponds to the excessive charge within the channel before the stroke The lower plate of C with opposite charge resembles the Earth The lossy inductance (the R-L combination in Figure 24) corresponds to the

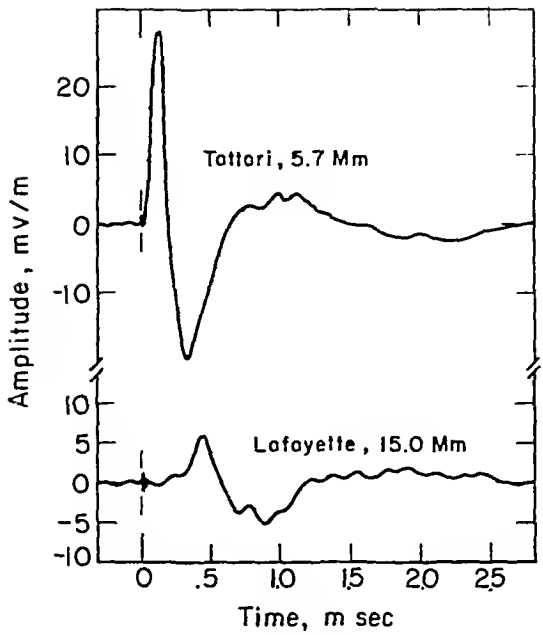

FIGURE 18. Example of slow tail wave forms. Orientation of electric field is according to Equation 6 (positive downward). (From Taylor, W. L., and Sao, K., *Radio Sci.*, 5, 1453, 1970. With permission. Copyrighted by American Geophysical Union.)

electrically conductive lightning channel. The switch is closed at time t = 0, i.e., the channel establishes electric contact with the Earth. The discharging current flowing at time $t \geqq 0$ is then given by[104]

$$I = -\bar{Q}(\gamma^2 + \delta^2)\frac{\sin \delta t}{\delta} e^{-\gamma t} = -\frac{\bar{Q}c}{\bar{R}} G_2(t) \qquad (28)$$

with

$$\gamma = \frac{R}{2L} \quad ; \quad \delta = \sqrt{\omega_o^2 - \gamma^2} \quad ; \quad \omega_o^2 = \frac{1}{LC} \quad ; \quad G^2 \text{ from Table 1}^*$$

which is the same as Equation 15 for $\gamma, \delta > 0$, real. Equation 28 reduces to Equation 12 for imaginary δ where now

$$\left.\begin{matrix}\alpha \\ \beta\end{matrix}\right\} = \gamma \mp |\delta| \qquad (29)$$

This is evidently the case when $\gamma > \omega_o$, where ω_o is the resonance frequency of the lossless circuit, i.e., when $R > 2Z$ where $Z = \sqrt{L/C}$ is the wave resistance.

* The resistance R should not be confused with the distance R in Equations 21 and 28.

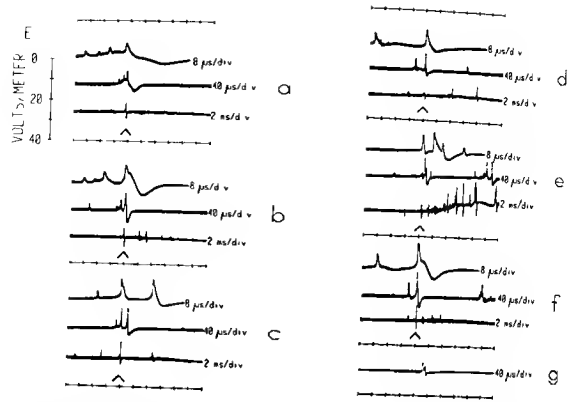

FIGURE 19 Electric fields radiated by lightning discharges at distances of 15 to 30 km Each discharge is shown on time scales of 2 msec/div, 40 μsec/div, and 8 μsec/div Orientation of electric field is positive upward (From Weidman, C D and Krider, E P *J Geophys Res*, 84, 3159, 1979 With permission Copyrighted by American Geophysical Union)

The voltage between the condenser plates is

$$U = \frac{1}{C}\int_t^\infty I\,dt = -\frac{\bar{Q}}{C}\left(\cos\delta t + \frac{\gamma}{\delta}\sin\delta t\right)e^{-\gamma t} = \frac{\bar{Q}}{C}G_3(t) \quad (30)$$

with G_3 from Table I The total charge on the upper plate of C at time $t = 0$ is then indeed

$$\bar{Q} = -C\,U(0) \quad (31)$$

The total energy dissipated within the circuit is

$$P = \int_0^\infty R\,I^2\,dt = \frac{(\gamma^2+\delta^2)}{4\gamma}R\bar{Q}^2 = \frac{\bar{Q}^2}{2C} \quad (32)$$

This model can also simulate intracloud discharges if one puts a positive charge on the upper plate of the condenser and a negative charge on the lower plate These charges correspond now to the charge distribution within a channel without contact to the Earth, and the discharging current flows only internally The net charge is zero

Wave Guide Model

Outline of Theory

A more realistic model of lightning channels must take into account the finite di-

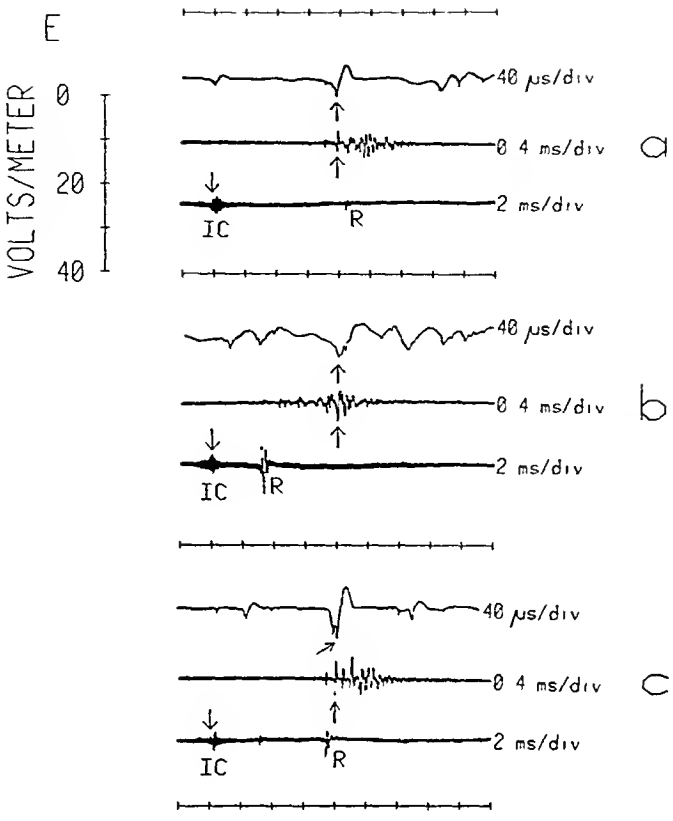

FIGURE 20. Electric fields radiated by lightning discharges at distances 50 to 100 km. The arrows indicate the same event on time scales of 2 msec/div, 0.4 msec/div, and 40 μsec/div. Orientation of electric field is positive upward. (From Weidman, C. D. and Krider, E. P., *J. Geophys. Res.*, 84, 3159, 1979. With permission. Copyrighted by American Geophysical Union.)

ameter and the finite length of the channel. Consider the channel to be a cylindrical straight wire of length ℓ and diameter d, with an electric conductivity σ. At times $t \geqq 0$ this wire has contact with the Earth in the case of return strokes, or else spontaneous discharging sets in at time $t \geqq 0$ without contact with the Earth in the case of intracloud strokes. The orientation of the channel (wire) may in general be oblique. To simplify matters, however, a vertical wire simulating return strokes with contact to the Earth is considered first.

The maximum spectral amplitude of return strokes is near 5 kHz (Figure 22) corresponding to a wavelength of 60 km in free space. This is much longer than the channel length which is assumed to be smaller than 10 km on the average. The propagation of electromagnetic waves within this wire must therefore be treated by full wave theory, and a straight wire model will be a reasonable approximation for the low-order wave modes with wavelengths $\lambda_n \geqq \ell$. The vertical electric field and current must disappear at the top of the wire ($z = \ell$), and the horizontal electric field strength must be zero at the contact to the perfectly conducting Earth ($z = 0$). The wire thus behaves like a resonant wave guide in which only standing waves of discrete frequencies ω_n can be excited.

The problem of electromagnetic wave propagation in a wire was solved long ago by Sommerfeld.[104] It can be shown that transverse magnetic and transverse electric waves

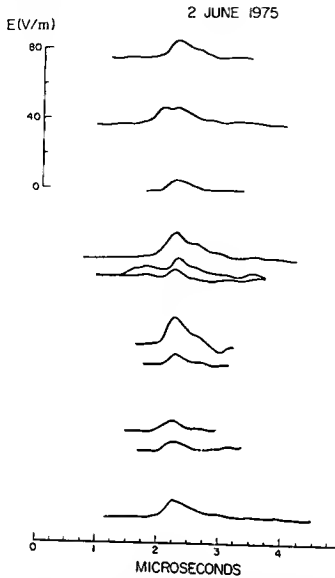

FIGURE 21 Fast time resolved records of stepped leader pulses produced by lightning discharges over seawater at distances of 20 to 30 km or less Orientation of electric field is according to Equation 6 (positive downward) (From Krider, E P , et al , *J Geophys Res* , 82, 951 1977 With permission Copyrighted by American Geophysical Union)

can exist in a wire However, only the cylindrically symmetric transverse magnetic waves are of significance for the energy transport In a resonance cavity of length l and resistance R with the boundary conditions given above, the electric and the magnetic fields of the nth mode within the wire ($\rho \leq d/2$) are[135]

$$(I_\rho)_n = \frac{R\bar{I}_n h_n K_n}{\varrho k_n^2} J_1(K_n\rho) \sin h_n z\, e^{-i\omega_n t}$$

$$(E_z)_n = \frac{R\bar{I}_n K_n^2}{\varrho k_n^2} J_0(K_n\rho) \cos h_n z\, e^{-i\omega_n t} \qquad (33)$$

$$(cB_\phi)_n = \frac{R\bar{I}_n c K\mu\sigma}{\varrho k_n^2} J_1(K_n\rho) \cos h_n z\, e^{-i\omega_n t}$$

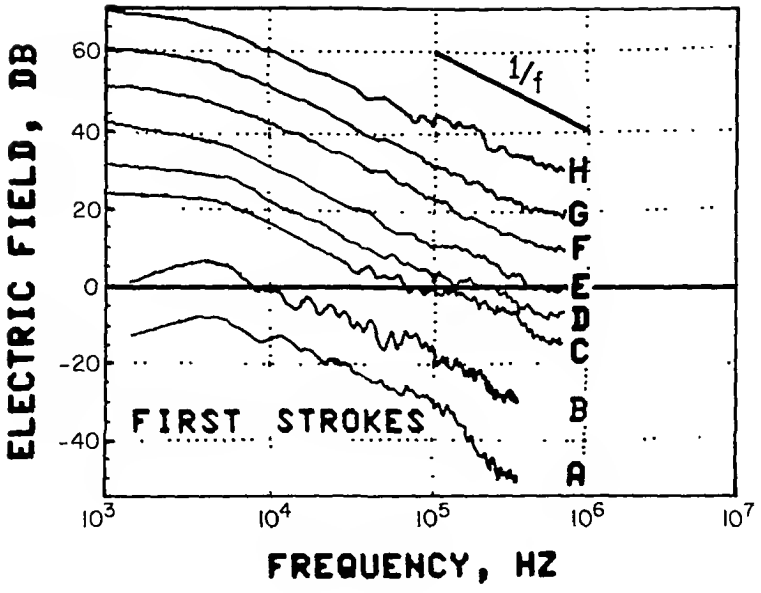

FIGURE 22. Average spectra of electric fields for first return strokes at distances (A) 200 km; (B) 50 km, (C) 10 km; (D) 7 km; (E) 4 km; (F) 2.5 km; (G) 1.5 km, and (H) 0.9 km. (From Serhan, G. I. et al , *Radio Sci.*, 15, 1089, 1980. With permission. Copyrighted by American Geophysical Union.)

with

$$h_n = \frac{(2n-1)\pi}{2\ell} \quad ; \quad (n = 1,2,3\ldots) \tag{34}$$

the vertical wave number chosen such that the upper boundary condition for E_z and the lower boundary condition for E_ρ is fulfilled. Furthermore,

$$k_n = \omega_n \sqrt{\mu\epsilon_n} \simeq \sqrt{\imath\sigma\mu\omega_n}$$

is the total wave number,

$$\epsilon_n = \epsilon' + \frac{i\sigma}{\omega_n} \simeq \frac{i\sigma}{\omega_n}$$

is the complex dielectric constant, $\mu = \mu_o$ is the permeability of free space, and

$$K_n = \sqrt{k_n^2 - h_n^2}$$

is the horizontal wave number. I_n is an amplitude to be determined later, and J_0 and J_1 are Bessel functions of order 0 and 1, respectively.

Discussion of Eigenvalue Equation

Continuity of the horizontal components E_ρ and B_ϕ/μ at the surface of the wire at d/2 yields an eigenvalue equation for the eigenfrequencies ω_n. Within a thin wire of

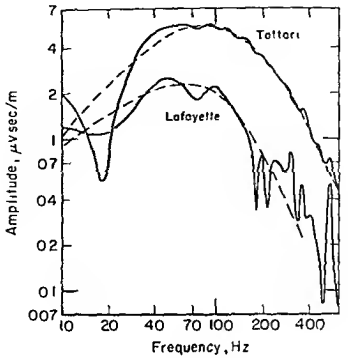

A

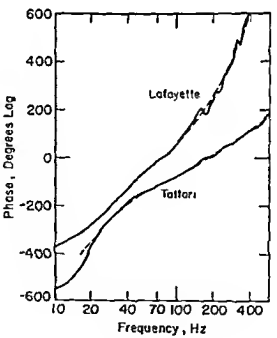

B

FIGURE 23 ELF spectra of the slow tail atmospherics in Figure 18 (A) Amplitude, (B) Phase (From Taylor, W. L. and Sao, K., *Radio Sci.* 5 1453, 1970 *With permission* Copyrighted by American Geophysical Union.)

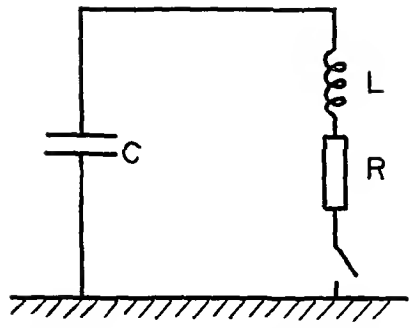

FIGURE 24 Lumped circuit model of a return stroke, adapted from Oetzel.[84]

moderate conductivity where $|K_n d/2| \lesssim 1$ is valid, the eigenvalue can be approximated as follows

$$u \ln u = -v \tag{35}$$

with

$$u = \left(\frac{\kappa d}{4c}\right)^2 (c^2h^2 - \omega^2) \qquad v = \frac{i\omega\kappa^2}{\sigma\mu\, c^2}$$

$\varkappa = 1.781$ is the Euler-Mascheroni constant. The indices 'n' have been dropped in Equation 35 and the following for convenience.

To fulfill the radiation condition outside the wire, u must possess a negative imaginary term. Introducing

$$u = -\frac{v}{\ln u} = \frac{1}{\sigma}(i\omega D - E) \qquad (D,E > 0, \text{ real}) \tag{36}$$

and eliminating u with its definition above, one arrives at

$$i\omega = \gamma \mp i\delta \tag{37}$$

with

$$\gamma = \frac{A^2 D}{2} > 0 \qquad \delta = \sqrt{\omega_0^2 - \gamma^2}$$

$$A = \frac{4c}{\kappa d\sqrt{\sigma}} \qquad \omega_0^2 = c^2h^2 + A^2E$$

The constants D and E must be determined by a numerical iterative method. ω in general is complex. If $\gamma > \omega_o$ ω becomes purely imaginary. Therefore, the solution of the eigenvalue equation leads indeed to eigenfunctions of the form of Equation 28. An (α,β) plot is shown in Figure 25 with a reduced channel length $\ell_n = \ell/(2n-1)$ (in

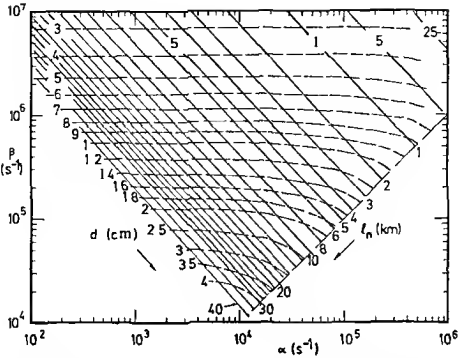

FIGURE 25 Solution of eigenvalue Equation 35 α, β—plot Isolines of reduced channel length $\ell_n = \ell/(2n-1)$ (solid lines) and of channel diameter d (dashed lines) At the dashed dotted line α is $\alpha = \beta$

km, solid lines) and the channel diameter d (in cm, dashed lines) as parameters The electric conductivity of the channel is assumed to be $\sigma = 10^4$ Sm^{-1} It can be shown that the plot in Figure 25 changes only slightly if d is replaced by the product $\sqrt{\sigma}\,d$ (in $\sqrt{\mathrm{Sm}}$) Therefore, Figure 25 can still be used for arbitrary values of σ ($10^3 < \sigma < 10^5$ Sm^{-1}) if d is replaced by $\sqrt{\sigma}\,d$

Figure 26 is a (d,γ) plot for type 2 waves, again using ℓ_n and d as parameters The validity of Equation 36 breaks down beyond the dotted line in the lower right corner where $|K_n\, d/2| > 1$ The transition from the (γ,d) regime (damped oscillations of type 2) occurs at the dash-dotted line in Figure 25 where $\alpha = \beta = \gamma$. This transition takes place at the critical resistance

$$R_{crit} = \frac{4\varrho_n}{\sigma\pi d^2} \simeq C_1 - C_2 \log \gamma \quad \text{(in k}\Omega\text{)} \tag{38}$$

with

$$C_1 = \quad = 3.50 \quad , \quad C_2 = 0.225 \quad , \quad \gamma \text{ in s}^{-1}$$

For a typical value of $\sigma d^2 = 1$, one arrives at $R_{crit} = 2.3$ kΩ Comparing Equation 37 with Equation 28, one can define a resistance R, an inductance L_n, a capacitance C_n and a wave resistance Z_n of the nth mode as

$$R = \frac{4\varrho}{\sigma\pi d^2} \quad , \quad L_n = \frac{R}{2\gamma_n} = \frac{R}{(\alpha_n + \beta_n)}$$

$$C_n = \frac{1}{(\gamma_n^2 + \delta_n^2)L_n} = \frac{1}{\alpha_n\beta_n L_n} \quad , \quad Z_n = \sqrt{L_n/C_n} \tag{39}$$

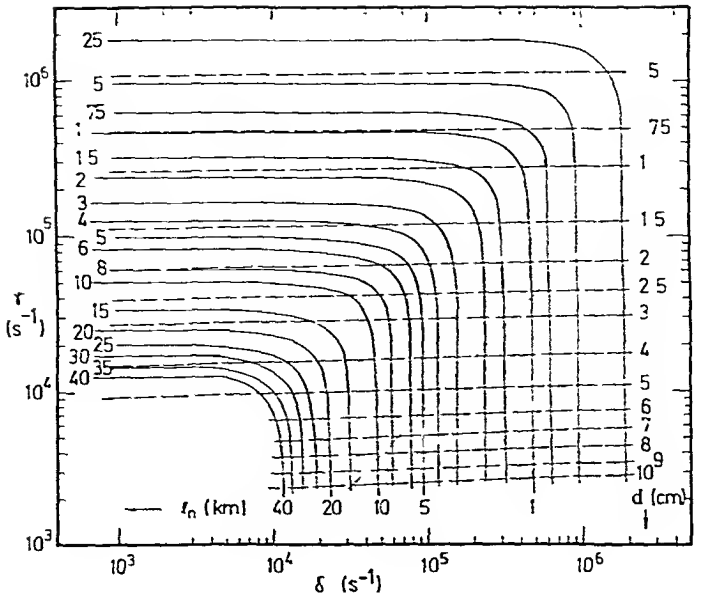

FIGURE 26. Solution of eigenvalue Equation 35. γ, δ-plot. Isolines of reduced channel length $l_n = l/(2n-1)$ (solid lines) and of channel diameter d (dashed lines). In the lower right corner beyond the dotted line, the approximation (Equation 35) breaks down.

Furthermore, the wavelength of the nth mode is

$$\lambda_n = \frac{2\pi}{h_n} = \frac{4l}{(2n-1)} = 4l_n \tag{40}$$

with $l_n = l/(2n-1)$ the reduced channel length.

Electric Current and Charge Configuration

Mode Structure of Ground Discharges

The eigenvalues (α,β), or (γ,δ), respectively, appear as pairs. Since the total electric current should be zero at time $t \leqq 0$, it is reasonable to assume that the two eigenfunctions are combined in the form given by Equation 28. Since $J_0(x) \simeq 1$ and $J_1(x) \simeq x/2$ for $x < 1$, the assumption used for the derivation of Equation 35, the skin effect within the wire is negligible for the lower order modes, and the whole interior of the wire is thus filled with the same current density. The vertical electric current of the nth mode within the wire is therefore

$$I_n(z,t) = 2\pi\sigma \int_0^{d/2} (E_z)_n \rho d\rho = -\bar{Q}_n(\gamma_n^2 + \delta_n^2) \cos h_n z \frac{\sin \delta_n t}{\delta_n} e^{-\gamma_n t} \tag{41}$$

The parameter $\bar{Q}_n$ in Equation 41 is related to the amplitude $\bar{I}_n$ in Equation 33 by

$$\bar{I}_n = -\frac{\bar{Q}_n(\gamma_n^2 + \delta_n^2)}{2\delta_n} \tag{42}$$

At large distances from the channel the lightning behaves like a dipole with the electric dipole moment

$$\bar{M}_n = 2\bar{Q}_n \int_0^{\ell} \cos h_n z \, dz = 2(-1)^{n+1} \bar{Q}_n \bar{\varrho}_n \tag{43}$$

where

$$\bar{\varrho}_n = \frac{1}{h_n} = \frac{2}{\pi}\varrho_n = \frac{2\ell}{(2n-1)\pi} \tag{44}$$

is an effective antenna length of the mode of order n It may be noted that Equations 15 and 12 are verified with the channel length ℓ in Equation 4 replaced by the effective length $\bar{\ell}_n$ of Equation 44

The charge density per unit length can be derived from the equation of continuity and is given by

$$q_n = \frac{\bar{Q}_n}{\bar{\varrho}_n} \sin h_n z \left\{ \cos \delta_n t + \frac{\gamma_n}{\delta_n} \sin \delta_n t \right\} e^{-\gamma_n t} \tag{45}$$

from which the total change of the nth mode can be determined as

$$\bar{Q}_n = \int_0^{\ell} q_n(z,0)\, dz \tag{46}$$

The energy of the nth mode dissipated during the discharging process within the channel is

$$P_{dis} = 2\pi\sigma \int (L_z)_n^2 \rho d\rho \, dz \, dt = \frac{\bar{Q}_n^2}{4C_n} \tag{47}$$

with C_n as defined in Equation 39 The radial Poynting vector integrated over the surface of the channel and over time gives the electromagnetic energy radiated from the channel This is

$$P_{em} = \frac{\pi d}{\mu} \int (F_z B_\phi)_n \, dz \, dt = \frac{\bar{Q}_n^2}{4C_n} \tag{48}$$

It has the same value as the dissipated energy. The total energy of the nth mode is therefore

$$P_n = P_{dis} + P_{em} = \frac{\overline{Q}_n^2}{2C_n} \tag{49}$$

which just corresponds to the energy P of the lumped circuit in Equation 32.

Dominance of Fundamental Mode

A lightning channel of length ℓ can carry a multitude of modes of order n. Evidently, all modes will be excited after grounding, but their amplitudes will depend on the charge density distribution along the channel just before ground contact. In an imperfect wave guide such as the tortuous lightning channel with branches etc., resonance loses its meaning for the higher order modes which have wavelengths small compared with the channel length ($n \gtrsim 10$). These modes propagate like free waves. They are partially reflected at inhomogeneities and damped along their propagation path. Although they are generated at all times during the flash, they are ineffective for transporting electric charge because they interfere destructively. Their contribution to channel heating is probably of minor importance. These waves give rise to the quasi-continuous radio noise at frequencies $\gtrsim$ 100 kHz (see the chapter, "High Frequency Radio Noise" by Lewis).

Waves of intermediate wave number ($3 \lesssim n \lesssim 10$) have wavelengths comparable with the large-scale inhomogeneities of the channel. On the other hand, their wavelengths are too large to allow propagation as free waves. Therefore, these waves cannot develop to their full impulse form, and mode coupling from that range of wave numbers into the other wave modes is expected.

The waves of lowest wave number ($n \lesssim 3$) are the only modes where resonance effects can lead to the full development of pulse forms like Equation 41. In particular, the first mode ($n = 1$) has a wavelength of four times the channel length. This is large even compared with the large-scale inhomogeneities of the channel. This is the mode which most effectively transports and redistributes electric charge within the lightning channel and also heats the gas within the channel to temperatures where liminous events can be observed. A discharging process where the first mode is involved probably starts after the channel has reached some kind of stable configuration.

Figure 27a shows the vertical structure of the electric charge density and current of the first two modes ($n = 1$ and 2). In the case of the first mode, the vertical current is upward (positive) within the whole channel, and the total negative charge is drained to the Earth. The wavelength is $\lambda_1 = 4\ell$. This contrasts with the second mode, for which only the negative excess charge within the lower part of the channel gives rise to an upward current from the Earth. An internal downward current discharges the regions of opposite electric charge in the upper part of the channel. Both the height integrated electric current and the total charge $\overline{Q}$ are negative as apparent from Equation 43. The situation is analogous for the higher order modes. The region of downward draining of electrons to the Earth is only the fraction $1/(2n-1)$ of the total channel length, and the internal discharging currents are alternatively upward and downward.

Mode Structure of Intracloud Discharges

No current can flow across the lower boundary for intracloud strokes so that the vertical electric field must also vanish there. Nevertheless, the results just presented can still be used if the channel ℓ of the return stroke is replaced by a channel of length

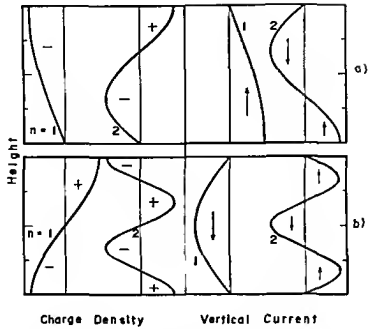

FIGURE 27 Height distribution of charge density q_n (left) and of vertical electric current I_n (right) for the two first modes of order n = 1 and 2 (A) Return stroke, (B) intracloud stroke

2ℓ with the lower half of the channel behaving symmetrically with respect to the upper half If H is the height of the center of the intracloud strokes, the total charge within the upper half of the channel is

$$\bar{Q}_n = \int_{H}^{H+\ell} q_n (z - H,0)\, dz \qquad (50)$$

The total charge within the whole channel is zero, and the total energy is

$$P_n = \bar{Q}_n^2/C_n \qquad (51)$$

with an effective antenna length

$$\bar{\ell}_n = \frac{4\ell}{(2n-1)\pi} \qquad (52)$$

instead of Equation 44

Figure 27b shows the vertical distribution of charge and current density of the first two modes of intracloud strokes The discharging current of the first mode is directed downward (or negative) within the whole channel if positive charge is stored within the upper half of the channel The current direction changes alternatively for the second mode, but the net current is upward directed Analogous distributions exist for the higher order modes.

Channel Heating

The waves in Figure 27 are standing waves which are excited instantaneously along the whole channel This would seem to be in conflict with photographic measurements

during R strokes where luminosity is observed to travel from the ground with velocities of the order of 10^8 m/sec. The upward velocity generally decreases from the bottom to the top.[113] This discrepancy may result from the fact that luminous events cannot be seen before a certain threshold of heating within the channel is exceeded. Since that threshold depends on the second power of the electric current integrated over the time, it will be reached later at greater heights because the electric current of the dominant first mode decreases upward (see Figure 27a). The luminous event may thus only give the illusion of a propagating wave front which does not actually exist. To obtain a rough estimate, one can use the energy equation in the form

$$\rho c_v \frac{\partial T}{\partial t} \simeq \frac{RI^2}{V} \tag{53}$$

with $\varrho \simeq$ the constant gas density, c_v the specific heat at constant volume, T the temperature, R the total resistance of the channel, I the electric current of the first mode from Equation 41, and V the volume of the channel. Integrating Equation 53, one may calculate the height z_m where the temperature $T_m \simeq 10{,}000$ K is reached at time t_m

$$z_m \simeq \frac{2\varrho}{\pi} \arccos \left\{ \frac{\Pi_{therm}}{\Pi_{joule}} \right\}^{1/2} \tag{54}$$

where

$$\Pi_{therm} \simeq \rho c_v (T_m - T_o) \lessapprox 9 \text{ MJ m}^{-3} \tag{55}$$

is the thermal energy density necessary to heat the channel to a temperature of T_m where luminosity starts,[113] T_o is the temperature of the channel prior to the discharge, and

$$\Pi_{joule} = \frac{R\bar{I}_1^2}{V} \int_0^{t_m} \left(e^{-\alpha_1 t} - e^{-\beta_1 t} \right)^2 dt \lessapprox \frac{2 P_{dis}}{V} = \frac{\bar{Q}_1^2}{2C_1 V} \tag{56}$$

is the total dissipated energy density with P_{dis} from Equation 47. According to Equation 54, the channel can never be illuminated up to its very top. In fact, luminous events can only be initiated when $2P_{dis}/V > \Pi_{therm}$.

Channel Parameters Derived from Observations

Type 1 First Return Strokes

Dennis and Pierce[16] have summarized the observed wave forms of electric currents of R strokes (see also Reference 55). These wave forms belong to type 1. Their parameters $\bar{I}$, α, and β are given in Table 2 for the first R stroke (R_f). The currents are proportional to G_2 in Table 1. The R_f wave configuration was given in Figure 5.

If one assumes that the parameters (α,β) of the R_f stroke in Table 2 represent the mode of order n = 1, it follows from Equation 35 or from Figure 25, that the channel length is ℓ = 7.9 km and the channel diameter is d = 1.55 cm for an assumed value for the electric conductivity of $\sigma = 10^4$ S/m. Since ℓ and d uniquely determine the configuration of the straight cylindrical channel, the reduced channel lengths ℓ_n of the higher order modes follow immediately from Equation 40.

The values of the diameter d, the total charge derived from Equation 42, and the total power derived from Equation 49 for the first mode (Table 1) are quite consistent with the corresponding values reported in the literature [5,35,113]. Note, however, that the theory determines only the product σd^2, and the diameter may vary if another value is adopted for σ. The channel length ℓ = 7.9 km appears to be larger than the value of 4 km determined mainly from photographic measurements [77,101]. One should recall, however, that the luminous effects are secondary processes occuring after heating the channel above a certain threshold. With the values from Table 2 and Equations 54 to 56, one may estimate a maximum height of 3.6 km, where luminous events can be expected, i.e., much closer to the measurements of Malan and Schonland [77].

Type 1 Subsequent Return Strokes

The electric current configuration of subsequent R strokes has been simulated by

$$I = \bar{I}(e^{-\alpha t} - e^{-\beta t}) + \bar{I}_1 e^{-\alpha_1 t}\left\{-\bar{I}_1 e^{-\beta_1 t}\right\} \qquad (57)$$

with

α = 0.014 μs^{-1}, β = 6 μs^{-1}, $\bar{I}$ = 10 kA (From Reference 16)

α_1 = 0.001 μs^{-1}, $\bar{I}_1$ = 2.5 kA (From Reference 113)

$\beta_1 = \beta$

The last term in brackets in Equation 57 has been added in order to conform with the theory. That term is negligible except for the first microsecond. The first term on the right hand side in Equation 57 cannot belong to the mode of first order because, according to Figure 25, a channel length of only 1.9 km would result in that case. The observations show, however, that the channel lengths of subsequent strokes are in general longer than the channel lengths of R_f strokes [113]. If one tentatively assumes the same channel length for the first and the subsequent strokes, and if one adopts the value β_1 = 6 μsec^{-1}, then the channel diameter d = 0.32 cm, and the values for α_n of the three first modes lie between 8.6×10^{-4} μsec^{-1} and 0.019 μsec^{-1} (see R, in Table 2). All three modes belong to type 1. Apparently, the experimentally derived form (Equation 57) is the sum of the three first modes. With the parameters for $\bar{I}_n$ given in Table 2, Equation 57 can, in fact, be well simulated by these three modes.

Because of the large dissipated energy and the small channel volume of the typical subsequent return strokes in Table 2, Equation 54 would suggest that nearly the entire channel length will be illuminated. This gives the impression of having a longer channel than that of the R_f stroke.

Type 2 Strokes

Type 2 return strokes with the parameters in Table 3, which represent observed sferic wave forms (Figures 12 and 13), have values of ℓ and d which are surprisingly large. They imply that the associated channels are huge and oblique to the ground. Since the dissipated energy is relatively small, the luminosity of these channels may be faint. The diameters of about 3 to 5 cm are within the upper range of data expected from other measurements [5]. The parameters used in Figure 6 are from the first return stroke R_f in Table 3.

The values 2ℓ = 4.3 km and d = 1.6 cm (with $\sigma = 10^4$ S/m) can be deduced from the parameters of the type 2 K stroke in Table 3 and Figure 7. Again, the channel need not be vertically orientated.

ELECTROMAGNETIC RADIATION FROM LIGHTNING CHANNELS

Vector Potential of a Line Current

Vertical Channel

Most theoretical calculations of the electromagnetic radiation field from lightning approximate the real lightning channel by a vertical straight line in which flows a one-dimensional electric current. The vector potential of the vertical line current in free space is[105]

$$A = (0, 0, A_z) \tag{58}$$

with the z-component

$$A_z = \frac{\mu}{4\pi} \int [I] \frac{dz'}{R} \tag{59}$$

[I] is the current to be taken at the retarded time

$$t_r = t - R/c \tag{60}$$

where (see Figure 28a)

$$R^2 = \rho^2 + (z - z')^2 \quad ; \quad \sin\theta = \rho/R \quad ; \quad \cos\theta = (z - z')/R \tag{61}$$

(0, z') are the coordinates of the lightning channel. (ϱ, z) are the coordinates of the receiving point P. The magnetic and electric fieldstrengths are then derived from

$$B = \nabla \times A \quad ; \quad E = -\frac{\partial A}{\partial t} - c^2 \nabla \int_t^\infty \nabla \cdot A \, dt \tag{62}$$

where by definition $E = 0$ as $t \to \infty$. In a cylindrical coordinate system the only non-vanishing components of the electromagnetic field are E_ρ, E_z, and B_ϕ. The reflection of the waves at the highly conducting earth can be taken into account in the usual manner by adding an image line current located at the height -H (see Figure 28a). Its field components have the same form as those obtained from Equation 62 if one replaces H by -H, z' by -z', R by $\tilde{R}$, θ by $\tilde{\theta}$, and $|I(z')|$ by $|I(-z')|$. For a receiving point on the ground ($z = 0$), $\tilde{R} \to R$, $\tilde{\theta} \to \pi - \theta$, and the horizontal component of E disappears while the remaining components double:

$$E_\rho + \tilde{E}_\rho = 0 \quad ; \quad E_z + \tilde{E}_z = 2E_z \quad ; \quad B_\phi + \tilde{B}_\phi = 2B_\phi \tag{63}$$

where $\tilde{E}_\rho$, $\tilde{E}_z$, and $\tilde{B}_\phi$ are the field components of the image line current.

Oblique Channel

The wave field of an arbitrarily orientated line current can be determined simply

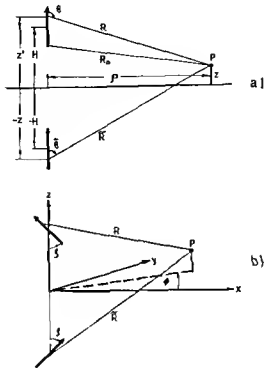

FIGURE 28 Geometry of lightning channels and their images (A) Vertical channel (B) oblique channel

from a transformation of the coordinate system and by an appropriate orientation of the image current (see Figure 28b) Rotating the line current by an angle ξ with respect to an axis in the (x,z) plane, one obtains the following components (now in a Cartesian coordinate system)

$$
\begin{aligned}
E_x &= (E_\rho + \tilde{E}_\rho)\cos\xi\cos\phi - (E_z - \tilde{E}_z)\sin\xi \\
E_y &= (E_\rho + \tilde{E}_\rho)\sin\phi \\
E_z &= (E_\rho - \tilde{E}_\rho)\sin\xi\cos\phi + (E_z + \tilde{E}_z)\cos\xi \\
B_x &= -(B_\phi + \tilde{B}_\phi)\cos\xi\sin\phi \\
B_y &= (B_\phi + \tilde{B}_\phi)\cos\phi \\
B_z &= -(B_\phi - \tilde{B}_\phi)\sin\xi\sin\phi
\end{aligned}
\qquad (64)
$$

If one has a horizontally orientated line current ($\xi = 90°$) and a receiving point on the ground ($z = 0$), the field reduces to the simple form

$$
\begin{aligned}
E_z &= 2E_\rho\cos\phi \\
B_y &= 2B_\phi\cos\phi
\end{aligned}
\qquad (65)
$$

Field Components

Effects of Finite Channel Length

The components of the electromagnetic field derived from Equations 62 and 64 depend on the electric current model to be included in Equation 59 and on the orientation of the channel. Most authors use a vertical channel and either the Bruce-Golde model or the transmission line model for the lightning current.[50,51,68,73,79,92,114-116] LeVine and Meneghini[69] simulated the lightning channel by using arbitrarily oriented piecewise linear current elements. The currents were taken from the transmission line model. All calculations assume propagation above a perfectly conducting Earth.

In the following, a vertical channel centered at height H above ground with the model current from Equation 41 is considered. For each mode of order n (for convenience, the index "n" is dropped) the cylindrical components of the electromagnetic field over a perfectly conducting Earth with the receiver on the ground are

$$E_z = \frac{\bar{Q}}{2\pi\epsilon_0 \bar{R}^3} \int_{H-L}^{H+\ell'} \left\{ \sin^2\theta \frac{G_1}{D} + \left(1 - 3\cos^2\theta\right)\left(\frac{G_2}{D^2} + \frac{G_3}{D^3}\right)\right\} \cos h(z' - H)\, dz' + \text{residuum} \tag{66}$$

$$cB_\phi = -\frac{\bar{Q}}{2\pi\epsilon_0 \bar{R}^3} \int_{H-L}^{H+\ell'} \sin\theta \left(\frac{G_1}{D} + \frac{G_2}{D^2}\right) \cos h(z' - H)\, dz'$$

with $G_m(t_r)$ in Table 1 taken at the retarded time

$$t_r = t - R/c = t' + R_o/c - R/c \tag{67}$$

Again it is $D = R/\bar{R}$ with $\bar{R} = 1$ km a normalizing distance, and $R_o = \sqrt{\rho^2 + (H-L)^2}$ is the shortest distance between lightning channel and the receiving point P (see Figure 28a). H is the height of the center of the channel above ground, $\bar{Q}$ is the total charge within the region (H, H + ℓ) at time t = 0. For return strokes, one has H = L = 0 and the channel reaches from the ground to the height ℓ. For intracloud strokes, the total channel length is 2ℓ, and L = ℓ. The time t is the channel time, and the discharging process is assumed to start at t = 0. The time $t' = t - R_o/c$ is the receiver time and the first signal will reach the receiving point P at t' = 0. The length ℓ' is that location on the channel where the last signal reaches the point P at time t':

$$\ell' = \begin{cases} \sqrt{(ct' + R_o)^2 - \rho^2} - H & \text{for } ct' < ct'_m \\ \ell & \text{for } ct' \geq ct'_m \end{cases} \tag{68}$$

with

$$ct'_m = \sqrt{(H + \ell)^2 + \rho^2} - R_o$$

giving the time when radiation from the whole channel reaches the receiver. The resid-

uum of E_z takes into account the finite charge stored within the channel at time $t' < 0$ It is

$$\text{residuum} = -\frac{\bar{Q}}{2\pi\epsilon_0 \bar{R}^3} \int_{H+\ell'}^{H+\ell} \frac{(1 - 3\cos^2\theta)}{D^3} \cos h(z' - H)\, dz' \quad (69)$$

The expressions for the field components become somewhat more complicated and the integration boundaries change for a receiving point at height $z > 0$

The G_{nm} can be taken before the integrals in Equation 66 for distances $R \gg \ell$, and the field components then become identical with the fields of a vertical electric dipole (Equation 21) with dipole moment $\bar{M}$ from Equation 43 and an effective antenna length $\bar{l}$ from Equation 44 for R strokes, or from Equation 52 for intracloud strokes

Numerical Results

The time dependence of the electromagnetic field components for a ground-based observer ($z = 0$) calculated from Equation 66 are shown in Figure 29 using the parameters of the type 1 first return stroke R_1 in Table 2 at the three distances 1, 10, and 200 km The dashed lines in Figure 29 give the radiation component ($m = 1$), induction component ($m = 2$), and electrostatic component ($m = 3$) of the vertical electric field E, and of the azimuthal magnetic field B. In order to compare these curves with observed sferic wave forms, the values ΔE_z from Equation 6 are plotted The left ordinate is for the electric field scaled in volts per meter, and the right ordinate is for the magnetic field scaled in tesla Note that the unit of cB_ϕ is volts per meter, and the left ordinate scales also cB_ϕ

The solid lines give the total field which is the sum of the three components For comparison, the dash-dotted lines are the dipole approximations of the total field according to Equation 21 with $\theta = 90°$ Except for the first microseconds, that dipole field is an excellent approximation of the radiation field at 200 km distance The real wave forms peak near 1 μsec and have maximum amplitudes reduced by a factor of about 1 4 as compared with the maximum of the dipole field which peaks at $t = 0$ Both the electric and the magnetic components are nearly identical

At a distance of 10 km, all three components are of the same order of magnitude The first relative maximum of the E field at 3 μsec is due to the radiation component At times larger than the crossover time of that component, the electrostatic component dominates and increases the total field This is called the "ramp" by Lin et al [72] The radiation component and the induction component of the magnetic field lead to a maximum at time $t < t_3$ which is called the "hump" by Lin et al [72] The dipole approximation is still a reasonable approximation apart from the first few microseconds

At a distance of 1 km, the situation is similar to that at 10-km distance except that the influence of the radiation component has been reduced At this distance, however, the dipole approximation grossly overestimates the magnitudes of the fields although the wave forms remain similar Note the logarithmic scale for the dipole field at 1-km distance

The calculation of the wave forms of the subsequent type 1 strokes (R_n in Table 2) give similar results as for the first R stroke with the difference that the peak of the radiation component occur at around 0 1 μsec and the crossover times have shifted to a few microseconds Furthermore, the higher order modes ($n = 2$ and 3 in Table 2) exhibit a rather complicated behavior during the first few microseconds because of the complex vertical electric current configurations within the channel

Figure 30 shows the calculated electric and magnetic fields vs time of the type 2

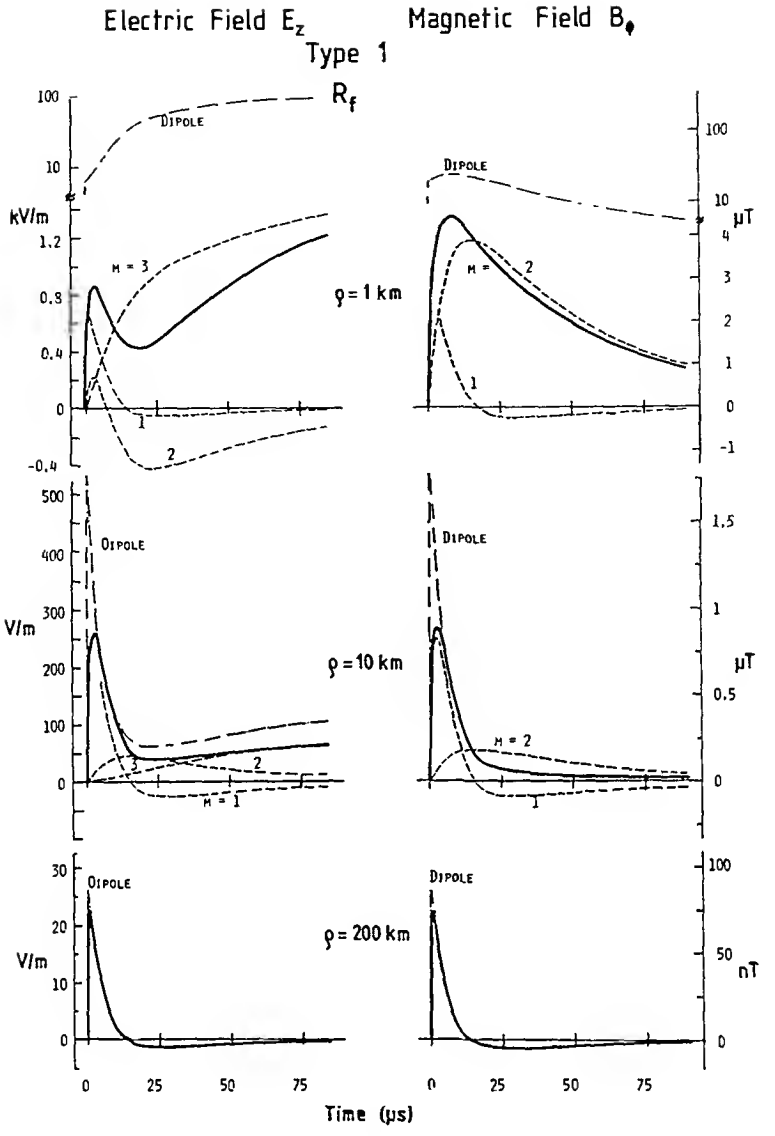

FIGURE 29. Type 1 first return stroke with the parameters of R_f from Table 2. Calculated vertical electric field (left) and azimuthal magnetic field (right) vs. time at three distances 1, 10, and 200 km. Solid lines: total field; dashed lines: radiation component (m = 1), induction component (m = 2), and electrostatic component (m = 3). Dash-dotted lines: total field of dipole approximation (Equation 21). The scaling on the right in μT (10^{-6} Tesla) and nT (10^{-9} Tesla), respectively, equals the scaling on the left in volts per meter if the magnetic field is multiplied by the speed of light c. Note that the scaling of the dipole field at 1 km distance is logarithmic. Orientation of the electric field is according to Equation 6 (positive downward).

first return stroke with the parameters of R_f in Table 3, plotted in the same manner as in Figure 29 at the three distances 1, 10, and 200 km. The dotted lines are observations of a first return stroke reproduced from the data of Lin et al.[72] in Figure 12.

The agreement between the observations and the model is excellent at 200-km distance. In fact, the parameters in Table 3 have been selected such that the fit at 200-km distance is optimal. The theoretical amplitudes are somewhat smaller than the ob-

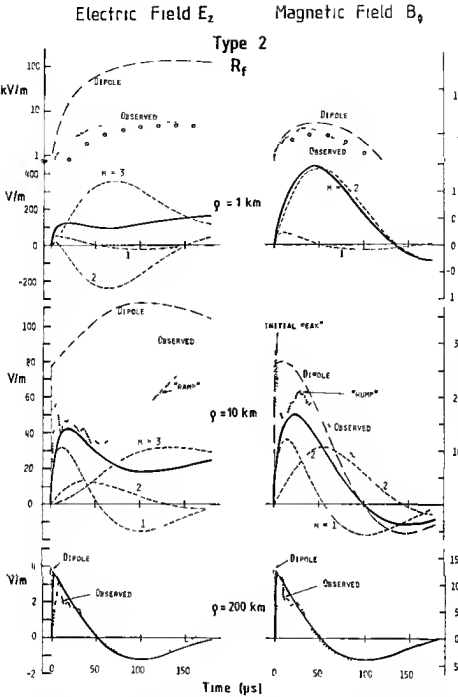

FIGURE 30 Type 2 first return stroke with the parameters of R_f from Table 3 Notation as in Figure 29 The dotted lines are observed wave forms of first return strokes reproduced from Lin et al [72] (the solid curves in Figure 12) The open circles at 1 km distances have been calculated for a dipole situated at a height of 670 m over ground Orientation of the electric field is positive downward

served data at 10 km, although the agreement between the wave forms is reasonable In particular, the "ramp" due to the electrostatic component (m = 3) in the E-field and the "hump" in the B-field are clearly visible The electrostatic component of the E-field is too small to adequately reproduce the "ramp" The model also does not simulate the "initial peak" in the data of Figure 12 At 1-km distance, the calculated field strengths are an order of magnitude too small compared with the observations although again the wave forms are similar This discrepancy may be not too surprising

in view of the simplified model here which only simulates the vertical part of a real oblique channel. The huge channel length of nearly 20 km already indicates that the channel must possess a significant horizontal extent, and it is well known that the horizontal part of an antenna near the ground contributes significantly to the electromagnetic field only in the immediate vicinity of the antenna.[105] This idea is supported by the behavior of the dipole approximation (the dash-dotted lines in Figure 30). While a reasonable approximation at 200 km, it somewhat overestimates the observed field at 10 km, and it grossly overestimates the field at 1-km distance. On the other hand, the calculated field of the vertical channel underestimates the measurements. Hence, a vertical antenna having a dimension between $\bar{\ell} = 0$ (dipole) and ℓ would reproduce the measurements at 1 km although many details would be lost.

For example, a dipole located at a height of only H = 670 m produces total electric and magnetic fields at 1-km distance as given by the open circles in Figure 30, and thus simulates rather well the observations at those distances. The reduction of the fields is due to the $\sin\theta$ – and $\cos\theta$ – terms in Equation 66. At distances $\varrho \gtrsim 10$ km, that elevation of the dipole is of no relevance for the field components.

The results for the type 2 subsequent return stroke (R_s in Table 3) are similar to those of Figure 30. However, because of the smaller channel length of about 13 km, the agreement between the measurements in Figure 12 (dotted lines) and theory is somewhat better at 10-km distance than in the case of R_f in Figure 30. The model is still inadequate at 1-km distance. The same arguments concerning the effect of radiation from oblique channels at short distances hold here as in the case of the R_f stroke.

Lin et al.[72] state that their observed wave forms in Figure 12 are typical for first and subsequent return strokes. This is consistent with Taylor's[107] findings that about 80% of all observed wave forms belong to type 2 (according to our nomenclature). On the other hand, the Bruce-Golde formula (Equation 12), based on direct current measurements at the base of the channel is of type 1. The question thus arises why type 1 sferic wave forms are apparently so rare. A possible answer may be as follows: the dissipated energy in type 1 return strokes is much larger than the threshold energy necessary for illuminating the channel (compare P_{em} in Table 2 with the threshold energy computed in the previous section). A significant part of the channel will therefore be visible. However, the average type 2 return current associated with the observed wave forms of sferics in Figure 12 dissipates a much smaller amount of energy (see column P_{em} in Table 3), so that the lightning stroke may be at or even below the threshold of visibility.

Figure 31 shows the radiation component (m = 1) of a typical intracloud K stroke situated at a distance of 25 km from the observer and centered at a height of 5 km above ground. The channel parameters were derived from the wave form in Figure 19b and are given in Table 3 and Figure 7. The solid line in Figure 31 is the dipole approximation. The dotted line is the exact solution from Equation 66. The signal from the bottom of the channel reaches the receiver about 1 μsec earlier than the signal from the dipole at the center of the channel. This explains the time difference at the beginning of the wave form.

The Energy of the Radiation Component

Considering a dipole approximation over an ideal Earth, the total radiated energy from the lightning antenna at great distances is[104]

$$P_{rad} = \frac{2\pi c}{\mu} \int_0^{\infty} \int_0^{\pi/2} B_\phi^2 r^2 \sin\theta \, d\theta \, dt = \frac{\mu \bar{M}^2 \alpha^2 \beta^2}{24\pi c (\alpha + \beta)} \qquad (70)$$

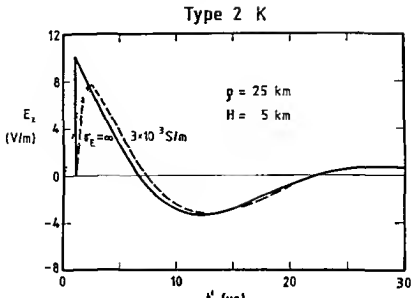

FIGURE 31 Radiation component (m = 1) of a type 2 intracloud stroke with the parameters of K from Table 3 The distance from the lightning channel is 25 km the center of the channel is located at 5 km height Solid line dipole approximation over a perfectly conducting Earth (Equation 21) Dashed line dipole approximation over an imperfectly conducting Earth with conductivity $\sigma_E = 3 \times 10^{-3}$ S/m (Equation 76) Dotted line exact calculation over a perfectly conducting Earth (Equation 66)

The ratio between P_{rad} and the energy of the Poynting vector P_{em} of mode n just outside the channel (Equation 48) is

$$\left[\frac{P_{rad}}{P_{em}}\right]_n = \frac{8\mu\sigma\bar{\omega}_n^2 V}{3c\pi^3(2n-1)^2} \tag{71}$$

with $\bar{\omega}_n$ the maximum spectral frequency from Table 4, and $V = \ell\pi d^2/4$ the channel volume The fractions Equation 71 for the strokes considered are included in Tables 2 and 3 (expressed in percent) The most efficient antenna is the type 2 K stroke, which transmits 16% of its electromagnetic radiation in the radiation component to the far field The type 1 subsequent stroke is a poor radiator due to its small channel volume Only 0 1% of its electromagnetic energy is transferred into the radiation component

Pulse Dispersion in the Atmospheric Wave Guide

Ground Wave

The finite electric conductivity of the Earth and ionosphere influence the propagation characteristics of electromagnetic waves [21 123] If the transmission function of the wave guide between Earth and ionosphere is W (ϱ, ω), then the radiation component of the electric field of a vertical electric dipole can be obtained from the Fourier transform

$$L_z(\varrho,t) = \frac{1}{2\pi}\int_{-\infty}^{\infty} \hat{L}_z(\varrho,\omega)\, e^{-i\omega t}\, d\omega \tag{72}$$

where

$$\hat{E}_z(\rho,\omega) = \frac{9\bar{M}}{D}\,\hat{G}_1(\omega)\,e^{i\omega R/c}\sin^2\theta\,W(\rho,\omega) = \left|\hat{E}_z\right| e^{i\Psi} \qquad (73)$$

with $\hat{G}_1(\omega)$ the Fourier transform of the field over a perfectly conducting Earth as derived in Equation 25 and also tabulated in Table 4.

The ground wave dominates of distances smaller than about 300 km. The transmission function of the ground wave for the case of transmitter and receiver on the ground can be approximated by

$$W_0(\rho,\omega) = \frac{X^2}{2(C - i\omega)(D - i\omega)} \qquad (74)$$

with

$$X = \sqrt{\frac{2c\sigma_E}{\epsilon_0\rho}} = 260\sqrt{\frac{\sigma_E}{\rho}} \qquad C = XA \qquad D = \frac{X}{2A}$$

$$A = 0.496 + 0.853\,i \quad (\rho \text{ in km} \;;\; \sigma_E \text{ in } Sm^{-1} \;;\; X \text{ in } \mu s^{-1})$$

σ_E is the electric conductivity of the surface of the Earth.

$$\Lambda = \frac{\omega^2}{X^2} \qquad (75)$$

is the numerical distance.[105]

The radiation component of the vertical electric field of the dipole in Equation 21 is modified by the Earth according to Equations 72 and 74 as

$$E_z(\rho,t) = \frac{\bar{I}\,\bar{\ell}\mu_0 X^2}{4\pi\rho}\,\text{Real}\left(\frac{\alpha\,e^{-\alpha t_r}}{(\alpha-D)(\alpha-C)} - \frac{\beta\,e^{-\beta t_r}}{(\beta-D)(\beta-C)} + \frac{(\beta-\alpha)}{(D-C)}\left\{\frac{C\,e^{-Ct_r}}{(\alpha-C)(\beta-C)} - \frac{D\,e^{-Dt_r}}{(\alpha-D)(\beta-D)}\right\}\right) \qquad (76)$$

with $t_r = t - \rho/c$ the retarded time. Figure 32a shows the effect of distance on the radiation component of the vertical electric field of the dipole situated on the ground simulating the type 2 first return stroke in Table 3. The conductivity is $\sigma_E = 10^{-3}$ Sm^{-1}. The time of minimum and the crossover point shift to later times, and the minimum amplitude decreases with increasing distance. In Figure 32b the electric conductivity is varied at a constant distance (ρ = 100 km). The minimum shifts to later times and the minimum amplitude decreases for a decrease in the conductivity. The dashed line shows for comparison the radiation component of the dipole over a perfectly conducting Earth. The observed rise times of about 3 μsec[17,71] are best fitted by an electric conductivity of about 3×10^{-3} S/m.

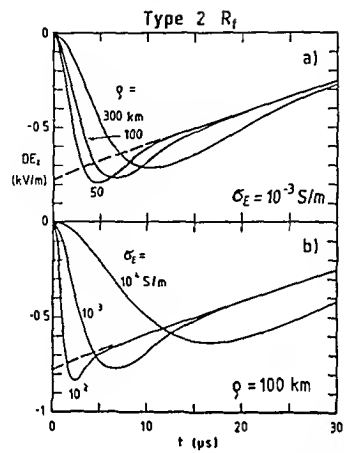

FIGURE 32 Type 2 first return stroke with the parameters of R_f from Table 3. Radiation component (multiple dipole approximation over imperfectly conducting Earth (Equation 76)) vs. time normalized to a distance of 1 km. (a) Constant electric conductivity $\sigma_E = 10^{-3}$ S/m, three different distances 50, 100, and 300 km. (b) Constant distance ϱ = 100 km, three different conductivities 10^{-4}, 10^{-3}, and 10^{-2} S/m.

The dashed line in Figure 31 takes this propagation effect into account for the dipole radiation of the K stroke at a distance of 25 km. The propagation effect is evidently similar to the effect of a finite antenna length, thus decreasing the maximum amplitude and shifting the rise time to later times.

The magnitude of the spectral function of the type 2 R_f stroke, $|\tilde{G}_1| \cdot |W_n|/D$ is plotted in Figure 33 vs. frequency for $\varrho = 200$ km and $\sigma_E = 3 \times 10^{-3}$ S/m. The dotted line is taken from Figure 8. The influence of the imperfectly conducting Earth becomes important at frequencies $\omega > X$, or for $f \geq 200$ kHz. In that range the spectral function falls off as f^{-3}.

Sky Waves

The propagation of VLF waves can be described by ray theory at distances $\varrho \lesssim 1000$ km. Within that range the transmission function of the vertical electric field is (see the chapter on Low Frequency Wave Propagation by Harth in Volume II)[11]

$$W = W_0 + \Sigma W_n \tag{77}$$

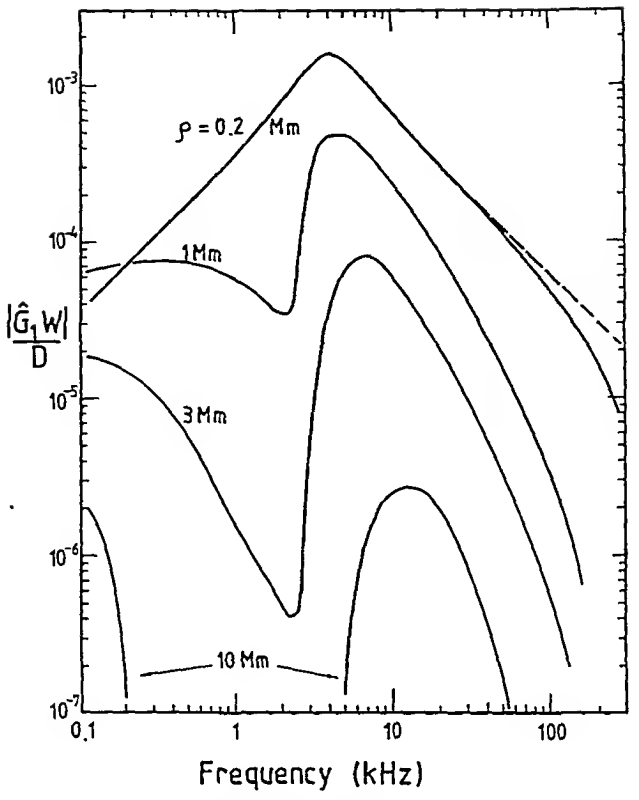

FIGURE 33. $|\hat{G}_1 W/D|$ vs. frequency for four different distances. Dashed line at 200 km distance is for W = 1 (perfectly conducting Earth).

where W_o is the transmission function of the ground wave (Equation 74), and

$$W_n = 2\, R_i^n\, R_e^{n-1}\, \frac{(1+R_e)^2}{4}\, \sin^3\theta_n e^{i\frac{\omega}{c}(r_n-\rho)} \tag{78}$$

is the transmission function of the n-hop sky wave. R_i and R_e are the reflection factors of the ionospheric D layer and the surface of the Earth, respectively. Finally,

$$\tan\theta_n = \frac{\rho}{2nh_n} \quad ; \quad r_n^2 = \rho^2 + 4n^2h_n^2 \tag{79}$$

with h_n the virtual height of the n-sky wave, θ_n the angle of incidence and r_n the phase path of that wave.

Within the VLF range and at distances $\rho < 500$ km one may approximate $R_e \simeq 1$ and $R_i \simeq A$ $(0.1 < A < 1)$.[120] The radiation component of sky waves from a vertical dipole are thus modified according to Equations 72 and 78 as

$$E_z\Big|_{\text{sky wave}} \simeq 2A^n \sin^3\theta_n \frac{9\bar{M}}{D}\, G_1(t_r') \tag{80}$$

with

$$t_r' = t_r - \frac{(r_n - \rho)}{c} = t - r_n/c \tag{81}$$

t_r is the retarded time from Equation 76, and

$$\Delta t_n = \frac{(r_n - \rho)}{c} \tag{82}$$

is the difference between the arrival times of the n-hop sky wave and the ground wave The symbol "s" in Figure 13 indicates the arrival time of the first hop sky wave

A clear separation between ground wave and first hop sky wave is possible only if the time difference Δt_n in Equation 82 is comparable or larger than the pulse length of the sferic With a pulse length of the order of 100 to 200 μsec in the case of R strokes, the limiting distance where separation is possible is about $\rho \lesssim 125$ to 300 km during daytime ($h_i \simeq 70$ km) and $\rho \lesssim 250$ to 500 km at night ($h_i \simeq 90$ km) For K strokes with their much shorter pulse lengths of about 20 μsec, the limiting distance increases to more than 1500 km during the day and about 3000 km at night Multihop propagation may even be possible, especially during the night

The method of locating thunderstorms by determining the delay time Δt_n between ground wave and first or multihop waves was used extensively in earlier times[67 80] and is still used today [67 78 108]

Far Field

Mode theory more appropriately describes VLF propagation than ray theory at distances greater than about 1000 km, because at these distances normally not more than two modes are involved in the transport of wave energy The transmission functions of the modes are[21 123]

$$W_n = \frac{1}{h}\sqrt{\frac{\Theta}{\sin\Theta}}\sqrt{\frac{2i\pi\rho c}{\omega}}\,k_n e^{(-A_n + iB_n)\rho} \tag{83}$$

$(\rho \gtrsim 500 \text{ km})$

$\Theta = \rho/a$ is the pole distance between receiver and transmitter (a is the radius of the Earth) K_n is an amplitude factor, A_n an attenuation factor, and B_n a propagation factor All three factors depend in a complicated way on frequency, geographic locations of receiver and transmitter, and time of day, and season

For the first mode, which dominates within the VLF range, one may approximate

$$K_1 \simeq 1 \quad , \quad A_1 \simeq \frac{a_1\pi^2c^2}{4\omega^2h^2} + \frac{b_1}{h} \quad , \quad B_1 \simeq -\frac{\pi^2c}{8\omega h^2 a_2} + \frac{b_1}{h} \tag{84}$$

$(3 \lesssim f \lesssim 15 \text{ kHz})$

with

$$a_1 = 0.001\,\omega^{2/3} \quad , \quad b_1 = \sqrt{\frac{\epsilon_0\omega}{2\sigma_E}}$$

$$a_2 = 4.5 \times 10^{-3}\sqrt{\omega} \quad (\omega \text{ in } s^{-1})$$

$h \simeq 70$ km at day time; $h \simeq 90$ km during night. For the mode of zero order, which dominates within the ELF range, the approximation is

$$K_o \simeq 0.5 \quad : \quad A_o \simeq B_o \simeq \frac{a_o}{h} \quad (100 \leqq f \leqq 2000 \text{ Hz}) \qquad (85)$$

with $a_o = 2.35 \times 10^{-4}\, \omega^{2/3}$ (ω in sec^{-1}). h is the virtual height of the wave guide.

The higher order modes become more and more important within the LF range ($f >$ 30 kHz), and the effective attenuation factor due to superposition of several modes increases with frequency. That factor can be simulated during daytime conditions by the function

$$A \simeq \exp\left\{F(f)\right\} \qquad (3 \leqq f \leqq 100 \text{ kHz}) \qquad (86)$$

with $F(f) = a (\log f)^2 + b \log f + c$; (f in kHz); $a = 0.95$; $b = -2.53$; $c = -1.83$. Since formulae Equations 84 to 86 can be expected to give only rough estimates, the exact values may differ substantially in individual cases.

Figure 34 shows the magnitude of W as derived from Equations 83 to 86 as a function of frequency for the three different distances 1000, 3000, and 10,000 km. One clearly notices a window of low attenuation shifting from 7 kHz at 1000 km to 18 kHz at 10,000 km in the VLF range, and a second window within the ELF range. Maximum attenuation occurs near 2 to 3 kHz. The bandpass effect of the atmospheric wave guide becomes more pronounced with increasing distance.

Figure 33 shows the function $|\hat{G}_1\ W/D|$ vs. frequency for the type 2 first return stroke R_f from Table 3 as determined for the ground wave at 200 km and from Figure 34. Due to the spectral function $\hat{G}_1$, the bandpass effect at large distances becomes even more remarkable. It is that bandpass effect which gives rise to the slow tail wave forms in Figure 18. According to Pierce,[86] the most frequent ratio between VLF to ELF amplitudes is 10:1. On the other hand, the bandwidths of the two windows in Figure 34 have a ratio of about 100:1, and spectral amplitudes in the ratio of 1:10. The type 2 R stroke thus has a VLF/ELF ratio of about 100:1, which is an order of magnitude too large to account for the observed ELF slow tail. Only a type 1 subsequent stroke R_s (Figure 8), which has a spectral amplitude ratio between VLF and ELF of 1:1 and thus a VLF/ELF ratio of about 10:1, is able to generate a significant ELF slow tail.

Phase Velocity and Group Time Delay

The phase of the spectral function in Equation 73 is

$$\Psi = \left(\frac{\omega}{c} + B_n\right)\rho + \Phi_1 + \frac{\pi}{4} \qquad (87)$$

The phase velocity v_p, defined from $\partial\Psi/\partial t = \omega$, is

$$v_p = \frac{\partial\rho}{\partial t} = \frac{c}{1 + B_n c/\omega} \qquad (88)$$

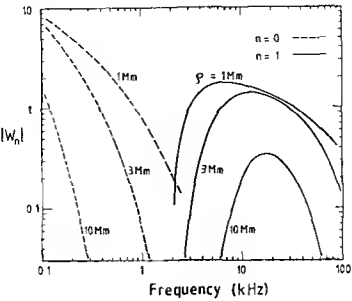

FIGURE 34 Transmission functions $|W_n|$ from Equation 83 during day time conditions (h = 70 km) vs. frequency for three different distances (1 Mm = 1000 km). Solid lines: first order mode (n = 1) with the parameters from Equation 84 and 86. Dashed lines: zeroth order mode with the parameters from Equation 85.

v_p becomes larger than the speed of light c if $B_n < 0$. That is the case for the first mode (Equation 84) within the lower VLF range.[122] Since $B_n > 0$ for the mode of zero order (Equation 85), v_p is less than c within the ELF range. The group velocity, defined from $\partial\Psi/\partial\omega = t_g$, is

$$v_g = \frac{\rho}{t_g} = \frac{c}{1 + c\partial B_n/\partial\omega + \frac{c}{\rho}\partial\Phi_1/\partial\omega} \tag{89}$$

The group time t_g is then

$$t_g = \frac{\rho}{c} + \rho\frac{\partial B_n}{\partial\omega} + \frac{\partial\Phi_1}{\partial\omega} \tag{90}$$

and the group time delay difference (GDD) between two spectral bands becomes

$$GDD = t_g\Big|_{f_0} - t_g\Big|_{f_1} = -\left\{\rho\frac{\partial^2 B_n}{\partial\omega^2} + \frac{\partial^2\Phi_1}{\partial\omega^2}\right\}\Delta\omega \quad (f_0 < f_1) \tag{91}$$

where the last term of the right-hand side is valid if both frequencies are sufficiently close together. The first and the second derivatives of Φ_1 are listed in Table 4. The time difference between the two pulses in Figure 18 is the group time delay between $F_0 \simeq 100$ Hz and $F_1 \simeq 20$ kHz according to Equation 90.

$$\Delta t_g = \left(\frac{\partial B_0}{\partial\omega}\Big|_{f_0} - \frac{\partial B_1}{\partial\omega}\Big|_{f_1}\right)\rho + \left(\frac{\partial\Phi_1}{\partial\omega}\Big|_{f_0} - \frac{\partial\Phi_1}{\partial\omega}\Big|_{f_1}\right) \tag{92}$$

For the type 1 subsequent R stroke during nighttime conditions (h = 90 km), it follows from Equations 84, 85 and Table 4 that

$$\Delta t_g = 0.2\rho + c_n \qquad (\rho \text{ in Mm; } \Delta t_g \text{ in msec}) \tag{93}$$

with $c_1 = 0.76$ for wave n = 1, $c_2 = 0.14$ for wave n = 2 in Table 2. Equation 93 corresponds nicely to the formula for the so-called separation time between the oscillation head and the ELF minimum such as in Figure 18, which has been experimentally established by Hepburn and Pierce.[31] The group time delay difference (Equation 91) applied to the lower VLF range has been used by Volland et al.[121] and Schäfer et al.[99] See also the section which follows.

SOURCE AND WAVE GUIDE PROPERTIES DERIVED FROM SFERICS

Probability Distribution of Sferics from Single Thunderstorm Centers

Spectral Amplitudes (SA)

It has been shown in the previous sections, that two types of lightning currents can exist which have either an aperiodic wave form (type 1) or are damped oscillations (type 2). Their individual wave forms depend on the channel characteristics. The parameters of several typical lightning currents are tabulated in Tables 2 and 3. One expects to observe a broad spectrum of sferic wave forms. In principle, it is possible to determine the channel parameters from each sferic arriving at a broad band receiver if the distance between source and receiver is known (see the section on "Channel Parameters Derived from Observations").

In order to perform a systematic statistical investigation, it is more convenient to observe at a few frequency bands with narrow band receivers. The output voltage U of an ordinary narrow band receiver gives the spectral amplitude from Equation 73 multiplied by a factor χ which depends on the bandwidth, the amplification of the receiver, and on the antenna properties:

$$U = \chi\,|\hat{E}_z| = \chi\, g(\omega)\, b(\rho, \omega) \tag{94}$$

with $g(\omega) = 9\overline{M}\hat{G}_1$ and $b(\varrho,\omega) = |W|/D$; $SA = g\,b$ is a spectral amplitude. Given a receiver threshold S, only signals exceeding that threshold will be recorded:

$$U \geqq S \tag{95}$$

If the spectral functions g at the source have a probability distribution P(g) at frequency ω, the number of sferics exceeding the threshold S from a thunderstorm center at the distance ϱ within a certain time interval is

$$N(\rho,\omega,S) = N_0 \int_{\frac{S}{\chi b}}^{\infty} P(g)\, dg \tag{96}$$

where N_o is the total number of sferics generated within the activity center during the time interval considered.

The statistical mean of g is defined by

$$\bar{g} = \int_0^\infty g\,P(g)\,dg \qquad (97)$$

The probability function does not contain only one type of lightning, but rather represents a weighted mean of all lightning types (cloud-to-ground as well as intracloud strokes) each of these types having a stochastic distribution of electric charges stored within the channel (or of its electric moment $\overline{M}$). Therefore, the statistic mean $\bar{g}$ cannot be compared directly with one of the spectral functions in Figure 8, and it may vary with geographic location and time of day and season depending on the relative abundance of the lightning types within an activity center

The probability function P(g) can be determined from observations by counting the number of sferics arriving from an activity center which are within a certain voltage range (U_1, U_2). It is convenient to scale the voltage amplitude logarithmically

$$L = 20 \log \frac{U}{S} \qquad (L \text{ in decibel}) \qquad (98)$$

Figure 35 shows two examples of distributions of the number of sferics vs. L registered on October 10, 1979 (04 40 to 04 55 GMT) near Bonn, Germany, with the automatic equipment described in "Instrumentation," Volume II. The frequency is 5 kHz. The two distributions belong to thunderstorms situated 4600 km WNW, and 7300 km W from Bonn. The behavior of these distributions which are typical examples, is not very regular. It can be fitted by a number of Gauss distributions.

The dashed lines in Figure 35 are single Gauss curves each with the distribution

$$N\,dL = N_0 W(L)\,dL = \frac{N_0}{\sqrt{2\pi}\sigma} \exp\left\{-\frac{(L-\bar{L})^2}{2\sigma^2}\right\} dL \qquad (99)$$

with N_0 the total number per minute, $\bar{L}$ the mean, and σ the standard deviation. By transforming from L to g, one obtains a logarithmic normal distribution in g

$$W(g) = \frac{C}{\sqrt{2\pi}\sigma g} \exp\left\{-\frac{C^2}{2\sigma^2}(\ln g - \ln \bar{g})^2\right\} \qquad (100)$$

with $C = 20/\ln 10 = 8.69$ where the statistical mean of g from Equation 97 is

$$\bar{g} = \tilde{g} \exp\left(\frac{\sigma^2}{2C^2}\right) = \frac{S}{\chi b} \exp\left(\frac{\bar{L}}{C} + \frac{\sigma^2}{2C^2}\right) \qquad (101)$$

One can therefore derive the function W (g), the product $\bar{g}b$, and N_0 from the dashed lines in Figure 35. The corresponding numbers are given in Figure 35. The receiver parameter in Figure 35 is $S/\chi = 0.8\ \mu V/m/Hz$ ($L = 0$).

If the distance between receiver and activity center is known, the product $\bar{g}b$ can be determined purely experimentally. If the transmission function b is known in addition, the mean $\bar{g}$ can be found.[120] Unfortunately, the distributions in Figure 35 depend on

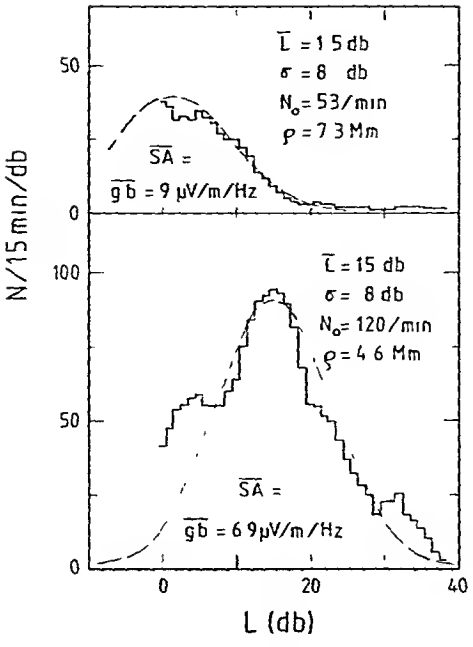

FIGURE 35. Histograms of spectral amplitudes (SA) of sferics from two thunderstorms located at 4600 km, west north west, and at 7300 km, west of Bonn, at October 10, 1979, 4.40 to 4.55 GMT. Dashed lines represent Gauss fits with the parameters indicated in the figure.

the three stochastically distributed parameters electric charge (or moment $\overline{M}$), channel length ℓ and channel diameter d (see the section "Antenna Characteristics of Lightning Currents") which may vary more or less independently from each other. Moreover, the maximum values of N in Figure 35 are often situated near or even below the receiver threshold S, thus further aggravating an exact determination of W (L). That threshold depends mainly on the dead time of the narrow band receiver. Impulses can only be recorded if they arrive at the receiver after the voltage due to a previous impulse has sufficiently decayed. In general, not more than about 1000 pulses per minute can be recorded.[120] Whether or not the secondary relative maxima in Figure 35 have any physical meaning remains to be investigated.

Spectral Amplitude Ratio (SAR) and Group Time Delay Difference (GDD)

The automatic equipment described in the chapter "Instrumentation", Volume II, records the ratio of the spectral amplitudes at the two frequencies f_1 = 5 kHz and f_2 = 9 kHz of each sferic. This spectral amplitude ratio (SAR) is given in decibels by:

$$\mathrm{SAR} = 20 \log \left| \frac{g(\omega_1)\, b(\rho,\omega_1)}{g(\omega_2)\, b(\rho,\omega_2)} \right| = 20 \log \left| \frac{\hat{G}_1(\omega_1)\, W(\rho,\omega_1)}{\hat{G}_1(\omega_2)\, W(\rho,\omega_2)} \right| \quad (102)$$

Since this ratio is independent of the moment $\overline{M}$, the number of stochastic parameters has been reduced to two (ℓ and d). Figure 36 shows as an example the SAR for the same two activity centers as in Figure 35 during the same time interval. The Gauss fit (solid lines) is clearly much better than in Figure 35, and the parameters $\overline{L}$, σ and N_o can be determined more exactly.

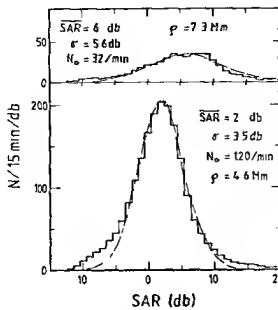

FIGURE 36 Histograms of spectral amplitude ratios (SAR) of the same two thunderstorms as in Figure 35 Dashed lines represent Gauss fits with the parameters indicated in the figure

Figure 37 shows the group time delay difference (GDD) between 6 and 8 kHz of each sferic, again for the same activity centers as in Figure 35 According to Equation 91, the GDD is proportional to the second derivative of the phase of $\hat{E}_v$, which is independent of the electric moment $\bar{M}$ The distribution also fits well to a Gauss curve The values of N_0 derived separately from the SAR and GDD are reasonably close, so they can be considered as reliable estimates of the total number of lightning strokes per minute within the activity center

Locating Thunderstorms

Multiple Station Techniques

A basic instrument for sferics measurements is the direction finder originally described by Watson-Watt and Herd,[125] by which the magnetic component of sferics is resolved using mutually perpendicular loop antennas The simultaneous measurements of the bearing angle of a sferic from two or more stations allows a determination of its location by triangulation Several sferic networks of this type are or have been operating, e g , the European sferic net of the British Meteorological Office,[130] sferic nets of the U S Air Force,[18 66] and a Japanese net [48 49]

Bearing errors of the order of several degrees are possible depending on frequency, distance, time of day and season, propagation path, and channel geometry These errors are largest in the VLF range, at distances smaller than 1000 km, during night, over a mixed propagation path (land-ocean or day-night), and for oblique channels [36 82 131] Interference of two or more sferics leads to additional bearing errors [81 85] Most of these errors are systematic errors and can be accounted for if sufficient observations at one station are available for various values of azimuth, time of day and season, and distance Apart from these bearing errors, the accuracy of this method depends on the location of the source with respect to the baselines of the sferic net Generally, only sferics at distances smaller than or comparable to the length of the baseline can be located

Bearing errors due to near distant ($\lesssim$ 1000 km) oblique lightning channels can be

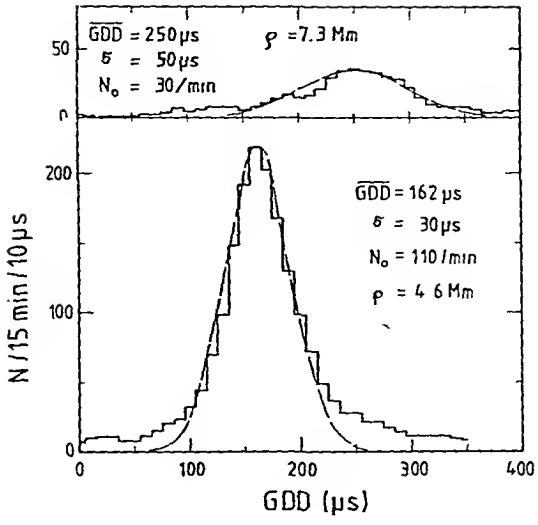

FIGURE 37. Histograms of group time delay differences (GDD) of the same two thunderstorms as in Figure 35. Dashed lines represent Gauss fits with the parameters indicated in the figure.

minimized if only the initial few microseconds of a wide band return stroke wave form are utilized.[62 118] The measurement of the difference in pulse arrival time at two or more stations is another possibility to eliminate bearing errors.[70]

Single Station Techniques

Using a net of several stations and allowing for the correction of bearing errors, the direction finding method just described can generally yield a reliable location of sferic sources. One serious disadvantage is the complex logistics required for synchronous observation at widely spaced stations. Moreover, the range is limited to distances comparable with the length of the baselines of the network.

Single station techniques can overcome these disadvantages. These techniques, which use the same direction finding methods, are all based on the wave guide characteristics of the atmospheric wave guide outlined in the section, "Pulse Dispersion in the Atmospheric Wave Guide."

At distances smaller than about 500 km, the separation between ground wave and first-hop sky wave described in "Sky Waves" (page 226) allows a determination of the distance between receiver and sferic source. Corrections are necessary due to the curved surface of the Earth[78] and the dispersion of the pulse of the ground wave (Equation 75) and of the sky wave.[95] Taylor[108] has used the separation between ground wave and first hop wave to determine the lightning stroke height. Application of this method to distances greater than 500 km should be undertaken with caution, because interference between several sky waves having group travel time differences smaller than the pulse length of the sferic prevents a unique separation of the various waves. Mode theory appropriately describes VLF- and ELF-propagation within the atmospheric wave guide beyond 1000 km. If only one mode is involved in the transport of wave energy, the Fourier component of the vertical electric field from Equation 73, and Equation 83 is (indices have again been deleted):

$$\hat{E}_z = g(\omega)\, b(\rho,\omega)\, e^{i\Psi} \qquad (103)$$

From measurements like those in Figures 35 to 37, the relationships with

$$g(\omega)\, b(\rho,\omega) \propto \frac{\overline{M\hat{G}k}}{\sqrt{\rho f}}\, e^{-\Lambda\rho} \qquad \text{(See Equation 94)}$$

and ψ from Equation 87

$$\overline{SA} = \bar{g}\, b \tag{104}$$

$$\overline{SAR} = 20 \log \frac{\overline{\hat{G}(f_1)}}{\hat{G}(f_2)} + 20 \log \frac{\sqrt{f_2}\, K(f_2)}{\sqrt{f_1}\, K(f_2)} + \frac{2 \times 10^4}{\ln 10} \left\{ A(f_2) - A(f_1) \right\} \frac{\rho}{\rho_0} = a + b\rho \tag{105}$$

$$\overline{GDD} = -\frac{\Delta f}{2\pi} \left\{ \frac{\partial^2 \overline{\Phi}}{\partial f^2} + \frac{\partial^2 B}{\partial f^2} \rho \right\} = c + d\rho \qquad (\rho_0 = 1000 \text{ km}) \tag{106}$$

can be derived $\overline{SAR}$ and $\overline{GDD}$ are linear functions of distance One can thus determine ϱ directly from Figures 36 and 37, if the parameters a, b, c, and d in Equations 105 and 106 are known The wave guide properties can be considered as constant for an observation interval of 20 min The scattering of the data in Figures 35 to 37 is therefore due to the scattering of the source properties and to interference between sferics from closely subsequent strokes The statistical approach applied in Figures 35 to 37 *yields time averaged mean source properties* $\bar{g}$, $\overline{\hat{G}(f_1)/\hat{G}(f_2)}$, *and* $\overline{\partial^2\Phi/\partial f^2}$, *which certainly* have a much smaller scatter for different thunderstorms than for individual strokes within one thunderstorm

The dependence of the factors b and d on time of day and on the propagation direction with respect to the geomagnetic field have been calculated by Harth[25,27] (see also chapter on Theory of Low Frequency Wave Propagation in Volume II) Typical values for north-to-south propagation in the northern hemisphere are

$$b = 8\ (3) \text{ db/Mm at day (night)} \qquad (f_1 = 9 \text{ kHz}, f_2 = 5 \text{ kHz}$$

$$d = 40\ (25)\ \mu\text{sec/Mm at day (night)} \qquad (f_m = 7 \text{ kHz}, \Delta f = 2 \text{ kHz})$$

These factors can vary by $\pm$ 50% for east-to-west or west-to-east propagation The factors derived from Figures 36 and 37 valid for west-to-east propagation at night are

$$a = -5 \text{ db}, \quad b = 1.5 \text{ db/Mm}, \quad c = 9\ \mu\text{s}, \quad d = 33\ \mu\text{s/Mm} \tag{107}$$

The mean values of the source terms are contained in a and c The factor

$$20 \log \left\{ \sqrt{f_2/f_1}\ \left(K(f_1)/K(f_2) \right) \right\} \simeq -3 \text{ db}$$

Table 5
SOURCE TERMS OF SAR AND GDD

Type	Stroke	SAR (9/5) (db)	GDD (7/2) (μs)
		$20 \log\{\hat{G}(f_1)/\hat{G}(f_2)\}$	$-\frac{\Delta f}{2\pi}\,\partial^2\Phi/\partial f^2$
1	R_f	0.74	4.2
	R_s	0.002	0.3
2	R_f	−6.0	19.4
	R_s	−1.2	13.2
	K	5.3	−0.2

Note. Source terms of SAR and GDD of the type 1 and type 2 strokes considered in Tables 2 and 3. The frequencies involved are: f_1 = 9 kHz, f_2 = 5 kHz (SAR); f_m = 7 kHz, Δf = 2 kHz (GDD).

must be added to the source terms in a. Table 5 gives average source terms for the four typical strokes considered in Tables 2 and 3. Since the intracloud strokes are probably of minor importance at great distances and at frequencies smaller than 10 kHz, the main contribution to SAR and GDD comes from the type 2 R strokes.

Locating thunderstorm centers with the SAR and GDD method has been performed by Volland et al.,[121] Frisius et al.,[20] Harth,[26] Harth and Pelz,[29] Frisius and Heydt,[19] Heydt,[33] and Harth.[28] A new network of automatically operating atmospherics analyzers was installed in early 1980.[99]

The interference of several modes gives rise to some ambiguity in the interpretation of the data at distances between about 500 and 2000 km. Fortunately, the simultaneous use of GDD and SAR can be used to help resolve that ambiguity (see "Frequency of Low Wave Propagation", Volume II). At distances smaller than about 300 km, however, the GDD and SAR approach is no longer possible.

The measurement of the difference in the arrival times of VLF/ELF pulses, as discussed in the section "Phase Velocity and Group Time Delay,"[41,52,94,109] is another GDD approach. It also leads to a linear relationship between distance and GDD Equation 93. Hepburn and Pierce[31] established experimentally empirical laws such as Equation 93. Their value δ is approximately equal to GDD in Equation 93:

$$\delta = t + \tau/4 = \begin{cases} 0.15 + 0.56\,\rho \text{ (day)} \\ 0.36 + 0.21\,\rho \text{ (night)} \end{cases} \qquad (108)$$

(δ in ms; ρ in Mm)

Here, t is the time separation between oscillation head and the slow tail, and $\tau/4$ is the first quarter cycle of the slow tail.

Contrary to the GDD method in the lower VLF band, which allows a statistical approach, the GDD measurement at VLF/ELF can only be applied to single sferics

having significant amplitudes of their slow tails Thus, the source term c in Equation 108 is expected to scatter widely for each individual sferic as is obvious from Figure 37

All single station techniques have the disadvantage that it is impossible to separate the source terms from the propagation terms directly from the measurements They also suffer from the same bearing errors as do the multistation techniques However, given some independent check of the location of the sources, it should be possible to arrive at empirical formulae for each station depending on azimuth, time of day, and season, which allows a localization of thunderstorm sources with an accuracy of at least 5%

Determination of Propagation Characteristics

Attenuation Rate

Sferics provide a means for studying the VLF and ELF characteristics of the atmospheric wave guide Since virtually no commercial transmitters operate at frequencies under 10 kHz, lightning strokes are the only available transmitters in that frequency range

The determination of SA, SAR, and GDD as explained in the last section is one way to derive the factors A and B of the transmission function (Equation 83) at one frequency Another method is to determine the attenuation factor A as a function of frequency from individual sferic wave forms as follows If the wave form of the same sferic is observed at two known distances ϱ_1 and ϱ_2, a Fourier transformation can yield the spectral functions $\hat{E}_z(\varrho_1, f)$ and $\hat{E}(\varrho_2, f)$ Provided only one mode is involved, the attenuation rate α (in db/Mm) at frequency f is obtained from Equation 83 to be

$$\alpha(f) = \kappa A = \frac{1}{(\varrho_2 - \varrho_1)} \left\{ 20 \log \left| \frac{\hat{E}_z(\varrho_1, f)}{\hat{E}_z(\varrho_2, f)} \right| + 10 \log \frac{\sin\Theta_2}{\sin\Theta_1} \right\} \tag{109}$$

with

$$\kappa = \frac{2 \times 10^4}{\ln 10} = 8686 \quad (\varrho \text{ in Mm})$$

This method has been utilized by many people Figure 38 shows some earlier determinations of α within the ELF and VLF range as summarized by Chapman et al [13] The minimum attenuation near 15 to 20 kHz and the region of maximum attenuation near 2 kHz are clearly visible Other data compilations have been made by Croom,[15] Rao,[93] and Watt[123] (see also References 3, 9, and 53) ELF attenuation rates derived from slow tail sferics are given by Jean et al ,[54] Sao et al ,[98] Taylor and Sao,[109] and Hughes and Gallenberger [42] Figure 39A shows Taylor and Sao's[109] results in the range 20 to 400 Hz during nighttime conditions for east-to-west and for west-to-east propagation Russian work on attenuation rates in the frequency range from 60 to 30 kHz has been summarized by Alpert et al [1]

Phase Velocity

The propagation factor B of the transmission function W in Equation 83 is a measure of the phase velocity at frequency f (Equation 88) Given the phases $\Psi(\varrho_i, f)$ of the same spectral functions $\hat{E}_z(\varrho_i, f)$ as in Equation 109 at two distances ϱ_1 and ϱ_2, B

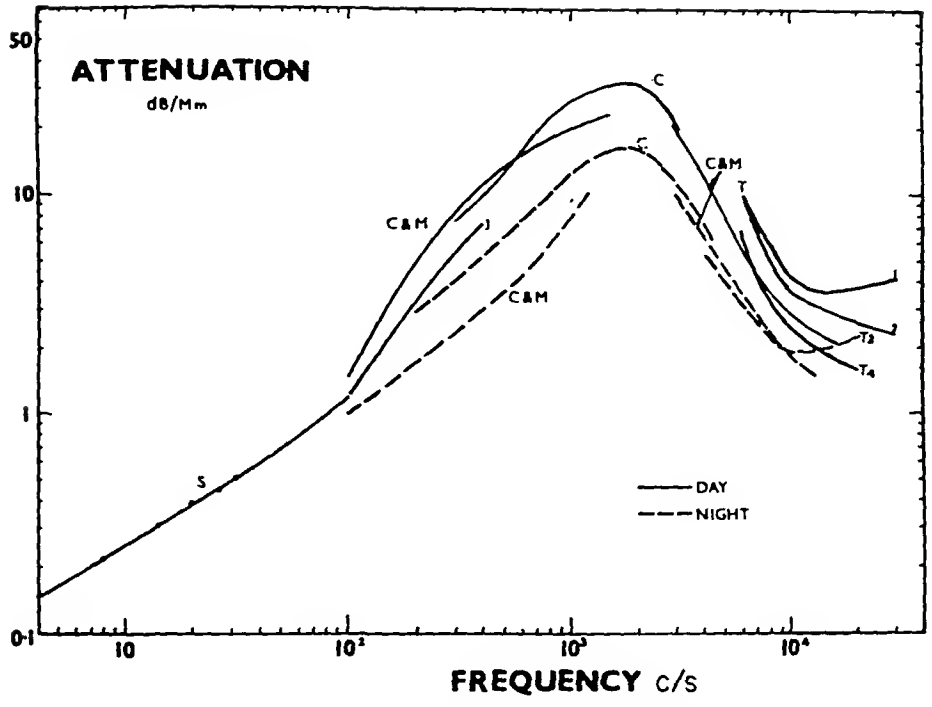

FIGURE 38 Variation of attenuation rate α with frequency during day and during night S from Schumann resonances; C and M from Chapman and Macario,[12] C from two station observations; T from Taylor, W. and Lange, J.[133] (From Chapman, F W., et al ,[13] *Radio Sci.*, I, 1273, 1966. With permission. Copyrighted by American Geophysical Union)

can be eliminated, and the phase velocity can be derived from

$$v_p = \frac{\omega(\rho_1 - \rho_2)}{\left\{\Psi(\rho_1,f) - \Psi(\rho_2,f)\right\}} \tag{110}$$

Figure 40 shows the ratio v_p/c vs. frequency for both day and night conditions as derived from sferics observations[13] (see also References 9 and 122). One notices the region of $v_p/c > 1$ in the VLF range and the decrease of v_p/c to values less than unity in the ELF range. Figure 39B shows the behavior of v_p/c in the ELF range for west-to-east and for east-to-west propagation at night.[109] Hughes and Gallenberger[42] evaluated slow tail sferics propagating over a mixed day-night path to determine the phase velocity.

Integrated Atmospherics Activity

Omnidirectional Observations

The most frequently used methods to record atmospheric noise are to either count sferic pulses arriving from all directions that exceed a given threshold of a narrow band or a broad band receiver, or to integrate the output voltage of all the pulses. It is not a trivial matter to compare results from different types of receivers (e.g., References 32 and 37), and the interpretation of the data is often rather ambiguous. If sferics are counted by a narrow band receiver, the number of sferics arriving from all directions depends on the frequency f and the threshold S is (see Equation 96):

$$N(f,S) = a \int_0^{a\pi} \int_0^{2\pi} n(\rho,\phi) \sin\frac{\rho}{a}\, d\rho\, d\phi \int_S^{\infty} \frac{P\left\{g(f)\right\} dg}{\chi\, b\,(\rho,\phi,f)} \tag{111}$$

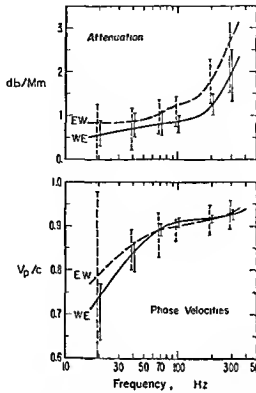

FIGURE 39 Average attenuation rates α and phase velocities in the ELF range derived from slow tail atmospherics Solid curves W-E propagation, Dashed curves E-W propagation Vertical lines error bars (From Taylor, W L and Sao K , *Radio Sci* , 5, 1453 1970 With permission Copyrighted by American Geophysical Union)

where $n(\varphi, \phi)$ is the number density of sferics per area and time, and a is the radius of the Earth

Obviously, it is impossible to quantitatively separate propagation effects from source effects Nevertheless, the data obtained by these methods are useful for telecommunication system performance More details on this subject are given in the chapter on Atmospheric Noise by Spaulding in this volume

Figure 41 shows as an example the daily variation of the impulse rate observed at 27 kHz in Kuhlungsborn, East Germany and in Spitzbergen during summer 1958 (left panels) and during summer 1962 (right panels) [23] The nighttime attenuation rate of the atmospheric wave guide is small at middle and low latitudes Although near field sources are absent in Kuhlungsborn, sferics from large distances (mainly from Middle and South America) arrive at the receiver and give rise to the high level The attenuation reaches a maximum at sunrise Since local sources are still weak at this time, the counting rate reaches its absolute minimum (points d in Figure 41) Local sources in Kuhlungsborn predominate during the day, while the distant sources are suppressed due to the large daytime attenuation of the wave guide The counting rate attains its maximum during the afternoon at points e The attenuation maximum at sunset is responsible for the relative minimum at points f Finally, the increase to nighttime condition takes place with a maximum at points g in the Kuhlungsborn records. That maximum occurs before midnight since local sources still contribute at this time in addition to the far field sources

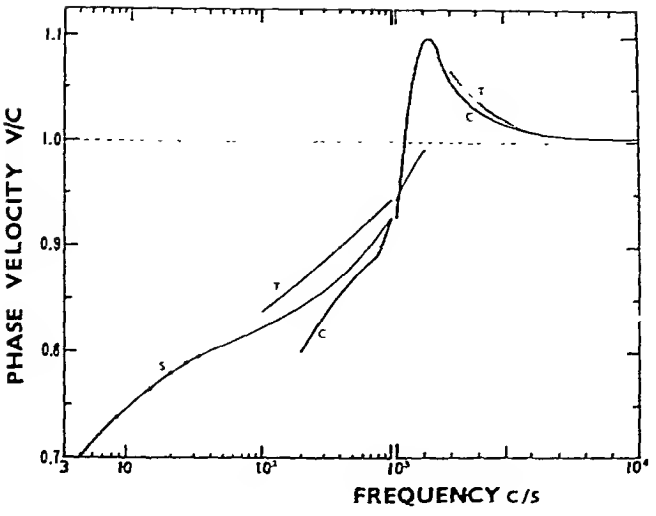

A

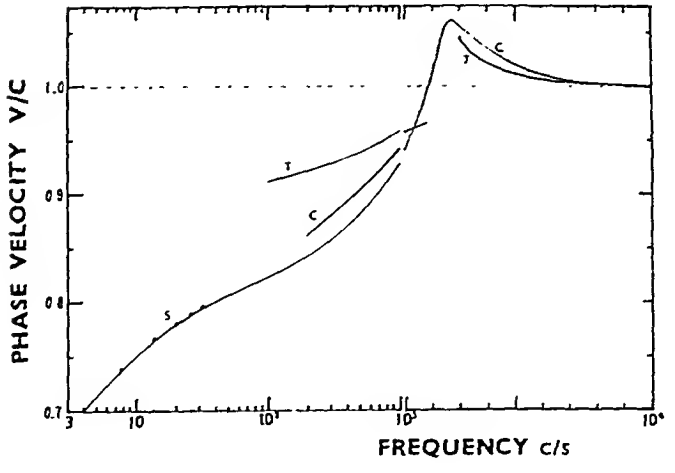

B

FIGURE 40. (A) Daytime variation of phase velocity with frequency. Results derived from S, Schumann resonances; T, single-station observations, and C, two-station observations. (B) Nighttime variation. (From Chapman, F. W. et al., *Radio Sci.*, 1, 1273, 1966. With permission. Copyrighted by American Geophysical Union.)

The arctic stations in Spitzbergen register mainly sferics from far field sources because the local thunderstorm activity is virtually absent. Therefore, the counting rate in Figures 41B and 41D represents mainly the daily variation of the attenuation rate of the atmospheric wave guide. The time differences of the maxima and minima at points e, d and f at Kühlungsborn and Spitzbergen are particularly good indicators of the influence of the local sources at the midlatitude station. Since the sun does not set at Spitzbergen during summer, the propagation from the main sources south of Spitzbergen during night is over a mixed day-night path with an extremely high attenuation rate. The counting rates at night thus do not reach the daytime values in Figures 41B

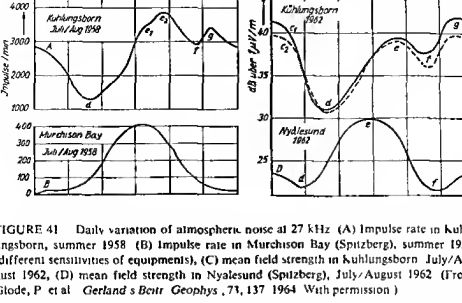

FIGURE 41 Daily variation of atmospheric noise at 27 kHz (A) Impulse rate in Kuhlungsborn, summer 1958 (B) Impulse rate in Murchison Bay (Spitzberg), summer 1958 (different sensitivities of equipments), (C) mean field strength in Kuhlungsborn July/August 1962, (D) mean field strength in Nyalesund (Spitzberg), July/August 1962 (From Glode, P et al *Gerland's Beitr Geophys*, 73, 137 1964 With permission)

and 41D During northern winter, however, the counting rates at the stations have their maximum at night [76]

The sunspot cycle also influences the attenuation rate For example, the attenuation decreases with increasing sunspot number during daylight hours The daytime maximum at point e in Figure 41A (sunspot maximum) is thus larger than the nighttime maximum at point g contrary to the behavior in Figure 41C during the declining phase of the sunspot cycle The missing minima at points d and f in Figure 41B during the sunspot maximum are probably also related to the sunspot cycle effect

More recent observations of VLF integrated atmospheric noise have been reported by Clarke et al ,[14] Ibukun,[45 46] Schoute-Vanneck and Wright,[102] Schaning and Cumme,[100] and Huang [40] A nearly complete bibliography about sferics observations before 1970 can be found in Israel's[47] work

Narrow Sector Observations

The combination of integrated atmospheric noise measurements with direction finding methods at a preset receiver threshold eliminates one degree of ambiguity in Equation 111 and gives a number $\Delta N(f, S, \phi)$ of sferics arriving from within a narrow sector $\Delta\phi$ at azimuth ϕ In fact, it largely resolves the ambiguity concerning the distribution of n (ϱ, ϕ) along the direction ϕ, because experience shows that thunderstorm centers are normally concentrated within relatively small areas not much larger than 100 × 100 km in extent The signals arriving from one narrow sector therefore belong mainly to the nearest thunderstorm center along that direction Of course, the distance to that center cannot be determined from those observations

Lugeon[73] has developed a narrow sector recorder which allows continuous recordings in simple fashion (see also Reference 76) Modern computer techniques are able to document the morphology of the diurnal and annual variations by isocontours Figure 42 shows a contour plot of sferic rates at 5 kHz arriving from a receiving sector of 12° width during a time interval of 2 min [36] The values shown are monthly means obtained during 1971 and 1972 in San Miguel, near Buenos Aires, Argentina Sources from the South American continent located mainly north and northeast of San Miguel are the primary sources in Figure 42 Oceanic regions comprise only a minor contribution to the observed sferic rate Two maxima, marked 1 and 2 in Figure 42, occurred

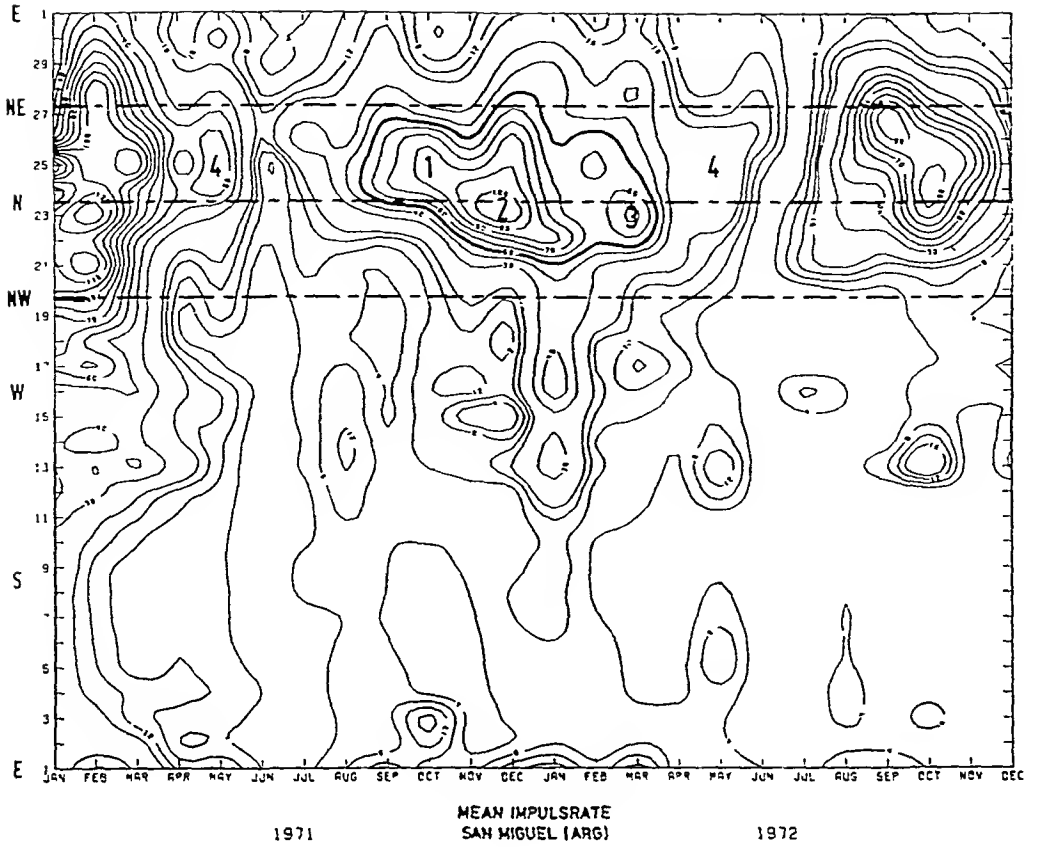

FIGURE 42. Monthly mean atmospherics rate at 5 kHz as a function of direction of incidence during 1971 to 1973 in San Miguel, Argentina. The intensity along each contour is constant. (From Harth, W. et al., *J. Geophys. Res.*, 83, 6231, 1978. With permission. Copyrighted by American Geophysical Union.)

in southern summer 1971/72. The later maximum marked 3 is followed by a weaker spur labeled 4. Most of these sources are within 2000 km of San Miguel. Remarkable is the repetition of the summer structures from one year to the next.

The daily mean during September to December 1971 observed in San Miguel is plotted in Figure 43.[134] It clearly shows quasi-periodic changes in the strength of the main source north of San Miguel with typical repeat periods of 2 to 6 days. These are evidently related to tropospheric planetary waves.

Sudden Enhancement (SEA) and Sudden Decrease (SDA) of Atmospherics

The role of the upper boundary for VLF/ELF propagation in the atmospheric wave guide, the ionospheric D layer during the day, and the E layer at night, has been stressed repeatedly in the previous sections. In particular, the increase of the virtual height and the improvement of the reflection characteristics of the upper boundary at night have been discussed (see also the chapter, "Theory of Low Frequency Wave Propagation", Volume II). The ionospheric electron density profile can be determined from observed spectral attenuation rates from sferics.[10,38,43,44]

Solar flares can increase the electron density of the daytime ionospheric D layer by orders of magnitude within a time interval of 5 to 10 min. The whole event lasts for about 1 hr before normal conditions are restored (e.g., Whitten and Poppoff[129]). The virtual reflection height h can decrease during such an event by as much as 10 km

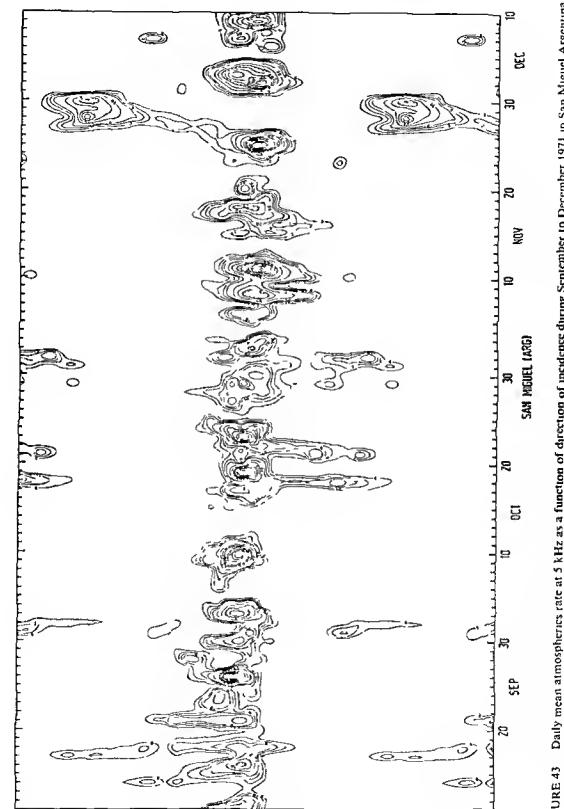

FIGURE 43 Daily mean atmospherics rate at 5 kHz as a function of direction of incidence during September to December 1971 in San Miguel Argentina The intensity along each contour is constant (Courtesy of Harth, W Scientist, Institute for Radioastronomy Bonn)

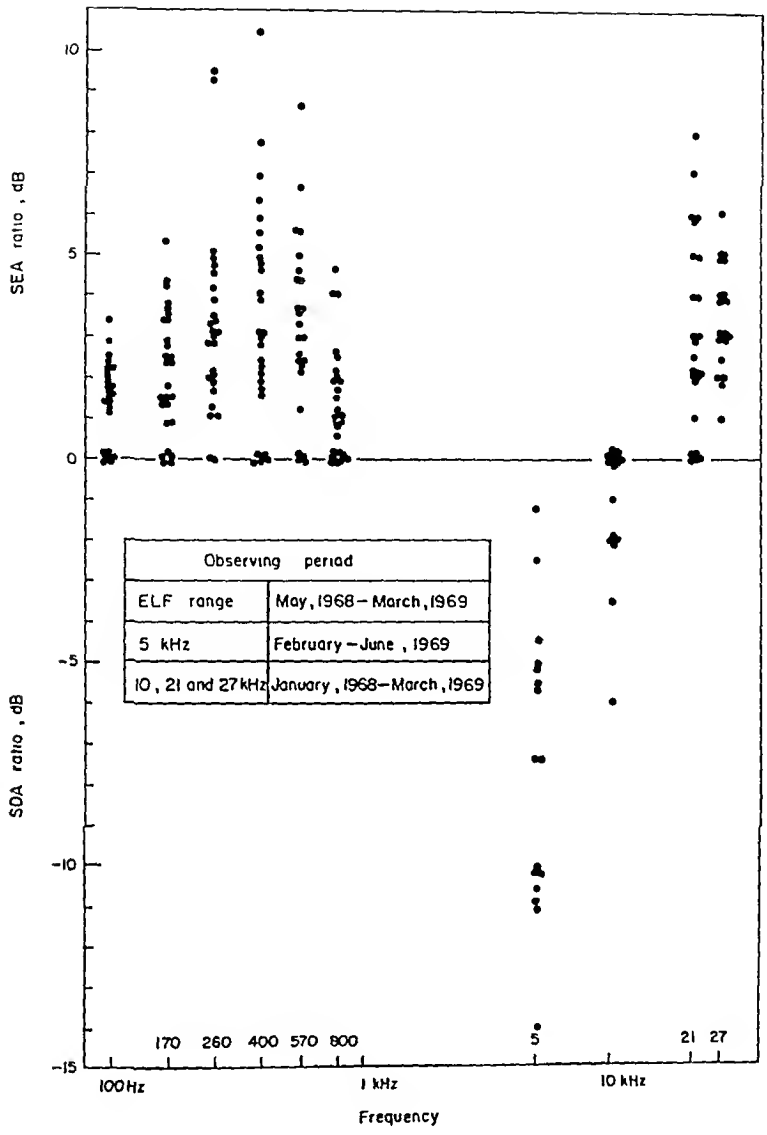

FIGURE 44. Frequency spectrum of SEA and SDA ratio. (From Sao, K., Yamashita, M., Tanahashi, S., Jindoh, H., and Ohta, K., *J. Atmos. Terr. Phys.*, 32, 1567, 1970. With permission.)

depending on the strength of the solar flare, and the attenuation rate increases correspondingly as function of frequency. The integrated sferics rate reacts to such events as shown in Figure 44. The sferics rate increases at frequencies larger than about 15 kHz with the strongest effect near 30 kHz (sudden enhancement of atmospherics or SEA). It decreases between about 15 and 1 kHz (sudden decrease of atmospherics or SDA) with the strongest effect near 5 kHz, and increases again in the lower ELF range. The SEA in the VLF range was first recorded by Bureau,[8] and the SDA in the lower VLF range was detected by Gardner.[22] The SEA in the ELF range was detected by Sao et al.[96] Local thunderstorm centers ($\varrho < 2000$ km) contribute mainly to the sferics noise during daytime at middle and lower latitudes. The ratio between the spectral amplitude

of the dominant mode during disturbed (D) and normal (N) conditions (Equation 83) is

$$\left|\frac{\hat{E}_D}{\hat{E}_N}\right| = \frac{h_N}{h_D} e^{(A_N - A_D)\rho} \qquad (112)$$

with $h_D < h_N$ and $A_D > A_N$

In the range of minimum attenuation in the upper VLF band and in the lower ELF band (see Figures 38 and 39), the influence of the height factor h_N/h_D in Equation 112 on the amplitude ratio outweighs that of the attenuation rate for medium distant sferic sources ($\rho < 2000$ km) The amplitude ratio (Equation 112) thus increases, causing an SEA The situation is reversed in the range of maximum attenuation within the lower VLF band, and an SDA is expected This qualitatively explains the result of Figure 44 More details on the observation and theory of SEAs and SDAs can be found in Obayashi,[83] Pierce,[87] Kamada,[36 37] Volland,[105] Sao et al ,[36 87] Tříška and Laštovička,[112] and Harth [46]

Nuclear events can create disturbances in the height distribution of the ionospheric ionization, the most significant processes occurring at altitudes between 60 and 100 km The effects on VLF propagation are therefore very similar to those during solar flare events (e g , Pierce[48]) Observations of SEAs and SDAs during nuclear explosions have been reported by Kimpara[50] and Kamada [38]

Nuclear explosions produce also electromagnetic pulses (EMP) [74] Sensors to detect EMP inside and away from nuclear source regions are described by Baum et al [4]

REFERENCES

1 Alpert, J L , Fligel, D S , and Michailova, G A , The propagation of atmospherics in the earth-ionosphere waveguide *J Atmos Terr Phys* , 29, 29, 1967

2 Arnold, H R and Pierce, E T , Leader and junction processes in the lightning discharge as a source of VLF atmospherics *Radio Sci* ,68D, 771, 1964

3 Barr, R , The ELF and VLF amplitude spectrum of atmospherics with particular reference to the attenuation band near 3 kHz *J Atmos Terr Phys* ,32 977 1970

4 Baum, C E , Breen, E L , Giles, J C , O'Neill, J , and Sower, G D , Sensors for electromagnetic pulse measurements both inside and away from nuclear source regions, *IEEE Transact Antennas Propag* ,26 22 1978

5 Berger, K , The earth flash, in *Lightning Vol 1*, Golde R H Ed , Academic Press London, 1977, 119

6 Brook, M and Ogawa, T , The cloud discharge in *Lightning Vol 1*, Golde, R H , Ed , Academic Press, London, 1977, 191

7 Bruce, C E R and Golde, R H , The lightning discharge *J Inst Electr Eng* 88 (Part II) 487, 1941

8 Bureau, R , Abnormalities of the ionosphere and bright solar eruptions, *Nature (London)*, 139, 110, 1937

9 Challinor, R A , The phase velocity and attenuation of audio-frequency electromagnetic waves from simultaneous observations of atmospherics at two spaced stations, *J Atmos Terr Phys* , 29, 803, 1967

10 Challinor, R A , The interpretation of recently measured propagation constants for audio frequency electromagnetic waves in terms of model ionosphere profiles, *J Atmos Terr Phys* 29, 995, 1967

11 Chalmers, J A , The so called "induction" component in the electric field of a lightning discharge, *J Atmos Terr Phys* ,27, 1027, 1965

12. Chapman, F. W. and Macario, R. C. V., Propagation of audio-frequency radio waves to great distances, *Nature (London)*, 177, 930, 1956.
13. Chapman, F. W., Jones, D. L., Todd, S. D. W., and Challinor, R. A., Observations on the propagation constant of the earth-ionosphere wave guide in the frequency band 8 c/s to 16 kc/s, *Radio Sci.*, 1, 1273, 1966.
14. Clarke, C., Bradley, P. A., and Mortimer, D. E., Characteristics of atmospheric radio noise observed at Singapore, *Proc. IEE (London)*, 112, 849, 1965.
15. Croom, D. L., The frequency spectra and attenuation of atmospherics in the range 1 — 15 kHz, *J. Atmos. Terr. Phys.*, 26, 1015, 1964.
16. Dennis, A. S., and Pierce, E. T., The return stroke of the lightning flash to earth as a source of VLF atmospherics, *Radio Sci.*, 68D, 777, 1964.
17. Fisher, R. J. and Uman, M. A., Measured electric field risetimes for first and subsequent lightning return strokes, *J. Geophys. Res.*, 77, 399, 1972.
18. Freeman, W. B., The distribution of thunderstorm and lightning parameters over the eastern hemisphere for 1972, M.S. thesis, Texas A & M University, College Station, May 1974.
19. Frisius, J. and Heydt, G., Statistical analysis of data from the atmospherics analyzer, in Proc. Waldorf Conference on Long Range Geographic Estimation of Lightning Sources, NRL Report 7763, Naval Research Laboratory, Washington, D.C., 1974, 381.
20. Frisius, J., Heydt, G., and Harth, W., Observations of parameters characterizing the VLF atmospherics activity as function of azimuth, *J. Atmos. Terr. Phys.*, 32, 1403, 1970.
21. Galejs, J., *Terrestrial Propagation of Long Electromagnetic Waves*, Pergamon Press, Oxford, 1972.
22. Gardner, F. F., The use of atmospherics to study the propagation of very long radio waves, *Philos. Mag.*, 41, 1259, 1950.
23. Glöde, P., Lauter, E. A., and Schäning, B., Daily variations of VLF atmospheric noise during summer at different latitudes, *Gerland's Beitr. Geophys.*, 73, 137, 1964.
24. Gupta, S. P., Rao, M., and Tantry, B. A. P., VLF spectra radiated by stepped leaders, *J. Geophys. Res.*, 77, 3924, 1972.
25. Harth, W., The description of VLF atmospherics parameters with the Wait-Walters-model, *Z. Geophys.*, 38, 153, 1972.
26. Harth, W., VLF atmospherics: their measurement and interpretation, *Z. Geophys.*, 38, 815, 1972.
27. Harth, W., The delay time difference and the amplitude ratio of spectral groups within various propagation models, in Proc. Waldorf Conference on Long Range Geographic Estimation of Lightning Sources, NRL Report 7763, Naval Research Laboratory, Washington, D.C., 1974, 147.
28. Harth, W., Daily variation of VLF atmospherics parameters for long-lasting thunderstorms, in Proc. Waldorf Conference on Long Range Geographic Estimation of Lightning Sources, NRL Report 7763, Naval Research Laboratory, Washington, D.C., 1974, 462.
29. Harth, W. and Pelz, J., Eastern thunderstorms located by VLF atmospherics parameters, *Radio Sci.*, 8, 117, 1973.
30. Harth, W., Hofmann, C. A., Falcoz, H., and Heydt, G., Atmospherics measurements in San Miguel, Argentina, *J. Geophys. Res.*, 83, 6231, 1978.
31. Hepburn, F. and Pierce, E. T., Atmospherics with very low frequency components, *Nature (London)*, 171, 837, 1953.
32. Heydt, G., Remarks on the comparability of VLF atmospherics counters in small band and wide band receivers, *Meteor. Rundsch.*, 25, 20, 1972.
33. Heydt, G., Observation of single storm complexes with the atmospherics analyser network, in Proc. Waldorf Conference on Long Range Geographic Estimation of Lightning Sources, NRL Report 7763, Naval Research Laboratory, Washington, D.C., 1974, 420.
34. Hill, R. D., Electromagnetic radiation from the return stroke of a lightning discharge, *J. Geophys. Res.*, 71, 1963, 1966.
35. Hill, R. D., A survey of lightning energy estimates, *Rev. Geophys. Space Phys.*, 17, 155, 1979.
36. Horner, F., Very low frequency propagation and direction-finding, *Proc. IEE (London)*, 104, 73, 1957.
37. Horner, F., Analysis of data from lightning-flash counters, *Proc. IEE (London)*, 114, 916, 1967.
38. Horner, F., The use of atmospherics for studying the ionosphere, *J. Atmos. Terr. Phys.*, 32, 609, 1970.
39. Horner, F. and Bradley, P. A., The spectra of atmospherics from near lightning discharges, *J. Atmos. Terr. Phys.*, 26, 1155, 1964.
40. Huang, Y-N., Variations of atmospheric radio noise at Ping-Cheng, Taiwan, China, *Radio Sci.*, 12, 239, 1977.
41. Hughes, H. G., On the directional dependency of "slow tail" extremely low-frequency atmospheric waveforms, *J. Atmos. Terr. Phys.*, 29, 545, 1967.

42 Hughes, H G and Gallenberger, R J , Propagation of extremely low-frequency (ELF) atmospherics over a mixed day-night path, *J Atmos Terr Phys* , 36, 1643, 1974

43 Hughes, H G and Pappert, R A , Propagation prediction model selection using VLF atmospherics, *Geophys Res Lett* , 2, 96, 1975

44 Hughes, H G, Gallenberger, R J , and Pappert, R A , Evaluation of nighttime exponential ionospheric models using VLF atmospherics, *Radio Sci* , 9, 1109, 1974

45 Ibukun, O , On the predictions of atmospheric radio noise levels in the tropics, *J Atmos Terr Phys* , 27, 1059, 1965

46 Ibukun, O , Variations of radio noise parameters at a tropical station, *J Atmos Terr Phys* , 27, 1081, 1965

47 Israel, H , *Atmospheric Electricity, Volume II* Israel Program for Scientific Translations, Jerusalem, 1973

48 Iwai, A , Ohtsu, J , Nishino, M , and Kashiwagi, M , A new direction finding network for locating the sources of atmospherics, *Proc Res Inst Atmos Nagoya Univ* , 16, 17, 1969

49 Iwai, A , Kashiwagi, M , Nishino, M , and Satoh, M , Triangulation direction finding network for fixing the sources of atmospherics, *Proc Res Inst Atmos Nagoya Univ* , 26 1, 1979

50 Iwata, A , Calculation of waveforms radiating from return strokes, *Proc Res Inst Atmos Nagoya Univ* 17, 115 1970

51 Iwata, A , Calculation of wave forms radiating from return strokes (2) *Proc Res Inst Atmos Nagoya Univ* 18, 103, 1971

52 Iwata, A , Ishikawa, H , and Takagi, M , Slow tail atmospherics and their origin, *Proc Res Inst Atmos Nagoya Univ* 17, 13, 1970

53 Jayendran, A , A study of ELF and VLF radiowave propagation in the south north direction near the magnetic equator, *J Atmos Terr Phys* 33 13, 1971

54 Jean, A G , Murphy, A C , Wait, J R , and Wasmundt, D F , Observed attenuation rate of ELF radio waves, *J Res Nat Bur Stand* 65D, 475, 1961

55 Jones, D L , Electromagnetic radiation from multiple return strokes of lightning *J Atmos Terr Phys* 32 1077 1970

56 Kamada, T , Statistical properties of the sudden enhancement of atmospherics in the VLF range, *Proc Res Inst Atmos Nagoya Univ* , 7, 28, 1960

57 Kamada, T , Mode IV sudden enhancement of atmospherics, *Proc Res Inst Atmos Nagoya Univ* , 8, 7, 1961

58 Kamada, T , SEA effect due to high altitude nuclear explosion *Proc Res Inst Atmos Nagoya Univ* , 12, 19, 1965

59 Kimpara, A , The wave form of atmospherics in the daytime and at night, *Proc Res Inst Atmos Nagoya Univ* 4, 1, 1956

60 Kimpara, A , SEA phenomena due to nuclear explosion, *Proc Res Inst Atmos Nagoya Univ* , 7, 89 1960

61 Kinzer, G D , Cloud to ground lightning versus radar reflectivity in Oklahoma thunderstorms, *J Atmos Sci* , 31, 787, 1974

62 Krider, E P , Noggle, R C , and Uman, M A , A gated, wideband magnetic direction finder for lightning return strokes, *J Appl Meteorol* , 15, 301, 1976

63 Krider, E P , Radda, G J , and Noggle, R C , Regular radiation field pulses produced by intracloud lightning discharges, *J Geophys Res* , 80, 3801, 1975

64 Krider, E P , Weidman, C D , and Noggle, R C , The electric fields produced by lightning stepped leaders, *J Geophys Res* , 82, 951, 1977

65 Krider, E P , Weidman, C D , and LeVine, D M , The temporal structure of the HF and VHF radiation produced by intracloud lightning discharges, *J Geophys Res* , 84, 5760, 1979

66 Krider, E P , Piper, A E , and Uman, M A , An automatic location system for cloud to-ground lightning, in *Proc Symposium on Lightning Technology*, NASA Conference Publ 2128, FAA-RD 80-30, NASA Langley Research Center, Hampton, Va , 1980, 205

67 Laby, T H , McNeill, J J , Nicholls, F G , and Nickson, A F B , Wave form, energy and reflection by the ionosphere of atmospherics, *Proc R Soc London Ser A* , 174, 145, 1940

68 Leise, J A and Taylor, W L , A transmission line model with general velocities for lightning, *J Geophys Res* , 82, 391, 1977

69 LeVine, D M and Meneghini, R , Simulation of radiation from lightning return strokes The effect of tortuosity, *Radio Sci* , 13, 801, 1978

70 Lewis, E A , Harvey, R B , and Rasmussen, J E , Hyperbolic direction finding with sferics of transatlantic origin, *J Geophys Res* , 65, 1879, 1960

71 Lin, Y T. and Uman, M A , Electric radiation fields of lightning return strokes in three isolated Florida thunderstorms, *J Geophys Res* , 78, 7911, 1973

72. Lin, Y. T., Uman, M. A., Tiller, J. A., Brantley, R. D., Beasley, W. H., Krider, E. P., and Weidman, C. D., Characterization of lightning return stroke electric and magnetic fields from simultaneous two-station measurements, *J. Geophys. Res.*, 84, 6307, 1979.
73. Lin, Y. T., Uman, M. A., and Standler, R. B., Lightning return-stroke models, *J. Geophys. Res*, 84, 1571, 1980.
74. Longmire, C. L., On the electromagnetic pulse produced by nuclear explosions, *IEEE Trans. Antennas Propag.*, 26, 3, 1978.
75. Lugeon, J., Le radiogoniographe de la station centrale Suisse de Meteorologie et son utilisation pour la prévision du temps, *Ann. Meteorol. Zentralamt*, 76, 433, 1939.
76. Lugeon, J., Junod, A., Wasserfallen, P., and Rieker, J., Mesures des parasites atmospheriques d'électricité atmosphérique et de radioactivité de l'air à Murchison Bay (Spitzberg), Payerne et Zurich, Zürich, 1960.
77. Malan, D. J. and Schonland, B. E. J., The distribution of electricity in thunderclouds, *Proc R Soc. London Ser. A.*, A209, 158, 1951.
78. McDonald, T. B., Uman, M. A., Tiller, J. A., and Beasley, W. H., Lightning location and lower-ionospheric height determination from two-station magnetic field measurement, *J Geophys Res* 84, 1727, 1979.
79. McLain, D. K. and Uman, M. A., Exact expression and momentum approximation for the electric field intensity of the lightning return stroke, *J. Geophys Res.*, 76, 2101, 1971
80. Nakai, T., The distance of the source and the height of reflection deduced from the waveforms of ionospheric reflection type, *Proc. Res. Inst. Atmos. Nagoya Univ*, 4, 20, 1956
81. Nakai, T. and Frisius, J. , The random scatter of spectral parameters of VLF-atmospherics, *J. Atmos. Terr. Phys.*, 40, 61, 1978.
82. Nishino, M., Kashiwagi, M., and Iwai, A., Error investigation for the location of the sources of atmospherics by radio direction finding, *Proc. Res. Inst Atmos Nagoya Univ.*, 19, 1, 1972.
83. Obayashi, T., Measured frequency spectra of very low frequency atmospherics, *J Res Nat Bus. Stand.*, 64D, 41, 1960.
84. Oetzel, G. N., Computation of the diameter of a lightning return stroke, *J Geophys. Res* , 73, 1889, 1968.
85. Outsu, J. and Shiga, T., Calculation of interference error on a crossed-loop type CRDF, *Proc. Res Inst. Atmos. Nagoya Univ.*, 2, 63, 1955.
86. Pierce, E. T., Some ELF phenomena, *J. Res Nat. Bur. Stand.*, 64D, 383, 1960.
87. Pierce, E. T., Attenuation coefficients for propagation at very low frequencies (VLF) during a sudden ionospheric disturbance (SID), *J. Res. Nat. Bur. Stand.*, 65D, 543, 1961
88. Pierce, E. T., Nuclear explosion phenomena and their bearing on radio detection of the explosions, *Proc. IEEE*, 53, 1994, 1965.
89. Pierce, E. T., Atmospherics and radio noise, in *Lightning, Vol. 1*, Golde, R. H , Ed , Academic Press, London, 1977, 351.
90. Price, G. H. and Pierce, E. T., The modeling of channel current in the lightning return stroke, *Radio Sci.*, 12, 381, 1977.
91. Rai, J., Current and velocity of the return stroke lightning, *J. Atmos. Terr Phys* , 40, 1275, 1978.
92. Rai, J. and Bhattacharya, P. K., Impulse magnetic flux density close to the multiple return strokes of a lightning discharge, *J. Phys. D.*, 4, 1252, 1971.
93. Rao, M., Some experimental results of the study of VLF-propagation by means of sferics, *J Atmos. Terr. Phys.*, 30, 1667, 1968.
94. Sao, K. and Jindoh, H., Real time location of atmospherics by single station techniques and preliminary results, *J. Atmos. Terr. Phys.*, 36, 261, 1974.
95. Sao, K. and Shiga, T., Some considerations of the wave form of atmospheric due to ionospheric reflection, *Proc. Res. Inst. Atmos. Nagoya Univ.*, 3, 47, 1955.
96. Sao, K., Yamashita, M., and Jindoh, H., SEA phenomena on e.l.f. atmospherics, *J. Atmos Terr. Phys.*, 28, 97, 1966.
97. Sao, K., Yamashita, M., Tanahashi, S., Jindoh, H., and Ohta, K., Sudden enhancements (SEA) and decreases (SDA) of atmospherics, *J. Atmos. Terr. Phys.*, 32, 1567, 1970.
98. Sao, K. Yamashita, M., Tanahashi, S., and Taylor, W. L., Genesis of slow tail atmospherics deduced from frequency analysis and association with VLF components, *J. Atmos. Terr. Phys.*, 32, 1147, 1970.
99. Schäfer, J., Volland, H., Ingmann, P., Heydt, G., and Eriksson, A. J., A network of automatic atmospherics analysers, *Proc. Symposium on Lightning Technology*, NASA Conference Publ. 2128, FAA-RD-80-30, NASA Langley Research Center, Hampton, Va., 1980, 215.
100. Schäning, B. and Cumme, C., Frequency dependence of atmospheric noise intensity from 1 to 1000 kHz at low and medium latitudes, *J. Atmos. Terr. Phys.*, 31, 135, 1969.

101 Schonland, B F J , The lightning discharge, *Handb Physik*, 22, 576, 1956
102 Schoute-Vanneck, C A and Wright, A G , 27 kHz atmospherics observed at sunset and sunrise in South Africa, *J Atmos Terr Phys* 30, 609 1968
103 Serhan, G I , Uman, M A , Childers, D G , and Lin, Y T , The RF spectra of first and subsequent lightning return strokes in the 1—200 km range *Radio Sci* , 15, 1089, 1980
104 Sommerfeld, A , *Lectures in Theoretical Physics Vol III* Academic Press New York, 1952
105 Sommerfeld, A , *Lectures in Theoretical Physics, Vol VI*, Academic Press, New York, 1952
106 Taylor, W L , Daytime attenuation rates in the very low frequency band using atmospherics, *J Res Nat Bur Stand* 64D 349, 1960
107 Taylor, W L , Radiation field characteristics of lightning discharges in the band 1 kc/s to 100 kc/s, *J Res Nat Bur Stand* 67D 539, 1963
108 Taylor, W L , Determining lightning stroke height from ionospheric components of atmospheric waveforms, *J Atmos Terr Phys* 31 983 1969
109 Taylor, W L and Sao, K , ELF attenuation rates and phase velocities observed from slow tail components of atmospherics *Radio Sci* 5, 1453 1970
110 Teer, T L and Few, A A , Horizontal lightning, *J Geophys Res* , 79 3436, 1974
111 Tiller, J A , Uman, M A , Lin, Y T , Brantley, R D , and Krider, E P , Electric field statistics for close lightning return strokes near Gainesville Florida, *J Geophys Res* 81 4430 1976
112 Trška, P , and Laštovička, J , Sudden decrease of atmospherics at 5 kHz *J Atmos Terr Phys* , 34, 1065 1972
113 Uman, M A , *Lightning* McGraw Hill, New York 1969
114 Uman, M A and McLain, D K , Magnetic field of lightning return strokes, *J Geophys Res* 74, 6899, 1969
115 Uman, M A and McLain, D K , Radiation field and current of the lightning stepped leader, *J Geophys Res* 75, 1058 1970
116 Uman, M A , Brantley, R D , Lin, Y T , Tiller, J A , Krider, E P , and McLain, D K , Correlated electric and magnetic fields from lightning return strokes, *J Geophys Res* 80 373 1975
117 Uman, M A , Beasley, W H , Tiller, J A , Lin, Y T , Krider, E P , Weidman, C D , Krehbiel, P R , Brook, M , Few, A A , Bohannon, J L , Lennon, C L , Poehler, H A , Jafferis, W , Gulick, J R , and Nicholson, J R , An unusual lightning flash at Kennedy Space Center, *Science* 201 9 1978
118 Uman, M A , Lin, Y T , and Krider, E P , Errors in magnetic direction finding due to non vertical lightning channels, *Radio Sci* , 15 35 1980
119 Volland, H , On the theory of the sudden enhancement of atmospherics (SAR) *J Atmos Terr Phys* 28, 409, 1966
120 Volland, H , *The Propagation of Long Waves* (in German) Vieweg Verlag Braunschweig, 1968
121 Volland, H , Heydt, G , and Harth, W , The statistical measurement of the spectral amplitudes and phases of atmospherics in the VLF range in *Phase and Frequency Instabilities in Electromagnetic Wave Propagation* Davies K Ed AGARD Conference Proc 33, 1970, 55
122 Wadehra, N S and Tantry, B A P , Phase spectra of distant atmospherics, *J Atmos Terr Phys* , 29 1453, 1967
123 Wait, J R , *Electromagnetic Waves in Stratified Media* Pergamon Press, Oxford, 1970
124 Wang, C P , Interpretation of atmospheric wave forms *J Atmos Terr Phys* 25, 35, 1963
125 Watson-Watt, R A and Herd, J F , An instantaneous direct reading radiogoniometer, *J Inst Electr Eng* 64, 611, 1926
126 Watt, A D , *VLF Radio Engineering*, Pergamon Press Oxford, 1967
127 Weidman, C D and Krider, E P , The fine structure of lightning return stroke wave forms, *J Geophys Res* , 83, 6239 1978
128 Weidman, C D and Krider, E P , The radiation field wave forms produced by intracloud lightning discharge processes *J Geophys Res* , 84 3159 1979
129 Whitten, R C and Poppoff, I G , *Fundamentals of Aeronomy*, John Wiley & Sons, New York, 1971
130 World Meteorological Organization Technical Note 12 *Atmospheric Techniques* Secretariat of the WMO, Geneva, 1955
131 Yamashita, M and Sao, K , Some considerations of the polarization error in direction finding of atmospherics I Effect of the earth's magnetic field, *J Atmos Terr Phys* , 36, 1623 1974
132 Yamashita, M and Sao, K , Some considerations of the polarization error in direction finding of atmospherics II Effect of the inclined electric dipole, *J Atmos Terr Phys* , 36, 1633 1974
133 Taylor, W and Lange, J , Some characteristics of VLF propagation using atmospheric waveforms, in *Proc 2nd Conf on Atmospheric Electricity*, Pergamon New York, 1958, 609
134 Harth, W , private communication
135 Volland, A wave guide model of lightning currents *J Atmos Terr Phys* , 43, 191, 1981

HIGH FREQUENCY RADIO NOISE

Edward A. Lewis

TABLE OF CONTENTS

INTRODUCTION

This chapter primarily deals with radio noise of atmospheric origin, but cosmic noise from sources external to the atmosphere is discussed in the last section The frequencies of interest here range from 100 kHz to 100 GHz corresponding to wavelengths from 3 km to 3 mm Commonly used designations of bands within this range are shown in Table 1 There are two principal sources of atmospheric noise in this frequency range (1) the acceleration of electric charges associated with the sudden breakdown of the dielectric properties of air under locally intense electric fields, and (2) thermally emitting molecular constituents of the air Thermal noise is especially important at high micro-wave frequencies near the molecular resonances of water and oxygen In cosmic noise sources, the acceleration of charges moving with velocities close to that of light is one of the more important emission mechanisms

The strength of the radio noise at a given time and place depends on the properties of the sources and on wave propagation factors which control how much of the radiated power reaches the receiving antenna The properties of the noise incident on the antenna, the characteristics of the antenna, and those of the receiver, together determine the voltage fluctuations at the receiver output terminals These noise fluctuations are a nuisance in practical radio circuits, but on the other hand they provide important diagnostic information on the noise sources themselves

The following section summarizes the basic features of the generation and propagation of the radio waves, and the section, "Specifications of Atmospheric Noise," discusses quantitative measures of the radiation Subsequent sections discuss source strengths and the estimation of noise fields under different conditions

RADIO WAVE GENERATION AND PROPAGATION

Radiation from Accelerated Charges

The subjects of wave generation and propagation have a very extensive literature, here it is possible to give only a brief summary of those aspects which are of particular interest in determining the levels of radio noise For classical electromagnetic theory see Stratton,[72] for ionospheric propagation, see, for example, Rishbeth,[42] and Davies[11] and Rawer,[40] for propagation at higher frequencies, see, for example, Reed[41] and Steinberg [70]

Electrical discharges in air vary tremendously in scale from a few milliamperes flowing over a distance of a few millimeters for a few nanoseconds, to full-fledged lightning strokes with thousands of amperes flowing in channels several kilometers in length for 50 μsec or longer If the motions of the electric charges involved in a lightning discharge could be specified as functions of time, the electric field E and the magnetic field H produced at a distant point in free space could be calculated from classical electromagnetic theory

An individual charge q moving with vector velocity v and vector acceleration v at time t produces radiation fields, at distance R and later time t + R/c, given by the relativistically correct expressions in MKS units

$$E = \frac{\mu_0}{4\pi}\frac{qa^2}{R}\left[\alpha(\mathbf{R}_\alpha - \mathbf{v}/c)(\mathbf{R}_\alpha \cdot \dot{\mathbf{v}}) - \dot{\mathbf{v}}\right] \quad \text{(volt m}^{-1}\text{)} \quad (1)$$

$$H = \frac{\mu_0}{4\pi Z_0}\frac{qa^2}{R}\left[\alpha\left(\frac{\mathbf{v}}{c} \times \mathbf{R}_\alpha\right)(\mathbf{R}_\alpha \cdot \dot{\mathbf{v}}) + (\dot{\mathbf{v}} \times \mathbf{R}_\alpha)\right] \quad \text{(amp m}^{-1}\text{)} \quad (2)$$

Table 1
FREQUENCY BANDS AND COMMONLY USED DESIGNATIONS

Band		Designations	
Frequency	Wavelength	Frequency	Wavelength
30.0—300 kHz	10—1 km	LF	Kilometric
0.3—3 MHz	1000—100 m	MF	Hectometric
3.0—30 MHz	100—10 m	HF	Decametric
30.0—300 MHz	10—1 m	VHF	Metric
0.3—3 GHz	1—0.1 m	UHF	Decimetric
3.0—30 GHz	10—1 cm	SHF	Centimetric
30.0—300 GHz	10—1 mm	EHF	Millimetric

where

$$\gamma \equiv \left(1 - \frac{\mathbf{v}\cdot\mathbf{R}_0}{c}\right)^{-1} \tag{3}$$

R_o is the unit vector from the charge to the observer, c is the velocity of radio waves in free space (3×10^8 m s^{-1}), $\mu_o = 4\pi \times 10^{-7}$ hy m^{-1}, and $Z_o = 120\pi$ ohms.[72] It follows that

$$\mathbf{E} = Z_0(\mathbf{H} \times \mathbf{R}_0) \tag{4}$$

Even though the tip of a lightning discharge may advance with a velocity in the order of c/3, it is usually assumed that the individual electrons and ions have velocities much less than c, and that low-velocity approximations are valid:

$$\mathbf{E} \simeq 10^{-7} \frac{q}{R} \mathbf{R}_0 \times (\mathbf{R}_0 \times \dot{\mathbf{v}}) \tag{5}$$

$$\mathbf{H} \simeq 10^{-7} \frac{q}{Z_0 R} \dot{\mathbf{v}} \times \mathbf{R}_0 \tag{6}$$

A short segment $\boldsymbol{l}$ of a thin channel carrying a macroscopic current I(t) has a current moment $m = I(t)\,\boldsymbol{l}$. The current might consist of a large number M of small charges q moving with low velocity v(t) such that

$$M q v(t) = m \qquad \text{ampere meters} \tag{7}$$

The radiation field of the segment would then be the sum of the fields of the individual charges so that by Equation 5,

$$\mathbf{E} \simeq 10^{-7} \frac{1}{R} \mathbf{R}_0 \times (\mathbf{R}_0 \times \dot{\mathbf{m}}) \tag{8}$$

where now R_o and R are unit vector and distance respectively from the segment to the observer, and where m is the time-derivative of m The field of a long current channel is the vector sum of fields of the segments with proper allowance being made for different R/c propagation time delays

By Fourier transform theory (see the subsection "Spectrum of a Single Impulse") m can be regarded as consisting of the sum of sinusoidally time-varying components Such a sinusoidal element, or dipole, may be represented by $m = m_o \sin \omega t$ (amp m) where $\omega = 2\pi f$, f is the oscillation frequency, and m_o is a constant vector Then

$$E = 10^{-7} \frac{R_o \times (R_o \times M_o)}{R} \omega \cos \omega (t - R/c) \qquad (9)$$

and its magnitude,

$$E = 10^{-7} m_o \frac{\sin \Theta}{R} \omega \cos \omega (t - R/c) \qquad (10)$$

where Θ is the angle between the directions of m_o and R_o

There are also nonradiation fields, varying as R^{-2} and R^{-3}, which are not included in Equations 1 and 2, but these are usually relatively unimportant at large distances For the oscillating dipole, the radiation field exceeds the R^{-2} field when $R > \lambda/2\pi$ where $\lambda = c/f$ is the wavelength At f = 100 kHz for example this distance is less than 500 m

The power radiated in all directions by the sinusoidal dipole, averaged over one cycle, is

$$W = \frac{4}{9} \pi^2 10^{-15} f^2 m_o^2 \qquad \text{(watts)} \qquad (11)$$

The peak instantaneous power is twice this value For $m_o = 1$ amp m and $f = 10^5$ Hz, $W = 4\ 39 \times 10^{-5}$ W, and the peak electric field at $\theta = 90°$ and $R = 10^4$ m is $2\pi\ 10^{-4}$ vm^{-1} If S is the time-average intensity of the wave in watts m^{-2}, at distance R in the $\theta = 90°$ direction,

$$W = \frac{8\pi R^2}{3} S = \frac{R^2 E_o^2}{90} \qquad \text{(watts)} \qquad (12)$$

where E_o is the peak field at the same point

Dipole above the Earth

In the simplest model, the Earth is regarded as a flat perfect conductor so that a transmitting dipole at altitude h has a perfect image at depth h below the surface The electric field of a vertical dipole and its image is given by

$$E = 2 \times 10^{-7} \frac{m_o}{R} \sin \chi \cos \left(\frac{2\pi h}{\lambda} \cos \chi \right) \omega \cos \omega (t - R/c) \qquad (13)$$

In the plane broadside to a horizontal dipole and its image the field is

$$E = 2 \times 10^{-7} \frac{m_0}{R} \cdot \sin\left(\frac{2\pi h}{\lambda} \cos\chi\right) \omega \cos\omega(t - R/c) \qquad (14)$$

where λ is the wavelength, and χ is the zenith angle. In these equations R is measured from the midpoint between the dipole and its image, and $R \gg h$. If the Earth is not perfectly conducting, an approximate result can be obtained by allowing for the finite conductivity σ (mho m^{-1}), and the relative dielectric constant ε, by reducing the field of the image, and adjusting its phase in accordance with the plane wave reflection coefficient of the surface. This method is not valid for directions near 90°—see, for example, Reed.[61] For a homogeneous Earth, the reflection coefficient may be calculated from the Fresnel formulas:[72]

Magnetic vectors parallel to surface: Transverse Magnetic (TM) polarization

$$r_{TM} = \left| \frac{\epsilon' \cos\Theta - u}{\epsilon' \cos\Theta + u} \right| \qquad (15)$$

Electric vectors parallel to surface: Transverse Electric (TE) polarization

$$r_{TE} = \left| \frac{\cos\Theta - u}{\cos\Theta + u} \right| \qquad (16)$$

where

$$u = \sqrt{\epsilon' - \sin^2\Theta} \qquad (17)$$

$$\epsilon' = \epsilon + i \frac{1.798 \times 10^{10}\sigma}{f} \qquad (18)$$

and θ is the angle of incidence. Here it is assumed that the Earth surface is homogeneous, isotropic, and nonmagnetic. Some typical values of σ and ε for frequencies up through UHF are given in Table 2, but these constants are somewhat frequency-dependent especially at microwave and millimeter wavelengths.[64] Table 3 gives values of the reflectivities of flat seawater at 400 MHz, and illustrates the monotone behavior of $r_{TE}(\theta)$, and the quasi Brewster angle minimum of $r_{TM}(\theta)$, which in this case is near 86°.

A mathematically correct approach to computing the fields of dipoles over a smooth Earth is based on the concepts of inhomogeneous waves and complex directions of propagation.[72] Data for the total field, or "Ground Wave", have been published in the form of amplitude-distance curves, e.g., Bell Telephone Lab,[2] Wait,[82] Reed,[61] and International Telephone and Telegraph Corporation.[36] The four examples of ground-wave vertical electric field strengths shown in Figure 1 were calculated with a computer program for a smooth round Earth of $\sigma = 2 \times 10^{-2}$ mho m^{-1}, and a vertical 1-A meter-transmitting dipole at 2-km altitude.[29] These curves show that the lower frequency waves are better able to diffract into the region below the horizon.

Radio waves penetrate down into the Earth to a degree depending on the conductivity and frequency. For a homogeneous Earth of nonmagnetic material the electric field

Table 2
TYPICAL SURFACE CONDUCTIVITIES AND DIELECTRIC CONSTANTS

Type of surface	σ(mho/m)	ε
Sea water	4	80
Fresh water	10^{-3}	80
Ice	2×10^{-5}	5
Good soil	10^{-2}	20
Poor soil	10^{-3}	10

at depth d is less than the surface value by a factor of approximately $e^{d/D}$ where the skin-depth $D \approx 503\,(\sigma f)^{-1/2}$ meters For example, in seawater of conductivity 4 mho m^{-1}, the skin depth is about 0 8 m at a frequency of 10^5 Hz Since low frequencies penetrate more deeply than high frequencies, the waveform of a sferic observed at a depth may differ from that at the surface

When the radiation wavelength is comparable with the scale of surface roughness, wave scattering and absorption become important In estimating line-of-sight microwave propagation over heavily vegetated terrain, the ground-reflected waves can often be ignored Thus in Figure 1, the fields for 1 GHz and 10 GHz are shown as simply inversely proportional to distance out to the radio horizon

Atmospheric Effects

In a normal atmosphere, the refractive index decreases slightly with increasing height above the ground, and this gradient helps radio waves bend around the curved earth Typically the radio horizon distance is about 15% larger than the geometric distance which is approximately $\sqrt{2ha}$, where the altitude h is much less than the Earth radius a Thus for h = 2 km and a = 6400 km the geometric horizon is at 160 km, while the radio horizon is at about 184 km as indicated in Figure 1 Under super-refractive conditions, microwaves launched at certain altitudes may propagate far beyond the normal horizon, but with correspondingly weak fields at other altitudes Scattering by small scale irregularities in the refractive index, and by terrestrial objects can also inject wave energy into the shadow zone beyond the geometric horizon

At centimeter and millimeter wavelengths, atmospheric absorption is an important factor on line-of-sight paths even in the absence of precipitation or clouds This clear-air absorption is due to (collision-broadened) molecular resonance lines, primarily those of water vapor and oxygen Between these lines there are absorption minima or windows Table 4 shows typical maxima and minima attenuation rates in dB/km for propagation near the surface of the Earth [12] The rates decrease with altitude because of the decreased densities of water vapor and oxygen The 100 GHz curve in Figure 1 is based on a numerical integration assuming 0 74 dB/km at the surface of the Earth.

The total attenuations from selected altitudes (h) to the top of the atmosphere in the zenith direction[13] are given in Table 5 for selected frequencies At the 60-GHz oxygen line the total atmosphere is practically opaque (200-dB attenuation) For a given h, directions tangential to the Earth encounter more air than those that are more nearly vertical, and the total attenuations are greater (see Table 6)

The presence of rain, snow, and fog particles in the propagation path produces additional attenuation which is highly variable but generally increases with frequency Table 7 shows some attenuation rates vs frequency for several categories of rain and fog [12] Evidently centimetric radiation produced in a thunderstorm could be somewhat attenuated in propagating through the associated precipitation

Table 3
REFLECTIVITY OF SEAWATER AT 400 MHZ

	Polarization	
θ	TE	TM
0	0.887	0.887
10	0.889	0.886
20	0.894	0.881
30	0.902	0.871
40	0.913	0.856
50	0.926	0.830
60	0.942	0.788
70	0.960	0.706
80	0.979	0.509
(86)	0.992	0.294
90	1.000	1.000

Ionospheric Propagation

At frequencies below about 30 MHz, free electrons in the ionsphere may strongly reflect radio waves. The electrons, set in motion by the electric field of the incident wave, generate the reflected wave. The ionosphere may be regarded as an anisotropic propagation medium with a complex refractive index given by the Appleton formula (see, for example, Davies[19]), which takes into account the coherent interactions of the electrons with the geomagnetic field, and collisions with neutral particles.

In the daytime, at an altitude of 55 km, the electron density is typically in the order of $1/cm^3$ but it can be much greater under disturbed ionospheric conditions. The daytime electron density reaches a maximum of about 3×10^5 cm^{-3} between 250 and 400 km, and thereafter decreases slowly out to about 1200 km where a more sudden drop-off marks the plasmapause (see Carpenter[9]). The electron densities are usually greatest near the subsolar point, and are less at night, and at higher latitudes. Within narrow (600-km) "troughs" running east-west, the density may be less by a factor of 10.

Electromagnetic waves cannot propagate in a field-free, collision-free region with an electron density N cm^{-3} unless the wave frequency is greater than the plasma frequency,

$$f_p = 8.98 \times 10^3 \, N^{1/2} \quad \text{(Hz)} \qquad (19)$$

The maximum value of f_p above a given place on the Earth, at a given time, is called the critical frequency, f_c. For example, if $N = 3 \times 10^5$ cm^{-3}, $f_c = 4.9$ MHz. In a simple propagation model which neglects the geomagnetic field, a wave is either reflected or transmitted by the ionosphere depending on whether its frequency is less than, or greater than, $f_c \sec \theta$, where θ is the angle of incidence on the ionosphere. This gives rise to ray patterns of the type qualitatively illustrated in Figure 2, for a transmitter (or lightning stroke) near the ground. The more steeply incident rays B, C, D, C′, B′, for which $f > f_c \sec \theta$, penetrate the ionosphere, while the more grazing rays, A, A′ are reflected. The area inside the "skip-zone" ATA′ is inaccessible to ionospherically reflected rays from that transmitter. Thus radio noise from a thunderstorm near the skip distance might actually increase with increasing distance. The ionospherically reflected

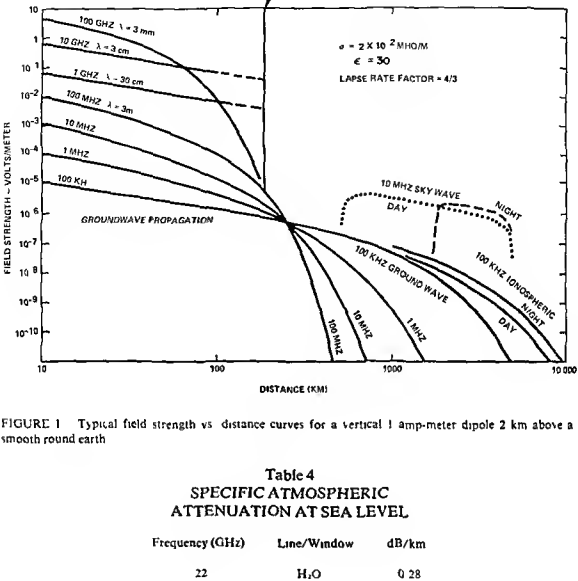

FIGURE 1 Typical field strength vs distance curves for a vertical 1 amp-meter dipole 2 km above a smooth round earth

Table 4
SPECIFIC ATMOSPHERIC ATTENUATION AT SEA LEVEL

Frequency (GHz)	Line/Window	dB/km
22	H_2O	0 28
31	W	0 12
60	O_2	13 0
75	W	0 56
118	O_2	2 40
126	W	1 32
184	H_2O	42 0
212	W	3 6
322	H_2O	51 0
339	W	12 2

waves reflect at the surface of the Earth, and again at the ionosphere, and so on Under low loss conditions, HF waves can propagate with significant field-strength to many thousands of kilometers around the Earth Earth-curvature prevents θ from approaching 90°, and consequently the practical upper limit for conventional HF ionospheric communication may not exceed 30 or 40 MHz Each time an HF wave reflects from high in the ionosphere, it must pass twice through the lower ionosphere, or D-region, where partial absorption occurs due to electron collisions with neutral atoms In the MF broadcast band, the daytime D-region absorption is severe, the ionospheric reflections are weak, and radio noise comes mainly from storms within groundwave range of the receiving antenna The absorption loss can also be large in the HF band

Table 5
TOTAL ONE-WAY ATTENUATION (DB) FROM HEIGHT h TO THE TOP OF THE ATMOSPHERE IN THE ZENITH DIRECTION

		Height (km)				
Frequency (GHz)	Line/window	2	4	8	12	16
1	—	3.2E − 2	1 6E − 2	8.1E − 3	3.4E − 3	1.1E −3
10	—	5.0E − 2	1.9E −2	8.3E − 3	3 5E − 3	1 2E − 3
22	H_2O	4.6E − 1	1 0E − 1	3.1E − 2	1 5E − 2	5.3E − 3
25—30	W	2 1E − 1	4.3E − 2	1 5E − 2	5 1E − 3	1.7E − 3
60	O_2	≈ 2.0E + 2	7.0E + 1	3.8E + 1	2.0E + 1	6.9
90—100	W	1.0	2.1E − 1	6.9E − 2	2.9E − 2	1.0E − 2
118	O_2	9.2E + 1	4.6	≈ 1	≈ 1	≈ 1

Note: E ± n = × 10±ⁿ.

Table 6
TOTAL ONE-WAY ATTENUATION (db) FROM HEIGHT h TO THE TOP OF THE ATMOSPHERE IN THE TANGENTIAL DIRECTION

		Height (km)				
Frequency (GHz)	Line/window	0	4	8	12	16
1	—	1.5	7.4E − 1	3.7E − 1	1.7E − 1	6.0E − 2
10	—	3.0	1.0	4.3E − 1	1.9E − 1	6.6E − 2
22	H_2O	3.2E + 1	5.6	1.3	4.2E − 1	2.4E − 1
28—30	W	1.6E + 1	2.5	7.0E − 1	2.8E − 1	9 6E − 2
60	O_2	≈ 5.5E + 3	2.8E + 3	1.3E + 3	1.0E + 3	4.0E + 2
85—100	W	6.5E + 1	1.3E + 1	3.7	1.6	5.1E − 1
118	O_2	1.5E + 3	—	—	—	>2.0E + 1

Note: E ± n = x10±ⁿ.

Table 7
SPECIFIC ATTENUATION (DB/KM) IN PRECIPITATION

		Rain (mm/hr)			Fog (g/m³)
Frequency (GHz)	Wavelength (cm)	150	25	0.25	0.1
3	10.0	0.055	0.011	—	—
10	3.3	4	0.43	—	0.006
30	1.0	24	4.4	0.033	0.050
100	0.3	50	12	0.33	0.44
300	0.10	50	13	0.66	2.7
1000	0.03	40	10	0.50	6.0

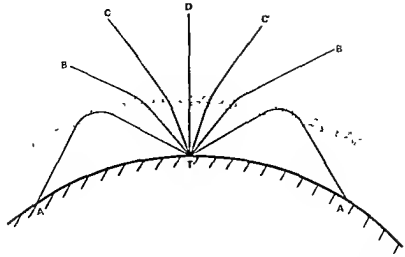

FIGURE 2 Ionospheric refraction of HF rays from a point on the ground

especially at high latitudes when high energy particles precipitate into the D-region and cause unusually high levels of ionization On the other hand, at very low frequencies, the waves partially reflect from the D-region itself, and ionospheric propagation may still take place

Figure 1 shows illustrative field-strength vs distance curves for ionospheric propagation at 10 MHz[40] and 100 kHz [44]

Wave Propagation through the Ionosphere

As a wave travels upward out of the collision-dominated lower ionosphere, the effects of the magnetic field of the Earth become more important An electron with a component of velocity perpendicular to the geomagnetic field is subject to a force which causes its trajectory to curve The resulting interaction of the wave with the field makes it possible for radiation to penetrate the ionosphere in the "whistler mode"[71] even if $f < f_c \sec\theta$, providing f is also less than the gyro frequency $f_H = 2.80 \times 10^{10} B$, where B is the magnetic flux density in webers m^{-2} For $B = 5 \times 10^{-5}$, corresponding to ½ gauss, $f_H = 1.4$ MHz The penetration loss incurred by a plane wave incident at an arbitrary angle upon the bottom of a horizontally stratified model ionosphere can be calculated using "full-wave" computer programs Table 8[44] shows theoretical full wave penetration losses for two TM-polarized waves, both incident on a model nighttime ionosphere at 20° but at different angles (0° and 40°) with respect to the geomagnetic field direction The loss is less for the wave launched in the direction of the magnetic field line, but in both cases the loss increases with frequency In similar calculations for a daytime model ionosphere the loss was greater than 60 dB in both cases

Figure 3[4] gives daytime and nighttime losses calculated for an extended range of frequencies and two angles of incidence assuming a vertical geomagnetic field At 3 MHz the penetration loss exceeds 90 dB in all four cases, while above about 80 MHz the loss is negligible

SPECIFICATION OF ATMOSPHERIC NOISE

Spectrum of a Single Impulse

Figure 4 illustrates an individual impulse of atmospheric noise incident upon a receiving antenna Let E(t) represent the time-variation of the electric field (volts m^{-1}) in the polarization to which the antenna responds The noise impulse causes a voltage

Table 8
PLANE WAVE IONOSPHERIC PENETRATION LOSSES (DB) FOR A 70° GEOMAGNETIC DIP ANGLE.

Frequency (kHz)	Angle between wave direction and field line (degrees)	
	0	40
100	3.0	25.6
200	3.5	45.2
300	6.5	57.2
500	24.0	>60

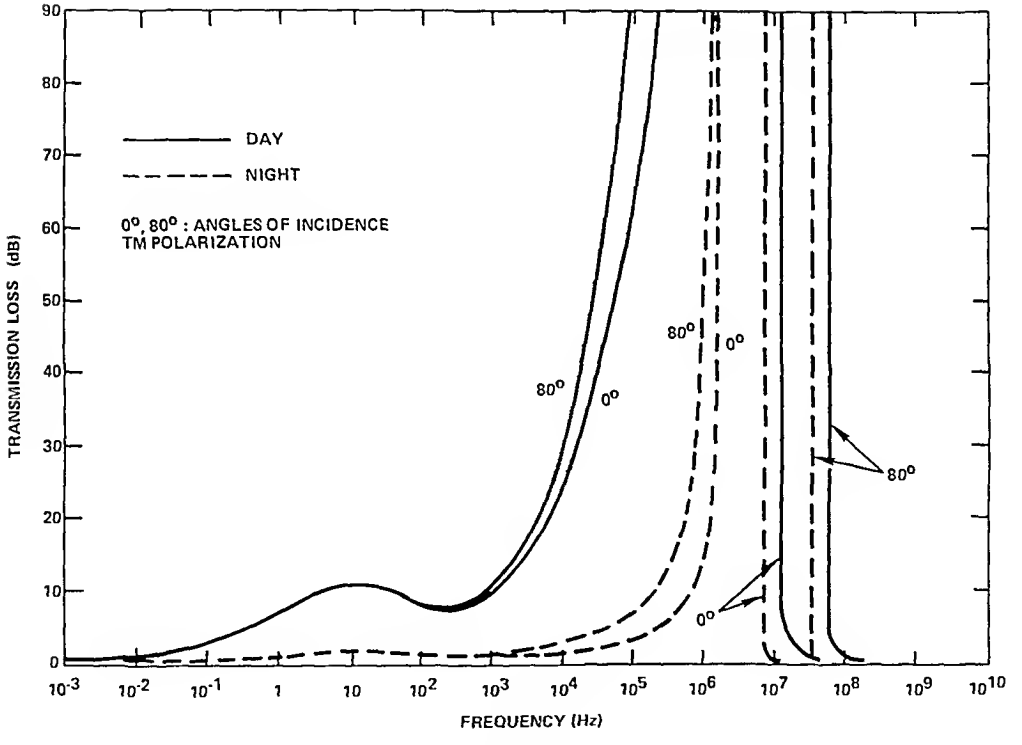

FIGURE 3. Ionospheric penetration losses for a 90° geomagnetic dip angle.

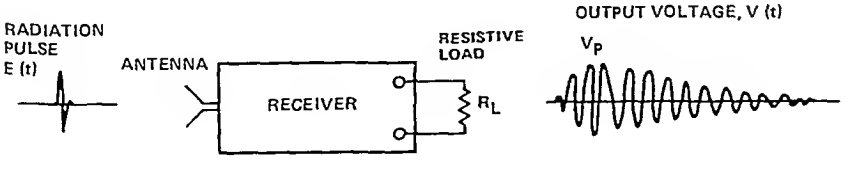

FIGURE 4. Response of a narrow frequency band linear receiver to a radiation pulse.

transient V(t) to appear across the resistive load R_L of a linear receiver whose effective frequency band-pass Δf is centered on frequency f It is V(t), or some feature of it, that is actually observed

By Fourier transform theory, E(t) is the sum of sinusoidal fields whose amplitudes and phases vary with frequency

$$E(t) = \int_0^\infty \left|A(f)\right| \cos(\omega t - \phi)\, df \qquad (20)$$

$$= \mathrm{Re} \int_0^\infty A(f)\, e^{-i\omega t}\, df \qquad (21)$$

where $\omega = 2\pi f$, and ϕ is the argument of the complex amplitude spectral density,

$$A(f) = 2 \int_{-\infty}^{\infty} E(t)\, e^{i\omega t}\, dt \qquad (V\ m^{-1}\ Hz^{-1}) \qquad (22)$$

The spectral density of the wave-energy incident on a unit area transverse to the direction of propagation (spectral energy intensity) is

$$\mathcal{E}'(f) = \frac{|A|^2}{2 Z_0} \qquad (\text{joule m}^{-2}\ \text{Hz}^{-1}) \qquad (23)$$

assuming a plane wave in essentially free space with $Z_0 = 120\pi$ ohms

The energy intensity $\mathcal{E}$, in joules per square meter may be found by integrating either with respect to time, or frequency

$$\mathcal{E}(f) = \frac{1}{Z_0} \int_0^\infty I^2(t)\, dt = \int_0^\infty \mathcal{E}'(f)\, df \qquad (24)$$

If A is the absorption cross section of the antenna for the direction from which the impulse is received, and if G is the power gain of the matched receiver, the energy P delivered to the receiver load is $AG\,\mathcal{E}'(f)\Delta f$ (joules) provided $\mathcal{E}'(f)$ does not vary too much across the pass-band Δf But also

$$P = \frac{1}{R_L} \int_{-\infty}^{\infty} V^2(t)\, dt \qquad (25)$$

so that

$$\mathcal{E}'(f) \approx \frac{1}{XGR_L \Delta f} \int_{-\infty}^{\infty} V^2(t)\, dt \qquad (26)$$

Thus by observing V(t), or P, the spectral energy intensity $\mathcal{E}'$ may be deduced

If the radiation pulse E(t) is much shorter in duration than the ringing time of the frequency selective networks responsible for the restricted bandwidth Δf, the form of V(t) will be more characteristic of the receiver than of the incident pulse Then if V_p is the peak of the envelope of V(t)

$$V(t) \approx V_p\, w(t) \tag{27}$$

where w(t), an oscillating function of unit peak amplitude, describes the ringing. Then

$$\mathcal{E}'(f) = \frac{V_p^2}{XGR_L \Delta f} \int_{-\infty}^{\infty} w^2(t)\,dt \tag{28}$$

If the value of this integral is not measured, a rough estimate may be made from fundamental considerations which suggest the effective duration of w(t) is in the order of $(\Delta f)^{-1}$. It is then reasonable to expect the integral to be in the order of $(4\Delta f)^{-1}$ seconds. A more detailed analysis by Horner[35] suggests that $(2\sqrt{2}\,2\Delta f)^{-1}$ is a better value to use with multistage band-pass circuits. Then

$$\mathcal{E}'(f) \approx \frac{V_p^2}{2\sqrt{2}\,XGR_L(\Delta f)^2} \tag{29}$$

$$|A(f)| \approx \frac{V_p}{\Delta f}\sqrt{\frac{Z_o}{2AGR_L}} \tag{30}$$

The narrow band (Fourier) parameters A(f) and $\mathcal{E}'(f)$ provide conceptually attractive descriptions of the spectrum of a single sferic. If wider bandwidths are used, the relation between output voltage and energy in the absence of phase information becomes less clear. For example, if the bandwidth is 1 kHz, the ringing time is comparable with the duration of many sferics bursts, and the assumption underlying Equation 28 is not valid. Thus if data measured with one (wide) bandwidth is to be extrapolated to a different one, the exercise of judgment may be required.

Spectra of Pulse Sequences

If the pulse E(t) is repeated endlessly with a precise repetition frequency f_R, the spectrum consists of discrete lines of amplitude $|A_n|$, frequency nf_R, and angular frequency $\omega_n = 2\pi n f_R$:

$$E(t) = \sum_{n=1}^{\infty} |A_n| \cos(\omega_n t - \phi_n) \tag{31}$$

$$= \mathcal{R}e \sum_{n=1}^{\infty} A_n e^{-i\omega_n t} \tag{32}$$

where $\varnothing_n$ is the argument of

$$A_n = 2 f_R \int E(t)\, e^{i\omega_n t}\, dt \qquad (V\,m^{-1}) \tag{33}$$

the integration being over one repetition interval (Since E(t) is a radiation pulse, $A_\infty = 0$)

If the source emits individual random pulses at an average rate f_A, and of average spectral energy intensity $\mathcal{E}'_A$, the spectral power intensity is

$$S'(f) = f_A \mathcal{E}'_A(f) \qquad \text{(watt m}^{-2}\text{ H}_Z^{-1}\text{)} \qquad (34)$$

The peak amplitude A^{**} of an equivalent sinusoidal wave which would deliver the same average power as the noise in a bandwidth Δf is given by

$$A_{eq} = \sqrt{2 Z_0 S' \Delta f} \qquad (35)$$

Because of the proportionality to the square root of the bandwidth, A^{**} is not a spectral density in the usual sense

Radio noise from electrical discharges in the atmosphere is irregular, the power delivered to the receiver load fluctuates, and the fraction of the time that a given level is exceeded is a parameter of importance in the design of radio systems Probability curves based on average power, average envelope voltage, and average logarithm of envelope voltage are available [17] The use of nonlinear (limiting) circuits may be advantageous in reducing the effects of impulsive noise in some applications

Brightness Temperature of Extended Noise Sources

When radio noise sources are distributed over a range of azimuthal and elevation angles, the concept of brightness, borrowed from optics, provides an appropriate measure of the emission An element of an extended monochromatic source at free-space distance (R) from an observer, appears to have a projected area (dF) transverse to the viewing direction The radiation power intensity dS in watts per square meter of transverse area at the observer, is evidently proportional to dF and inversely proportional to R^2 The brightness (b) of the source is then defined as the constant of proportionality in the equation

$$dS = \frac{b\,dF}{R^2} \qquad \text{(watt m}^{-2}\text{)} \qquad (36)$$

$$= b\,d\Omega \qquad (37)$$

where $dF = d\Omega/R^2$ is the solid angle subtended by the source Thus b may be regarded as the power intensity per steradian w m^{-2} $ster^{-1}$, a quantity which would be *infinite* for a mathematical point source If the radiation is not monochromatic, the corresponding quantity is spectral brightness (b') in w m^{-2} $ster^{-1}$ Hz^{-1}

Brightness can also be stated in terms of a brightness temperature, or noise temperature, which is the temperature T of a black body whose brightness b'_{BB} would equal that of the source By the Planck radiation law,

$$b'_{BB} = \beta f^3 (e^{\xi f/T} - 1)^{-1} \qquad \text{(watt m}^{-2}\text{ ster}^{-1}\text{ Hz}^{-1}\text{)} \qquad (38)$$

where $\xi = 4\ 772 \times 10^{-11}$ deg Hz^{-1}; $\beta = 1\ 453 \times 10^{-50}$ w m^{-2} $ster^{-1}$ Hz^{-4}, T is in degrees

kelvin, and f is the radiation frequency in hertz. An integration shows that one square meter of black body surface receives, and hence also radiates, $\pi b'_{BB}$ watts per hertz.

At radio frequencies $\zeta f/T$ is usually small, and the exponential may be replaced by the first two terms of its power series, giving the Rayleigh-Jeans approximation:

$$b'_{BB} \approx \frac{\beta}{\zeta} f^2 T = 2kT\lambda^{-2} \tag{39}$$

where k is Boltzmann's constant (1.38×10^{-23} joules deg^{-1}), $\beta/\zeta = 2k/c^2 = 3.045 \times 10^{-40}$, and λ is the wavelength in meters. The error in this approximation is less than about 5% if $f \leqslant 2 \times 10^9 T$. On inverting Equation 38,

$$T = \frac{\zeta f}{\ln(\beta f^3/b'_{BB} + 1)} \tag{40}$$

$$\approx \lambda^2 b'_{BB}/2k \tag{41}$$

when $\beta f^3/b'_{BB}$ is small.

Under thermal equilibrium conditions, a thermally insulated matched resistive load of an ideal antenna immersed in black body radiation of temperature T will also be at temperature T. The power received by the antenna and delivered to the load is then equal to the power delivered by the load to the antenna and radiated. By the Nyquist formula this power is $kT\Delta f$, where Δf is the frequency bandwidth. (For a more detailed discussion see for example, Steinberg.[70])

The concepts of brightness, and brightness temperature, provide measures of radio noise largely independant of the type of antenna used. However if the noise is not isotropic, the measured noise temperature will be a directional average, weighted with respect the antenna directional pattern.

The power intensity S of a sinusoidal plane wave incident on an antenna in the direction of highest gain, and with the optimum polarization, which would deliver a power to the load equal to the noise power is $kT\Delta f/X$, where X is the receiving cross section of the antenna in m^2. For very short dipole antennas $X = 0.1194\lambda^2$, while for half-wave dipoles $X = 0.1305\lambda^2$. More generally, $X = G\lambda^2/4\pi$ where G is the gain of the antenna. From Equation 35 it follows that the peak plane wave field strength equivalent to the noise,

$$E_{eq} = \sqrt{2Z_0 kT\Delta f/X} \tag{42}$$

SOURCE STRENGTHS OF SFERICS

Observational Techniques

The observation of the radiation fields produced by atmospheric discharges at some standard short distance, for example 10 km, provides a measure of radiation source-strength which is relatively free of propagation uncertainties. The distance can be found by triangulation with direction-finders of the field-resolving type,[40] of the time-of-arrival type,[48,59,77] or by using wide-aperture directional antennas (see the subsection "Mapping of VHF/UHF Sources in Clouds"), and lightning discharge channels can be located by radar. Some of these techniques can also provide information on the altitude of the radiation sources, provided the radial distances are not too large.

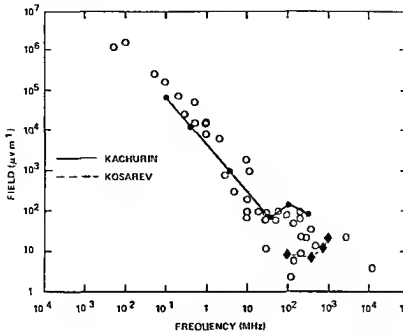

FIGURE 5 Peak sferics amplitudes in a 1-kHz bandwidth at 10 km distance

Especially at long wavelengths, the electromagnetic boundary conditions at the Earth surface may largely determine the polarization of the received atmospheric noise, see the section "Radio Wave Generation and Propagation." In making field measurements on or near the ground it has been common practice to observe the vertical electric field or the associated horizontal magnetic field, either of which provides information on the Transverse Magnetic (TM) polarization-component of the radiation. Balloon-borne sensors have been used to a limited extent to observe noise in the Transverse Electric polarization in the LF spectral region.

Data Adjusted to Standard Distance and Bandwidth

Published data on sferics observed from nearby storms have been adjusted to a standard distance and standard bandwidth by Pierce,[57] Kimpara,[42] Clanos,[14] and Kachurin,[38] thus providing a basis of comparison over a wide range of frequencies. Figure 5 shows individual points from Clanos,[14] who normalized available data to a 10-km distance and a 1-kHz bandwidth. The ordinate shows peak voltages in this bandwidth, referred to equivalent plane wave field strengths. The solid line in Figure 5 links data points from more recent work[38] at six different frequencies, each point representing at least 30 measurements.

The scatter of the data is worst around 100 MHz, where the range of variation is about 100-fold in field strength, or 10,000 times in intensity. The general trend of the data is one of decreasing field strength with increasing frequency, and is roughly represented by the relation

$$\Gamma_{peak} \approx 6500\, f^{-1.2} \quad (10^{-2} \leq f \leq 10^{2}) \tag{43}$$

where here E_{peak} is in microvolts per meter, and f is in MHz. The data of Kosarev,[43] (solid diamonds in Figure 5), show a minimum at a frequency around 300 MHz. Kosarev speculated that this might indicate the onset of a different source mechanism.

In addition to the discrete atmospheric noise bursts, Kachurin[38] also reported that

thunderclouds emitted a continuous radiation consisting of short pulses at rates as high as 400 sec^{-1}, and lasting for times in the order of 1 hr. The equivalent field strength of this noise in a 1 kHz bandwidth at a distance of 10 km was about 1 $\mu V \cdot m^{-1}$ from 1 MHz to 300 MHz.

Spectral Densities at 10-km Distance

As discussed in the section "Specification of Noise," information for a finite bandwidth, as in Figure 5, is not exactly convertible to a Fourier spectral density. Points indicated by solid dots in Figure 6 show spectral densities A(f) from Horner,[35] allowance being made for A(f) being twice Horner's S(f). Points indicated by diamonds show spectral data of Kosarev[43] converted to amplitude.

Power measurements at 600 MHz reported by Hewitt[33] and converted to amplitude spectral density at 10 km, are also shown in Figure 6. This noise appeared either as trains of individual impulses lasting for 0.1 msec to 3 msec preceding the appearance of radar echoes from discharge channels, or as a general increase in receiver noise.

Krider[45] observed noise bursts with durations of 100 to 400 μsec with sufficient time resolution to show that they consisted of individual short impulses separated by about 5 μsec with a standard deviation of about 1.8 μsec. As observed at distances around 50 km, a typical individual impulse rose to a peak of about 1 V m^{-1}in 0.1 μsec, decreased to zero in about 1 μsec, and ended in a low amplitude tail of opposite sign. Krider attributed these pulses to an intra cloud dart-stepped leader discharge process. (For a discussion of discharge mechanisms see Brook,[7] Shonland,[65] and the chapter "The Lightning Current.") Extrapolated to 10-km distance, an individual impulse would have a spectral peak in the order of 2×10^{-5} V $m^{-1}Hz^{-1}$ at 200 kHz. Considering a 40-impulse burst as a single pulse, and allowing for partial coherency, the spectral density of the burst would be in the order of 10^{-4} V $m^{-1}Hz^{-1}$, which is comparable with the data in Figure 6.

Figure 7 shows burst durations estimated from data reported by different observers, arranged by radio frequency. While burst-lengths may vary with the type of storms and other factors, there seems to be a tendency toward shorter bursts at higher frequencies. See also the subsection on "Mapping of VHF/UHF Sources in Clouds."

Current Moments

A variety of electromagnetic events are associated with what might be perceived visually as a single lightning flash. The event responsible for the low frequency radio noise is the sudden flow of a large current which may be in the order of 30,000 A or more.[87] Some aspects of the low frequency radiation may be illustrated by an oversimplified model which represents the downward electric field at a distance of 10 km by the function

$$E(t) = 60(1 - 10^5 t/60)e^{-10^6 t/60} \quad (V\ m^{-1}) \qquad (44)$$

where time t is in seconds, and where $E = 0$ for $t < 0$. This field has a peak amplitude of 60 V m^{-1}; changes sign at 60 μsec; has a shallow minimum of -8 V m^{-1} around 120 μsec; and decreases to zero at infinite time. The integral of E(t) over all time is zero. Except for the discontinuity at $t = 0$, the waveform represented by E(t) is quite typical of many waveforms observed experimentally, for example see Kalakowsky.[40]

By Equation 8, a short upward-directed current moment

$$m(t) = 3 \times 10^{12}\, t e^{-10^6 t/60} \quad (amp\ m) \qquad (45)$$

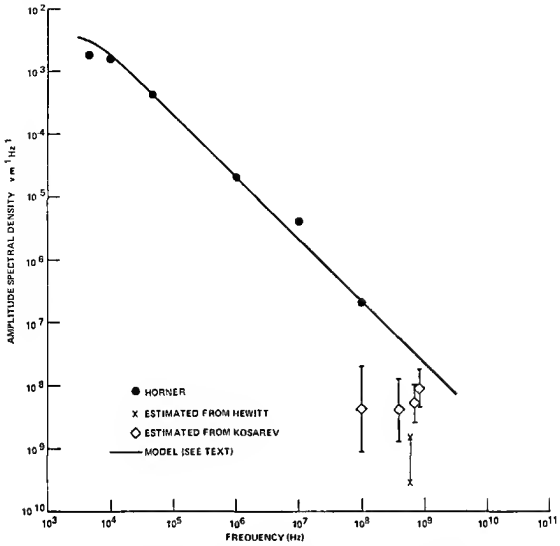

FIGURE 6 *Amplitude spectral density of sferics normalized to 10-km distance*

together with its ground reflection, could produce the field of Equation 44 This moment rises in 60 μsec to a maximum of $6\ 6 \times 10^7$ amp m, then gradually decreases to zero, reaching 1/10 of its maximum around 300 μsec The maximum value of dm/dt is 3×10^{12} amp m sec^{-1}, and would be equivalent to a current-column of 30,000 A advancing at 10^8 m sec^{-1}, a velocity typical of a return stroke [8]

The computed spectral density A (f) of the field described by Equation 44 is shown in Figure 6, and is in fair agreement with experimental data points from 10 kHz to 10 MHz However the agreement at the high frequencies is largely fortuitous because this part of the spectrum, with its f^{-1} frequency variation, is a mathematical consequence of the nonphysical discontinuity of E(t) at t = 0 A seemingly slight modification of the current moment would make dm/dt continuous, give E(t) a finite rise-time, and result in a faster high-frequency roll-off without substantially changing the spectral amplitude around 10 kHz

A much more complicated model would be required to account correctly for the high-frequency spectrum which is due to the complex of smaller current moments in a discharge For example, an individual impulse, of the type shown by Krider to occur repetitively (see "Spectral Densities at 10-km Distance" above), could be produced by a current moment in the order of only 2×10^5 amp m, or less than 1% of the moment discussed above

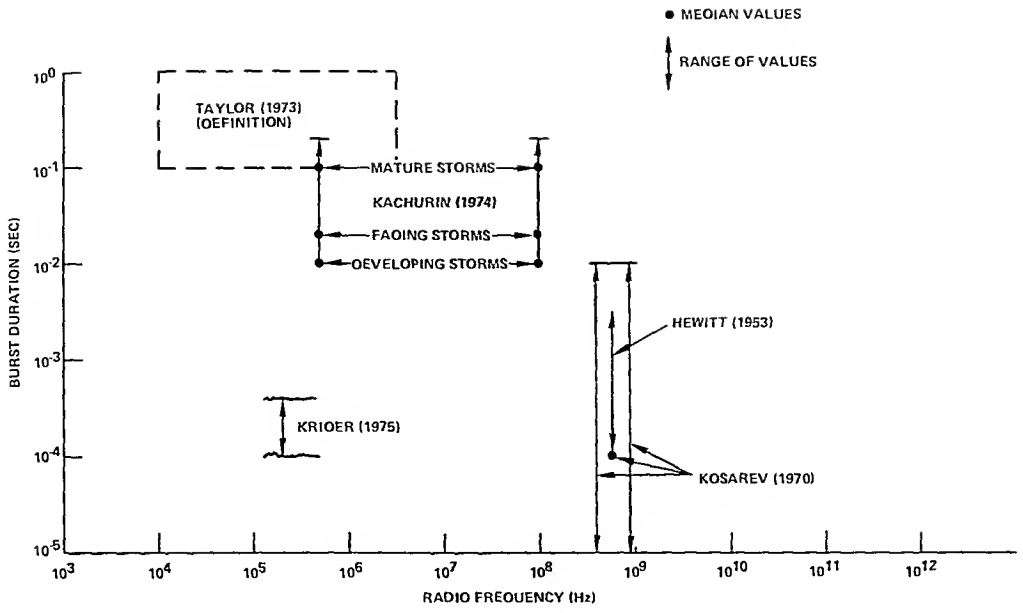

FIGURE 7. Estimated burst-durations.

Mapping of VHF/UHF Sources in Clouds

The hyperbolic, or time-of-arrival, technique[48] uses an array of synchronized receivers and data processing to determine directions of incoming pulses. With receiver base lines comparable to the propagation distances, and by observing VHF or higher frequencies it is possible to locate pulse sources in three dimensions with considerable accuracy.[59,77] Another, and in some respects simpler, mapping technique is to scan the sky with large diameter parabolic antenna. With a 6-m antenna, Harvey[27] obtained azimuth and elevation patterns of electrical activity in the vicinity of Kennedy Space Center, Florida, at 250 and 925 MHz. Individual impulses from clouds at distances of 60 km or more could be recorded. The previously described dense-burst type of sferics was frequently observed, but impulses also occurred singly, or in groups containing only a few. This small-group emission was observed even when no lightning flashes were seen, raising the possibility that the early stages of electrical build-up in clouds might be detectable at considerable distances thus warning of a developing hazard. Kachurin[38] also mentioned possible diagnostic and predictive applications of "prethunderstorm emissions".

NOISE FROM WORLD-WIDE ATMOSPHERICS

Thunderstorm Distribution.

If lightning strokes radiated equally, and were distributed with equal probability over the surface of a flat Earth, the more distant strokes would contribute more impulses to a receiving antenna than nearby strokes, simply because the element $2\pi RdR$ of surface area would increase with distance R. Since, in general, the radiation fields decrease faster with distance than R^{-1} there would tend to be more weak sferics than strong ones. Although the distribution of sources over the world is far from uniform, HF atmospheric noise does tend to consist of strong impulses superimposed on a more steady background.[16]

The geographical distribution of atmospheric noise sources relates to the average number of "thunderstorm days" in an area in a given time period. Maps of the world

with contours of thunderstorm days[83] show that thunderstorms are most frequent in equatorial regions, especially South Central America, Indonesia, and Africa. The relative activity varies with local time of day and the season, and so does the HF radio propagation from the area to a distant receiver. In principle it might be possible to calculate and predict noise levels from a knowledge of these factors — an approach which has been developed for VLF[50] — but conventional practice makes use of noise charts which are based on noise measurements.

Noise Charts

The charts of the U.S. National Bureau of Standards[46] and of the International Radio Consultative Committee[41] give average noise levels for short vertical receiving dipoles as functions of frequency for each 4-hr time-block of the day, for each of four 3-month periods corresponding to the seasons. The noise levels are parametric in noise grade, which varies from 1 to 5 depending on the observer's location on a contour map specific for the season. The thickness of the lines in Figure 8 shows the approximate range of seasonal variation in noise level for noise grade 3 for the time blocks 0000 to 0400 and 1200 to 1600. In summer, noise grade 3 would be appropriate for parts of the U.S. and Europe for example. In winter the same geographic areas would have a noise grade between 2 and 3, and the noise levels would be lower than in Figure 8. In summer the spread between noise grades 2 and 4 is a factor of 10^4 for the time block 1200 to 1600 and a frequency of 1 MHz. For the 0000 to 0400 time block the corresponding spread is only about a factor of 160.

The standard reference antenna for noise measurements is a vertical electric dipole which is equally sensitive for all azimuthal directions. With a high gain antenna it might be expected that the noise level would vary considerably with azimuthal direction, but according to the International Radio Consultative Committee (CCIR)[11] the variation may be only about 6 dB or less on the average.

Extrapolations to UHF and Higher Frequencies

A very rough estimate of the global average level of sferics noise at frequencies too high for ionospheric propagation might be made by assuming that lightning strokes occur over the 5×10^{14} m^2 surface area of the Earth at the rate of about 100/sec,[83] and that there is one noise burst per lightning stroke. Taking an average burst duration of 200 μsec, and spectral density from Figure 6, an average brightness temperature can be calculated for the whole Earth. Estimates obtained in this way are less than 1 K for the frequency range 100 MHz to 1000 MHz, so that on average, this noise is probably negligible compared to that from other sources.

CORONA NOISE

When a conductor accumulates static charge, the electric field at the tip of any sharp point or edge is especially large and may be strong enough to ionize the air locally and, in effect, permit charge to escape into the air in the form of ions. The charge-flow may appear as a direct current on a microammeter, but when observed with an oscilloscope it is seen to consist of individual current impulses, each one corresponding to a sudden brief breakdown of the insulating properties of the air. The rapidly changing currents in the air, and on the associated electrical conductors, radiate radio noise.

Coronal discharges in air are easily produced in the laboratory using DC voltage-sources of 5 kV or more. In vicinity of thunderstorms the electrostatic fields can be strong enough to induce corona discharges from grounded metal towers and other conductors.

The type of discharge and its electromagnetic parameters depend on many factors,

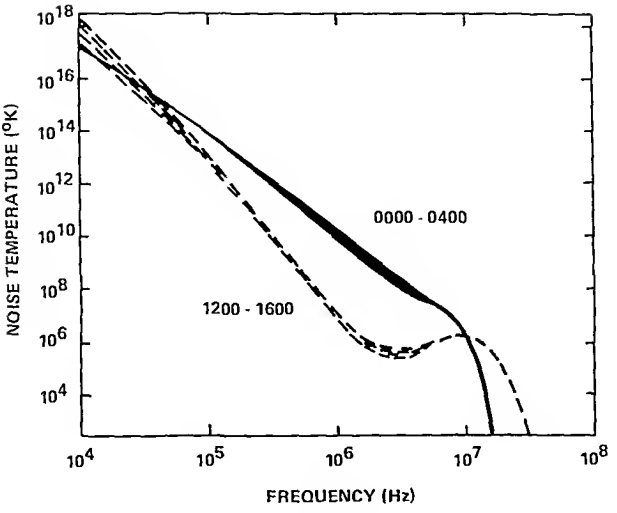

FIGURE 8. Sferics noise temperatures for noise grade 3.

including the magnitude and sign of the driving field, conductor resistivity, contaminants on the surface, conditions of illumination, composition of the atmosphere, its temperature, pressure, particle content, and velocity of air flow at the point.[49] In standard air the discharge may vary from quite regular small events, to streamers and small sparks, on up to arc-over conditions.

In the common type of discharge described by Trichel,[76] the charge released into the air in each individual ionization is in the order of 2×10^{-10} C but is more or less, depending on whether the discharge point is rounded or sharp. For a 10 μa average corona current, there are about 5×10^{4} discharges per second. In a typical individual Trichel discharge, the current may rise to a peak of about 8×10^{-3} amp in 10^{-9} sec, and decay to half value in about 8×10^{-9} sec. The corresponding current spectrum would have a value of about 2×10^{-10} amp Hz^{-1} up to around 10^{7} Hz, and then would decrease.

From tests with corona artificially induced at the upper end of a vertical quarter-wave monopole receiving antenna at 200 MHz, a tentative value of the spectral energy delivered to a matched receiver by an individual corona impulse is 1.5×10^{-20} joules Hz^{-1}.[29] With an incoherent pulse rate of 10^{4} sec^{-1}, the power spectral density would be 1.5×10^{-16} watt Hz^{-1} which is equivalent to an antenna temperature of about 10^{7} K, which is much larger than typical sferics noise at 200 MHz. Ways of reducing corona noise on receiving antennas include increasing the radius of the tip to decrease the local electric field, and coating the antenna with an insulating material that resists electrical breakdown.

Electrical sparks from electrostatic processes may constitute a fire or explosion hazard in certain industrial environments, for example, in oil tankers. However, to ignite a given inflamable mixture a minimum threshold spark energy is required. The early detection of corona-like radio noise from low energy discharges has been proposed[13] as possibly providing a warning of developing conditions likely to produce more dangerous discharges.

Aircraft become electrically charged when flying through clouds, due to particles impacting the surface of the fuselage and wings. Charging rates in the order of 500 μa have been observed with large jet aircraft,[73] and under equilibrium conditions an equal current is discharged into the air by corona. The radio noise from the corona is picked up by on-board receiving antennas at levels depending on certain electromagnetic coupling factors, but Tanner[73] reported noise levels in terms of equivalent free-space plane

waves in a 1-kHz bandwidth Examples of noise at the fin-cap of a 707-type aircraft flying at 20 kft (6km) and discharging a current of 250 μa varied from around 2000 μVm^{-1} at 500 kHz, to 20 μVm^{-1} at 8MHz Radio interference from corona noise on aircraft can be reduced by providing discharge points of electrically resistive material

Corona noise from high-voltage power transmission lines contributes to the overall level of man-made radio noise which comes from many sources including electrical machinery and ignition circuits of gasoline engines From estimates given by Pierce,[57] the man-made noise temperature of a short vertical antenna in an urban environment is approximately

$$T_{urb} = 9 \times 10^5 f^{-2.2} \text{ K}, \quad (0.1 \leq f \leq 100) \tag{46}$$

where here f is in megahertz In urban areas, especially in the daytime, man-made noise can exceed the atmospheric noise level For rural areas the estimate of man-made noise is about 1/200 of that given by Equation 46

ATMOSPHERIC THERMAL NOISE

As discussed in the section "Radio Wave Generation and Propagation," the atmosphere is significantly absorbing at centimeter and millimeter wavelengths, and it follows from thermodynamics that the atmosphere must also emit thermal radiation at these frequencies Atmospheric thermal noise is of molecular origin and is essentially unrelated to the impulsive noise from electrical discharges A directional antenna looking up from the ground at zenith angle χ receives thermal radiation emitted by each elemental thickness ds of air at distance s in that direction The height h of the element above the spherical Earth of radius a is given by

$$h = \sqrt{a^2 + s^2 + 2as\cos\chi} - a \tag{47}$$

$$\approx s\cos\chi \qquad (s << a\cos\chi) \tag{48}$$

If $\eta(h)$ is the absorption coefficient at altitude h, the absorption factor of the element ds is ηds, and hence the element radiates with spectral brightness $b'_{BB}\eta$ds, where b'_{BB} is the spectral brightness of a black body at thermodynamic temperature T(h) at altitude h (see Reference 21) The absorption in the air along the path s to the antenna reduces the brightness by the factor

$$e^{-\int_0^s \eta ds}$$

so that the total atmospheric brightness at the antenna is

$$b' \approx \int_0^\infty \eta b'_{BB}\, e^{-\int_0^s \eta ds}\, ds \tag{49}$$

If b'_c is the spectral brightness of the cosmic noise from beyond the atmosphere (see the last section) this will appear to the antenna as an additional brightness

$$b'_c\, e^{-\int_0^\infty \eta ds} \tag{50}$$

Table 9
CALCULATED ATMOSPHERIC THERMAL NOISE TEMPERATURES (K) VS. ZENITH ANGLE, FOR ANTENNAS AT ZERO ALTITUDE.

Frequency (GHz)	Line/window	Zenith angle (degrees)					
		0	20	40	60	80	90
1	—	2.01	2.14	2.62	4.00	11.1	75.7
22	H_2O	29.1	30.8	37.3	55.1	130 3	287.4
35	W	16.4	17.5	21.3	31.9	81.6	281.5
60	O_2	286	286	287	287	288	288
94	W	59.8	63.2	75.4	107	210	288
118	O_2	259	262	270	280	286	288
140	W	99.6	105	122	164	260	288

Within the range of validity of the Rayleigh-Jeans approximation (see the section "Radio Wave Generation and Propagation") the equivalent noise temperatures may replace brightness in the above. Typical results of numerical integrations for a model (clear-air) atmosphere for 45° N Latitude in July[88] (see Reference 80) are shown in Table 9 for directional antennas on the ground.[22] An elevated antenna at point Q, looking down toward a point P on the Earth at incidence angle χ, receives radiation consisting of four components: (1) thermal radiation originating on the path PQ, (2) thermal radiation from the Earth surface, attenuated by the path PQ, (3) atmospheric thermal radiation reduced by the reflection coefficient of the Earth at angle χ, and attenuated by the path PQ, and (4) cosmic radiation reduced by the entire air-path and by the Earth-reflection. These contributions can be estimated numerically in specific cases.

Rough, vegetated Earth-surfaces are generally good absorbers of short microwaves, and hence the radiation is approximately that of a black body at air temperature. The reflectivity of snow-cover can vary over a wide range depending on the condition of the snow.[28] If the surface is smooth water, for example, the power reflectivity is r^2, and the surface emissivity is $(1 - r^2)$, where r is the Fresnel amplitude reflection coefficient appropriate to the wave polarization (see Equations 15 and 16). The brightness of the surface is then $(1 - r^2)\, b'_{BB}$, where b'_{BB} is the brightness of a black body at Earth temperature T. At centimetric and millimetric wavelengths most of the absorption, and emission, for many common natural materials takes place quite close to the surface, and the effective value of T may be close to the surface temperature.

As noted in the section "Radio Wave Generation and Propagation," the reflection coefficient can be markedly different for the TE- and TM-polarizations, especially with smooth flat surfaces, and angles of incidence near the Brewster angle. Because of the high TM-wave absorption at the Brewster angle the thermal emission in the TM polarization can be significantly larger. This was demonstrated experimentally by observing the thermal radiation from calm seawater at 24.2 GHz[47] (see also Reference 69). For typical natural land-surfaces, the microwave emissivity varies less with wave polarization.

At MF and HF wavelengths the D-region may be strongly absorbing (see the section on radio wave generation) and hence must also radiate.[85] The electron temperature in the D-region extrapolated from higher altitude data[5] is probably only a few hundred degrees Kelvin; about the same as the neutral temperature. The MF-HF thermal radiation from the D-region may therefore be expected to be negligible compared with sferics noise.

ATMOSPHERIC NOISE AT SATELLITE ALTITUDES

Factors in Noise Estimation

In estimating atmospheric noise levels for altitudes above the ionosphere, four cases may be distinguished. In Case 1 the frequency is so high ($f \gg fc$) that ionospheric reflection, refraction and absorption are negligible. The noise from the direction of the Earth consists of atmospheric thermal noise, atmospherically attenuated thermal radiation from the Earth, sferics, and man-made noise. If the observation point is at height h high above the surface of the Earth of radius a, the area of the Earth contained within the observer's geometric horizon, and from which radiation is receivable, is approximately $2\pi a^2 h/(a + h)$, neglecting atmospheric refraction.

In Case 2, the frequency is higher than the critical frequency, but low enough for ionospheric refraction to be important. The qualitative illustration, Figure 9 shows a point P, effectively above the ionosphere, receiving waves for only a limited area of the Earth lying between the rays B and B′ for which $f > f_c \sec\theta$ (see the subsection "Ionospheric Propagation"). As f approaches f_c the cone of directions and the corresponding area on the Earth shrink down to zero, and the ionosphere becomes nearly opaque. A more quantitative discussion of the closing aperture effect has been given by Herman [32]. The ionosphere is not perfectly uniform, and for this and other reasons the boundaries of the aperture are somewhat blurred (see Reference 57).

Because the ionosphere transmits some frequencies and not others, the wave-form E(t) of an individual sferic observed at satellite altitudes will be different from that observed below the ionosphere. Pierce[57] gave field strength estimates of individual sferics at satellite altitudes, assuming a model ionosphere with a 5-MHz critical frequency. For an altitude of 1000 km, and a 1-MHz bandwidth, these estimates range from 2000 μVm^{-1} at 10 MHz to 100 μVm^{-1} at 100 MHz.

In Case 3 the frequency is less than the ionospheric critical frequency, but greater than about 1 MHz. This is the spectral region in which the ionosphere is nearly opaque (see Figure 3). In Case 4, from below 1 MHz to 100 kHz, the attenuation is large in the daytime, but may be less than 10 db at night depending on the propagation direction with respect to the geomagnetic field.

Satellite Data

Herman[31] has reviewed HF noise information obtained from satellites at distances from 1.3 to 31 Earth radii. At 2 MHz the ionosphere is so nearly opaque most of the time that sferics noise is less than the cosmic noise background at that frequency. At 3 MHz, sferics are occasionally found to penetrate the ionosphere when the critical frequency is low, as would be the case on winter nights at the times of solar minima, or over the main ionospheric trough where the critical frequency can be lower than 4 MHz. Above these frequencies, on up to about 30 MHz or higher, sferics noise is generally dominant. Although based on only 120 data points, a contour map of terrestrial radio noise temperatures at 9.18 MHz, derived from measurements by the RAE-I satellite,[32] shows major noise peaks roughly coincident with the areas of maximum thunderstorm activity (see the section "Noise From World Wide Atmospherics").

In the range between 100 and 600 kHz, noise of magnetospheric origin can be very intense ($> 10^{-15} Wm^{-2}Hz^{-1}$) above the ionosphere.[24,39] Most of this noise is reflected back out into space by the ionosphere and hence does not reach the ground with appreciable intensity.

SPECIAL SOURCES OF ATMOSPHERIC NOISE

Certain special sources of atmospheric noise are of interest even though they may

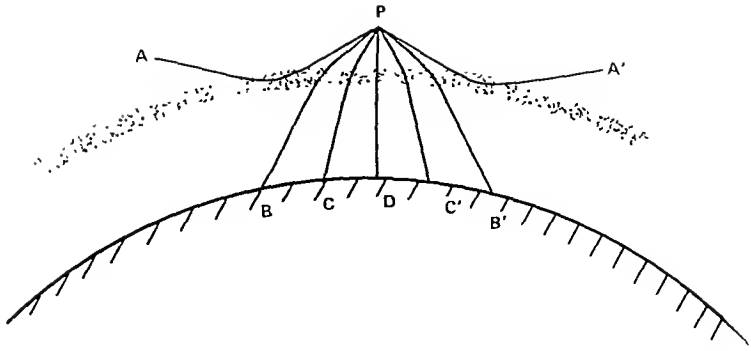

FIGURE 9. Ionospheric refraction of HF rays from a point above the ionosphere.

not be major contributors to world-wide noise levels. For instance, wind-blown snow particles impinging on a receiving antenna produce radio noise whose equivalent radiation field-strength decreases with increasing frequency, at a rate depending on wind velocity.[30] Dust storms can cause atmospheric fields of many thousands of volts per meter; enough to produce corona currents from sharp points, and perhaps even cause lightning discharges.[41]

Tornadoes have long been considered to be strong emitters of radio noise. This noise may differ significantly from that of ordinary thunderstorms; for example, the rate at which sferics bursts occur in tornadoes has been proposed as an index for tornado warning. Taylor[75] concluded from measurements from 10 KHz to 3 MHz that the noise sources are not always confined to close proximity of the funnel and are probably in the parent cloud. Harvey[27] observed noise from a distant tornado with a parabolic antenna at 925 MHz and concluded that the sources of the noise extended to unusually high altitudes.

Lightning-like flashes have been observed near erupting volcanoes, probably the earliest account being that of Pliny[58] who described the eruption of Vesuvius. Presumably radio noise emissions accompany such flashes. The detonation of chemical explosives in air is said to cause electromagnetic radiation.[79] A source-mechanism which has been suggested, involves the sudden exclusion of preexisting static fields in the volume of air made electrically conducting by ionization from the explosion. In the case of nuclear explosions, lightning-like discharges have been photographed around the periphery of the resulting cloud-mass. The powerful electromagnetic-pulse which occurs at the instant of an airburst nuclear explosion, is explained by a quite different mechanism: a sudden burst of gamma rays enters the air, and an outward flow of Compton electrons results. Any asymmetry of this electron flow such as might be caused by the ground, or even the density gradient in the air, would produce a net current-moment in one direction thus causing the radiation.[23]

In an unusual experiment, regions of high electrostatic fields in thunderstorms were seeeded with millions of short chaff-fibers.[63] A 35-GHz radiometer antenna directed toward the chaff indicated noise temperatures in the order of 300 K. This noise was attributed to coronal discharges from the fibers.

The influx of high energy particles into the upper atmosphere is usually accompanied by a decrease in the high frequency cosmic radio noise received on the ground because of the additional absorption from the ionization produced by the particles. Recent measurements[3] indicate an increase in noise level in the frequency range 8.0 to 25.5 MHz several hours before the cosmic noise absorption occurs. The noise increase was

attributed to the deceleration (braking) of electrons with energies greater than 40 keV entering the ionosphere

Newman[51] showed that lightning could be triggered artificially by rapidly thrusting a long grounded conductor up toward thunderclouds In 1969 lightning struck the Apollo 12 space vehicle twice shortly after lift off, and it is generally thought that the conducting exhaust trail played a role in that event Conventional aircraft are occasionally struck by lightning, and in these cases electromagnetic fields, but not necessarily the radiation fields per se, can be responsible for damaging or causing malfunction of electronic and other equipment In many cases pilots have reported severe noise interference in radio equipment well in advance of receiving a lightning strike Such events sometimes take place with no known thunderstorms nearby [25]

Many anecdotal reports describe the appearance of ball lightning, see for example the discussion by Singer [67] Most of the reports describe a glowing sphere, or ball of light, with a diameter of perhaps 30 cm The glow persists for some seconds, and may hover or move about slowly The glow may fade silently, or in some cases ends with explosive force Of those theories which seek a physical explanation, probably that of Kapitza[69] has been most widely discussed In this theory the visible glow is ascribed to a high radio-frequency gas discharge, with thunderstorms as a possible source of the electromagnetic energy

RADIO NOISE FROM EXTRATERRESTRIAL SOURCES

Introduction

In some cases, noise from sources external to the Earth may be more important than atmospheric noise The sun and other members of the solar system contribute part of the extraterrestrial background, and the remaining cosmic noise has both galactic and extragalactic components Galactic noise comes from sources in the Earth's own galaxy (Milky Way) which contains something in the order of 10^{11} stars, vast quantities of interstellar dust, and gases — especially atomic hydrogen Most of the material of the galaxy is distributed in the form of a thin flat disk, with a bulge near its center The disk diameter is about 8×10^4 light years, and the solar system is located in the disk about 3×10^4 light years from the center The disk has spiral-like features, but when viewed edge-on from the eccentric position of the Earth, the spiral structure is not conspicuous, and the maximum density appears in the general direction of the galactic center The rest of the galactic material, stars, and globular clusters, is dispersed throughout a sphere or 'halo' about $1\ 3 \times 10^5$ light years in diameter, with its center near the center of the disk There are many other galaxies at still more remote distances beyond the Milky Way, some of which radiate radio noise which reaches the Earth with appreciable intensity

The "positions" (actually directions) of astronomical objects can be described in an angular coordinate system on a Celestial Sphere concentric with the Earth Intersections of the sphere by the axis of the Earth define North and South Celestial Poles, and hence also a Celestial Equator Degrees of astronomical latitude or "declination" (δ) are measured northward from the equator, and astronomical longitude or "Right Ascension" (α) is measured in hours (24 hr = 360°) eastward from a reference meridian which contains the point where the sun crosses the equator at the Vernal (March) Equinox Figure 10 illustrates the Northern Hemisphere of the celestial sphere as if seen from a great distance above the North Pole The plane of the Galaxy intersects the sphere in a great circle whose northern half appears semielliptical in the projection of Figure 10 The direction opposite to the center of the Galaxy, is indicated by the point GAC That diameter of the sphere which is perpendicular to the galactic plane,

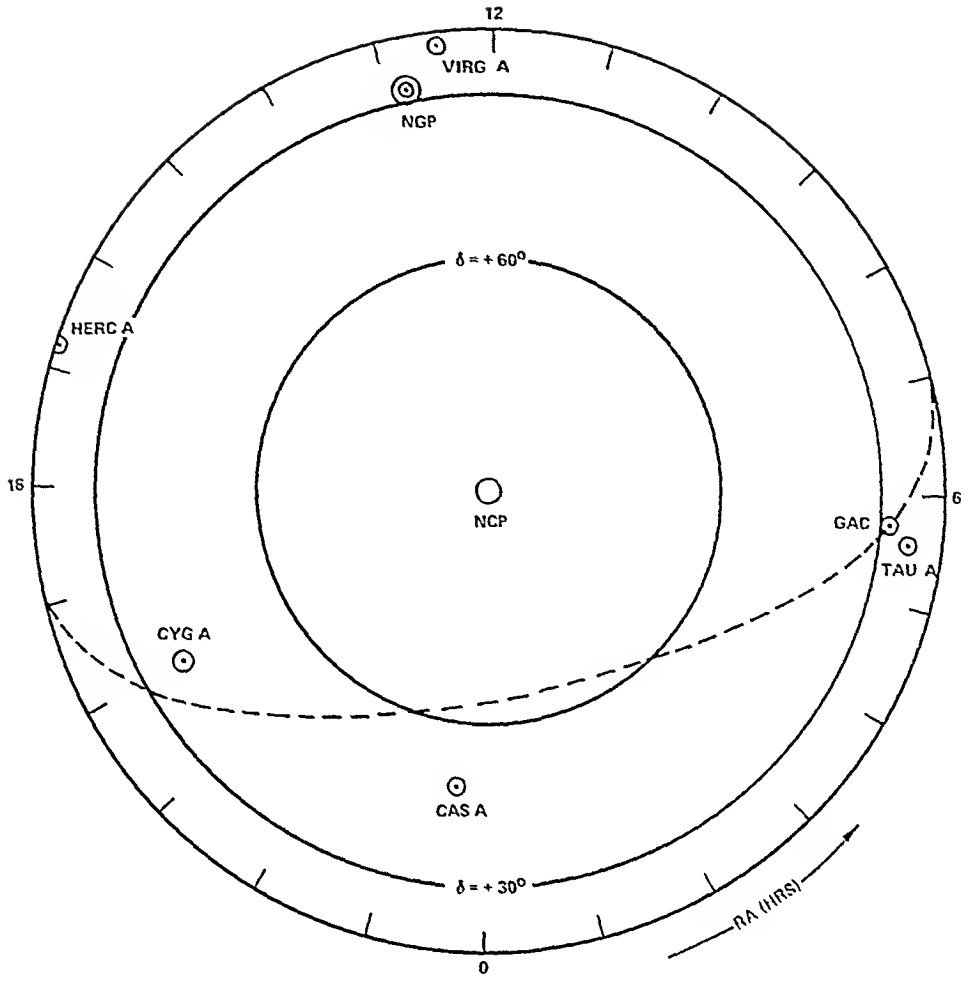

FIGURE 10. Celestial sphere viewed from above the North Celestial Pole.

defines the Galactic poles; the Northern Galactic Pole (NGP) is shown in Figure 10. The position of certain discrete sources of radio noise (see the section "Discrete Sources" following) are also shown. The geometrical relations of points on the celestial sphere may be found by spherical trigonometry, or by vector analysis. In a rectangular coordinate system XYZ, with OZ in the direction of the North pole and OX in the reference meridian, the unit vector in the direction δ, α is

$$r_0 = \cos\alpha \cos\delta\, x_0 + \sin\alpha \cos\delta\, y_0 + \sin\delta\, z_0 \qquad (51)$$

where x_0, y_0, z_0 are unit vectors in the coordinate directions.

Since an observer's view of the sky is limited by the local horizon, not all of the cosmic sources contribute to the noise at a given time and place. Neglecting refraction effects, a source having declination δ will always be above the horizon of a sea-level observer at geographic latitude L if $\tan\delta\tan L > +1$, and will never be above if $\tan\delta\tan L < -1$. For intermediate cases the fraction of the time that the source is above the horizon is given by $(1/180°)\cos^{-1}(-\tan\delta\tan L)$. At L = 45°, for example, the galactic center with $\delta = -29°$ (approximate direction of Sagittarius A) is above the horizon about 31% of the time.

A number of different emission mechanisms are involved in the generation of extra-terrestrial noise. A discrete spectral line observed at $\lambda = 21$ cm is due to quantum transitions in neutral hydrogen. In the case of the moon and most of the planets, the radiation is of thermal origin. The continuous radiation from hot stellar gases can be attributed to the acceleration of charges with high thermal velocities. The mass motion of charges in plasma oscillations may be a source of noise in stellar atmospheres, and certainly the plasma critical frequencies play a role in determining what radiation can escape. In other sources, the relatively high intensities of low frequency radio noise, and the presence of linearly polarized noise components are evidence of synchrontron radiation, so called because it was first recognized in the form of visible light from accelerated electrons in high energy machines of that name. The basic classical theory was developed around the beginning of the century[80] and can be derived from the relativistically correct formulas for radiating charges (Equations 1, 2) by assuming the point charge q is orbiting in a free-space circle of radius ϱ, with constant velocity v, and a centripetal acceleration v^2/ϱ provided by a magnetic field perpendicular to the circle. As the charge velocity approaches the velocity (c) of electromagnetic waves, the radiated power increases, and the increase appears in spectral lines at increasingly high harmonics of the orbital period. For high energy electrons, the strongest line occurs at a harmonic number $n \approx 3.4\ k,^2$ where K_e is the kinetic energy of the electron in millions of electron volts. Thus for $K_e = 100$ mev, $n \approx 3.4 \times 10^6$. The radiation is strongest in directions very close to the orbital plane, where it is polarized with the electric vector parallel with the plane. In an astronomical source there would be distributions of particle types, energies, and directions with respect to the ambient magnetic field, thus producing a complex radiation-mix.

Much of the information in this section may be found in far greater detail in one or more of the following references: 1, 34, 66, 70, 80, 81 and 84. Many original papers may be found in *The Astrophysical Journal* and in the *Royal Astronomical Society Monthly Notices*.

Cosmic Noise Maps

Radio noise maps of the entire celestial sphere are becoming increasingly available, and earlier text books give examples and references to partial maps. A typical map for a given frequency, shows contours of equal brightness temperature on a projection in which δ and α appear as rectangular coordinates. Other maps use galactic coordinates with the galactic plane as the equator.

Noise maps typically show higher temperatures in a band perhaps 20° wide along the galactic plane, and the highest temperatures in the band are approximately in the direction of the galactic center. Maps for 136 and 400 MHz, prepared for a cosmic noise study by NASA,[74] show brightness temperatures for about 20 contour-intervals. With this degree of resolution, the 136-MHz maps show about 7 peak-regions with temperatures ranging from 600 K to over 3200 K, and the 400-MHz map shows about 5 peaks from 60 K to 240 K. An antenna pointed at the sky has a temperature equal to the average temperature of the sky within its beam so if the directional pattern is known, it can be combined with the temperature information, and the effective antenna temperature calculated by numerical integration. If appropriate, estimates of ionospheric and tropospheric effects may also be folded in. If the antenna has a very narrow beam it may be necessary to take individual discrete sources into account (see the subsection below, "Discrete Sources").

Average Cosmic Noise Temperatures

In many cases, a rougher estimate of cosmic noise than that obtained by a detailed numerical integration may be adequate. For example, a low gain antenna, such as half-

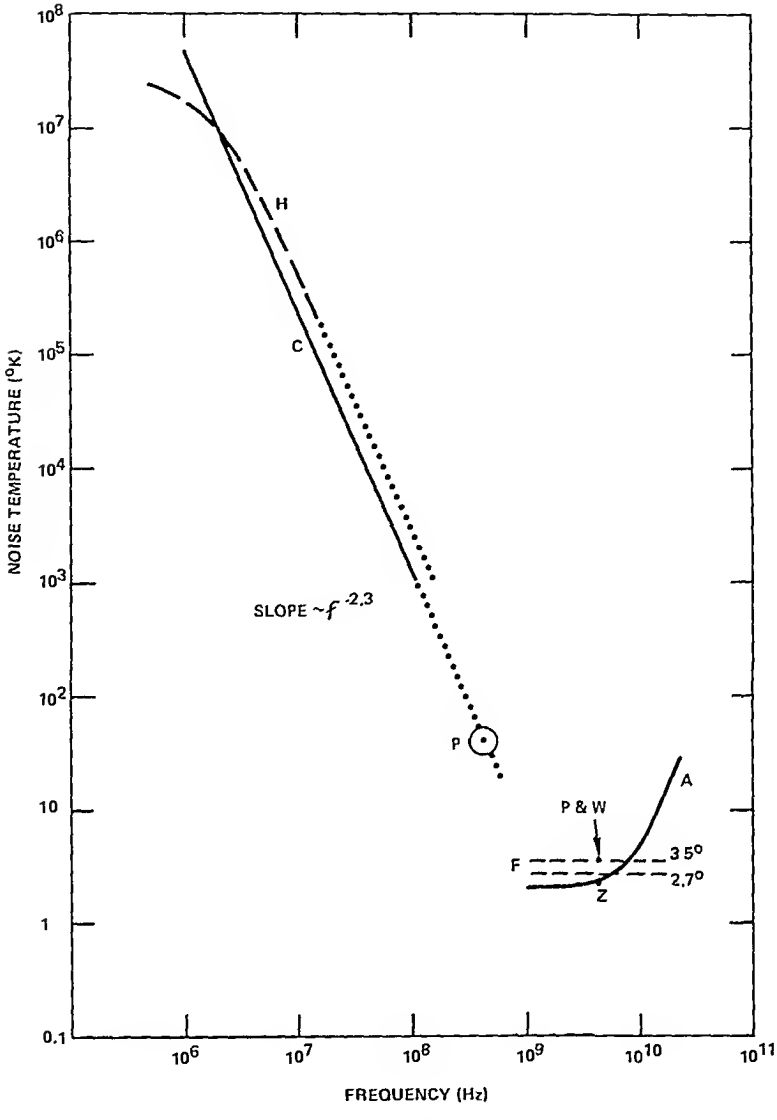

FIGURE 11. Estimates of average cosmic noise temperatures.

wave dipole receives cosmic noise over a wide range of directions and the received noise power will be a time-varying average, and it may suffice to know typical values.

Line C in Figure 11 is an approximation of the cosmic noise levels from 1 to 100 MHz adopted by Crichlow and Smith[16] as being appropriate for vertical half-wave dipoles near the surface of the Earth. On this line, antenna temperature is proportional to $f^{-2.3}$. Curve H in Figure 11 summarizes many data points from Alouette satellite observations[26] which were relatively free of ionospheric effects. More limited data reported from a variety of other space measurements, tend to run higher by perhaps 3 dB.

A frequency variation of $f^{-2.3}$ also approximates the temperature trend found by Piddington,[56] who analyzed data at frequencies as high as 3 GHz. Although this trend applied primarily to noise from near the galactic center, it can perhaps be used with some caution for estimating temperature averages in the present context; see dotted lines in Figure 11. An inspection of the radio noise maps of Pauling-Toth[54] and of Taylor[74] suggests that a numerical integration might yield an average noise temperature

in the order of 40 K around 400 MHz This estimate (point P, in Figure 11) is consistant with the $f^{-2.3}$ line However, continuing this line much beyond 1 GHz would conflict with the conclusions of Penzias and Wilson[55] who reported a background temperature of 3 5 K at 4 08 GHz (λ = 7 3 cm) It is now generally accepted that this temperature, or the more recent value 2 7 K (see for example Verschur[81]), is nearly constant in all directions on the celestial sphere, and represents the background temperature of the universe, consistant with the "big bang" theory of cosmological development This temperature imposes a floor (F) shown in Figure 11 For comparison, the line A is an estimate of atmospheric thermal noise in the zenith direction for an antenna on the ground, based on a computer model [22] Point Z (2 3 K) is the zenith atmospheric noise temperature quoted by Penzias and Wilson [55]

Discrete Sources

When observed with increasingly high angular resolution, the distribution of cosmic noise over the celestial sphere shows distinct radiation peaks, or "discrete sources", many of which have been identified with objects known to optical astronomy Thousands of discrete noise sources have been catalogued, some of them subtending angles much less than one degree Table 10 lists a few such sources with their nominal dimensions given in minutes of arc Sources which are part of the Milky Way, and those which are extragalactic are distinguished by G or XG, respectively Distances are given in light years All the sources listed in Table 10 are considered synchrotron emitters, except Orion, which being thermal, has a power flux spectral density which increases with frequency, see Table 11 The radio sources Cassiopeia A and Taurus A are remnants of supernova explosions which occurred in the years 1700 and 1054, respectively The approximate positions of the five sources in Table 10 having positive declinations are indicated in Figure 9

To place in perspective the power of an individual localized discrete source, consider a half-wave 100-MHz antenna oriented to receive the strong source, Cassiopeia A, whose spectral power intensity is about $1\ 9 \times 10^{-22}$ w $m^{-2}Hz^{-1}$ Since the absorption cross section of the antenna is about 1 2 m^2, the received spectral power is $2\ 2 \times 10^{-22}$ wHz^{-1}, which on dividing by Boltzmann's constant, gives an equivalent temperature of only about 18 K This would require a special low-noise receiver to detect, even if there were no noise from the rest of the sky If the antenna had 100 times (20 dB) more gain, the temperature from Cassiopeia A would be around 1800 K, which would be comparable to, or larger than, the estimated 1000 K average temperature of cosmic noise from Figure 11 However, to obtain a gain of 20 dB over a half-wave dipole at this frequency with a conventional parabolic reflector, its diameter would have to be in the order of 16 m

Radio Noise from the Solar System

In its quiet state the sun thermally emits radio noise, producing power flux spectral densities on the Earth which increase with frequency as indicated in Table 12 Solar disturbances, which are most frequent near times of maxima in the 11-year solar sunspot cycle, are often accompanied by strong bursts of radio noise The bursts associated with solar flares can be particularly intense, see Table 12, they typically build to a peak in a few minutes, then fade away in 10 to 100 min X-rays from the flares may increase the ionization-density in the lower ionosphere on the illuminated side of the Earth, thereby temporarily improving low frequency wave propagation and causing an apparent increase of atmospheric noise There may also by an emission of high energy particles, especially protons, which arrive at the Earth later than the X-rays because of their lower velocities The particles produce longer-lasting ionospheric effects, especially in polar latitudes, and can interfere with high frequency propagation

Table 10
EXAMPLES OF STRONG LOCALIZED SOURCES OF COSMIC RADIO NOISE.

Source	G/XG	Dist. (LY)	Type	RA – α (hr)	Dec – δ (degrees)	Approximate size (min)
Cassiopeia A	G	1.1E4	Supernova remnant (1700 AD)	23.4	58.6	3 7
Cygnus A	XG	5.5E8	Double galaxy	20 0	40.6	1 × 2
Virgo A	XG	3.5E7	Radio galaxy (core-halo-jet)	12.5	12.6	6 × 10
Taurus A	G	3.5E3	Crab Nebula supernova remnant (1054 AD)	5.5	22.0	5×7
Hercules A	XG	1.5E9	Double galaxy	16.8	5.1	1 × 2
Orion	G	1.6E3	Nebula	5.5	−5.4	30

Note: En = × 10^{n}

Table 11
APPROXIMATE SPECTRAL POWER FLUX DATA FOR SOURCES OF TABLE 10

	Frequency (GHz)/wavelength (m)						
Source	0.03 10	0.1 3	0.3 1	1 0.3	3 0.1	10 0.03	30 0.01
Cassiopeia A	4.4E − 22	1.9E − 22	7.1E − 21	2.8E − 23	6.5E − 24	4.3E − 24	1.8E − 24
Cygnus A	2.0E − 22	1.1E−22	5.6E − 23	2.2E − 23	6.3E − 24	1.6E − 24	—
Virgo A	4.1E − 23	1.5E − 23	5.8E − 24	2.0E − 24	7 9E − 25	3.0E − 25	—
Taurus A	2.0E − 23	1.6E − 23	1.3E − 23	9.1E − 24	6.3E − 24	4.4E − 24	2.5E − 24
Hercules A	1.6E − 23	5.5E − 24	1.8E − 24	5.6E − 25	1.7E − 25	5.6E − 26	—
Orion	2.5E − 25	8.5E − 25	2.6E − 24	4.1E − 24	4.4E − 24	—	—

(w $m^{-2}Hz^{-1}$)

Note: E − = × 10^{-n}.

Table 12
POWER FLUX SPECTRAL DENSITIES FROM THE SUN, THE MOON, AND JUPITER.

	Frequency (GHz)/Wavelength (m)						
Source	0.03 10	0.1 3	0.3 1	1 0.3	3 0.1	10 0.03	30 0.01
Solar bursts	2.8E − 17	9.1E − 18	5.0E − 18	3.7E − 18	2.7E − 18	1.3E − 18	5.3E − 19
Quiet sun	1.0E − 22	1.0E − 21	2.6E − 21	3.5E − 21	6.5E − 21	2.9E − 20	—
Average moon	—	—	4.4E − 25	4.6E − 24	3.9E − 23	4.4E − 22	3.6E − 21
Jupiter	4.0E − 26	6.2E − 26	7.9E − 26	8.5E − 26	7.6E − 26	1.7E − 25	1.8E − 24

(w $m^{-2}Hz^{-1}$)

Table 13
NOISE-RELATED DATA FOR THE PLANETS MERCURY, VENUS, MARS, SATURN, AND URANUS

	Mercury	Venus	Mars	Saturn	Uranus
Average distance from sun (km)	6 0E + 7	1 0E + 8	2 2E + 8	1 4E + 9	2 8E + 9
Approximate noise temperature at 3 GHz (K)	≈1000	660	200	<300	130
Diameter (km)	4 8E + 3	1 2E + 4	6 8E + 3	1 2E + 5	5 1E + 4
Distance with sunlit side toward Earth (km)	2 1E + 8	2 6E + 8	7 8E + 7	1 3E + 9	2 7E + 9
Corresponding solid angle (steradians)	4 1E − 10	1 6E − 9	6 0E − 9	6 7E − 9	2 8E − 10
Calc noise at 3 GHz (w m $^{-2}$Hz $^{-1}$)	≈1 1E − 28	2 9E − 27	3 3E − 27	<5 5E − 27	1 0E − 28

for hours, or even days At 100 MHz, under quiet-sun conditions (10 $^{-21}$w m^{-2} Hz^{-1}) a half-wave dipole antenna could receive about 10^{-23}w Hz $^{-1}$, which is equivalent to an antenna temperature of about 90 K Under solar-burst conditions (10^{-17}w m^{-2} Hz^{-1}) the antenna temperature would be 10^{4} times higher, or nearly a million degrees The intense noise from the disturbed sun was first discovered when it interfered with radar operations in February 1942 [34]

The moon is about 3 8 × 10^{5} km from the Earth, and subtends about the same solid angle as the sun, 6 7 × 10^{-5} steradians The lunar surface is heated by the sun, and emits thermal radio noise The infrared and millimetric radiation comes from material close to the surface, and varies as the surface temperature follows the changing conditions of solar illumination The temperature of the deeper layers which are responsible for the longer wavelength radiation vary less The noise temperature of the full moon is around 220 K, and some values of power flux spectral density averaged over a lunar cycle are given in Table 12

The planet Jupiter is about 7 6 × 10^{8} km from the sun, and comes within about 6 3 × 10^{8} km of the Earth when it subtends a solid angle of 3 9 × 10^{-8} steradians Spectral power intensities are given in Table 12 At wavelengths less than about 3 cm, the radiation is primarily of thermal origin with a noise temperature around 145 K, but at wavelengths greater than about 10 cm the noise temperature is much higher (600 K) indicating a nonthermal emission process, see for example, Smith [68] Also, Jupiter occasionally emits intense bursts of noise around 18 MHz, with spectral power intensities in the order of 10^{-20} to 10^{-19}w m^{-2} Hz^{-1} These bursts last for a tenth second or longer, and have been observed as often as several times in a few days

The planets Mercury, Venus, Mars, Saturn, and Uranus are primarily thermal emitters of radio noise, with noise temperatures at 3 GHz given in Table 13 The last line in this table gives estimates of spectral power intensities calculated from the noise temperatures and the listed geometric parameters, assuming that the sides of the planets facing the Earth are nearly all sunlit For the inner planets, Mercury and Venus, this condition holds when they are farthest from the earth For the outer planets, Mars, Saturn, and Uranus, the approximate distances of closest approach to the Earth were used The noise intensities in Table 13 are less than those of many discrete galactic and extragalactic noise sources

APPENDIX

LIST OF SYMBOLS

Symbol	Meaning	Units
q	electric charge	coulombs
v	velocity	meters second^{-1}
t	time	seconds
R	distance	meters
R_o	unit vector	none
E	electric field	volts meter^{-1}
H	magnetic field	amperes meter^{-1}
Z_o	impedance of space	ohms
c	wave velocity	meters second^{-1}
μ_o	mag permeability	henry meter^{-1}
γ	relativistic factor	none
I	current	amperes
m	current moment	ampere meter
ℓ	length of segment	meter
M	a number	none
m_o	peak sinusoidal current moment	ampere meter
f	frequency	hertz
ω	angular freq.	hertz
Θ	angle between M_o and R_o	degrees or radians
S	power intensity	watts meter^{-2}
E_o	peak sinusoidal wave field	volts meter^{-1}
W	power	watts
λ	wavelength	meters
χ	zenith angle	radians
h	height	meters
σ	electrical conductivity	mho meter^{-1}
ε	relative dielectric const.	none
r_{TM}	reflection coefficient	none
r_{TE}	reflection coefficient	none
u	a parameter	none
ε'	complex dielectric constant	none
θ	angle of incidence	radians
d	depth	meters
D	skin depth	meters
e	base, natural logs	none
a	radius of Earth	meters

N	electron density	meters^{-3}
f_p	plasma frequency	hertz
f_c	critical frequency	hertz
B	mag flux density	Webers meters^{-2}
f_H	gyro frequency	hertz
V	voltage transient	volts
R_L	resistive load	ohms
A (f)	field amplitude spectral density	volt meter^{-1} hertz^{-1}
ϕ	phase angle	radians
$\mathcal{E}'$	spectral energy intensity	joule meter^{-2} hertz^{-1}
$\mathcal{E}$	energy intensity	joule meter^{-2}
X	antenna cross section	meters^2
P	energy to load	joules
G	receiver gain	none
V_p	envelope peak	volts
w	damped oscillation of unit amplitude	none
A_n	amplitude of nth spectral line	volt meter^{-1}
n	a running integer number	none
ω_n	angular frequency of nth spectral line	hertz
f_R	repetition frequency	hertz
ϕ_n	phase of nth spectral line	radians
f_A	av rate of random pulses	hertz
A_{eq}	amplitude of equivalent sinusoidal wave	volt meter^{-1}
$\mathcal{E}'_A$	av value of $\mathcal{E}'$	joule meter^{-2} hertz^{-1}
S	spectral power intensity	watt meter^{-2} hertz^{-1}
F	projected area	meter^2
b	brightness of extended source	watt meter^{-2} steradian
Ω	solid angle	steradians
b′	spectral brightness	watt meter^{-2} steradian^{-1} hertz^{-1}
T	absolute temperature	degrees Kelvin
b'_{BB}	spectral brightness of black body	watt metter^{-2} steradian^{-1} hertz^{-1}
k	Boltzmann's constant	joule degree^{-1}
ζ	constant	degree hertz^{-1}

β	constant	watt meter^{-2} steradian^{-1} hertz^{-1}
E_{eq}	equivalent field	volts meter^{-1}
E_{peak}	peak electric field	micro-volts meter^{-1}
T_{urb}	noise temp in urban environment	degrees Kelvin
s	distance along propagation path	meters.
b'_c	spectral brightness of cosmic noise	watts meter^{-2} steradian^{-1} hertz^{-1}
η	absorption coef.	meter^{-1}
r	complex reflectivity	none
δ	declination	degrees or radians
α	right ascension	degrees or radians
r_o	*unit vector in direction* δ, α	none
L	latitude	degrees or radians
x_o	unit vector along x-axis	none
y_o	unit vector along y-axis	none
z_o	unit vector along z-axis	none
ϱ	radius of circular orbit	meters
K_e	kinetic energy	million electron volt (abbrev: MEV)

REFERENCES

1. Baker, R. H., *Astronomy*, 9th ed., Van Nostrand, Princeton, N.J., 1971.
2. Bell Telephone Laboratories, Inc., Propagation Curves, Report 966-6c, October, 1944.
3. Blagoveshchenskii, D. V. and Degtyarev, V. I., Radio noise in the decameter range during auroral substorms, *Izv. Vyssh. Uchebn. Zaved. Radiofiz.* 22(3), 262, 1979.
4. Booker, H. G., Crain, C. M., and Field, E. C., Transmission of Electromagnetic Waves Through Normal and Disturbed Ionospheres, Report R-558-PR, Rand Corporation, Santa Monica, Calif., November 1970.
5. Booker, H. G. and Smith, E. K., A comparative study of ionospheric measurement techniques, *J. Atmos. Terr. Phys.*, 32, 467, 1970.
6. Brook, M. and Kitagawa, N., Radiation from lightning discharges in the frequency range 400 to 1000 Mc/s, *J. Geophys. Res.*, 69(12), 2431, 1964.
7. Brook, M. and Ogawa, T., The cloud discharge, in *Lightning*, Vol. 1, Golde, R. H., Ed., Academic Press, New York, 1977.
8. Bruce, C. E. R. and Golde, R. H., The lightning discharge *J. Inst. Elec. Eng. (London)*, 88, 487, 1941.
9. Carpenter, D. L. and Park, C. G., On what ionospheric workers should know about the plasmapause-plasmasphere, *Rev. Geophys. Space Phys.*, 11, 133, 1973.
10. Casey, J. P., Lewis E. A., and O'Neil, J. F., Thermal Radiation: Additional Airborne Observations and Guidance Tests, Technical Report 55-11, Air Force Cambridge Research Center, Cambridge, Mass., June 1955.

11 International Radio Consultative Committee World Distribution and Characteristics of Atmospheric Radio Noise, Report 322 International Telecommunication Union, Geneva, 1963
12 International Radio Consultative Committee, Report 719, in Recommendations and Reports of the CCIR 1978 Vol 5, Plenery Assembly International Telecommunication Union/International Radio Consultative Committee Geneva
13 Chubb, J N , Erents, S K , and Pollard, I E , Radio detection of low energy electrostatic sparks, *Nature (London)*, 245 1973
14 Cianos, N and Pierce, E T , A Ground-Lightning Environment for Engineering Usage, Technical Report 1, Stanford Research Institute 1972
15 Crane, R K , Propagation phenomena affecting satellite communication systems operating in the centimeter and millimeter wavelength bands *Proc IEEE*, 59, 173 1971
16 Crichlow, W Q , Smith, D F , Morton, R N , and Corliss, W R , Worldwide Radio Noise Levels Expected on the Frequency Band 10 Kilocycles to 100 Megaeyeles *Natl Bur Stand (U S) Circ* , No 557, 1955
17 Crichlow, W Q , Spaulding, A D , Roubique, C J , and Disnet, R T , Amplitude probability distributions for atmospheric radio noise, *Natl Bur Stand (U S) Monogr* No 23, 1960
18 Disnet, R T , Amplitude probability distributions for atmospheric radio noise, *Natl Bur Stand Monogr* 23 1960
19 Davies, K , *Ionospheric Radio Waves* Blaisdell, Waltham, Mass 1969
20 Elkins, T , Personal communications, 1979
21 Falcone, V J , Calculations of apparent sky temperature at millimeter wavelengths *Radio Sci* 1(10), 1205, 1966
22 Falcone, V J , personal communication, 1980
23 Pierce, E T , Nuclear explosion phenomena and their bearing on radio detection of the explosions, *Proc IEEE* 53(12) 1994 1965
24 Gurnett, D A , The earth as a radio source terrestrial kilometric radiation, *J Geophys Res* , 79, 4227, 1974
25 Harrison, H T , UAL Turbojet Experience with Electrical Discharges, Meteorology Circular No 57 United Air Lines Chicago 1965
26 Hartz, T R , Radio noise levels within and above the ionosphere, *Proc IEEE* 57(6), 1042, 1969
27 Harvey, R B and Lewis, E A , Radio mapping of 250 and 925-megahertz noise sources in clouds, *J Geophys Res* ,78(12) 1944, 1973
28 Hayes, D T , Lammers, U H , Marr, R A , and McNally, J J , Millimeter propagation measurements over snow in *Conference Records*, Vol 2 Institute of Engineers and Electrical Engineers, 1979
29 Heckseher, J L , personal communication, 1979
30 Herman, J R , Radio noise problems in arctic regions, in *Arctic Communications*, Pergamon Press, Elmsford N Y , 1964
31 Herman, J R , Space Environment Radio Noise and Propagation Analysis, Contract F19628-760-C-0001 Radio Sciences Company, Melbourne, Fla February 1976
32 Herman, J R , Caruso, J A , and Stone, R G , Radio astronomy explorer — 1 Observations of terrestrial radio noise *Planet Space Sci* 21 443, 1973
33 Hewitt, F J , The study of lightning streamers with 50 cm radar, *Proc Phys Soc London*, 66 B, 895, 1953
34 Hey, J S , *The Radio Universe*, Pergamon Press Elmsford, N Y 1971
35 Horner, F , Radio noise from thunderstorms, in *Advances in Radio Research* Vol 2, Ed , Saxton, J A , Academic Press, New York 1964
36 International Telephone and Telegraph Corporation Reference Data for Radio Engineers 4th ed , New York , 1956
37 Israel, H , *Atmospheric Electricity*, Vol 2, Israel Program for Scientific Translations, Jerusalem, 1973
38 Kachurin, L G Karmov, M I , and Medaliyev, Kh Kh, The principal characteristics of the radio emission of convective clouds, *Izv Atmos Oceanic Phys* 10(11), 1163 , 1974
39 Kaiser, M L and Stone, R G , Earth as an intense planetary radio source similarities to Jupiter and Saturn, *Science*, 189, 285 1975
40 Kalakowsky, C B and Lewis, E A , VLF Sferics of Very Large Virtual Source Strength, *Proc Inst Electr Eng Conference on MF, LF and VLF Radio Propagation*, C Baldwin Ltd , Kent, England, 1967, 228
41 Kamra, A K , Measurements of the electrical properties of dust storms, *J Geophys Res* , 77(30), 5856, 1972
42 Kimpara, A , Electromagnetic energy radiated from lightning in *Problems of Atmospheric and Space Electricity*, Coroniti, S C , Ed , Elsevier Amsterdam, 1965

43. Kosarev, E. L., Zatsepin, V. G., and Mitrofanov, A. V., Ultrahigh frequency radiation from lightnings, *J. Geophys. Res.*, 75(36), 7524, 1970.
44. Kossey, P. K., personal communication, 1979.
45. Krider, E. P., Radda, G. J., and Noggle, R. C. Regular radiation field pulses produced by intracloud lighning discharges, *J. Geophys. Res.*, 80, 951, 1975.
46. Lewis, E. A., Radiation from idealized shock excitation currents in a straight conductor rising from a perfect earth at an arbitrary angle, in *Electromagnetic Wave Propagation*, Academic Press, New York 1958.
47. Lewis, E. A., Casey, J. P., Vaccaro, A. J., Polarized Radiation from Certain Thermal Emitters, Technical Report 54-6, Air Force Cambridge Research Center, Cambridge, Mass., February 1954.
48. Lewis, E. A., Harvey, R. B., and Rasmussen, J. E., Hyperbolic direction finding with sferics of trans-Atlantic origin, *J. Geophys. Res.*, 65(7), 1879, 1960.
49. Loeb, L. B., *Electrical Coronas*, University of California Press, Berkley, 1965.
50. Maxwell, E. L. and Stone, D. L., VLF Atmospheric Noise Predictions, Report 92-F-1, Deco Electronics, Inc., Boulder, Colo., April 15, 1966.
51. Newman, M. M., Stahmann, J. R., Robb, J. D., Lewis, E. A., Martin, S. G., and Zinn, L. V., Triggered lightning strokes at very close range, *J. Geophys. Res.*, 72, 4761, 1967.
52. Oh, L., Huang, G. C., Goldman, R., Natural and Induced Electrical Effects on Integrated Antennas and Circuits at Frequencies to 10 GHz, Technical report AFAL-TR-69-210, Boeing Aerospace Company, Seattle, Wash., September 1969.
53. Orville, R. E. and Spencer, D. W., Global lightning flash frequency, *Mon. Weather Rev.*, 107, 934, 1979.
54. Pauling-Toth, I. I. K. and Shakeshaft, J. R., A survey of the background radiation at a frequency of 404 Mc/s, *Mon. Not. R. Astron. Soc.*, 124, 61, 1962
55. Penzias, A. A. and Wilson, R. W., A Measurement of Excess Antenna Temperature at 4080 Mc/s, *Astrophys. J.*, 142, 419, 1965.
56. Piddington, J. H., The Origin of Galactic Radio Frequency Radiation, *Mon. Not. R. Astron. Soc.*, 111, 45, 1951.
57. Pierce, E. T., Atmospherics and Radio Noise, in *Lightning*, Vol. 1, Golde, R. H., Ed., Academic Press, New York, 1977.
58. Pliny, The Younger, Plin, Epp VI, 16, 79 A.D.
59. Proctor, D. E., VHF Radio Pictures of Lightning, Council for Scientific and Industrial Research, Special Report TEL 120, Pretoria, Union of South Africa, 1974; Brook, M. and Ogawa, T., The cloud discharge, in *Lightning*, Vol. 1, Academic Press, New York, 1977, 191.
60. Rawer, K. and Suchy, K., Radio observations of the ionosphere, in *Handbuch der Physik*, Bd 49, Springer-Verlag, Berlin, 1967.
61. Reed, H. R. and Russel, C. M., *Ultra High Frequency Propagation*, 2nd ed., Boston Technical Publishers, Inc., Boston, Mass., 1966.
62. Rishbeth, H. and Garriott, O. K., *Introduction to the Ionosphere*, Academic Press, New York, 1969.
63. Rust, W. D. and Krehbiel, P. R., Microwave radiometric detection of corona from chaff within thunderstorms, *J. Geophys. Res.*, 82(27), 3945, 1977.
64. Saxton, J. A. and Lane, J. A., The anomalous dispersion of water at very high radio frequencies, in *Meteorological Factors in Radio-Wave Propagation*, The Physical Society, London, 1946.
65. Schonland, B. F. S., The lightning discharge, in *Handbuch der Physik*, Bd. 22, Springer-Verlag, Berlin, 1956.
66. Shklovsky, I. S., *Cosmic Radio Waves*, (transl.), Harvard University Press, Cambridge, Mass., 1960.
67. Singer, S., Ball lightning, in *Lightning*, Golde, R. H., Ed., Academic Press, New York, 1977.
68. Smith, A. G., Lubo, G. R., Six, N. F., Jr., Carr, T. D., Bollhagen, H., May, J., and Levy, J., Decameter-wavelength observations of Jupiter, *Astrophys. J.*, 141, 457, 1965.
69. Stogryn, A. The emissivity of sea foam at microwave frequencies, *J. Geophys. Res.*, 77(9), 1658, 1972.
70. Steinberg, J. L. and Lequeux, J., *Radio Astronomy*, (transl.) Bracewell, McGraw-Hill, New York, 1963.
71. Storey, L. R. O., *Monograph* on *Radio Noise of Terrestrial Origin*, Horner, F., Ed., Elsevier, Amsterdam, 1962, 134.
72. Stratton, J. A., *Electromagnetic Theory*, McGraw-Hill, New York, 1941.
73. Tanner, R. L. and Nanevicz, J. E., Precipitation Charging and Corona-Generated Interference in Aircraft, Stanford Research Institute, Tech. Rep. 73, Stanford Calif., April 1961.
74. Taylor, R. E., 136-MHz/400 MHz radio-sky maps, *Proc. IEEE*, 61, 469, 1973.
75. Taylor, W. L., Electromagnetic radiation from severe storms in Oklahoma during April 29 to 30, 1970, *J. Geophys. Res.*, 78(36), 8761, 1973.

76 Trichel, G W , The mechanism of the positive point-to plane corona in air at atmospheric pressure, *Phys Rev* , 55, 382, 1939
77 Uman, M A , Beasley, W H , Tiller, J A , Lin, Y-T, Krider, E P , Weidman, C D , Krehbiel, P. R , Brook, M , Few, A A , Bohannon, J L , Lennon, C L , Poehler, H A , Jafferies, W , Gulick, J R and Nicholson, J R , An unusual lightning flash at Kennedy Space Center, *Science*, 201, 9, 1978
78 Uman, M A , Seacord, D F , Price, G H , Pierce, E T , Lightning induced by Thermonuclear detonations, *J Geophys Res* , 77(9) 1591, 1972
79 United States Atomic Energy Commission, The Effects of Nuclear Weapons, Washington, D C , April 1962
80 Valley, S ,Ed , Handbook of Geophysics and Space Environments, Air Force Cambridge Research Laboratories Cambridge Mass 1965
81 Verschur, G L and Kellerman, K I , *Galactic and Extra Galactic Radio Astronomy*, National Radio Astronomy Observatory Springer Verlag, 1974
82 Watt, J R and Campbell, L L , Transmission Curves for Ground Wave Propagation at Low Radio Frequencies Report R I, Defense Research Telecommunication Establishment, Ottawa Canada, April 1953
83 World Meteorological Organization, World Distribution of Thunderstorm Days, Geneva, Switzerland, 1953
84 Zheleznyakov, V V , *Radio Emission of the Sun and Planets* (transl), Massey, Pergamon Press, Elmsford N Y 1970
85 Hsieh, H C , A theory of ionospheric thermal radiation, *J Atmos Terr Phys* , 28 769, 1966
86 Stogryn, A , The apparent temperature of the sea at microwave frequencies, *IEEE Trans Antennas Propag* , AP 15 278 1967
87 Golde, R H ,Ed , Lightning currents and related parameters, in Lightning Vol I, Academic Press, New York 1977, 309
88 Environmental Science Services Administration U S Standard Atmosphere Supplements, U S Government Printing Office Washington D C 1966
89 Kapitza, P L , The nature of ball lightning (transl) *Dokl Acad Nauk SSSR*, 101, 245, 1955
90 Schott, G A , *Electromagnetic Radiation* Cambridge University Press, Cambridge, Mass , 1912, 83

ATMOSPHERIC NOISE AND ITS EFFECTS ON TELECOMMUNICATION SYSTEMS PERFORMANCE

A. D. Spaulding

TABLE OF CONTENTS

INTRODUCTION

Atmospherics are electromagnetic "signals," impulsive in nature, which means they are spectrally broadband processes The lightning which radiates these atmospherics radiates most of its energy at frequency at and below HF (3 to 30 MHz) It is also frequencies at and below HF which are used for long-range communications, since propagation is supported by the Earth-ionosphere waveguide While this means that atmospherics can be used to study this propagation media, the density and location of thunderstorms and other geophysical phenomena, it also means that long-range communications systems can receive interference from these atmospherics At any receiving location, atmospherics can be received from the entire surface of the Earth (at low enough frequencies) Therefore, the satisfactory design of a radio communications system must take into account the level and other characteristics of this atmospheric noise It is the purpose of this chapter to treat this nature of atmospherics, i e , the relationships between atmospheric noise and telecommunication systems It should also be noted that in spite of satellite systems for long-range communications, the use of systems using the ionsophere to achieve long-range communications is continually increasing

The satisfactory design of a radio communications system depends on consideration of all the parameters affecting operation This requires not only the proper choice of terminal facilities and an understanding of propagation of the desired signal between the terminals, but also a knowledge of the interference environment This environment may consist of signals that are intentionally radiated, or of noise, either of natural origin or unintentionally radiated from man-made sources, or various combinations of these It has long been recognized that the ultimate limitation to a communication link will usually be the radio noise

There are a number of types of radio noise that must be considered in any design, though, in general, one type will be the predominate noise and will be the deciding design factor In broad categories, the noise can be divided into two types — noise internal to the receiving system and noise external to the receiving antenna Noise power is generally the most significant parameter (but seldom sufficient) in relating the interference potential of the noise to system performance Since the noise level often results from a combination of external and internal noise, it is convenient to express the resulting noise by means of an overall operating noise factor which characterizes the performance of the entire receiving system The next section of this chapter, therefore, defines the receiving system operating noise factor and shows how the internal and external noises must be combined It then gives estimates of the minimum (and maximum) environmental noise levels likely at any location on the surface of the Earth The frequency range 0 1 Hz to 100 GHz is covered, and so the interference potential of atmospheric noise can be compared to that of other external noises (e g , man-made and galactic)

After the broad look of the next section, the section on "Worldwide Atmospheric Radio Noise Estimates" goes on in much more detail concerning atmospheric noise, giving its level as a function of time and geographic location In addition, the required statistical characterizations (in addition to level) are defined and examples given Finally, this section provides a historical summary of mathematical models for the atmospheric-noise process, since, quite often, proper system design requires more information (obtained by modeling) about the process than can be obtained by measurement alone

The last section summarizes the effects of atmospheric noise on system performance and then gives various means of improving system performance in impulsive noise.

WORLDWIDE MINIMUM ENVIRONMENTAL RADIO NOISE LEVELS (0.1 Hz to 100 GHz)

Predetection Signal-to-Noise Ratio and Operating Noise Factor

As mentioned in the introduction, it is desirable to express the external noise levels in a form which will allow the external noises to be appropriately combined with noise internal to a telecommunications system. In so doing, it is then possible to make decisions concerning required receiving system sensitivity; that is, a receiver need have no more sensitivity than that dictated by the external noise. Also, the noise levels can then be compared to the desired signal level to determine the predetection signal-to-noise (s/n) ratio. The predetection s/n ratio is an important system design parameter and is always required knowledge (required but seldom sufficient) when determining the effects of the external noise on system performance. It is useful to refer (or translate) the noise from all sources to one point in the system for comparison with the signal power (desired signal). A unique system reference point exists: the terminals of an equivalent lossless antenna having the same characteristics (except efficiency) as the actual antenna (see Reference 9). Consider the receiving system shown in Figure 1. The output of block (a) is this unique reference point. The output of block (c) represents the actual (available) antenna terminals to which one could attach a meter or a transmission line. Let s represent the signal power and n the average noise power in watts which would be observed at the output of block (a) in an actual system (if the terminals were accessible). We can define a receiving system overall operating noise factor, f, such that $n = fkT_ob$, where k = Boltzmann's constant = 1.38×10^{-23} J/K, T_o = the reference temperature in K taken as 288K, and b = the noise power bandwidth of the receiving system in hertz.

We can also define a system overall operating noise figure $F = 10 \log_{10} f$ in dB. The ratio s/n can be expressed:

$$(S/N) = S - N \tag{1}$$

where
S = the desired average signal power in dB (1W) = $10 \log_{10} s$, and N = the average system noise power in dB (1W) = $10 \log_{10} n$. Let us now explore the components of n in greater detail with emphasis on environmental noise external to the system components.

For receivers free from spurious responses, the system noise factor is given by

$$f = f_a + (\ell_c - 1)\left(\frac{T_c}{T_o}\right) + \ell_c(\ell_t - 1)\left(\frac{T_t}{T_o}\right) + \ell_c\ell_t(f_r - 1) \tag{2}$$

where
f_a = the external noise factor defined as

$$f_a = \frac{p_n}{kT_o b} \tag{3}$$

and F_a = the external noise figure defined as $F_a = 10 \log f_a$; p_n = the available noise power from a lossless antenna (the output of block (a) in Figure 1); ℓ_c = the antenna circuit loss (power available from lossless antenna/power available from actual an-

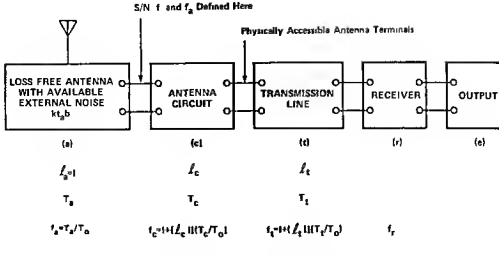

FIGURE 1 The receiving system and its operating noise factor, f

tenna), T_c = the actual temperature, in K, of the antenna and nearby ground, ℓ_t = the transmission line loss (available input power/available output power), T_t = the actural temperature, in K, of the transmission line, and f_r = the noise factor of the receiver (F_r = 10 log f_r = noise figure in dB) Let us now define noise factors f_c and f_t, where f_c is the noise factor associated with the antenna circuit losses,

$$f_c = 1 + (\ell_c - 1)\left(\frac{T_c}{T_o}\right) \tag{4}$$

and f_t is the noise factor associated with the transmission line losses,

$$f_t = 1 + (\ell_t - 1)\left(\frac{T_t}{T_o}\right) \tag{5}$$

If $T_c = T_r = T_a$, (2) becomes

$$f = f_a - 1 + f_c f_t f_r \tag{6}$$

Note specifically that when $f_c = f_t = 1$ (lossless antenna and transmission line), then $F \neq F_a + F_r$

Relation (3) can be written

$$P_n = F_a + B - 204 \text{ dB(1W)} \tag{7}$$

where P_n = 10 log p_n (p_n = available power at the output of block (a) in Figure 1, in watts), B = 10 log b, and −204 = 10 log kT$_o$. For a short ($h \ll \lambda$) grounded vertical monopole, the vertical component of the rms field strength is given by

$$E_n = F_a + 20 \log f_{MHz} + B - 95.5 \text{ db}(1\ \mu\text{V/m}) \tag{8}$$

where E_n is the field strength in bandwidth b and f_{MHz} is the center frequency in MHz. Similar expressions for E_n can be derived for other antennas.[31] For example, for a halfwave dipole in free space,

$$E_n = F_a + 20 \log f_{MHz} + B - 98.9 \text{ dB}(1\ \mu\text{V/m}) \tag{9}$$

The external noise factor is also commonly expressed as a temperature, T_a, where by definition of f_a

$$f_a = \frac{T_a}{T_0} \tag{10}$$

and T_0 is the reference temperature in K and T_a is the antenna temperature due to external noise.

More detailed definitions and discussions (including the case with spurious responses) are contained in CCIR Report 413.[9] Additional discussions on natural noise are given in the next section of this chapter. Discussions on man-made noise are given in the chapter on Man-Made Noise and CCIR Report 258.[10]

Relationships among F_a, Noise Power, Spectral Density, and Noise Power Bandwidth

Note that f_a is a dimensionless quantity, being the ratio of two powers. The quantity f_a, however, gives, numerically, the available power spectral density in terms of kT_0 and the available power in terms of kT_0b. The relationship between the noise power, P_n, the noise power spectral density, P_{sd}, and noise power bandwidth, b, are summarized in Figure 2.[57] When F_a is known, then P_n or P_{sd} can be determined by following the steps indicated in the figure. For example, if the minimum value of F_a = 40 dB and b = 10 kHz, then the minimum value of noise power available from the equivalent lossless antenna is $P_n = -124$ dB(1W).

If $\ell_c = 3$, then the noise power available from the actual receiving antenna is −128.8 dB(1W).

Estimates of Minimum (and Maximum) Environmental Noise Levels

The best available estimates of the minimum expected values of F_a along with other external noise levels of interest are summarized in this section as a function of frequency. Figure 3 covers the frequency range 0.1 Hz to 10 kHz. The solid curve is the minimum expected values of F_a at the surface of the Earth based on measurements (taking into account all seasons and times of day for the entire Earth), and the dashed curve gives the maximum expected values. Note that in this frequency range there is very little seasonal, diurnal, or geographic variation. The larger variability in the 100 to 10,000 Hz range is due to the variability of the Earth-ionosphere waveguide cutoff.

Figure 4 covers the frequency range 10^4 to 10^8 Hz, i.e., 10 kHz to 100 MHz. The minimum expected noise is shown via the solid curves and other noises that could be of interest as dashed curves. For atmospheric noise ($f > 10^4$ Hz), the minimum values expected are taken to be those values exceeded 99.5% of the time, and the maximum values are those exceeded 0.5% of the time. For the atmospheric noise curves, all times of day, seasons, and the entire surface of the Earth have been taken into account. More precise details (geographic and time variations) can be obtained from CCIR Report 322,[8] which is discussed in the next section of this chapter. These atmospheric noise data are of average background. Local thunderstorms can cause higher noise levels. The man-made noise (quiet receiving site) is that noise measured at carefully

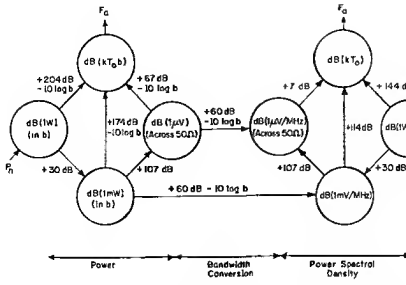

FIGURE 2 Relationships between power, power spectral density, and noise bandwidth (rms detector) (From Spaulding A D , Report OT 76-85 U S Government Printing Office Washington D C , 1976)

selected, quiet sites worldwide as given in CCIR Report 322 [9] The atmospheric noise below this man-made noise level was, of course, not measured, and the levels shown are based on theoretical considerations[8] and engineering judgment [14] Also shown is the median expected business area man-made noise Further details concerning man-made noise and its variation can be obtained from the following chapter, CCIR Report 258,[10] Spaulding and Disney[55] and references therein, and Hagn and Shepherd [23]

On Figure 5, the frequency range 10^8 to 10^{11} is covered, i e , 100 MHz to 100 GHz Again, the minimum noise is given by solid curves while some other noises of interest are again given by dashed curves

The majority of the results shown on the three figures is for omni-directional vertically polarized antennas (except as noted on the figures) The average value of F_a for directional antennas will be the same if we assume random direction Studies have indicated that at HF (for example), for atmospheric noise from lightning, there can be as much as 10 dB variation (5 dB above to 5 dB below the average F_a value shown) with direction for very narrowbeam antennas

For galactic noise, the average value (over the entire sky) is given by the solid curve labeled galactic noise (Figures 4 and 5) Measurements indicate a ± 2 dB variation about this curve The minimum galactic noise (narrowbeam antenna towards galactic pole) is 3 dB below the solid galactic noise curve shown on Figure 5 The maximum galactic noise for narrowbeam antennas is shown via a dashed curve on Figure 5

Example Determination of Required Receiver Noise Figure

We now want to consider a simple example to show how to determine the required receiver noise figure. At 10 kHz, for example, the minimum external noise is F_a = 145 dB (see Figure 4) If we assume $T_e = T_r = T_o$, and $\ell_c = \ell_r = 1$ (that is, no antenna or transmission line losses), then

$$f = f_a - 1 + f_r \tag{11}$$

We can take f_r to be that value which will increase F by only 1 dB This gives us a noise figure, F_r, of 140 dB or an overall noise figure, F, of 147 dB Any smaller noise

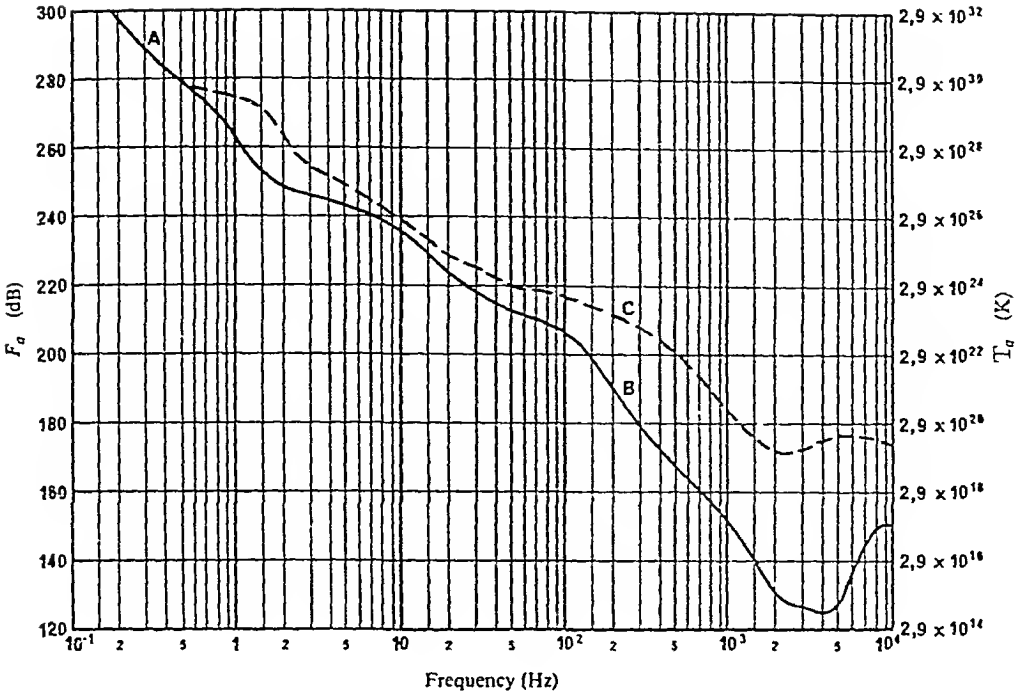

FIGURE 3. F_a, minimum and maximum, vs. frequency (0.1 to 10^4 Hz). A — micropulsations, B — minimum value expected of atmospheric noise, C — maximum value expected of atmospheric noise.

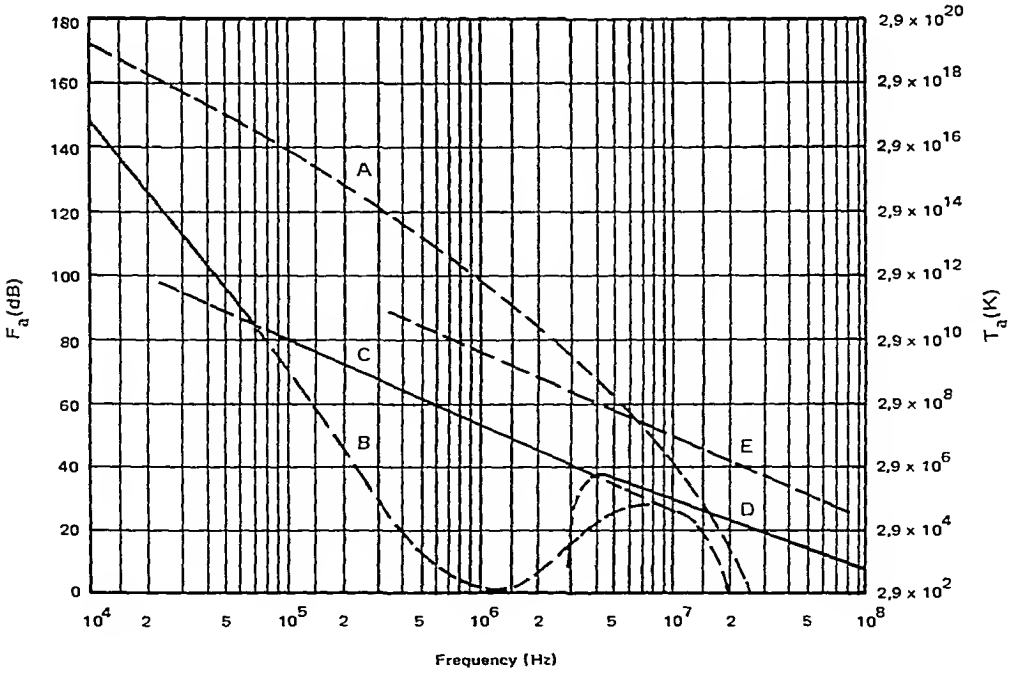

FIGURE 4. F_a vs. frequency (10^4 to 10^8 Hz). A — atmospheric noise, value exceeded 0.5% of time; B — atmospheric noise, value exceeded 99.5% of time; C — man-made noise, quiet receiving site; D — galactic noise; E — median business area man-made noise; minimum noise level expected.

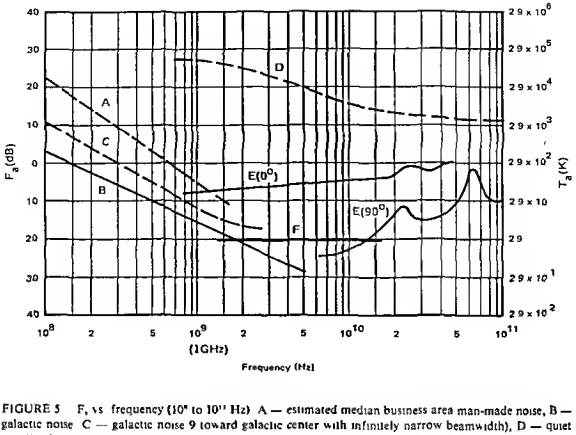

FIGURE 5 F, vs frequency (10^8 to 10^{11} Hz) A — estimated median business area man-made noise, B — galactic noise C — galactic noise 9 toward galactic center with infinitely narrow beamwidth), D — quiet *sun* (½ degree *beamwidth directed at sun*), E — sky noise due to oxygen and water vapor (very narrow beam antenna), upper curve, 0° elevation angle lower curve, 90° elevation angle, F — black body (cosmic background), 2 7 k, minimum noise level expected

figure, F_a, no matter how small, cannot decrease F below 146 dB Consider now that $l_c = l_r = 100$, i e , 20 dB antenna losses and 20 dB transmission losses Then,

$$1 = f_a - 1 + 10000\, f_r \qquad (12)$$

In order to raise the F no more than 1 dB (to 147 dB) for the above situation, F_a can only be as large as 100 dB As this example shows, it makes no sense to attempt to use sensitive receivers at low frequencies

As another example, consider a VHF receiver at 100 MHz The minimum noise level is now due to galactic noise and is approximately an F_a of 7 dB Suppose that $l_r = 100$ and $l_c = 1$, now, in order not to raise F more than 1 dB, F_a can only be as large as −19 8 dB

In the first example above, the interfering noise was atmospheric noise, and in the second example the noise was galactic These two types of noise are quite different in character — atmospheric noise being very impulsive and galactic noise being white Gaussian Correspondingly, these two types of noise will affect system performance quite differently, even if they have the same level (i e , available power) In specifying system performance, the detailed statistical characteristic of the noise must be taken into account. One consequence of this is that the external noise can still limit performance even though the receiver noise (Gaussian in character) is made as high as possible so as not to increase the overall operating noise factor f System performance depends on more than the noise level, and so far we have considered only noise level via f_a In the last two sections of this chapter, then, we continue on, taking a closer look at the character of atmospheric noise and its effects on system performance as well as some techniques to overcome degradation caused by impulsive noise

WORLDWIDE ATMOSPHERIC RADIO NOISE ESTIMATES

Introduction

In the previous section we defined f_a (and T_a), the most useful and common way of specifying the external noise level. We also noted that when one is concerned with determining the effects of the external noise (e.g., atmospheric noise) on system performance, more information about the received noise process than just its energy content (level) is almost always required. In the following paragraphs, then, we will define these more detailed statistics which are required and show, via examples for atmospheric noise, their general characteristics. Having the definitions in hand, we will discuss CCIR Report 322, which gives the available worldwide estimates for atmospheric noise, its level, f_a, and also the most useful statistic, the amplitude probability distribution of the received noise envelope along with the time, frequency, and geographic variations of these parameters.

Since the impulsive atmospheric noise can have serious effects on the performance of communication systems, various techniques can be used to minimize these effects. This means that receiving systems must be designed to function as well as possible in impulsive noise. In general, in order to carry out such system designs, more knowledge about the noise process is required than can be obtained by measurement alone. Therefore, at the end of this section, a summary of the mathematical models that have been developed for the atmospheric noise process is given. In addition to system performance and design problems, some of these models can be used, coupled with measured noise data, to study various geophysical phenomena such as radio wave propagation, thunderstorm occurrence rates, the nature of lightning, etc.

Definition and Examples of Measured Received Atmospheric Noise Envelope Statistics

Atmospheric noise is a random process. The fact that we are dealing with a random process means that the noise can be described only in probabilistic or statistical terms and cannot be represented by a deterministic waveform or any collection of deterministic waveforms. In addition, atmospheric noise is basically nonstationary; therefore, great care must be exercised in the planning and making of measurements and in the interpretation of the results. We must measure long enough to obtain a good estimate of the required parameter but be certain that the noise remains "stationary enough" during this period. This is no small point and is frequently overlooked in the design of measurement experiments. We assume that the random noise process is stationary enough over some required time period for us to obtain the required statistics. Of course, how these statistics then change with time, as from day to day, as well as with location, now becomes important.

The basic description of any random process is its probability density function (pdf) or distribution function. The first order pdf of the received interference process is almost always required to determine system performance (i.e., always necessary but sometimes not sufficient).

Although a random process, X(t), is said to be completely described if its hierarchy of distributions is known, there are other important statistical properties (important to communications systems) which are not immediately implied by this hierarchy. Moments and distributions of level crossings of X(t) within a time interval, moments and distributions of the time interval between successive crossings, distribution of extremes in the interval, and so on are typical examples.

We now want to define, in a unified way, the atmospheric noise parameters that have been measured and their interrelationships.

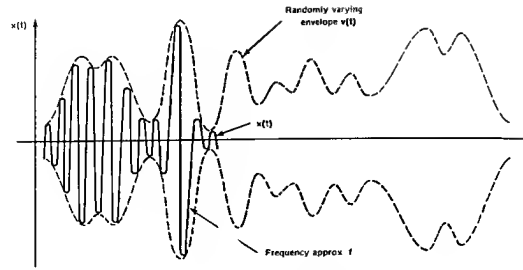

FIGURE 6 Noise at the output of a narrowband filter

For analysis of a communication system, the noise process of interest is the one seen by our receiving system This means that we are almost always interested in "narrowband" noise processes A narrowband process results whenever the bandpass of the system is a small fraction of the center frequency, f_c, and means that the received noise is describable in terms of its envelope and phase as shown on Figure 6 The noise process, x(t), at the output of a narrowband filter is given by

$$x(t) = v(t)\cos[\omega_c t + \phi(t)]$$

where v(t) is the envelope process and $\phi(t)$ is the phase process For atmospheric noise in the absence of discrete signals, ϕ is uniformly distributed, that is

$$p(\phi) = \frac{1}{2\pi}, \quad -\pi \leq \phi < \pi$$

Therefore, we will concentrate on the statistics of the envelope process, v(t) In general, for system analysis, the required statistics that determine performance are either the envelope statistics directly or are obtainable from the envelope and phase statistics For noise from some discrete sources or for general background atmospheric noise plus interfering signals, $\phi(t)$ is not uniformly distributed, and the statistics of the $\phi(t)$ process must also be known

As an example, let x(t) (Figure 6) be a white Gaussian process, then the pdf's for x, v, and ϕ are

$$p(x) = \frac{1}{\sqrt{\pi N_0}} \exp\left[-\frac{x^2}{N_0}\right]$$

$$p(v) = \frac{2v}{N_0} \exp\left[-\frac{v^2}{N_0}\right], \quad v \geq 0$$

$$p(\phi) = \frac{1}{2\pi}, \quad -\pi \leq \phi < \pi$$

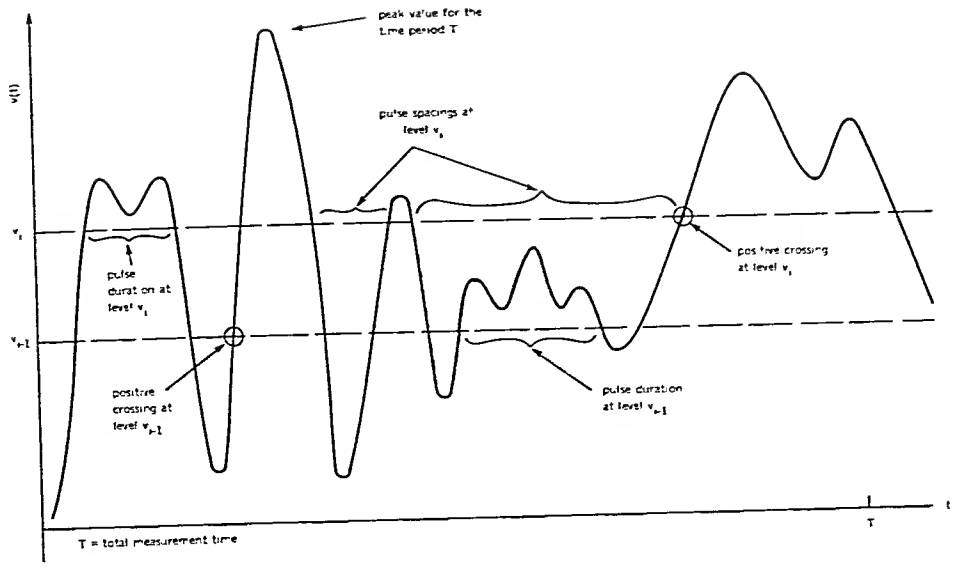

FIGURE 7. Noise envelope of a sample of atmospheric noise.

where N_o is the noise power spectral density (watts/Hz). That is, the envelope voltage v is Rayleigh distributed and the phase is uniformly distributed.

Figure 7 shows the noise envelope of a sample of atmospheric noise along with definitions of the various noise parameters that have been measured. From Figure 7 we have:

The amplitude probability distribution (APD) is the fraction of the total measurement time, T, for which the envelope was above level v_i;

$$D(v) = \text{Prob}\,[v \geq v_i] = 1 - P(v)$$

where P(v) is the cumulative distribution function. The pdf of v is given by the derivative of P(v).

The average crossing rate characteristic (ACR) is the average number of positive crossings of level v_i = total number/T. For impulsive noise and at high envelope voltage levels, an average noise pulse rate (pulses per second) at the receiver input can be inferred from the ACR. The requirement for the pulse rate to be essentially equal to the ACR is that the noise envelope (at the level v_i) be composed of isolated filter impulse responses.[61]

The pulse spacing distribution (PSD) for level v_i is the fraction of pulse spacings at level v_i that exceeds time τ. That is, the PSD is the distribution for the random variable τ.

The pulse duration distribution (PDD) for level v_i is the fraction of pulse durations at level v_i that exceeds time τ.

To specify time dependence in the received wave form, the *autocorrelation function, R(τ)*, is used.

$$R(\tau) = \int_{-\infty}^{\infty} \int_{-\infty}^{\infty} v_1 v_2 \, p_2(v_1, v_2, \tau)\, dv_1 dv_2$$

$$= \lim_{T \to \infty} \frac{1}{T} \int_0^T v(t)\, v(t+\tau)\, dt$$

where v_1 is $v(t)$ at time t_1, v_2 is $v(t)$ at t_2, and $\tau = t_2 - t_1$, with $p_2(v_1, v_2)$ the 2nd order pdf of $v(t)$. The autocovariance of $v(t)$ is the covariance of the random variables $v(t_1)$ and $v(t_2)$. For zero mean processes, the autocorrelation and autocovariance are identical.

The power spectral density, $S(\omega)$, for a stationary random process is given by the Fourier transform of $R(\tau)$. This is similar to the Fourier transform pair relationship between the time domain representation and the frequency domain representation of deterministic waveforms. Note, however, that while for deterministic waveforms the spectrum gives the amplitude of each frequency component and its phase, no phase information is possible for the spectrum of a random process. If the process is time independent (correlated only for $\tau = 0$), then

$$R(\tau) = N_0\,\delta(\tau - 0)$$

and

$$S(\omega) = N_0$$

Noise with the above property is termed "white."

The average envelope voltage is termed the expected value of v, $E[v]$,

$$v_{av} = E[v] = \frac{1}{T}\int_0^T v(t)\,dt = -\int_0^\infty v\,dD(v)$$

where $-dD(v) = p(v)dv$.

The rms voltage squared (proportional to energy or power), $E[v^2]$, is

$$v^2_{rms} = E[v^2] = \frac{1}{T}\int_0^T v^2(t)\,dt = -\int_0^\infty v^2\,dD(v)$$

The average logarithm of the envelope voltage, $E[\log v]$, is

$$v_{log} = E[\log v] = -\int_0^\infty \log v(t)\,dt = -\int_0^\infty \log v\,dD(v)$$

The peak voltage for time period T is the maximum of $v(t)$ during T.

Because the rms voltage level can be given in absolute terms (i.e., rms field strength or available power as given in the first part of the second section), it is common to refer the other envelope voltage levels to it. The dB difference between the average voltage and the rms voltage is termed V_d,

$$V_d = -20 \log \frac{v_{av}}{v_{rms}}$$

The dB difference between the antilog of the average log of the envelope voltage and the rms voltage is termed L_d,

$$L_d = -20 \log \frac{10^{v_{log}}}{v_{rms}}$$

Knowledge of the behavior of the above statistics with time and location is also important.

Figures 8 and 9 show a 200 msec sample of atmospheric noise taken from a 6 min noise recording at 2.5 MHz in a 4 kHz bandwidth and the autocorrelation for this sample. Note from the autocorrelation that some time correlation (for small τ) is indicated. While some samples of atmospheric noise show no time correlation, the situation depicted in Figure 9 can be considered to be typical for atmospheric noise. Figures 10, 11, 12, and 13 show the APD, ACR, PDD, and PSD for this 6-min sample of atmospheric noise. In Figure 10 the dashed curve is that for a Rayleigh distribution (envelope of Gaussian noise). The impulsive nature of atmospheric noise at 2.5 MHz can easily be seen from Figure 10. In general, atmospheric noise is much more impulsive still (larger dynamic range) at lower frequencies (e.g., LF, MF, etc.). This example of the statistics of the received atmospheric noise was selected to only give a general "feel" of the statistical nature of atmospheric noise. Even so, the example shown is quite typical.

CCIR Report 322

Previously, the various atmospheric noise parameters that have been measured were defined and examples given. How these parameters (e.g., f_a) vary with time and location is also required knowledge. Research pertaining to atmospheric noise dates back to at least 1896;[45] however, the research leading to the first publication of predictions of radio noise levels was carried out in 1942 by a group in the United Kingdom at the Interservices Ionosphere Bureau and in the U.S. at the Interservice Radio Propagation Laboratory.[27] Predictions of worldwide radio noise were published subsequently in RPU Technical Report No. 5[49] and in National Bureau of Standards (NBS) Circulars 462[39] and 557,[40] and CCIR Report 65.[7] All these predictions for atmospheric noise were based mainly on weather patterns and measurements at very few locations and over rather short periods of time.

Starting in 1957, average power levels (f_a) of atmospheric noise were measured on a worldwide basis starting with a network of 15 identical recording stations. Figure 14 shows the location of these recording stations. The frequency range 13 kHz to 20 MHz was covered, and measurements of F_a, V_d, and L_d were made using a bandwidth of 200 Hz. In addition, APD measurements were made at some of the stations.

The data from this worldwide network were analyzed by the Central Radio Propagation Laboratory (CRPL) of NBS and the results published in the NBS Technical Note Series 18. The first in this series was published in July 1959 and covered July 1957 through December 1958. After this, one in the series was published every quarter until No. 18—32 for September, October, and November 1966. These Technical Notes gave, for each frequency and location, the month-hour median value of F_a along with D_u and D_l, the upper and lower decile values; i.e., the values exceeded 10% and 90% of the time. The median values of V_d and L_d were also given. In addition, the corresponding season-time block values were given for the four seasons, winter (December, January, and February; June, July, and August in the southern hemisphere), spring (March, April, May), summer (June, July, August), and fall (September, October, November) and six 4-hr time blocks (0000-0400, etc.).

A method was developed to obtain the APD from the measured statistical moments V_d and L_d.[12] Later it was shown that for atmospheric noise there is strong correlation between V_d and L_d, and a good approximation of the APD could be obtained from V_d alone.[52] Also, a means of converting the APD from one bandwidth to another was developed.[52] It has since been shown, based on numerous measurements, that this bandwidth conversion method is strictly valid for only small changes in bandwidth (5 to 1, say).

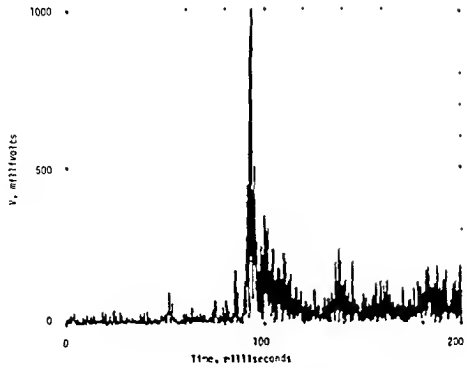

FIGURE 8 Randomly selected 200 msec sample of atmospheric noise envelope from a 6 min noise recording at 2.5 MHz in a 4 kHz bandwidth

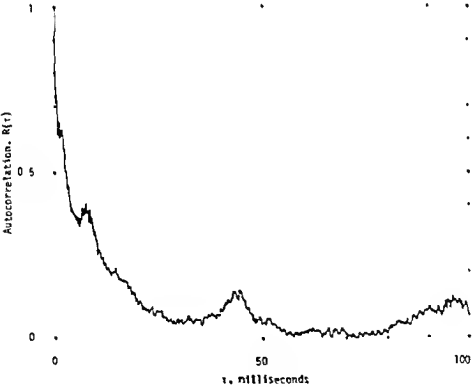

FIGURE 9 Autocorrelation for the noise sample of Figure 8

In 1963, CCIR Report 322, **World Distribution and Characteristics of Atmospheric** Radio Noise, was published by the **International** Telecommunications Union in Geneva This report (small book, actually) **presents** the worldwide predictions of F_a, V_a

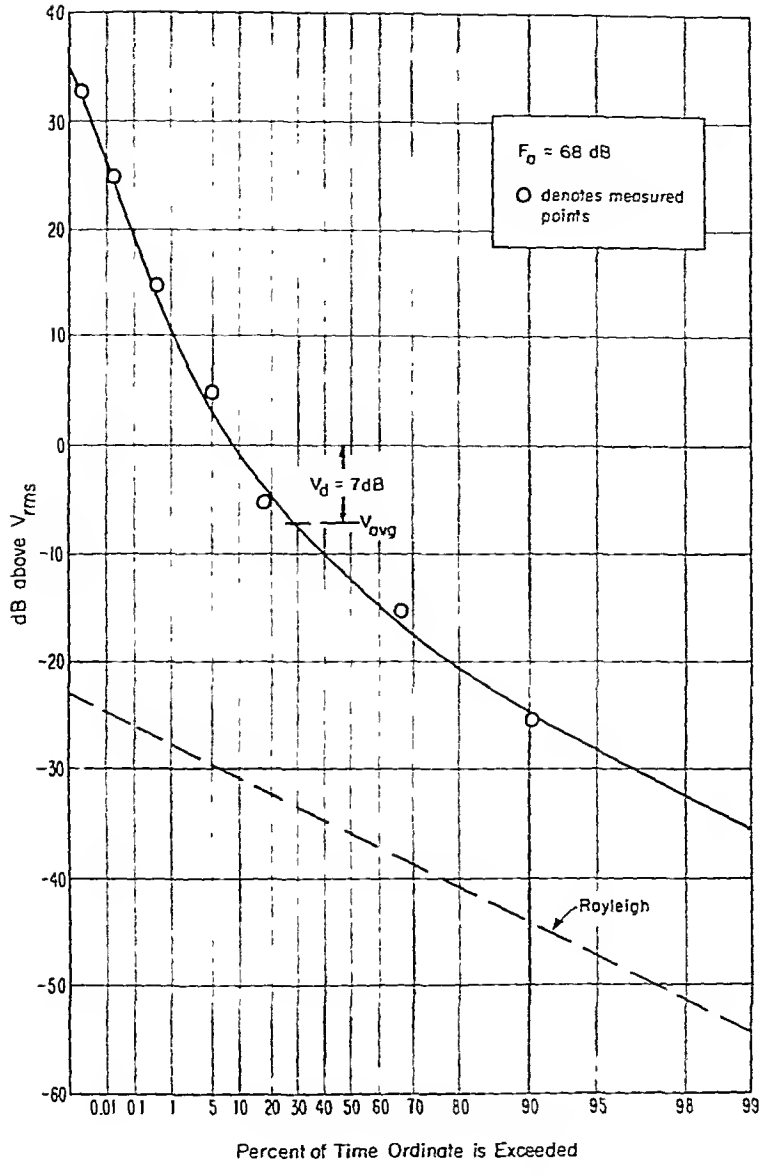

FIGURE 10. Amplitude probability distribution for a 6-min sample of atmospheric noise recorded at 2.5 MHz in a 4 kHz bandwidth.

and their statistical variations for each season-time block and is based on all the available measurements to that date, primarily the recording network shown in Figure 14. The expected APD for various values of V_d (1.05 dB for Rayleigh to 30 dB) are also given along with the expected variation in the APD.

Figure 15 shows Figure 19A of CCIR Report 322. This figure gives F_{am} at 1 MHz as a function of latitude and longitude for the summer season and the time block 2000-2400. Since this map is for local time, there is a discontinuity at the equator (corresponding to summer being 6 months apart in the northern and southern hemispheres). World maps of atmospheric radio noise in universal time are also available.[66] To obtain F_{am}, Figure 16 is used to convert the 1 MHz value to any frequency between 10 kHz and 30 MHz. Finally, the median value of V_d, V_{dm}, and the statistical variations of F_a about its median value F_{am} are given in Figure 16. The expected APD for a given V_d is

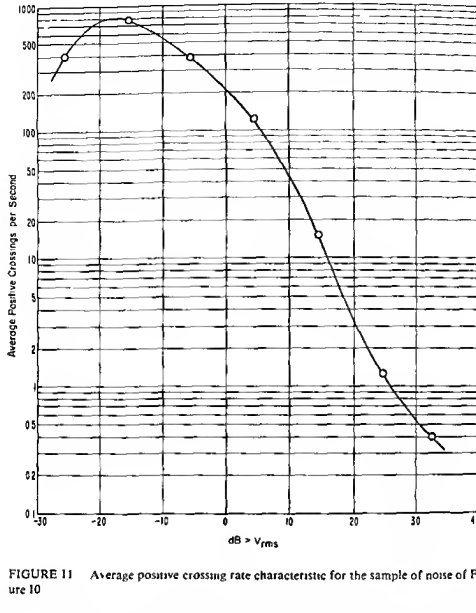

FIGURE 11 Average positive crossing rate characteristic for the sample of noise of Figure 10

given in Figure 17 Also, numerical representation of CCIR Report 322 is available [34] While the title of Lucas and Harper says that only HF (3-30 MHz) is covered, the results there will reproduce all of Report 322 This numerical representation is also contained in the ITU HF propagation prediction programs A numerical representation (computer program) of the APD as a function of V_d is also available [1]

It has been shown that the variation of f_a for a given season and time block can be adequately represented by two log-normal distributions (i e , dB values normally distributed), one above the median value and one below Therefore, the variation is given by F_{am}, D_u, and D_l This is best explained via an example Suppose we want F_a and its variation for the summer season, 2000-2400 time block for Boulder, Colo , at 500 kHz (As mentioned in the previous section, F_a is independent of bandwidth) From Figure 15, the 1 MHz F_{am} value is 90 dB From Figure 16 then, the 500 kHz F_{am} is 102 dB with D_u = 9.0 dB, D_l = 7 7 dB, σ_{Du} = 3 1 dB, and σ_{Dl} = 2 0 dB A value for σ_{Fam} is also given (4.7 dB) and is designed to account for the difference between observations and the results obtained by the numerical mapping routines that produced CCIR Report 322, to account for year-to-year variations, and also to account for the expected variation in the median value when extrapolations were made to geographic areas where measurements did not exist Figure 18 shows the distribution of F_a values esti-

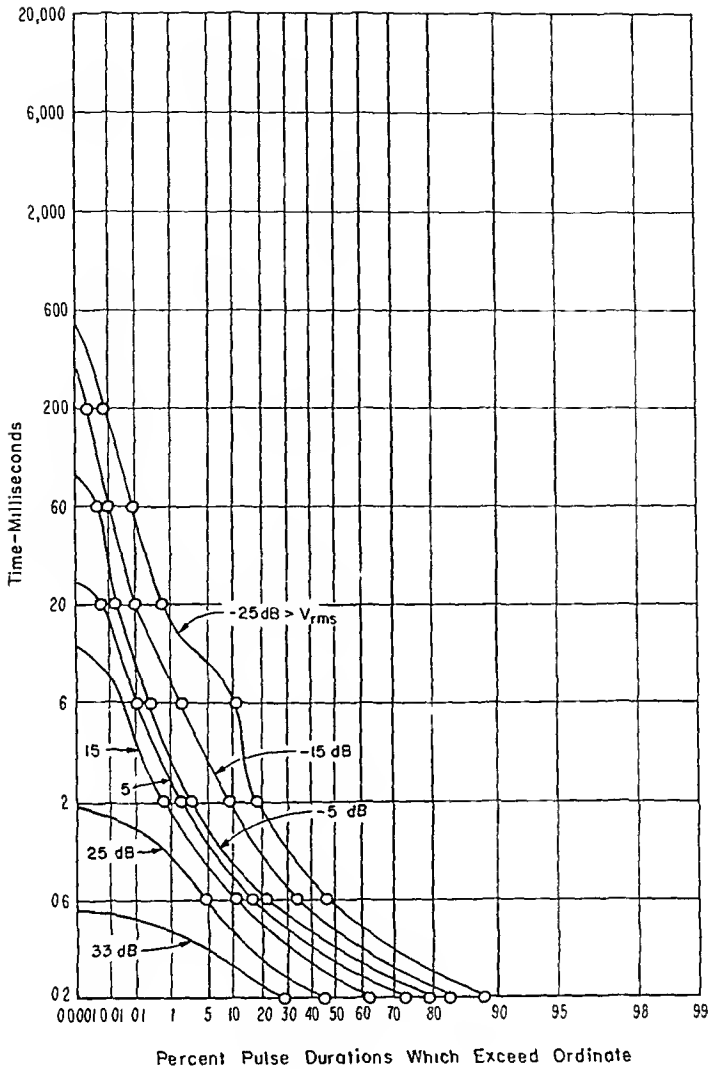

FIGURE 12. Pulse duration distributions for the sample of noise of Figure 10.

mated via the data above (F_{am}, D_u, D_t, σ_{Du}, and σ_{Dt}). On Figure 18, all the measured values of F_a measured at Boulder at 500 kHz will essentially lie between the two dotted lines with the solid line being the estimate of the distribution of F_a for this season and time block. The σ_{D_t} and σ_{D_u} values account for the year-to-year variation in D_t and D_u and also the geographic variation, since only one value of D_u is given for the entire surface of the Earth. Now the value of F_a exceeded any percent of time for this season-time block can be determined.

CCIR Report 322 gives examples of using the noise data to determine the required signal strength in order for various communications systems to operate according to some given specifications. What these specifications usually are in order to take into account the noise (and signal) variability with time and location are covered in the last section of this chapter.

Summary of Mathematical Models for Atmospheric Radio Noise Processes

In order to be able to determine the optimum receiving system for a given class of

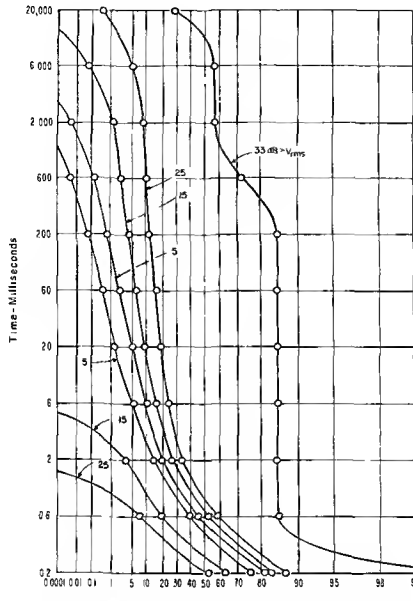

FIGURE 13 Pulse spacing distributions for the sample of noise of Figure 10

signals and analyze its performance, a mathematical model for the random interference process is required That is, for optimal system studies and also for determining the performance of some of the existing suboptimum systems, more information about the interference process is required than can generally be obtained by measurement alone The problem is to develop a model for the interference that fits all the available measurements, is physically meaningful when the nature of the noise sources, their distributions in time and space, propagation, etc are considered, is directly relatable to the physical mechanisms giving rise to the interference, and is still simple enough so that the required statistics can be obtained for solving signal detection problems While various models have been proposed in the past (to be summarized later) that meet these requirements in particular instances, the only general (canonical) model proposed to date that meets all the above requirements is that proposed by Middleton [35,36]

Models that have been developed to date can be categorized into two basic types.

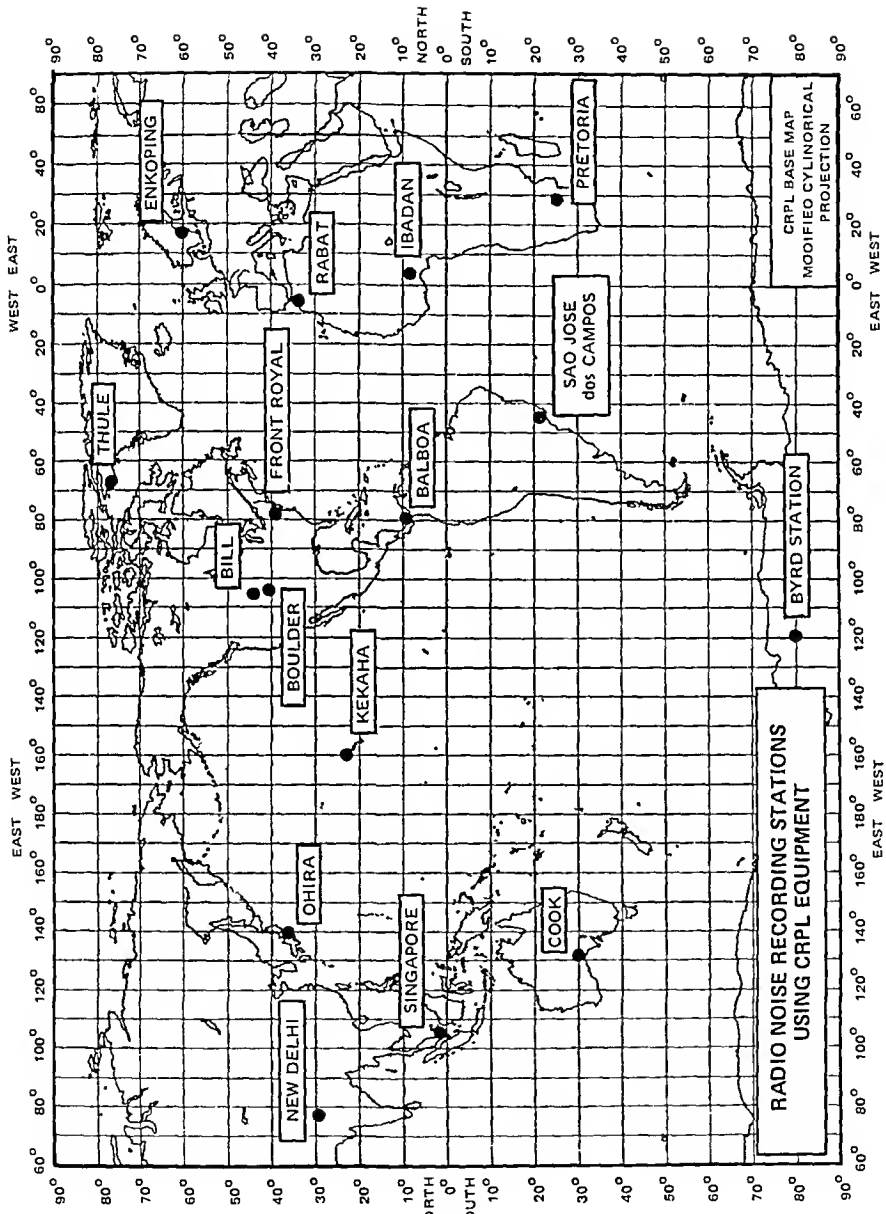

FIGURE 14. Radio noise recording stations used to obtain most of the data used for CCIR Report 322 [8]

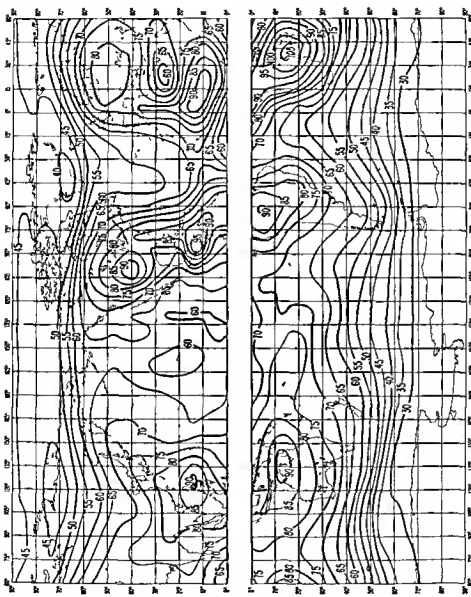

FIGURE 15 Expected values of atmospheric radio noise, F_{am}, in dB above kTb at 1 Mc/sec for summer season, 2000-2400 hr.[4]

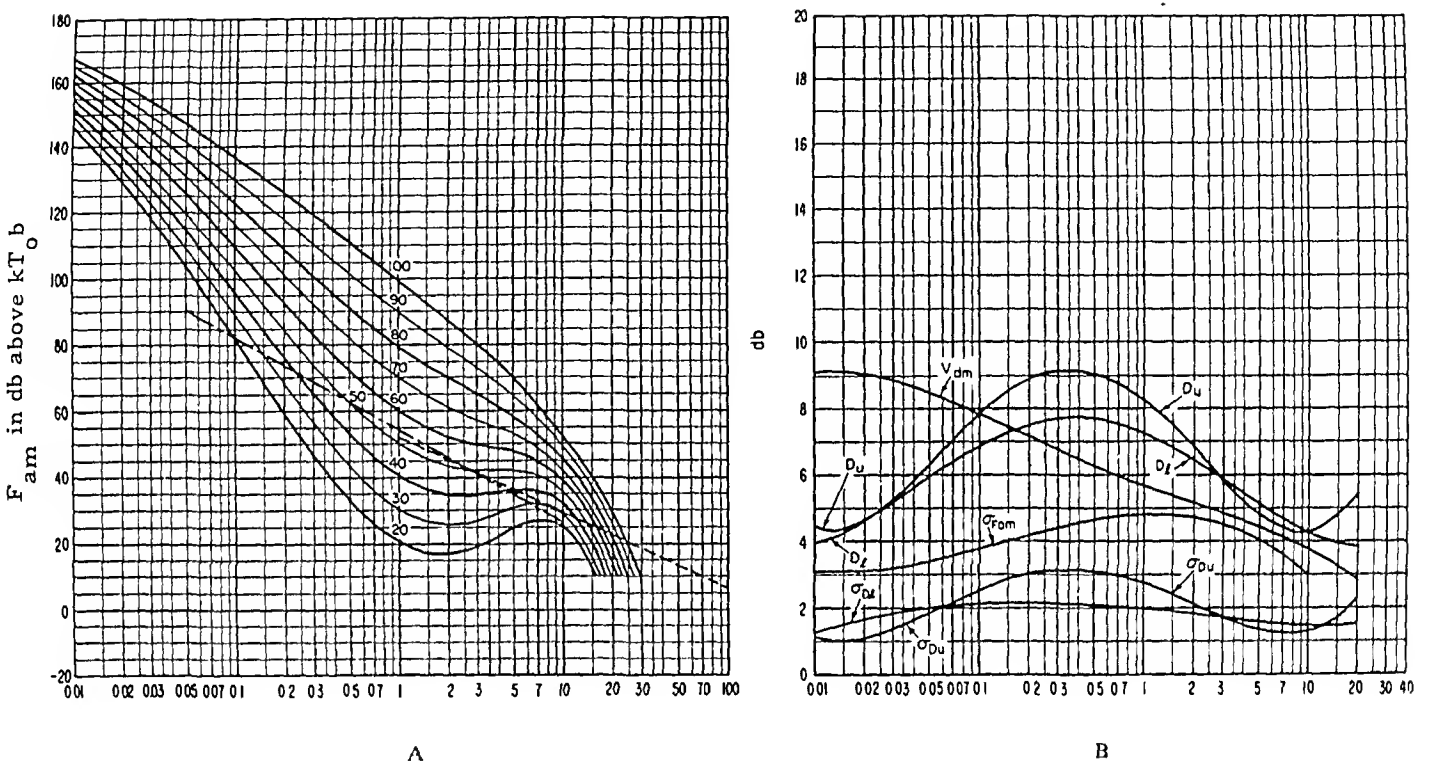

FIGURE 16. A. Variation of radio noise with frequency summer season, 2000-2400 hr. B. Data on noise variability and character summer season, 2000-2400 hr. Frequency in Mc/sec: ——— expected values of atmospheric noise; —·—·— expected values of man-made noise at a quiet receiving location; – – – – – – expected values of galactic noise. Frequency in Mc/sec: σ_{Fam} — standard deviation of values of F_{am}; D_u — ratio of upper decile to median value, F_{am}; σ_{Du} — standard deviation of values of D_u; D_l — ratio of median value, F_{am} to lower decile; σ_{Dl} — standard deviation of values of D_l; V_{dm} — Expected value of median deviation of average voltage. The values shown are for a 200 c/s bandwidth. (From Figure 19B and 19C of CCIR Report 322.[6])

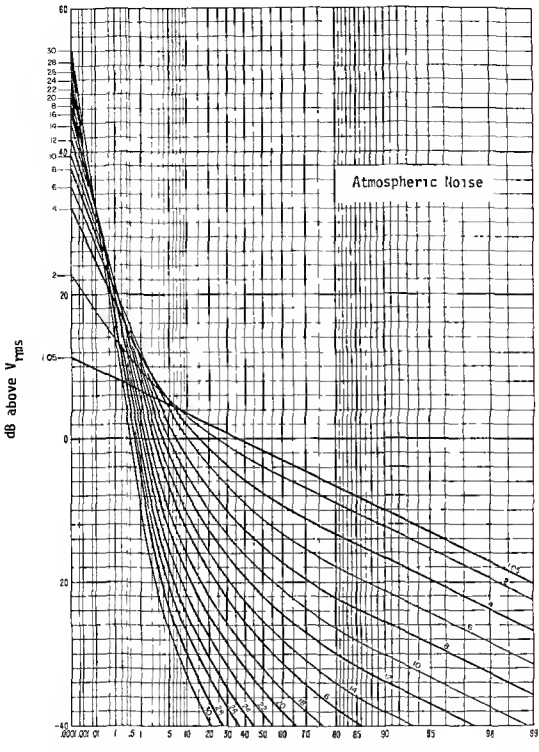

FIGURE 17 Amplitude probability distributions for atmospheric radio noise for various V_r values [4]

The first type (and earliest models) are empirical models which do not represent the interference process itself but which propose various mathematical expressions designed only to fit the measured statistics of the interference The second type of model is that which is designed to represent the entire random interference process itself The majority of these models represents the received interference waveform as a summation of filtered impulses

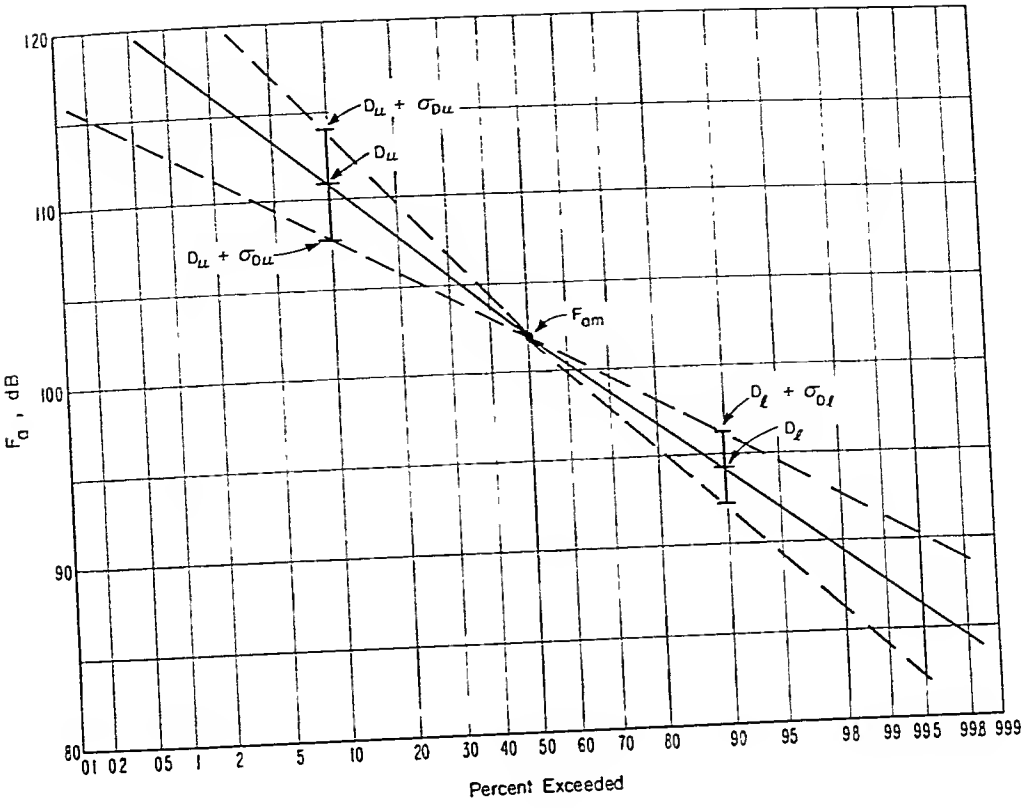

FIGURE 18. The distribution of F_a values expected at Boulder, Colo., 500 kHz, for the summer season, 2000-2400 hr.

Most of the empirical models have concentrated on the amplitude probability distribution (APD) of the noise envelope, $P(V > V_o)$. This distribution has been measured extensively for atmospheric noise (see the bibliography by Spaulding et al.[56] which deals with man-made noise but also contains an extensive section on atmospheric noise).

The first "model" for the noise envelope was the Rayleigh distribution

$$P(V > V_0) = e^{-aV_0^2}$$

This simply assumes that the interference is Gaussian and was quickly recognized to be quite inappropriate, since the envelope distribution of atmospheric and man-made noise exhibits large impulsive tails (e.g., Figure 10).

In 1954, Hesperper, Kessler, Sullivan, and Wells independently proposed the log normal distribution for atmospheric noise (see Reference 16),

$$P(V) = \frac{1}{\sigma\sqrt{2\pi}} e^{-\frac{1}{2}\left(\frac{\log V - \log \mu}{\sigma}\right)^2}$$

This approach gave reasonable approximations to the impulsive tail of the distribution but did not match the Rayleigh (Gaussian) character of the interference at the lower amplitude levels.

Likhter[33] used a combination of two Rayleigh distributions for atmospheric noise

$$P(V > V_o) = (1 - c)\, e^{-aV_o^2} + c\, e^{-bV_o^2}$$

This distribution gave poor agreement with actual data

Also in 1956 Watt proposed a variation on the Rayleigh distribution (see Reference 16),

$$P(V > V_o) = e^{-x^2}$$

where

$$x = a_1 V_o + a_2 V_o (b + 1)/2 + a_3 V_o^b$$

$$b = 0.6\,[20 \log (V_{rms}/V_{ave})]$$

This distribution was designed for atmospheric noise and was claimed to give better results at high and low probabilities than the previously proposed distributions

Ishida[28] proposed a combination for atmospheric noise,

$$P(V > V_o) = (1 - c)\, e^{-aV_o} + c(\text{log normal distribution})$$

Nakai[28] recommended this same combination Ibukun[26] found good agreement with some measured data for this log normal, Rayleigh combination

In 1956 Horner and Harwood (see Reference 29) used

$$P(V > V_o) = \frac{\gamma^2}{(V_o^q + \gamma^2)}$$

to represent the APD of atmospheric noise, and also in 1956 the Department of Scientific and Industrial Research of Great Britain proposed the following distribution (see Reference 26)

$$P(V > V_o) = \frac{1}{\left[1 + \left(\frac{\alpha V_o}{V_o}\right)^r\right]^{-1}}$$

obtaining experimental values for α and r of 2.7 and 1.4, respectively, using atmospheric noise data from Nakai [28]

Crichlow et al [12] represented the APD of atmospheric noise by a Rayleigh distribution at the lower amplitude levels and a "power" Rayleigh distribution at the higher levels

$$P(V > V_o) = e^{-(a V_o^3)^{1/s}}, \quad y > B$$

with these two distributions being joined by a third expression for the middle range of

amplitudes. These APDs were found to fit data very well over a wide range of bandwidths and are still the "standard" representation for atmospheric radio noise.[8] Means of obtaining the distribution for bandwidths other than the measurement bandwidth was also obtained.[52] It has been this empirical representation that has generally been used in determining the performance of digital systems in atmospheric noise (see Reference 1 and the bibliography by Spaulding et al.[56]).

Galejs[17] used a variation of the Rayleigh distribution

$$P(V > V_0) = (1 - \delta)\, e^{-\alpha_1 V_0} + \delta e^{-\alpha_2 V_0}$$

He reported satisfactory agreement with atmospheric noise data using appropriate values of the parameters δ, α_1, and α_2. Galejs[18] also used a more complicated version for atmospherics

$$P(V > V_0) = \left[1 - \left(\frac{b}{a}\right)^2 - \left(\frac{d}{a}\right)^2\right]^{-\left(\frac{V_0}{\sigma}\right)^2} + \frac{b^2}{(V_0^2 + a^2) + V_0(V_0^2 + a^2)^{1/2}} + \left(\frac{d}{a}\right)^2 e^{-sV_0}$$

Finally, Ponhratov and Antonov[46] used a variation of the normal distribution with mean μ to represent the instantaneous amplitude

$$p(x) = \frac{\nu}{2\sqrt{2}\ \Gamma(1/\nu)\mu} \exp\left(-\frac{|x|^\nu}{2^{\nu/2}\mu^\nu}\right), \quad -\infty < x < \infty$$

with $1/2 < \nu < 1$. They found this to be a good approximation for the probability density of atmospheric noise.

Almost all of the above empirical models concentrated on the envelope of the received noise process. Such models, while useful in determining the performance of "idealized" digital systems using matched filter or correlation receivers (i.e., those optimum for white Gaussian noise), give no insight into the physical processes that cause the interference. Neither can they be used to determine performance of "real" systems which employ various kinds of nonlinear processing nor can they be used in optimum signal detection problems. Various investigators have developed models for the entire interference process. The most significant of these models are as follows.

Furutsu and Ishida[16] represented atmospheric noise as a summation of filtered impulses and considered two cases: (1) Poisson noise, consisting of the superposition of independent, randomly occurring impulses and (2) Poisson-Poisson noise, consisting of the superposition of independent, randomly occurring Poisson noise — each Poisson noise forming a wave packet of some duration. They represent the response of the receiver for an elementary pulse to be

$$r = r(t,a)\cos(\omega t + \psi)$$

express this response as a vector and take the summation of n(n random) such vectors. They obtain, for the envelope amplitude for Poisson noise,

$$P(V) = \int_0^\infty \lambda V J_0(\lambda V)\, f(\lambda, T)\, d\lambda$$

where the characteristic function f(λ, T) is given by

$$f(\lambda,T) = \exp\left[\nu\int_0^T dt \int da\, p(a)\left\{J_0(\lambda r) - 1\right\}\right]$$

and ν is the mean rate of occurrence of pulses in the Poisson distribution, T is the total time period of interest, and p(a) is the pdf of a They also obtain

$$P(V < V_o) = V_o\int_0^\infty J_1(\lambda V_o)\, f(\lambda,T)\, d\lambda$$

Corresponding results are obtained for Poisson-Poisson noise (ν becomes Poisson distributed) and for second-order distributions, i e , p(V₁, V₂) and f(λ₁, λ₂, T) Furutsu and Ishida[16] proceeded to evaluate P(V <V$_o$) for two "typical" cases of discrete and continuous spatial distributions of sources (using f[λ,∞]) Their results showed good agreement with measurements

Beckmann[3,4] developed a theoretical model for the received envelope of atmospheric noise and related his results to the number of sources (atmospheric discharges) and the properties of the propagation paths from these sources to the receiver He assumed that the shape of the envelope of an individual atmospheric (attaining its peak value E_p at time t_o) was of the form

$$u_o(t) = \begin{cases} I_p \exp\left(-\dfrac{t - t_o}{a}\right) & \text{for } t > t_o \\ I_p \exp\left(\dfrac{t - t_o}{b}\right) & \text{for } t < t_o \end{cases}$$

The total signal at time t_o is given as

$$\hat{U} = \hat{u}_o + \sum_{k=1}^{\infty} \hat{u}_k + \sum_{k=1}^{\infty} \hat{s}_k$$

where the circumflex accents denote uniformly distributed phase vectors, the u_k are atmospherics that have reached their peak values at times previous to t_o, and the s_k are atmospherics that have not yet reached their peak values For any arbitrary time, t (between two successive peaks), the amplitude is

$$V = U e^{-t/a}$$

A Poisson distribution is assumed for the occurrence times of the atmospherics and a log-normal distribution is postulated for the peak amplitude, E_p; i.e ,

$$I_p = e^{\Delta}$$

where Δ is normally distributed with mean μ and variance σ² Beckmann's results from the above are

$$V_{rms} \approx \sqrt{Nc \ln(1/Nc)}\; e^{\sigma^2 + \mu}$$

where N is the number of discharges per unit time and c = (a + b)/2, and

$$P\left(\frac{V}{V_{rms}} > V_o\right) = \frac{2}{Nc\sigma\sqrt{2\pi}} \int_{V_o}^{\infty} dx \int_{o}^{\infty} dy \frac{x}{y} \quad \exp\left[-\frac{x^2+y^2}{Nc} - \frac{(\ln y+\sigma^2)}{2\sigma^2}\right] I_o\left(\frac{2xy}{Nc}\right)$$

which reduces for large and small values of V_o to

$$P\left(\frac{V}{V_{rms}} > V_o\right) \approx \frac{1}{2}\left[1 - \text{erf}\left(\frac{\ln V_o + \sigma^2}{\sigma\sqrt{2}}\right)\right]$$

for large V_o, and

$$P\left(\frac{V}{V_{rms}} > V_o\right) \approx e^{-V_o^2/Nc}$$

for small V_o, respectively.

These results showed good agreement with measurements and were the first results which related measurements to the physical properties giving rise to the noise. The parameter Nc depends on the properties of atmospheric discharges, and μ and σ^2 are the mean and variance of the total attenuation, which is determined by the properties of the propagation path. Beckmann's analysis, however, gave no consideration to the characteristics of the receiver.

Hall[23] applied work on the applicability of a class of "self similar" random processes as a model for certain intermittent phenomena to signal detection problems considering LF atmospheric noise. The concept introduced is that of a random process that is controlled by one "regime" for the duration of observation, while this regime is itself a random process. The model that Hall proposed for received impulsive noise is one that takes the received noise to be a narrowband Gaussian process multiplied by a weighting factor that varies with time. Thus, the received atmospheric noise x(t) is assumed to have the form

$$x(t) = a(t)\, n(t)$$

where n(t) is a zero-mean narrowband Gaussian process with covariance function $R_n(\tau)$, and a(t), the regime process, is a stationary random process, independent of n(t), whose statistics are to be chosen so that x(t) is an accurate description of the received atmospheric noise. For a(t), Hall chose the "two-sided" chi distribution, $\chi_2(m, \sigma)$, for the reciprocal of a(t), resulting in

$$p(a) = \frac{(m/2)^{m/2}}{\sigma^m \Gamma(m/2)} \frac{1}{|a|^{m+1}} \exp\left[-\frac{m}{2a^2\sigma^2}\right]$$

and

$$p(n) = \frac{1}{\sqrt{2\pi\sigma_1^2}} \exp\left[-\frac{n^2}{2\sigma_1^2}\right]$$

Using the two equations above, Hall found the pdf of the noise to be given by

$$p(x) = \frac{\Gamma\left(\frac{\theta}{2}\right)}{\Gamma\left(\frac{\theta-1}{2}\right)} \frac{\gamma^{\theta-1}}{\sqrt{\pi}} \frac{1}{[x^2+\gamma^2]^{\theta/2}}$$

where $\gamma = m^{1/2}\sigma_t/\sigma$ and $\theta \equiv m + 1 > 1$. For the special case $\sigma_t = \sigma$, p(x) is Student's "t"-distribution. Hall terms the above the generalized "t"-distribution with parameters θ and λ. Hall shows that θ in the range $2 < \theta \leq 4$ is appropriate to fit measured data of atmospheric noise and that $\theta \simeq 3$ is appropriate to fit a large body of data at VLF and LF. (Unfortunately, for θ in the range $2 < \theta \leq 3$, x(t) has infinite variance and therefore cannot be a model for physical noise, although it fits the data very closely.)

Hall then considers the envelope and phase of the received noise, i.e.,

$$x(t) = V(t)\cos[\omega_0 t + \phi(t)]$$

Using

$$p_{V,\phi}(V,\phi) = V\, p_{y\tilde{y}}(V\cos\phi,\ V\sin\phi)$$

where $V = (y^2 + \tilde{y}^2)^{1/2}$, $\phi = \tan^{-1}(\tilde{y}/y)$, and $\tilde{y}(t)$ is the Hilbert transform of y(t), Hall showed that the phase is uniformly distributed and that the envelope distribution is given by

$$p(V) = (\theta - 1)\gamma^{\theta-1} \frac{V}{[V^2+\gamma^2]^{(\theta+1)/2}}$$

For his model, Hall also obtains expressions for the average rate of envelope level crossings and the distribution of pulse widths and pulse spacings. The envelope distributions and level crossing rates show good agreement with measurements but poor agreement with measurements of pulse width and pulse spacing distributions.[23,54]

Hall uses his model to determine the optimum receiver for coherent ON-OFF signaling and analyzes its performance. While the Hall model results in expressions that are mathematically simple enough for solving detection problems, the parameters of the model, θ and γ, have no relation to the physical processes causing the interference.

Omura[43] presented a noise process similar to that of Hall.[23] He defined

$$x(t) = A\,X(t)\sin(\omega_0 t + \phi(t))$$

where

$$X(t) = \text{a log normal process} = e^{b(t)}$$

where $b(t)$ is a stationary Gaussian process with zero mean and autocorrelation $R_b(\tau)$ and A is a constant to be determined from noise power estimates. This results in the

phase being uniformly distributed, and

$$p(AX) = \frac{1}{\sigma\sqrt{2\pi}} \exp\left\{-\frac{1}{2}\left[\frac{\log\left(\frac{X}{A}\right)}{\sigma}\right]^2\right\}$$

where $\sigma \equiv \sigma_{\log x}$. Omura also obtained expressions for the average rate of envelope level crossings and pulse width and pulse spacing distributions. The model showed agreement with measurements only at the higher envelope levels. Omura used his model to calculate the performance of various LF and VLF digital modems.

Giordano[20,21] used a filtered impulse model to obtain results similar to Furutsu and Ishida[16] for the envelope distribution of atmospheric noise. He obtained

$$p(V) = V\int_0^\infty d\lambda\, H(\lambda)\, J_1(\lambda V)$$

where $H(\lambda)$ is a characteristic function obtained along the lines of Furutsu and Ishida's[16] development. Giordano evaluates p(V) for various spacial distributions and propagation situations. Each such assumption results in a different "model." One case of interest that Giordano treats is (1) uniform spatial distribution of sources, (2) field strength that varies inversely with distance, and (3) arbitrary receiver envelope response. The result is a distribution of the Hall[23] form, and so Giordano gave a physical rationale to the Hall model.

Giordano considered numerous other cases of propagation and source distributions and also developed expressions for the average rate of envelope crossings and pulse spacing distributions.

Recent work by Middleton[35,36] has led to the development of a physical-statistical model for radio noise. The Middleton model is the only general one proposed to date in which the parameters of the model are determined explicitly by the underlying physical mechanisms (e.g., source density, beam-patterns, propagation conditions, emission waveforms, etc.). The model is also canonical in nature in that the mathematical forms do not change with changing physical conditions.

As in past models, Middleton's model postulates the familiar Poisson mechanism for the initiation of the interfering signals that comprise the received waveform X(t). The received interfering process is

$$X(t) = \sum_j U_j(t, \underline{\theta})$$

where U_j denotes the jth received waveform from an interfering source and $\underline{\theta}$ represents the random parameters that describe the waveform scale and structure. It is next assumed that only one type of waveform, U, is generated with variations in the individual waveforms taken care of by appropriate statistical treatment of the parameters $\underline{\theta}$.

With the assumption that the sources are Poisson distributed in space and emit their waveforms independently according to the Poisson distribution in time, the first-order characteristic function of X(t) is obtained in a manner similar to the analyses of Furutsu and Ishida[16] and Girodano.[20,21] These investigators have made various assumptions for the distributions required to perform averages needed to obtain a characteristic function that could be transformed to obtain the corresponding probability

density function Each different assumption, of course, leads to a different model (mathematical form) A unique approach of Middleton's model is to develop expressions for the transform of the characteristic function without performing these averages explicitly, thereby obtaining a canonical model

For atmospheric noise, the results are for the instantaneous amplitude

$$p(x) = \frac{e^{-x^2}}{\pi} \sum_{m=0}^{\infty} \frac{(-1)^m}{m!} A_\alpha^m \Gamma\left(\frac{m\alpha+1}{2}\right) {}_1F_1\left(-\frac{m\alpha}{2}, \frac{1}{2}, x^2\right)$$

where ${}_1F_1$ is a confluent hypergeometric function The model has the two parameters α and A_α Both these parameters are intimately involved in the physical processes causing the interference That is, the model is sensitive to source distributions and the propagation law Specifically,

$$\alpha = \frac{2-\mu}{\gamma}, \quad 0 \leq \alpha < 2$$

where source density $\sim 1/\lambda^\mu$, and propagation law $\sim 1/\lambda^\gamma$, where λ denotes distance The parameter A_α includes the parameter α and other terms depending on the physical mechanisms The normalization in the above is to the power in the Gaussian portion of the distribution, since as with the Hall[23] model or the Furutsu and Ishida[16] model, we obtain infinite variance for some values of the parameters α and A_α For the case $\alpha = 1$, $p(x)$ reduces to a distribution of the Hall form (A more complete model[35,36] exists which does not have this infinite variance problem, i e , a model for which all moments exist)

The corresponding results for the envelope APD are

$$P(V > V_0) = e^{-V_0^2}\left[1 - V_0^2 \sum_{m=1}^{\infty} \frac{(-1)^m}{m!} A_\alpha^m \times \Gamma\left(1+\frac{m\alpha}{2}\right) {}_1F_1\left(1-\frac{m\alpha}{2}, 2, V_0\right)\right]$$

While the Middleton model is somewhat more mathematically complex than others, it still can be (and has been) used with good success to develop optimum receiving systems and analyze the performance of existing systems (e g , see Reference 59)

EFFECT OF ATMOSPHERIC NOISE ON SYSTEM PERFORMANCE

Introduction

Here we want to briefly discuss the wide variety of interference effects atmospheric noise (or similar forms of impulsive noise) has on system performance In the next section, we give a broad overview or summary of known effects of atmospheric noise on communication systems, primarily digital, but with some measured results for analog voice systems included After that various means of improving system performance in impulsive noise are covered.

General Effects of Atmospheric Noise on System Performance

Until recently, most analyses of communication systems have been based on the

additive, Gaussian noise channel. It has long been recognized that in most communications situations the additive noise is not Gaussian in character, but rather it is impulsive in nature. Many investigators have studied the effects of impulsive broadband noise on digital communication systems (see the bibliography by Spaulding et al.[56] which lists some 315 references pertaining to system performance in impulsive noise).

For digital signaling, the receivers in general use are those designed to be optimum (minimum probability of error) in white Gaussian noise (usually termed matched filter or correlation receivers). The early work analyzed these receivers in impulsive atmospheric noise by following the steps of the Gaussian analysis but using the appropriate distributions of the atmospheric noise.

Following Montgomery,[37] we have the following results for any arbitrary additive noise which is independent from one integration period (bit length) to the next and which has uniformly distributed phase. For the symmetric binary NCFSK (noncoherent frequency shift keying) system, the probability of a bit being in error is given by one half the probability that the noise envelope exceeds the signal envelope, and for symmetric binary CPSK (coherent phase shift keying), the probability of an error is given by one half the probability that the quadrature component of the noise envelope exceeds the signal. While Montgomery's result for FSK is in terms of the noise and signal envelopes at the input to an ideal discriminator, it has been shown[65] that the result is also directly applicable to most common FSK receivers (bandpass-filter, discriminator receivers and matched-filter, envelope detection receivers). Using the above, Conda[11] has given results for NCFSK for the entire range of atmospheric noise conditions likely to occur and for a wide range of flat fading signal conditions. Shepelavey[51] and Spaulding[53] have given results for impulsive noise for the CPSK binary system. The CFSK binary system has the same error characteristic as CPSK with a 3 dB shift in S/N ratio; that is, a given error rate requires a 3 dB greater S/N ratio for CFSK than for CPSK. Here S/N ratio is the ratio of the energy per received signal to the noise power density. In the bi-phase DCPSK (differentially coherent phase shift keying) system, the receiver compares the phase ϕ of a noisy signal with a reference phase $\bar{\phi}$ to decide whether the corresponding pure-signal relative phase ψ was 0 or π ($\psi = 0$ is selected if $|\phi - \bar{\phi}| < \pi/2$, and $\psi = \pi$ otherwise). The reference phase is obtained from the previously received signals; usually it is just the phase of the previous signal. Thus the analysis of this system is complicated by the fact that both ϕ and $\bar{\phi}$ are affected by noise. This system also has adjacent symbol dependency, and, therefore, the occurrence of paired errors and other error groupings cannot be obtained easily, even with independent noise. Halton and Spaulding[24] have given results for this system, including the occurrence of various groupings or errors.

In general, the results of such analyses for suboptimum receivers (i.e., those designed to be optimum in Gaussian noise) correspond to experimental observations and can be summarized as follows:

1. For digital systems and constant signal, white impulsive noise is much more harmful (causes more errors) than Gaussian noise of the same energy at the higher S/N ratios, while Gaussian noise is more harmful for the lower S/N ratios. This is illustrated by Figure 19 which shows the APD for a sample of atmospheric noise (see Figure 10) along with the probability of binary bit error for a CPSK system with constant signal. Since the noise distribution is given relative to its rms level, the ordinate scale can also serve as a S/N ratio scale. Gaussian noise is also shown for contrast. By presenting the error rate characteristic jointly with the APD, it is easy to see how the impulsive nature of atmospheric noise effects system performance. Figure 20 shows the probability of character error for a

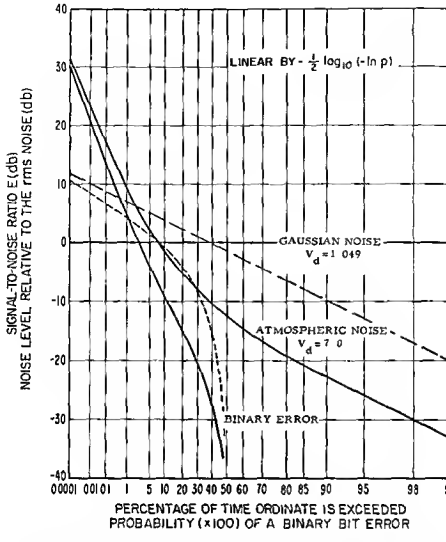

FIGURE 19 Amplitude probability distributions of the noise envelope for Gaussian noise and a sample of atmospheric noise shown with the corresponding probabilities of binary bit error for a CPSK system

four-phase DCPSK system for various atmospheric noise conditions (given by V_d).

2 When the signal is Rayleigh fading, Gaussian noise is more harmful at all S/N ratios. For diversity reception, however, impulsive noise is again more harmful at higher S/N ratios. For diversity reception, impulse noise, and Rayleigh fading signal, the degree of statistical dependence between the noise on the different diversity branches has a relatively minor effect on system performance for low order of diversity. For nondiversity operation of a binary system with Rayleigh fading signal, the error probability for a large S/N ratio is essentially independent of the additive noise statistics. Other flat fading situations (e.g., log-normal fading) do arise for which impulsive noise will cause more errors than Gaussian noise at some S/N ratios. Figure 21 illustrates some of these results using a binary NCFSK system for example.

3. For analog voice systems, impulsive noise is less harmful than Gaussian noise in the sense that understandability can be maintained at much lower S/N ratios, although the impulse interference is quite bothersome. Figure 22[40] shows an example for AM voice in atmospheric noise.

4 In addition to the above additive noise and flat fading signal effects, systems are

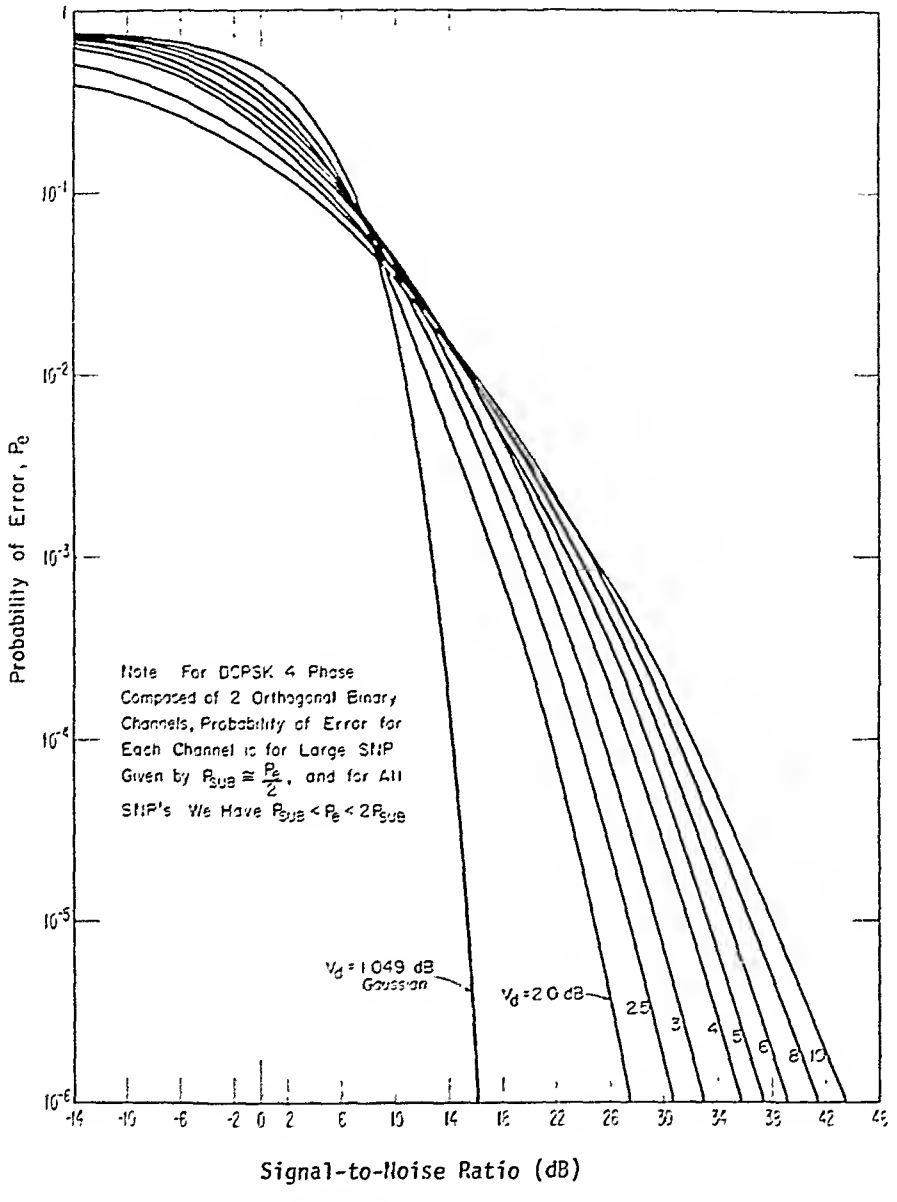

FIGURE 20. Probability of character error for a range of atmospheric noise conditions (V_d) for constant signal for a 4-phase DCPSK system.

also subject to multiplicative noise. This form of signal distortion is sometimes termed frequency selective fading. In digital systems, the effect of multiplicative noise is generally to produce a P_e threshold; that is, a value of P_e which cannot be lowered by increasing signal power. For examples of this phenomena, see Watterson and Minister.[64]

In general, the studies and example-results above obtain a single number (e.g., error rate) to describe the system performance. A long-term average, such as error rate, gives a good measure of the performance of a system only if we are dealing with stationary noise and signal processes (Gaussian noise and constant signal, for example). Since atmospheric noise is is a nonstationary random process and the signal processes

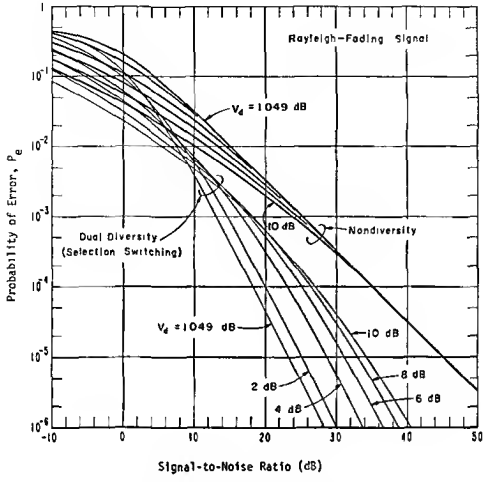

FIGURE 21 Probability of binary error for a slow flat Rayleigh fading signal for NCFSK system for both nondiversity and dual diversity reception

are also, in general, nonstationary, information in addition to the error rate (or a similar measure for analog systems) is required to specify the performance of a given system

It has become common to give two additional measures the percentage of time a given error rate or better will be achieved (termed time availability) and the probability that a given system will achieve a specified time availability and error rate (termed service probability) The service probability is designed to account for the probable errors in the prediction of noise and signal distributions, antenna gains, and the like These concepts are illustrated in the following quantitative definition of detrimental interference detrimental interference will exist for a particular receiving system whenever the available power of the wanted signal at the receiving antenna terminals is less than the operating threshold of this receiving system, corresponding to a specified required grade of service, g_r, for the specified required fraction, q_r, of some specified period of time, T (see Reference 9) This quantitative definition of detrimental interference depends on the quantitative specification of g_r, q_r, and T The determination of the grade of service, g, depends on the detailed statistical characteristics of the desired signal and the noise environment An example of grade of service is given by a P_e vs S/N ratio characteristic The determination of the fraction of time, q, depends on the long-term changes in the desired signal and the noise, since in general both of these random processes are nonstationary

Note further that both the available power of the wanted signal and the operating

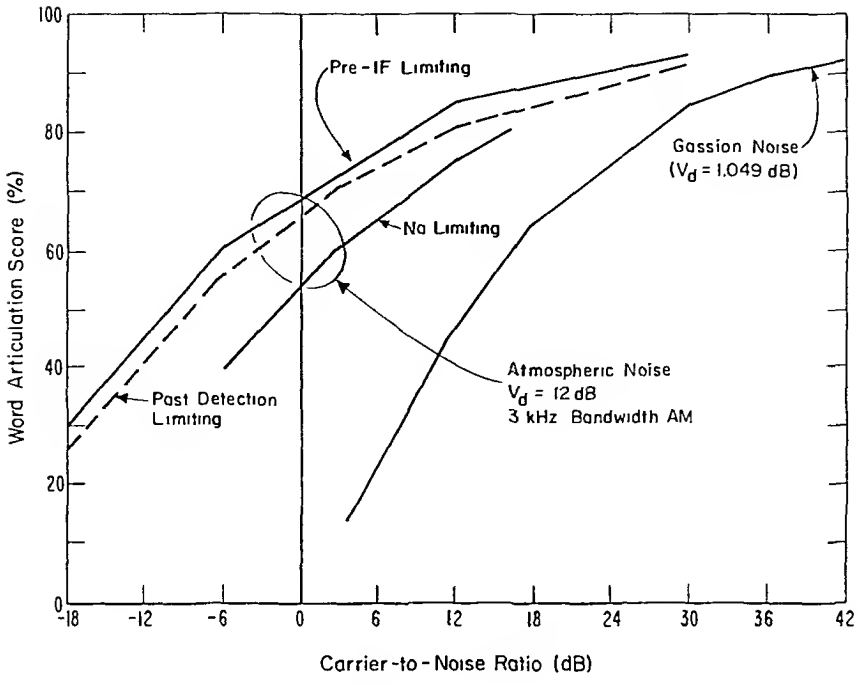

FIGURE 22. Comparison of performance of AM voice system in Gaussian and atmospheric noise (V_d = 12).[60]

threshold power of the receiving system are predicted values, and, as such, are subject to error.

Assuming that the errors of prediction are known (statistically), it is possible to determine a service probability, $Q(g_r, q_r, T)$ (statistical confidence factor), that service of a specified required grade, g_r, or better, will be available for a specified required fraction, q_r, of the specified period of time, T; i.e., will have a "time availability" of qT equal or greater than its required value, q_rT. It is also possible to define an interference probability $P(g_r, q_r, T) = 1 - Q(g_r, q_r, T)$. Note that the service probability and interference probability are simply numbers between 0 and 1. Finally, detrimental interference may be said to exist at the antenna terminals of a particular receiving system if the service probability $Q(g_r, q_r, T)$ is less than some specified value (e.g., 0.95). Once an error rate or like measure has been obtained, examples of obtaining the time availability and service probability are given in the references (e.g., References 8 and 9).

Means of Improving System Performance in Impulsive Noise

As shown above, impulsive atmospheric noise can cause serious systems degradation, especially when "normal" communication systems are employed (i.e., those designed for Gaussian noise). In view of this, recent emphasis has been on the application of various ad hoc nonlinear processing, designed to make the additive noise more Gaussian in character so that the existing receivers would be better matched to the interference, thereby improving performance. These techniques take the form of hard limiting, hole punching, and "smear-desmear" filtering. The analysis of the effectiveness of such techniques now requires appropriate mathematical models of the interference process. Bello and Esposito[5,6] use the now-customary model in which the noise takes the form of a summation of filtered impulses, the arrival times of the impulses being Poisson distributed. Bello and Esposito evaluate error rates for PSK and DPSK

with and without hard-limiting In their analyses, the impulses are assumed to be non-overlapping Ovchinnikov[44] and Richter and Smits[45] present analyses which include the intermediate case where impulses overlap but not so frequently as to approach Gaussian noise Richter and Smits[45] also evaluate the case of "smear-desmear" filtering, which is shown to be helpful at high S/N ratios and harmful at low S/N ratios A quite extensive analysis of system performance in atmospheric noise when limiting is employed has been given by Gamble [19] Signal design techniques to combat impulsive noise have been given by Silver and Kurtz [20] A useful general analysis has also been given by Fang and Shimbo [15]

While the various kinds of nonlinear processing mentioned above can be quite helpful in improving system performance, they generally are quite wasteful of spectrum (i e , time-bandwidth product) Recent studies have also been concerned with developing optimum detection algorithms for impulsive interference — that is, designing receivers that match the interference rather than attempting to change the interference to match some particular type of receiver In order to obtain improvement using any technique, the time-bandwidth product must be expanded over that normally required by the Gaussian receiver in Gaussian noise However, the optimum or near optimum detection techniques require a much smaller time-bandwidth product expansion than do the various ad hoc techniques

The first such optimum receiver was that proposed by Hall [22] Hall termed his optimum receiver for broadband impulsive noise a "log correlator" receiver Figure 23 shows the optimum performance compared to the performance of a "standard" CPSK receiver for a range of atmospheric noise conditions On Figure 23, the time-bandwidth product is denoted 2TB and is 500, compared to the normal time-bandwidth product of 1 for a binary CPSK system The atmospheric noise to be combated is received in a bandwidth of 4 kHz (three examples shown), but the effective noise bandwidth is 8 Hz, achieved by using 500 times as much time as "normal" to detect a given binary bit The performance of the matched-filter receiver for this situation is shown along with the performance of Hall's log-correlator receiver for the same situation (m is a parameter in the Hall model and was defined in the previous section) Also shown is the standard performance of a matched-filter receiver in Gaussian noise (for a time-bandwidth product = 1) Note the rather large savings in time-bandwidth product and/or signal energy that can, theoretically, be achieved

Much recent work has been centered on obtaining optimum threshold receivers, that is, receivers which approach optimality as the signal becomes small In this situation, it is possible to derive a canonical receiver structure, meaning a structure which is independent of the particular additive noise distribution The general result which has been obtained by numerous investigations is that the optimum threshold receiver for both coherent and incoherent signals is the same receiver that is optimum for Gaussian noise but preceded by a particular nonlinearity This nonlinearity is given by the derivative of the logarithm of the probability density function of the instantaneous amplitude of the interference process (See, for example, Reference 2) It should be noted that this nonlinearity does not "Gaussianize" the noise Kushner and Levin[30] and Ribin[42] have shown that these canonical threshold receivers are asymptotically optimum That is, as the decision time becomes infinite and/or the signal becomes vanishing small, the threshold receiver yields a probability of error no larger than that obtained by any other receiver Nirenberg[42] has shown that the threshold results extend to M-ary digital systems, that the receiver is independent of the signal fading characteristics, and that, if the desired signal contains desired amplitude modulation, the threshold receiver takes a more complicated form, requiring additional nonlinear processing The threshold results have been extended to narrowband non-Gaussian noise by Zachepitsky et al [47] and to cases where the observational data represent a sequence of

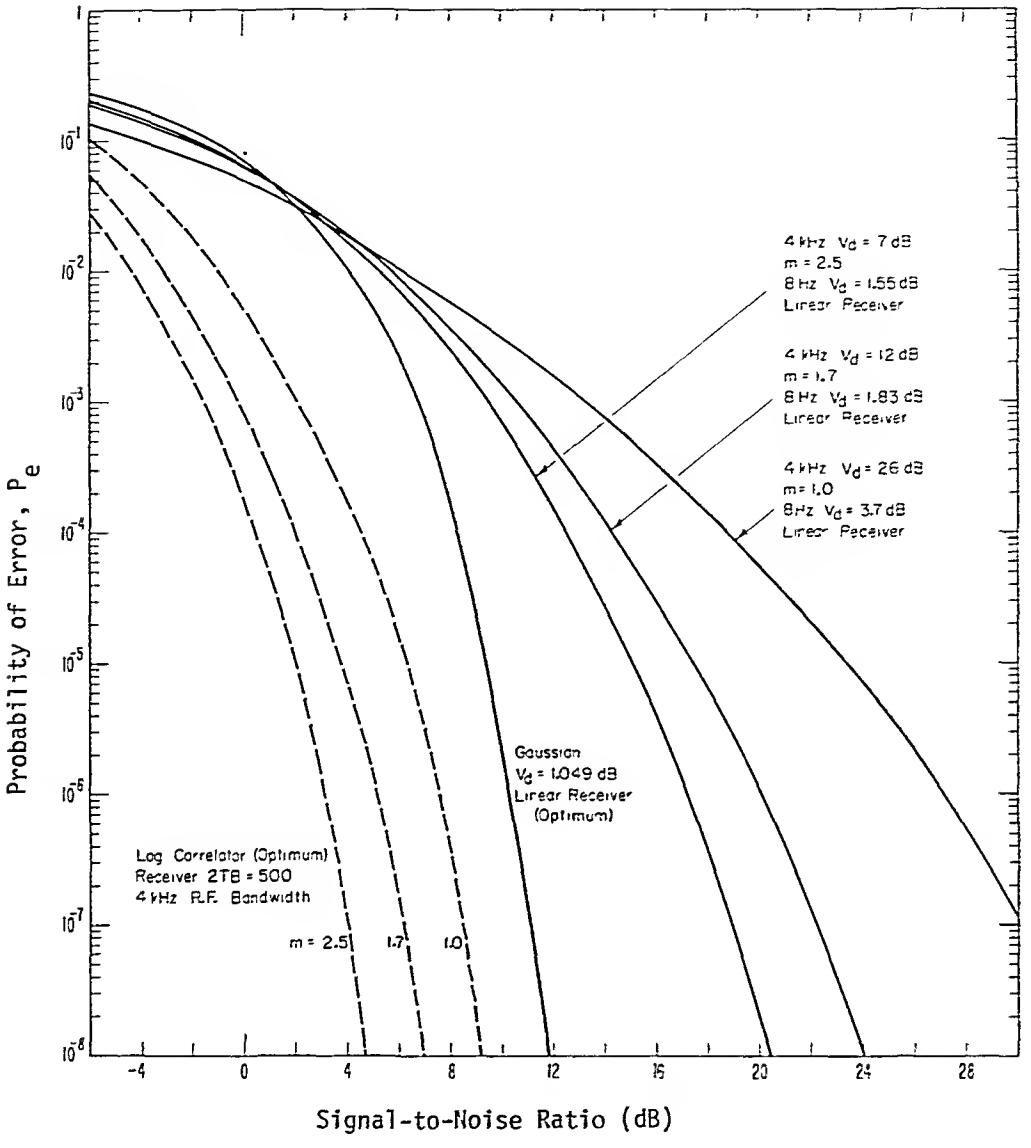

FIGURE 23. Comparison of the performance of an optimum receiving system for atmospheric noise with the performance of a standard matched filter receiver for constant CPSK binary signals for a range of noise conditions.

quantized random quantities by Levin and Baronkin.[32] Spaulding and Middleton[58] have derived and analyzed the performance of threshold receivers for a wide range of system types. In addition, Spaulding[59] has analyzed optimum threshold detection using both time and spacial sampling.

These optimum receivers are required to be adaptive. They must be able to change themselves to match the changing noise environment. This complicates the receiver structure so that, in addition to the basic receiver, there must also be equipment to estimate the required noise parameters. Nirenberg[42] has treated this problem for the Hall receiver; and Griffiths,[22] Valeyev,[62] and Valeyev and Gonopol'sky[63] have attacked the estimation problem for threshold receivers.

REFERENCES

1 Akima, H , A Method of Numerical Representation for the Amplitude Probability Distribution of Atmospheric Radio Noise, Office of Telecommunications Research and Engineering Report OT/TRER 27 (U S Government Printing Office Washington D C , March 1972
2 Antonov, O Y , Optimum detection of signals in non Gaussian noise (transl), *Radio Eng Electron Phys* 12, 541, 1967
3 Beckmann, P , The Amplitude Probability Distribution of Atmospheric Radio Noise, No 26, Institute of Radio Engineering and Electronics, Czechoslovak Academy of Sciences, Prague, Czechoslovakia 1962
4 Beckmann, P , Amplitude probability distribution of atmospheric radio noise *Radio Sci* , 68D, 723, 1964
5 Bello, P A and Esposito, R , A new method for calculating probabilities of errors due to impulsive noise, *IEEE Trans Commun Technol* COM-17 368 1969
6 Bello, P A and Esposito, R , Error probabilities due to impulsive noise in linear and hard limiting DPSK systems, *IEEE Trans Commun Technol* COM-19, 14 1971
7 Revision of Atmospheric Radio Noise Data, International Radio Consultative Committee, International Telecommunications Union, Geneva 1957
8 World Distribution and Characteristics of Atmospheric Radio Noise, Report 322 International Radio Consultative Committee, International Telecommunications Union, Geneva, 1963
9 Operating Noise-Threshold of a Radio Receiving System Report 413, International Telecommunications Union, Geneva 1966
10 Man-Made Noise, Report 258-2 International Radio Consultative Committee, International Telecommunications Union, Geneva 1976
11 Conda, A M , The effect of atmospheric noise on the probability of error for an NCFSk system, *IEEE Trans Commun Technol* ,13(3), 280 1965
12 Crichlow, W Q , Roubique, C J , Spaulding, A D , and Beery, W M , Determination of the amplitude probability distribution of atmospheric radio noise from statistical moments, *J Res Nat Bur Stand Sect* D Radio Propagation 64-(1), 49, 1960
13 Crichlow, W Q , Spaulding, A D , Roubique, C J , and Disney, R T , Amplitude-probability distributions for atmospheric radio noise, *Nat Bur Stand (U S) Monogr* ,23, 1960
14 Crichlow, W Q , private communication 1966
15 Fang, R and Shimbo, O , Unified analysis of a class of digital systems in additive noise and interference, *IEEE Trans Commun* COM-21(10), 1075 1973
16 Furutsu, K and Ishida, T , On the theory of amplitude distribution of impulsive random noise and its application to the atmospheric noise *J Radio Res Lab Jpn* ,7(32), 279, 1960
17 Galejs, J , Amplitude distributions of radio noise at ELF and VLF, *J Geophys Res* , 71, 201, 1966
18 Galejs, J , Amplitude statistics of lightning discharge currents and ELF and VLF radio noise, *J Geophys Res* 72, 2943 1967
19 Gamble, J T , An Analysis of Linear and Non-linear Coherent Detection in Atmospheric Noise at Very Low Frequency, Rome Air Development Center Technical Report TR-74 289, National Technical Information Service Springfield, Va , 1974
20 Giordano, A A , Modeling of Atmospheric Noise Ph D thesis, University of Pennsylvania, Philadelphia, Pa , 1970
21 Giordano, A A and Haber, F , Modeling of atmospheric noise, *Radio Sci* , 7(11), 1011, 1972
22 Griffiths, A S , ELF Noise Processing, Lincoln Laboratories Technical Report 490, Massachusetts Institute of Technology, Lexington Mass , 1972
23 Hall, H M , A New Model for "Impulsive" Phenomena Application to Atmospheric noise Communications Channels Stanford University Electronics Laboratories Technical Report 3412-8 and No 7050-7, SU SEL 66 052, Stanford Calif , 1966
24 Halton, J H and Spaulding, A D , Error rates in differentially coherent phase systems in non Gaussian noise *IEEE Trans Comm Tech* , COM 14(5), 594, 1966
25 Hagn, G H and Shepherd, R A , Man-Made Electromagnetic Noise from Incidental Radiators A summary, Accession No AD-A 018980, NATO/AGARD Meeting of Electromagnetic Noise, Interference, and Compatibility AGARD, National Technical Information Service, Springfield, Va , 1974
26 Ibukun, O , Structural aspects of atmospheric radio noise in the tropics, *Proc IEEE*, 54, 361, 1966
27 Interservice Radio Propagation Service, Radio Propagation Handbook, U S Dept of Commerce, National Bureau of Standards, November 1943
28 Ishida, T , Bulletin of the XIIth Symposium of the Radio Research Laboratory, (in Japanese), October 23 to 24, Tokyo, p 113 1956

29. Ishida, T., Statistical Characteristics of Atmospheric Noise 1966-1969, Radio Research Laboratories Ministry of Posts and Telecommunications, Tokyo, 1969, 1.
30. Kushner, A. F. and Levin, B. P., Optimal ranking algorithms for the detection of signals in noise, (transl.), *Problemy Peredachi Inform.*, 4, 1968.
31. Lauber, W. R. and Bertrand, J. M., Preliminary urban VFH/UHF radio noise intensity measurements in Ottawa, Canada, in *Electromagnetic Compatibility 1977*, Institute of Engineers and Electrical Engineers, 1977, 357.
32. Levin, B. R. and Baronkin, V. M., Asymptotically optimum algorithms of detection of signals from quantized observations (transl.,) *Radio Eng. Electron. Phys.*, 5, 682, 1973.
33. Likhter, J. I., Concerning the statistical characteristics of atmospheric noise, *Radiotekh i Electron*, 1, 1295, 1956.
34. Lucas, D. L. and Harper, J. D., A Numerical Representation of CCIR Report 322: High Frequency (3-30 Mc/s) Atmospheric Radio Noise Data, NBS Technical Note 318, U.S. Department of Commerce, Washington, D.C., 1965.
35. Middleton, D., Statistical-physical models of electromagnetic interference, *IEEE Trans. Electromagn. Compat.*, EMC-19, 106, 1977.
36. Middleton, D., Canonical non-Gaussian noise models: their implications for measurement and for prediction of receiver performance, *IEEE Trans. Electromagn. Compat.*, EMC-21, 209, 1979.
37. Montgomery, G. F., Comparison of amplitude and angle modulation for narrow-band communication of binary-coded messages in fluctuation noise, *Proc. Inst. Radio Eng.*, 42, 447, 1954.
38. Nakai, T., The study of amplitude probability distribution of atmospheric radio noise, *Proc. Res. Inst. Atmos.*, (Japan), 7, 12, 1960.
39. Ionospheric Radio Propagation, Circular 462, U.S. Department of Commerce, National Bureau of Standards, Washington, D.C., 1948.
40. World-wide Noise Levels Expected in the Frequency Band 10 kc/s to 100 Mc/s, Circular 557, U.S. Department of Commerce, National Bureau of Standards, Washington, D.C., 1955.
41. Nirenberg, L. M., Parameter estimation for an adaptive instrumentation of Hall's optimum receiver for digital signals in impulse noise, *IEEE Trans. Comm.*, COM-22(6), 798, 1974.
42. Nirenberg, L. M., Low SNR digital communication over certain additive non-Gaussian channels, *IEEE Trans. Comm.*, COM-23(3), 332, 1975.
43. Omura, J. K., Statistical Analysis of LF/VLF Communications Modems, Special Technical Report 1, SRI Project 7045, Stanford Research Institute, Menlo Park, Calif., 1969.
44. Ovchinnikov, L. M., Noise Immunity of PSK and ASK Coherent Receivers to Quasi-impulsive Interference (transl.), Telecommun. Radio Eng., 28(10), 64, 1973.
45. Popoff, A. C., Apparatus for the detection and registration of electrical vibrations, *Russian Physical and Chemical Societies' Journal*, 28, 1, 1896.
46. Ponhratov, V. S. and Antonov, O. Y., Optimal reception of binary signals in a background of non-Gaussian noise, *Telecommunications*, 19, 19, 1967.
47. Ribin, A. K., Classification of weak signals in non-Gaussian noise, *Eng. Cybern.*, 10, 901, 1972.
48. Richter, W. J. and Smits, T. I., Numerical evaluation of Rice's integral representation of the probability density function for Poisson impulsive noise, *J. Acoust. Soc. Am.*, 56(2), 481, 1974.
49. Minimum Required Field Intensities for Intelligent Reception of Radio Telephony in Presence of Atmospheric or Receiving Set Noise, Radio Propagation Unit Technical Report 5, Holabird Signal Depot, Baltimore, Md., December 1945.
50. Silver, H. I. and Kurz, L., A class of discrete signal-design problems in burst noise, *IEEE Trans. Inf. Theory*, IT-18, 258, 1972.
51. Shepelavey, B., Non-Gaussian noise in binary data phase coherent communications systems, *IEEE Trans. Commun. Syst.*, CS11, 280, 1963.
52. Spaulding, A. D., Roubique, C. J., and Crichlow, W. Q., Conversion of the amplitude probability distribution function for atmospheric radio noise from one bandwidth to another, *J. Res. Nat. Bur. Stand. Sect. D.*, 66, 713, 1962.
53. Spaulding, A. D., Determination of error rates for narrowband communication of binary-coded messages in atmospheric radio noise, *Proc. IEEE*, 52(2), 220, 1964.
54. Spaulding, A. D., Disney, R. T., and Espeland, L. R., Samso Phase C — Final Report — Noise Data and Analysis Hard Rock Silo Development, Program 12JB, Report ESSA/ITS ERLTM-ITS 184 (NTIS AD861428), National Technical Information Service, Springfield, Va., 1969.
55. Spaulding, A. D., and Disney, R. T., Man-Made Radio Noise. 1. Estimates for Business, Residential, and Rural Areas, Report OT 74-38, Office of Telecommunications, U.S. Department of Commerce, Boulder, Colo., U.S. Government Printing Office, Washington, D.C., 1974.
56. Spaulding, A. D., Disney, R. T., and Hubbard, A. G., Man-Made Radio Noise, Part II: Bibliography of Measurement Data, Applications, and Measurement Methods, Office of Telecommunications Report OT 75-63, U.S. Government Printing Office, Washington, D.C., 1975.

57 Spaulding, A D , Man-Made Noise The Problem and Recommended Steps Toward Solution, Report OT 76-85, Office of Telecommunications U S Department of Commerce, Boulder, Colo U S Government Printing Office, Washington, D C 1976
58 Spaulding, A D and Middleton, D , Optimum reception in an impulsive interference environment I Coherent detection II Incoherent reception, *IEEE Trans Commun* COM 25, 910, 1977
59 Spaulding, A D , Optimum Threshold Detection in Broadband Impulsive Noise Employing Both Time and Spatial Sampling, in Proc 3rd Symp Tech Exhibition on Electromagnetic Compatibility, Rotterdam, May 1 to 3, 1979, 377
60 Systems Development Corporation, Santa Monica, Calif Decision Information Distribution System, Intelligibility Study Report January 1968
61 URSI, *The Measurement of Characteristics of Terrestrial Radio Noise* Special Report 7 Elsevier, Amsterdam 1962
62 Valeyev, V G , Nonlinear normalization in optimum detection of signals in the presence of non-Gaussian interference (transl), *Radio Eng Electron Phys U S S R* ,4 623 1973
63 Valeyev, V G , and Gonopol'sky, V B , Reception of signals in the presence of unknown probability density of noise (transl) *Radio Eng Electron Phys U S S R* 8, 1176 1973
64 Watterson, C C , and Minister, C M , HF Channel Simulator Measurements and Performance Analysis on the USC10, ACQ6 and MX190 PSK Modems Office of Telecommunications Report 75-56, U S Government Printing Office Washington, D C 1975
65 White, H E , Atmospheric noise FSk error probabilities for an envelopedetection receiver, *IEEE Trans Commun Technol* 2 188 1966
66 Zacharisen, D H , and Jones, W B , World Maps of Atmospheric Radio Noise in Universal Time by Numerical Mapping Telecommunications Research Report OT/ITS/TRR2 U S Department of Commerce Washington D C 1970
67 Zacheptsky, A A , Mareskin, V M , and Paknomov, Yu I , Detection of weak signals in narrow band noises, Radio Eng Electron Phys , *U S S R* 10, 1637 1972

MAN-MADE RADIO NOISE

G. H. Hagn

TABLE OF CONTENTS

INTRODUCTION

Electromagnetic noise can be defined as "all electromagnetic energy from both intentional and unintentional radiators, except the desired signal for a specific system of interest "[1,2] Such noise (a cause) should not be confused with interference (an effect), which is the degradation that the noise can cause to the performance of a telecommunications or an electronic system [3] Other terms used in the literature for man-made radio noise include incidental noise, unintentionally generated radio noise, etc

There is a large body of literature on man-made electromagnetic noise The International Union of Radio Science (URSI) has produced triennial reviews and occasional summaries (e g , References 4 through 8), and the International Special Committee on Interference (CISPR) has given considerable attention to the allowable radiation limits for specific sources of noise [9-12] The International Radio Consultative Committee (CCIR) has produced a report on environmental noise [13] The Joint Technical Advisory Committee of the Institute of Electrical and Electronics Engineers (IEEE) and the Electronic Industries Association (EIA) considered radio noise as it impacts on the use of the spectrum [14] Spaulding has discussed the problems associated with man-made noise and recommended steps for solutions in the U S [15] Two recent books have been devoted almost entirely to man-made noise [16,17] These publications, and the references therein, when combined with a bibliography by Spaulding, Disney, and Hubbard,[18] cover the major work on man-made noise published through 1980

The composite electromagnetic noise environment observed (or observable) by a given receiving system at a given time and location can arise from various categories of natural and man-made sources (see Figures 1 and 2) This chapter will discuss the noise from man-made sources

SOURCES OF MAN-MADE NOISES

The intended coherent radiation from intentional radiators produces the largest electromagnetic fields The density of intentional radiators is highly correlated with population density [14,17] Janes, et al [19,20] have measured the integrated power density levels in the band 54 to 900 MHz at 72 locations in the U S urban areas and found that the integrated power density levels (including that of subbands) were log-normally distributed with a median of 0 03μW/cm^2 The FM band (88 to 108 MHz) had the largest median (1 3 × 10^{-2}μW/cm^2), the high VHF-TV band (174 to 216 MHz) was next highest (2 9 × 10^{-3}μW/cm^2), followed by the UHF-TV band (470 to 806 MHz) with 2 1 × 10^{-3}μW/cm^2, the low VHF TV band (54 to 88 MHz) with 1 7 × 10^{-3}μW/cm^2, whereas, the land mobile bands (150 to 182 MHz, and 450 to 470 MHz) were the lowest with 2 8 × 10^{-5}μW/cm^2 In addition to their desired emissions, such powerful transmitters can radiate broadband noise,[21] harmonics, and other unintended radiation, and they can cause problems to nearby receivers such as desensitization, adjacent channel interference, and intermodulation products [22,23]

Unintentional man-made radiators also contribute to the composite electromagnetic environment Table 1 summarizes some of the primary categories of such radiators The level of radiation from these equipments and devices is typically much less than the levels from intentional radiators Figure 3 is an example of the relative contributions to the composite noise environment at 155 MHz as observed with a scanning receiver with memory [1,24,25] Notice the relative contributions of the land-mobile transmitter and the ignition noise This 3-dimensional display of amplitude vs frequency and time is a useful way to observe the short-term variability and complexity of the environment (see also References 17 and 25 for numerous other examples of the 3-

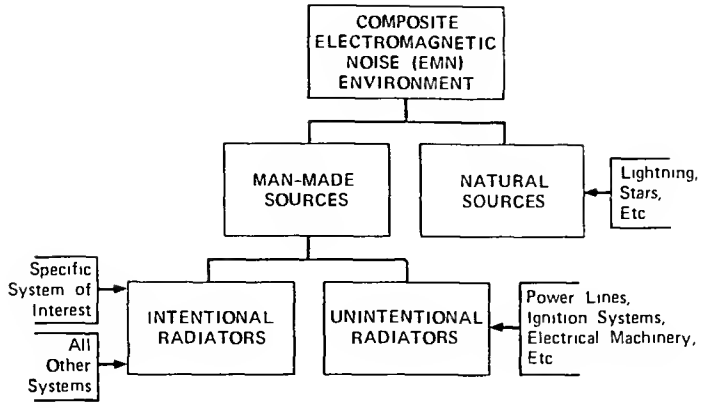

FIGURE 1. Basic categories of sources contributing to the composite electromagnetic noise environment. (After Hagn, G. H , Definitions and Fundamentals of Electromagnetic Noise, Interference, and Compatibility, No. AD-A-018980, National Technical Information Service, Springfield, Va., 1975.)

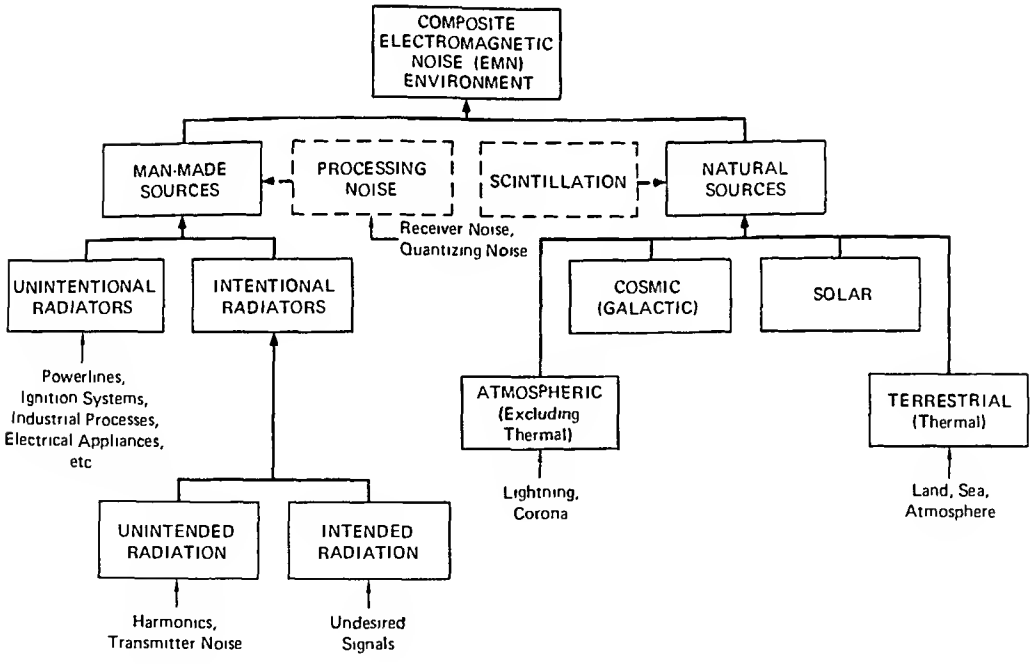

FIGURE 2. Detailed sources of the composite electromagnetic noise (EMN) environment. (After Hagn, G. H., Definitions and Fundamentals of Electromagnetic Noise, Interference, and Compatibility, No. AD-A-018980, National Technical Information Service, Springfield, Va., 1975.)

dimensional "signatures" of specific sources). Let us now consider these unintentional sources that contribute to the ambient noise levels observed on signal-free radio channels.

The list of potential incidental radiators (Table 1) which can cause interference is very great (see also References 16 and 17). Frequently, the closest noise source to your receiving antenna will dominate the ambient level while it is operating. It is possible to identify specific sources which make major contributions to the noise background

Table 1
CATEGORIES OF UNINTENTIONAL RADIATORS

Overhead power transmission and distribution lines
Ignition systems (e g , automotive, aircraft, small engines, etc)
Industrial fabrication and processing equipment (including arc welders)
Electric motors and generators
Electric buses and trains (excluding their power lines)
Contact devices (e g , thermostats bells, and buzzers)
Electrical control, switchings, and converting equipment (e g , SCRs, and ac/dc converters)
Medical and scientific apparatus
Lamps (e g , gaseous discharge devices and neon signs)
Various electrical consumer products (including electronic games and computers)

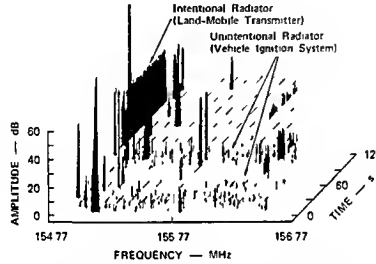

FIGURE 3 Examples of contributions to the composite electromagnetic environment by intentional and unintentional radiators (After Vincent, W R *IEEE Trans EMC*, 19(3), 241 1977 Copyright © 1977, IEEE With permission)

by noting verified complaints (e g , Reference 26) or by correlating their characteristics with observed ambient levels Since we are dealing with man-made noise, let us first consider the correlation of the composite man-made noise level with population density before addressing its measured correlation with specific electromagnetic sources It seems reasonable that man-made noise levels should correlate, at least broadly, with population in urban areas [16] Allen[27] presented data relating quasi-peak field strength values measured at street level to urban population He computed the probability of various levels being exceeded at 1 MHz as a percentage of locations in an urban area. This was done over a population range from 10^3 to 10^6 persons Although Allen reported a gross correlation between population and noise levels, attempts to correlate average noise power levels with population density, as measured on a finer scale in U S Census Bureau standard location areas (SLAs) of 1 to 5 square miles, have not been successful [28] Spaulding[29] investigated the relationship between population density and average noise power spectral density, F_a, in decibels above kT_o, in signal-free channels in the band 250 kHz to 48 MHz In the population density range of 1,000 to 25,000 per square mile (San Antonio, Texas) he found no significant correlation between the average population density of an SLA and the average values of noise level taken at several locations within the SLA (see Figure 4) Correlation on a finer scale (down to an individual city block) has not been attempted

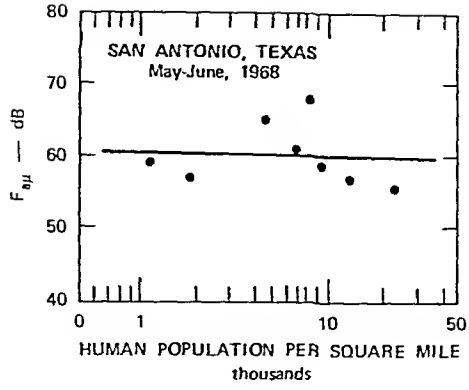

FIGURE 4. Regression of 5.0 MHz $F_{a\mu}$ with log population density. (From Spaulding, A. D., *IEEE 1972 NTC Record*, IEEE Cat. No. 72CH0601-5-NTC, 1972. Copyright © 1972, IEEE. With permission.)

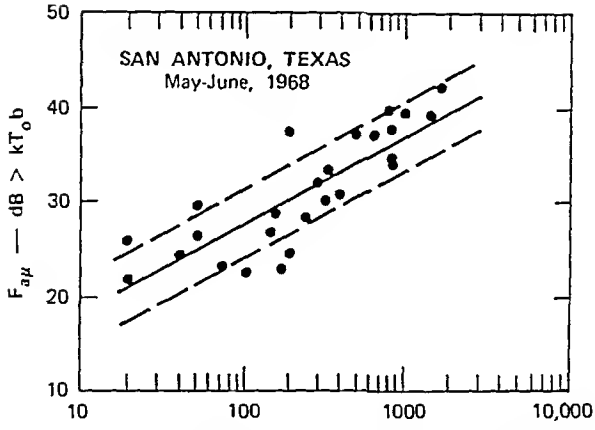

FIGURE 5. Linear regression of the mean of F_a values along a thoroughfare ($F_{a\mu}$) vs. log hourly traffic count along the thoroughfare at 48 MHz (26 thoroughfares). (From Spaulding, A. D., *IEEE 1972 NTC Record*, IEEE Cat. No. 72CH0601-5-NTC, 1972. Copyright © 1972, IEEE. With permission.)

Spaulding et al.,[28] Disney,[30] Spaulding,[29] and Spaulding and Disney[31] did find significant correlation between vehicular traffic density and average noise power spectral density (Figure 5), especially for frequencies above 20 MHz (Figure 6). Data taken later than those in Figure 6 indicate that the correlation remains high between 50 and 250 MHz. Therefore, it seems reasonable to conclude that vehicle ignition systems will be potentially important sources of interference to radio systems operating above 20 MHz, especially near roads. In rural areas remote from power lines and other sources, automobiles, gasoline-powered tractors, snowmobiles, etc. may be dominant noise sources below 20 MHz.

Overhead power lines are known to be an important source of man-made noise below 15 to 20 MHz. Spaulding and Disney,[31] reported relatively good correlation between electrical power consumption in an area and the root mean square (rms) value of the radio noise below 20 MHz. They noted, however, that information on local power consumption in the U.S. is difficult to obtain. Overhead lines also can be im-

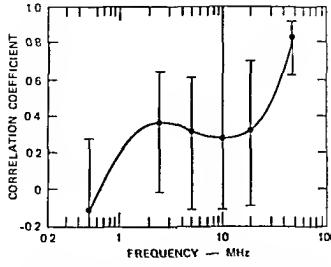

FIGURE 6 Correlation coefficients along with the 95% confidence limits for each of the measurement frequencies F_m vs log hourly traffic count (From Spaulding, A. D., *IEEE 1972 NTC Record* IEEE Cat. No. 72CH0601-5 NTC, 1972. Copyright © 1972, IEEE. With permission.)

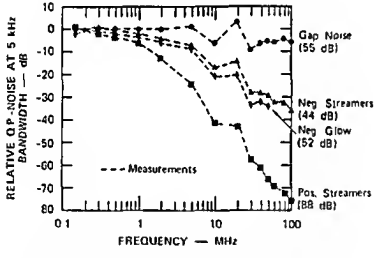

FIGURE 7 Relative frequency spectra for different power line noise types. The numbers in parentheses are the absolute values measured at 0.150 MHz. (From Juette, G. H., *IEEE Trans. Power Appar. Syst.* 91(3), 1972. Copyright © 1972, IEEE. With permission.)

portant above 15 MHz[32] and the interference to television from power lines has been discussed (e.g., References 33 to 35). Let us now consider in more detail the technical characteristics of the noise from power lines and automobiles and some other specific sources.

Power lines can be categorized by their function (power transmission or distribution), which determines their operating voltage and the mechanisms by which they produce radio noise under normal operating conditions. In general, the lower-voltage distribution and transmission lines (below about 70 kV) produce noise from various types of discharges in gaps, while the higher-voltage transmission lines (110 kV and higher) generate noise by various kinds of corona.[36] The high rate of current rise transforms to a broader spectrum for gap noise than for corona noise, as observed with peak detectors[37] and with quasi-peak detectors (see Figure 7). The low-voltage lines

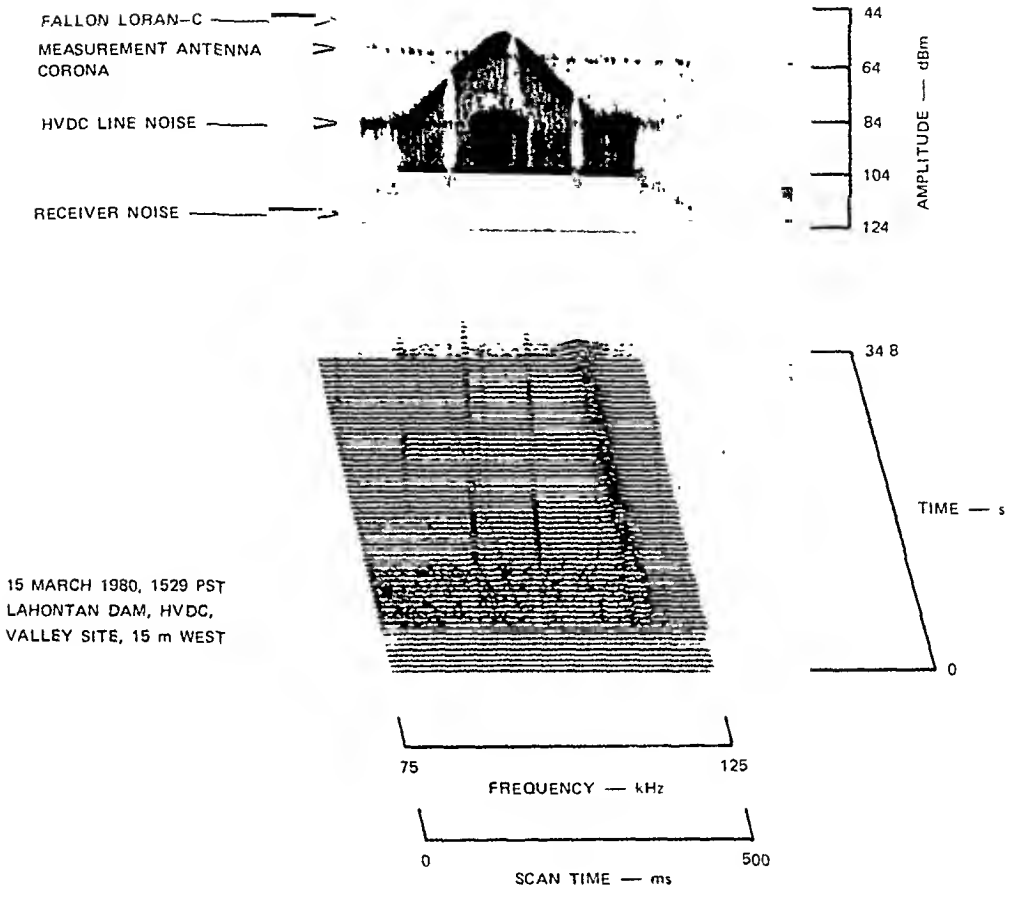

FIGURE 8. HVDC line noise, antenna breakdown noise, and Loran-C signals. (From Vincent, W. R., IEEE Cat. No. 80, CH1538-8-EMC, 1972. Copyright © 1972, IEEE. With permission.)

may also radiate noise resulting from switching transients and other effects and from devices connected to the lines.(See Table 1.)

High-voltage DC transmission lines are coming into use.[38] Annestrand[39] points out that noise is generated at the converter stations, which then propagates on the lines. Vincent[40] has been studying this noise, and he has observed that corona from the measurement antenna can be a problem (see Figure 8 where noise on a 9-ft rod was observed at 15 m with a 3 kHz bandwidth).This only adds to the problems regarding noise measurements already noted by Hubbard.[41]

The noise from power lines is greatly influenced by the weather and by the state of maintenance of the line. Fair-weather noise levels measured by using peak and quasi-peak detectors have been reported in the literature of the IEEE Power Engineering Society. Indeed, most of the measurements of power-line noise reported in the literature have been made by using quasi-peak detectors, although some data on powerline noise measured with peak and average detectors are available. Measurements made with an rms detector are not generally available in the literature,[42] but some data of this type were given by Disney and Longley[43] and Spaulding and Disney.[31] Figure 9

presents median values of average noise power spectral density data obtained in the near field by several investigators at MF, HF, and VHF with rms detectors Vertical monopole antennas were used, the antennas were positioned directly under the line, with the exception of the 15-kV/16 67-Hz line One of the most interesting observations is that the 115-kV lines were noiser than the lines with higher or lower operating voltage The absolute calibration is only approximate, however the relative calibration is ±3dB At any given frequency, the difference between measured medians for the noisiest and the quietest line was about 30 dB for these fair weather data Pakala and Chartier[37] stated that noise increases of 17 dB on a quasi-peak meter were likely during rain They observed that, in 60% of their measurements, those made with horizontally polarized dipoles produced greater noise than those made with vertically polarized dipoles The differences ranged from 0 to 10 dB over the frequency band 15 kHz to 10 GHz The IEEE[45] indicated increases of 15 to 25 dB during foul weather and subsequently[46] indicated increases of 20 dB during bad weather Data on radio interference (RI) levels (i e , data at about 1 MHz) taken on a Bonneville Power Administration 345-kV line between May 1965 and May 1966 (Figure 10) show an average RI level during rain of approximately 20 dB above that shown during clear weather, while during snow the average level was nearly 26 dB higher than the clear-weather level [47] Forrest[48] pointed out that "defect" noise on lower-voltage (11- to 66-kV) lines, caused by sparks and microsparks, tended to determine the fair-weather RI levels above 10 MHz He noted that wet weather could cause RI increases of 5 to 15 dB in the band 100 kHz to 10 MHz, due to corona on lines above 100 kV, while causing RI levels above 10 MHz to decrease, due to the shorting out of arcing gaps Lauber[49] and Lauber and Bertrand[50] have reported on power line amplitude probability distributions (APDs, see also Reference 51) The IEEE[52] has just completed an excellent summary of the technical aspects of power line noise pertinent to establishing limits on this important noise source

Ignition noise is generally found wherever automobiles or other vehicles using spark-initiated power systems (e g , trucks, boats, aircraft, and snowmobiles) are used The sources of ignition noise include the distributor, spark plugs, and generator Typically, in a given frequency band, one of these is the dominant source This noise is highly *impulsive and spreads over much of the frequency spectrum At the low end of the* spectrum (below about 20 MHz), ignition noise is generally believed to be exceeded by power-line noise when both sources are present The actual lower limit will, of course, be determined by specific situations, including the density of automobile traffic and the proximity of power lines The high frequency limit to the automobile ignition noise spectrum has not been as well studied Generally, instrumentation capability or investigator interest tapers off before the establishment of a clear upper limit Increased traffic intensity associated with the rush hour in the U S commonly produces noise spikes 30 to 40 dB above the receiver noise in a 100-kHz bandwidth at 1 2 and 2.9 GHz for a 30 dB noise figure receiver (spectrum analyzer)

The APDs of three vehicles measured in an 8 kHz bandwidth[53] are shown in Figure 11 and single-vehicle APDs (averaged over four vehicles) are shown in Figure 12 as a function of receiver bandwidth [54] Note the change in the shape of the APD in Figure 11 as a function of engine speed Shepherd et al[56] have also surveyed a vehicle population using a spectrum analyzer (peak detector) to measure impulse field strength (see Figure 13) This survey was extended at 50 MHz and 153 MHz to include over 10,000 vehicles in the U S [57] Figure 14 shows the distribution of noise levels observed at 10 m using the procedures of the Society of Automotive Engineers (SAE)[58] as applied to passing vehicles Figures 15 and 16 show similar distributions vs vehicle type and country of origin (for non-U S vehicles), respectively Other sources of noise have

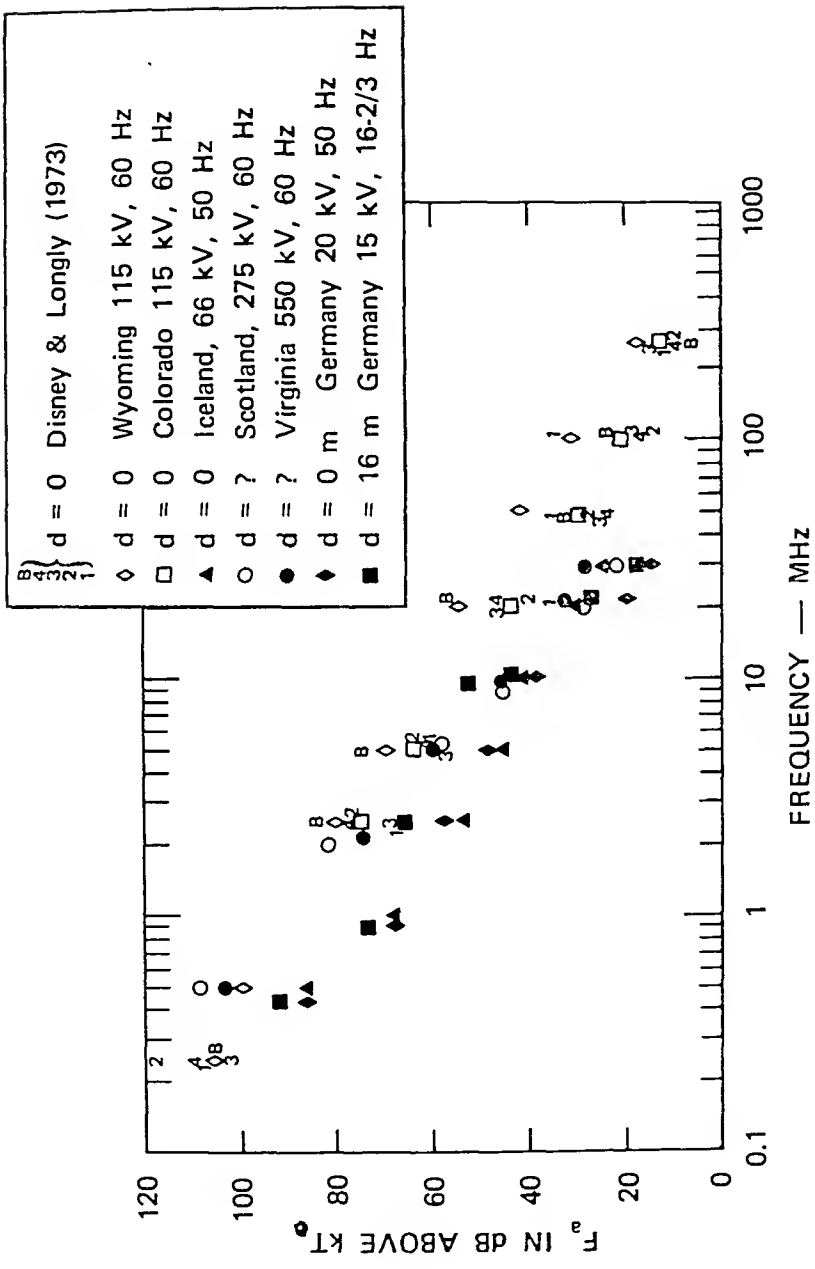

FIGURE 9. Average noise power approximately underneath selected power lines.

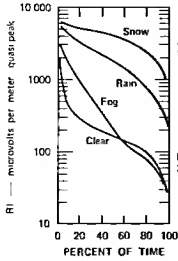

FIGURE 10 RI distribution, percent of time RI level equals or exceeds ordinate (From Bailey, B M and Belsher, M W, *IEEE Trans Power Appar Syst*, 87(4) 1968 Copyright © 1968, IEEE With permission)

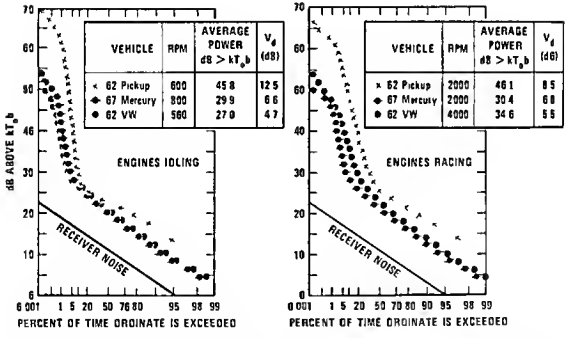

FIGURE 11 APDs of three vehicles, right side at 10 m, 24 11 MHz, 8 kHz noise bandwidth (From Shepherd, R A, *IEEE Trans Vehic Technol*, 23(3), 1974 Copyright © 1974, IEEE With permission)

also been studied[89] but they will not be discussed further here (see References 16, 17, and 44)

EXAMPLE MEASURES OF MAN-MADE NOISE

Due to the variability of man-made noise it is necessary to treat it statistically The noise envelope statistics discussed in the chapter, "High Frequency Radio Noise," for describing atmospheric noise are equally applicable to man-made noise These statistics

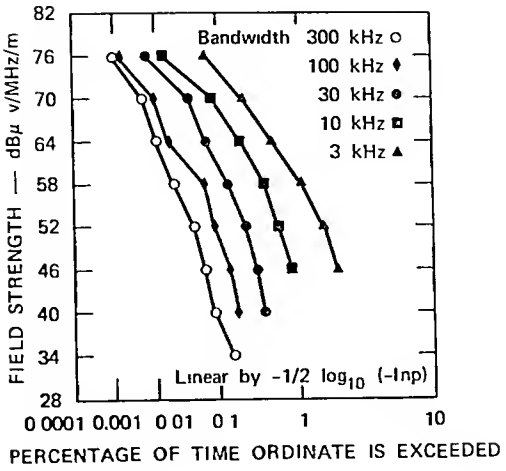

FIGURE 12. Single-vehicle APD data (average of four vehicles). (From Schultz, R. B and Southwick, R. A., *IEEE Electromagnetic Compatibility Symp. Record*, 74CH0803-7EMC, 1974, 50. Copyright © 1974, IEEE. With permission.)

include the rms voltage, the average voltage (and V_d the dB difference between rms and average) and the various distributions (e.g., APD). The quasi-peak (qp) voltage, measured by passing the noise envelope waveform through a circuit with a very short charging time and a long discharge time and averaging the output, has been used by CISPR workers and others. For power line noise the qp meter typically reads about 10 to 15 dB higher than an rms meter (Lauber, 1980). Under certain circumstances the relationship between the qp and rms values of a given envelope observed in the same bandwidth can be computed for random noise,[60] but in the general case no analytical relationship exists. Another measure used is the peak voltage (for the period, T).

Examples of the APD, ACR, PDD, and PSD (see the chapter by Spaulding on Atmospheric Noise for definitions) for the magnetic field strength of man-made noise in a coal mine are given in Figures 17 to 20[61,62] for comparison with Figures 10 to 13 in the Spaulding chapter.

As previously mentioned, the 3-dimensional display of amplitude vs. frequency and time is most descriptive of the details of the noise variation. The narrow band scanning receiver approach used by Vincent[25] and the broadband Fourier transform approach of Bensema[63] are both most useful.

EMPIRICAL PREDICTIONS OF THE COMPOSITE NOISE ENVIRONMENT FROM INCIDENTAL RADIATORS

Spaulding and Disney[31] have discussed two methods of predicting man-made radio noise average power levels. One method is based directly on past measurements in specified environments; the other depends on the correlation of past noise measurements with some predictable parameter(s) of the environment (e.g., traffic density for frequencies above 20 MHz). Skomal[16] has developed empirical formulas for noise level vs. frequency and distance from the center of a metropolitan area measured along or above the surface of the Earth. Vincent[64] observed "hot spots" and "cold spots" in the Los Angeles area at 100 kHz and observed that noise levels than the downtown area (with mostly underground power lines) were lower than in the surrounding area

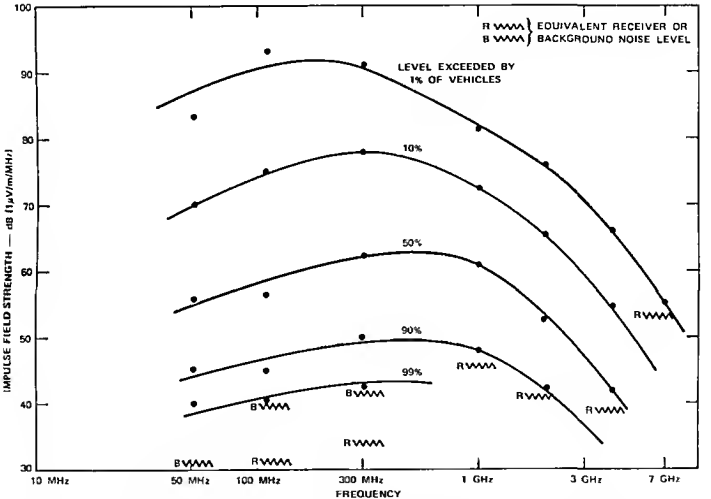

FIGURE 13 Exceedence distribution vs frequency for ignition noise levels from individual moving vehicles at about 13 m

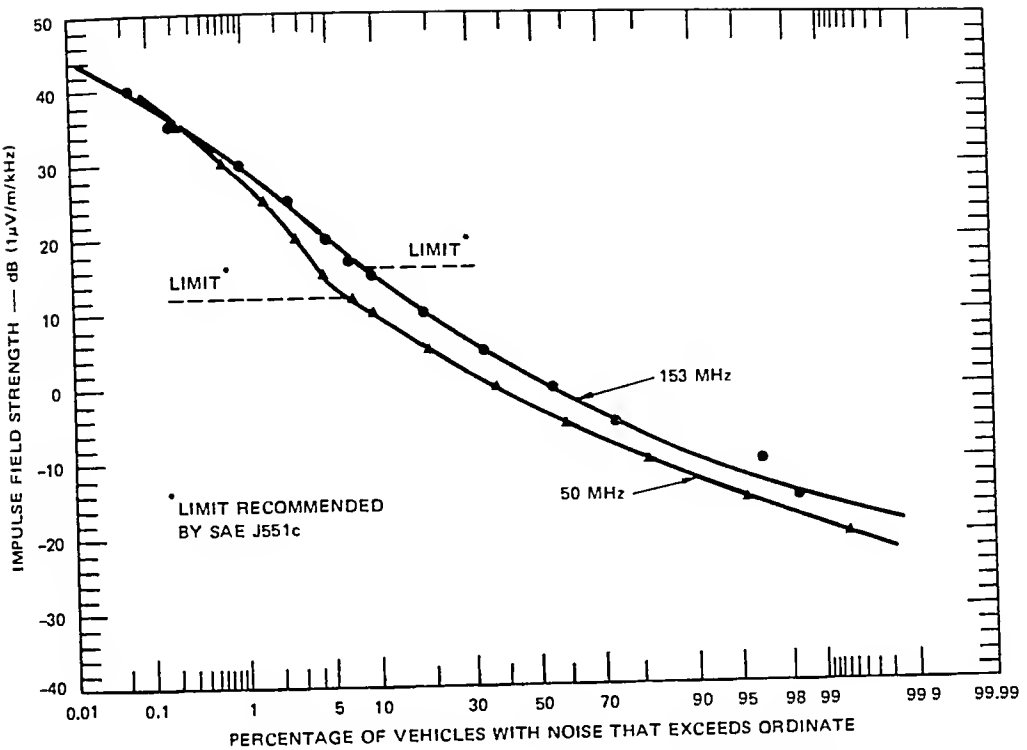

FIGURE 14. Ignition noise distributions of the U.S. vehicle population in mid-1977-developed from Regional Distributions. (From Shepherd, R. A., Gaddie, J. C., and Bell, P. J., Electromagnetic Radio Statistics at 50 MHz and 153 MHz of the United States Vehicle Population, SRI International, Menlo Park, Calif., August 1977. With Permission.)

— in contrast to Skomal's model which predicts contours of levels decreasing with distance from the center of the city. In some cities, it is difficult to specify a central reference location in order to use Skomal's model at the shorter distances.

Let us consider now Spaulding and Disney's first prediction method. This method which assumes that the behavior patterns noted at "typical" locations will be the same at similar locations in the future. Analysis of the available data base for each category of location (i.e., each type of environment) will then provide the estimates of the man-made radio noise conditions to be found at other locations in the same category of environment. The user must determine the category that best describes the location for which he desires to predict the noise level, and he must make modifications if he uses a different antenna or detector than the ones used to generate the predictions.

Spaulding and Disney[31] used essentially the same measurement system with an rms detector to obtain data in the band 250 kHz to 250 MHz with a short vertical antenna near ground at various sites in the U.S. Over 300 hr of data were obtained simultaneously on ten frequencies over the period from 1966 through 1971 in six states and in the District of Columbia. Three environmental categories were defined: rural, residential, and business. Rural areas were defined as locations where land usage is primarily for agricultural or similar pursuits, and dwellings are no more than one every five acres. Residential areas (urban or suburban) were defined as any area used predominantly for single or multiple family dwellings with a density of at least two single family units per acre and with no large or busy highways nearby. A business area was defined as any area where the predominant usage throughout the area is for any type of business (e.g., stores and offices, industrial parks, large shopping centers, main streets or highways lined with various business enterprises, etc.).

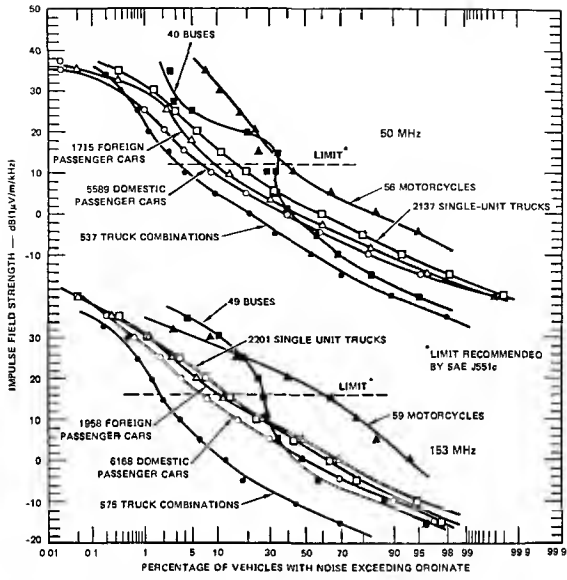

FIGURE 15 Ignition noise distributions for various vehicle types (From Shepherd, R A , Gaddie, J C , and Bell, P J , Electromagnetic Radio Statistics at 50 MHz and 153 MHz of the United States Vehicle Population, SRI International, Menlo Park, Calif , August 1977 With Permission)

These results were analyzed statistically, and the least-squares fit for F_{am}, the median values of F_a, for each environmental category is reproduced as Figure 21 The slope with frequency was found to be −27 7 dB/decade for each environmental category (at the 95% confidence level) The equations for F_{am} in dB(kT$_a$) for each category are rural, $F_{am} = -27\ 7 \log_{10} f_{MHz} + 67\ 2$, residential, $F_{am} = -27\ 7 \log_{10} f_{MHz} + 72\ 5$, business, $F_{am} = -27\ 7 \log_{10} f_{MHz} + 76\ 8$ The other man-made noise prediction shown is for a quiet rural location [65] $F_{am} = -28\ 6 \log_{10} f_{MHz} + 53\ 6$ These quiet rural predictions are typical of the lowest levels at sites chosen to ensure a minimum amount of man-made noise Data are also given for urban parks and college campuses $F_{am} = -27\ 7 \log_{10} f_{MHz} + 69\ 3$, although the same sample size was smaller for this case For comparison, the curve for galactic noise is $F_{am} = -23\ 0 \log_{10} f_{MHz} + 52\ 0$ These results have been adopted by the International Radio Consultative Committee[13] as the best available estimates for use worldwide

These man-made noise data are daytime values At night these 20- to 50-MHz levels can drop 5 to 10 dB to a minimum around 0400 hr, and at 100 MHz and 250 MHz

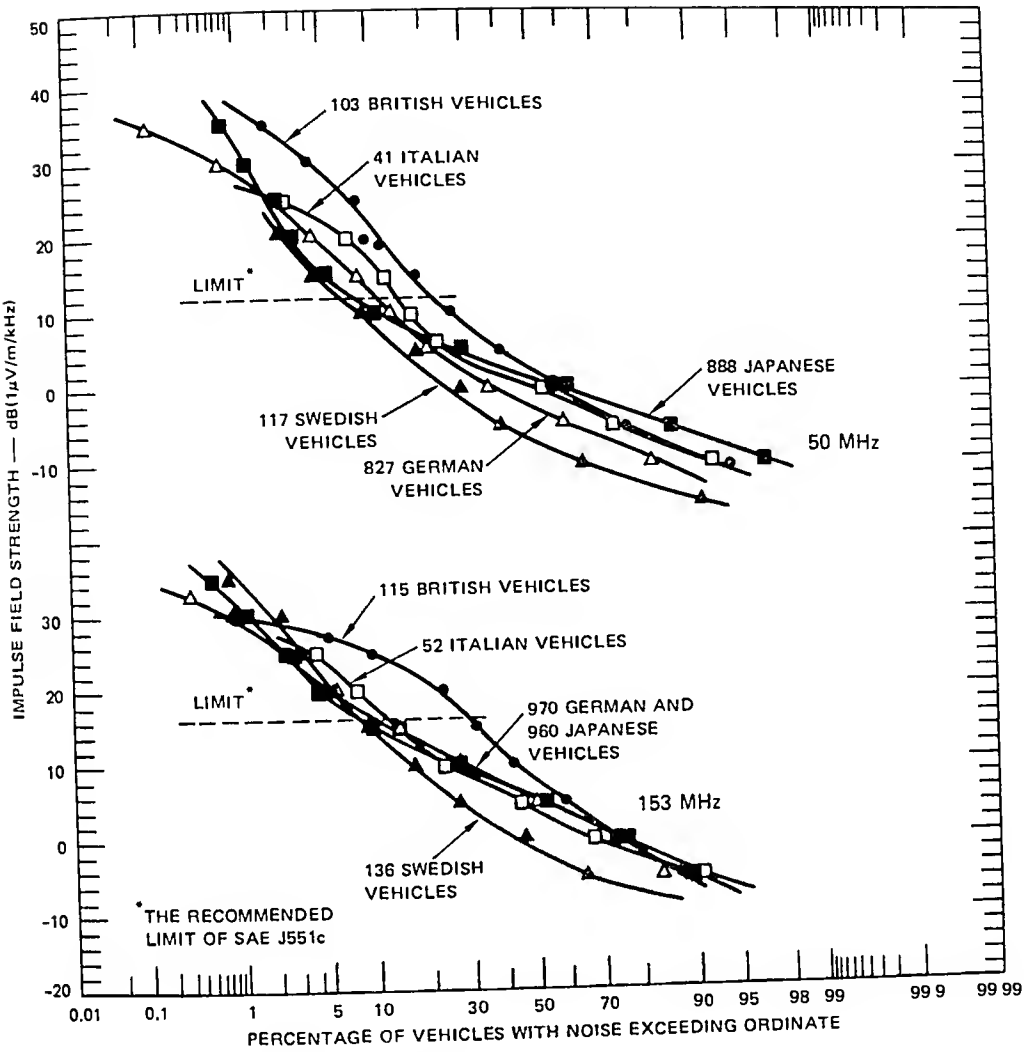

FIGURE 16. Ignition noise distributions for vehicles separated by national origin. (From Shepherd, R. A., Gaddie, J. C., and Bell, P. J., Electromagnetic Radio Statistics at 50 MHz and 153 MHz of the United States Vehicle Population, SRI International, Menlo Park, Calif., August 1977. With Permission.)

they can drop 3 to 5 dB. At the lower frequencies in the HF band the night levels are frequently controlled by atmospheric noise from lightning, and the man-made levels cannot be observed (see Figure 21). The diurnal variation decreases for the MF band and is again only 3 to 5 dB at 0.25 MHz, with values at night being slightly higher than during the day.

Let us now consider the variability about these median values due to location within a given generic environmental category and with time while at a given location.

An example distribution of local median values of man-made noise at 20 MHz in residential areas is given as Figure 22. The value σ_T is the standard deviation of all measured medians about the regression line for F_{am} vs. frequency (5.0 dB for residential areas and 6.5 dB and 7.0 dB for rural and business areas, respectively). σ_{NL} is the standard deviation for location variability at each of the measurement frequencies. Values for σ_{NL} are given in Table 2 for each frequency and environmental category.

Figure 23 gives the distribution of F_a values obtained on 20 MHz during an hour (0839 to 0939 hr local time) in a residential area in Boulder, Colo. The median and

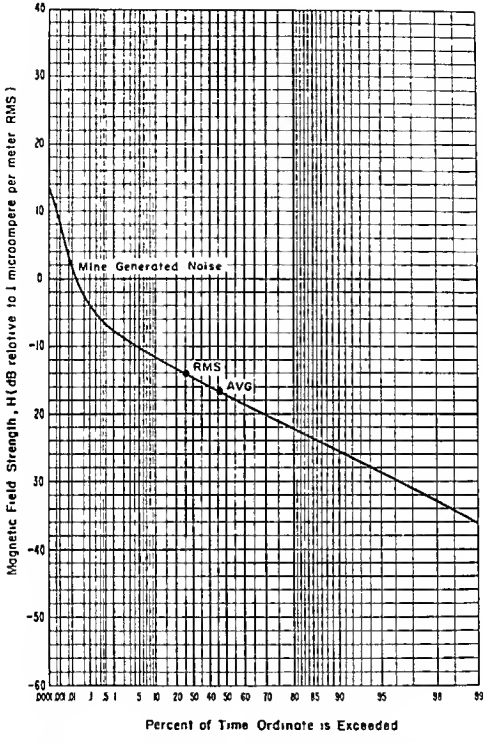

FIGURE 17 APD, 1 MHz, vertical component, 1 2 kHz predetection bandwidth (From Kanda, M., NBSIR 74-378, National Bureau of Standards, Boulder, Colo., 1974.)

the upper and lower deciles are indicated to help illustrate the variability of F_a. The time variability for the different environmental categories has been estimated by Spaulding and Disney[31] for each of the ten measurement frequencies in terms of the upper and lower deciles, D_u and D_l (in dB, relative to the median). These values, summarized in Table 2, are the root-mean squares of all the location values for each frequency and environmental category. Let us now consider the models derived from this empirical data base.

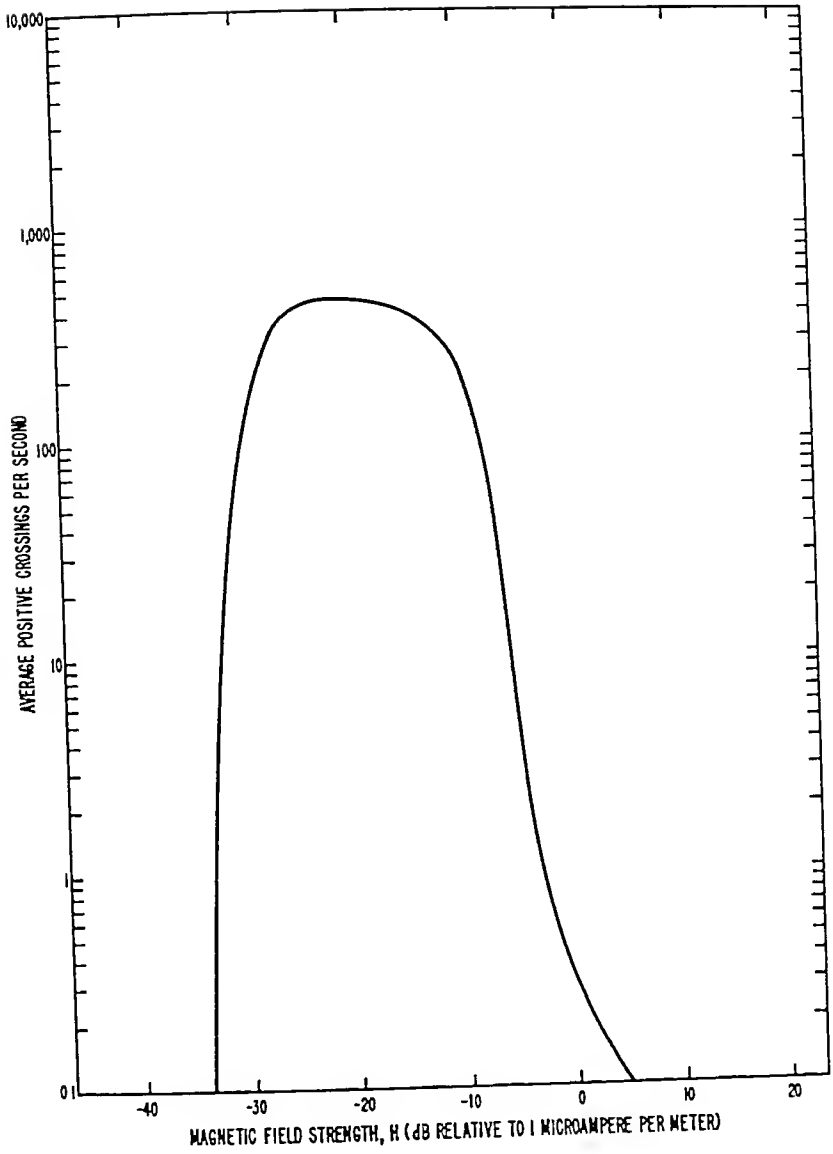

FIGURE 18. ACR, 1 MHz, vertical component, 1.2 kHz predetection bandwidth. (From Kanda, M., NBSIR 74-378, National Bureau of Standards, Boulder, Colo., 1974.)

Hagn and Sailors[66] presented four models for the probability distribution of the short-term ($\approx$ 1 min) mean values of man-made radio noise available power spectral density levels based upon the data of Spaulding and Disney:[31] a model based upon a single Gaussian distribution (simple Gaussian), a slightly more complicated model based upon two Gaussian distributions (composite Gaussian), a more complex model based upon the Chi-square distribution, and a Gaussian model with the parameters estimated using the Chi-square results for the mean and standard deviation. These models assume that the mean value is given by the F_{am} expressions for the appropriate environmental categories. The mean and standard deviations are summarized in Table 2 and approximate expressions for the standard deviations are given in Table 3. The simple Gaussian model assumes the mean is F_{am} (in dB) and the standard deviation is

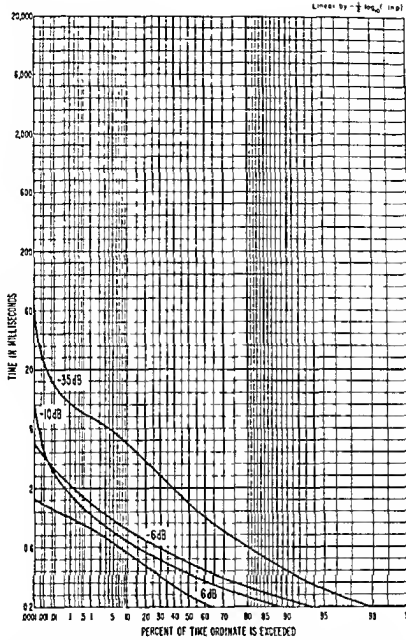

FIGURE 19 PDD, 1 MHz, vertical component, 1 2 kHz predetection bandwidth (From kanda, M , NBSIR 74-378, National Bureau of Standards, Boulder, Colo 1974)

σ_N, whereas, the composite Gaussian model uses the same mean with the upper half of the distribution being described by O_{N_r} and the lower half being described by σ_{N_l}. For the Chi-square model, the mean is given by $\overline{F}_n = a + b\nu$ and the standard deviation by $\sigma_{N_r} = b\,(2\nu^{1/2})$, where ν is the degrees of freedom Figure 24 presents an example at 20 MHz of a comparison of the model with data When the skew is negligible and the distribution between the deciles is required, the simple Gaussian model (or the Gaussian derived from the Chi-square) is often adequate, whereas the two-part Gaussian model or the Chi-square model is needed when there is significant skew These model distributions should not be confused with the amplitude probability distribution (APD) of the envelope of the noise waveform at the output of the predetection filter of a communication receiver.

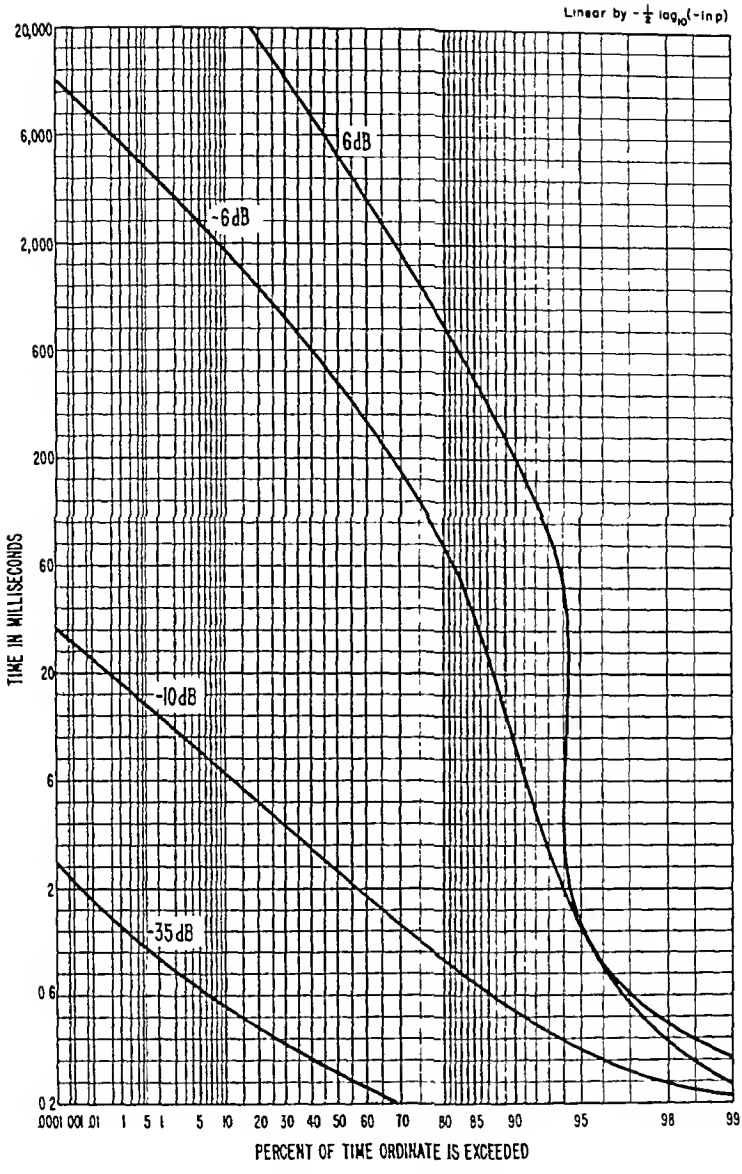

FIGURE 20. PSD, 1 MHz, vertical component, 1.2 kHz predetection bandwidth. (From Kanda, M., NBSIR 74-378, National Bureau of Standards, Boulder, Colo., 1974.)

ANALYTICAL MODELS OF THE COMPOSITE ELECTROMAGNETIC NOISE ENVIRONMENT

Spaulding in the preeceeding Chapter has reviewed noise models for the envelope statistics of atmospheric noise, and Skomal[16] has summarized the theory of envelope statistics of man-made radio noise developed by Middleton.[67-72]

The statistical-physical model of the composite electromagnetic environment developed by Middleton[69,70] is truly comprehensive. Analytical first-order probability densities and distributions, as observed at the output of the initial (linear) stages of typical narrow-band receivers (of bandwidth Δf_R), are obtained for three basic classes of elec-

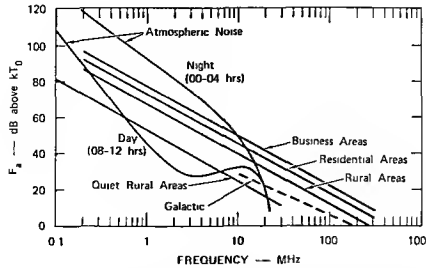

FIGURE 21 Estimates of median values of man-made, atmospheric, and galactic noise expected near Washington, D C during summer (References 13 and 65)

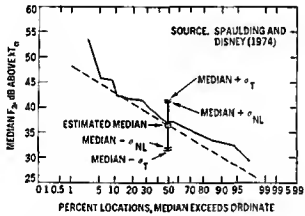

FIGURE 22 Example distribution of local median F_a values for different locations for 20 MHz in a residential area (From Spaulding, A D and Disney, R T , OT Report 74-38, Office of Telecommunications, U S Department of Commerce, Boulder, Colo , 1974)

tromagnetic noise These are, respectively (1) Class A noise, characterized by input bandwidths Δf_N less than Δf_R, (2) Class B noise, where Δf_N is larger than Δf_R, and (3) Class C noise, which is a linear combination of Class A and Class B components Middleton has recently noted that the conditions for Class A noise correspond to the case where the transient responses of the receiver are negligible relative to the steady-state responses caused by an incident wave [73]

These models combine statistical and physical structures the noise sources are assumed to be independently and randomly distributed in space, and they emit arbitrary waveforms randomly in time, so that the basic statistics are Poisson The emitted waveforms obey appropriate propagation laws (e g , the wave equations) and explicitly include the effects of source and receiver antenna patterns, relative doppler effects, source distributions in space, and other geometrical factors The results are highly nongaussian, as would be expected, but they are analytically tractable and canonical

Table 2

SUMMARY OF HAGN AND SAILORS' NOISE MODEL PARAMETERS

		Simple Gaussian						Composite Gaussian		Chi-square						
Environmental category	Freq. (MHz)	F_{am} dB (kT_o)	D_u (dB)	D_l (dB)	σ_{NT} (dB)	σ_{NL} (dB)	σ_N (dB)	σ_{Nu} (dB)	σ_{Nl} (dB)	D_{Nu} (dB)	D_{Nl} (dB)	ν	a	b	$\overline{F}_a$ dB (kT_o)	$\sigma_{N_X}^2$ (dB)
Business	0.25	93.5	8.1	6.1	5.6	6.1	8.3	8.8	7.8	11.3	9.9	92.16	37.51	0.61	93.9	8.3
	0.50	85.1	12.6	8.0	8.2	8.2	11.6	12.8	10.3	16.4	13.2	32.12	39.26	1.46	86.1	11.7
	1.00	76.8	9.8	4.0	5.8	2.3	6.3	8.0	3.9	10.2	5.0	3.51	69.77	2.46	78.4	6.5
	2.50	65.8	11.9	9.5	8.4	9.1	12.4	13.0	11.8	16.7	15.1	142.29	−38.56	0.74	66.3	12.4
	5.00	57.4	11.0	6.2	7.0	6.1	9.2	10.5	7.8	13.5	10.0	16.58	31.70	1.62	58.5	9.3
	10.00	49.1	10.9	4.2	6.4	4.2	7.7	9.5	5.3	12.1	6.8	4.95	38.38	2.49	50.7	7.8
	20.00	40.8	10.5	7.6	7.2	4.9	8.7	9.6	7.7	12.3	9.9	32.66	6.18	1.08	41.5	8.7
	48.00	30.2	13.1	8.1	8.5	7.1	11.1	12.5	9.5	16.0	12.2	20.91	−4.69	1.73	31.4	11.2
	102.00	21.2	11.9	5.7	7.3	8.8	11.4	12.8	9.8	16.4	12.6	21.95	−15.62	1.73	22.3	11.5
	250.00	10.4	6.7	3.2	4.1	3.8	5.6	6.4	4.5	8.3	5.8	12.28	−2.80	1.13	11.1	5.6
Residential	0.25	89.2	9.3	5.0	5.8	3.5	6.8	8.1	5.3	10.3	6.8	8.67	75.88	1.66	90.3	6.9
	0.50	80.8	12.3	4.9	7.3	4.3	8.5	10.5	5.7	13.5	7.4	4.67	69.42	2 84	82.7	8.7
	1.00	72.5	10.0	4.4	6.0	2 5	6.5	8.2	4.3	10.5	5.5	4.02	64.49	2.37	74.0	6.7
	2.50	61.5	10.1	6.2	6.5	8.1	10.4	11.3	9.4	14.4	12.0	45.36	12.58	1.09	62 2	10.4
	5.00	53.1	10.0	5.7	6.4	5.5	8.4	9.6	7.1	12.3	9.1	17.11	29.28	1.45	54.1	8.5
	10.00	44.8	8.4	5.0	5.4	2.9	6.1	7.2	4.9	9.2	6.2	10.38	31.57	1.36	45.7	6.2
	20.00	36.5	10.6	6.5	6.9	4.7	8.3	9.5	6.9	12.2	8.8	14.80	14.75	1.54	37.5	8.4
	48.00	25.9	12.3	7.1	7.8	4.0	8.8	10.4	6.8	13.3	8.7	8.90	8.53	2.11	27.3	8.9
	102.00	16.9	12.5	4.8	7.4	2.7	7.9	10.1	4.6	13.0	5.9	3 09	8.98	3.35	19.0	8.2
	250.00	6.1	6.9	1.8	3.9	2.9	4.9	6.1	3.2	7.8	4.1	4.13	0.00	1.74	7.2	5.0
Rural	0.25	83.9	10.6	2.8	6.0	3.9	7.2	9.1	4.5	11.7	5.7	3.52	75 82	2.80	85.7	7.4
	0.50	75.5	12.5	4.0	7.2	4.4	8.5	10.7	5.4	13.7	6.9	3.78	65.57	3.17	77.6	8.7
	1.00	67.2	9.2	6.6	6.2	7.1	9.5	10.1	8.8	13 0	11.3	75.34	9.41	0.77	67.7	9.5
	2.50	56.2	10.1	5.1	6.2	8.0	10.2	11.2	9.0	14.4	11.5	28.78	18.36	1.35	57.1	10.2
	5.00	47.8	5.9	7.5	5.3	7.7	9.4	9.0	9.7	11.5	12.4	260.87	154.61	0.41	47.6	9.4
	10.00	39.5	9.0	4.0	5.4	4 0	6.8	8.1	5.1	10 4	6.5	7.49	27 37	1.78	40.7	6.9
	20.00	31.2	7.8	5.5	5.3	4.5	6.9	7.6	6.2	9.7	8 0	39.08	0.87	0.79	31.7	7.0
	48.00	20.6	5.3	1.8	3.1	3.2	4.5	5.2	3.5	6.7	4.5	9.84	11.27	1.02	21.3	4.5
	102.00	11.6	10.5	3.1	6.0	3.8	7.1	9.0	4.5	11.6	5.8	3.72	3.25	2.71	13.3	7.4
	250.00	0.8	3.5	0.8	2.0	2.3	3.0	3.5	2.3	4.5	3.0	9.20	−5.29	0.71	1.2	3.0

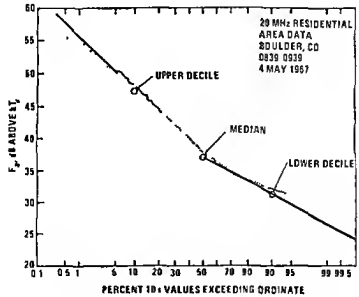

FIGURE 23 Example distribution of short-term local median average noise power spectral density at one location (for 20 MHz, residential area) (From Spaulding, A D and Disney R T, OT Report 74-38, Office of Telecommunications, U S Department of Commerce Boulder, Colo, 1974)

Table 3
HAGN AND SAILORS' APPROXIMATE FORMULAS FOR THE STANDARD DEVIATIONS, IN dB

Environmental category	Simple Gaussian and Chi-Square	Composite Gaussian
Business	for $0.25 \leq f_{MH} < 2.5$ $\sigma_N \cong \sigma_{N_2}^2 \cong 9.0$	for $0.25 \leq f_{MH} < 100$ $\sigma_N \cong 10.5$, $\sigma_{N_1} \cong 8.0$
	for $2.5 \leq f_{MH} < 10$ $\sigma_N \cong \sigma_{N_2}^2 \cong 8.0 - 4 \log_{10}[f_{MH}/10]$	for $100 \leq f_{MH} \leq 250$ $\sigma_N \cong 9.5$ $\sigma_{N_1} \cong 7.5$
	for $10 \leq f_{MH} \leq 100$ $\sigma_N \cong \sigma_{N_2}^2 \cong 8.0 + 4 \log_{10}[f_{MH}/10]$	
Residential	for $0.25 \leq f_{MH} \leq 250$ $\sigma_N \cong \sigma_{N_2}^2 \cong 8.0$	for $0.25 \leq f_{MH} < 100$ $\sigma_N \cong 9.0$ $\sigma_{N_1} \cong 6.0$
		for $100 \leq f_{MH} \leq 250$ $\sigma_N \cong 8.0$, $\sigma_{N_1} \cong 4.0$
Rural	for $0.25 \leq f_{MH} \leq 2.5$ $\sigma_N \cong \sigma_{N_2}^2 \cong 9.0 + 4 \log_{10} f_{MH}$	for $0.25 \leq f_{MH} < 100$ $\sigma_N \cong 9.0$, $\sigma_{N_1} \cong 6.0$
	for $2.5 \leq f_{MH} \leq 250$ $\sigma_N \cong \sigma_{N_2}^2 \cong 8.0 - 4 \log_{10}[f_{MH}/10]$	for $100 \leq f_{MH} \leq 250$ $\sigma_N \cong 6.3$, $\sigma_{N_1} \cong 3.5$

(*i e*, the form of the probability structures are essentially invariant of the waveform and of kinematic and geometric details) This is strongly true of Class A noise (such as some man-made noise and communications signals), but only moderately so for Class B noise (such as atmospheric noise and automobile ignition noise) whose statis-

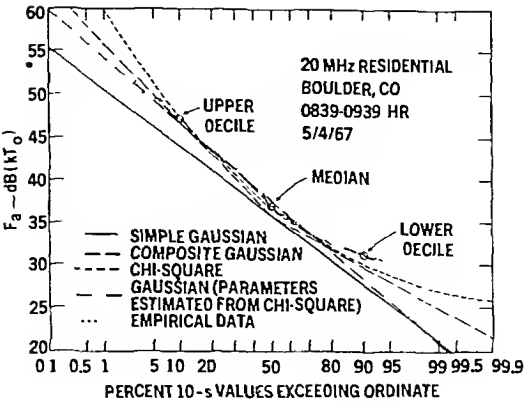

FIGURE 24. Comparison of Hagn and Sailors' model predictions with measured data at 20 MHz in a residential area. (From Hagn, G. H. and Sailors, D. B., in Electromagnetic Compatibility in 1979, Proc 3rd Symp. Tech. Exhibition on Electronic Compatibility, Rotterdam, May, 1 to 3, 1979, 355. With permission.)

tics are more sensitive to the source distribution and propagation laws. Excellent agreement of the statistical-physical model with experiment is found for the relative APDs of both basic Classes A and B (see Figure 25 for an example.) These quantitative models, appropriately calibrated to reality by simple experiment, are useful for: (1) the assessmcnt of electromagnetic environments for the purposes of spectrum management; (2) the evaluation of receiver performance related to the design of optimum receivers for use in these strongly nongaussian noise situations; and (3) analytical determination of system performance.

Middleton's analytical formula for the probability of successful communications in a land mobile environment (Class A noise) has been shown by Berry[74] to produce identical answers to his own numerical computer program for identical inputs. He noted that one assumption of Middleton's Class A model (specifically, that interferring sources transmit randomly) does not apply for radio services that employ circuit discipline (e.g., land mobile radio); whereas, Berry's model does not have this limitation. In order to use Middleton's formula to compute the probability of successful communications for a detailed Class A scenario, the parameters for Class A noise must be determined from scenario descriptors. This nontrival task is discussed by Berry[74] and by Middleton.[75]

Techniques have been developed to estimate the Middleton model parameters from experimentally measured APDs.[70] It should be noted that this is not simply curve fitting. The model, once the parameters are determined, is capable of predicting the APD quite well in dB relative to the rms value (see Figure 25). Currently, an empirical model (e.g., Reference 66) is still required to predict the probability of occurrence of a given rms value for a given environmental category of Class B noise (e.g., business, residential, or rural).

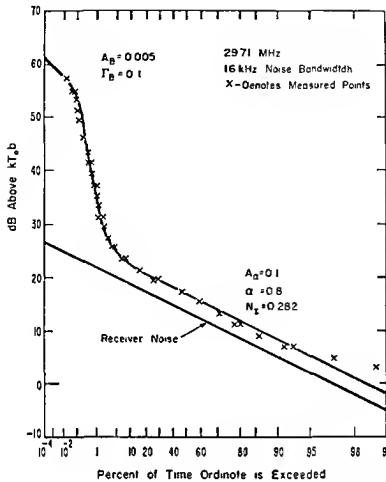

FIGURE 25 Comparison of measured envelope amplitude probability distribution of automotive ignition noise from moving traffic with Middleton class B model (From Middleton, D , NTIA Contractor Rep 80-7, National Telecommunications and Information Administration, U S Department of Commerce, Boulder, Colo , June 1980)

REFERENCES

1 Hagn, G H , Definitions and Fundamentals of Electromagnetic Noise, Interference and Compatibility, in *AGARD Conf Proc* , No 159 (AGARD-CP-159), p I-1, National Technical Information Service Springfield Va as AD A-018980, 1975

2 Hagn, G H , Definitions of Electromagnetic Noise and Interference, in Symp Record of IEEE Int Symp on EMC, Seattle, IEEE Cat No 77CH 1231-OEMC, August 1977, 122

3 CCIR, Definitions of radio communication interference, recommendation 506, in *Recommendations and Reports of the CCIR 1978*, Vol I , International Radio Consultative Committee, International Telecommunication Union, Geneva, 1978, I

4 Herman, J R , Survey of man made radio noise, in *Progress in Radio Science, 1966-1969*, Vol I, Brown, G M , Clarence, N D , and Rycroft M J , Eds , International Union of Radio Science (URSI), Brussels, 1971 315

5 Rivault, R , Bruit Radioelectrique d'origine Terrestre in *Review of Radio Science, 1969-1971*, Minnis, C M and Bogitch, Y , Eds , International Union of Radio Science, Brussels, Belgium, 1972

6 Hagn, G H , Commission 8 radio noise of terrestrial origin 8 4 man made noise environment, *Radio Sci* , 8(6), 613, 1973

7 Hagn, G H , Radio noise of terrestrial origin, *Review of Radio Science, 1972-1974*, Bowhill, S A , Ed , International Union of Radio Science, Brussels, Belgium, 1975

8. Hagn, G. H., The electromagnetic noise and interference environment, *Review of Radio Science, 1975-1977*, Bowhill, S. A., Ed., International Union of Radio Science, Brussels, Belgium, 1978
9. Spaulding, A. D., Electromagnetic noise and interference, *Review of Radio Science.*, Bowhill, S. A., *Ed., International Union of Radio Science, Brussels, Belgium, 1981.*
10. Stumpers, F. L. H. M., Progress in the work of CISPR, *IEEE Trans. Electromagn Compat* , 12, 29, 1970.
11. Stumpers, F. L. H. M., The activities of CISPR during recent years and their impact on society, in *International Electromagnetic Compatibility Symp. Record,* Cat. No 73CHO751-8 EMC, IEEE, New York, 1973, 5-10.
12 Stumpers, F. L. H. M., New developments in CISPR — results of the EMC Symp. in Montreux, *IEEE Trans. EMC*, 17(4), 1975, 269.
13. CCIR, Man-Made Radio Noise, Report 258 (Revised), International Radio Consultative Committee, International Telecommunication Union, Geneva, 1980.
14. Joint Technical Advisory Committee, Spectrum Engineering — The Key to Progress, IEEE, New York, 1968.
15. Spaulding, A. D., Man-Made Noise: The Problem and Recommended Steps Toward Solution, Report OT 76-85, U.S. Department of Commerce, Boulder, Colo., April 1976.
16. Skomal, E. N., *Man-Made Radio Noise*, Van Nostrand Reinhold, New York, 1978.
17. Herman, J. R., *Electromagnetic Ambients and Man-Made Noise, Vol. 3, Multi-Volume EMC Encyclopedia Series*, Don White Consultants, Gainesville, Va., 1979
18. Spaulding, A. D., Disney, R. T., and Hubbard, A. G., Man-Made Radio Noise. II. Bibliography of Measurement Data, Applications, and Measurement Methods, OT Report 75-63, U S. Department of Commerce, Boulder, Colo., 1975.
19. Janes, D. E., Tell, R. A., Athey, T. W., and Hankin, N. N., Radio-frequency radiation levels in urban areas, *Radio Sci.*, 12(6), 49, 1977.
20. Janes, D. E., Radiofrequency environments in the United States, in *ICC '79 Conf. Record*, Vol. 2, Cat. No. 79CH1435-7 CSCB, IEEE, New York, 1979.
21. Shepherd, N. and Smith, J., The Gaussian curse — transmitter noise limits spectrum utilization, *IRE Trans. Veh. Commun.*, 10, 1958.
22. Lustgarten, M. N., Duff, W. G., Hagn, G. H., Hill, J. S , Mohr, R J., Schulz, R. B., and Shepherd, N. H., Special issue: final report of ad hoc committee on an electromagnetic compatibility figure of merit (EMC FOM) for single-channel voice communications equipment, *IEEE Trans. EMC*, 17(1), 1975.
23 CCIR, An electromagnetic compatibility figure of merit for single channel voice communications systems, Report 660, in *Recommendations and Reports of the CCIR, 1978*, Vol 1., International Radio Consultative Committee, International Telecommunication Union, Geneva, 1978, 150.
24. Vincent, W. R. and Dayharsh, T. I., A Study of Land Mobile Spectrum Utilization, Part B: Analysis of the Spectrum Management Problem, Final Report, Contract RC-10056, Stanford Research Institute, Menlo Park, Calif., 1969; PB 182918, National Technical Information Service, Springfield, Va.
25. Vincent, W. R., Examples of signals and noise in the radio-frequency spectrum, *IEEE Trans. EMC*, 19(3), Part II, 241, 1977.
26. Robertson, E., Some examples of powerline interference and suggested remedial measures, *Proc. IEEE*, 396, 1971.
27. Allen, E. W., Man-made radio noise, in *The Radio Noise Spectrum*, Menzel, D. H , Harvard University Press, 1960, 1.
28. Spaulding, A. D., Ahlbeck, W. H., and Espeland, L. R., Urban Residential Man-Made Radio Analysis and Predictions, OT/ITS Telecommunications Research and Engineering Report 14, Office of Telecommunications, U.S. Department of Commerce, Boulder, Colo., 1971.
29. Spaulding, A. D., The Determination of Received Noise Levels from Vehicular Traffic Statistics, IEEE 1972 *NTC Record, IEEE Cat. No. 72CHO601-5-NTC, 1972.*
30. Disney, R. T., Estimates of Man-Made Radio Noise Levels Based on the Office of Telecommunications, ITS Data Base, Conference Record, IEEE International Conference on Communications, Philadelphia, IEEE Cat. No. 72CHO6224-COM, 1972, 13.
31. Spaulding, A.D. and Disney, R. T., Man-Made Radio Noise. I. Estimates for Business, Residential and Rural Areas, OT Report 74-38, Office of Telecommunications, U.S. Department of Commerce, Boulder, Colo., 1974.
32. Warburton, F. W., Laio, T. W., and Hoglund, N. A., Power line radiations and interference above 15 MHz, *IEEE Trans. Power Appar. Syst.*, 88(10), 1992, 1969.
33. Loftness, M. O., The location of power line TVI: some reduction considerations, *IEEE Trans. Power Appar. Syst.*, 89(3), 1970.
34. Juette, G. W., Evaluation of television interference from high voltage transmission lines, *IEEE Trans. Power Appar. Syst.*, 91(3), 1972.

35 March, D N , Electromagnetic Communications Quality Measurements at Residences Before and After Construction of Nearby Powerlines 1977 IEEE International Symposium on EMC Record, IEEE Cat No CH 1231 OEMC, 1977, 254

36 Pakala, W E , Taylor, E R , Jr , and Harrold, R T , Radio Noise Measurements on High Voltage Lines from 2 4 to 345 kV, 1968 IEEE Electromagnetic Compatibility Symposium Record, IEEE Cat No 68C12-EMC, 96, 1968

37 Pakala, W E and Chartier, V L , Radio noise measurements on overhead power lines from 2 4 to 800 kV, *IEEE Trans Power Appar Syst* ,90(3) 1155, 1971

38 Kaufeile, J , Using DC links to enhance AC system performance, *IEEE Spectrum*, 9(6) 31, 1972

39 Annestrand, S A , Radio interference from HVDC converter stations, *IEEE Trans Power Appar Syst* , 91(3), 1972

40 Vincent, W R , Practical Aspects of Man-Made Radio Noise That Affect Radio-Spectrum Management, IEEE Cat No 80 CH 1538 8EMC, 1980 IEEE Int Symp on EMC Record, Baltimore, October 1980 (See also Vincent, W R , Smith, D , and Jauregui, S , Temporal and Spectral Properties of Powerline Noise, IEEE Cat No 80-CH 1538 EMC, 1980 IEEE Int Symp on EMC Record, Baltimore, October 1980

41 Hubbard, A G , Man Made Noise Measurements An Unsolved Problem?, IEEE 1972 National Telecommunications Conference Record, IEEE Cat No 72CHO601-5-NTC, Institute of Electrical and Electronics Engineers, New York, 1972, 19E1

42 Hagn, G H and Shepherd, R A , Discussion on 'a field comparison of RI and TVI instrumentation,' by task force of the radio noise and corona subcommittee of the transmission and distribution committee *IEEE Trans Power Appar Syst* 96(3), 872, 1977

43 Disney, R T and Longley, A G , Preliminary Telemetry Link Performance Estimate for Department of Transportation High-Speed Test Track, Report No OTM 73 130 Institute for Telecommunications Sciences, U S Department of Commerce, Boulder Colo , 1973

44 Hagn, G H and Shepherd, R , Man Made Electromagnetic Noise from Unintentional Radiators A Summary, NATO Advisory Group for Aerospace Research and Development (AGARD), in Proceedings of Conference on Electromagnetic Noise, Interference and Compatibility, AGARD-CP-159, November 1975, 1 National Technical Information Service Springfield, Va as AD-A 018980

45 IEEE Radio Noise Subcommittee of the IEEE Transmission and Distribution Committee, Transmission system radio influence *IEEE Trans Appar Syst* 84(8), 1965

46 IEEE Radio Noise Subcommittee — Working Group No 3, Radio noise design guide for high voltage transmission lines, *IEEE Trans Power Appar Syst* ,90(2) 1971

47 Bailey, B M and Belsher, M W , Discussion of Newell H H , et al *IEEE Trans Power Appar Syst* 87(4), 1968

48 Forrest, J S , Discussion of paper by Warburton, F W , et al *IEEE Trans Power Appar Syst* , 88(10), 1498, 1969

49 Lauber, W R , Amplitude probability distribution measurements at the Apple Grove 775 kV project, *IEEE Trans Power Appar Syst* , Vol 2 95(4), 1254, 1976

50 Lauber, W R and Bertrand, J M , Statistical Measurements and Modeling of HVDC Powerline Noise, 1979 IEEE EMC Symp Record, San Diego IEEE Cat No 79CH 1383-9 October, 1979

51 Shepherd, A and Hagn, G H , Discussion of 'amplitude probability distribution measurements at the Apple Grove 775 kV project' by Wilfred R Lauber, *IEEE Trans Power Appar Syst* , 95(4), 1263, 1976

52 IEEE, Review of Technical Considerations on Limits to Interference from Power Lines and Stations, *IEEE Trans Power Appar Syst* 99(1) 1980

53 Shepherd, R A , Measurements of amplitude probability distributions and power of automobile ignition noise at HF, *IEEE Trans Veh Technol* ,23(3), 1974

54 Schulz, R , Southwick, R , and Smithpeter, C , Measurement of Electromagnetic Emissions Generated by Vehicle Ignition Systems, report prepared for Motor Vehicle Manufacturers Association under MVMA Agreement SW 7303-C359, Southwest Research Institute, San Antonio, Tex , 1973

55 Schulz, R B and Southwick, R A , APD Measurements of V-8 Ignition Emanations, IEEE Electromagnetic Compatibility Symp Record IEEE, Cat No 74 CHO803-7EMC, 1974, 50

56 Shepherd, R A , Gaddie, J C , and Shobara, A , Measurement Parameters for Automobile Ignition Noise, Final Report, SRI Project 3930, MVMA Agreement No SRI 7502 C2 10, Stanford Research Institute, Menlo Park, Calif , June 1975

57 Shepherd, R A , Gaddie, J C , and Bell, P J , Electromagnetic Radiation Statistics at 50 MHz and 153 MHz of the United States Vehicle Population, Final Report, SRI Project 5959, MVMA Agreement No SRI-7706-C2 10, SRI International, Menlo Park, Calif , August 1977 (See also Shepherd, R A and Gaddie, J C , Ignition noise of foreign and domestic vehicles in use in the United States, *IEEE Trans Vehic Tech* , Vol VT-29, No 3, pp 338-345, August, 1980)

58. SAE, Measurement of Electromagnetic Radiation from a Motor Vehicle or Other Internal-Combustion-Powered Device (Excluding Aircraft) (20-1000 MHz), SAE J551c, Society of Automotive Engineers, Warrendale, Pa., 1974.
59. Vincent, W. R. and Ellison, R. W., RF Noise Radiated by a Rapid Transit System, IEEE Electromagnetic Compatibility Symp. Record, IEEE Cat No. 74CH) 803-7 EMC, 1974.
60. Cook, J. H., Quasi-peak-to-RMS voltage conversion, *IEEE Trans. Electromagn Compat.*, 21(1), 9, 1979.
61. Kanda, M., Time and Amplitude Statistics for Electromagnetic Noise in Mines, NBSIR 74-378, National Bureau of Standards, Boulder, Colo., 1974.
62. Kanda, M., Time and amplitude statistics for electromagnetic noise in mines, *IEEE Trans. EMC*, 17(3), 122, 1975.
63. Bensema, W. D., A noise spectrum management system using the fast fourier transform, *IEEE Trans EMC*, 19(2), 37, 1977.
64. Vincent, W. R., private communication, 1980.
65. CCIR, World Distribution and Characteristics of Atmospheric Radio Noise, Report 322, International Radio Consultative Committee, International Telecommunication Union, Geneva, 1964.
66. Hagn, G. H. and Sailors, D. B., Empirical Models for Probability Distributions of Short-Term Mean Environmental Man-Made Radio Noise Levels, in Electromagnetic Compatibility in 1979, Proc of 3rd Symp and Technical Exhibition on Electromagnetic Compatibility, Rotterdam, May 1 to 3, 1979, 355. (Available from Netherlands Normalization Institute, Polakweg 5, Postbus 5810, Rijswijk, 228 OHV, The Netherlands.)
67. Middleton, D., Statistical-physical models of urban radio-noise environments I. *IEEE Trans Electromagn. Compat.*, 14, 38, 1972.
68. Middleton, D., Man-made noise in urban environments and transportation systems, *IEEE Trans Commun.*, 21, 1232, 1973.
69. Middleton, D., Statistical-physical models of electromagnetic interference, *IEEE Trans. Electromagn. Compat.*, 19, 106, 1977.
70. Middleton, D., Canonical non-Guassian noise models· their implications for measurement and for prediction of receiver performance, *IEEE Trans Electromagn. Compat* , 21, 209, 1979
71. Middleton, D., Procedures for determining the parameters of the first-order canonical models of class A and B electromagnetic interference, *IEEE Trans Electromagn Compat* , 21, 190, 1979
72. Middleton, D., A Tutorial Review of the New EMI Models and Their Effects on Receiver Performance, NTIA Contractor Report-80-7, National Telecommunications and Information Administration, U.S. Department of Commerce, Boulder, Colo , May 1980
73. Middleton, D., private communication, September 1980.
74. Berry, L. A., Comparisons of Analytical and Numerical Calculations of Communications Probability, NTIA Report 80-41, National Telecommunications and Information Administration, U.S. Department of Commerce, Boulder, Colo., June 1980.
75. Middleton, D., Performance of Telecommunications Systems in the Spectral-Use Environment: VII, Interference Scenarios and the Canonical and Quasi-Canonical First-Order Probability Models of Class A Interference, NTIA Contractor Report 80-80, National Telecommunications and Information Administration, U.S. Department of Commerce, Boulder, Colo., 1980.

INDEX

A

D

E

F

G

H

I

J

K

L

M

P

Q

R

S

W

X

Z